Physics of the Solid State, Vol. 42, No. 2, 2000, pp. 199–200. Translated from Fizika Tverdogo Tela, Vol. 42, No. 2, 2000, pp. 193–195.

METALS AND SUPERCONDUCTORS

Heat Capacity, Root-Mean-Square Displacements of Atoms and Thermal Expansion Coefficient of Europium Hexaboride

N. N. Sirota, V. V. Novikov, and A. A. Sidorov

Moscow State University of Environmental Engineering, ul. Pryanishnikova 19, Moscow, 127550 Russia

Bryansk State Pedagogical University, Bezhitskaya ul. 14, Bryansk, 241036 Russia

Received in final form, December 29, 1998

Abstract—The temperature dependences of the specific heat capacity $c_p(T)$, thermal expansion coefficient $\alpha(T)$ of europium hexaboride, and root-mean-square displacements of Eu and B atoms are determined in the temperature range from helium to room temperature (5–300 K). © *2000 MAIK "Nauka/Interperiodica".*

In order to carry out the measurements, the EuB_6 compound was synthesized from a mixture of thoroughly mixed powders of high-purity grade europium oxide and chemically pure amorphous boron. The synthesis was performed under vacuum at a temperature of ~2000 K according to the procedure described in [1]. The X-ray powder diffraction analysis did not reveal traces of any foreign phase. The spectral analysis of the sample did not show impurities of carbon, oxygen, hydrogen, iron, and tungsten with an accuracy up to 0.01%. The total amount of aluminum, silicon, and magnesium impurities was about 0.3%.

Calorimetric measurements were carried out in a low-temperature adiabatic calorimeter of the Nernst–Strelkov type with a periodic heat input in steps of 0.3–1 K at low temperatures (below 20 K) and 3–5 K at higher temperatures. The calorimetric setup and the technique of measurements are similar to those described earlier [2]. The error of measurements at temperatures below 20 K did not exceed 1% and above 20 K was about 0.3%. The dispersion of experimental points with respect to the smoothed curve was less than the above errors of measurements.

The thermal expansion coefficient was determined from the data of low-temperature X-ray measurements of interplanar distances by the Bragg–Brentano method on powder samples. The measurements were carried out in a low-temperature vacuum X-ray chamber under isothermal conditions with an automatic monitoring of the temperature with an accuracy of ±0.2 K. Positions and intensities of the (411) and (410) reflections were determined. The change in the interplanar distance d_{411} was determined with an accuracy up to 2×10^{-5} Å. The changes in the linear thermal expansion coefficient were determined from the temperature dependence $d_{411}(T)$. The error of the determination at room temperature did not exceed 2%. A decrease in the temperature below 100 K led to an increase in the error up to 10%.

For the EuB_6 structure, the metal and boron atoms have the following coordinates in units of the lattice period: Eu(000); B(1/2 0.207 1/2, 0.207 1/2 1/2, 1/2 0.793 1/2, 0.793 1/2 1/2, 1/2 1/2 0.793, 1/2 1/2 0.207). The structure factors of the reflections studied have the form

$$|F_{410}|^2 = (f_{Eu} - 2.41 f_B)^2,$$

$$|F_{411}|^2 = (f_{Eu} - 0.126 f_B)^2.$$

Here, the atomic scattering factor f_i at a given temperature is related to the atomic scattering factor f_{i0} at absolute zero, the root-mean-square displacement $\overline{u_i^2}$ of the

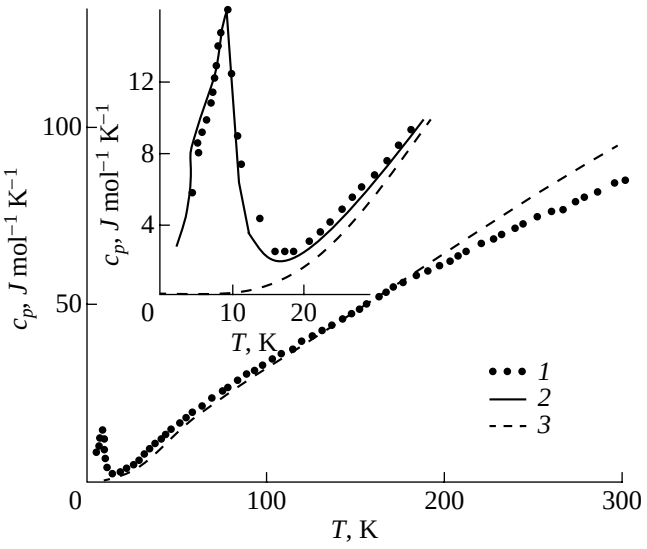

Fig. 1. Molar heat capacity of (*1*, *2*) EuB_6 and (*3*) LaB_6 according to the data taken from (*1*) this work, (*2*) [3], and (*3*) [4].

1063-7834/00/4202-0199$20.00 © 2000 MAIK "Nauka/Interperiodica"

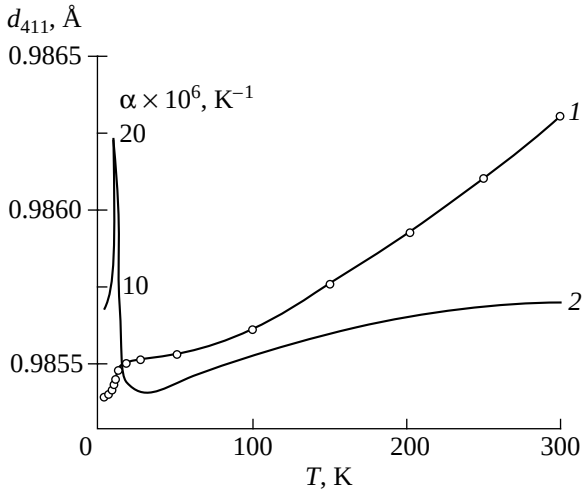

Fig. 2. (*1*) Interplanar distance d_{411} of EuB_6 and (*2*) linear thermal expansion coefficients $\alpha(T)$.

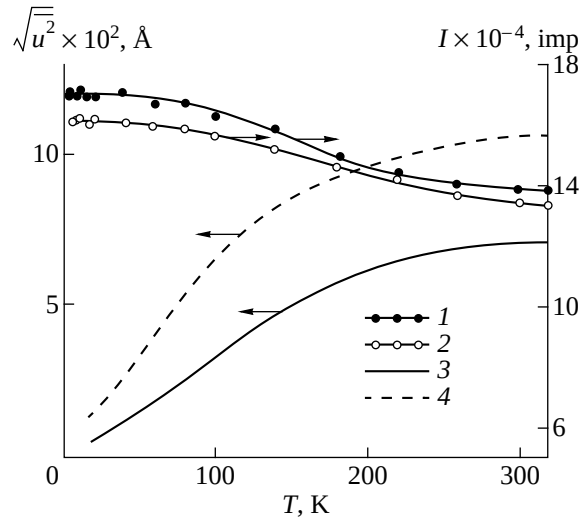

Fig. 3. Intensity of X-ray reflections (*1*) I_{411} and (*2*) I_{410} and root-mean-square displacements of (*3*) europium and (*4*) boron atoms in EuB_6.

*i*th ion, and the scattering vector $S = \frac{\sin\theta}{\lambda}$,

$$f_B = f_{0_B}\exp(-8\pi\overline{u_B^2}S^2),\ f_{Eu} = f_{0_{Eu}}\exp(-8\pi\overline{u_{Eu}^2}S^2).$$

The root-mean-square dynamic displacements of europium and boron atoms are calculated from the temperature dependences of the I_{hkl} reflections.

The experimental isobaric heat capacities of EuB_6 are given in Fig. 1. In the range 0–10 K, the dependence exhibits an anomaly with a sharp maximum at 9.41 K. The low-temperature part of the $c_p(T)$ curve is shown on an enlarged scale in the inset, which also displays the data taken from [3]. As is seen, the results of the present work agree well with the data obtained in [3].

In the range 0–8 K, the temperature dependence of the heat capacity for ferromagnetic europium hexaboride is approximated by the expression

$$c_1(T) = a_eT + a_{f-m}T^{3/2} + a_lT^3$$

and at temperatures of 16–25 K, above T_c, by the relationship

$$c_2(T) = a_eT + a_{p-m}T^{-2} + a_lT^3.$$

Here, the coefficients a_e, a_{f-m}, a_{p-m}, and a_l determine the electronic, ferromagnetic, paramagnetic, and lattice contributions to the heat capacity [5]. The best agreement with the experimental data is achieved at $a_e = 0.04$ J/mol K^2, $a_{f-m} = 0.89$ J/mol K$^{5/2}$, $a_{p-m} = 160$ J K/mol, $a_l = 2.01 \times 10^{-4}$ J/mol K^4.

The variation in the d_{411} interplanar distance as a function of temperature is shown in Fig. 2. The temperature changes in the linear thermal expansion coefficient $\alpha(T)$ are determined from the dependence $d_{411}(T)$ (Fig. 2). The linear thermal expansion coefficient of EuB_6 is positive over the entire temperature range studied.

The temperature changes in the intensities of the I_{411} and I_{410} reflections and the root-mean-square dynamic displacements of europium and boron atoms in the EuB_6 lattice, which were calculated from these changes, are displayed in Fig. 3.

No anomaly in the range of ferromagnetic transformation is revealed in the temperature dependences $\overline{u^2}(T)$ of the root-mean-square displacements of ions. This is most likely connected with a negligible difference in reflection intensities at absolute zero and at temperatures of magnetic transformations. This question requires further elucidation.

ACKNOWLEDGMENTS

This work was supported in part by the Ministry of General and Professional Education of the Russian Federation, grant no. 97-5-1.1-25.

REFERENCES

1. G. V. Samsonov, T. I. Serebryakova, and V. I. Neronov, *Borides* (Atomizdat, Moscow, 1975).
2. N. N. Sirota, A. M. Antjukhov, V. V. Novikov *et al.*, Cryst. Res. Technol. **17** (3), 279 (1982).
3. T. Fujita, M. Suzuki, and Y. Isikawa, Solid State Commun. **33** (9), 947 (1980).
4. N. N. Sirota, V. V. Novikov, V. A. Vinokurov, *et al.*, Zh. Fiz. Khim. **72** (11), 1967 (1998).
5. K. P. Belov, *Magnetothermal Phenomena in Rare-Earth Magnetic Materials* (Nauka, Moscow, 1990).

Translated by T. Galkina

Physics of the Solid State, Vol. 42, No. 2, 2000, pp. 201–206. Translated from Fizika Tverdogo Tela, Vol. 42, No. 2, 2000, pp. 196–201.

METALS AND SUPERCONDUCTORS

A Generalized Critical-State Model for Low-Dimensional Superconductors with an Edge Barrier

A. A. Elistratov and I. L. Maksimov

Nizhni Novgorod State University, pr. Gagarina 23, Nizhni Novgorod, 603000 Russia

Received, in final form, August 18, 1999

Abstract—A generalized model of the critical state in low-dimensional superconductors is proposed, which includes the effects of bulk and edge pinning of the magnetic flux. The conditions are determined for the penetration of Pearl–Abrikosov vortices into the superconductor, and metastable flux structures in these systems are described. A diagram of different vortex states is constructed for a complete cycle of variations of the external magnetic field. © *2000 MAIK "Nauka/Interperiodica".*

INTRODUCTION

The study of the structure and features of the critical state in type II superconductors is an important problem in the physics of superconductivity. The development of the theory of the critical state in bulk superconductors, including the bulk and surface pinning of Abrikosov vortices, is now completed for the most part (see, e.g., [1–3]). However, in low-dimensional superconductors (thin films, single crystals with a high demagnetizing factor, etc.), the structure, dynamics, and magnetic properties of the critical state still remain hardly investigated. At the same time, the principally unremovable nonlocality of the interaction between vortices and the possible existence of an edge barrier, which prevents vortices from entering and (or) leaving the superconductor, may lead to overheating of the Meissner state [4] and to the formation of nontrivial flux structures [5, 6]. The significant influence of the barrier on the resistive characteristics of a vortex state in high-T_c superconductors was observed in [7]. Because the electromagnetic and dissipative characteristics of such systems have been hardly investigated, the concept of the critical state in low-dimensional superconductors should be developed in order to quantitatively describe these systems.

In this paper, we propose a generalized model of the critical state in low-dimensional superconductors, which takes into account the effects of bulk and edge pinning of the flux. On the basis of this model, we find the conditions for the penetration of Pearl–Abrikosov vortices into the superconductor and describe the metastable flux structures in these systems. A diagram of different vortex states is constructed for a complete cycle of variations of the external magnetic field. We also demonstrate the transition to the Bean model of the critical state, in which bulk pinning is dominant, and discuss the conditions for observing the predicted flux structures.

1. THE MODEL

Let us consider a long superconducting film strip of a thickness d ($-d/2 < z < d/2$) and a width $2W$ ($-W < Y < W$), which is placed in a magnetic field perpendicular to its surface, $\mathbf{H} = (0, 0, H)$. The film thickness is assumed small as compared to the London penetration depth λ, $d < \lambda$, and its width satisfies the condition $W \gg \lambda_{\text{eff}} = \lambda^2/d$.

When the edge barrier and the bulk pinning exist simultaneously, it is important to determine the conditions under which flux vortices really enter the superconductor, i.e., they enter and penetrate deep into the sample. When a system has a high demagnetizing factor and a high edge barrier, vortices enter it at a field exceeding the field H_S at which the barrier is suppressed [8]. In this case, the near-edge current density i_e becomes equal to the value i_S sufficient for the barrier to be suppressed and for a vortex to enter the superconductor, $i_S = H_S W^{1/2}/[2\pi(2\lambda_{\text{eff}})^{1/2}]$ [8]. Here and henceforth, by a current density we mean the linear one; its definition is given in Subsection 2.1.

In the case where bulk pinning takes place, of importance is the ratio r between the barrier-suppressing current density i_S and the vortex-depinning current density i_p, $r = i_S/i_p$. When $r > 1$, a vortex that enters the sample will be certain to penetrate into it to the point $y = y_0$ (where $y = Y/W$ is the dimensionless coordinate), at which the Lorentz force is balanced by the pinning force. Using the well-known distribution of the Meissner current in the strip, $i_m(y) = Hy/[2\pi(1 - y^2)^{1/2}]$, it is easy to find that $y_0 = 1/[1 + (H_S/2\pi i_p)^2]^{1/2}$. It is seen that, at $H_S/2\pi i_p \geq 1$, we have $y_0 < 1$ and, hence, a region with vortices appears in the bulk of the superconductor. Physically, this is due to Meissner currents, which displace vortices from the periphery to the central part of the sample. Metastable flux distributions that are formed under these conditions can be interpreted as a

1063-7834/00/4202-0201$20.00

self-organized critical state controlled by edge flux pinning [9].

In the case where the barrier entry the vortex is suppressed [$(H_S/2\pi i_p)^2 < 2\lambda_{\text{eff}}/W \ll 1$ or, what is the same, $r < 1$], the current density i_S and field H_S for vortex entering are still related by the equation that follows from the condition that the Gibbs barrier to vortex entering is suppressed. However, the vortices that entered the film are clustered near its edge and cannot, without a noticeable increase in the external field, penetrate the sample to a distance exceeding λ_{eff}. For them to really go forward, an increase in the external field is required that will induce extra currents such that the total current density will become equal to the depinning current density i_p. As a result, a critical state will be formed in the sample, which is controlled by bulk pinning of vortices. In the literature, this state is commonly described in terms of the critical-state model [1, 10].

By analogy with the case mentioned above (high barrier), we can identify i_p with the current density for vortex entering into the sample i_{en}^*. Thus, when the edge barrier is suppressed, the current density i_{en}^* sufficient for the real vortex entering (i.e., entering and going forward, $i_{\text{en}}^* \approx i_p$) and the field for vortex entering H_S ($H_S \approx h_{c1}$, where H_{c1} is the lower critical field) are independent parameters of the system. In commonly used models of the critical state controlled by bulk pinning (see, e.g., [10, 11]), the vortex-entering field is assumed negligible, which essentially corresponds to the situation where the edge barrier is completely suppressed. In the generalized critical-state model, the vortex-entering field is an independent parameter characterizing the quality of the sample surface. The current density for the real vortex entering is defined as $i_{\text{en}} = \max\{i_S, i_p\}$ in this model.

As the external field is decreased, the magnetic flux begins to be expelled from the sample after the barrier to the vortex leaving the sample is suppressed [4]. The latter occurs when the field becomes equal to H_{ex} (see Subsection 2.3). As the field is further decreased, the current near the edge monotonically decreases until it reaches the value $i_{\text{en}}^{(-)}$ ($i_{\text{en}}^{(-)} \approx -i_{\text{en}}$), at which antivortices begin to enter the sample.

The general approach outlined above allows us to describe the flux distribution in a wide class of materials and samples. In what follows, we present the results of the analysis of the characteristics of the critical state in general cases.

2. EQUILIBRIUM VORTEX DISTRIBUTIONS

2.1. Basic Equations

The distributions of the magnetic-flux density $n(y)$ and the steady-state current density $i(y)$ over the film width are described by the Maxwell–London equation, which can be written in the following form in the case of films with a large width, such that $\lambda_{\text{eff}} \ll W$:

$$\int_0^1 \frac{i^*(\tau)d\tau}{\tau - y^2} = h - b^*(y^2). \tag{1}$$

Here, $h = H/2i_p$ and $b^*(y) = \Phi_0 n(y)/2i_p$ are the dimensionless external magnetic-field strength and the magnetic-flux density in the film, respectively; Φ_0 is the flux quantum; and $i^*(y) = i(y)/i_p$ is the dimensionless current density with $i(y)$ being the linear (integrated over the film thickness) current density

$$i(y) = -\int_{-d/2}^{d/2} j_x(y, z)dz.$$

Equation (1) relates two unknown functions $i^*(y)$ and $n^*(y)$; hence, additional conditions are required in order to find these quantities unambiguously. These conditions are dictated by the nature of variations of the external magnetic field and also by the history of the flux distribution in the sample (see below). One of them is the universal requirement that, in the region where vortices are located, the local current density be less than the depinning current density $i_p(b^*) = i_p\phi(b^*)$ [1, 5, 6]. The dimensionless function $\phi(b^*)$ reflects the influence of the magnetic flux in the sample on the magnitude of the local depinning current density [1].

The integral equation (1) with a singular kernel of the Cauchy type can be solved by reducing it to the Riemann boundary value problem [12]. Following this method, we represent $i^*(y)$ in the form

$$i^*(y) = \frac{y}{\pi\sqrt{1-y^2}} \times \left\{h + \frac{1}{\pi}\int_0^1 \sqrt{\frac{1-\tau}{\tau}} b^*(\tau)\frac{d\tau}{\tau - y^2}\right\}, \tag{2}$$

where $b^*(y)$ is formally considered as a known function. Further analysis should be performed for each specific case separately, with allowances made for the magnetic history of the process.

2.2. Initial Flux Penetration into the Superconductor

After the field value H_{en} is reached, vortices begin to penetrate the film from its edges, forming two stripes situated symmetrically about the center of the film, $\Theta_1 < |y| < \Theta_2$. In these stripes, according to the critical-state model, the current density is $i(y) = i_p(b^*)\,\text{sgn}(y)$. The additional conditions on the unknown functions in (1) have the form

$$b^*(y) = 0,\ i^*(y) \neq \phi(b^*)\,\text{sgn}(y),\ |y| \notin [\Theta_1, \Theta_2]; \tag{2a}$$

$$b^*(y) \neq 0,\ i^*(y) = \phi(b^*)\,\text{sgn}(y),\ |y| \in [\Theta_1, \Theta_2]. \tag{2b}$$

With (2b), the range of integration in (2) is reduced to the interval $[\Theta_1, \Theta_2]$, in which the $i^*(y)$ dependence is given by the critical-state equation $i^*(y) = i_p[b^*(y)]$. In principle, equation (2) can be solved for $b^*(y)$ by taking the inverse of the Cauchy-type integral, thereby finding $b^*(y)$ and $i^*(y)$ in the entire interval $|y| \in [-1, 1]$. However, in the general critical-state model, where $\phi(b^*)$ is an arbitrary function, the problem cannot be solved analytically. Below, we present the results obtained with the Bean approximation to the depinning current $[\phi(b^*) = 1]$. In this case, the inversion of the singular integrals can be performed by a common method, and we find

$$b^*(y) = -R(y^2, \alpha_1, \alpha_2)\int_{\alpha_1}^{\alpha_2}\frac{1}{R(\tau, \alpha_1, \alpha_2)}\frac{d\tau}{\tau - y^2}, \quad |y| \in [\Theta_{1],\Theta 2}]; \tag{3a}$$

$$i^*(y) = \pm\frac{1}{\pi}R(y^2, \alpha_1, \alpha_2)\int_{\alpha_1}^{\alpha_2}\frac{1.}{R(\tau, \alpha_1, \alpha_2)}\frac{d\tau}{\tau - y^2}\operatorname{sgn}(y), \quad |y| \notin [\Theta_{1],\Theta 2}]. \tag{3b}$$

This result is valid provided that

$$h = \int_{\alpha_1}^{\alpha_2}\frac{d\tau}{R(\tau, \alpha_1, \alpha_2)}, \tag{3c}$$

where

$$R(x, \beta_1, \beta_2) = \sqrt{\frac{x|(\beta_2 - x)(x - \beta_1)|}{1 - x}}.$$

In the foregoing expressions, we have introduced the notation $\alpha_1 = \Theta_1^2$, $\alpha_2 = \Theta_2^2$; the upper sign (plus) in (3b) is taken if $|y| \in [\Theta_2, 1]$ and the lower sign (minus), if $|y| \in [0, \Theta_1]$. Condition (3c) prevents the appearance of a nonphysical singularity in the current distribution at $y = 0$.

To determine the boundaries Θ_1 and Θ_2 of the region where vortices are located, condition (3c) should be supplemented by the condition that, at the film edge, the current density be saturated and equal the vortex-entering current density i_{en}, i.e., $i(1 - \xi) = i_{en}$, where $\xi = \lambda_{eff}/W$. Thus we arrive at the equation

$$h_{en} = -\sqrt{(1 - \alpha_1)(1 - \alpha_2)}\int_{\alpha_1}^{\alpha_2}\frac{1}{1 - \tau}\frac{d\tau}{R(\tau, \alpha_1, \alpha_2)}, \tag{4}$$

where $h_{en} = H_{en}/2i_p$.

Analysis shows that, in the case of $r > 1$ ($H_{en} = H_S$), a solution to (3c) combined with (4) exists only when the external field exceeds the vortex-entering field h_S, i.e., when $h > h_S$. In this case, as $h \Rightarrow h_S$, Θ_1 approaches the point y_0 from the left and Θ_2 approaches this point from the right. It is also easy to verify that, in the case of $r \ll 1$, where the edge barrier is essentially suppressed ($h_S \sim \xi^{1/2} \ll 1$), expressions (3a) and (3b) reduce to the corresponding expressions in the Bean model [10], because $y_0 \approx 1 - h_S^2 \approx 1$.

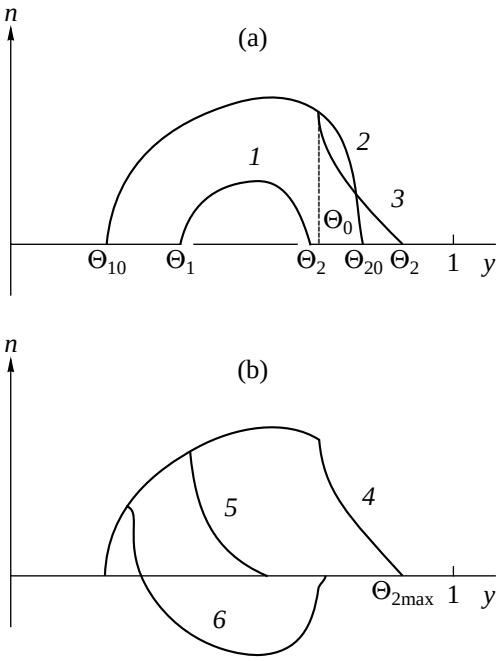

Fig. 1. Vortex density distribution over the film width for various values of the external field: (a) (*1*) $H_1 < H < H_0$ (field increase, flux entry); (*2*) $H_{df} < H < H_0$ (field decrease, frozen flux); (*3*) $H_{ex} < H < H_{df}$ (flux conservation); and (b) (*4*) $H^* < H < H_{ex}$ (flux exit from the periphery); (*5*) $H_{en}^{(-)} < H < H^*$ (flux-region contraction); and (*6*) $H_0 < H < H_{en}^{(-)}$ (antivortex entry).

Thus, when the magnetic flux penetrates the film, its profile has two maxima (Fig. 1a). As h increases, the flux profile expands towards both the center and the edges of the superconducting film. The changes in the position of the profile boundaries are shown in Fig. 2 ("vortex-entry" regime).

In superconductors with a high edge barrier, the onset of the vortex-entry regime corresponds to a marked discontinuity in slope of the magnetization curve $M(H)$ (see Fig. 3), which is due to the avalanche-like penetration of magnetic flux into the sample. As the barrier is lowered, the $M(H)$ curve is noticeably smoothed out and, in the limit of $r \ll 1$, the $M(H)$ dependence becomes monotonic in the vicinity of the vortex-entering field H_S ($\approx H_{c1}$).

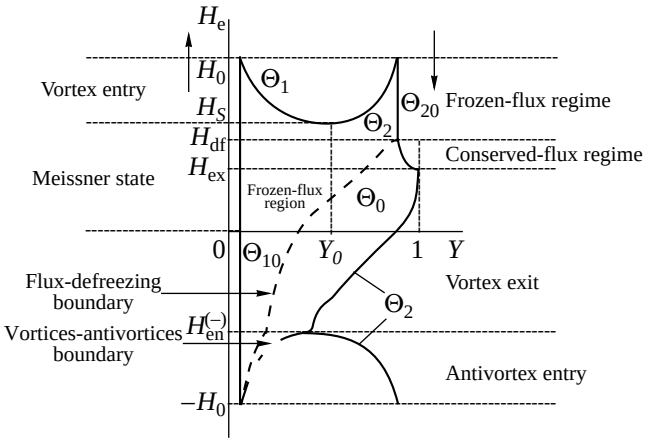

Fig. 2. Magnetic-flux distribution diagram.

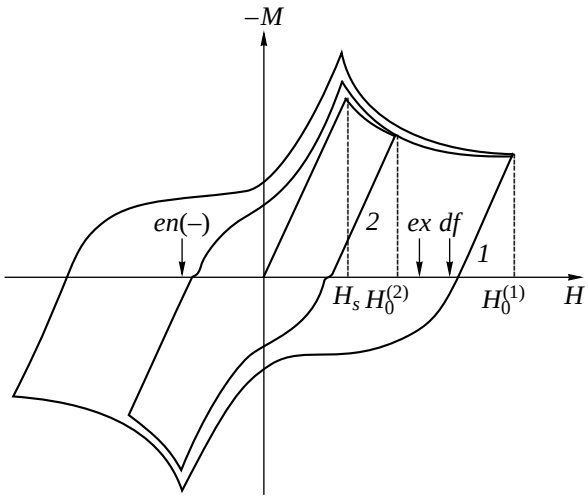

Fig. 3. Family of magnetization curves of a film for $H_S/i_p = 10$: (*1*) $H_0/i_p = 30$ and (*2*) $H_0/i_p = 16$.

2.3. The Field-Decreasing Regime

Now, we consider the case where the external magnetic field is decreased from its amplitude value $h_0 > h_S$. The values of Θ_1 and Θ_2 corresponding to the field h_0 will be designated as Θ_{10} and Θ_{20}, respectively.

In a certain range of fields near h_0 ($h_0 > h > h_{df}$), the vortices will be immobile ("frozen") at their initial pinning points in the region $\Theta_{10} < |y| < \Theta_{20}$ (see Fig. 2, the frozen-flux regime). In this field range, we have $b^*(y, h) = b_0^*(y)$, where $b_0^*(y, h_0) = b_0^*(y)$, and the current distribution can be found using the superposition principle

$$i^*(y, h) = i^*(y, h_0) + \frac{h - h_0}{h} i_m^*(y), \tag{5}$$

where $i_m^*(y)$ is the dimensionless Meissner component of the total current density $i^*(y)$.

This regime takes place until the current density reaches a value of –1 at some point of the sample (the dimensional current density being $-i_p$). This will first occur at the point $|y| = \Theta_{20}$. Hence, the flux-defreezing field is determined by the conditions $i^*(\Theta_{20}, h_{df}) = -1$ and $i^*(\Theta_{20}, h_0) = 1$, from which we obtain

$$h_{df} = h_0 - 2\pi \sqrt{\frac{1 - \Theta_{20}^2}{\Theta_{20}^2}}. \tag{6}$$

As the field is decreased further, a region of "defrozen" vortices appears near the point Θ_{20} ($\Theta_0 < |y| < \Theta_2$) and expands towards the center and the edges of the film. In this region, the vortices are arranged in such a way that $i^*(y) = -1$ for $\Theta_0 < |y| < \Theta_2$; this corresponds to the formation of the critical state for vortex exit. The $i^*(y)$ and $n^*(y)$ distributions are described by (1) with modified additional conditions

$$b^*(y) = 0, \quad i^*(y) \neq \operatorname{sgn}(y), \quad |y| \in [0, \Theta_{10}] \cup [\Theta_2, 1];$$

$$b^*(y) = b_0^*(y), \quad i^*(y) \neq \operatorname{sgn}(y), \quad |y| \in [\Theta_{10}, \Theta_0];$$

$$b^*(y) \neq b_0^*(y), \quad i^*(y) = \operatorname{sgn}(y), \quad |y| \in [\Theta_0, \Theta_2].$$

A solution is found in much the same way as in the previous case (see Subsection 2.2), and we obtain

$$b^*(y) = -R(y^2, \alpha_0, \alpha_2)\left\{\frac{1}{\pi}\int_{\alpha_{10}}^{\alpha_0} \frac{n_0^*(\tau)}{R(\tau, \alpha_0, \alpha_2)}\frac{d\tau}{\tau - y^2} - \int_{\alpha_0}^{\alpha_2} \frac{1}{R(\tau, \alpha_0, \alpha_2)}\frac{d\tau}{\tau - y^2}\right\}, \quad |y| \in [\Theta_0, \Theta_2], \tag{7a}$$

$$i^*(y) = \pm R(y^2, \alpha_0, \alpha_2)\left\{\frac{1}{\pi}\int_{\alpha_{10}}^{\alpha_0} \frac{n_0^*(\tau)}{R(\tau, \alpha_0, \alpha_2)}\frac{d\tau}{\tau - y^2} - \int_{\alpha_0}^{\alpha_2} \frac{1}{R(\tau, \alpha_0, \alpha_2)}\frac{d\tau}{\tau - y^2}\right\}, \quad |y| \in [0, \Theta_0] \cup [\Theta_2, 1]. \tag{7b}$$

This solution is valid provided that

$$h = \frac{1}{\pi}\int_{\alpha_{10}}^{\alpha_0} \frac{n_0^*(\tau)}{R(\tau, \alpha_0, \alpha_2)}d\tau - \int_{\alpha_0}^{\alpha_2} \frac{1}{R(\tau, \alpha_0, \alpha_2)}d\tau. \tag{7c}$$

In these expressions, $\alpha_0 = \Theta_0^2$, $\alpha_{10} = \Theta_{10}^2$, $\alpha_2 = \Theta_2^2$; the upper sign (plus) in (7b) is taken if $|y| \in [0, \Theta_0]$ and the lower sign (minus), if $|y| \in [\Theta_2, 1]$. The physical meaning of (7c) is identical to that of (3c).

The boundaries of the defrozen-vortex region Θ_0 and Θ_2 are determined from (7c), combined with the condition for total-flux conservation. The latter is reduced to the following integral relation with allowances made for the flux-defreezing effect [13]:

$$\int_{\Theta_0}^{\Theta_2} n^*(y)dy = \int_{\Theta_0}^{\Theta_{20}} n_0^*(y)dy. \quad (8)$$

Figure 2 shows the changes in position of the boundaries Θ_0 and Θ_2 in the field range where the critical state for vortex exit is formed ("conserved-flux" regime). The corresponding redistribution of the flux density is shown in Fig. 1 (curve *3*).

The frozen-flux regime and the conserved-flux regime will only be clearly observed in samples with a high edge barrier at small (compared to h_S) amplitudes h_0 of the varying external magnetic field. The distinctive feature of the conserved-flux regime is a rectilinear portion of the magnetization curve (Fig. 3).

The conserved-flux regime will take place in the film until the outer boundary Θ_2 of the region occupied by vortices reaches the film edge or until the barrier to vortex exit is suppressed (at a certain value $\Theta_2 = \Theta_{2\max}$). We designate the corresponding (vortex-exit) field as h_{ex}. As the field is varied in a certain range $h^* < h < h_{ex}$, the boundaries of the region of vortices will remain unchanged, but vortices will leave the film, causing the slope of the defrozen-flux profile to change (curve *4* in Fig. 1 and the "vortex-exit" regime in Fig. 2). Further, at $h^* < h$, the region of vortices will begin to contract (through Θ_2 decreasing), because the vortices will be forced out of the periphery of the film by the Meissner current (curve *5* in Fig. 1). The position of the outer boundary of the vortex region corresponds to the maximum value of Θ_2, at which the vortex density is still an unambiguous (positive) quantity everywhere in the vortex region.

An $M(H)$ curve corresponding to a large amplitude of the flux in the film (curve *1* in Fig. 3) has a clearly defined plateau, which is due to defrozen vortices being rearranged, according to Faraday's law of electromagnetic induction, in such a way as to compensate for any variation in the magnetic moment of the sample. As the vortices leave the film, the near-edge Meissner currents play a progressively larger role and the magnetization curve becomes practically rectilinear.

As the field is further decreased, the current density at the film edges reaches the value $-i_S$ and from this time on, vortices of an opposite sign begin to enter the film (curve *6* in Fig. 1 and the "antivortex-entry" regime in Fig. 2). We designate the corresponding (antivortex-entry) field as $h_{en}^{(-)}$. To determine the boundaries of the region occupied by magnetic flux, we should use an additional condition similar to (4),

$$h_1 = \sqrt{(1-\alpha_0)(1-\alpha_2)}\left\{-\frac{1}{\pi}\int_{\alpha_{10}}^{\alpha_0}\frac{n_0(\tau)}{1-\tau}\frac{d\tau}{R(\tau, \alpha_0, \alpha_2)} + \int_{\alpha_0}^{\alpha_2}\frac{1}{1-\tau}\frac{d\tau}{R(\tau, \alpha_0, \alpha_2)}\right\}. \quad (9)$$

Analysis shows that, at $h \in [-h_0, h_{en}^{(-)}]$, vortices and antivortices coexist in the film. At $h = -h_0$, vortices completely disappear and antivortices have a distribution identical to that of vortices at $h = h_0$.

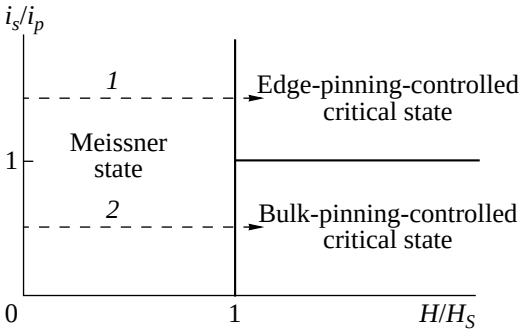

Fig. 4. Critical-state diagram.

3. DISCUSSION

Figure 4 shows the calculated critical-state diagram in the parameter plane. This diagram allows one to predict the transition from the Meissner state to a critical state of a certain type. If the parameter r is large, the transition to the critical state controlled by edge pinning must occur when the external field is increased; in the other extreme case, $r \ll 1$, the transition to the Bean critical state takes place. The parameter r is temperature dependent. Let us suppose that $i_p = i_{p0}(1-\tau)^q$ and $i_S = i_{S0}(1-\tau)^n$, where $\tau = T/T_c$. Then r decreases with increasing T if $q > n$. Therefore, at low temperatures, materials with $q > n$ will exhibit properties characteristic of the Bean critical state, whereas near T_c the edge barrier will dominate. Such behavior was observed in experimental spin-resonance studies of the magnetic-flux profile in single crystals of bismuth [14]. It was in this consecutive order that the crossover occurred from one critical state to the other in the experiment in [14].

Our model allows one to follow the evolution of the $M(H)$ magnetization curve as the parameter r is varied

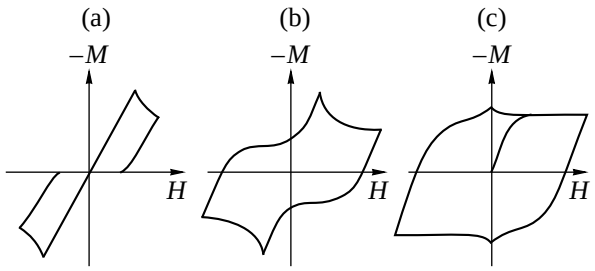

Fig. 5. Evolution of the magnetization curve with varying parameter r (see text).

(Fig. 5). When the edge pinning of vortices dominates ($r \gg 1$), the $M(H)$ dependence is identical to that calculated earlier in [15, 16] (Fig. 5a). In the other extreme case, $r \ll 1$, where bulk pinning is dominant, the magnetization curve is basically similar to that presented in [10]; the distinctions are due to the parameter r having a finite value. In the intermediate case of $r \sim 1$, where the surface and bulk pinning forces are comparable in magnitude, the magnetization curve has a rather nontrivial shape (like that of a curved carpet). Such curves were observed in experimental studies of single crystals of bismuth [14] and BSCCO ribbons [17] of a certain shape.

It is important that the model proposed here can be used to describe the properties of macroscopic superconductors with a high demagnetizing factor (single crystals [14], superconducting ribbons [17] and plates), for which the inequality $d \ll W$ takes place. Indeed, macroscopic electrodynamics of systems of this type are described by equations (the Ampere equation [18]) formally coinciding with (1). The method under discussion allows one to calculate the local magnetization (along Y), to determine the demagnetizing factor of a sample with a trapped flux, and also to describe refraction of magnetic-flux lines of a tilted magnetic field.

The analytical model proposed here can form the basis of calculations of magnetic and dissipative characteristics of low-dimensional superconductors. In particular, the model allows one to calculate the impedance of thin-film microbridges in time-varying fields and to quantitatively describe the generation of higher harmonics in magnetization.

ACKNOWLEDGMENTS

The authors are grateful to E.H. Brandt and G.M. Maksimova for helpful discussions and assistance throughout this work and to J. Clem and E.Yu. Klimenko for their interest in this work, and our correspondence.

This work was supported in part by the Ministry of Science of the Russian Federation (project no. 98-012), the Russian Foundation for Basic Research (grant no. 97-02-17437), and the INCAS (grant no. 97-2-10).

REFERENCES

1. R. G. Mints and A. L. Rakhmanov, *Instabilities in Superconductors* [in Russian] (Nauka, Moscow, 1984), p. 28.
2. J. R. Clem, J. Appl. Phys. **50** (5), 3518 (1979).
3. V. S. Gorbachev and S. E. Savel'ev, Zh. Éksp. Teor. Fiz. **109** (5), 1387 (1996).
4. I. L. Maksimov and G. M. Maksimova, Pis'ma Zh. Éksp. Teor. Fiz. **65** (5), 405 (1997).
5. E. Zeldov, A. Larkin, V. Geshkenbein, *et al.*, Phys. Rev. Lett. **73** (10), 1428 (1994).
6. I. L. Maksimov and A. A. Elistratov, Pis'ma Zh. Éksp. Teor. Fiz. **61** (3), 204 (1995).
7. D. T. Fuchs, E. Zeldov, M. Rappaport, *et al.*, Nature **391** (6665), 373 (1998).
8. K. K. Likharev, Izv. Vyssh. Uchebn. Zaved., Radiofiz. **14** (6), 919 (1971).
9. I. L. Maksimov, Europhys. Lett. **32** (9), 753 (1995).
10. E. H. Brandt and M. V. Indenbom, Phys. Rev. B: Condens. Matter **48** (17), 12893 (1993).
11. E. Zeldov, J. R. Clem, M. McElfresh, *et al.*, Phys. Rev. B: Condens. Matter **49** (14), 9802 (1994).
12. N. I. Muskhelishvili, *Singular Integral Equations* [in Russian] (Fizmatgiz, Moscow, 1963).
13. I. L. Maksimov and A. A. Elistratov, Appl. Phys. Lett. **72** (13), 1650 (1998).
14. R. Khasanov, Yu. I. Talanov, W. Assmus, *et al.*, Phys. Rev. B: Condens. Matter **54** (18), 13339 (1996).
15. I. L. Maksimov, Pis'ma Zh. Éksp. Teor. Fiz. **22** (20), 56 (1996).
16. M. Benkrauoda and J. R. Clem, Phys. Rev. B: Condens. Matter **53** (9), 5716 (1996).
17. Yu. N. Likhanin (private communication).
18. E. H. Brandt, Phys. Rev. B: Condens. Matter **48** (9), 6699 (1993).

Translated by Yu. Epifanov

Physics of the Solid State, Vol. 42, No. 2, 2000, pp. 207–214. Translated from Fizika Tverdogo Tela, Vol. 42, No. 2, 2000, pp. 202–209.

SEMICONDUCTORS AND DIELECTRICS

Effect of the Mutual Dragging of Electrons and Phonons on the Thermomagnetic Effects in HgSe

Kh. M. Bikkin, A. T. Lonchakov, and I. I. Lyapilin

Institute of Metal Physics, Ural Division, Russian Academy of Sciences, ul. S. Kovalevskoĭ 18, Ekaterinburg, 620219 Russia

Received May 11, 1999

Abstract—The longitudinal and transverse Nernst–Ettingshausen (NE) effects were measured in HgSe samples doped with various concentrations of gallium, $0.6 \times 10^{18} < N(\mathrm{Ga}) < 4.7 \times 10^{18}$ cm^{-3}. The NE measurements were performed for the classical interval of magnetic field strengths (0–40 kOe) in the temperature range from 20 to 60 K. It was established that the low-temperature NE coefficients change sign with increasing Ga concentration or the applied magnetic field strength. It is shown that all unusual features of the NE effects observed in HgSe crystals can be attributed to the effect of mutual dragging of electrons and phonons. This implies that the effect of mutual electron–phonon dragging can be experimentally detected in semiconductors with high concentration of conduction electrons. *© 2000 MAIK "Nauka/Interperiodica".*

INTRODUCTION

It was demonstrated [1–5] that measurements of the thermo emf of a degenerate electron gas in the classical range of magnetic field strengths provides information about the mechanism of charge carrier scattering in $A^{II}B^{VI}$ semiconductors. Investigations of the field dependence of the longitudinal Nernst–Ettingshausen (NE) effect in mercury selenide [1, 2] and lead chalcogenides [3, 4] in the region of comparatively high temperatures ($T \geq 77$ K) showed that thermo emf α exhibits saturation in the classical region of strong magnetic fields H, irrespective of the dominating mechanism of charge carrier scattering in the conduction band. However, measurements of the longitudinal NE effect in iron-doped HgSe samples at low temperatures (15 K $\leq T \leq$ 60 K) [5] revealed the presence of maxima in the plot of $\Delta\alpha(H) = |\alpha(H)| - |\alpha(0)|$. Until now, the reasons for nonmonotonic variation of the $\Delta\alpha(H)$ value in HgSe:Fe remained unclear. In particular, the maxima could be related to some special features of the HgSe:Fe system containing iron ions of mixed valence. In order to clarify this problem, it was necessary to thoroughly study the longitudinal NE effect in HgSe crystals doped with shallow donors. As for the transverse NE effect, this point was never experimentally studied in $A^{II}B^{VI}$ semiconductors in a wide classical range of magnetic field strengths and sufficiently low temperatures.

The measurements of thermo emf in a zero magnetic field [2, 6, 7] and the study of temperature variation of the thermomagnetic effects [7, 8] showed that analysis of the thermoelectric and thermomagnetic coefficients in $A^{II}B^{VI}$ semiconductors must be performed with an allowance for the effect of the carrier dragging by phonons. This effect is related to deviation of the phonon distribution function from equilibrium in the presence of a temperature gradient and leads, in particular, to a nonmonotonic temperature variation of the coefficient of the longitudinal NE effect in HgSe : Fe [7, 8]. An analysis of the effect of electron dragging by phonons in strongly doped semiconductors of the $A^{II}B^{VI}$ type, in contrast to a similar phenomenon in the pure semiconductors, must take into account the scattering of phonons on electrons in addition to the contributions of scattering from sample boundaries and the phonon–phonon scattering. As is known, the transition from scattering on impurities to the electron–phonon mechanism in HgSe crystals with $n \sim 10^{18}$ cm^{-3} is observed at a temperature of $T \approx 40$ K [9]. Measurements of the thermo emf in HgSe in zero magnetic field [2, 7] showed that another effect, which must be also taken into account in this temperature region, is related to the phenomenon of electron dragging by phonons. For this reason, it is not excluded that the phonon scattering on electrons may contribute to the drugging effect. This factor markedly complicates analysis of the phenomenon of dragging because the kinetic equations for the phonon and electron distribution functions have to be solved jointly. The dragging effect in this case is called the mutual electron–phonon dragging [10–12].

The fact of mutual dragging implies that a part of the momentum transferred from phonons to electrons is returned back to the phonon system as a result of mutual collisions. If electrons and phonons are scattered primarily from each other, the effect is referred to as the strong mutual electron–phonon dragging [10, 11]. Evidently, the strong mutual dragging cannot take place in degenerate semiconductors at a sufficiently low temperature (i.e., when $\tau_{pp} \gg \tau_{pe}$, τ_{pe} and τ_{pp} being the phonon relaxation times for the scattering on electrons and other centers, respectively) because electrons are scattered predominantly from charged centers ($\tau_{ep} \gg \tau_{ei}$, where τ_{ep} and τ_{ei} are the electron relaxation times for the scattering

1063-7834/00/4202-0207$20.00 © 2000 MAIK "Nauka/Interperiodica"

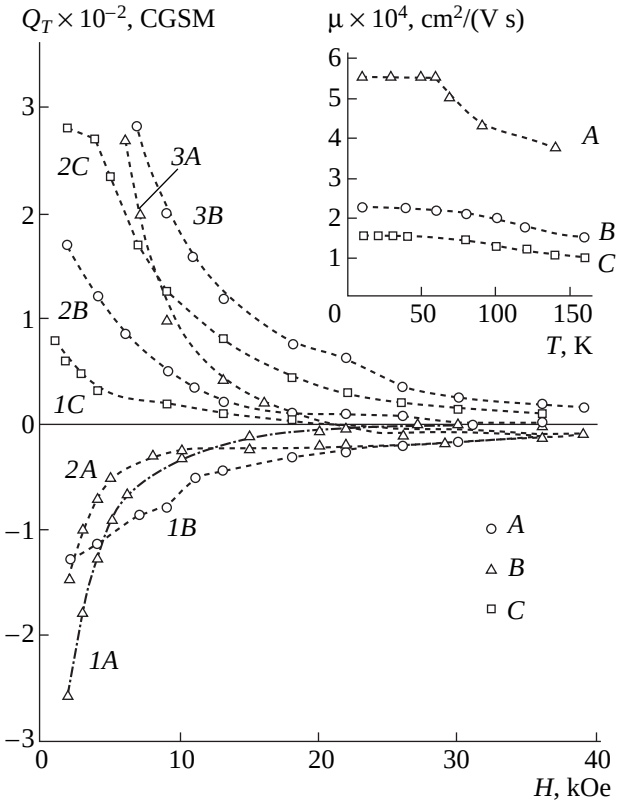

Fig. 1. Plots of the coefficient Q_T of the transverse NE effect versus magnetic field strength for three HgSe samples (*A*, *B*, and *C*, see the table) at various temperatures: (*1A*) 21 K; (*2A*) 40 K; (*3A*) 60 K; (*1B*) 29 K; (*2B*) 48 K; (*3B*) 60 K; (*1C*) 29 K; (*2C*) 50 K. The inset shows the plots of electron mobility μ versus temperature for samples *A*, *B* and *C*.

on phonons and impurities). However, we cannot a priori exclude any influence of the mutual dragging on the thermomagnetic effects in the temperature region where the relaxation times are comparable ($\tau_{ep} \sim \tau_{ei}$, $\tau_{pp} \sim \tau_{pe}$). The relaxation of phonons on electrons (provided the electron concentration is sufficiently high) becomes a significant factor and we cannot restrict the consideration to simple mutual dragging of electrons and phonons. As was demonstrated in [10, 11], the mutual electrons–phonon dragging in degenerate semiconductors leads to an increase in the thermo emf and influences the temperature dependence of the NE coefficients.

As demonstrated below, the region of temperatures where the effect of mutual electrons–phonon dragging can be anticipated in HgSe extends approximately from 20 to 60 K. Therefore, it was of interest to establish experimentally the degree of influence of the mutual dragging on the field dependence of the longitudinal and transverse NE effects in degenerate semiconductors. We selected mercury selenide doped with various concentrations of gallium, $N(\mathrm{Ga}) \sim (0.6\text{–}4.8) \times 10^{18}$ cm^{-3}, as the object for investigation. Here we present the data of measurements of the thermomagnetic effects in this system in the classical range of magnetic field strengths and the results of theoretical analysis of these effects.

EXPERIMENTAL RESULTS

The longitudinal and transverse NE effects were measured in a range of temperatures (20 K ≤ T ≤ 60 K) and magnetic fields (0–40 kOe) on a series of three HgSe : Ga samples.

The main electrical characteristics (i.e., the concentration of conduction electrons n and their mobility μ at T = 4.2 K) of HgSe samples (denoted by *A*, *B*, and *C*) doped with gallium are presented in the table. The average dimensions of the samples were 9 × 2 × 1 mm. The temperature was measured by the (Au + 0.012% Fe)–Cu thermocouples with a sensitivity of ~10 μV/K. The temperature differences measured did not exceed 10% of an average sample temperature.

Figure 1 shows the plots of the transverse NE coefficient Q_T versus magnetic field strength H for the HgSe samples studied at various temperatures. The main feature in variation of the $Q_T(H)$ value is that the coefficient of the transverse NE effect changes sign from negative to positive with increasing concentration of charged centers (and, hence, the concentration of charge carriers in the sample) at fixed temperature in the interval $T \sim$ 20–40 K and a magnetic field strength $H \leq$ 20 kOe (cf. curves *1B*, *1C* and *2A*, *2B* in Fig. 1). It should be noted that a similar change of the sign of the transverse NE effect from negative to positive was previously observed in HgSe : Fe crystals with increasing content of iron [5] and explained by a change in the energy dependence of the relaxation time in the vicinity of the Fermi energy as a result of increasing degree of correlation in the system of Fe^{3+} ions. However, this mechanism evidently cannot be operative in HgSe : Ga where the charged centers are distributed in a random manner.

Another feature in the behavior of $Q_T(H)$ is observed in the region of strong magnetic fields ($\mu H/c > 1$), where the $Q_T(H)$ value changes sign from positive to negative (curves *1C*, *2B*, *3A* in Fig. 1). As seen in Fig. 1, this change takes place at different temperatures in various samples: the lower the electron concentration, the higher the temperature at which the coefficient $Q_T(H)$ changes sign. These features in the behavior of $Q_T(H)$ cannot be explained within the framework of the conventional theory of thermomagnetic effects. According to this theory, first, the sign of $Q_T(H)$ at sufficiently low temperatures is always negative (which is related to the dominating electron scattering on charged centers) and, second, the absolute value of the coefficient $|Q_T(H)|$ in the classical region of strong magnetic fields must decrease (irrespective of the sign) proportionally to $(H)^{-2}$ with increasing field strength.

The data presented in Fig. 1 show that the transverse NE effect in samples A and B changes sign from negative to positive with increasing temperature (cf. curves *1A*, *3A* and *1B*, *3B*). The temperature-induced change in sign of the NE coefficient reflects a change from the

electron scattering predominantly on charged centers to the scattering on acoustic phonons. This effect is also manifested in the temperature variation of the electron mobility μ depicted on the inset in Fig. 1. As seen, the mobility in all samples does not vary with the temperature in the region $T \leq 40$ K, which corresponds to dominating role of the charge carrier scattering on impurity centers. Note that the onset of transition from the scattering on impurity centers to the scattering on acoustic phonons (at $T \cong 40$ K) is rather smooth, especially in the samples doped to a greater level (see curves *B* and *C* on the inset in Fig. 1).

Figure 2 shows the plots of the dimensionless field $\varepsilon_x(H)$ versus magnetic field strength H for the longitudinal NE effect:

$$\varepsilon_x(H) = \frac{e}{k_B}(|\alpha(H)| - |\alpha(0)|).$$

The values of $\alpha(H)$ were averaged with respect to two directions of the magnetic field H. An important feature of the $\varepsilon_x(H)$ curves is the absence of the effect of thermo emf saturation in the classical region of strong magnetic fields for all samples in the entire temperature range studied (from 20 to 60 K). Apparently, this behavior is due to the presence of some negative contribution to the longitudinal NE effect. This contribution results either in monotonic decrease in thermo emf with increasing magnetic field strength at sufficiently low temperatures $T \sim 20$–30 K (Fig. 2, curves *1A*, *1B*, *2A*, *2B*) or in the appearance of maximum at higher temperatures (curves *3A*, *3B*, *2C*, *3C*). In the latter case, a decrease in the absolute value $|\alpha(H)|$ may be accompanied by the change in sign of the longitudinal NE effect from positive to negative (Fig. 2, curves *3A*, *3B*, *2C*). As noted above, analogous maxima were observed for the HgSe crystals doped with iron. Therefore, we may suggest that factors responsible for the appearance of these maxima are not related to the type of dopant distribution (random or spatially correlated).

For a fixed magnetic field, the aforementioned negative contribution to the thermo emf depends both on the temperature and on the electron concentration. As seen from Fig. 2, the absolute α value decreases with increasing concentration at a constant temperature (curves *2B*, *2C*, *3A*, *3B*, *3C*), while the longitudinal NE effect changes sign from negative to positive. As noted above, the same behavior is characteristic of the transverse NE effect. This experimental fact cannot be explained within the framework of a simple diffusion theory of thermomagnetic effects. Indeed, according to these notions, a growth in the concentration of charged centers leads to an increase in the probability of scattering on these centers, so that the thermomagnetic effects must retain the negative sign.

On more feature to be noted is the unusual (nonmonotonic) variation of the dimensionless field $\varepsilon_x(H)$ with the temperature observed for sample A (Fig. 2). This behavior indicates that the negative contribution to

Electrical properties of HgSe : Ga samples

Sample	$n \times 10^{18}$, cm^{-3}	$\mu \times 10^{-4}$ cm^2/(V s)
A	0.6	5.40
B	2.4	2.25
C	4.7	1.60

$\varepsilon_x(H)$ for this sample, in contrast to that for samples *B* and *C*, increases when the temperature grows from 20 to 40 K (curves *1A* and *2A*) and drops on the further increase in the temperature (curve *3A*).

Thus, the thermo emf measurements revealed a number of peculiarities in the field dependence of the longitudinal and transverse NE effects in mercury selenide. The main features are the change in the sign of both thermomagnetic effects from positive to negative observed with increasing magnetic field strength, and from negative to positive—with increasing concentration of charged centers. The inset on Fig. 2 shows an experimental plot of the thermo emf $|\alpha(0)|$ in a zero magnetic field versus temperature for sample *B*, which is typical of the HgSe samples studied. As is seen, the temperature interval from 20 to 60 K corresponds to the region of minimum in $|\alpha(0)|$, which is related to the phonon contribution to the thermo emf being compara-

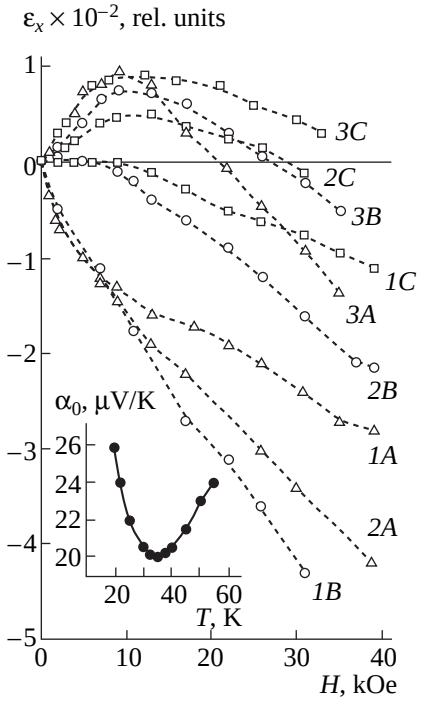

Fig. 2. Plots of the dimensionless field ε_x in the longitudinal NE effect versus magnetic field strength for three HgSe samples (*A*, *B*, and *C*, see the table) at various temperatures: (*1A*) 21 K; (*2A*) 40 K; (*3A*) 60 K; (*1B*) 29 K; (*2B*) 48 K; (*3B*) 60 K; (*1C*) 29 K; (*2C*) 50 K; (*3C*) 60 K. The inset shows the plot of the absolute thermo emf α_0 in zero magnetic field versus temperature for samples *B*.

ble with the diffusion contribution [7]. Therefore, we may suggest that an analysis of the field dependence of the thermomagnetic effects (Figs. 1 and 2) must take into account the phenomenon of electron dragging by phonons. Moreover, this phenomenon should be considered with an allowance for the phonon scattering both on the other phonons and on the charge carriers. In other words, the dragging has to be considered as the mutual effect. As demonstrated below, only this approach allows the experimentally observed field dependences of the thermomagnetic coefficients to be adequately described.

SYSTEM OF KINETIC EQUATIONS

In order to take into account the effect of mutual electron–phonon dragging it is necessary to include a term describing the scattering of acoustic phonons on electrons into a kinetic equation determining the phonon distribution function N_q. The kinetic equation for the phonon distribution function can be written in the following form:

$$\frac{sk_0}{q\hbar\omega_q}\nabla T = -\frac{k_0 T\mathbf{b}(q)}{(\hbar\omega_q)^2\tau_{pp}(q)} + \frac{1}{2\tau_{ep}(k)kq} \times \int_{q/2}^{\infty} k\left(\mathbf{b}(q) - \frac{\hbar}{m}\boldsymbol{\chi}\right)\left(\frac{\partial f^0}{\partial\varepsilon}\right)dk. \quad (1)$$

In deriving equation (1), we assumed that deviations of the distribution functions from the equilibrium values f_0 and N_q^0 are small:

$$f = f^0 + f', \quad N_q = N_q^0 + N_q'.$$

Then the nonequilibrium increments to the equilibrium functions can be presented as

$$f_k' = \left(-\frac{\partial f_k^0}{\partial\varepsilon_k}\right)\left(\frac{\hbar k}{m}\boldsymbol{\chi}(\varepsilon_k)\right), \quad N_q' = \left(-\frac{\partial N_q^0}{\partial\hbar\omega_q}\right)(\mathbf{qb}(q)), \quad (2)$$

where the unknown functions $\boldsymbol{\chi}$ and $\mathbf{b}$ characterizing deviations of the system from equilibrium depend only on the absolute values of the corresponding wavevectors. In addition, we introduce the characteristic time of electron relaxation on acoustic phonons $\tau_{ep}(k)$:

$$\frac{1}{\tau_{ep}(k)} = \frac{E_0^2 k_0 T m k}{\pi\rho s^2\hbar^3}, \quad (3)$$

where E_0 is the deformation potential constant, s is the velocity of light, k_0 is the Boltzmann constant, m is the effective mass of electron, and ρ is the crystal density.

Of the two possible non-electron mechanisms of the phonon relaxation–the scattering from sample boundaries and the phonon–phonon scattering–equation (1) takes into account only the latter factor (represented by the corresponding relaxation time τ_{pp}). Contribution due to the scattering from sample boundaries can be neglected, which is confirmed by the absence of the corresponding phonon peak in the $|\alpha_0(T)|$ plot within the temperature intervals studied (see the inset on Fig. 2).

Upon separating an explicit term to describe the electron scattering on acoustic phonons in the collision integral entering into the kinetic equation for the electron distribution function, we obtain the following expression:

$$\left.\frac{\partial f}{\partial t}\right|_s = -\frac{f'}{\tau(k)} - \frac{\tau(k)}{4\tau_{ep}(k)\hbar k^4}\int_0^{2k} q^3(\hbar\mathbf{kb}(q))\left(\frac{\partial f^0}{\partial\varepsilon}\right)dq, \quad (4)$$

where τ_k determines the time of electron relaxation on the impurity centers. Taking into account the field and diffusion terms, the kinetic equation for the conduction electrons can be written in the following form:

$$\mathbf{B}(k) = \boldsymbol{\chi}(\varepsilon_k) - (\mathbf{a}\times\boldsymbol{\chi}(\varepsilon_k)) - \frac{\tau(k)m}{4\hbar\tau_{ep}(k)k^4}\int_0^{2k} q^3\mathbf{b}(q)dq,$$

$$\mathbf{B}(k) = -\tau(k)\left[e\boldsymbol{\varepsilon} + \frac{\varepsilon_k - \zeta}{T}\nabla T\right], \quad (5)$$

$$\mathbf{a} = \omega_0\tau_{ep}(k)h, \quad \omega_0 = \frac{eH}{mc}, \quad \boldsymbol{\varepsilon} = \mathbf{E} - \nabla\xi/e,$$

where $\boldsymbol{\varepsilon}$ is the electrochemical potential gradient, ζ is the chemical potential of electrons, and $\mathbf{h}$ is the unit vector oriented along the magnetic field vector $\mathbf{H} = (0, 0, H)$.

Equations (1) and (5) form the initial set of equations for determining the kinetic coefficients of the mutual electron–phonon dragging. As can be seen, this set of equations is readily solved if the collision integral, entering into the kinetic equation for the phonon distribution function, is transformed so as to take into account a stepwise character of the electron distribution function related to a strong degeneracy of the electron gas. This simplification allows the set of equation to be solved exactly. Upon calculating a correction to the electron distribution function on the Fermi surface $\boldsymbol{\chi}(\varepsilon_F)$, we may turn back to solution of the set of equations (1) and (5) for the arbitrary values of ε_k. Leaving only a contribution on the Fermi surface in the collision integral in the right-hand part of equation (5), we obtain an algebraic set of equations relative to $\boldsymbol{\chi}(\varepsilon_k)$. This procedure is fully equivalent to the scheme of solution used in [1] and leads to analogous expressions for the unknown functions $\mathbf{b}(q)$ and $\boldsymbol{\chi}$.

It should be noted that particular calculations for the temperatures $T > 20$ K would require the phonon–phonon relaxation mechanism to be specified in an explicit form. Using the algorithm of solution of the set

of equation described above and assuming that the phonon–phonon relaxation proceeds by the Simons mechanism [7],

$$\tau_{pp}^{-1} = \lambda_s q, \quad \lambda_s = \frac{\hbar}{\rho}\left(\frac{k_0 T}{\hbar s}\right)^4, \tag{6}$$

we obtain the following equation for $\boldsymbol{\chi}(\varepsilon_k)$:

$$\mathbf{B} = \boldsymbol{\chi} - (\mathbf{a}\times\boldsymbol{\chi}) - G\mathbf{K} + \mathbf{F},$$

$$\mathbf{B}(\varepsilon_F) = -\tau(k_F)\left(e\boldsymbol{\varepsilon} + \frac{4}{3}\Pi k_0 T\frac{\nabla T}{T}\right),$$

$$G = \frac{\Pi}{(1-\Pi^*)}\frac{\tau(k)}{\tau_{ep}(k)}\frac{1}{R(k_F)},$$

$$K = \{\mathbf{B}(\varepsilon_F) + \nu^2(k_F)\mathbf{h}(\mathbf{h}\mathbf{B}(\varepsilon_F)) + \nu(k_F)\mathbf{h}(\mathbf{h}\times\mathbf{B}(\varepsilon_F))\},$$
$$\mathbf{F} = \frac{4}{3}\Pi k_0\tau(k)\frac{\nabla T}{T}, \tag{7}$$

$$R(k_F) = 1 + \nu^2(k_F), \quad \nu(k_F) = \tau(k_F)\omega_0(1-\Pi^*)^{-1},$$

$$\Pi = \frac{1}{1+\Pi_1}, \quad \Pi_1 = \frac{2k_0 T\hbar^2 kq}{m(\hbar\omega_q)^2}\frac{\tau_{ep}(k)}{\tau_{pp}(q)} = \frac{2\pi(k_0 T)^4}{E_0^2(ms^2)^2},$$

$$\Pi^* = \frac{\tau(k_F)}{\tau_{ep}(k_F)}\Pi.$$

Note that the other mechanisms in the phonon relaxation, for example, the Herring mechanism [7], can be taken into account in a similar manner.

As seen, the general structure of equations (7) is the same as that in the classical theory of thermomagnetic phenomena. All changes are related only to renormalization of the thermodynamic forces and the electron mean free path.

Introducing, in addition to $\boldsymbol{\varepsilon}^*$, an effective thermodynamic force $\nabla T^{\cdot}$, we may rewrite equation (7) in the following form:

$$\boldsymbol{\chi}(\varepsilon_k) = -e\tau(k)\left\{(\mathbf{h}\boldsymbol{\varepsilon}^*)\mathbf{h} + \frac{\omega_0\tau(k)(\mathbf{h}\times\boldsymbol{\varepsilon}^{\cdot}) - (\mathbf{h}\times(\mathbf{h}\times\boldsymbol{\varepsilon}^*))}{1+(\omega_0\tau(k))^2}\right\}$$
$$-\tau(k)\frac{(\varepsilon_k-\zeta)}{T}\left\{(\mathbf{h}\nabla T)\mathbf{h} + \frac{\omega_0\tau(k)(\mathbf{h}\times\nabla T) - (\mathbf{h}\times(\mathbf{h}\times\nabla T))}{1+(\omega_0\tau(k))^2}\right\} \tag{8}$$
$$-\tau(k)k_0\left\{(\mathbf{h}\nabla T^*)\mathbf{h} + \frac{\omega_0\tau(k)(\mathbf{h}\times\nabla T^*) - (\mathbf{h}\times(\mathbf{h}\times\nabla T^{\cdot}))}{1+(\omega_0\tau(k))^2}\right\},$$

where

$$\nabla T_i^* = \nabla T_j(A_\phi\delta_{ij} + A_{\phi ij}), \quad \varepsilon^* = \varepsilon_j(1+S_\Phi)\delta_{ij} + S_{\Phi ij},$$

$$S_{\Phi ij} = S_\Phi\begin{pmatrix} 0 & -1 & 0 \\ -1 & 0 & 0 \\ 0 & 0 & \sqrt{k_F} \end{pmatrix}, \tag{9}$$

$$S_\phi = \frac{\Pi^*}{(1-\Pi^*)}\frac{\tau_{ep}(k_F)}{\tau_{ep}(k)}\frac{1}{1+\nu^2(k_F)},$$

$$A_\phi(k) = \frac{4}{3}\Pi(1+S_\phi(k)) \quad A_{\phi ij} = \frac{4}{3}\Pi S_{\phi ij}.$$

Using an equation for the correction to the electron distribution function $\boldsymbol{\chi}(\varepsilon_k)$, we may write an expression for the components of the charge flux density in the sample $J_i = \sigma_{ij}\varepsilon_j - \beta_{ij}\nabla_j T$, find the components of the electric conductivity tensor σ_{ij}, and the components of the β_{ij} tensor. The latter quantities can be used to express the kinetic coefficients under consideration.

In particular, expressing the coefficient Q_T of the transverse NE effect in terms of the kinetic coefficients σ_{ij} and β_{ij},

$$Q_T = \frac{\sigma_{xx}\beta_{xy} - \sigma_{xy}\beta_{xx}}{H(\sigma_{xx}^2 + \sigma_{xy}^2)},$$

we finally obtain

$$Q_T = -\frac{\pi^2}{3}\frac{k_0}{e}\frac{k_0 T}{\varepsilon_F H} \times \frac{(1+S_F)D\nu_0 - \nu_0 S_F\left[\frac{3}{2}(1+\nu_0^2) + D\right]}{(1+\nu_0^2)[(1+S_F)^2 + (\nu(k_F)S_F)^2]}, \tag{10}$$

where $\nu_0 = \omega_0\tau(\varepsilon_F)$ and $D = \varepsilon_F\tau'(\varepsilon_F)/\tau(\varepsilon_F)$.

By the same token, we may write an expression for the coefficient of the differential thermo emf in a magnetic field. This coefficient can be represented as a sum

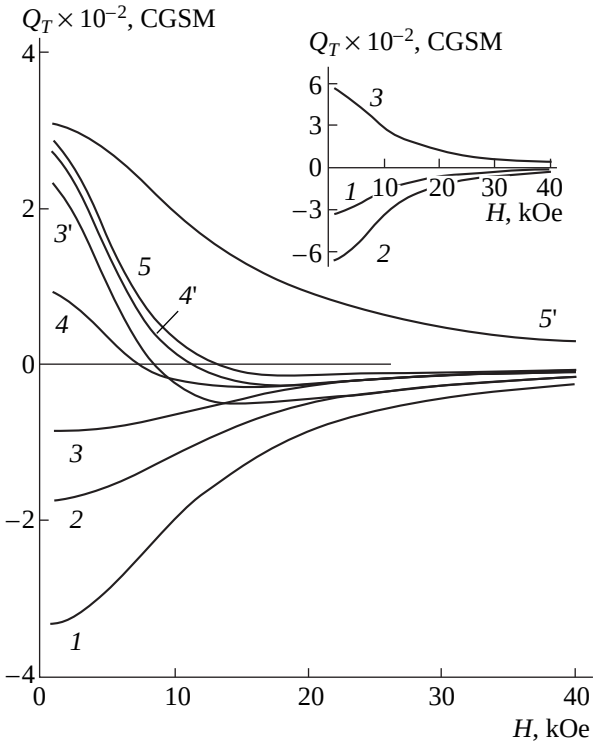

Fig. 3. Calculated plots of the coefficient Q_T of the transverse NE effect versus magnetic field strength H at various temperatures T = 20 (*1*–*4*); 30 (*3*'–*4*', *5*); and 60 K (*5*') and electron concentrations $n = 0.7 \times 10^{18}$ cm^{-3} (*1*); 1×10^{18} cm^{-3} (*2*); 2×10^{18} cm^{-3} (*3*, *3*'); 3×10^{18} cm^{-3} (*4*, *4*'); and 4×10^{18} cm^{-3} (*5*, *5*'). The inset shows the plots of Q_T versus H for HgSe with $n = 1 \times 10^{18}$ cm^{-3} calculated with neglect of the mutual dragging effect for T = 20 K (*1*); 30 K (*2*); and 50 K (*3*).

of two contributions: $\alpha_{xx} = \alpha_{xx}^{diff} + \alpha_{xx}^{u}$, where α_{xx}^{diff} is the diffusion part:

$$\alpha_{xx}^{diff} = -\frac{k_0}{e}\frac{\pi^2 k_0 T}{\varepsilon_F} \times \frac{\left[\frac{3}{2}(1+\nu_0^2)+D\right](1+S_\phi)+DS_\phi\nu_0^2(1-\Pi^*)^{-1}}{(1+\nu_0^2)[(1+S_\phi)^2+\nu_0^2 S_\phi^2]}. \quad (11)$$

and α_{xx}^{u} is the dragging thermo emf, which has a nonzero value in the zero-order approximation with respect to the parameter k_0T/ε_F:

$$\alpha_{xx}^{u} = -\frac{k_0}{e}\frac{4}{3}\Pi,\ \Pi = \frac{1}{1+\Pi_1},\ \Pi_1 = \frac{2\pi(k_0T)^4}{E_0^2(ms^2)^2}. \quad (12)$$

Equations (10) and (11) fully determine dependence of the thermoelectric forces and thermomagnetic coefficients on the temperature and the field strength in the region of classical magnetic fields.

RESULTS OF NUMERICAL CALCULATION

Using equations (10) and (11) we may analyze the pattern of variation of the coefficient Q_T in the transverse NE effect and of the dimensionless longitudinal field $\varepsilon_x(H)$ in the longitudinal NE effect as functions of the magnetic field strength for HgSe crystals with various concentrations of charge carriers in the conduction band.

First, we will consider the field dependence of the coefficient Q_T in the transverse NE effect. For the numerical analysis, we have taken the following values of the parameters: effective mass $m = 0.065m_0$ (m_0 is the free electron mass); crystal density $\rho = 8$ g/cm^3; deformation potential constant $E_0 = 10$ eV (this value was obtained from analysis of the temperature dependence of the electron mobility using the condition $\tau_{ei} = \tau_{pe}$ at $T = 40$ K).

The results of the numerical analysis of the Q_T coefficient characterizing the transverse NE effect are presented in Fig. 3. The inset on this figure shows the curves calculated by formula (10) for the case of zero dragging effect ($S_F = 0$), assuming that the main contribution to scattering at low temperatures ($T < 40$ K) is due to the system of impurity centers ($D = 3/2$), while at elevated temperatures ($T > 40$ K), the dominating process is the electron scattering on acoustic phonons ($D = -1/2$). As expected, the sign of the NE effect at $T < 40$ K is negative (see curves *1* and *2* in the inset on Fig. 3) ad the coefficient Q_T decreases in proportion to $\sim H^{-2}$ with increasing field strength. Curve *3* in the inset corresponds to $T = 50$ K. Here, the effect is positive and Q_T decreases with increasing field strength by the same law as in the case of scattering on the charged centers. Note that a similar field dependence of the coefficient of the transverse NE effect is observed for the usual dragging effect when $\tau_{pp} \gg \tau_{ep}$ [7].

Let us consider the results of numerical calculations taking into account the mutual electron–phonon dragging effect under the same assumptions concerning the main mechanisms of scattering of the charge carriers in the conduction band (Fig. 3). Curves *1*–*5*, *3*', and *4*' refer to the case of predominant scattering on the system of impurity centers, and curve *5*' corresponds to the dominating scattering from acoustic phonons. The results of the calculation show that a change in the sign of the Q_T coefficient in samples possessing a higher concentration of the conduction electrons must be observed in greater magnetic fields (Fig. 3, curves *3*', *4*', *5*). A seen from Fig. 3 (curves *1*–*4*) for a weak magnetic field ($H < 10$ kOe), the Q_T value changes its sign from negative to positive with increasing concentration of the charged centers—in agreement with the experimental data (Fig. 1, curves *1A* and *1C*). At elevated temperatures, where the electron scattering on acoustic phonons dominates and the drugging effect is comparatively small, the coefficient $Q_T(H)$ of the transverse NE effect is always positive (Fig. 3, curve *5*').

Let us turn to analysis of the dimensionless coefficient ε_x in the longitudinal NE effect calculated as a function of the magnetic field strength (Fig. 4). The inset on Fig. 4 shows the results of numerical calculations of the dimensionless field ε_x for various magnetic field strengths with neglect of the mutual electron-phonon dragging effect. Here, curves *1* and *2* refer to the lower temperatures (T = 20 and 30 K), and curve *3* corresponds to an elevated temperature (T = 50 K) where the main contribution to the electron relaxation is due to their scattering on acoustic phonons. As seen, the calculation yielded the "classical" $\varepsilon_{xx}(H, T)$ functions exhibiting saturation of the thermo emf with increasing magnetic field strength.

The results of the calculation with an allowance for the mutual dragging effect are presented in Fig. 4 by curves *1–5* and *3*'–*5*'. As seen, the mutual electron–phonon dragging leads (similarly to the case of the transverse NE effect) to a qualitative change in the temperature and field dependence of the dimensionless coefficient of the longitudinal NE effect. This is most clearly manifested by the appearance of maxima in the calculated curves $\varepsilon_{xx}(H)$ and by a change in the sign of the longitudinal NE effect from positive to negative with increasing magnetic field strength (Fig. 4, curves *2–4* and *3*').

Dependence of the calculated $\varepsilon_{xx}(H, T)$ coefficient on the concentration of conduction electrons also agrees with experiment (Fig. 4, curves *1–4*): as the charge carrier concentration in the conduction band increases, the longitudinal NE effect changes sign from negative to positive.

Thus, the results of our numerical analysis showed that the change of sign of the thermomagnetic coefficients with increasing magnetic field strength and concentration of charged centers (i.e., the concentration of charge carriers in the conduction band) observed in mercury selenide, which cannot be explained within the framework of the "classical" theory of thermomagnetic effects, is caused by the mutual electron–phonon dragging.

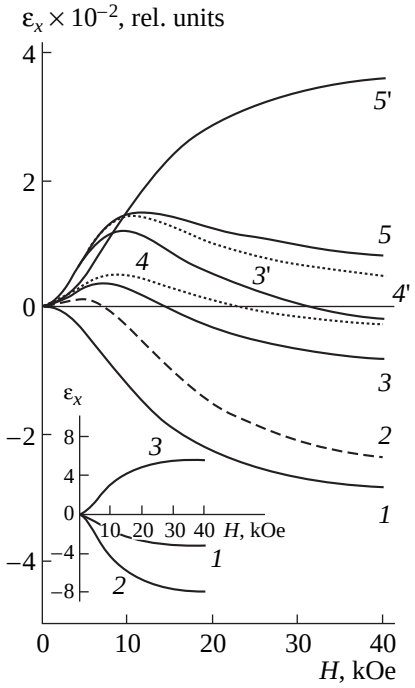

Fig. 4. Calculated plots of the dimensionless field $\varepsilon_x(T, H)$ in the longitudinal NE effect versus magnetic field strength H at various temperatures T = 20 (*1–4*); 30 (*4', 5*); 40 (*3*'); and 60 K (*5*') and electron concentrations $n = 0.5 \times 10^{18}$ cm^{-3} (*1*); 1×10^{18} cm^{-3} (*2*); 2×10^{18} cm^{-3} (*3, 3*'); 3×10^{18} cm^{-3} (*4, 4*'); and 4×10^{18} cm^{-3} (*5, 5*'). The inset shows the plots of ε_x versus H for HgSe with $n = 1 \times 10^{18}$ cm^{-3} calculated with neglect of the mutual dragging effect for T = 20 K (*1*); 30 K (*2*); and 50 K (*3*).

CONCLUSIONS

We have interpreted data for the HgSe crystals doped with various concentrations of gallium, where unusual variation of the transverse and longitudinal NE effects at sufficiently low temperatures in the region of classical magnetic field strength was observed, including a change in the sign of both NE effects and nonmonotonic field dependence of the longitudinal NE effect.

It was demonstrated that all the experimentally observed features in the dependence of the thermomagnetic coefficients on the magnetic field strength and the donor impurity concentration can be related to the mutual dragging of electrons and phonons, the role of this effect increases in semiconductors with high concentration of charge carriers in the conduction band.

It should be noted that the mutual electron–phonon dragging effect, which is so clearly manifested in the field and concentration dependence of the coefficients of the NE effects in HgSe : Ga crystals may play even greater role in the thermomagnetic properties of HgSe : Fe solid solutions. There are grounds to expect that a decrease in the level of charge carrier scattering in the conduction band on the system of spatially ordered charged impurity centers, which was observed in the latter compounds at sufficiently low temperatures [7], would lead to an increasing role of the phonon system in relaxation processes and, hence, to more pronounced manifestations of the mutual electron–phonon dragging effect.

ACKNOWLEDGMENTS

This work was supported by the INTAS Foundation, grant no. 93-3657.

REFERENCES

1. S. S. Shalyt and S. A. Aliev, Fiz. Tverd. Tela **6** (7), 1979 (1964).

2. S. A. Aliev, L. L. Korenblit, and S.S. Shalyt, Fiz. Tverd. Tela **7** (6), 1973 (1965).
3. I. N. Dubrovnaya and Yu. I. Ravich, Fiz. Tverd. Tela **8** (5), 1455 (1966).
4. V. I. Tamarchenko, Yu. I. Ravich, L. Ya. Morgovskiĭ, *et al.*, Fiz. Tverd. Tela **11** (11), 3506 (1969).
5. I. G. Kuleev, I. I. Lyapilin, A. T. Lonchakov, *et al.*, Zh. Éksp. Teor. Fiz. **106** (4), 1205 (1994); **103** (4), 1447 (1993).
6. S. S. Shalyt, V. M. Muzhdaba, and A. D. Galetskaya, Fiz. Tverd. Tela **16** (5), 1277 (1968).
7. I. G. Kuleev, I. I. Lyapilin, A. T. Lonchakov, *et al.*, Fiz. Tekh. Poluprovod. **28** (6), 937 (1994).
8. I. G. Kuleev, I. I. Lyapilin, A. T. Lonchakov, *et al.*, Semicond. Sci. Technol. **10**, 314 (1995).
9. T. Dietl and W. Szymanska, J. Phys. Chem. Sol. **39** (10), 1041 (1978).
10. A. L. Natadze and A. L. Éfros, Fiz. Tverd. Tela **4** (10), 2931 (1962).
11. L. É. Gurevich and I. Ya. Korenblit, Fiz. Tverd. Tela **6** (3), 856 (1964).
12. I. G. Lang and S. T. Pavlov, Zh. Éksp. Teor. Fiz. **63** (4), 1495 (1973).

Translated by P.P. Pozdeev

Physics of the Solid State, Vol. 42, No. 2, 2000, pp. 215–223. Translated from Fizika Tverdogo Tela, Vol. 42, No. 2, 2000, pp. 210–217.

SEMICONDUCTORS AND DIELECTRICS

Effect of Pressure and Anionic Substitution on the Electrical Properties of HgTeS Crystals

V. V. Shchennikov, A. E. Kar'kin, N. P. Gavaleshko, and V. M. Frasunyak

Institute of Metal Physics, Ural Division, Russian Academy of Sciences, ul. S. Kovalevskoĭ 18, Yekaterinburg, 620219 Russia
e-mail: phisica@ifm.e-burg.ru

Received June 24, 1999

Abstract—The resistivity ρ and the Hall constant R for the $HgTe_{1-x}S_x$ ($0.04 \le x \le 0.6$) crystals have been investigated in the temperature range 4.2–350 K in the magnetic fields B up to 14 T. The pressure dependences of the resistivity ρ have been measured at the pressures P as high as 1 GPa at temperature T = 77–300 K and magnetic field B = 0–2 T. It is found that the samples with $x \le 0.20$ exhibit a decreasing dependence $\rho(T)$ typical of zero-gap semiconductors, whereas the samples with $x \ge 0.27$ show the dependence $\rho(T)$ characteristic of semimetals. For the semiconducting crystals with $x \approx 0.20$ and $x \approx 0.14$, the temperature coefficient of $\rho(T)$ changes sign at T = 265 and T > 300 K, respectively. Under a pressure of ≈ 1 GPa, the temperature of the sign inversion decreases by ≈ 30 K. An increase in the magnetic field B and a rise in the temperature T lead to a change in the sign of the Hall constant R for the semiconducting samples, but do not affect the electronic sign of R for the semimetallic samples. The behavior of R and ρ correlates with the thermoemf data obtained at the quasi-hydrostatic pressure P up to 3 GPa. It is demonstrated that the substitution of sulfur atoms for tellurium atoms brings about an increase in the concentration of electrons and a decrease in their mobility. The transition to the wide-gap semiconductor phase is observed at P > 1–1.5 GPa. The conclusion is drawn that the semimetallic crystals $HgTe_{1-x}S_x$ with $x \ge 0.27$ and HgSe are similar in properties. © *2000 MAIK "Nauka/Interperiodica".*

At atmospheric pressure, mercury telluride, mercury selenide, and cubic mercury sulfide belong to the class of zero-gap semiconductors, in which the conduction band is immediately adjacent to the valence band [1–6]. The available experimental data allow the inference that there exists a small overlap in energy of bands $\Delta\varepsilon_t$ that provides a high concentration of charge carriers at low temperatures [1–6]. Different theoretical models that describe this overlap with allowance made for the influence of fluctuations, an acceptor band overlapping with the conduction band, or the bending of the valence band have been considered in [1–6]. A decrease in the atomic number of the anion in a series from tellurium to sulfur leads to an increase in the magnitude of the energy gap $\varepsilon_g = \varepsilon(\Gamma_6) - \varepsilon(\Gamma_8)$ between the Γ_6 and Γ_8 electron energy bands in the electronic spectrum of mercury chalcogenides and an increase in the band overlap $\Delta\varepsilon_t$ and the electron concentration brought about by this overlap [1, 4–6]. In this respect, the temperature dependences of the resistivity ρ for these crystals substantially differ from each other: the resistivity of HgTe decreases with an increase in the temperature, which is characteristic of semiconductors with zero band gap, whereas the temperature dependences of the resistivity for HgSe and β-HgS are typical of semimetals [1, 4–6].

The substitution of sulfur atoms for tellurium and selenium atoms in the anionic sublattice of HgTe and HgSe should change the electronic structure of the initial phases and, correspondingly, the electron concentration and character of the dependence $\rho(T)$ [5, 6]. Indeed, our earlier investigations of crystals in the $HgSe_{1-x}S_x$ system [7, 8] demonstrated that an increase in the sulfur content x brings about an increase in the concentration of electrons and a decrease in their mobility, and the electrical properties of crystals exhibit qualitative agreement over wide ranges of temperatures from 4.2 to 300 K and magnetic fields from 0 to 14 T. Moreover, we studied the thermoemf S and the resistivity ρ of the $HgTe_{1-x}S_x$ crystals with low sulfur content x < 0.3 under the quasi-hydrostatic pressure P up to 30 GPa [9, 10] and found the transformations, first, to the wide-gap semiconductor phase and, then, to the metallic phase. According to the available data [5, 6, 11–14], the electrical properties of the $HgTe_{1-x}S_x$ crystals with a high sulfur content were not investigated thoroughly. The purpose of the present work was to investigate the influence of the anionic substitution and hydrostatic pressure on the electrical and galvanomagnetic properties of the $HgTe_{1-x}S_x$ crystals over a wide range of compositions ($0 < x < 1$) at temperatures of 4.2–350 K in magnetic fields up to 14 T.

1. EXPERIMENTAL

The $HgTe_{1-x}S_x$ crystals were synthesized by the melting of high-purity components (99.9999%). The sample composition was determined by X-ray microanalysis on a Superprobe-JCXA-733 spectrometer. We studied the crystals with the sulfur content

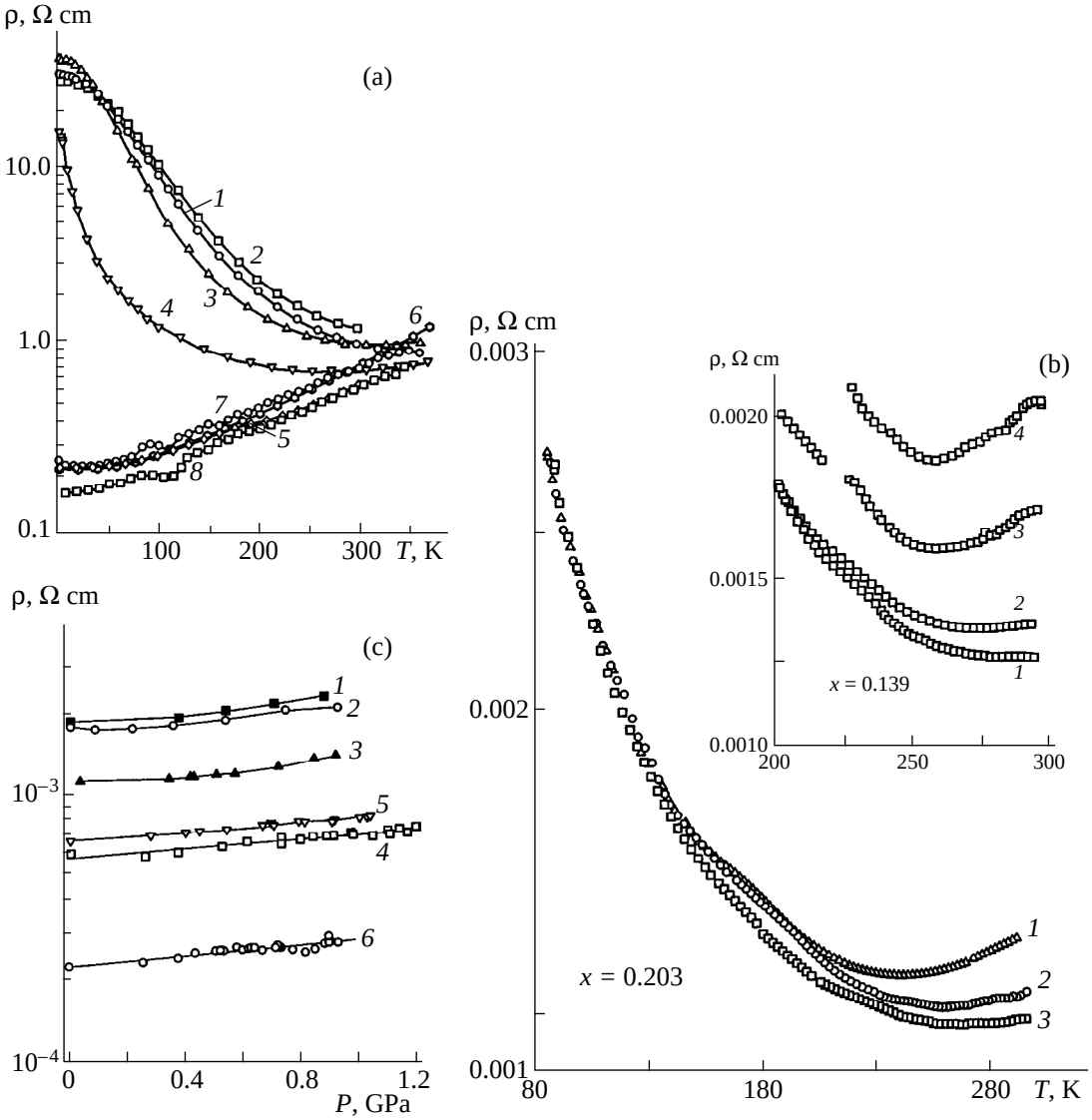

Fig. 1. Dependences of the resistivity on (a, b) the temperature and (c) the hydrostatic pressure for the $HgTe_{1-x}S_x$ samples. (a) Atmospheric pressure, sulfur content x = (*1*) 0.042, (*2*) 0.094, (*3*) 0.139, (*4*) 0.203, (*5*) 0.297, (*6*) 0.396, (*7*) 0.482, and (*8*) 0.60; (b) x = 0.203, hydrostatic pressure P, GPa: (*1*) 0.887, (*2*) 0.505, and (*3*) 0.256. The inset shows fragments of the dependences for the sample with x = 0.139 at hydrostatic pressure P, GPa: (*1*) 0.31, (*2*) 0.57, (*3*) 0.84, and (*4*) 0.89. (c) T = 293 K, sulfur content x = (*1*) 0.094, (*2*) 0.139, (*3*) 0.203, (*4*) 0.271, (*5*) 0.396, and (*6*) 0.6.

x = 0.042, 0.094, 0.139, 0.203, 0.271, 0.296, 0.397, 0.482, and 0.60. The samples intended for galvanomagnetic measurements were prepared in the form of parallelepipeds $\approx 0.5 \times 0.5 \times 5$ mm in size. Current and voltage contacts were soldered by indium to end and side faces of a parallelepiped, respectively.

The Hall constants R and the transverse magnetoresistance (MR) were measured in dc magnetic fields up to 14 T induced with an "Oxford Instruments" solenoid [15]. The experiments under hydrostatic pressure P = 0–1.2 GPa were carried out in "piston–cylinder" chambers fabricated from nonmagnetic titanium alloys. The pressures P in a kerosine–oil mixture (1 : 1) were measured using a manganin manometer with an accuracy of 0.01 GPa. As a whole, the procedure of measurements was identical to that used in the investigation of crystals in the HgSeS system [8]. The thermoelectric measurements of crystals in the pressure range 0–3.5 GPa were performed with the use of "Toroid"-type steel chambers [16] with a solid pressure-transferring medium (pyrophyllite). In this case, the pressure was determined with an error of ≈ 10% from the calibrated dependence, which was constructed according to the phase transitions in the reference compounds Bi, CdSe, etc. [8, 9]. The relative error of thermoemf measurements was equal to ≈ 20% [9, 10]. No variations in the geometric sizes of the samples with pressure [17] were taken into account.

Parameters for the $HgTe_{1-x}S_x$ samples at atmospheric pressure

x	0.042	0.094	0.139	0.203	0.271	0.296	0.397	0.482	0.60
n_0, 10^{18} cm^{-3} (B = 12 T)	–3.9	–2.7	–1.0	+0.15	+0.49	+1.0	+1.1	+2.3	+4.6
S, mV K^{-1}	–0.16	–0.17	–0.15	–0.11	–0.09	–0.08	–0.07	–0.07	–0.08
B_0, T	–	–	–	–	–93	38	29	–	–
B_1, T	–	–	–	–	–172	189	211	–	–
μ_0, m^2 V^{-1} s^{-1}	–	–	–	5.0*	6.0	2.8	2.6	1.2	0.8
μ_h, m^2 V^{-1} s^{-1} (T = 4.2 K)	0.08	0.085	0.09	0.15	–	–	–	–	–

* The value is obtained by the extrapolation of the MR data at T = 77 K.

2. RESULTS

The temperature coefficient of $\rho(T)$ changes sign when the sulfur content in the studied crystals reaches $x \approx 0.2$–0.27 (Fig. 1). For the samples with $x \approx 0.04$–0.1, the resistivity $\rho(T)$ increases with a decrease in the temperature down to ≈ 40 K, which is characteristic of zero-gap semiconductors, and with a further decrease in the temperature, remains virtually constant [1–5]. The crystals with x = 0.3–0.6 is characterized by a typical semimetallic behavior of the dependence $\rho(T) = \rho_0 + \rho_1 T^2$, where ρ_0 and ρ_1 are constants. A similar variation in the resistivity $\rho(T)$ is observed in crystals of the $HgTe_{1-x}S_x$ system, for which the temperature coefficient changes sign at larger values of $x \geq 0.6$ [18]. The sample with x = 0.20 shows the first type of the $\rho(T)$ dependence at T < 265 K and a weak increase in $\rho(T)$ at T > 265 K (Fig. 1). Under hydrostatic pressure, the transition from the semiconducting behavior of the $\rho(T)$ curve to the semimetallic dependence is observed at lower temperatures, so that the semimetallic character of the $\rho(T)$ dependence for the sample with x = 0.14 manifests itself at P > 0.5 GPa (Fig. 1b). Similar dependences $\rho(T)$ for the semimetallic crystals with $x \geq 0.27$ remain qualitatively unchanged at the pressure P up to ≈ 1 GPa. The pressure dependences of ρ at room temperature are approximately identical for the semiconducting and semimetallic samples: ρ only slightly increases with an increase in the pressure P up to ≈ 1–1.2 GPa (Fig. 1c).

The Hall effect in the semiconducting samples with x = 0.04–0.14 reverses sign with both a decrease in the temperature at magnetic field B = 12 T and an increase in the magnetic field at T = 4.2 K (Fig. 2). This behavior observed earlier for HgTe [1, 4, 5, 17] suggests that the conductivity is provided by electrons of the conduction band and also by holes of the Γ_8 valence band. The experimental dependences were described within the standard model of a two-band impurity semiconductor [19]

$$n = \frac{n_0}{2} + \left[\left(\frac{n_0}{2}\right)^2 + (4A_C A_V)^2 \exp\left(-\frac{E_g}{kT}\right)\right]^{1/2},$$
$$p = -\frac{n_0}{2} + \left[\left(\frac{n_0}{2}\right)^2 + (4A_C A_V)^2 \exp\left(-\frac{E_g}{kT}\right)\right]^{1/2}. \quad (1)$$

where n and p are the electron and hole concentrations, respectively; n_0 is the difference between the donor and acceptor concentrations; E_g is the thermal band gap in the electronic spectrum; and A_C and A_V are the densities of states in the conduction and valence bands, respectively. For the HgTe crystal ($E_g \approx 0$), formulas (1) are applicable in the range of intrinsic conductivity at T > 60 K [1, 5]. With allowance made for the contribution of several bands, the kinetic coefficients take the form [20]

$$R = \frac{\langle R_\sigma^2 \rangle}{\langle \sigma \rangle^2 + (\langle R_\sigma^2 \rangle B)^2},$$
$$\rho = \frac{\langle \sigma \rangle}{\langle \sigma \rangle^2 + (\langle R_\sigma^2 \rangle B)^2}, \quad (2)$$
$$\langle \sigma \rangle = \sum_i \frac{\sigma_i}{1 + (R_i \sigma_i B)^2}, \quad \langle R_\sigma^2 \rangle = \sum_i \frac{R_i \sigma_i^2}{1 + (R_i \sigma_i B)^2},$$

where σ_i and R_i are the conductivities and the Hall constants of individual bands, respectively. The $R(B)$ and $R(T)$ dependences were fitted to the theoretical curves by varying the parameters n_0 and $A = 4A_C A_V$. For all the samples, it was assumed that $E_g \approx 0$ [1–6, 17]. In the case when the experimental curves could not be described within the two-band model, the contribution from charge carriers of three bands was taken into consideration. The parameters of charge carriers, which were evaluated for the studied samples according to the above procedure, are listed in the table. The n_0 and A

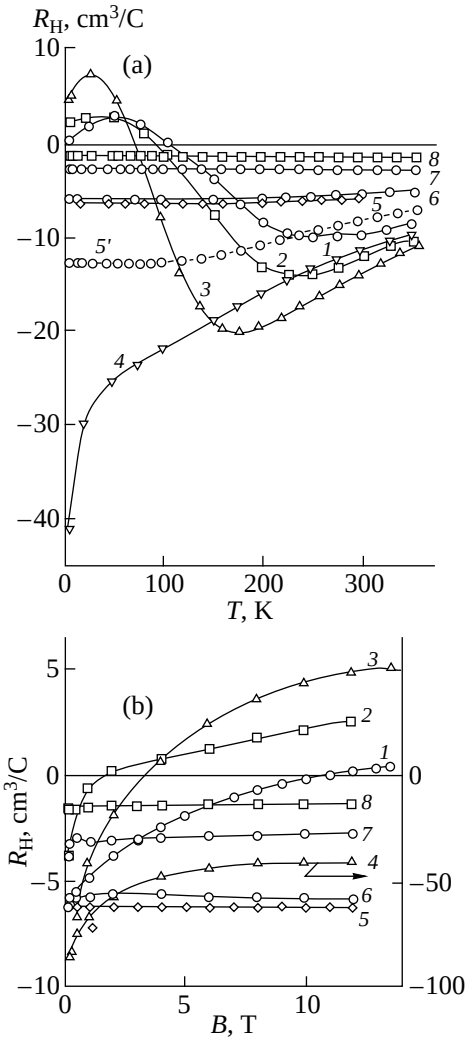

Fig. 2. Dependences of the Hall constant on (a) the temperature in the magnetic field $B = 12$ T and on (b) the magnetic field at $T = 4.2$ K for the $HgTe_{1-x}S_x$ samples with the sulfur content x = (*1*) 0.042, (*2*) 0.094, (*3*) 0.139, (*4*) 0.203, (*5*') 0.271, (*5*) 0.297, (*6*) 0.396, (*7*) 0.482, and (*8*) 0.60.

parameters obtained by the fitting of the $\rho(T)$ curves (Fig. 1) with the use of formulas (1) and (2) differ by ≈20% from the parameters determined from the Hall effect.

The experimental dependences of the Hall constant R for the semimetallic samples ($x \geq 0.27$) can be described with the inclusion of only one band. In these crystals, the n concentration increases with an increase in the sulfur content, which agrees with a higher electron concentration in the HgS cubic phase as compared to the electron concentration in HgTe [5, 6]. For the semiconducting samples, a decrease in $R(T)$ at high temperatures reflects an increase in the concentration of intrinsic charge carriers $n_{int} \sim T^{3/2}$ [1–6] when this concentration is higher than the concentration of impurity electrons. At low temperatures, when n_{int} is smaller than the latter concentration, the value of $R(T)$ remains unchanged [1–5]. It is evident that, in the sample with $x = 0.20$, for which the saturation of $R(T)$ is not observed, the concentration of impurity electrons is small. The inversion of the R sign for the samples with $x = 0.04$–0.14 indicates that holes become the majority carriers in a magnetic field of 12 T (at $T = 4.2$ K). In a weak field, the electron contribution remains predominant.

The fact that the conductivity in the semiconducting ($x \leq 0.20$) and semimetallic ($x \geq 0.27$) samples at low temperatures is provided by charge carriers of different bands becomes evident from the dependences of the magnetoresistance on the magnetic field (Fig. 3). A strong magnetoresistance effect was observed in the semimetallic samples with a high electron mobility. In weak magnetic fields, the magnetoresistance effect was quadratic in B and, then, became a linear function of B. The Shubnikov–de Haas quantum oscillations were observed in these crystals at a temperature of 4.2 K (Fig. 3b). For the semiconducting samples, the dependence of the magnetoresistance was weakly parabolic (Fig. 3). The experimental magnetoresistance curves were fitted using the following relationship [5, 8, 20]:

$$\rho(B) = \rho_1(B)(1 + \rho_2(B)), \qquad (3)$$

where $\rho_1(B)$ is monotonic dependence (2), and $\rho_2(B)$ is the oscillating term

$$\rho_2(B) = g\exp(-B_1/B)\sin(B_0/B + \varphi), \qquad (4)$$

which takes into consideration the dependence of the oscillation amplitude on the magnetic field and the oscillation periodicity [5, 20, 21]. Here, g, B_1, B_0, and φ are the fitting parameters. The B_1 parameter accounts for the thermal and defect-induced smearing of oscillations. The oscillation period B_0^{-1} is determined by the section of the Fermi surface in the plane perpendicular to the magnetic field $S_F = 2\pi eB_0/h$. The found value was used to estimate the electron concentrations, which, for the studied samples, are in good agreement with those obtained from the Hall effect (see table).

The magnetoresistance was measured under hydrostatic pressure in the temperature range 77–300 K. The magnetoresistance of the samples with $x = 203$ and 0.139 increases with an increase in the pressure P (Figs. 3c, 3d). According to the data obtained from the Hall effect (Fig. 2), the conductivity of the former sample is predominantly contributed by electrons, whereas the conductivity of the latter samples at low temperatures also involves the hole contribution. The electron mobilities μ, which were estimated from the magnetoresistance of these samples at high temperatures, are in reasonable agreement with the Hall electron mobilities $\mu_H = R/\rho$ (Figs. 4a, 4b) with allowance made for the probable mechanisms of scattering from optic and acoustic lattice vibrations [20, 21]. The μ mobilities determined from the magnetoresistance of the crystal with $x = 0.14$ at nitrogen temperatures (Fig. 4b) are less

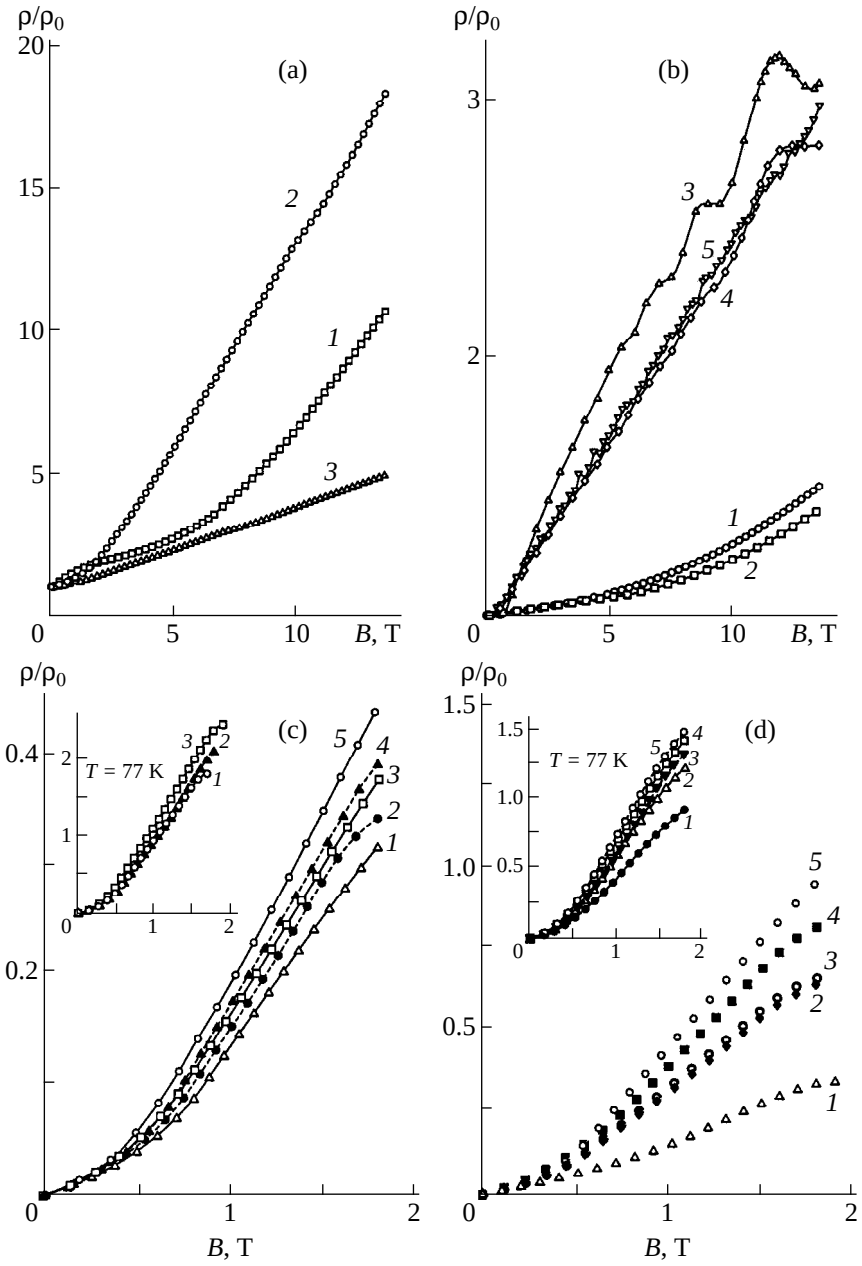

Fig. 3. Dependences of the transverse magnetoresistance on the magnetic field B for the $HgTe_{1-x}S_x$ samples at T = (a, b) 4.2 and (c, d) 293 K. (a) Sulfur content x = (*1*) 0.203, (*2*) 0.271, and (*3*) 0.482. (b) x = (*1*) 0.042, (*2*) 0.094, (*3*) 0.297, (*4*) 0.396, and (*5*) 0.60. (c) x = 0.203, hydrostatic pressure P, GPa: (*1*) 0.165, (*2*) 0.293, (*3*) 0.515, (*4*) 0.887, and (*5*) 0.924. (c, inset) T = 77 K, x = 0.203, hydrostatic pressure P, GPa: (*1*) 0.256, (*2*) 0.505, and (*3*) 0.887. (d) x = 0.139, hydrostatic pressure P, GPa: (*1*) 0.086, (*2*) 0.311, (*3*) 0.572; (*4*) 0.84, and (*5*) 0.885. (d, insert.) T = 77 K.

than the electron mobility and characterize the total contribution of electrons and holes to the effect (at the same concentrations, $\mu \approx (\mu_h/\mu_e)^{1/2}$ [21]).

For the HgTeS semimetallic samples, as for HgSeS [8], the Hall mobility $\mu_H = R/\rho$ over the entire range of temperatures is well described by the dependence $\mu_H = (\mu_0^{-1} + aT^2)^{-1}$, where a is the constant (Fig. 4). By using the ratio between the mobilities determined from the magnetoresistances at nitrogen and room temperatures (Fig. 3d), it is possible to extrapolate the high-temperature portion of the $\mu_H(T)$ dependence for the sample with x = 0.203 to the low-temperature range. The temperature dependence of μ_H for this crystalline compound and the other semiconducting crystals, as for the semimetallic crystals, is described by the formula given above (Fig. 4). The R/ρ values deviate from this dependence at low temperatures when the holes substantially contribute to the Hall effect. The partial contributions of electrons and holes to the Hall and magnetoresis-

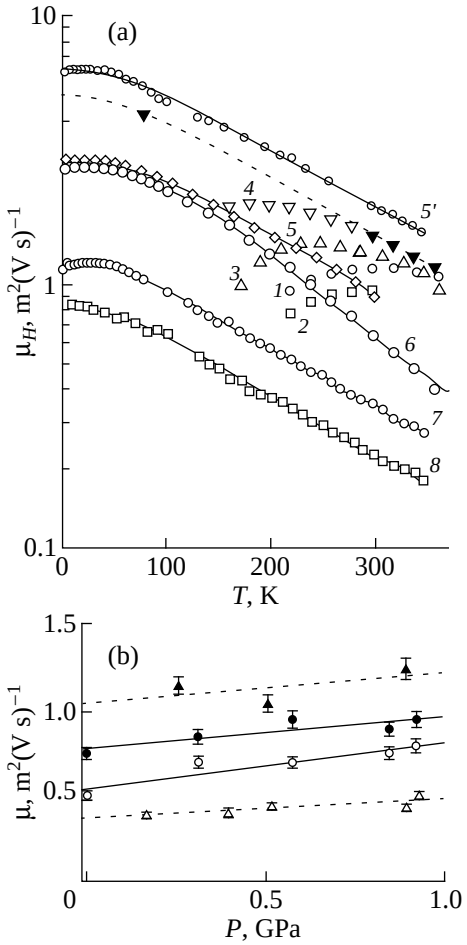

Fig. 4. Dependences of the electron mobility on (a) the temperature and (b) the hydrostatic pressure for the $HgTe_{1-x}S_x$ samples. (a) Atmospheric pressure, points are the experimental Hall mobilities, solid lines demonstrate the approximation (see text), numbering of curves corresponds to that in Fig. 1a, and the dashed line represents the fitting from the μ mobilities evaluated from the magnetoresistance for the sample with $x = 0.203$ (closed triangles). (b) $T = 293$ (open symbols) and 77 K (closed symbols), $x = 0.203$ (triangles) and 0.149 (circles).

tance effects significantly differ: the magnetoresistance is governed by the most mobile carriers (in our case, electrons), whereas the R constant is determined by the carriers with a high concentration and conductivity [20, 21]. At 4.2 K, in the field $B = 12$ T, the μ_H mobilities for the samples with $x = 0.042$ and 0.094 are ≈ 50 times less than the μ_0 mobility of electrons in the semimetallic crystals (see table) and characterize the mobility of holes ($R > 0$) and heavy electrons (at $B \approx 0$). In the study of the Hall effect for the HgTe crystal in a magnetic field of ≈ 1 T, Lombos *et al.* [18] approximated the ratio between the hole and electron mobilities $b = \mu_h/\mu_e$ by the formula $b(T) = 20 + 0.06\ T$. The μ_H mobilities are ≈ 1.5 times as high as the mobilities estimated from the magnetoresistance, which corresponds to the calculated ratio upon scattering by impurity ions [21].

The anionic substitution also strongly affects the pressure dependence of the thermoemf S for the HgTeS crystals (Fig. 5). In the presence of electron and hole contributions, the thermoemf S is defined as [20, 21]

$$S = (\sigma_n/\sigma S_n + \sigma_p/\sigma S_p), \qquad (5)$$

where σ_n and σ_p are the electron and hole conductivities, respectively; $\sigma = \sigma_n + \sigma_p$ is the total electrical conductivity; $S_n = k/e(g_n + \zeta/kT)$ and $S_p = k/e(g_p + \zeta_p/kT)$ are the electron and hole components of the thermoemf S; ζ and ζ_p are the corresponding chemical potentials; and g_n and g_p are the coefficients determined by the parameters of electron and hole scattering [20, 21]. The thermoemf $S(T)$ for the samples with $x \le 0.042$ decreases in magnitude with an increase in P. At a certain pressure, the thermoemf S of semiconducting crystals changes sign, which suggests an increase in the hole contribution to the conductivity. Kwan *et al.*, [22] observed a decrease in $|S|$ for the HgTe crystals at the hydrostatic pressure P up to 1.2 GPa in the case when the electronic sign of S remained unchanged, which can be associated with the high electron concentration. In the study of the Hall effect in the HgCdTe crystals, Piotrzkowski *et al.* [23] also observed an increase in the hole contribution to the conductivity under pressure and revealed an enhancement of this contribution in samples with $\varepsilon_g > 0$. For the semimetallic crystals, the absolute value of S somewhat increases with an increase in the pressure P. The observed decrease in $|S|$ with an increase in the sulfur content correlates with both the increase in electron concentration, which was found from the data on the Hall effect (Fig. 2), and the decrease in $|S|$ [20, 21].

A drastic increase in the resistivity ρ at $P = 0.8$–1.5 GPa corresponds to the onset of structural transformation to the cinnabar phase [9, 10, 24–30] (an increase in $|S|$ manifests itself at a higher pressure due to the shunting effects of initial phase inclusions [31]). The resistivity of the new phase increases with an increase in x, because the band gap increases [1, 5, 6, 9, 10], and the thermoemf S of the "semiconducting" ($x \le 0.20$) and "semimetallic" ($x \ge 0.27$) samples is opposite in sign. The hole-type conductivity of the high-pressure phases in HgTe and alloys on its base is corroborated by the data on the Hall effect [26–28].

An increase in the sulfur content x leads to a decrease in the pressure of the onset of structural transformation. The theoretical calculations [32] and the experimental data for HgTe-based compounds [25–30] demonstrate that, compared to the cationic substitution, the substitution of atoms in the anionic sublattice of the A_2B_6 crystals produces a weaker effect on the pressure of the phase transition. Note also that the cationic and anionic substitution in HgTe-based crystals more weakly affects the pressure of the phase transformation to the cinnabar structure (according to the data of the present work and [9, 10, 28, 33]) as compared to a similar substitution in HgSe-based crystals, in which this pressure increases or decreases more than two times [7, 10, 25]. In solids, the

pressure of the onset of phase transformations due to shear stresses is less than that under hydrostatic conditions [24–30], at which the initial phase is stable up to a pressure of ≈ 1 GPa (Figs. 1, 5).

3. DISCUSSION

The composition dependence of the electrical properties for the $HgTe_{1-x}S_x$ crystals is in good agreement with the experimental data for HgTe and β-HgS [3–6, 11–14]. From the optical spectra of the $HgTe_{1-x}S_x$ crystals, it follows that an increase in x results in a monotonic shift of electron energy bands [13], which should be attended by changes in the electrical properties of materials. Furthermore, the crystal and electronic structures are affected by the disordered distribution of substituting atoms [34, 35]. According to the calculations [34], in HgCdTe and HgZnTe, the difference in electronic configurations of the original and substituting cations and also the mismatch of their sizes lead to splitting the peak of the density of states in the valence band and at the bottom of conduction band. The vacancy concentration in mercury chalcogenide crystals can change upon anionic and cationic substitution [35], which also should influence the concentration of impurity electrons [1, 3–6].

The experimental dependences indicate three types of charge carriers whose partial contributions to the conductivity are determined by the level of the chemical potential ζ. For the samples with $x \le 0.14$, at 4.2 K, ζ lies in the valence band, and holes and heavy electrons (in the impurity energy band or in the region of valence band with the positive curvature [1–6]) are involved in the conductivity. At room temperature, ζ is boosted to the conduction band, which provides the contribution of mobile electrons (Figs. 1–3). At $x \ge 0.27$, ζ resides in the conduction band, and, as in HgSeS [8], electrons are charge carriers. The parameters of charge carriers were evaluated by the fitting of experimental dependences with different degrees of accuracy. This procedure led to close values of the electron mobility μ(T) in the semiconducting and semimetallic crystals (Fig. 4). The μ mobilities of holes and the n_0 parameter were estimated with a lower accuracy. The n_0 parameter is negative (acceptors predominate) at low values of x, and it is positive at $x \ge 0.2$. The dependence of the n_0 parameter on x correlates with the behavior of $R(B)$, $R(T)$, and $S(T)$ and suggests a decrease in the hole contribution to the conductivity with an increase in the sulfur content. The A parameter proportional to the effective masses of electrons and holes was only qualitatively estimated by the fitting procedure. As the sulfur content x increases, the A parameter decreases (this corresponds to a decrease in the effective mass) and reaches a minimum at the sulfur content $x = 0.27$, at which the electron mobility μ is maximum. (In [12], the maximum value of μ was observed for the sample with $x = 0.4$.) The parameters of heavy electrons can be esti-

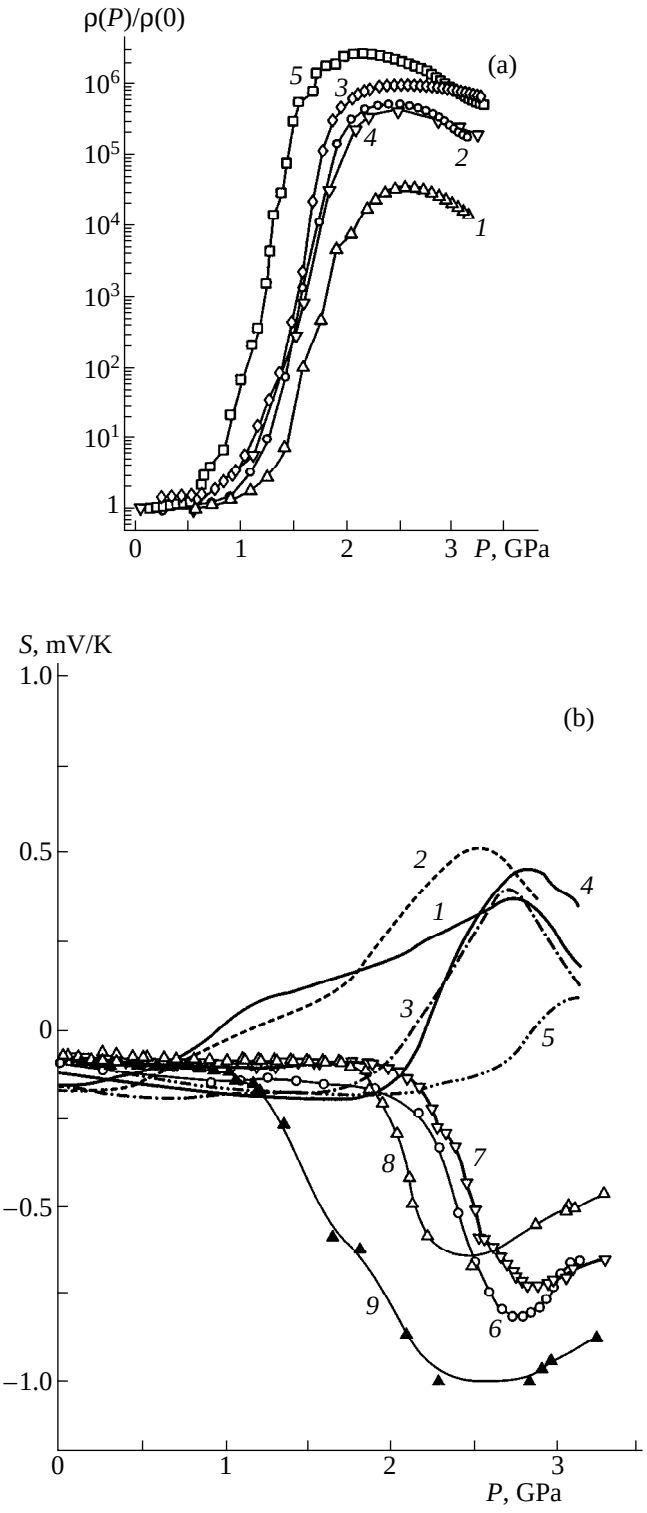

Fig. 5. Dependences of (a) the resistivity and (b) the thermoemf on the hydrostatic pressure for the $HgTe_{1-x}S_x$ samples at T = 293 K. Sulfur content x: (a) (*1*) 0.203, (*2*) 0.297, (*3*) 0.396, (*4*) 0.482, and (*5*) 0.60 and (b) (*1*) 0, (*2*) 0.042, (*3*) 0.094, (*4*) 0.139, (*5*) 0.203, (*6*) 0.297, (*7*) 0.396, (*8*) 0.482, and (*9*) 0.60. Curves *1–5* are taken from [9], and the points are the data of the present work.

mated from the data obtained in the present work with a large error.

By and large, the experimental composition and pressure dependences obtained for the $HgTe_{1-x}S_x$ crystals are consistent with the model of electronic structure that is currently accepted for mercury chalcogenides [1–6]. Actually, an increase in the concentration of electrons (Fig. 2) and a decrease in their mobility (Fig. 4), with an increase in the sulfur content x, can be explained by an increase in $\Delta\varepsilon_t$ and $|\varepsilon_g|$ and, hence, by an increase in the effective mass of electrons [1, 4, 5]. (A decrease in the mobility μ can also be partly caused by the scattering from nonuniformly distributed substituting atoms.) The shift of the n_0 parameter toward the positive values with an increase in x corresponds to an expected increase in the band overlap $\Delta\varepsilon_t$ in going from HgTe to β-HgS [1–6]. An increase in the electron mobility μ under pressure (Figs. 3, 4) is in agreement with the decrease in ε_g and in the effective mass of electrons, which follows from the model [1, 4] and is confirmed experimentally ($\partial|\varepsilon_g|/\partial P$ = –0.12 eV/GPa [1, 4–6]). In the open-gap semiconductors $Hg_{1-g}Cd_xTe$ ($x \geq 0.27$) and $Hg_{1-x}Zn_xTe$ ($x = 0.15$) with the reverse location of the Γ_8 and Γ_6 electron energy bands, the electron mobility μ, on the contrary, decreases [28, 33], because ε_g increases with an increase in the pressure P ($\partial\varepsilon_g/\partial P$ = 0.12 eV/GPa) [1, 4–6]. Since the concentration of intrinsic electrons in the $HgTe_{1-x}S_x$ crystals at $x \leq 0.20$ decreases with an increase in the pressure P (owing to a decrease in the effective mass), the partial contribution of "impurity" electrons to the conductivity increases, which can provides an explanation for an increase in the positive slope of the $\rho(T)$ curves (Fig. 1c). Note that, up to now, there has been no unambiguous interpretation for the origin of the band responsible for impurity electrons [1, 4–6]. This is likely the reason why for the $HgTe_{1-x}S_x$ crystals, the correct description of a similar change of the $\rho(T)$ dependence from semiconducting to semimetallic behavior with an increase in x has failed in the framework of the above model [18].

At room temperature, the inversion of the Γ_8 and Γ_6 electron energy bands (determined from the inflection point in the pressure dependences of R) is observed at $P = 0$ in the $Hg_{1-g}Cd_xTe$ crystals with $x \approx 0.1$ [1–6] and at $P \approx 0.9$ GPa in HgTe [28]. This agrees with the value and the baric coefficient of ε_g [1–6]. It is of interest that the thermoemf of the HgTe crystal in the vicinity of this pressure changes sign (see [30] and Fig. 5). For the $HgCd_xTe_{1-x}$ and $HgMg_xTe_{1-x}$ crystals, with an increase in $x \longrightarrow 0.1$, the inflection point in the $R(P)$ dependence and the change in sign of $S(P)$ are observed at lower pressures $P \longrightarrow 0$ in accord with a decrease in $|\varepsilon_g| \longrightarrow 0$ [28, 30]. By contrast, for crystals in the $HgTe_{1-x}S_x$ system, $|\varepsilon_g|$ increases with an increase in x [5, 6], and S changes sign at higher pressures P (Fig. 5). In the $HgTe_{1-x}S_x$ semimetallic crystals with $x > 0.27$, variations in the pressure P, temperature T, and magnetic field B do not change the sign of the thermoemf S, and these crystals in their properties (Figs. 1–5) are analogs of the HgSe and HgSeS crystals [7, 8].

ACKNOWLEDGMENTS

This work was supported by the Russian Foundation for Basic Research (project no. 98-03-32656) and the State Scientific and Technical Program "Physics of Quantum and Wave Processes," ("Statistical Physics," project no. VIII-8).

REFERENCES

1. I. M. Tsidil'kovskiĭ, *Zero-Gap Semiconductors—A New Class of Materials* (Nauka, Moscow, 1986).
2. A. A. Abrikosov and S. D. Beneslavskiĭ, Zh. Éksp. Teor. Fiz. **59** (4), 1280 (1970).
3. B. L. Gel'mont and M. I. D'yakonov, Zh. Éksp. Teor. Fiz. **62** (2), 713 (1972).
4. B. L. Gel'mont, V. I. Ivanov-Omskiĭ, and I. M. Tsidil'kovskiĭ, Usp. Fiz. Nauk **120** (3), 337 (1976).
5. I. M. Tsidil'kovskiĭ, *Electrons and Holes in Semiconductors* (Nauka, Moscow, 1972).
6. N. N. Berchenko, V. E. Krevs, and V. G. Sredin, *Semiconducting Solid Solutions and Their Applications* (Voenizdat SSSR, Moscow, 1982).
7. V. V. Shchennikov, N. P. Gavaleshko, V. M. Frasunyak, *et al.*, Fiz. Tverd. Tela (S.-Peterburg) **37** (8), 2398 (1995).
8. V. V. Shchennikov, A. E. Kar'kin, N. P. Gavaleshko, *et al.*, Fiz. Tverd. Tela (S.-Peterburg) **39** (10), 1717 (1997).
9. V. V. Shchennikov, N. P. Gavaleshko, and V. M. Frasunyak, Fiz. Tverd. Tela (S.-Peterburg) **37** (11), 3532 (1995).
10. V. V. Shchennikov, V. I. Osotov, N. P. Gavaleshko, *et al.*, in *High Pressure Science and Technology*, Ed. by W. A. Trzeciakowski (World Sci., Singapore, 1996), pp. 493–495.
11. E. I. Nikol'skaya and A. R. Regel', Zh. Tekh. Fiz. **25** (8), 1347 (1955).
12. E. I. Nikol'skaya and A. R. Regel', Zh. Tekh. Fiz. **25** (8), 1352 (1955).
13. B. F. Bilen'kiĭ, V. G. Savitskiĭ, and A. K. Filatova, Ukr. Fiz. Zh. (Russ. Ed.) **18** (10), 1729 (1973).
14. R. Zallen and M. Slade, Solid State Commun. **8** (16), 1291 (1970).
15. A. E. Kar'kin, V. V. Shchennikov, B. N. Goshchitskiĭ, *et al.*, Zh. Éksp. Teor. Fiz. **113** (5), 1787 (1998).
16. L. G. Khvostantsev, L. F. Vereshchagin, and N. M. Uliyanitskaya, High Temp.–High Press. **5** (3), 261 (1973).
17. A. J. Miller, G. A. Saunders, Y. K. Yogurtcu, *et al.*, Philos. Mag. A **43** (6), 1447 (1981).
18. B. A. Lombos, E. Y. M. Lee, A. L. Kipling, *et al.*, J. Phys. Chem. Solids **36** (11), 1193 (1975).
19. W. Paul and D. M. Warschauer, in *Solids under Pressure*, Ed. by W. Paul and D. M. Warschauer (McGraw-Hill, New York, 1963).

20. P. S. Kireev, *Physics of Semiconductors* (Vysshaya Shkola, Moscow, 1975).
21. K. Seeger, *Semiconductor Physics* (Springer-Verlag, Vienna, 1973; Mir, Moscow, 1977).
22. C. C. Kwan, J. Basinsky, and E. Burstain, Phys. Status Solidi B **48,** 699 (1971).
23. R. Piotrzkowski, S. Porowski, Z. Dziuba, *et al.*, Phys. Status Solidi **8,** K135 (1965).
24. J. Blair and A. L. Smith, Phys. Rev. Lett. **7** (4), 124 (1961).
25. I. M. Tsidil'kovskiĭ, V. V. Shchennikov, and N. G. Gluzman, Fiz. Tverd. Tela (Leningrad) **24** (9), 2658 (1982).
26. G. D. Pitt, J. H. McCartney, J. Lees, *et al.*, J. Phys. D: Appl. Phys. **5** (7), 1330 (1972).
27. J. H. Morrissy, G. D. Pitt, and M. K. R. Vyas, J. Phys. C: Solid State Phys. **7** (1), 113 (1974).
28. S. Narita, M. Egawa, K. Suizu, *et al.*, J. Appl. Phys. **2** (3), 151 (1973).
29. A. Lacam, J. Peyronneau, L. J. Engel, *et al.*, Chem. Phys. Lett. **18** (1), 129 (1973).
30. V. V. Shchennikov, N. P. Gavaleshko, and V. M. Frasunyak, Fiz. Tverd. Tela (Leningrad) **35** (2), 389 (1993).
31. V. V. Shchennikov, Fiz. Met. Metalloved. **67** (1), 93 (1989).
32. J. A. Majewski and P. Vogl, Phys. Rev. Lett. **57** (11), 1366 (1986).
33. J. C. Gonthier, A. Raymond, J. L. Robert, *et al.*, Semicond. Sci. Technol. **5** (3S), S217 (1990).
34. S.-H. Wei and A. Zunger, Phys. Rev. B: Condens. Matter **43** (2), 1662 (1991).
35. M. A. Berding, A. Sher, and A.-B. Chen, J. Appl. Phys. **68** (10), 5064 (1990).

Translated by O. Borovik-Romanova

Physics of the Solid State, Vol. 42, No. 2, 2000, pp. 224–229. Translated from Fizika Tverdogo Tela, Vol. 42, No. 2, 2000, pp. 218–223.

SEMICONDUCTORS AND DIELECTRICS

A Model of Hopping and Band DC Photoconduction in Doped Crystals

N. A. Poklonskiĭ and S. Yu. Lopatin

Belarus State University, Leningradskaya ul. 14, Minsk, 220080 Belarus
e-mail: Poklonski@phys.bsu.unibel.by

Received March 18, 1999; in final form, July 6, 1999

Abstract—Expressions for the screening length and the ambipolar diffusion length are derived, for the first time, for the case where hopping conduction and band conduction coexist in semiconductors with hydrogen-like impurities. A method is proposed for calculating the diffusion coefficient of electrons (holes) hopping between impurity atoms from data on the Hall effect, in the case where the hopping and band conductivities are equal. An interpretation is given of available experimental data on hopping photoconduction between acceptors (Ga) and donors (As) in *p*-Ge at $T = 4.2$ K doped by a transmutation method. It is shown that the relative magnitude of the mobilities of electrons hopping between donors and holes hopping between acceptors can be found from the hopping photoconductivity measured as a function of the intensity of band-to-band optical carrier excitation. © *2000 MAIK "Nauka/Interperiodica".*

1. Conventional methods for describing photoelectrical phenomena in crystals [1–3] take no account of the hopping mechanism of electron transport. At the same time, it is electron (hole) hopping between impurity atoms that determines the charge transfer at low temperatures, where the electron concentration in the conduction band (*c*-band) and the hole concentration in the valence band (*v*-band) are negligibly small.

Since its discovery [4, 5], the hopping photoconduction has been studied extensively [6, 7], for the most part in weakly compensated crystalline semiconductors, in which, when carriers are generated by light corresponding to the impurity absorption region, the A^+-band (D^--band) conductivity is dominant—holes (electrons) hop between neutral acceptors (donors) [7, 8]. The photoelectric phenomena in such semiconductors were treated under the assumption that hydrogen-like impurities of one kind may be in three charge states, –1, 0, and +1. For instance, the energy levels of boron atoms were assumed [7, 8] to form two energy bands,[1] A^0 and A^+, in the forbidden band of Si. In terms of the model proposed in [9], the fact that the hopping photoconductivity in Si : B decreases when the intensity of exciting light increases was explained by the complete ionization of A^0 centers (neutral boron atoms) and the formation of A^+ centers (positively charged B atoms) [8].

At the same time, only a qualitative explanation was given of experimental data [5] on hopping photoconductivity in partially compensated *p*-Ge, in which, when illuminated by low-intensity light corresponding to fundamental absorption in Ge, the A^+ (D^-) impurity centers are not involved in the process.

The objective of this paper is to describe the screening of an external electrostatic field and the electron (hole) diffusion including their hopping between immobile hydrogen-like impurity atoms in photoexcited covalent crystals.

First, we consider the linear response of an *n*-type semiconductor to an electric field in the case where combined, band and hopping, electron transport takes place. Then we calculate the changes in screening length and diffusion length caused by light illumination that corresponds to the impurity absorption and excites electrons from a donor level to the *c*-band. And, finally, we describe the hopping dc photoconduction in *p*-Ge characterized by the transfer of both holes from neutral to negatively charged acceptors (Ga) and electrons from neutral to positively charged donors (As). The light illumination is assumed to change the carrier concentration, but their mobility remains unchanged.

2. Let us consider a crystalline semiconductor having electrons with equilibrium concentration n in the *c*-band. The concentration of donors is $N = N_0 + N_+$ and that of acceptors is KN, where K is the degree of compensation of donors by acceptors; $n + KN = N_+$ is the electrical neutrality condition. Here and henceforth, N is the concentration of the majority doping impurity. We assume that donors in the (0) and (+1) charge states exchange electrons via the *c*-band or through thermally activated tunneling (hopping).

According to [9, 10], the concentration of electrons hopping between donors is $N_h = N_0N_+/N$. At the same time, according to [11], N_h is equal to the concentration of those donors in the (0) and (+1) charge states that are

[1] In heavily doped, weakly compensated semiconductors, in addition to A^+ (D^-) impurity levels, there are also long-lived excited states of hydrogen-like acceptors (donors) [6].

mutually closest to each other.[2] The mobility M_h of hopping electrons exponentially increases with a decrease in the mean distance between donors and determines the temperature dependence of the conductivity $\sigma_h = qN_hM_h$, where q is the absolute value of the electronic charge.

In the hydrodynamic approximation, the steady-state band [1–3] and hopping [9, 10] charge transfer and the generation and recombination of carriers are described by the set of equations

$$\frac{d(\delta n)}{dx} = -\frac{\mu_n}{D_n}(n+\delta n)E + \frac{j_n}{qD_n},$$

$$\frac{d(\delta N_+)}{dx} = \frac{M_h}{D_h}\frac{(N_0+\delta N_0)(N_+ + \delta N_+)}{N}E - \frac{J_h}{qD_h},$$

$$\frac{dE}{dx} = \frac{q}{\varepsilon}(\delta N_+ - \delta n), \qquad (1)$$

$$\frac{dj_n}{dx} = q\alpha(n+\delta n)(N_+ + \delta N_+) - q\beta(N_0 + \delta N_0),$$

$$\frac{dJ_h}{dx} = -\frac{dj_n}{dx},$$

where δn, δN_0, and $\delta N_+ = -\delta N_0$ are the deviations of the corresponding concentrations from their equilibrium values; E is the external electric field in the crystal; x is the coordinate; j_n is the electron current density in the c-band [1–3] with mobility μ_n and diffusion coefficient D_n; J_h is the current density of electrons hopping between donors [9, 10] and characterized by mobility M_h and diffusion coefficient D_h; $\varepsilon = \varepsilon_r\varepsilon_0$ is the static dielectric permittivity of the crystal lattice ($\varepsilon_r = 15.4$ for Ge); α is a coefficient characterizing the electron capture from the c-band by a donor in the (+1) charge state; and $\beta = \alpha n N_+/N_0$ is the coefficient characterizing the electron excitation from a neutral-donor level into the c-band caused by thermal atomic vibrations or equilibrium background radiation [1–3].

According to [1, 10], the ratio of the diffusion coefficient of electrons to their mobility is $D_n/\mu_n = D_h/M_h = \xi k_BT/q$, where k_BT is the thermal energy. The parameter $\xi \geq 1$ characterizes the influence of fluctuations of the electrostatic potential in the crystal on the electronic states; $\xi = 1$ for a nondegenerate electron gas in the c-band [13] and for a donor band whose width is smaller than, or of the order, of the thermal energy [14].

In the case of small deviations from the equilibrium state ($\delta n/n \ll 1$ and $\delta N_+/N_+ \ll 1$), the set of equations (1) can be linearized and its solution, according to [15], has the form

$$\begin{pmatrix}\delta n\\ \delta N_+\\ E\\ j_n\\ J_h\end{pmatrix} = C_1\begin{pmatrix}-1\\ N_h/N_+\\ \lambda_1\xi k_BT/(qn)\\ 0\\ 0\end{pmatrix}\exp(\lambda_1 x)$$

$$+ C_2\begin{pmatrix}-1\\ -N_h/N_+\\ \lambda_1\xi k_BT/(qn)\\ 0\\ 0\end{pmatrix}\exp(-\lambda_1 x) + C_3\begin{pmatrix}A_1\\ A_2\\ A_3\\ A_4\\ A_5\end{pmatrix}\exp(\lambda_3 x) \qquad (2)$$

$$+ C_4\begin{pmatrix}-A_1\\ -A_2\\ A_3\\ A_4\\ A_5\end{pmatrix}\exp(-\lambda_3 x) + C_5\begin{pmatrix}0\\ 0\\ \xi k_BT/q^2\\ nD_n\\ N_hD_h\end{pmatrix},$$

where the coefficients C_1, C_2, C_3, C_4 and C_5 are determined from the boundary conditions

$$A_1 = \frac{D_h\lambda_3(\alpha\varepsilon\xi k_BTN_+ - q^2D_nN_h)}{q\xi k_BT\alpha N_+},$$

$$A_2 = \frac{D_n\lambda_3(\alpha\varepsilon\xi k_BTN_+ - q^2D_hN_h)}{q\xi k_BT\alpha N_+},$$

$$A_3 = q(D_n - D_h), \quad A_4 = -A_5 = \varepsilon q D_nD_h(\lambda_3^2 - \lambda_1^2).$$

The nonzero characteristic numbers $\lambda_1 = -\lambda_2$ and $\lambda_3 = -\lambda_4$ are real; hence, the original set of differential equations (1) and the linearized one have the same solutions in the vicinity of the equilibrium point.

If $j_n = J_h = 0$ (i.e., $C_3 = C_4 = C_5 = 0$) and $E \neq 0$, from (2) we find the screening length L_s (the penetration depth of an electrostatic field into the semiconductor)

$$L_s = \lambda_1^{-1} = \left[\frac{\varepsilon\xi k_BT}{q^2(n+N_h)}\right]^{1/2}. \qquad (3)$$

When the electron concentration in the c-band is much lower than that of the electrons hopping between donors [$n \ll N_h \approx K(1-K)N$] and the donor band width is much smaller than the thermal energy ($\xi = 1$), from (3) and the electric neutrality condition $N_+ = n + KN \approx KN$, it follows [16, 17] that $L_s^2 = \varepsilon k_BT/q^2(1-K)KN$.

In (2), the characteristic number λ_3 determines the ambipolar diffusion length of electrons in the c-band

[2] Two particles (not necessarily distinguishable [12]), belonging to a collection of particles characterized by a random (Poisson) distribution over a crystal, are each other's nearest neighbors if they are mutually closest to each other.

and of electrons hopping between donors in the (0) and (+1) charge states (for $j_n \neq 0$ and $J_h \neq 0$)

$$L_d = \lambda_3^{-1} = \left[\frac{N_0 D_n D_h}{\alpha N(nD_n + N_h D_h)}\right]^{1/2}. \quad (4)$$

The coexistence of the currents j_n and J_h leads to a single ambipolar diffusion coefficient of charges in the semiconductor (in much the same way as with the simultaneous transport of electrons in the *c*-band and holes in the *v*-band [1])

$$D = \frac{D_n D_h (n + N_h)}{nD_n + N_h D_h}. \quad (5)$$

With (4) and (5), we find the ambipolar recombination time between electrons in the *c*-band and positively charged donors

$$\tau_d = \frac{L_d^2}{D} = \frac{N_h}{\alpha N_+ (n + N_h)}. \quad (6)$$

The ambipolar dielectric relaxation time is $\tau_s = L_s^2/D$. Using (3)–(6), we find the ratio τ_d/τ_s, which characterizes the response of the semiconductor to an external electric field [18]; its response is predominantly relaxation if $\tau_s > \tau_d$, and recombination if $\tau_d > \tau_s$.

From (6) it is seen that the hopping electron transport via donors decreases the ambipolar recombination (and generation) time τ_d. This is due to the migration in the crystal of both the electrons in the *c*-band and the positive-charge states of immobile donors. In the case of $n \ll N_h$, in particular, from (6) one obtains a well-known expression [1–3] for the electron lifetime in the *c*-band associated with its capture by a positively charged donor, $\tau_d \longrightarrow 1/\alpha N_+$. In the other extreme case, $n \gg N_h$, from (6) we have $\tau_d \longrightarrow N_h/\alpha N_+ n$, which can be considered, if $N_h \approx N_0$, as the lifetime of the (0) charge state of a donor associated with the electron excitation from the donor into the *c*-band. Indeed, at $n \gg N_h \approx N_0$, we have $\tau_d \longrightarrow 1/\beta$.

3. Let us now consider the features of the Hall effect in the case of the coexistence of the hopping and band conductivities. The relevant experimental data and calculations are contradictory in many respects [19], but common to all of them is the conclusion that the Hall effect is much weaker for the hopping than for the band conduction.

We will show here that the concentration and (or) the diffusion coefficient of hopping holes can be calculated from Hall effect data for *p*-type germanium crystals doped with Ga atoms by a transmutation method and compensated with As (and, to a small extent, Se) atoms [20]. The electrical neutrality equation for *p*-Ge is $N_- = p + KN$, where p is the hole concentration in the *v*-band, $N = N_- + N_0$ is the concentration of Ga atoms, and K is the degree of compensation (the ratio between the donor and the acceptor concentrations). We note that (3)–(6) are also true for a *p*-type semiconductor with n being replaced by p and N_+ by N_-.

From experimental data for Ge : Ga [21, 22] one can determine the temperature T_h at which the *v*-band hole conductivity σ_p equals the conductivity due to hopping holes between Ga atoms. At $K \approx 0.35$, we have the following estimates for T_h and the mean ionization energy ε_1 of Ga atoms in Ge in the concentration range $3 \times 10^{14} < N < 2 \times 10^{16}$ cm^{-3}:

$$T_h \approx 5.3 \times 10^{-4} N^{0.27};$$
$$\varepsilon_1 = 11.3 \text{ meV} - 7.7 \times 10^{-6} N^{0.35}, \quad (7)$$

where $[T_h] = $ K, $[N] = $ cm^{-3}, and $[\varepsilon_1] = $ meV.

If the expressions $\sigma_p = qp\mu_p$ for the band conductivity and $\sigma_h = qN_h M_h = qM_h N_0 N_-/N$ for the hopping conductivity are true, then the equality $\sigma_p = \sigma_h$ at $T = T_h$ reduces to $pD_p = N_h D_h$, where $D_p/\mu_p = D_h/M_h = \xi k_B T_h/q$. We will put $\xi \approx 1$ at the temperature T_h.

The *v*-band hole concentration $p(T_h)$ in *p*-Ge at $T = T_h$ is determined from the electrical neutrality condition $p + KN = N_-$. At $k_B T_h \ll \varepsilon_1$, for $p(T_h) \ll K(1 - K)N$, we have

$$p = \frac{(1-K)N_v}{K\beta_a} \exp(-\varepsilon_1/k_B T_h), \quad (8)$$

where $N_v(T_h) = 4.831 \times 10^{15} (m_p/m_0)^{3/2} T_h^{3/2}$ cm^{-3}; $m_p = 0.384 m_0$ is the density-of-states effective mass of a hole in the *v*-band; and $\beta_a = 4$ is the degeneracy of the energy level of a hydrogen-like acceptor in a Ge crystal.

With $\sigma_p = \sigma_h$ at $T = T_h$, the experimental value of the Hall coefficient R_H in *p*-Ge becomes (see, e.g., [1–3, 21, 22])

$$R_H = (R_v \sigma_p^2 + R_a \sigma_n^2)/(\sigma_p + \sigma_h)^2 \approx \frac{R_v}{4} = \frac{r_p}{4qp},$$

where the Hall coefficient R_a for hopping holes between acceptors is much less than R_v for the *v*-band; and $p(T_h) = r_p/4qR_H$ is the hole concentration in the *v*-band, in which the special features of the Hall coefficient for *p*-Ge [23] are taken into account.

With $p(T_h)$ and $D_p(T_h) = \sigma_p k_B T_h/qp$, calculated from the measured Hall coefficient $R_H(T_h)$ and conductivity $\sigma_p + \sigma_h = 2\sigma_p$ at $T = T_h$, one finds the diffusion coefficient of hopping holes between Ga atoms as

$$D_h = \frac{D_p N_v}{\beta_a K^2 N} \exp(-\varepsilon_1/k_B T_h). \quad (9)$$

From (9) and (7), it follows that, as the concentration of Ga atoms in *p*-Ge increases from $N = 3 \times 10^{14}$ cm^{-3} to 2×10^{16} cm^{-3} at $K \approx 0.35$, the ratio between the diffusion coefficients of hopping holes D_h and *v*-band holes D_p increases from $D_h/D_p \approx 4 \times 10^{-11}$ to 8×10^{-3}.

Thus, $p(T_h)$ and $D_p(T_h)$ can be calculated from the experimentally measured Hall coefficient R_H and conductivity at $T = T_h$. Then, putting $N_h(T_h) \approx K(1-K)N$, one can calculate the ambipolar diffusion length L_d from (4) and compare it with its experimental value at $\sigma_p = \sigma_h$.

4. When light illumination of the crystal is uniform over its volume and causes the ionization of donors, both the concentrations of hopping electrons and of *c*-band electrons are changed. We assume that the irradiation does not result in the crystal heating and, hence, does not increase the coefficient $\beta = \alpha n N_+/N_0$, characterizing the thermal ionization of neutral donors. Therefore, in the above solution of the set of equations (1), the equilibrium concentrations n, N_0, and N_h should be replaced by $n(\gamma)$, $N_0(\gamma) = N - N_+(\gamma)$, and $N_h(\gamma)$, respectively, that are determined from the equations

$$n(\gamma) + KN = N_+(\gamma);$$
$$\alpha\frac{nN_+}{N_0} + \gamma = \alpha\frac{n(\gamma)N_+(\gamma)}{N_0(\gamma)}, \qquad (10)$$

where γ is the product of the donor photoionization cross section and the steady-state irradiation intensity inducing the transition of an electron from the donor energy level to the *c*-band. It may be noted that both γ and α [24] depend on the temperature T, the dopant concentration N, and the degree of compensation K.

Thus, in the case where the donor photoionization occurs, the screening length $L_s(\gamma)$ and the diffusion length $L_d(\gamma)$ are given by (3) and (4), respectively, in which n should be replaced by $n(\gamma)$, N_0 by $N_0(\gamma)$, and N_h by $N_h(\gamma)$, determined from (10).

If $\gamma/\beta \ll 1$ (thermal generation of carriers dominates over their photogeneration), then from (3), (4), and (10), it follows that $L_s(\gamma) < L_s$ and $L_d(\gamma) < L_d$. At low temperatures, where in the absence of irradiation we have $n \ll N_h \approx K(1-K)N$ and $N_+ \approx KN$, from (6) it follows that $\tau_d(\gamma) = \tau_d - (2-K)\gamma/\alpha^2 N^2 K^3$. It is seen that the irradiation decreases the *c*-band electron lifetime associated with the electron capture by a positively charged donor.

If $\gamma/\beta \gg 1$ (high intensity of external photoexcitation), then we obtain from (10) that $n(\gamma) \longrightarrow (1-K)N$ and $N_h(\gamma) \propto 1/\gamma$, and from (3)–(5) it follows at $n(\gamma) \gg N_h(\gamma)$ that $L_s^2(\gamma) \longrightarrow \varepsilon\xi k_B T/(q^2(1-K)N)$; $L_d^2(\gamma) \propto 1/\gamma$; and $D(\gamma) \longrightarrow D_h$. At $\gamma \geq 10\alpha N$ and $0 < K < 1$, the lifetime of the (0) charge state of a donor associated with the electron optical excitation from the donor into the *c*-band is obtained from (6) to be $\tau_d(\gamma) \approx 1/\gamma$.

It is noteworthy that, in the limit of a high illumination intensity, where $L_d(\gamma) \longrightarrow 0$, from (2), it is seen that the hopping-carrier current disappears ($J_h \longrightarrow 0$), as does the diffusive component of the *c*-band electron current ($j_n \longrightarrow qn\mu_n E$) when the electric field E is independent of the x coordinate.

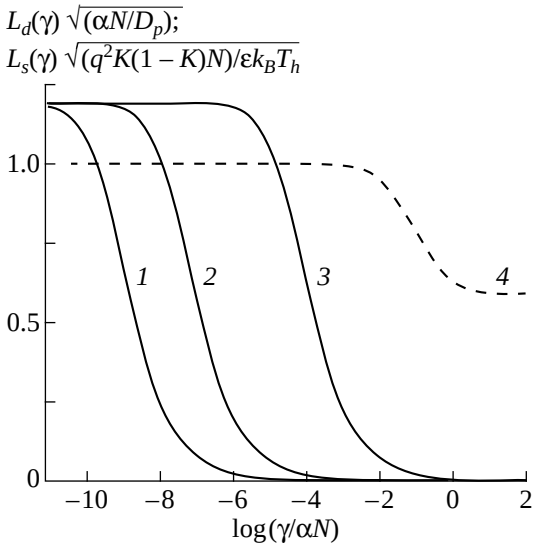

Fig. 1. Calculated ambipolar diffusion lengths $L_d(\gamma)$ of *v*-band holes and hopping holes between Ga atoms in *p*-Ge for $K = 0.35$ and $T = T_h$ as functions of the illumination intensity γ causing the ionization of gallium atoms for different values of N: (*1*) 5×10^{14}, (*2*) 10^{15}, and (*3*) 5×10^{15} cm^{-3}; and the calculated electrostatic-field screening length $L_s(\gamma)$ at the temperature $T_h(N)$. Calculations are performed with (3) and (4) combined with (10) and (9).

Let us apply the expressions obtained above to the specific case of *p*-Ge doped with Ga atoms and compensated with As and Se ($K \approx 0.35$) and of illumination causing the ionization of Ga.

Figure 1 shows the diffusion length $L_d(\gamma)$ in units of $\sqrt{D_p/\alpha N}$ and the screening length $L_s(\gamma)$ in units of $\sqrt{\varepsilon k_B T_h/(q^2K(1-K)N)}$ as functions of the impurity photoexcitation intensity γ at $T = T_h$. The lengths $L_s(\gamma)$ and $L_d(\gamma)$ are calculated from (3), (4), and (10); the ratio between the diffusion coefficients, D_h/D_p, is calculated from (9). In the limit of a low illumination intensity ($\gamma \longrightarrow 0$), at $\sigma_p = \sigma_h$ and $p(T_h) \ll N_h \approx K(1-K)N$, we obtain that the diffusion length $L_d(\gamma)\sqrt{\alpha N/D_p}$ tends to $1/\sqrt{2K}$. In the limit of a high illumination intensity ($\gamma \gg \alpha N$), the screening length $L_s(\gamma)\sqrt{q^2K(1-K)N/(\varepsilon k_B T_h)}$ tends to $\sqrt{K}$.

In Fig. 1, the coefficients α and γ are determined at $T = T_h$. Here, γ is the product of the photoionization cross section of neutral Ga atoms and the illumination intensity. The illumination is assumed to change the concentration of holes in the *v*-band and that of holes hopping between Ga atoms in the (0) and (–1) charge states.

5. We represent the conductivity as $\sigma_h = qN_hM_h$ when interpreting the data on the hopping-carrier pho-

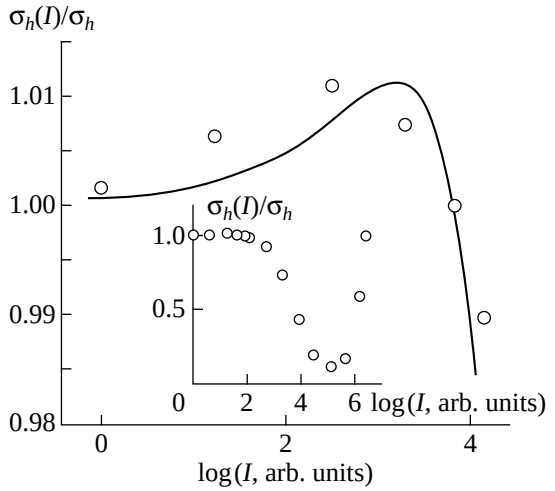

Fig. 2. Reduced dc hopping conductivity of *p*-Ge at $T = 4.2$ K as a function of the illumination intensity I causing band-to-band transitions; open circles are experimental data [5] for $N = 3.4 \times 10^{15}$ cm^{-3} and $K \approx 0.40$ and the solid line is calculated with (14) for $b_h = 0.34$. The inset shows the total conductivity as a function of the illumination intensity.

toconduction [5] in *p*-Ge crystals doped with Ga and As atoms by a transmutation method[3] (Fig. 2). The measurements were performed on a series of *p*-Ge samples with Ga concentration ranging from $N = N_0 + N_- \approx 4 \times 10^{14}$–$8 \times 10^{16}$ cm^{-3} for $K \approx 0.40$. The samples were immersed in liquid helium and prevented from heating during the band–band photogeneration of electron–hole pairs.

In the dark, the holes in the v-band and the electrons on donors (the ratio between the concentrations of As and Ga atoms is $K = 0.4$) can be ignored at $T = 4.2$ K. The hole transport is solely via Ga atoms in the (0) and (–1) charge states. For example, at $N = 3.4 \times 10^{15}$ cm^{-3} and $T = 4.2$ K, the hopping-hole conductivity is dominant ($\sigma_h \gg \sigma_p$); from (7), it follows that the equality $\sigma_h = \sigma_p$ takes place at $T_h \approx 8.3$ K. Hence, the dark steady-state hopping conductivity is [9, 10]

$$\sigma_{h1} = qN_{h1}M_{h1} = q(1-K)KNM_{h1}, \qquad (11)$$

where $N_{h1} = N_0N_-/N$ is the concentration of hopping holes between Ga atoms with mobility M_{h1}.

When electron–hole pairs are generated by light in the fundamental-absorption region, the electrons are captured by positively charged donors (As) and the holes by negatively charged acceptors (Ga). At $K = 0.4$, the hole capture by neutral Ga atoms is negligible [5, 25]. Therefore, under irradiation, the concentration of hopping holes between Ga atoms is varied and the hopping electron conduction through As atoms appears in the sample. The photoconduction becomes stationary owing to donor–acceptor recombination.

[3] The degree of compensation of Ge depends on the hardness of the reactor neutron spectrum [20].

In the general case, the concentration of negatively charged gallium atoms is $N_-(I) = [1 - F(I)]KN$, where $1 \geq F(I) \geq 0$ is a function of the interband illumination intensity I. When the deviation of $N_-(I) = N - N_0(I)$ from its dark value $KN \geq N_-(I)$ is small, one can employ the approximation $F(I) = cI$, where c is the coefficient of proportionality. In this case, the concentration of hopping holes between Ga atoms is given by

$$N_{h1}(I) = (1 - K + cIK)(1 - cI)KN; \qquad (12)$$

and the corresponding hopping photoconductivity is $\sigma_{h1}(I) = qN_{h1}(I)M_{h1}$.

Under the influence of interband illumination, the concentration of neutral As atoms $cIKN$ increases, whereas the concentration of positively charged As atoms $(1 - cI)KN$ decreases. Hence, the concentration of hopping electrons between As atoms with mobility M_{h2} is

$$N_{h2}(I) = cI(1 - cI)KN, \qquad (13)$$

and the corresponding hopping photoconductivity is $\sigma_{h2}(I) = qN_{h2}(I)M_{h2}$.

With (11)–(13), the ratio of the hopping conductivity in the presence of illumination $\sigma_h(I) = \sigma_{h1}(I) + \sigma_{h2}(I)$ to its dark value $\sigma_h = \sigma_{h1}$ is obtained to be

$$\frac{\sigma_h(I)}{\sigma_h} = \frac{N_{h1}(I) + b_hN_{h2}(I)}{N_{h1}} = \frac{(1-cI)(1-K+cIK+cIb_h)}{(1-K)}, \qquad (14)$$

where $b_h = M_{h2}/M_{h1}$ is the ratio of the mobility of electrons hopping between As atoms in the (0) and (+1) charge states to the mobility of holes hopping between Ga atoms in the (0) and (–1) charge states.

From (14), it follows that, at $2K > 1 - b_h$ and the interband illumination intensity equal to $I_1 = (2K + b_h - 1)/2c(K + b_h)$, the hopping photoconductivity reaches its maximum value $\sigma_h(I_1) > \sigma_h$ and then, at $I_2 = 2I_1$, it becomes equal to its dark value, $\sigma_h(I_2) = \sigma_h$. Therefore, the quantities b_h and c can be determined if the intensity I and the degree of compensation K are known. We note that the relation $I_2 = 2I_1$ is consistent with experimental observations [5].

If the absolute value of the illumination intensity I is unknown, one can write (14) for $\sigma_h(I_1)$ and $\sigma_h(I_2)$ and eliminate cI between these equations by introducing I_1/I_2, which can be measured experimentally. This procedure allows one to find b_h. For example, from the data [5] presented in Fig. 2, we have $\sigma_h(I_1)/\sigma_h = 1.011$ and $\log I_2 = 1.92$, and from (14) we obtain $b_h \approx 0.34$.

It should be noted that an increase in the illumination intensity I leads to an increase of the number of both acceptors (Ga) and donors (As) in the neutral change state and, hence, to an increase in the probability of A^+ and D^- centers (positively charged acceptors and nega-

tively charged donors, respectively) [25, 26] being formed. Due to the involvement of A^+ and D^- centers in the hopping photoconduction, the experimentally measured $\sigma_h(I)/\sigma_h$ does not drop to zero [5], in contrast to (14) in the case of the linear approximation $F(I) = cI$, but passes through a minimum $\sigma_h(I) \approx 0.13\sigma_h$ at $\log I \approx 2.61\log I_2$ and then rises sharply (see the inset of Fig. 2). Photoconductivity–illumination intensity curves in which the initial range with positive photoconductivity was followed by a range with negative photoconductivity were clearly observed in [5] on *p*-Ge samples with gallium atomic concentration $N = 8 \times 10^{14}$–4×10^{16} cm^{-3} and the degree of compensation $K \approx 0.40$.

6. In summary, expressions are obtained for the first time for the screening length of an electrostatic field and for the carrier ambipolar diffusion length in the case where band- and hopping-carrier currents coexist.

For *p*-Ge crystals doped by a transmutation method, the temperature T_h is determined at which the *v*-band hole conductivity σ_p equals the conductivity σ_h due to holes hopping between Ga atoms. At $T = T_h$, the parameters of hopping holes N_h and D_h are shown to be related, by the ambipolar diffusion length L_d, to the *v*-band hole concentration p, diffusion coefficient D_p, and capture coefficient for negatively charged acceptors α. This allows one to find N_h and D_h from experimental data on the Hall effect (due to *v*-band holes) and the total conductivity $\sigma_p + \sigma_h = 2\sigma_p$.

The change in the hopping-electron (hole) concentration caused by impurity photoexcitation of the crystal is found. Expressions are obtained for the steady-state *c*-band electron lifetime due to their capture by positively charged donors and for the donor (0) charge state lifetime associated with the electron transitions from donors to the *c*-band.

An explanation is given for the first time for the nonmonotonic dependence of the hopping photoconductivity on the illumination intensity corresponding to the fundamental absorption in *p*-Ge crystals doped by a transmutation method.

ACKNOWLEDGMENTS

The authors are grateful to V.P. Dobrego and A.G. Zabrodskiĭ for helpful discussions.

REFERENCES

1. V. L. Bonch-Bruevich and S. G. Kalashnikov, *Semiconductor Physics* [in Russian] (Nauka, Moscow, 1990).
2. *Handbook on Semiconductors*, Vol. 1: *Basic Properties of Semiconductors*. Ed. by P. T. Landsberg (Elsevier Science, Amsterdam, 1993).
3. P. Y. Yu and M. Cardona, *Fundamentals of Semiconductors: Physics and Materials Properties* (Springer, Berlin, 1999).
4. V. P. Dobrego and S. M. Ryvkin, Fiz. Tverd. Tela (Leningrad) **6** (4), 1203 (1964) [Sov. Phys. Solid State **6** (4), 928 (1964)].
5. V. P. Dobrego, Fiz. Tekh. Poluprovodn. (Leningrad) **3** (11), 1665 (1969).
6. Ya. E. Pokrovskiĭ, O. I. Smirnova, and N. A. Khval'kovskiĭ, Zh. Éksp. Teor. Fiz. **112** (1), 221 (1997).
7. A. P. Mel'nikov, Yu. A. Gurvich, L. N. Shestakov, *et al.*, Pis'ma Zh. Éksp. Teor. Fiz. **66** (4), 232 (1997).
8. E. M. Gershenzon, F. M. Ismagilova, L. B. Litvak-Gorskaya, *et al.*, Zh. Éksp. Teor. Fiz. **100** (3), 1029 (1991) [JETP **73**, 568 (1991)].
9. N. A. Poklonskiĭ and S. Yu. Lopatin, Fiz. Tverd. Tela (St. Petersburg) **40** (10), 1805 (1998).
10. N. A. Poklonskiĭ and V. F. Stelmakh, Phys. Status Solidi B **117** (1), 93 (1983).
11. N. A. Poklonskiĭ, Candidate's Dissertation in Mathematical Physics (Minsk, 1982).
12. D. K. Pickard, J. Appl. Probab. **19** (2), 444 (1982).
13. P. T. Landsberg and A. G. Guy, Phys. Rev. B: Condens. Matter **28** (2), 1187 (1983).
14. N. A. Poklonskiĭ, Izv. Vyssh. Uchebn. Zaved., Fiz. **27** (11), 41 (1984).
15. S. J. Farlow, *An Introduction to Differential Equations and Their Applications* (McGraw-Hill, New York, 1994).
16. N. A. Poklonski, V. F. Stelmakh, V. D. Tkachev, *et al.*, Phys. Status Solidi B **88** (2), K165 (1978).
17. A. A. Uzakov and A. L. Éfros, Zh. Éksp. Teor. Fiz. **81** (5), 1940 (1981) [JETP **54**, 1028 (1981)].
18. J.-C. Manifacier and H. K. Henisch, J. Phys. Chem. Solids **41** (11), 1285 (1980).
19. Yu. M. Gal'perin, E. P. German, and V. G. Karpov, Zh. Éksp. Teor. Fiz. **99** (1), 343 (1991) [JETP **72**, 193 (1991)].
20. A. G. Zabrodskiĭ and M. V. Alekseenko, Fiz. Tekh. Poluprovodn. (Leningrad) **28** (1), 168 (1994).
21. L. V. Govor, V. P. Dobrego, and N. A. Poklonskiĭ, Fiz. Tekh. Poluprovodn. (Leningrad) **18** (11), 2075 (1984).
22. A. G. Andreev, V. V. Voronkov, G. I. Voronkova, *et al.*, Fiz. Tekh. Poluprovodn. (S.-Peterburg) **29** (12), 2218 (1995).
23. M. V. Alekseenko, A. G. Zabrodskiĭ, and L. M. Shterengas, Fiz. Tekh. Poluprovodn. (S.-Peterburg) **32** (7), 811 (1998).
24. V. N. Abakumov, V. I. Perel', and I. N. Yassievich, Fiz. Tekh. Poluprovodn. (Leningrad) **12** (1), 3 (1978).
25. L. V. Berman and A. I. Seliverstov, Fiz. Tekh. Poluprovodn. (Leningrad) **23** (11), 1959 (1989).
26. A. G. Zhdan, T. M. Lifshitz, and V. V. Ryl'kov, Fiz. Tekh. Poluprovodn. (Leningrad) **21** (2), 217 (1987).

Translated by Yu. Epifanov

Physics of the Solid State, Vol. 42, No. 2, 2000, pp. 230–235. Translated from Fizika Tverdogo Tela, Vol. 42, No. 2, 2000, pp. 224–229.

SEMICONDUCTORS AND DIELECTRICS

The Urbach Rule for the $PbO–SiO_2$ Glasses

I. A. Vaĭnshteĭn, A. F. Zatsepin, V. S. Kortov, and Yu. V. Shchapova

Ural State Technical University, ul. Mira 19, Yekaterinburg, 620002 Russia
e-mail: wia@dpt.ustu.ru

Received May 6, 1999; in final form, July 8, 1999

Abstract—An analysis is made of the behavior of optical spectra of lead-silicate glasses, with variable lead content near the UV absorption edge, and within the 80–470-K range. A generalized formulation of the modified Urbach rule, applicable to glassy materials within a broad temperature range, is proposed for the interpretation of experimental spectral relations. Within this approach, the effective energies of the phonons responsible for the temperature-induced shift of the Urbach edge have been calculated. It is shown that the spectral and temperature parameters of the modified Urbach rule are structure-sensitive, and that their concentration behavior reflects the change of the type of short-range order in the glassy matrix. © *2000 MAIK "Nauka/Interperiodica".*

The most important factor determining the optical, radiative, and emissive characteristics of glassy materials is the behavior of the fundamental absorption edge over a broad temperature range (from cryogenic to the glass-formation point T_g) [1]. For most amorphous media, the optical-absorption spectra measured near the transmission threshold exhibit an extended exponential tail, whose spectral and temperature behavior obeys the so-called "glassy" or modified Urbach rule (MOR) [2, 3]. By this rule, the slope of the spectral characteristics of a glass, unlike that of crystals [4], does not vary with temperature, so that they are shifted parallel to one another toward lower energies [3].

It is presently universally accepted [2,3,5–7] that the formation of the Urbach tail in crystalline and noncrystalline materials is associated in some way with the general structural disorder in the system. It is assumed that the MOR reflects the dominant role of static disorder in an amorphous matrix; however, the temperature-induced shift of the absorption edge indicates a certain effect of thermal (dynamic) disorder in glasses [8]. There are many publications dealing with investigation of the temperature behavior of the optical absorption edge in oxide glasses [9–12]. A study assuming equivalence of the static to dynamic types of disorder in the atomic lattice showed the "crystalline" and "glassy" modifications of the Urbach rule to be the extreme cases of a general exponential dependence of the absorption coefficient in the vicinity of the UV edge [13].

At the same time, one has to admit that, when using the MOR written in the traditional form [9], one cannot isolate, let alone interpret and quantify, the role of the dynamic effects. Incidentally, the region of applicability of the above MOR formalism is restricted only to the high-temperature domain, where one observes a linear dependence of the absorption edge on temperature [13].

This work deals with a study of the behavior of the fundamental absorption edge in binary lead-silicate glasses of variable composition. In our opinion, the $PbO–SiO_2$ system is very promising for the investigation of disorder effects, because it is characterized by a broad glass-formation region, which permits one to smoothly vary the atomic structure of the matrix, including short-range order inversion, by properly varying the concentration of the components [10, 14, 15]. Besides, the UV edge in lead-silicate matrices is not distorted by extrinsic effects, as is the case, for instance, with alkali-silicate glasses, where such studies are impeded by absorption due to iron microimpurities [11, 16].

This study is primarily aimed at obtaining a physical interpretation of the MOR parameters by taking into account the dynamic disorder, as applied to statically disordered glassy materials in the $PbO–SiO_2$ system.

EXPERIMENTAL

The samples to be studied were homogeneous, amorphous (as evidenced by x-ray diffraction measurements), and visually transparent $PbO–SiO_2$ glasses synthesized of particularly pure materials. The PbO content varied from 20 to 80 mol. %. Within the 45–50% PbO content region, the glasses under study exhibit a structural transformation, namely, the transition from the silicate glass-forming network to the lead-oxygen one, which involves a change in the short-range order type [15, 17]. We studied actual samples of two glass-forming systems: (a) low-lead glasses (silicate matrix with a lead modifier) and (b) high-lead glasses (lead-oxygen network with a silicon modifier). Chemical analysis showed the composition of the binary samples to coincide with the batch composition to within 1 mol. %.

After the final treatment, the samples were polished plane-parallel plates 0.4–0.6 mm thick with optical-grade surfaces, thus permitting measurement of the absorption coefficient in the region of the exponential

1063-7834/00/4202-0230$20.00 © 2000 MAIK "Nauka/Interperiodica"

Parameters of the modified Ohrbach rule for PbO–SiO_2 glasses

PbO content, mol. %	E_0, eV	T_0, K	β, $\times 10^{-4}$ eV K^{-1}	T', K	ω, cm^{-1}	A, eV
20	0.119	234	5.08	250	304	0.222
40	0.095	143	6.65	230	238	0.228
45	0.097	204	4.76	200	174	0.199
50	0.117	234	5.00	210	196	0.141
55	0.136	261	5.21	210	236	0.177
60	0.137	245	5.59	250	225	0.181
80	0.116	182	6.38	270	249	0.229

tail. All the measurements were made on a Specord-M40 spectrophotometer with a vacuum cryostat in the 80–470-K range.

The measured fundamental-absorption spectra of glassy lead silicates, displayed in Fig. 1, exhibit a low-lead region (20 mol. %), an inversion region (50 mol. %), and a high-lead region (80 mol. %). For all concentrations, the dependences of the absorption coefficient α on photon energy $h\nu$ and temperature T derived from the spectra obey the "glassy" Urbach rule [9,10]

$$\alpha(h\nu, T) = \alpha_g \exp\left(\frac{h\nu}{E_0} + \frac{T}{T_0}\right), \qquad (1)$$

where α_g is a constant, T_0 is the characteristic temperature derived from the experiment, and $1/E_0 = \partial \ln\alpha/\partial h\nu$ is the log slope of the spectral characteristic. The actual values of E_0 estimated for the same spectral curve may differ slightly, depending on the region of α within which the $\alpha(h\nu)$ function is approximated with an exponential [18].

The E_0 parameter was estimated for all samples within the α = 40–120 cm^{-1} region. Figure 2 presents absorption spectra for all samples measured at room temperature (T = 290 K). One readily sees that, as the lead oxide content increases, the absorption edge shifts toward longer wavelengths. The values of E_0 obtained for different lead concentrations at T = 290 K are listed in the table.

The absorption spectra shift toward the long-wavelength region with increasing temperature without any change in the slope parameter E_0 (Fig. 1). Figure 3 presents the temperature dependences of the E_0 parameter for three samples. The scatter shown in Fig. 3 is 2% of the measured slopes of the spectral characteristics. Within the temperature range studied, 80–470 K, the E_0 parameters are seen to remain constant within the limits specified. It is known [3] that such behavior is typical of most disordered structures and demonstrates the dominant role of static disordering, with the magnitude of E_0 being assumed to quantitatively characterize the degree of disorder in the system.

The temperature term in the exponent in Eq. (1) reflects the linear shift of the absorption edge along the energy axis. Besides the linear part, the $h\nu(T)$ relation also has an essentially nonlinear portion in a temperature range $T < T'$ (Fig. 4), where Eq. (1) no longer fits the experimental results. The position of the T' bound-

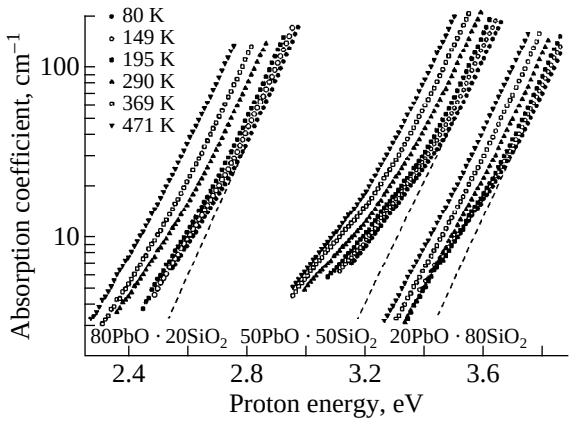

Fig. 1. Effect of temperature on optical absorption spectra of glasses. Dashed lines show the slope of the corresponding Ohrbach tails.

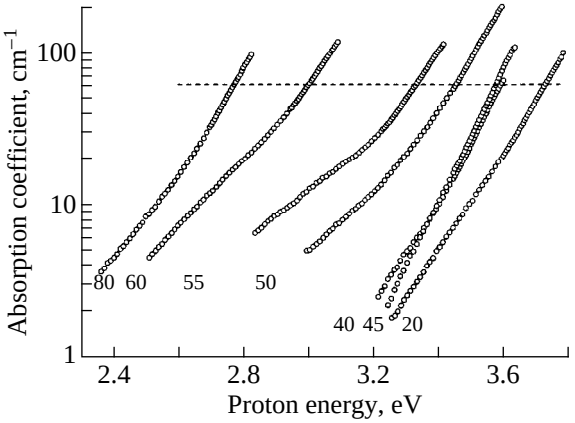

Fig. 2. Optical absorption spectra of glasses obtained at 290 K. The figures under the curves are PbO content in mol. %.

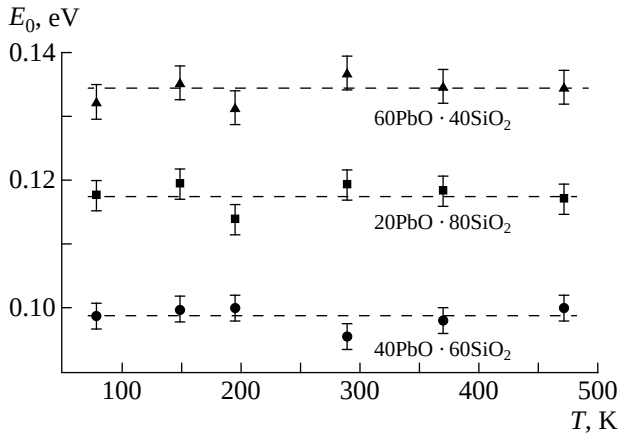

Fig. 3. Temperature dependences of the E_0 spectral parameter.

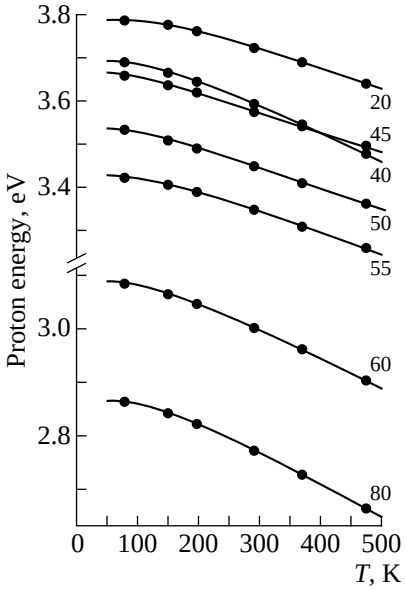

Fig. 4. Temperature dependences of the optical-absorption edge position for all samples: points are experiment and solid lines are fitting using (5). The figures adjoining the curves are PbO content in mol. %.

ary is characteristic of a glassy material and is found graphically. The values of T' obtained in this way for all samples are given in the table. The slope of the linear part yields the T_0 parameter, which is also a sample characteristic involved in the temperature-dependent term of the MOR (1) and, hence, it should likewise be sensitive to the extent of static disorder.

It should be pointed out that, in the conditions where the absorption edges are shifted parallel to one another, the $h\nu(T)$ function completely coincides in shape with the temperature-induced variation of the optical gap $E_g(T)$ of the material [8]:

$$h\nu(0) - h\nu(T) = E_g(0) - E_g(T). \qquad (2)$$

The shape of the experimentally observed relation (Fig. 4) is typical of most not only amorphous, but also crystalline systems [7, 19]. This suggests that the optical absorption edges in crystals and glasses are shifted by a common mechanism, and that the thermal (phonon) disorder plays a noticeable part in this mechanism. At the same time, Eq. (1) does not explicitly contain the physical quantities characterizing the dynamic component of the total atomic disorder. In other words, the MOR (1) does not describe the $h\nu(T)$ relation in the low-temperature domain and does not allow the estimation of the energy parameters of dynamic disorder (in particular, the atomic vibration energy) from experimental curves that are intimately connected with it.

Thus, using relation (1), we have determined the E_0 parameter of the spectral part of the MOR, which is connected, in disordered materials, with the static disordering of atoms. However, the physical meaning of the temperature parameters T_0 and T' remains unclear and requires dedicated consideration.

THEORY

The exponential dependence of the absorption coefficient in the vicinity of the UV transmission edge can be written in a general form [13,20]

$$\alpha(h\nu, T) = \alpha_0 \exp\left(\frac{h\nu - E_g(T)}{E_0(T, X)}\right), \qquad (3)$$

where α_0 is a constant. The $E_0(T, X)$ function in (3) is a measure of the disorder in the system and reflects, in a general case, the contribution of the dynamic (thermal phonons) and static (frozen-in phonons) disorder through the displacements **u** of atoms from their equilibrium positions [2, 21]:

$$E_0(T, X) = K(u_T^2 + u_X^2), \qquad (4)$$

where X is a geometrical parameter of the material [2] used to characterize the static disorder, $\langle u^2\rangle_T$ is the rms thermal displacement, and $\langle u^2\rangle_X$ is the rms atomic displacement due to the frozen-in phonons. The coefficient K has the meaning here of the constant of the second-order deformation potential [21].

In the high-temperature limit, the gap width function $E_g(T)$ allows a linear approximation [3] with a temperature coefficient $\beta = dE_g/dT$, which is usually derived from the slope of the experimental $E_g(T)$ relation.

In our previous work [13], the "crystalline" and "glassy" (1) modifications of the Urbach rule were obtained analytically from Eq. (3) using a linear approximation to the temperature dependence of E_g and the concept (4) of the equivalence between the static and dynamic types of disorder in an atomic lattice. The "crystalline" version is appropriate in the conditions where the lattice disorder is considered to be primarily of

thermal nature, i.e. for $\langle u^2\rangle_T \gg \langle u^2\rangle_X$ and $E_0(T, X) \sim kT$. Systems with predominantly static disorder, where $\langle u^2\rangle_X \gg \langle u^2\rangle_T$ and the $E_0(T, X) \equiv E_0$ function is temperature-independent, are characterized by the "glassy" modification (1).

In the low-temperature domain, $E_g(T)$ is an essentially nonlinear function, and relation (1) becomes invalid for the description of the temperature-induced shift of the optical absorption edge. With such an approach, the temperature boundary of applicability of (1) is determined by the parameters of the model used to describe $E_g(T)$.

The temperature dependence of the gap width, which is valid throughout the temperature range studied, can be written as [22]

$$E_g(T) = E_g(0) - A\langle n\rangle, \quad (5)$$

where $E_g(0)$ is the gap width at zero temperature, A is the Fan parameter depending on the microscopic properties of the material [23], and $\langle n\rangle = [\exp(\hbar\omega/kT) - 1]^{-1}$ is the Bose–Einstein factor for phonons with energy $\hbar\omega$.

Equation (5) explicitly takes into account only the phonon contribution to $E_g(T)$, which is dominant at low temperatures [24]. Moreover, the contribution due to lattice thermal expansion to the total temperature-induced variation of gap width does not exceed 20% for a number of materials, and can be neglected in a first approximation [24]. Note that, at high temperatures, the thermal expansion contribution to the energy level shift will be likewise proportional to $\langle n\rangle$ [24]. In this case, the calculated value of the A parameter takes into account both the internal (electron-phonon coupling) and external (thermal expansion) contributions to the $E_g(T)$ relation.

Thus, substituting (5) into (3), one obtains the following "glassy" modification of the Urbach rule, which is valid throughout the temperature range under study:

$$\alpha(h\omega, T) = \alpha_g \exp\left(\frac{h\nu + A\langle n\rangle}{E_0}\right). \quad (6)$$

At high enough temperatures, where $kT \gg \hbar\omega$, the second term in the numerator of the argument of the exponential in (6) is proportional to temperature, namely, $\langle n\rangle = kT/\hbar\omega$. In this case, Eq. (6) takes on the form of (1). The characteristic parameter T_0 and the temperature coefficient β can now be written as

$$T_0 = E_0\frac{\hbar\omega}{kA}, \quad \beta = A\frac{k}{\hbar\omega}. \quad (7)$$

The reasoning presented in this section is based to a certain extent on the validity of Fan's expression (5) derived for the case of disordered structures. The applicability of Eq. (5) to description of $E_g(T)$ for both crystalline and amorphous materials has already been pointed out by a number of authors [7, 8, 19].

Thus, the generalized formulation of the MOR (6) can be used to analyze the experimental relations $\alpha(h\nu, T)$ for glasses over a broad temperature range and permits one to explicitly estimate the parameters of static and dynamic disorder from optical absorption spectra.

DISCUSSION

An important consequence of the positional disordering of atoms in noncrystalline materials is the localization of electronic states in the energy band tails. The E_0 parameter of the spectral part of the MOR is a quantitative characteristic of dominant static disorder in the structure of the glasses under study and reflects the extent of band tails in the electronic density of states [3,25,26].

As seen from the table, the E_0 parameter lies within a range of 0.095–0.140 eV for all samples, which implies close extents of atomic disorder in the glasses under study. This conclusion agrees with the observation [6,13] that the slope parameter of the Urbach edge is of the same order of magnitude for diverse glass-forming systems, 0.05–0.25 eV. Note that the magnitude of E_0 remains constant under the temperature-induced shift of the spectral characteristics, and in a general case it is determined by the slope of the longest tail [5,18]. By the model of Abe–Toyozawa [5], the characteristic length of the band tail in the density of states is connected with atomic-potential fluctuations. Note that the most ordered from this point of view are glasses containing 40 and 45 mol. % PbO, for which E_0 = 0.095 and 0.097 eV, respectively. The concentration behavior of the E_0 parameter in the 45–50 mol. % PbO interval (see table) follows the transformation of the short-range order (the transition from low- to high-lead glasses) and the corresponding variation in the degree of static disorder [15].

The generalized formulation of the MOR proposed in the preceding section permits one to estimate the parameters of the dynamic disorder determining the temperature-induced shift of the absorption edge, in particular, the effective phonon energy. Figure 4 plots the $h\nu(T)$ relation for all samples under study. The points identify the experimental photon energies $h\nu$ obtained for the absorption coefficient $\log(\alpha) = 1.8$ (shown with a dashed line in Fig. 2) and corresponding to various measurement temperatures. The solid lines in Fig. 4 are fits to the experimental plots obtained using (5). $E_g(0)$, A, and ω were varied as temperature independent quantities. The values of these variables obtained in this manner are listed in the table.

As seen from Fig. 4, Eq. (5) reproduces quite well the experimental temperature dependence of the absorption edge position. The phonon frequencies obtained in this fitting are listed in the table. A comparison of the calculations with experimental Raman-scattering data [27–29] shows that the values obtained, on

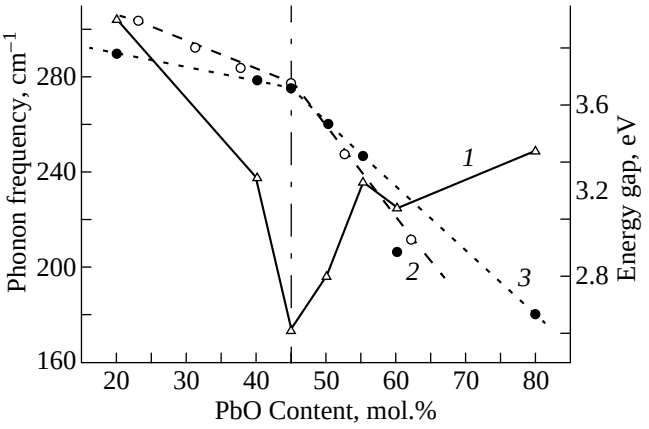

Fig. 5. Concentration dependences of the effective-vibration energy and optical-gap width: (*1*) phonon frequency, (*2*) E_g for $\alpha = 100$ cm^{-1} [17], and (*3*) $E_g(0)$. The vertical dot-and-dash line identifies the glass short-range order inversion region.

the one hand, somewhat exceed the frequencies associated with the vibrational motion of lead atoms, 95 and 140 cm^{-1}, while on the other they are below the bending and optical vibration frequencies of the silicate network (the glass-former sublattices), which lie within the 400–500 and 880–1200 cm^{-1} regions [27, 28]. Because Eq. (5) was derived within the one-phonon approximation [22], the phonon energy obtained from it reflects some effective quantity, which takes into account the contributions of all vibrational states in a system. Considered from this standpoint, the 170–300 cm^{-1} frequencies are intermediate figures characterizing effective vibrational states.

The values of the T_0 and β parameters of the temperature part of the MOR, which characterize the region of the linear temperature dependence $h\nu(T)$, were calculated using relations (7) (see table). The fictive boundary T' was found graphically using the plots of Fig. 4. Note that the T' values are fairly arbitrary. Strictly speaking, the $E_g(T)$ relation (5) is nowhere linear, and the values of the β coefficient and of the T_0 parameter have an asymptotic character. It should be stressed that all the above quantities characterize the dynamic component of the total structural disorder.

The relative magnitude of the static and dynamic contributions to the total structural disorder is determined to a considerable extent by the actual type of short-range order. As already pointed out in our analysis of the E_0 parameter, the observed quantitative changes are associated with the qualitative change that the nature of the glass-former sublattice undergoes within the interval 45–50 mol. % PbO. A similar relation can also be found for the dynamic MOR energy parameters.

Figure 5 presents the concentration dependences of the effective phonon energy and of the optical gap width at zero temperature $E_g(0)$. Also shown for comparison are independent experimental data obtained for the optical-absorption edge energy in lead-silicate glasses at $\alpha = 100$ cm^{-1} [17]. One readily sees that all concentration relations have a break in a region of 45–50 mol. % PbO, which corresponds to the change in the type of short-range order. Moreover, the concentration dependences of all quantities (except T_0) listed in the table also reach a minimum at the PbO content of 45 mol. %. Hence, the characteristic parameters of the MOR are indeed very sensitive to a short-range order transformation. In other words, the inversion of short-range order, which noticeably affects many physical properties of glasses [15,17], also manifests itself in the characteristics of dynamic disorder.

Thus, we have used the concept of equivalence of the static and dynamic components of structural disorder to obtain a generalized formulation of the modified Urbach rule, which describes the spectral and temperature behavior of statically-disordered materials. The proposed formulation (6) explicitly contains parameters characterizing both types of disorder and, in the limit of high temperatures ($kT \gg \hbar\omega$), reduces to the well-known form (1). This formalism has been employed to analyze the behavior of optical-absorption spectra of PbO–SiO_2 glasses within the 80–470-K temperature range. The effective phonon frequencies (170–300 cm^{-1}) responsible for the thermal shift of the Urbach edge have been calculated. The parameters of the proposed formulation (6) of the Urbach rule are structurally sensitive, and their concentration dependences reflect inversion in the glass short-range order.

ACKNOWLEDGMENTS

The authors express gratitude to A.A. Maslakov for his assistance in the experiment.

REFERENCES

1. Gan Fuxi, *Optical and Spectroscopic Properties of Glass* (Springer, Berlin, 1992).
2. J. Tauc, Mater. Res. Bull. **5**, 721 (1970).
3. N. F. Mott and E. A. Davis, *Electronic Processes in Non-Crystalline Materials* (Clarendon Press, Oxford, 1979; Mir, M., 1982).
4. B. L. Gel'mont, V. I. Perel', and I. N. Yassievich, Fiz. Tverd. Tela (Leningrad) **25** (3), 727 (1983).
5. S. Abe and Y. Toyozawa, in *Amorphous Semiconductor: Technologies and Devices*, Ed. by Y. Hamakawa (North-Holland, Amsterdam, 1983; Metallurgiya, M., 1986, p. 35).
6. Ya. G. Klyava, Fiz. Tverd. Tela (Leningrad) **27** (5), 1350 (1985).
7. G. D. Cody, in *Hydrogenated Amorphous Silicon*, Part B, Ed. by J. Pankove (Academic Press, New York, 1984), p. 11.
8. J. N. Zakis and H. Fritzsche, Phys. Status Solidi B **64**, 123 (1974).

9. L. B. Glebov and M. N. Tolstoĭ, Fiz. Khim. Stekla **1** (3), 239 (1975).
10. A. N. Trukhin, J. Non-Cryst. Solids **189**, 1 (1995).
11. V. I. Arbuzov, A. F. Zatsepin, V. S. Kortov, *et al.*, Fiz. Khim. Stekla **20** (6), 689 (1994).
12. I. A. Weinstein, A. F. Zatsepin, and Yu. V. Schapova, Physica B **263-264** (1–4), 167 (1999).
13. I. A. Vainshtein, A. F. Zatsepin, and V. S. Kortov, Fiz. Khim. Stekla **25** (1), 70 (1999).
14. L. B. Glebov, A. G. Plyukhin, E. L. Raaben, *et al.*, Fiz. Khim. Stekla **16** (2), 245 (1990).
15. A. F. Zatsepin, V. S. Kortov, and Yu. V. Shchapova, Radiotekhn. Élektron. **37** (2), 326 (1992).
16. L. B. Glebov, V. G. Dokuchaev, M. A. Petrov, *et al.*, Fiz. Khim. Stekla **16** (1), 39 (1990).
17. A. M. Tyutikov, N. V. Lobanova, M. N. Toiseeva, *et al.*, Fiz. Khim. Stekla **5** (5), 628 (1979).
18. S. K. O'Leary, S. R. Johnson, and P. K. Lim, J. Appl. Phys. **82**, 3334 (1997).
19. I. A. Vainshtein, A. F. Zatsepin, and V. S. Kortov, Fiz. Tverd. Tela (St. Petersburg) **41** (6), 994 (1999).
20. G. D. Cody, J. Non-Cryst. Solids **141**, 3 (1992).
21. G. D. Cody, T. Tiedje, B. Abeles, *et al.*, Phys. Rev. Lett. **47** (20), 1480 (1981).
22. H. Y. Fan, Phys. Rev. **82** (6), 900 (1951).
23. H. Fan, *Photon-Electron Interaction: Crystals Without Fields* (Springer, Berlin, 1967; Mir, M., 1969).
24. T. Skettrup, Phys. Rev. B **18** (6), 2622 (1978).
25. A. F. Zatsepin, V. S. Kortov, and Yu. V. Shchapova, Fiz. Tverd. Tela (St. Petersburg) **39** (8), 1366 (1997).
26. V. A. Gubanov, A. F. Zatsepin, V. S. Kortov, *et al.*, J. Non-Cryst. Solids **127**, 259 (1991).
27. E. M. Rabinovich, J. Mater. Sci. **11**, 925 (1976).
28. B. Piriou and H. Arashi, High Temp. Sci. **13**, 299 (1980).
29. V. O. Kabanov, T. M. Podol'skaya, and O. V. Yanush, Fiz. Khim. Stekla **22** (1), 25 (1996).

Translated by G. Skrebtsov

Physics of the Solid State, Vol. 42, No. 2, 2000, pp. 236–240. Translated from Fizika Tverdogo Tela, Vol. 42, No. 2, 2000, pp. 230–234.

SEMICONDUCTORS AND DIELECTRICS

Investigation of Free and Bound Excitons in Strained ZnTe Films Grown by MBE on GaAs(100) Substrates

V. V. Zaĭtsev, V. S. Bagaev, E. E. Onishchenko, and Yu. G. Sadof'ev

Lebedev Institute of Physics, Russian Academy of Sciences, Leninskiĭ pr. 53, Moscow, 117924 Russia
e-mail: zaitsev@sci.lebedev.ru

Received August 2, 1999.

Abstract—A study is reported of the reflectance and low-temperature photoluminescence (PL) spectra of ZnTe films grown by molecular-beam epitaxy (MBE) on GaAs substrates [(100) orientation, 3° deflection toward ⟨110⟩]. It is shown that the strain-induced splitting of the free-exciton energy level (ΔE_{ex}) does not depend on ZnTe film thickness within the 1–5.7 μm range and is due to biaxial in-plane film tension. The stresses are primarily determined by the difference between the thermal expansion coefficients of the film and the substrate. It is also shown that the residual stresses originating from incomplete relaxation of the film lattice parameter to its equilibrium value at the growth temperature likewise provide a certain contribution. The position of the spectral line of an exciton bound to a neutral acceptor (As) is well approximated in terms of the present models, taking into account the stresses calculated using the value of ΔE_{ex}. *© 2000 MAIK "Nauka/Interperiodica".*

ZnTe is a promising material for use in opto-electronics. Having a large gap (E_g = 2.26 eV at 300 K), it is widely employed, in particular, as barrier material in various low-dimensional structures [1–7]. ZnTe to be used in such structures is conventionally grown by various epitaxial techniques on GaAs substrates. One of the features of the heterostructures under study here is, as will be shown later, the presence in ZnTe films of strains caused by both thermal and residual stresses. The methods of low-temperature optical spectroscopy (the reflectance and photoluminescence spectra) employed in the work permit one, on the one hand, to investigate the effect of strains on the various optical transitions and, on the other hand, to perform quantitative calculations of the strain tensor, as well as to draw certain conclusions concerning the nature of these strains. The above aspects will be considered in this work based on an analysis of the optical transitions involving a free and neutral-acceptor-bound exciton.

EXPERIMENT

The samples for the experiment were grown on a KATUN MBE setup, whose molecular-beam formation system was substantially modified, with an ionization manometer introduced to monitor the beam equivalent pressure. The films were prepared by vaporization of elemental Zn and Te from separate sources.

Following removal of natural oxides from the GaAs substrate surface [(100) orientation, 3° deflection toward the ⟨110⟩ direction] by heating up to 570 ± 10°C, the substrate was cooled down to a temperature of 250–280°C, and maintained in a zinc vapor flow to prevent formation of the Ga_2Te_3 compound. The ZnTe epitaxial film was nucleated at the same temperatures. After a streak reflection system has appeared in the RHEED pattern, which occurs when the deposited coating becomes thicker than about 100 nm, the substrate temperature was raised to 320–350°C and maintained constant at this level to the end of the epitaxial growth. The growth rate of an epitaxial layer was 0.2 nm/s. By maintaining the equivalent-pressure ratio of Te_2 and Zn molecular beams at a level of 2.0, one could reach coexistence on the surface of a growing film of the $c(2 \times 2)$ and (2×1) reconstructions, which ensured growth conditions closest to stoichiometric ones.

The photoluminescence and reflectance spectra were obtained at a temperature of 5 K. The optical excitation was performed with an argon laser operated in the single-line lasing regime. The spectra were analyzed with a double monochromator having a limiting resolution of not worse than 0.01 nm. The PM tube output was fed into a narrow-band amplifier with a lock-in detector. The experimental data were processed in the CAMAC format.

EXPERIMENTAL DATA AND DISCUSSION

Prior to dealing with the results themselves, we would like to stress that Figs. 1–3 will present secondary luminescence spectra containing both emission and Raman scattering (RS) lines, which were obtained in excitation by different argon-laser lines. This permits one to more clearly reveal the features in secondary luminescence spectra that are due to photoluminescence. Obviously enough, this will be accompanied by the appearance at the ZnTe emission edge of different RS lines corresponding to different exciting photons [2, 3]. We are not going to consider the Raman scattering in what follows. Each of the RS lines in the second-

1063-7834/00/4202-0236$20.00

ary luminescence spectra will be denoted by *nLO*, where *n* specifies the number of the longitudinal optical phonons emitted in the RS process.

We will start the analysis of the results with a discussion of the spectra of free excitons in ZnTe films. Figures 1–3 present secondary-luminescence spectra of ZnTe films 3.2 and 5.7 μm thick obtained near the zinc telluride absorption edge. Figures 1 and 3 also display reflectance spectra, which clearly exhibit two minima resonantly coinciding in energy with the emission lines of the heavy-hole (X_{hh}) and light-hole (X_{lh}) free excitons with energies E_{hh} = 2.3793 and E_{lh} = 2.3743 eV, respectively; note that these energies do not depend on the ZnTe thickness within the 1–5.7 μm range (the oscillations in the reflectance spectra on the long-wavelength side of X_{lh} are due to the interference of light in the film). This interpretation of the *X* lines is based on the fact that the spectral reflectance feature associated with X_{hh} is pronounced much more clearly, which qualitatively agrees with the conclusion concerning the relative magnitude of the oscillator strengths for the X_{hh} and X_{lh} transitions in the quasicubic model [8]. Besides, the mere fact of the appearance of features in reflectance spectra implies their excitonic nature. The free-exciton line splitting is only natural to associate with the existence in ZnTe films of strains, which lower the cubic-lattice symmetry and thereby bring about the splitting of the degenerate valence band. Despite the apparent obviousness and simplicity of the above arguments, one could cite relatively recent works where the presence of strains in ZnTe/GaAs films was denied. References to these studies can be found in [9], where this problem was analyzed in detail, in particular, based on papers published in 1988–1989 and dealing with investigations of ZnTe films grown by MBE and vapor-phase epitaxy from organometallic compounds on GaAs and GaSb substrates.

At present, strains are considered to be proven to exist in other II–VI semiconducting films as well, which are grown by various epitaxial techniques on III–V substrates. In particular, Refs. [10–12] report on studies of the CdTe/GaAs heterostructures, and [13–15], on those of ZnSe/GaAs. The papers quoted above come to a general conclusion that strains in films depend both on the lattice mismatch parameter $f = \Delta a/a$ between the film and the substrate and on the difference between their thermal expansion coefficients. The difference consists in the actual contribution due to the residual stresses caused by the incomplete relaxation of the film lattice parameter to its equilibrium value at the growth temperatures, and in how these stresses depend on the film thickness.

Using the known expressions [8] for the strain-induced splitting of the exciton energy level in the pres-

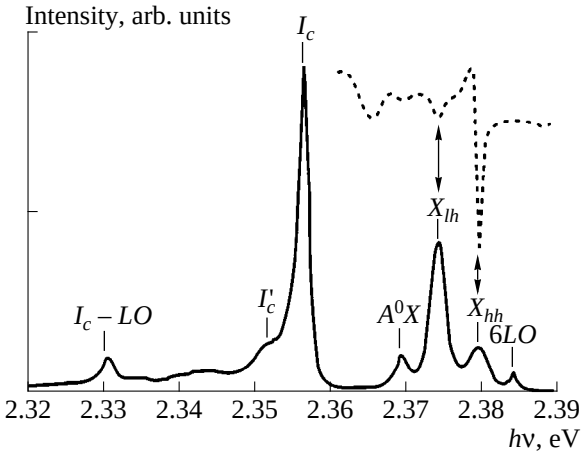

Fig. 1. Spectra of secondary luminescence (solid line, λ_{exc} = 488.0 nm) and of reflectance (points) of a 3.2 μm-thick ZnTe film.

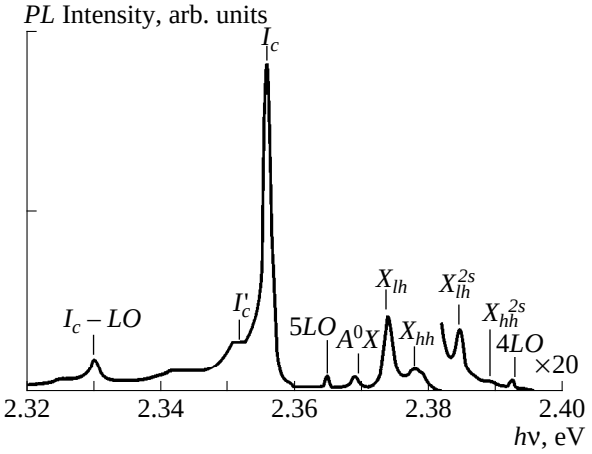

Fig. 2. Secondary-luminescence spectrum of a 5.7 μm-thick ZnTe film obtained for λ_{exc} = 496.5 nm.

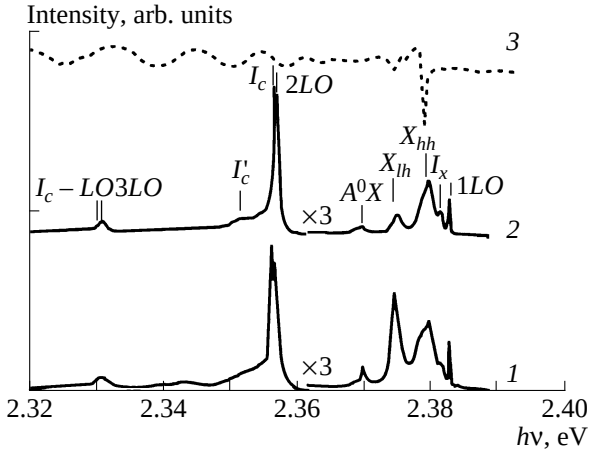

Fig. 3. Spectra of secondary luminescence [(*1*) W_{exc} = 20 W/cm^2, λ_{exc} = 514.5 nm; (*2*) W_{exc} = 4 W/cm^2, λ_{exc} = 514.5 nm] and of reflectance (*3*) obtained on a 5.7 μm-thick ZnTe film.

ence of stresses symmetric along the principal directions in the film plane ($\varepsilon_{xx} = \varepsilon_{yy} \equiv \varepsilon$ is the strain tensor)

$$\Delta E_{ex} = E_{hh} - E_{lh} = -2b\left(\frac{C_{11} + 2C_{12}}{C_{11}}\right)\varepsilon, \quad (1)$$

and for thermal stresses

$$\varepsilon_{\Delta T} = \int_{T_e}^{T_p} [\alpha^{\mathrm{ZnTe}}(T) - \alpha^{\mathrm{GaAs}}(T)]\,dT, \quad (2)$$

one can calculate the contribution to the exciton-line splitting ΔE_{ex} due to the difference between the thermal expansion coefficients of the film (α^{ZnTe}) and of the substrate (α^{GaAs}). Here, b is the shear-deformation potential constant [8], C_{11} and C_{12} are the elastic stiffness constants, T_{gr} and T_{exp} are the growth and experiment temperatures, respectively, and $\Delta T = T_{gr} - T_{exp}$. Taking the values of $\alpha^{\mathrm{ZnTe}}(T)$ and $\alpha^{\mathrm{GaAs}}(T)$ from [16, 17], the values of C_{11} and C_{12} from [16], and the most reliable figure $b = -13$ eV [9, 18, 19], one can show that the experimental value of ΔE_{ex} is smaller than that of $\Delta E_{ex}(\varepsilon_{\Delta t})$ by about a factor of 1.4. Accordingly, the experimental value $\varepsilon = 0.9 \times 10^{-4}$, whereas the thermal-expansion contribution is $\varepsilon_{\Delta t} = 1.3 \times 10^{-4}$. This implies the presence of residual stresses originating from incomplete relaxation of the film lattice parameter to its equilibrium value at the growth temperature. Indeed, because the film lattice parameter is larger than that of the substrate ($f \approx 7.6\%$), the residual stresses must have a negative sign, i.e., the sign opposite to that of the thermal stresses [$\alpha^{\mathrm{ZnTe}}(T) > \alpha^{\mathrm{GaAs}}(T)$]. Therefore, the resultant stress defined by (1) can be smaller than the thermal stress given by (2).

It should be pointed out that the stress calculated with (1) describes well the position of each of the exciton lines:

$$E_{hh,\,lh} = E_0 + \left[2a\left(\frac{C_{11} - C_{12}}{C_{11}}\right) \pm b\frac{C_{11} + 2C_{12}}{C_{11}}\right]\varepsilon. \quad (3)$$

In Eq. (3), the minus sign corresponds to the heavy-hole, while the plus sign, to the light-hole exciton; a is the hydrostatic deformation potential; and $E_0 = 2.381$ eV is the exciton energy in unstrained ZnTe. As this will be shown below, the same value of ε approximates closely the line position of the exciton bound to a neutral acceptor (A^0X).

Prior to turning to this item, we will make a few more remarks concerning the doublet structure, X_{hh} and X_{lh}, of the free-exciton emission lines. An analysis of the literature [20–25] (also see references in [9]) shows that the presence of a distinct exciton structure simultaneously in the emission and reflectance spectra is an exclusion rather than a rule. Quite frequently, the conclusions drawn in a study are based on emission spectra that are poorly resolved in the excitonic region, with no reflectance spectrum measured. Note that even if reflectance spectra do exhibit a distinct reflectance structure, the higher-energy excitons (X_{hh}) can become manifest in the emission spectrum only as a shoulder against the background of the X_{lh} excitons [21]. Considering that the difference between the X_{hh} and X_{lh} energies is about 5 meV, which is considerably in excess of kT at 5 K, it becomes clear that there is no thermal equilibrium between the light- and heavy-hole exciton bands. This consideration also accounts for the simultaneous manifestation in the emission of the 2s X_{hh} and X_{lh} excitons (Fig. 2), which indicates, by the way, that excitons do not become fully thermalized within each of the bands as well. The presence of a clearly seen doublet in the exciton emission at low temperatures correlates with the theoretical conclusion that the spin relaxation time of the hole in the exciton increases with increasing strain-induced splitting ΔE_{ex} [26].

Figure 3 presents secondary-luminescence spectra of 5.7-μm-thick ZnTe films obtained at $\lambda_{exc} = 514.5$ nm and two levels of optical excitation differing by about five times. As seen already from Fig. 3, X_{hh} and X_{lh} depend differently on the pumping. At still higher excitation levels, X_{lh} becomes dominant, with X_{hh} manifesting itself as a shoulder on the short-wavelength edge of X_{lh} (this spectrum is not shown in the figure). The increase in the X_{lh} exciton population is apparently due to a decrease of the hole spin-relaxation time with an increase of the excitation level, which can be caused by the generation of nonequilibrium acoustic phonons. Note also a weak (~1 meV) splitting of the X_{hh} line (see also Fig. 2), which is not observed in thinner ZnTe films (Fig. 1). Such a splitting is associated usually with polariton effects [24, 27]. For instance, the short-wavelength component of X_{hh} is assigned [24] to the upper, and the long-wavelength one, to the lower polariton branch. The polariton model allows, however, a somewhat different viewpoint as well [27]. We are not going to discuss this problem in more detail, and have mentioned it only to stress that this splitting is not connected in any way with strains.

Note that a new line I_x has appeared in Fig. 3 between the 1LO and X_{hh} lines, which manifests itself in secondary-luminescence spectra only when excited by 2.4097-eV photons ($\lambda_{exc} = 514.5$ nm), whose energy exceeds the heavy-hole exciton band bottom by slightly more than the energy of the optical LO phonon. This line originates from the resonant Mandelshtam–Brillouin light scattering (RMBLS) involving simultaneous emission of an optical and an acoustic phonon. As far as we know, RMBLS in ZnTe was earlier observed only in bulk crystals [28]. A comprehensive discussion of the I_x line in ZnTe/GaAs would go outside the scope of this paper. We note only that the presence in secondary-luminescence spectra of RMBLS, as well as of the radiation due to both ground and excited states of the

heavy- and light-hole excitons, implies a sufficiently high perfection of the ZnTe films.

We turn now to a consideration of the effect of strains on the A^0X line, i.e., on the exciton bound to a neutral acceptor. For the sake of brevity, we will denote this complex by NAE. We first note that, as shown in [9], the acceptor impurity in ZnTe/GaAs heterostructures is arsenic and that, by [29], the A^0X line in unstrained ZnTe lies at 2.375 eV.

The effect of biaxial strains on the radiation caused by the exciton localized at a neutral acceptor is more complex than the one associated with a free exciton. This is due to three particles, two holes, and one electron being localized in this case at a negatively-charged impurity (acceptor). This problem was considered theoretically in [30], where it was shown, in particular, that the NAE energy level should split into three, even if only strains are taken into account. The final state after the recombination of the electron and the hole in the NAE is the neutral acceptor (NA), whose ground state (only transitions to such states can be strong) splits into two levels in the field of a biaxial strain. Therefore, in principle, one could observe several lines originating from optical transitions between the various initial states of the NAE and the final states of the NA. However, at low temperatures, only the lowest NAE state is populated and, hence, the emission spectra should contain two lines (A^0X), whose energies, with only the strains taken into account, are given by the expressions [30, 31]

$$W_{1,2} = W_0 + \left[2a\left(\frac{C_{11} - C_{12}}{C_{11}}\right) \pm b_1\left(\frac{C_{11} + 2C_{12}}{C_{11}}\right)\right]\varepsilon, \quad (4)$$

which very much resemble Eq. (3), the only difference being that W_0 in (4) is the A^0X energy (2.375 eV) in unstrained ZnTe, whereas the deformation constant b_1 describes the splitting of the NA level. Note in connection with Eqs. (4), that the higher-energy photon corresponding to the transition to the lower NA level is an allowed optical transition [32], whose energy, as will be shown later on, practically coincides with the position of the A^0X line observed in ZnTe/GaAs spectra. The optical transition corresponding to the less energetic photon W_2 [the plus sign in (4)] is weakly allowed, provided $\Delta = |2b_1[(C_{11} + 2C_{12})/C_{11}]\varepsilon|$ considerably exceeds the exchange interaction between the holes, Δ_{exc} [32]. As follows from our estimates made using expressions from [30], which are more complex than (4) and are modified to cover the case of biaxial strains, this condition is upheld: $\Delta = 3.5$ meV $\gg \Delta_{exc} \approx 0.6$ meV. This is why low-temperature PL spectra of ZnTe/GaAs exhibit one A^0X line only.

The theoretical value of the b_1 constant for the NA was derived within the effective-mass approximation [33]

$$b_1 = b\left(1 - \frac{4\mu^2}{5} - \frac{12\mu\delta}{25}\right), \quad (5)$$

where b is the deformation constant entering (3), and $\mu = 6\gamma_3 + 4\gamma_2)/5\gamma_1$ and $\delta = (\gamma_3 - \gamma_2)/\gamma_1$ are expressed through the Luttinger parameters. Because, as already mentioned, the acceptor in ZnTe/GaAs films is As, and in this case the hole binding energy is close to the theoretical value obtained in the effective-mass approximation [29], we will use the value of b_1 obtained from (5). Substituting the values of γ_i ($i = 1, 2, 3$) from [16] yields $b_1 = -0.91$ eV. Inserting this value in (4), we obtain for the allowed transition a photon energy very close to the experimental value of the A^0X line energy (2.3693 eV): $E_{A^0X} - W_1 \approx 0.4$ meV. Using more complex relations from [30], taking into account the exchange interaction Δ_{exc}, we come to $E_{A^0X} = W_1(\Delta_{exc})$ for $\Delta_{exc} \approx 0.6$ meV.

Note that the presence of nonuniformities in the strain tensor can result in lifting of the forbiddenness of the transition involving the W_2 photon. Nonuniformities can be formed, for instance, through introduction of CdTe islands in ZnTe/GaAs. Such experiments will be discussed in a separate paper. We will restrict ourselves here to saying that we have succeeded in observing in such structures the manifestation of the forbidden transition, with the theoretical energy difference $W_1 - W_2 = -b_1[(C_1 + 2C_{12})/C_{11}]\varepsilon = 3.5$ meV very close to the experimental value of 3.2 meV for this quantity.

ACKNOWLEDGMENTS

The authors are indebted to A.F. Plotnikov for his assistance in the work.

Support of the Russian Foundation for Basic Research (grants nos. 98-02-16980, 97-02-16721, and 99-02-18161) and of the Ministry of Science of the RF (grant no. 97-1045) is gratefully acknowledged. The work was also partially supported by a Scientific School Support Grant (96-15-96341).

REFERENCES

1. A. M. Glass, K. Tai, R. B. Bylsma, *et al.*, Appl. Phys. Lett. **53** (10), 834 (1988).
2. V. S. Bagaev, V. V. Zaĭtsev, V. V. Kalinin, *et al.*, Pis'ma Zh. Éksp. Teor. Fiz. **58** (2), 82 (1993).
3. V. S. Bagaev, V. V. Zaĭtsev, V. V. Kalinin, *et al.*, Solid State Commun. **88** (10), 777 (1993).
4. S. L. Zhang, Y. T. Hou, M. Y. Shen, *et al.*, Phys. Rev. B **47** (19), 12937 (1993).
5. V. S. Bagaev, V. V. Zaĭtsev, V. V. Kalinin, *et al.*, Izv. Akad. Nauk, Ser. Fiz. **58** (7), 97 (1994).
6. J. Cibert, Y. Gobil, Le Si Dang, *et al.*, Appl. Phys. Lett. **56** (3), 292 (1990).
7. V. S. Bagaev, V. V. Zaĭtsev, V. V. Kalinin, *et al.*, Fiz. Tverd. Tela (S.-Peterburg) **38** (6), 1728 (1996).
8. G. L. Bir and G. E. Pikus, *Symmetry and Strain-Induced Effects in Semiconductors* (Nauka, M., 1972; Wiley, New York, 1974).

9. Y. Zhang, B. J. Skromme, and F. S. Turco-Sandroff, Phys. Rev. B **46** (7), 3872 (1992).
10. H. Tatsuoka, H. Kuwabara, Y. Nakanishi, *et al.*, J. Appl. Phys. **67** (11), 6860 (1990).
11. H. Tatsuoka, H. Kuwabara, Y. Nakanishi, *et al.*, J. Cryst. Growth **117** (1–4), 554 (1992).
12. T. Itoh, K. Shinone, N. Katagiri, *et al.*, J. Cryst. Growth **117** (1–4), 835 (1992).
13. K. Shahzad, Phys. Rev. B **38** (12), 8309 (1988).
14. K. Ohkawa, T. Mitsuyu, and O. Yamazaki, Phys. Rev. B **38** (17), 12465 (1988).
15. D. J. Olego, K. Shahzad, J. Petruzzello, *et al.*, Phys. Rev. B **36** (14), 7674 (1987).
16. *Numerical Data and Functional Relationships in Science and Technology*, Ed. by K.-H. Hellwege, Landolt-Bornstein, New Series (Springer, Berlin, 1982), vol. 17, Parts *a* and *b*.
17. S. I. Novikova, *Thermal Expansion of Solids* (Nauka, M., 1974).
18. W. Wardzynski, M. Giriat, Szymczak, *et al.*, Phys. Status Solidi B **49** (1), 71 (1972).
19. J. Calatayud, J. Allegre, H. Mattieu, *et al.*, Phys. Rev. B **47** (15), 9684 (1993).
20. Le Si Dang, J. Cibert, Y. Gobil, *et al.*, Appl. Phys. Lett. **55** (3), 235 (1989).
21. G. Kudlek, N. Presser, J. Gutowski, *et al.*, Semicond. Sci. Technol. **6** (9A), A90 (1991).
22. J. Gutowski, Semicond. Sci. Technol. **6** (9A), A51 (1991).
23. K. Kumazaki, F. Iida, K. Ohno, *et al.*, J. Cryst. Growth **117** (1–4), 285 (1992).
24. H. P. Wagner, S. Lankes, K. Wolf, *et al.*, J. Cryst. Growth **117** (1–4), 303 (1992).
25. G. Kudlek, N. Presser, J. Gutowski, *et al.*, J. Cryst. Growth **117** (1–4), 290 (1992).
26. G. E. Pikus and E. L. Ivchenko, in *Excitons*, Modern Problems in Condensed Matter Sciences (Nauka, Moscow, 1985), p. 148.
27. D. E. Cooper and P. R. Newman, Phys. Rev. B **39** (11), 7431 (1989).
28. Y. Oka and M. Cardona, Solid State Commun. **30** (4), 447 (1979).
29. H. Venghaus and P. J. Dean, Phys. Rev. B **21** (4), 1596 (1980).
30. H. Mathieu, J. Camassel, and F. Ben Chekroun, Phys. Rev. B **29** (6), 3438 (1984).
31. F. Dal'Bo, G. Lentz, N. Magnea, *et al.*, J. Appl. Phys. **66** (3), 1338 (1989).
32. V. D. Kulakovskiĭ, G. E. Pikus, and V. B. Timofeev, Usp. Fiz. Nauk **135** (2), 237 (1981).
33. M. Schmidt, Phys. Status Solidi B **79** (2), 533 (1977).

Translated by G. Skrebtsov

Physics of the Solid State, Vol. 42, No. 2, 2000, pp. 241–243. Translated from Fizika Tverdogo Tela, Vol. 42, No. 2, 2000, pp. 235–237.

SEMICONDUCTORS AND DIELECTRICS

Nonlinear Absorption of a Picosecond Pulse in *a*-Si : H

A. A. Bugaev, O. I. Kon'kov, and E. I. Terukov

Ioffe Physicotechnical Institute, Russian Academy of Sciences, Politekhnicheskaya ul. 26, St. Petersburg, 194021 Russia

Received August 5, 1999

Abstract—The results of a nonlinear-absorption research in a film of *a*-Si : H are reported. The absorption is induced by a picosecond laser pulse with quantum energy only slightly exceeding the band gap width of the material. Picosecond pulses obtained by optical methane and hydrogen pumping and stimulated Raman scattering were used in experiments for resonance excitation of the sample. The total absorption is shown to be the sum of the free carrier absorption and absorption by holes trapped on local levels in the "tail" of the conduction band. © *2000 MAIK "Nauka/Interperiodica".*

Amorphous hydrogenated silicon (*a*-Si : H) attracts significant attention due to the fact that is has the potential to be used as a solar-cell material or as a material for light-emitting integrated structures for telecommunication systems [1]. In the latter case, *a*-Si : H is used as a solid-state host doped by rare-earth ions, which allows luminescence to be excited by free charge carriers created by electron pumping [2, 3]. The emitting elements arranged this way are ideal for integrating into opto-electronic devices. The nonlinear interaction process associated with photoexcitation and relaxation of the excited state in *a*-Si : H was earlier investigated in a number of works using light pulses belonging to the pulse-width range from microseconds to femtoseconds [4–11]. These works studied the trapping of the excited carriers by shallow and deep trapping centers, investigated recombination mechanisms and mechanisms of light-induced absorption in the middle of the band gap of *a*-Si : H.

In the present work, we researched nonlinear absorption of picosecond light pulses with the quantum energy of 1.978 eV and 1.825 eV, which only slightly exceeded band gap width E_g in *a*-Si : H (E_g = 1.8 eV). The data obtained allowed us to determine the effective absorption cross section due to excited carriers as a sum of the free-carrier absorption and absorption by the carriers trapped at local electron levels.

In the experiments, we used a sample of amorphous hydrogenated silicon deposited on a fused silica substrate obtained by magnetron sputtering of Si in an argon and hydrogen atmosphere. The film was 2.32 μm thick. Dispersion of absorption and refraction was measured in this sample, applying reflectivity spectroscopy for *S*- and *P*-polarized light incident at an angle of 50°. For the energy of quanta used, the absorption coefficients for picosecond pulses were found to be 1.5×10^4 ($\hbar\omega$ = 1.978 eV) and 1.1×10^4 cm^{-1} (($\hbar\omega$ = 1.825 eV). The band gap width was obtained in *a*-Si : H as the energy of a quantum for which $\alpha = 10^4$ cm^{-1} and turned out to be of 1.8 V.

A single pulse of a YAG : Nd laser operating in the colliding pulse regime of the passive mode selflocking was used in the research of nonlinear absorption. After amplification, the laser pulse energy amounted to 5 mJ. The pulsewidth was 27 ps measured as FWHM. Laser radiation of the fundamental frequency ($\hbar\omega$ = 1.17 eV) was then converted into a second-harmonic pulse ($\hbar\omega$ = 2.34 eV), which, in the reflection schematic, was used for stimulated Raman scattering excitation in a gas chamber containing methane (CH_4) or hydrogen (H_2) at a pressure of 20 atm. The wavelengths and energies of the first Stokes components in the picosecond Raman-scattered pulse were 0.627 μm or 1.978 eV for CH_4 and 0.697 μm or 1.825 eV for H_2.

In the experiments, we investigated the energy dependence of the transmission of the Raman-scattered pulse through the film of *a*-Si : H; relaxation of the induced absorption was also investigated. In the first case, the sample of *a*-Si : H was positioned near the focused-beam waist (F = 150 mm) and calibrated filters provided variation of the exciting radiation level. To determine the peak energy density E_0 at the surface of the *a*-Si : H film, a CdS plate was used instead of the amorphous-silicon sample and the induced absorption was measured in CdS (E_g = 2.42 eV) corresponding to two-photon interband transitions. From this measurement, the peak intensity of the exciting pulse I_0 was estimated [12]. The two-photon absorption coefficients for the wavelengths of the Raman-scattered pulse were calculated according to relationships used in [13, 14] and turned out to be 6.12 cm/J W (for 0.627 μm) and 9.6 cm/J W (for 0.697 μm). In the second case, a conventional probing schematic with preceding excitation was used to investigate the induced-absorption relaxation; the polarizations of the exiting and probing pulses were mutually perpendicular. The results of measurements are shown on Figs. 1 and 2.

As is seen, the relaxation kinetics data obtained for the induced absorption at the initial carrier concentration N ~ 10^{19} cm^{-3} in the delay-time range below ~150 ps

1063-7834/00/4202-0241$20.00

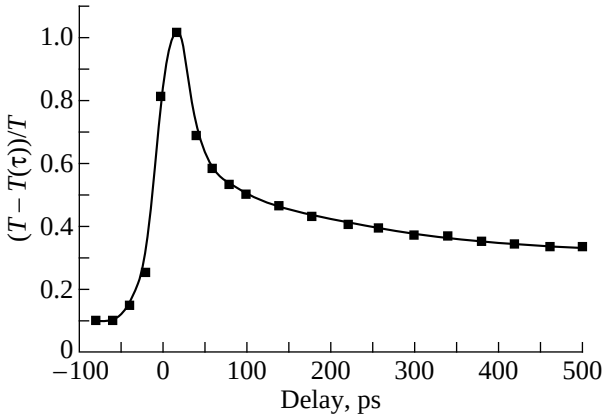

Fig. 1. Relaxation kinetics of the induced absorption for picosecond pulses in *a*-Si : H at a charge carrier concentration of 10^{19} cm^{-3}. Filled squares are experimental data. Solid curve is the best fit approximation.

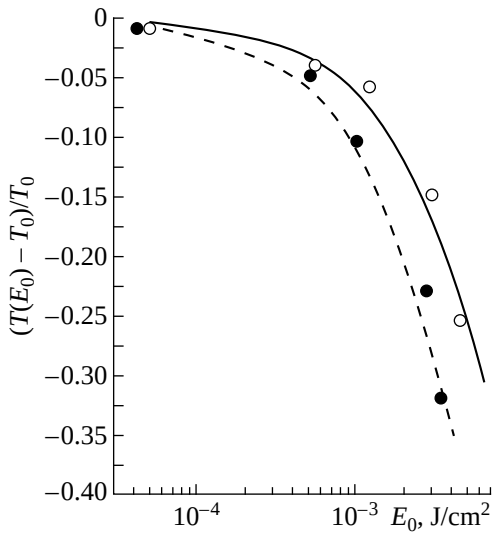

Fig. 2. Energy dependence of the nonlinear absorption in *a*-Si : H excited by picosecond Raman-scattered pulses with the energy of quanta 1.825 eV (solid curve) and 1.978 eV (dashed curve). The curves are results of the numerical fit (2), the circles indicate experimental data.

(Fig. 1) reveal approximately inversely proportional time dependence $(1/\tau)$. For longer delays, the relaxation significantly slows down. The relaxation behavior in the 150 ps range is in a good agreement with an earlier proposed mechanism [11], according to which the process of recombination belongs to the Auger type and involves two free electrons and one trapped hole. Under the condition of faster hole trapping compared to the trapping of an electron (due to longer "tail" of the density of states in the valence band) and in the case of high concentrations, i.e., for $n = p > N_t$ (N_t is the density of localized states), the kinetic equation for electrons corresponds not to a cubic but rather to a quadratic dependence $dn/dt = -\gamma_n N_t n^2$ and it is in agreement with the observed type of recombination with the coefficient $B = \gamma_n N_t$. According to the data of [6–10], the inequality $n = p > N_t$ begins to be fulfilled for the carrier concentration higher than $\sim 3 \times 10^{17}$ cm^{-3}, above which the recombination process is, in general, bimolecular with the time constant $B \sim 10^{-9}$ s. It is easy to see that even for the maximum achievable concentration levels ($\geq 10^{19}$ cm^{-3} in our experiments) the nonlinear absorption of a 27 ps pulse is weakly influenced by the recombination process, whose duration is $B^{-1}N^{-1} \geq 100$ ps.

As seen from Fig. 2, propagation of a laser pulse through the *a*-Si : H film is accompanied by a significant decrease of the transmission level amounting to 30% with the growth of incident energy. Such a transmission change ($\Delta T/T_0 \sim \Delta\alpha d = 0.3$) approximately corresponds to the induced absorption level $\Delta\alpha \sim 10^3$ cm^{-1}. The nature of the energy dependence of $\Delta T/T_0 = f(E_0)$ is close to that observed under analogous excitation conditions in *c*-Si [15, 16]. The last is known to originate from absorption by the free carriers created via an indirect interband transition in *c*-Si. We have no reason to assume that, in our case, the nonlinear absorption includes not only transient nonlinear susceptibility but also stationary (time-lag-free) nonlinear components, i.e., two-photon absorption. This allows us to analyze the results presented in Fig. 2, implying only a set of equations describing propagation of a light pulse in a medium with the transient cubic susceptibility and disregarding diffusion process,

$$\begin{aligned}\frac{\partial I(z,t)}{\partial z} &= -\alpha I(z,t) - \sigma_f N_f(z,t) I(z,t) \\ &\quad - \sigma N(z,t) I(z,t), \\ \frac{\partial N(z,t)}{\partial t} &= \frac{N_f(z,t)}{\tau_f} - BN^2(z,t), \\ \frac{\partial N_f(z,t)}{\partial t} &= \frac{\alpha I(z,t)}{\hbar\omega} - \frac{N_f(z,t)}{\tau_f},\end{aligned} \tag{1}$$

where N_f and σ_f are the concentration and absorption cross section for free electrons; N and σ are the same parameters for carriers trapped on local levels; τ_f is the trapping time; and α is the linear absorption coefficient.

As the data on τ_f are absent and the recombination of carriers during the pulse can be neglected, the set (1) can be written as

$$\begin{aligned}\frac{\partial I(z,t)}{\partial z} &= \alpha I(z,t) - \sigma_{\text{eff}} N_f(z,t) I(z,t), \\ \frac{\partial N_f(z,t)}{\partial t} &= \frac{\alpha I(z,t)}{\hbar\omega},\end{aligned} \tag{2}$$

where $\sigma_{\text{eff}} = \sigma_f N_f + \sigma N$ and σN are assumed to be a constant ($n = p > N_t$). We integrated set (2) numerically, under the assumption that σ_{eff} is a variable param-

eter. For the Gaussian spatial and temporal intensity profile $T = \int_0^\infty \int_{-\infty}^\infty I_{\text{out}}(r, t)dtdr / \int_0^\infty \int_{-\infty}^\infty I_{\text{in}}(r, t)dtdr$, we derived a solution for the energy transmission of the light pulse. The numerical fit of solution (2) to the experimental results is shown in Fig. 2 (solid lines). The best fit was complied with $\sigma_{\text{ef}} = 4 \times 10^{-17}$ (for $\hbar\omega = 1.978$ eV) and to $\sigma_{\text{eff}} = 6 \times 10^{-17}$ cm^2 (for $\hbar\omega = 1.825$ eV). The result obtained was in a good agreement with data of the work [6], according to which the change in extinction amounts to $\Delta k \sim 0.03$ at the carrier concentration of 10^{20} cm^{-3}, which, as is easily seen, corresponds to $\sigma \sim 7 \times 10^{-17}$ cm^2.

It is shown that the cross section for the charge carrier absorption in a-Si : H exceeds the cross section in *c*-Si approximately by an order of magnitude. In the last case, [17] reports $\sigma = 6 \times 10^{-18}$ cm^2. On the other hand, it was demonstrated in [4] that the induced absorption in a-Si : H is mostly due to transitions of holes trapped on local levels to the conduction band. These transitions have an absorption cross section $\sigma = 10^{-16}$ cm^2. Hence, it appears clear that the nonlinear absorption of a picosecond pulse in *a*-Si : H results from the free carrier absorption in combination with photoionization of holes trapped on the local levels in the "tail" of the conduction band.

ACKNOWLEDGMENTS

The authors are grateful to B.P. Zaharchenya for interest and support of the present work. The work was carried out in the frame of the project "Optics. Laser physics" of the Ministry of Science and Engineering of the Russian Federation.

REFERENCES

1. *Proceedings of MRS Symposium on Amorphous Silicon Technology*, Ed. by M. Hack, E. A. Schiff, S. Wagner, R. Schropp, and A. Matsuda (Pittsburgh, Pennsylvania, 1996), Vol. 420.
2. *Proceedings of MRS Symposium on Rare Earth Doped Semiconductors II*, Ed. by S. Coffa, A. Polman, and R. N. Schwartz (Pittsburgh, Pennsylvania, 1996), Vol. 422.
3. *Proceedings of MRS Symposium on Material and Devices for Silicon-Based Optoelectronics*, Ed. by A. Polman, S. Coffa, and R. Soref (Warrendale, Pennsylvania, 1997), Vol. 486.
4. P. O'Connor and J. Tauc, Phys. Rev. B **25** (4), 2748 (1982).
5. S. Komuro, Y. Aoyagi, Y. Segawa, *et al.*, Appl. Phys. Lett. **42** (1), 79 (1983).
6. A. Esser, K. Seibert, and H. Kurz, Phys. Rev. B **41** (5), 2879 (1990).
7. P. M. Fouchet, D. Hulin, R. Vanderhaghen, *et al.*, J. Non-Cryst. Solids **141** (2), 76 (1992).
8. R. Vanderhaghen, A. Mourchid, D. Hulin, *et al.*, J. Non-Cryst. Solids **137–138**, 543 (1991).
9. R. I. Devlen, G. S. Kanner, Z. Vardeny, *et al.*, Solid State Commun. **78** (7), 665 (1991).
10. G. Juska, M. Viliunas, K. Arlauskas, *et al.*, Phys. Rev. B **51** (23), 16668 (1995).
11. G. Juska, J. Kocka, M. Viliunas, *et al.*, J. Non-Cryst. Solids **164–166** (8), 579 (1993).
12. A. A. Bugaev and A. L. Stankevich, Fiz. Tverd. Tela **34** (5), 1622 (1992).
13. C. R. Pidgeon, B. S. Wherrett, A. M. Johnston, *et al.*, Phys. Rev. Lett. **42** (26), 1785 (1979).
14. B. S. Wherrett, J. Opt. Soc. Am. B **1** (1), 67 (1984).
15. T. F. Boggess, K. M. Bohnert, K. Mansour, *et al.*, IEEE J. Quant. Electron. **QE-22** (33), 2195 (1986).
16. A. A. Bugaev, B. P. Zaharchenya, Yu. B. Kiselev, *et al.*, Dokl. Akad. Nauk SSSR **296** (5), 1098 (1987).
17. K. G. Svantesson, J. Phys. D: Appl. Phys. **12** (3), 425 (1979).

Translated by S. Klimentov

Physics of the Solid State, Vol. 42, No. 2, 2000, pp. 244–252. Translated from Fizika Tverdogo Tela, Vol. 42, No. 2, 2000, pp. 238–245.

SEMICONDUCTORS AND DIELECTRICS

Tellurium Recrystallization under Microgravity Conditions and the Resulting Properties of Samples

R. V. Parfen'ev*, I. I. Farbshteĭn*, I. L. Shul'pina*, S. V. Yakimov*, V. P. Shalimov, A. M. Turchaninov**, A. I. Ivanov**, and S. F. Savin*****

**Ioffe Physicotechnical Institute, Russian Academy of Sciences, St. Petersburg, 194021 Russia*

***Kompozit Research and Production Corporation, Kaliningrad, Moscow oblast, 141070 Russia*

****Energiya All-Russia Space Corporation, Kaliningrad, Moscow oblast, 141070 Russia*

Received August 5, 1999

Abstract—Three experiments on the tellurium recrystallization by a modified Bridgman method were performed under microgravity conditions on board the Mir orbital space laboratory using a ChSK-1 Kristallizator furnace. The physical properties of samples were studied, including the final crystal structure, the distribution of impurities and defects, and the charge carrier concentration and mobility. The results were compared to the analogous parameters of crystals remelted using the same method under the normal gravity conditions. It is established that the samples recrystallized in a close volume under the on-board microgravity conditions "break off" from the container walls and touch the walls only in a few points. This circumstance gives rise to special effects, such as the growth of crystals with a free surface and deep supercooling. Study of the distribution of electrically active impurities over the length of ingots shows evidence of the presence of thermocapillary convective flows in the melt under the microgravity conditions. The flows tend to increase upon separation of the melt from the container walls. The contributions due to impurities and electrically active structural defects to the charge carrier distribution are taken into account. The single-crystal sample obtained upon the partial recrystallization of tellurium in a close container volume under the on-board microgravity conditions exhibits the electrical characteristics comparable to those of a crystal grown by the Czochralski technique under the normal gravity conditions. © *2000 MAIK "Nauka/Interperiodica".*

INTRODUCTION

Experiments involving the mass and heat transfer processes and crystallization at various levels of gravity—from tens of g_0 in centrifuges to $10^{-6}g_0$ on board of space vehicles and platforms—offer additional means of variation of the structure and properties of semiconductor materials.

Pure tellurium—a material with the intrinsic hole concentration at $T = 77$ K equal to $p(77\ \text{K}) \sim 10^{13}$ cm^{-3} and the impurity conductivity region at $T < 200$ K with $E_{g\text{Te}} \cong 340$ mV [1]–is a very convenient object for such experiments because of a comparatively low melting temperature ($T_m = 452$°C [1]) and extremely high sensitivity of the electrophysical properties of Te to the presence of structural defects and mechanical stresses arising during the crystal growth process [2]. A comparatively high concentration of defects in Te crystals grown under the normal conditions may probably account for the fact that tellurium behaves in the impurity conductivity region as a typical *p*-type semiconductor [1].

Effect of a high gravity level upon the crystallization process, the content of structural defects, and the distribution of impurities in tellurium samples was recently studied in experiments using a special furnace of the Meudon type [3, 4] placed in a TsF-18 centrifuge operating in the Cosmonaut Training Center (Russia).

A series of three experiments on the directional crystallization of tellurium under microgravity conditions was performed in August 1996 on board of the Mir orbital space laboratory using a furnace of the Kristallizator ChSK-1 type. Below, we will present the results of investigations of the electrophysical properties of tellurium samples with different crystal structures. The results are compared with the known reference data, with the properties of samples obtained in the course of the preliminary on-ground experiments using the same equipment as that employed on board [5], and with the parameters of specially synthesized tellurium crystals. Preliminary results were reported at conferences devoted to the space materials science [6, 7].

EXPERIMENTS ON TELLURIUM RECRYSTALLIZATION UNDER MICROGRAVITY CONDITIONS

The directional crystallization of tellurium was performed by the method of propagating temperature gradient in a furnace of the Kristallizator ChSK-1 type [8]. This method ensures the absence of vibrations–in contrast to the regime of propagating sample which was also possible in the experimental setup employed. Fig-

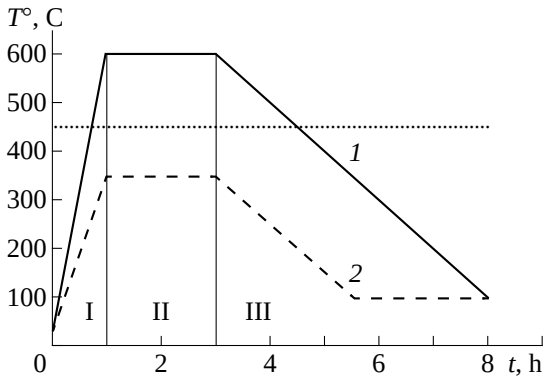

Fig. 1. Temperature–time schedule of tellurium recrystallization experiments: (*1*) hot zone; (*2*) cold zone. Dashed horizontal line shows the melting temperature of tellurium (452°C). Stages I–III are explained in the text.

ure 1 shows a temperature–time schedule of the experiment exhibiting tree sequential stages: (I) heating of the furnace and melting of the initial ingot; (II) homogenization of the melt; (III) cooling and solidification of the melt. A sample was positioned in the zone of temperature gradient (≅40 K/cm over a 60 mm distance) so as to provide for the partial or compete melting, depending on the experimental task. The ingot crystallization front occurred within the temperature gradient region and propagated at a velocity of $f \cong 4$ cm/h when the heater temperature was decreased according to stage III (Fig. 1).

In experiment 1, we studied recrystallization of a single-crystal tellurium sample with a length of $L = 52$ mm cleaved along the C_3 axis from a Czochralski grown single crystal with the hole concentration $p(77\ \mathrm{K}) = 5 \times 10^{14}$ cm^{-3}. A container (ampule) with the sample was mounted in the furnace so that 1/3 of the sample length (~17 mm) occurred at a temperature below the melting point and served a seed for crystallization. Then the directional crystallization was performed in the melted part of the sample at a velocity of 4 cm/h and the process was terminated in ~55 min, when the hot zone temperature decreased to 460°C and that of the cold zone, to 100°C.

In experiment 2, the initial sample was a polycrystalline tellurium ingot with a length of $L = 43$ mm fused with a 22-mm-long seed crystal cleaved along the C_3 axis from a tellurium single crystal and mounted parallel to the ampule axis. When the furnace was heated (stages I and II in Fig. 1), the polycrystalline ingot and a part of the seed melted and then recrystallized from melt at the same rate of temperature decrease as in the first experiment.

In experiment 3, the initial sample represented an ingot of high-purity tellurium with a length of $L =$ 44 mm and a hole concentration of $p(77\ \mathrm{K}) \sim 10^{14}$ cm^{-3} not provided with a seed. The sample was placed in the furnace so as to be completely melted in stages I and II and then spontaneously crystallized under the propagating temperature gradient conditions in stage III.

The photographs of tellurium samples after the recrystallization under the on-board microgravity conditions are shown in Fig. 2, and the dimensions of samples are given in Table 1.

REAL CRYSTAL STRUCTURE OF TELLURIUM SAMPLES RECRYSTALLIZED UNDER MICROGRAVITY CONDITIONS

In sample 1, one may distinguish three different parts oriented along the third-order axis C_3 (direction [0001]): non-remelted region, cylindrical recrystallized region in contact with the ampule walls, and recrystallized region with a hexagonal cross-section not touch-

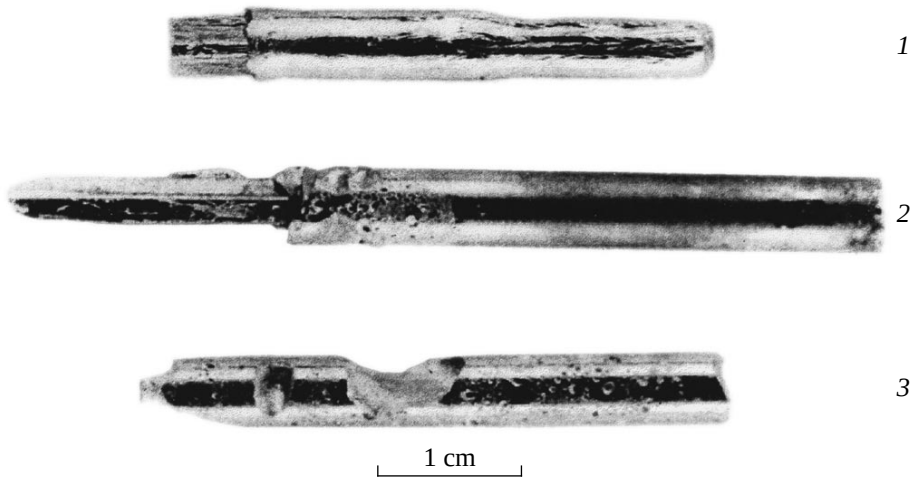

Fig. 2. Photographs of tellurium single crystals grown by the method of directional crystallization under the on-board microgravity conditions: (*1*) sample 1 obtained by partial recrystallization of initial single crystal; (*2*) sample 2 obtained by crystallization on a seed; (*3*) sample 3 obtained by complete recrystallization without seed.

Table 1. Sample dimensions

Sample	Sample length, mm	Sample diameter, mm	Seed length, mm
1	41	5.6–4.8	7
2	65	5.6	22
3	44	5.6	–

ing the ampule walls. The latter part, which can be observed only in samples crystallized under the microgravity conditions, is probably formed due to the action of surface tension forces developed in the field of temperature gradient. For the same reason, the non-melted region of the seed was partly pulled into the melt. As a result, the length of the non-remelted part of the sample upon treatment was less than 1/3 of the initial length.

After measuring the galvanomagnetic properties characteristic of the distribution of impurities and defects along the crystal, sample 1 was cleaved along the C_3 axis in the cleavage plane $(10\bar{1}0)$. The real crystal structure was studied by X-ray backscattering topography using one- and two-crystal setups [9]. The X-ray topographs are presented in Fig. 3.

The surface of cleaved sample 1 mostly coincides with the cleavage plane, but contains some flat steps. At a distance of 9.6 mm from anticipated boundary of the recrystallization region (indicated by the arrow in Fig. 3), the cleavage reveals bent and twisted boundaries near the ingot side surface (see region to the right of the arrow). The real structure of the initial single crystal (observed to the left of the arrows in Fig. 3) is evidently imperfect and exhibits the presence of macroscopic stresses. Position of the real recrystallization boundary can be determined by the shape of the ingot side surface (Fig. 2) and by the distribution of macrostresses determined using the X-ray topograph (see below). The misorientation of crystal blocks along the C_3 axis in the remelted region amounts to only a few seconds of arc, while misorientation around the C_3 axis is more pronounced (reaching a few minutes of arc).

Use of a monochromator for imaging of the ingot cleavage surface provides for a better resolution and higher sensitivity with respect to macrostresses, pores, and other inclusions. In particular, this techniques reveals macrostresses in the region of anticipated recrystallization boundary. The distribution of pores and inclusions exhibits a random character, that is, the pattern is related neither to the recrystallization boundary nor to the growth axis (coinciding with the central axis of the sample). A region with a length of ~6 mm adjacent to the recrystallization boundary possesses the most perfect structure, despite the presence of some crystal defects inherited from the seed.

The third portion of the sample crystallized with a free surface.

In sample 2, a single-crystal seed was fused with a polycrystalline ingot before the experiment on board. After recrystallization under the microgravity conditions, it was found that the seed separated from the sample ingot in the region of ampule narrowing. In the vicinity of the breakage site, there are blisters on the sample surface (Fig. 2). The X-ray topographic investigation of this sample revealed a fine-grained mosaic structure on the ingot surface. The crystal orientation of grains on the sample surface coincides, on the average, with that in the seed. The size of grains is 5–10 μm and they partly occur in a strongly stressed state.

The recrystallization of sample 3 was performed by completely remelting the initial ingot without seed under the microgravity conditions. The recrystallized ingot has

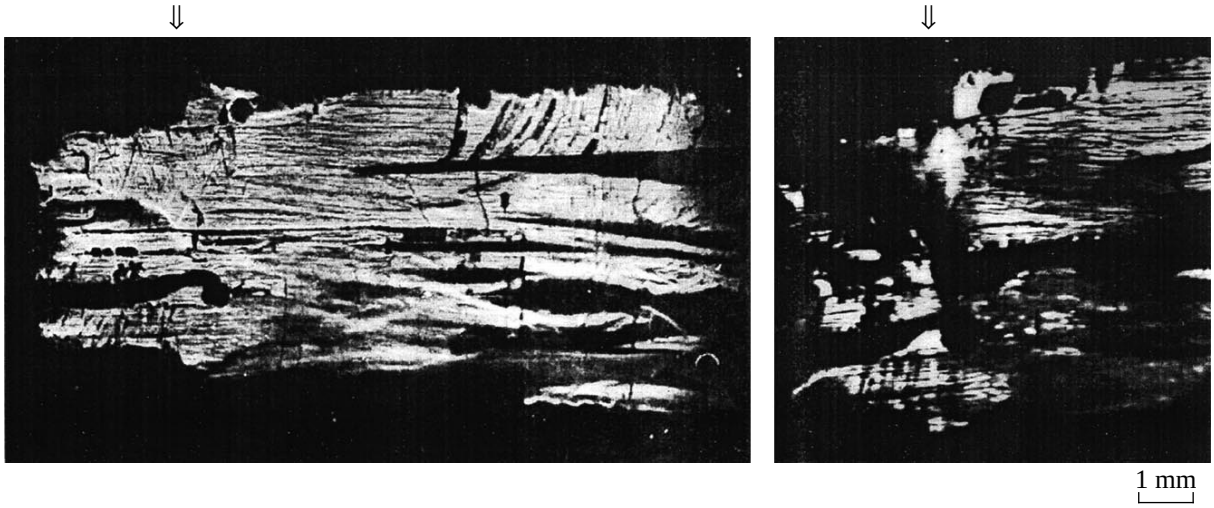

Fig. 3. X-ray topographs of the surface obtained upon cleavage of sample 1 by $(10\bar{1}0)$ plane [CuK_α radiation; $(20\bar{2}0)$ reflection]. Right-hand micrograph shows the expected region of the recrystallization onset [imaged using a Ge(111) single-crystal monochromator]. The arrows indicate positions of the expected recrystallization onset regions.

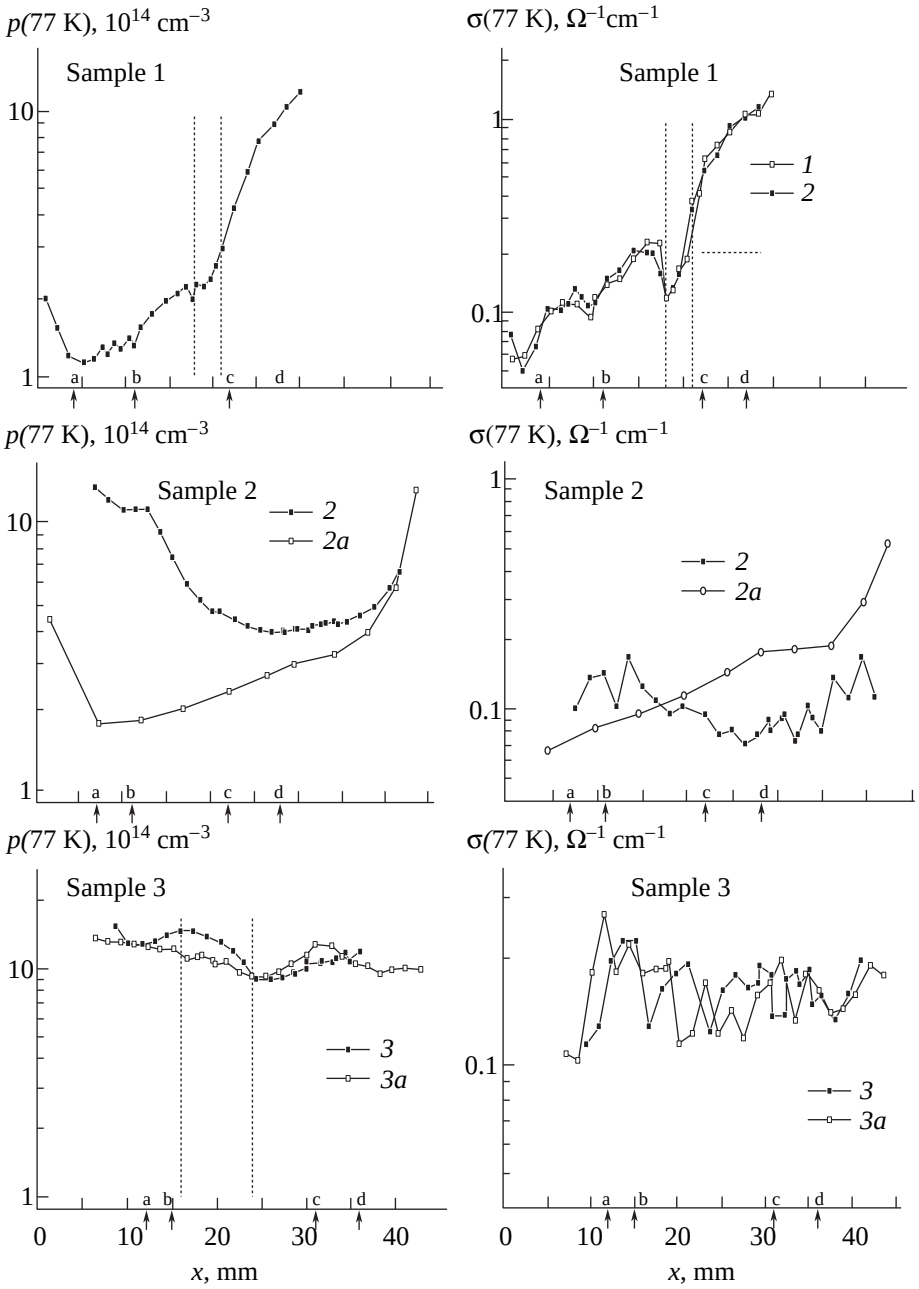

Fig. 4. Distributions of the hole concentration p(77 K) and conductivity σ(77 K) along the single-crystal tellurium samples grown on board of the Mir orbital space laboratory: sample 1 (*1*, before etching; *2*, after etching); sample 2 (*2a*, on-ground analog); sample 3 (*3a*, on-ground analog). The vertical lines indicate the onset of the break-off crystallization in sample 1 and the position of a large pore in sample 3.

a cylindrical shape with two large caverns and numerous small traces of bubbles on the surface (Fig. 2).

After measuring the galvanomagnetic properties, sample 3 was cut into three approximately equal parts across the longitudinal axis. X-ray topographic analysis of the cross-sections revealed a considerable difference in size of the crystal blocks in these sections. The first part of the crystal, which occurred in the region of minimum temperature in the course of solidification, contains large blocks (0.6–1.0 mm) and blisters of complicated shape. The distribution of blocks in this cross-section is not centrosymmetric relative to the longitudinal axis of the ingot. Large blocks possess a fragmentary structure and are strongly stressed. In the second cross-section, the ingot exhibits a homogeneous fine-grained structure with random orientation of the grains and the grain size varying from 5 to 50 μm. These data

Table 2. Averaged characteristics of samples

Sample	Length of recrystallized region, mm	σ (290 K), $\Omega^{-1}cm^{-1}$	$R\sigma$ (77 K), $cm^2/(V\,s)$	p (77.4 K), 10^{14} cm^{-3}
1	34	2.57	6140	2.59
			8155 (max)	1.13 (min)
Cz	65	2.70	7677	1.13
			8060 (max)	1.11 (min)
2	43	2.43	1423	5.96
			2351 (max)	3.87 (min)
2a	45	–	3833	4.00
			4669 (max)	1.76 (min)
3	44	1.79	1076	11.7
			1464 (max)	8.92 (min)
3a	48.5	–	1.075	11.1
			1.557 (max)	9.20 (min)

Note: Positions of the "min" and "max" points correspond to Figs. 3, 4; Cz denotes a single-crystal sample grown on the Earth by the Czochralski method.

indicate that the melt occurred in a supercooled state prior to solidification; the solidification process behind the second cross-section proceeded in a homogeneous spontaneous crystallization regime.

ELECTRICAL PROPERTIES OF RECRYSTALLIZED TELLURIUM SAMPLES

The electrical properties of samples grown under the microgravity conditions were studied by measuring conductivity and the Hall response in a weak magnetic field in the temperature range from 1.45 to 300 K. Distribution of these properties along the samples was studied at 290 and 77.4 K. The measured values were used to calculate the hole concentration $p = A/(Rec)$ [where A(77 K) = 1.18 and A(4.2 K) = 1.93 at the liquid nitrogen and liquid helium temperatures, respectively] and their Hall mobility $R\sigma$.

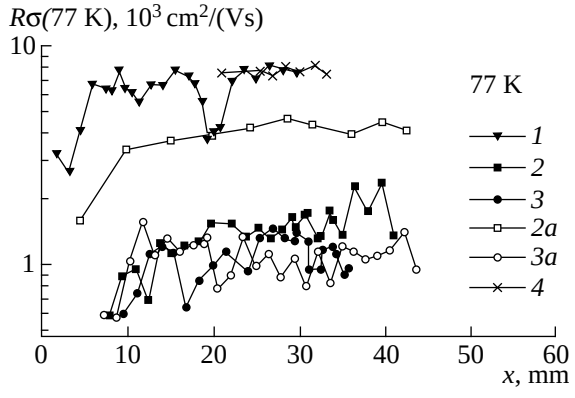

Fig. 5. Profiles of the Hall mobility $R\sigma$(77 K) in the recrystallized part of (*1–3*) space-grown samples *1–3*, respectively, and samples grown on the Earth by the (*4*) Czochralski and (*2a*, *3a*) Bridgman methods.

Figure 4 shows variation of the conductivity σ and the hole concentration p at 77 K along the samples grown on board of the Mir orbital space laboratory in comparison with analogous parameters of the samples grown on Earth by the Bridgman method using the same temperature–time schedule [on-ground analogs 2a (with seed) and 3a grown on the Earth]. Figure 5 presents the results of calculations of the Hall mobility $R\sigma$(77 K) distribution along the "space-grown" samples. For the comparison, also depicted are the hole mobility distributions in the initial Czochralski grown single crystal and in the on-ground analogs 2a and 3a.

After these measurements, the samples were treated for 2 min with a polishing etchant with the composition CrO_3–HCl–H_2O (1 : 1 : 3, w/w). Repeated measurements showed that the electrical properties of the samples remained virtually unchanged upon etching (cf. with the data for electric conductivity in Fig. 4). This result implies that the surface of samples was not contaminated in the course of remelting and acquired no additional defects, which could appear as a result of the difference in the coefficients of thermal expansion between tellurium and the container material. The absence of the latter effect is apparently related to a smaller role of the contact between melt and ampule walls during crystal growth under the microgravity conditions.

Table 2 presents averaged values of the parameters of space-grown tellurium samples and their on-ground analogs, together with the electrical properties of the initial tellurium single crystal grown by the Czochralski method (including data on the maximum mobilities and minimum hole concentrations).

Table 3. The values of parameters in equation (1) for various samples

Sample	k	C_0, 10^{14} cm^{-3}	$C_{0\text{def}}$, 10^{14} cm^{-3}	X_0, mm	V_0, mm^3	L, mm
1, region (ab)	0.2	5	2	4	726	34
1, region (cd)	0.45	7.8	–	–	–	–
2	0.8	4	60	4	1058	43
2a	0.42	3.5	6	2.2	1083	44
3	0.55	11	80	4	1083	4
3a	0.95	7	10	25	1194	48.5

DISCUSSION OF RESULTS

1. Charge carrier mobility. In samples remelted under the microgravity conditions, the concentrations of holes p(77 K) and their Hall mobilities $R\sigma$(77 K) at 77.4 K, as well as the distributions of these parameters along recrystallized ingots, were different in the samples of various types.

The $R\sigma$(77 K) value in sample 1, grown in a close volume under the microgravity conditions, was close to the mobility in a tellurium single crystal grown by the Czochralski technique (with a free surface) on the Earth. A significant decrease in mobility observed at a distance of 5 and 22 mm from the recrystallization boundary (Fig. 5) corresponds to the sample structure disturbances in the regions of variable ingot cross-section (Fig. 3). Generally lower mobility values in samples 2 and 3 are explained by the effect of hole scattering from structural defects and grain boundaries in these polycrystalline ingots.

2. Charge carrier concentration. In all samples obtained upon directional recrystallization under the microgravity conditions, the hole concentration p(77 K) exhibited an increase on the passage from beginning to end of the ingot. This pattern is characteristic of the process of impurity displacement in the course of directional crystallization, observed for impurities with a distribution coefficient $k < 1$. The process is usually described by the Scheil law, which is valid for k_0 = const and flat crystallization front [10]. In this case of tellurium, the dopant impurity is Sb with an equilibrium distribution coefficient of k_0(Sb) = 0.003 [3]. However, the character of the hole concentration variation observed in both space-grown samples 1 and 2 and in the on-ground analog 2a deviated from that predicted by the Scheil theory, the difference being especially pronounced in the initial parts of ingots. This behavior of the hole concentration in the initial parts of ingots can be explained by a decrease in the number of structural defects in the course of directional crystallization. In tellurium, these defects act both as the scattering centers and as acceptors [4]. For this reason, the character of the acceptor impurity distribution in ingots grown under the microgravity conditions, as well as in the samples obtained by directional crystallization at normal gravity, was described by the following expression [4]:

$$C = kC_0\left(1 - \frac{V(x)}{V_0}\right)^{k-1} + C^0_{\text{def}}\exp\left(\frac{x}{x_{0\,\text{def}}}\right), \qquad (1)$$

where k is the effective impurity distribution coefficient, V_0 is the total volume of a recrystallized part of the sample, $V(x)$ is the current volume recrystallized over the sample length x, C_0 is the initial impurity concentration in the melt, $x_{0\text{def}}$ is the relaxation length of the defect concentration, and $C_{0\,\text{def}}$ is the initial concentration of these defects. The results of analysis using this relationship are depicted in Fig. 6 and summarized in Table 3.

The first term in the right-hand part of equation (1) is valid in the case of ideal stirring of the melt during solidification. Under the microgravity conditions, the mechanism of gravitational mixing is virtually inoperative and the major role is played by a much weaker diffusion mechanism. This mass transfer mechanism is characterized by a constant impurity concentration in the major part of the ingot [11]. However, the experimental fact of the impurity displacement indicates that,

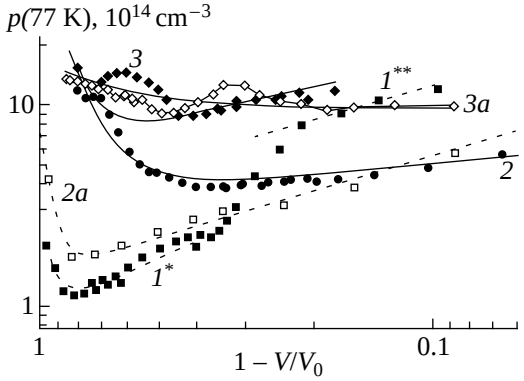

Fig. 6. Profiles of the hole concentration p(77 K) plotted on the relative scale $(1 - V/V_0)$ for (*1–3*) the single-crystal tellurium samples 1–3 grown on board of the Mir orbital space laboratory (microgravity conditions) and (*2a*, *3a*) their analogs grown on the Earth. Curves *1** and *1*** refer to regions (ab) and (cd) of sample 1. Points represent the data of measurements; curves show the results of calculations by equation (1) with the parameters given in Table 3.

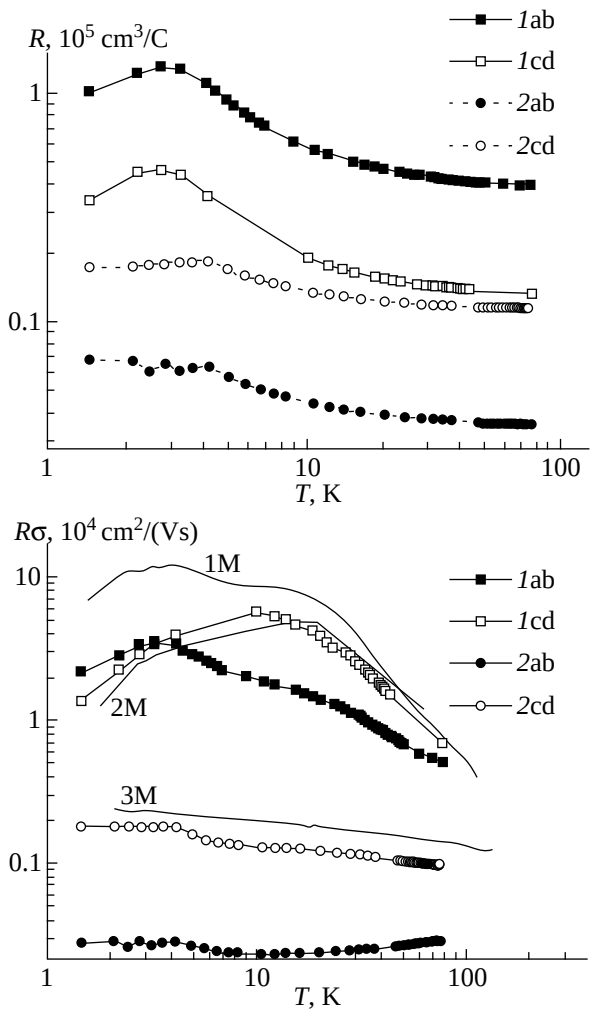

Fig. 7. Temperature dependence of the Hall coefficient R and the Hall mobility $R\sigma$ for various regions of single-crystal tellurium samples 1 and 2 grown on board of the Mir orbital space laboratory in comparison with the data for tellurium single crystals grown on the Earth using the (1M, 2M) Czochralski method and (3M) zone melting [16].

under conditions of the sample break-off from the walls, an increasing role is also played by the thermocapillary convective mixing (the Marangoni convection). Here, we may still use the Scheil law with the equilibrium distribution coefficient k_0 replaced by an effective coefficient k [12] dependent on the conditions of convection, the growth velocity, and the coefficient of impurity diffusion in the melt [13]:

$$k = \frac{k_0}{k_0 + (1 - k_0)\exp(-f\delta/D)}, \qquad (2)$$

where f is the growth velocity, δ is the thickness of the impurity-rich layer at the solid–liquid phase interface, and D is the coefficient of impurity diffusion in the melt. At a large growth rate, the effective coefficient k tends to unity, and at a small growth rate, this coefficient is close to the equilibrium value k_0.

According to the results of our numerical analysis, the case of "moderate" mixing corresponds to $k(g_0)$ = 0.1–0.9 under the normal gravity conditions for the experimental geometry employed. For a "weak" mixing (corresponding to the Marangoni convection) with the melt break-off from the walls, the effective distribution coefficient $k(g = 0)$ may approach unity. Indeed, a comparison of data on the impurity distribution in samples 2 and 2a shows that the pattern of impurity displacement during the directional crystallization on the Earth corresponds to $k = 0.42$, while the process observed under the microgravity conditions is less intensive and is characterized by $k = 0.8$. The weak convection increases the role of binding between structural elements of tellurium chains near the solid–liquid phase interface. This leads to a greater number of the structural centers of crystallization and, hence, to a higher value of C_{0def}.

It should be noted that liquid tellurium at temperatures near the melting point contains structural chains forming a kind of network [14], which results in increasing viscosity and anomalous temperature dependence of the melt density [15].

In sample 1, where the number of defects is much lower compared to that in samples 2 and 3, the conditions of mixing were different in part 1* (touching the ampule walls) and part 1** recrystallized with a free surface (Fig. 6). This difference may lead to a change in the effective distribution coefficient k both due to enhanced thermocapillary streams in the melt (leading to a flow of liquid at the crystal growth boundary with the resulting increase in the δ value) and due to variations in the growth velocity caused by changes in the thermal regime. In this case, formula (1) described the experimental results (sold curves in Fig. 6) for the k value increasing from 0.2 (in part 1*) to 0.45 (in part 1**). This fact accounts for the more rapid growth of the hole concentration p(77 K) in part 1** as compared to that in part 1*. The anomalous growth of p(77 K) can be explained by an increase in the k value as a result of changes in the crystal growth conditions related to the material break-off from ampule walls caused by enhanced thermocapillary streams in the melt. The enhanced thermocapillary streams lead to a flow of liquid along the crystal growth boundary with the resulting increase in the δ value.

The hole concentration profile observed in sample 3 can be formally also descried by relationship (1) with the parameters listed in Table 3. However, the hole concentration p(77 K) varies rather slightly along this sample and the variation may be as well explained by some defects (e.g., pores) not taken into account in the calculation. The on-ground analog remelted according to the same temperature–time schedule also exhibited a homogeneous concentration profile (Fig. 4). This fact confirms the above conclusion that sample 3 was characterized by a strong supercooling and featured spontaneous crystallization with the formation of numerous defects, including the electrically active ones

3. Temperature effects. The study of variation of the electrical properties of most perfect tellurium samples 1 and 2 in the broad temperature range 1.6–100 K showed that the mobility of holes in the ingots recrystallized under the microgravity conditions markedly depends both on the temperature and on the sample crystallization conditions (Fig. 7). In sample 1, the mobility of holes at temperatures below 77 K is greater in the region (cd) than in (ab), a maximum difference being observed at 10–20 K. This behavior may be related to a difference in the content of neutral defects in the two regions of sample 1, which determines the temperature-independent contribution to the hole scattering [2]. A decrease in concentration of these defects at the end of the ingot would result in that $R\sigma$(cd) > $R\sigma$(ab) at $T \approx 77$ K. As the temperature decreases to 1.5 K, the hole scattering from charged defects begins to dominate. Since the concentration of electrically active impurities is greater in the region (cd) than in (ab), the mobility of holes in the former region $R\sigma$(cd) at $T < 4$ K becomes lower than $R\sigma$(ab) (Fig. 7).

Dependence of the mobility of holes on their temperature-independent scattering from structural defects [2] is confirmed by a large difference between the hole mobilities of samples 1 and 2, as well as by the character of the temperature variation of this parameter. These data correlate with a large number of crystal block boundaries observed in part 1ab. In sample 3, characterized by the greater number of growth defects, the hole mobility has a minimum value and is almost independent of the temperature (Table 2).

Temperature variation of the hole mobility in samples 1 and 2 is qualitatively the same as that observed previously in the samples characterized by similar structures and impurity concentrations, grown on the Earth under the normal conditions (Fig. 7) [16].

In order to evaluate the temperature-independent contribution of hole scattering from the structural defects, we have used the Matthiessen rule as described in [2]. The defect concentration N_0 was calculated using the well-known relationship for the relaxation time $\tau = um^*/e$ (where u is the Ohm mobility and m^* is the carrier mass) of charge carriers scattered from neutral defects of the hydrogen atom type in a medium with the dielectric permittivity ε_0 [17]:

$$\frac{1}{\tau} = \frac{20\varepsilon_0\hbar^3}{m^{*2}e^2}N_0. \quad (3)$$

Using the average values of ε_0 and m ($\varepsilon_0 = 33.82$; $m^*/m_0 = 0.156$), we obtain $N_0 = 3.8 \times 10^{15}$ cm^{-3} for the region (ab) of sample 1, and $N_0 = 6.145 \times 10^{14}$ cm^{-3} for the region (cd) of the same sample. These values indicate that the number of defects is much smaller in the region (cd) crystallized without touching the walls than in the region (ab) contacted with the ampule. In sample 2, we have $N_0 = 2.4 \times 10^{16}$ cm^{-3} for the region (ab) and $N_0 = 5.0 \times 10^{16}$ cm^{-3} for the region (cd), both values being greater than in sample 1. The concentration of defects in sample 3 ($N_0 = 2.0 \times 10^{17}$ cm^{-3}) is even greater than that in sample 2, which is naturally explained by the polycrystalline structure of sample 3.

CONCLUSION

Experiments on the recrystallization of three different samples of pure tellurium by a modified Bridgman method were performed under microgravity conditions. Electrical properties of the final samples, studied in a broad temperature range, were compared to the known data and to the values obtained in additional experiments conducted on the Earth under otherwise analogous conditions. Data on the directional growth of tellurium single crystals under the microgravity conditions using the method of partial recrystallization of initial single-crystal samples showed that the electrical properties of the final crystals obtained by this technology are comparable with the properties of crystals grown on the Earth by the Czochralski method. It was established that development of the crystal block structure, as well as the size, orientation, and number of blocks, depend on the crystallization conditions that are different in the regions of melt contacting or not with the container (ampule) walls. The maximum mobility of holes was observed in the crystal regions formed with a free surface. This regime of crystallization is realized under the microgravity conditions, where the melt "breaks off" from the ampule walls. The amount of neutral defects reducing the hole mobility was evaluated to characterize the degree of perfection of the crystals grown using various sample preparation techniques.

It was found that complete remelting of a single-crystal tellurium sample under the microgravity conditions is accompanied by deep supercooling and leads to the formation of a fine-grained ingot. This phenomenon opens way to the obtaining of tellurium samples with the properties corresponding to those of a microcrystalline system composed of anisotropic structural elements.

Extremely high sensitivity of the electrical properties of tellurium at low temperatures, with respect to the presence of structural defects, allowed the distribution of impurities and electrically active defects (not detected by other methods) over the sample length to be studied. The concentrations of the electrically active impurities (determined on the level of 10^{-6} at %) and the neutral defects were evaluated from the results of low-temperature galvanomagnetic measurements.

ACKNOWLEDGMENTS

The authors are grateful to L.L. Regel' for his help in organization and participation in the preliminary on-ground work and experiments, including the growth of tellurium alloys at elevated gravity levels.

REFERENCES

1. P. Grosse, *Die Festkörpereigenschaften von Tellur*, in *Springer Tractats in Modern Physics* (Springer, Berlin, 1969), Vol. 48.
2. R. V. Parfen'ev, I. I. Farbshteĭn, and S. S. Shalyt, Fiz. Tverd. Tela (Leningrad) **2** (11), 2923 (1960).
3. L. L. Regel', A. M. Turchaninov, R. V. Parfen'ev, *et al*., J. Phys. III (Paris) **2**, 373 (1992).
4. I. I. Farbshtein, R. V. Parfeniev, N. K. Shulga, and L. L. Regel, in *Material Processing in High Gravity*, Ed. by L. L. Regel and W. R. Wilcox (Plenum Press, New York, 1994), pp. 81–84.
5. L. L. Regel, I. V. Vidensky, A. V. Mikhailov, A. M. Turchaninov, R. V. Parfeniev, I. I. Farbshtein, N. K. Shulga, and B. T. Melekh, Preprint IAF-86-283 (1986).
6. R. V. Parfeniev, I. I. Farbshtein, S. V. Yakimov, V. P. Shalimov, and A.M. Turchaninov, *Proceedings of the Joint Xth European and VIth Russian Symposium on Physical Sciences in Microgravity* (St. Petersburg, 15–20 June 1997), Abstract No. 98 (1997).
7. R. V. Parfeniev, L. L. Regel', and W. R. Wilcox, Proceedings IAAA-97, IAA 12.01.08 (1997).
8. L. L Regel', *Space Materials Science. Part II* [in Russian] (Achievements in Science and Technology, Ser. Space Research, Vol. 29) (VINITI, Moscow, 1987), p. 146.
9. A. R. Lang, in *Diffraction and Microscopic Techniques in Materials Science* [Russian translation] (Metallurgiya, Moscow, 1984).
10. E. Scheil, Z. Metallk. **34**, 70 (1942).
11. W. A. Tiller, K. A. Jackson, J. W. Rutter, *et al*., Acta Met. **1**, 428 (1953).
12. V. S. Avduevskiĭ, S. D. Grishin, and L. V. Leskov, in *Scientific Readings in Aviation and Cosmonautics-1980* (Nauka, Moscow, 1981), pp. 15–24.
13. J. A. Burton, R. C. Prim, and W. P. Slichter, J. Chem. Phys. **21** (11), 1987 (1953).
14. B. Cabane and J. Friedel, J. Phys. **32**, 73 (1971).
15. A. R. Regel' and V. M. Glazov, *Physical Properties of Electronic Melts* (Nauka, Moscow, 1980).
16. I. I. Farbshteĭn, A. M. Pogarskiĭ, and S. S. Shalyt, Fiz. Tverd. Tela (Leningrad) **7** (8), 2383 (1965).
17. C. Erginsoy, Phys. Rev. **79**, 1013 (1950).

Translated by P. Pozdeev

Physics of the Solid State, Vol. 42, No. 2, 2000, pp. 253–256. Translated from Fizika Tverdogo Tela, Vol. 42, No. 2, 2000, pp. 246–250.

SEMICONDUCTORS AND DIELECTRICS

Optical and Luminescent VUV Spectroscopy of $La_2Be_2O_5$ Crystals

V. A. Pustovarov, V. L. Petrov, É. I. Zinin*, M. Kirm, G. Tsimmerer**, and B. V. Shul'gin**

Ural State Technical University, ul. Mira 19, Yekaterinburg, 620002 Russia
**Budker Institute of Nuclear Physics, Siberian Division, Russian Academy of Sciences, pr. akademika Lavrent'eva 11, Novosibirsk, 630090 Russia*
***II Institute of Experimental Physics, Hamburg University, Hamburg, D22761 Germany*
e-mail: pva@dpt.ustu.ru

Received March 31, 1999

Abstract—Electronic excitations and the processes of their radiative relaxation are studied in pure and Ce^{3+} ion-doped crystals of lanthanum beryllate excited by synchrotron radiation in the x-ray and VUV ranges by methods of optical and luminescent vacuum ultraviolet time-resolved spectroscopy. Manifestations of excitons of the valence band are absent in the reflection spectra. However, a fast (τ = 1.7 ns) and a slow (microsecond range) channel corresponding to two possible types of self-trapped excitons (STE) are found in radiative relaxation of intrinsic electronic excitations at T = 10 K. The slow channel corresponds to emission of STE formed through recombination, the fast channel corresponds to emission of relaxed metastable excitons from the STE state. In the energy region higher than 14 eV ($E > 2E_g$), the effect of multiplication of electronic excitations due to generation of secondary electron–hole pairs resulting from inelastic scattering of both hot photoelectrons and hot photoholes is exhibited. © *2000 MAIK "Nauka/Interperiodica"*.

INTRODUCTION

Luminescence of triplet self-trapped excitons (STE) in alkali-halide crystals can appear through the pure exciton mechanism as a result of exciton self-trapping, as well as through recombination of electrons with self-trapped holes [1]. At the same time, for certain crystals of complex oxides, oxides of metals of the III group [2–4], branching of relaxation in independent channels takes place. As a result, direct optical generation of STE and their generation through electron–hole recombination produce different radiative states. In the series of complex oxides used in the laser and in the scintillation technologies, good promises are shown by lanthanum beryllate. Interest in this compound was created when the effect of stimulated emission was obtained in $La_2Be_2O_5$–Nd [5]. Detailed spectroscopic studies of these crystals in the transparency region were carried out in [6]. Optical properties and efficiency of excitation of luminescence in the region of fundamental absorption were briefly studied only in [7]. At the same time, detailed studies of the structure of electronic excitations (EE) and processes of their radiative relaxation make it possible to elucidate, in this context, typical features of EE in this class of oxides. On the one hand, the features of the crystal structure of $La_2Be_2O_5$ are similar to those of BeO crystals (deformed BeO_4 tetrahedrons), where excitonic states are clearly defined in both optical spectra and processes of radiative relaxation [8]. On the other hand, manifestations of anion exciton states in optical spectra are completely absent for compounds containing transition *d*-metals, for instance, Sc_2O_3 [2, 3] and LaF_3 [9]. This is determined by the *pd*-genealogy of the top of the valence band and the conduction band.

In this work, the time-resolved reflection and luminescence spectra and kinetics of luminescence decay in the case of x-ray and selective VUV excitation are studied, as well as the time-resolved excitation spectra of luminescence in the region of 5–40 eV for pure and Ce^{3+}-doped crystals of lanthanum beryllate at 295 and 10 K.

EXPERIMENTAL EQUIPMENT AND TECHNIQUE

The measurements were made on samples grown in the Institute of Geology and Geophysics, Siberian Division, Russian Academy of Sciences using the Czochralski technique. The crystal structure (monoclinic system, space group $C_{2h}^6(C2/c)$, z = 4, unit cell parameters a = 7.5356, b = 7.3436, c = 7.4387 Å, and β = 91°33′) is formed by distorted BeO_4 tetrahedrons with bonded angles, where La^{3+} ions (point group C_1) coordinated by ten oxygen ions are asymmetrically built in [10]. The crystals were certified by using the x-ray diffraction method. Polarized discs 1 mm thick and 10–15 mm in diameter were used for the study.

Luminescence was excited by synchrotron radiation (SR) of VÉPP-3 accumulators of the Institute of Nuclear Physics, Siberian Division, a RAS (excitation in the x-ray range) and a DORIS accumulator (excita-

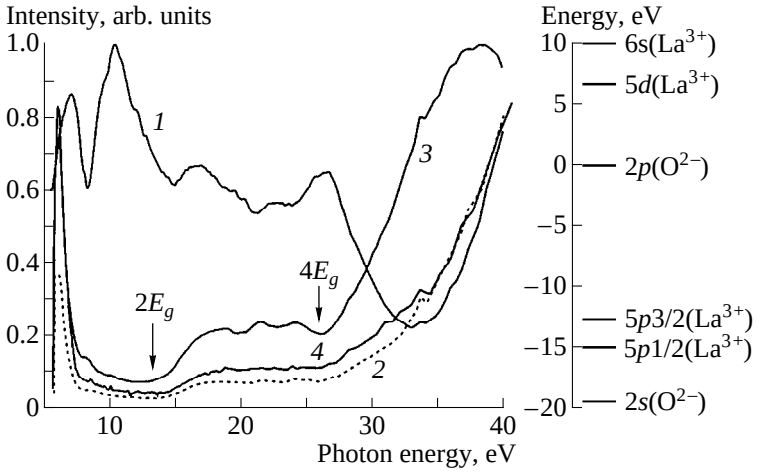

Fig. 1. Spectra of (*1*) reflection and (*2*, *3*) excitation of luminescence ($E_{emission}$ = 3.3 eV) (*2*) for the fast and (*3*) for the slow components of the kinetics of luminescence decay of $La_2Be_2O_5$ crystals; (*4*) time-integrated excitation spectrum of luminescence of Ce^{3+} centers ($E_{emission}$ = 2.7 eV) of $La_2Be_2O_5$ crystals (0.5 mol. %). T = 10.8 K. The diagram of energy levels is given on the right.

tion in the VUV range). SR pulses from VÉPP accumulators had a length δ = 430 ps, a pulse repetition frequency 4 MHz, and an energy 5–60 keV. A streak camera with a time resolution no worse than 200 ps on the basis of a LI-602 dissector was used for recording time-resolved spectra and kinetics of luminescence decay [11]. Measurements using a DORIS accumulator were carried out at the SUPERLUMI center of the HASYLAB laboratory [12]. Excitation spectra of luminescence were normalized to an equal number of photons incident on a crystal. Emission spectra were analyzed by a Czerny–Turner secondary monochromator and a R2059 (Hamamatsu) photoelectric multiplier. Luminescence and excitation spectra were measured for time-integrated luminescence as well as for luminescence detected in temporal windows (of width Δ_t) correlated with respect to the exciting SR pulse (delay relative to the beginning of the SR pulse is δ_t). The time delay and the width of a temporal window were set to 2.2 and 8.2 ns, respectively, for the fast component and 23 and 111 ns, respectively, for the slow component, on the basis of the decay kinetics. Parameters of the decay kinetics were determined in all experiments by the method of convolution. Reflection spectra were measured for an angle of incidence of SR equal to 17.5°.

EXPERIMENTAL RESULTS AND DISCUSSION

The reflection spectrum (RS) measured in the energy region of 5–40 eV has two groups of bands in the regions of 7–12 and 17–27 eV (Fig. 1). The analysis of x-ray–electronic spectra and calculations of the electronic structure within the framework of the MO LCAO model for $La_2Be_2O_5$ made in [13], as well as a deep analogy with RS of lanthanum trifluoride [9], make it possible to relate the low-energy bands 7.0 and 10.4 eV to electron transitions from the valence band formed by 2*p*-states of oxygen to the conduction band formed by 5*d*- and 6*s*-states of La^{3+}. Complete absence of manifestations of excitons of the valence band of the RS in the region of the long-wavelength edge of fundamental absorption (LEFA) should be noted. This hinders the determination of the minimum energy of interband transitions, whose estimate on the basis of the measurement of the excitation spectrum of low-temperature thermostimulated luminescence (TSL) and the Urbach rule [7] gives E_g = 6.2–6.5 eV at 80 K. The growth of the reflection coefficient for energies greater than 15 eV probably corresponds to transitions from 2*p* states of oxygen to higher regions of the conduction band, while the bands in the regions 19.5 and 22 eV correspond to the excitation of split $5p_{3/2}$ and $5p_{1/2}$ levels of La^{3+} (possibly, cation excitons). Transitions from 2*s* levels of O^{2-} form a peak at 26.5 eV in the RS. The energy level diagram for $La_2Be_2O_5$ constructed on the basis of this interpretation (Fig. 1) definitely agrees with the location of energy levels in x-ray–electron spectra of these crystals [13].

When crystals are excited by x-ray radiation, electron pulses, or photons with $E \geq 5.8$ eV at low temperatures, a broad band (E_m = 3.34 eV, FWHM = 0.82 eV, and quantum yield η = 0.5 with respect to sodium salicylate at 80 K) is observed in the spectrum of luminescence (SL) without time resolution (Fig. 2). The decay kinetics of this luminescence in the case of selective excitation by photons in the region of the LEFA or photons with energies $E > E_g$ at 10 K contains a fast (τ = 1.7 ns) and a slow (microsecond range) component (Fig. 3). The kinetics is not exponential for the slow component under the excitation by electron pulses with $\tau_{1/2}$ = 8 μs at 80 K. The SL of the slow component coincides with the SL measured without time resolution, while the SL of the fast component is insignificantly shifted to the long-wavelength side (E_m = 3.30 eV, FWHM = 0.78 eV) (Fig. 2).

Excitation spectra of luminescence (ESL) of the slow and fast components have no bands in the region of transparency. Both emissions are excited exclusively in the region of the LEFA and in the case of production of individual electron–hole pairs (Fig. 1). In the region of LEFA, there are differences between their ESL: the maximum of the ESL of the fast component (E_m = 5.94 eV, FWHM = 0.78 eV) is somewhat shifted to the long-wavelength side relative to the ESL peak of the slow component (E_m = 6.05 eV, FWHM = 1.02 eV). As the energy of exciting photons is increased above the LEFA, the yield of both emissions decreases. This is associated with an increase in the absorption coefficient in the region of interband transitions, which results in a decrease in the light penetration depth into the crystal and an increase in the number of acts of nonradiative decay of EE near the surface. For $E > 14$ eV, i.e., for $E > 2E_g$, an increase in the yield of both emissions is observed. In the region of 18–27 eV, corresponding to the excitation of 5*p* levels of lanthanum, ESL and RS behave in opposite ways. The second region of increasing quantum yield for the fast and the slow components and correspondingly emission integral in time is observed at $E > 4E_g$ (Fig. 1). The comparison of ESL with RS and with the absorption spectrum calculated from RS by the Kramers–Kronig method shows that the growth of the luminescence yield at $E > 2E_g$ is associated with the effect of multiplication of electronic excitations (MEE). X-ray–electron spectrum data on the structure of the valence band [13] testify that the width of the valence band in $La_2Be_2O_5$ is of order of 10 eV, hence, $E_v > E_g$ as for most of oxides. This fact, along with the presence of two thresholds of the growth of the quantum yield of luminescence in the region from $2E_g$ to $4E_g$, suggests, in correspondence with modern concepts of the MEE theory [14], that the electron–hole mechanism for MEE due to generation of secondary electron–hole pairs resulting from inelastic scattering of both hot photoelectrons and hot photoholes is realized in $La_2Be_2O_5$.

The introduction of Ce^{3+} ions leads to the appearance of intense luminescence (η = 0.4 at 300 K) in the region of 2.7 eV (Fig. 2). In the case of selective excitation by SR pulses in the absorption band of Ce^{3+} centers (E_{exc} = 4.7 eV), the luminescence kinetics is inertialess and is described by an exponential with τ = 29 ns at 300 K. In the case of excitation by an electron beam or SR in the x-ray range, the time constant of the decay kinetics of Ce^{3+} luminescence increases up to τ = 38–45 ns, which is due to migration and recombination processes in the host. In this case, intermediate localization of carriers is also attested by the appearance of the stage of build-up (4–6 ns at 300 K) in the luminescence kinetics of Ce^{3+} centers. Intracenter excitation in the region of 3.5–4.7 eV associated with 4*f* transitions in Cr^{3+} ions is observed in the ESL of Ce^{3+} centers of $La_2Be_2O_5$ crystals. Taking into account data of thermoactivation spectroscopy on irradiated crystals or crystals subjected to thermochemical processing [7], we should reason that excitation of Ce^{3+} centers in the region of the LEFA and interband transitions proceeds in accordance with the electronic recombination mechanism $Ce^{3+} + h^+ \longrightarrow Ce^{4+}$ and $Ce^{4+} + e^- \longrightarrow (Ce^{3+})^* \longrightarrow Ce^{3+} + h\nu$. In this case, all the features in the ESL of Ce^{3+} centers, including the MEE effect, correspond to the ESL of a pure crystal at 3.34 eV (Fig. 1). It should be noted that migration losses in energy transfer to spatially remote impurity centers are higher with respect to luminescence at 3.34 eV (see [15] for details). This is exhibited in a more pronounced dip in the ESL at energies somewhat above the LEFA. Nevertheless, a high efficiency of energy transfer, a high quantum yield at 300 K, and a clearly defined MEE effect, along with rapid kinetics of luminescence decay, explain the assumption made earlier in [16] concerning utilization of $La_2Be_2O_5$–Ce as a scintillation material.

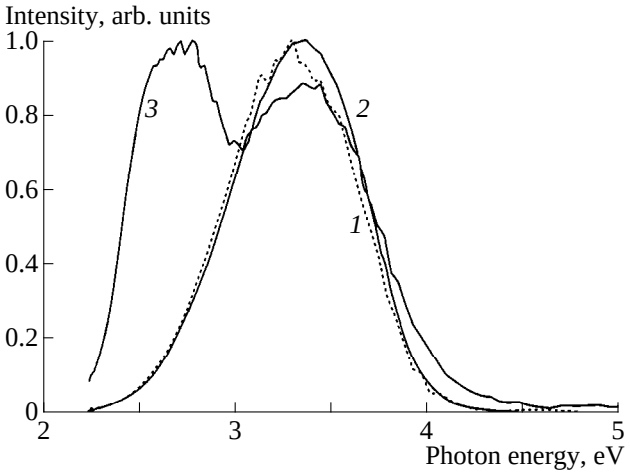

Fig. 2. Spectra of (*1*) fast, (*2*) slow, and (*3*) time-integrated luminescence of (*1* and *2*) $La_2Be_2O_5$ and (*3*) $La_2Be_2O_5$–Ce (0.5 mol. %) crystals. $E_{excitation}$ = 6.2 eV, T = 10.8 K.

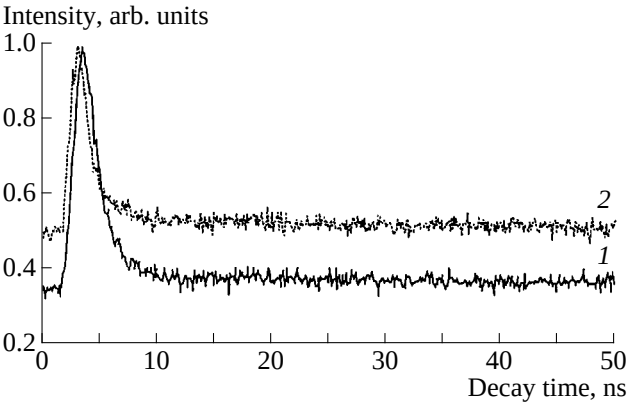

Fig. 3. Decay kinetics of luminescence at 3.3 eV for $La_2Be_2O_5$ crystals. $E_{excitation}$ = (*1*) 6.2 and (*2*) 21.4 eV, T = 10.8 K.

The experimental data presented above confirms the assumption made in [7] that emission at 3.34 eV in pure $La_2Be_2O_5$ crystals is of the intrinsic type. The presence of this emission in the spectral composition of TSL peaks is a direct indication of its recombination nature. It is typical of oxides that *p* states of the valence band are split in a field of low symmetry. As a result, one of the orbitals turns out to be of the nonbonding type [2]. Because of this, the mass of holes at nonbonding orbitals can considerably exceed their mass for other states in the valence band, i.e., a hole can be self-trapped. At present, we may believe, on the basis of the analogy with binary or complex oxides (for instance, $CaWO_4$ [4]), that emission at 3.34 eV appears in $La_2Be_2O_5$ as a result of recombination of electrons with self-trapped holes, which are polarons of small radius of the type of O^-.

The absence of manifestation of excitons in RS of $La_2Be_2O_5$ in the region of the LEFA is dictated, as in the case of compounds of transition *d* metals, by the *pd*-genealogy of the top of the valence band and the bottom of the conduction band. In addition, according to the assumption made in [9], the presence of unfilled 4*f* levels for LaF_3 can noticeably shorten the lifetime of 5*d* states of La^{3+} with the result that exciton states are metastable. At the same time, the parameter $\sigma_0 = 0.44$ for $La_2Be_2O_5$ involved in the Urbach rule is indicative of strong exciton–phonon interaction and of the possibility for exciton self-trapping. Efficient excitation of the fast component 3.30 eV in the region of the LEFA at energies smaller than the maximum of the ESL of slow emission 3.34 eV points to the branching of relaxation of EE in independent channels typical of oxides [2–4]. On this basis, we suppose that excitons in $La_2Be_2O_5$ are metastable and therefore they are not detected in the RS. Their presence is manifested only in processes of radiative relaxation; a radiative transition from the relaxed state of STE forms the spectrum of fast emission 3.30 eV. The allowed transitions indicate the manifestation of singlet STE. The ESL at 3.30 eV reflects the special feature of EE relaxation in $La_2Be_2O_5$ indicated above, although it does not quite correspond to the general trend of the formation of ESL of singlet STE in alkali-halid crystals studied (preferential excitation from $n = 2$ states of excitons) [17].

ACKNOWLEDGMENTS

The authors are grateful to V.N. Matrosov for placing samples at our disposal and A.V. Kruzhalov for the support of the work.

REFERENCES

1. Ch. B. Lushchik, *Excitons* (Nauka, Moscow, 1985).
2. A. I. Kuznetsov, V. N. Abramov, V. V. Mürk, *et al.*, Fiz. Tverd. Tela **33**, 2000 (1991).
3. V. Mürk and O. Svinarenkov, *Inorganic Scintillators and Their Applications* (Delft University Press, Delft, 1995).
4. V. Mürk, B. Namazov, and B. Yaroshevich, Radiat. Measurements **24** (4), 371 (1995).
5. H. P. Jenssen, R. F. Begley, R. Webb, *et al.*, J. Appl. Phys. **47** (4), 1496 (1976).
6. A. A. Kaminskiĭ, Ngoc Tran, S. E. Sarkisov, *et al.*, Phys. Status Solidi A **59** (1), 121 (1980).
7. A. V. Kruzhalov, V. A. Pustovarov, A. A. Maslakov, *et al.*, Opt. Spektrosk. **63** (2), 457 (1987).
8. V. Yu. Ivanov, V. A. Pustovarov, A. V. Kruzhalov, *et al.*, Nucl. Instrum. Methods Phys. Res., Sect. A **282**, 359 (1989).
9. C. G. Olson, D. W. Lynch, and M. Piacentini, Phys. Rev. B: Solid State **18** (10), 5740 (1978).
10. L. A. Harris and R. Yekel, Acta Crystallogr., Sect. B: Struct. Sci. **24**, 672 (1968).
11. V. A. Pustovarov, E. I. Zinin, A. L. Krymov, *et al.*, Rev. Sci. Instrum. **63** (6), 3521 (1992).
12. G. Zimmerer, Nucl. Instrum. Methods Phys. Res., Sect. A **308**, 178 (1991).
13. T. A. Betenekova, A. V. Kruzhalov, N. M. Osipova, *et al.*, Fiz. Tverd. Tela **25** (1), 175 (1983).
14. A. Lushchik, E. Feldbach, R. Kink, *et al.*, Phys. Rev. B: Condens. Matter **53** (9), 5379 (1996).
15. A. N. Vasil'ev, V. V. Mikhaĭlin, and I. V. Ovchinnikova, Izv. Akad. Nauk, Ser. Fiz. **49**, 2044 (1985).
16. L. V. Viktorov, A. V. Kruzhalov, A. A. Maslakov, *et al.*, USSR Inventor' Certificate No. 921328 Byull. Izobret. 14 (1982).
17. T. Matsumoto, M. Shirai, and K. Kanno, J. Phys. Soc. Jpn. **64**, 987 (1995).

Translated by A. Mozharovskiĭ

Physics of the Solid State, Vol. 42, No. 2, 2000, pp. 257–260. Translated from Fizika Tverdogo Tela, Vol. 42, No. 2, 2000, pp. 251–253.

SEMICONDUCTORS AND DIELECTRICS

^{7}Li NMR Study of the Mobility of Lithium Ions in One-Dimensional Channels of Nb_3Se_4

Yu. G. Kriger, A. V. Mishchenko, A. R. Semenov, S. V. Tkachev, and V. E. Fedorov

Institute of Inorganic Chemistry, Siberian Division, Russian Academy of Sciences, pr. akademika Lavrent'eva 3, Novosibirsk, 630090 Russia
e-mail: kriger@che.nsk.su

Received April 20, 1999

Abstract—The temperature dependence of the spin-lattice relaxation time T_1 and the ^{7}Li NMR spectra of the $Li_{0.7}Nb_3Se_4$ intercalation compound with one-dimensional channel structure have been studied. It is found that the temperature dependence of T_1 exhibits two relaxation minima, and the quadrupole splitting in the Li NMR spectra shows an anomalous temperature behavior. The inference is drawn that the observed effects are associated with the high-rate diffusive motion of lithium ions along one-dimensional channels and the interchannel transitions. *© 2000 MAIK "Nauka/Interperiodica".*

Recent studies on the ionic mobility in solids have attracted considerable attention. The purpose of these investigations is to search for new compounds with a high ionic mobility and to elucidate the mechanisms of ionic transport in solids.

The transition metal chalcogenide compounds are a very promising and interesting class of solids with high ionic mobility [1]. The structure of these compounds involves van der Waals cavities in the form of two-dimensional layers or one-dimensional channels. Free cavities can be partly or completely filled with molecules or ions on the "guest–host" principle, for example, by an intercalation reaction. As a rule, the intercalated molecules and ions possess a high mobility. Such a characteristic as the activation energy of diffusion of the guests in the host lattice strongly depends not only on the nature of atoms, but also on the relative sizes of cavities and intercalated ions or molecules. It is reasonable to expect that ions with a small ionic radius, such as lithium ions, should possess a high mobility and a low activation energy. Another intriguing property inherent in intercalation compounds is the possibility of forming incommensurate regions in their structure that arise from the difference in the mean distance between the intercalated guest ions and the host lattice spacing. This type of incommensurate structures was theoretically studied by Pokrovskiĭ and Talapov [2]. Later, these structures were investigated by the NQR and NMR techniques in the intercalation compounds based on thiourea clathrate [3] and niobium trichalcogenides [4]. In the last work, the authors studied the mobility of lithium ions in the $Li_{0.7}Nb_3Se_4$ intercalates with a quasi-one-dimensional channel structure. They also propose the model of the soliton mechanism of ionic diffusion in one-dimensional systems with an incommensurate structure that provides an adequate explanation for the experimental results. An essential feature of this model is the decrease in the activation energy of ionic diffusion with an increase in the ion concentration in the case of the incommensurate structure. By contrast, for the commensurate structure, the activation energy of ionic diffusion increases. It was noted that the activation energy of one-dimensional diffusion decreases with an increase in the guest concentration up to the values corresponding to 60–70% of the maximum occupation of a channel. An anomalous decrease in the ionic mobility in the intercalation compounds with an increase in the ion concentration was also described in other works [5].

For the purpose of further investigations into the ionic mobility and the soliton-like mechanism of diffusion in the intercalation compounds, we synthesized the Nb_3Se_4-based lithium intercalate with a lithium content of about 70% of the maximum value. It should be noted that the Nb_3Se_4 structure provides an ideal example of the structure involving one-dimensional linear hexagonal channels. Upon intercalation, the channels are occupied by lithium ions to a greater or lesser extent, and the parameters of the Nb_3Se_4 structure do not depend on the occupancy. The ^{7}Li NMR study of the Knight shift demonstrated that, during the intercalation into one-dimensional channels of the structure, the lithium atoms become almost completely ionized and donate their electrons to the host matrix. In the present work, the ionic mobility was investigated by the ^{7}Li NMR technique, which was successfully used in studies of solid electrolytes [6].

1. EXPERIMENTAL TECHNIQUE AND SAMPLE PREPARATION

The initial Nb_3Se_4 matrix was synthesized according to the procedure described in [7] and then was characterized by the X-ray diffraction method. Figure 1 dis-

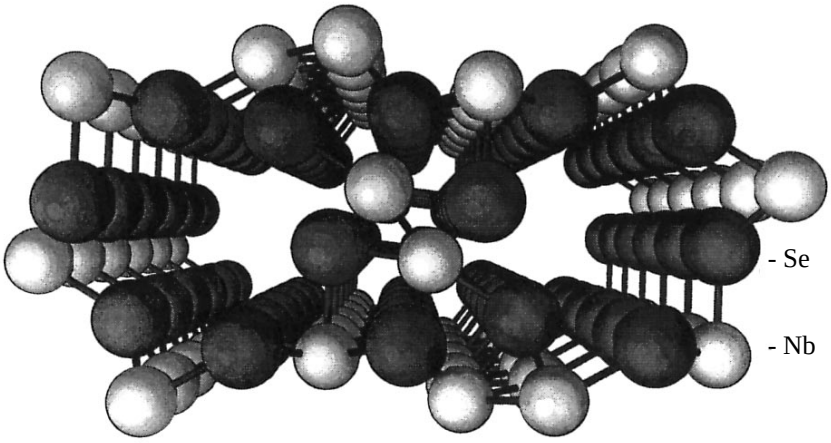

Fig. 1. One-dimensional channels in the structure of Nd_3Se_4.

plays the structure of Nb_3Se_4 [7]. The one-dimensional channels formed by the selenium atoms are clearly seen in the figure.

The intercalation was carried out in a hexane solution of butyllithium (*n*-BuLi). The lithium content in the intercalate corresponded to the ultimate concentration of lithium atoms in the product (about 70% of the maximum content). The sample was homogenized by the annealing in an inert gas atmosphere at 1100 K for 6 days. In order to eliminate the effects of thermal prehistory, the sample was repeatedly heated up to 800 K and cooled down to 77 K. According to the X-ray diffraction analysis, the compound obtained was a well-crystallized powder.

In order to examine the ionic mobility, the temperature dependence of the nuclear spin-lattice relaxation time T_1 for the lithium nuclei was measured at 12.5 MHz. The experimental error was no more than 5% (confidence interval, 95%) over the entire range of temperatures. To obtain additional information on the mobility of lithium ions and to determine the charge state of lithium nuclei, we recorded the ^{7}Li NMR spectra at different temperatures and found the Knight shifts. The experiments were performed at a frequency of 35 MHz. The chemical shifts were measured with respect to the $LiClO_4$ alcohol solution.

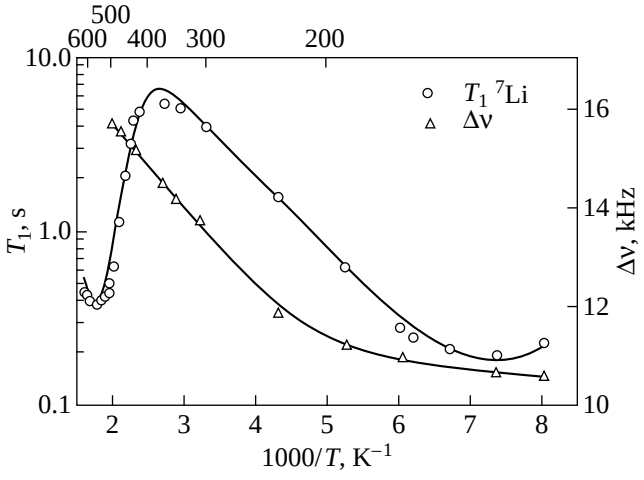

Fig. 2. Temperature dependences of the spin-lattice relaxation time for ^{7}Li nuclei and the quadrupole splitting in the ^{7}Li NMR spectra of $Li_{0.7}Nb_3Se_4$.

2. RESULTS AND DISCUSSION

The data on the spin-lattice relaxation time T_1 for the lithium nuclei in the temperature range 125–625 K are shown in Fig. 2. The temperature dependence of the T_1 time in the studied range exhibits two minima. As is known [8], each minimum is matched by the temperature range characterized by a high-rate diffusive motion with the diffusion correlation time τ_c, which meets the condition $\tau_c\omega \approx 1$, where ω is the Larmor precession frequency for the observed nuclei. In the general case, the relaxation time is defined by the expression [4]

$$1/T_1 = C[J(\omega) + 4J(2\omega)],$$

and the correlation time is usually described by the Arrhenius equation

$$\tau_c = \tau_0 \exp(E_{act}/RT),$$

where τ_0 is the preexponential factor, and E_{act} is the activation energy of diffusion.

Two minima observed in the temperature dependence of the T_1 time correspond to two types of ionic mobility with different activation parameters. The high-temperature and low-temperature minima are associated with the motions of lithium atoms with activation energies of 8.1 and 51.3 kJ / mol and preexponential factors of 2.28×10^{-12} and 5.7×10^{-14} s, respectively. The solid line in Fig. 2 shows the temperature dependence of the T_1 time,

which was calculated with the above activation parameters and $J(\omega) = \tau_c/(1 + \omega^2\tau_c^2)$ [8].

The ^{7}Li NMR spectra taken in the temperature range from 125 to 500 K are demonstrated in Fig. 3. At lower temperatures, we failed to record the spectra, and, hence, it was impossible to determine the relaxation times. As can be seen from Fig. 3, over the entire temperature range under consideration, the spectra exhibit a triplet consisting of an intense central line and two low-intensity satellites, which is typical of the ^{7}Li nuclear magnetic resonance ($I = 3/2$) in solids [9]. The width of the central line is a mere 700 Hz, which is extremely small for the ^{7}Li NMR spectra of solids and most likely reflects the high diffusive mobility of lithium ions. The satellites observed are caused by the first-order quadrupole effects. The splitting between satellites Δ is proportional to the electric field gradient at quadrupole lithium nuclei. The temperature dependence of the quadrupole splitting Δ is depicted in Fig. 2. The specific feature of this dependence is an anomalous increase in the splitting with an increase in temperature. The Knight shifts were also measured at different temperatures. In all the cases, their values are equal to 2.0 ± 0.5, which is characteristic of lithium compounds with the Li^+ charge state.

The ratios between the activation energies for two types of the lithium ion mobility and the data on the structure of the studied compound allow us to assume that the low-temperature minimum in the dependence $T_1(T)$ is explained by the diffusion of lithium ions along the channels. The low activation energy of this motion (8 kJ / mol) can argue for the fact that the effective diameter of channels in the Nb_3Se_4 structure is sufficiently large for the lithium ions to be located rather freely. This is indirectly evidenced by the constancy of the unit-cell parameters in the course of intercalation. Furthermore, the degree of occupation with lithium ions (according to [4], its value is chosen to be 70% of the maximum lithium content) is a prerequisite to the formation of an incommensurate structure or, at least, sufficiently large incommensurate regions.

The high-temperature minimum can be associated with the transitions of lithium ions between the adjacent channels. This type of motion is characterized by a rather high value of activation energy (51.3 kJ / mol). According to the correlation time τ_c estimated at ≈ 10 kHz from the temperature dependence of the quadrupole splitting Δ, the changes in the NMR spectra can be also attributed to this motion of lithium ions. The anomalous temperature dependence of Δ in the ^{7}Li NMR spectra is of particular interest. In general, the quadrupole splitting in the presence of ionic mobility decreases with an increase in temperature due to the averaging of the quadrupole (or dipole) interaction [9]. The found anomalous behavior of the quadrupole splitting Δ can be explained by assuming that the transitions of lithium ions between the adjacent channels occur through the

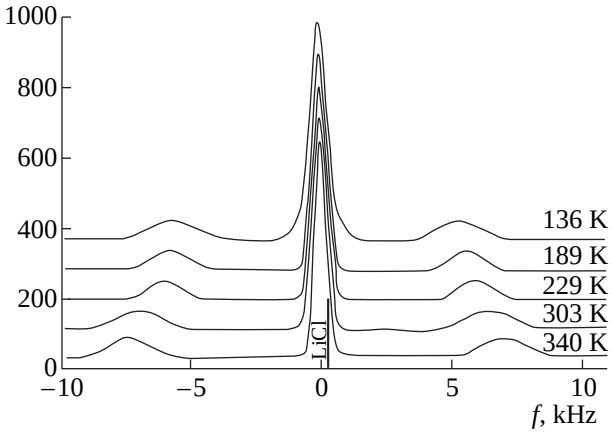

Fig. 3. ^{7}Li NMR spectra of $Li_{0.7}Nb_3Se_4$.

occupation of intermediate sites characterized by the substantially larger quadrupole splittings. A qualitative analysis of the structure of the studied compound confirms the possibility of two-stage transition of ions between channels through an intermediate site with a higher energy. Since, at low temperatures, the probability of occupation of intermediate sites is not very high, and the quadrupole splittings corresponding to these sites are rather large, the NMR spectra of the ions in these sites cannot be measured. However, an increase in the temperature gives rise to a high-rate ion exchange between the adjacent channels, and, hence, the lithium nuclei substantially affect the averaged value of the corresponding quadrupole splitting observed in the experiment. Thus, the anomalous behavior of the quadrupole splitting Δ corroborates the assumption that the transition of ions between channels proceeds through the two-stage mechanism.

The available data on the relaxation times, the quadrupole splittings in the ^{7}Li NMR spectra, and the Knight shifts provide sufficient grounds to argue that the $Li_{0.7}Nb_3Se_4$ compound is a superionic material with the low activation energy of diffusion of the lithium ions. The characteristic feature of this compound is the high ionic mobility observed even at rather low temperatures. Actually, the low-temperature minimum in the temperature dependence of T_1, which corresponds to the estimate of the effective frequency of lithium ion motion at about 5×10^7 Hz, is observed in the range of 135 K. It can be assumed that, as in $NbSe_3$ [3], the low activation parameters of ionic motion along the channels are caused by the incommensurate structure of the $Li_{0.7}Nb_3Se_4$ compound. A deeper insight into the mechanism of ionic diffusion in incommensurate structures requires detailed investigations of the dependence of the activation energy of diffusion on the lithium ion concentration. Additional information on the mechanism of transitions of lithium ions between the adjacent channels can be obtained from analysis of the angular dependences of the NMR spectra for the Nb_3Se_4 crystal.

REFERENCES

1. V. E. Fedorov, *Chalcogenides of High-Melting Transition Metals: Quasi-One-Dimensional Compounds* (Nauka, Novosibirsk, 1988).
2. V. L. Pokrovskiĭ and A. L. Talapov, Zh. Éksp. Teor. Fiz. **75** (3), 1151 (1978).
3. Yu. G. Kriger, S. G. Kozlova, S. P. Gabuda, *et al.*, Fiz. Tverd. Tela (Leningrad) **27** (10), 3121 (1985).
4. Yu. Kriger, G. V. Sikorskaya, and V. E. Fedorov, Zh. Fiz. Khim. **34** (6), 135 (1993).
5. S. Basu and W. L. Worrell, *Fast Ion Transport in Solids* (New York, 1979).
6. V. M. Buznik, *Nuclear Resonance in Ionic Crystals* (Nauka, Novosibirsk, 1981).
7. K. Selte and A. Kjekshus, Acta Crystallogr. **17** (2), 248 (1964).
8. Ch. Slicter, *Principles of Magnetic Resonance* (Springer-Verlag, Heidelberg, 1978; Mir, Moscow, 1981).
9. V. S. Grechishkin, *Nuclear Quadrupole Interactions in Solids* (Nauka, Moscow, 1973).

Translated by O. Borovik-Romanova

Physics of the Solid State, Vol. 42, No. 2, 2000, pp. 261–269. Translated from Fizika Tverdogo Tela, Vol. 42, No. 2, 2000, pp. 254–262.

SEMICONDUCTORS AND DIELECTRICS

Photoluminescence of Concentration Series of CaF_2 : Mn Phosphors Excited by VUV Radiation

V. P. Denks, M. P. Kerikmyaé*, A. L. Lust, and T. I. Savikhina**

Institute of Physics, Academy of Sciences of Éstoniya, Riia 142, Tartu, EE2400 Éstoniya

**Techological Center, Tartu University, Tartu, 51014 Éstoniya*

***Chemicophysical Institute, Tartu University, Tartu, 51014 Éstoniya*

Received June 15, 1999

Abstract—Fluorescent characteristics of a series of powder CaF_2 : Mn phosphors (from 0.01 to 2.47 wt. % of Mn in the mixture) excited by VUV radiation with quantum energies up to 14 eV at 293 K and up to 12 eV at 85 K are measured. Narrow excitation bands of Mn^{2+} centers found at 7.9 and 8.6 eV (at 293 K) are assigned to partially forbidden transitions of electrons from the ground state ^6S split by the crystalline field (10 Dq = 0.71 eV from the literature) in two sublevels to the excited level corresponding to the ^6D term of a free Mn^{2+} ion ($3d^5 \longrightarrow 3d^4 4s$ transitions). A wide nonelementary excitation band in the region of 9.1–10.3 eV is interpreted as photogeneration of near-activator *D*-excitations: allowed transitions of electrons from levels that are split from the top of the valence band under the influence of an impurity ion to the free 4*s*-orbital of a Mn^{2+} ion. Channels of energy transport in the CaF_2 : Mn system are briefly analyzed. © *2000 MAIK "Nauka/Interperiodica".*

INTRODUCTION

CaF_2 : Mn crystallophosphor has remained an object of comprehensive study for more than 40 years. The main reasons for this are the following. First, CaF_2 : Mn (3%) in the form of pressed pellets is one of several types of dosimeters utilized (see [1–3] and references therein; the Harshow firm produces it under the mark TLD-400 [2]). Second, the system CaF_2 : Mn, RE (RE are rare-earth elements) are model objects for the studies of mechanisms for sensitization energy transfer in solids, which is important for the development of phosphors, laser materials, etc. (see, for example, [3–5]). Third, isotropic fluorite crystals are almost the only promising material for short-wavelength ($h\nu$ > 6 eV) laser optics (see, for example, [6, 7]).

The study of luminescent processes in CaF_2 : Mn excited in the UV spectral region has been the subject of many experimental as well as theoretical works (see, for example, [3, 5, 8–10]). Low-energy excited states of centers of luminescence—Mn^{2+} ions (the $3d^5$ electron shell) at cation sites of the lattice, shift and splitting of their levels in the crystalline field in CaF_2—were studied in detail. On the other hand, as far as we know, there are only two works in the literature [11, 12], where the study of physical processes in CaF_2 : Mn under the excitation by photons with energies $h\nu$ > 6 eV was started. Thus, problems of high-energy excited states of impurity centers and processes of exciton and electron–hole energy, transported to them in the case of elementary excitations of the CaF_2 : Mn system, remain hardly studied. This situation hampers the elucidation of a number of physical processes in CaF_2 : Mn, in particular, the mechanism of operation of dosimeters on this basis remains unknown up to now [2, 3, 13, 14].

In this work, we start the study of luminescent processes in a concentration series of CaF_2 : Mn phosphors excited at various temperatures by photons with energies up to 14 eV, i.e., in the VUV spectral region. Preliminary results of the study of one of the members of this series were published in [7].

1. OBJECTS AND TECHNIQUE

Powder CaF_2 : Mn phosphors were synthesized by the method close to that described in [15]. Mixtures were produced by the method of coprecipitation of impurity ions and host-forming ions from solution to precipitate. Coprecipitation was carried out in a special Teflon vessel with the simultaneous addition of diluted solutions of calcium and manganese salts and hydrofluoric acid. All the reagents used were of a special purity. The content of heavy metals in HF was less than 10^{-5}%, the content of Ba and Sr was less than 10^{-3}%. The content of Al, Cu, Ag, Fe, Mn, and Mg in $CaCl_2$ was less than 10^{-5}%, and the content of Pb, W, Cr, and Si was less than 10^{-4}%. The reaction vessel was heated by water vapor, and the rate of the addition of solution was adjusted by peristaltic pumps. After precipitation, the precipitate was aged in the mother solution for 2–3 hours. The precipitate was separated, rinsed, dried, and heated in the air for two hours at 400° C. The manganese concentration was varied in the initial solution so that it varied in the mixture from 0.01% to 2.47 wt. %. High-temperature calcina-

1063-7834/00/4202-0261$20.00

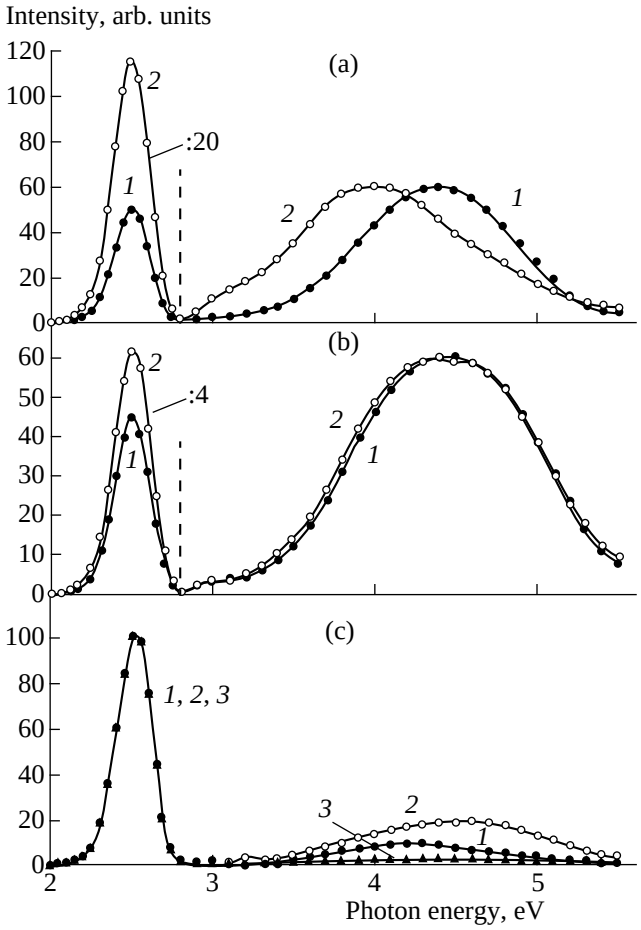

Fig. 1. Spectra of (a, b, *2*c, and *3*c) photoluminescence and (*1*c from [3]) x-ray luminescence of CaF_2 : Mn. Impurity concentration in the mixture is (a and b) 0.01 wt. %, (*1*c) 0.5 mol. %, and (*2*c and *3*c) 0.82 wt. %. Measurement temperature is (a) 85 K and (b and c) 293 K; exciting photon energy is (*2*a) 10.2, (*2*b) 10.7, (*1*a, *1*b, and *2*c) 11.3, and (*3*c) 13 eV.

tion was carried out at 1150°C for 30 minutes in the atmosphere of a specially purified inert gas (Ar).

Emission spectra of the objects were measured in the region of 1.8–5.5 eV with the help of a grating monochromator. Corrections were not introduced in the spectra presented below, because we did not propose to study the details of intracenter processes. Excitation spectra were measured by the standard method on the installation described in [7] at a temperature $T = 85$ K in the spectral region up to 12 eV and at $T = 295$ K up to 14 eV. The necessary emission band was usually selected by glass optical filters. In the measurements of the excitation spectra of phosphorescence, the magnitude of the afterglow within 2 s after the termination of excitation was taken as the phosphorescence intensity.

Below, we present the description of a part of the experimental results obtained and their analysis carried out with consideration for all familiar data from the literature and all the results obtained.

2. RESULTS AND THEIR ANALYSIS

2.1. The Main Emission Centers

In our basic (intentionally undoped) phosphor, practically only one band at 4.4 eV is observed in emission independent of temperature and the region of fundamental excitation as in [7]. In a sample with a minimum impurity concentration of 0.01%, a weak but easily detectable band at 2.5 eV appears already in the case of exciton excitation (see curves *1*a and *1*b in Fig. 1). Its intensity grows drastically in the case of excitation at the edge of fundamental absorption (see curves *2*a and *2*b in Fig. 1). As the impurity concentration increases, the intensity of this band rapidly grows. The steepest growth is observed in the case of interband excitation (see curves *2*c and *3*c in Fig. 1). No new bands appear in emission spectra of the samples. These very two emission bands also prevail in x-ray luminescence spectra of CaF_2 : Mn according to data from the literature (see curve *1*c in Fig. 1 [3] and [13, 16]) as well as our observations.

The nature of the emission centers responsible for the bands indicated was reliably established earlier. The band at 4.4 eV is conditioned by radiative decay of self-trapped excitons with the structure $V_k e^-$ [17]. At room temperature, this emission is quenched by approximately 40% (see [7] and references therein), so it is easily observed. The band at 2.5 eV results from radiative transitions of electrons between the levels (terms) $^4G(^4T_{1g}) \longrightarrow {}^6S(A_{1g})$ of Mn^{2+} ions residing at cation sites of the fluorite lattice (at the centers of cubes of eight F^- ions) [9, 16, 18]. In the temperature range that we used, the intensity of this emission does not depend on T [8].

The quality of synthesis of our objects of study is characterized by the following observation. We did not detect emission of oxygen centers (2.6 eV [19]), narrow emission bands of RE and Y impurities (UV and visible regions [3–5, 20]), α-luminescence (3.9 eV [7]), and other possible uncontrollable impurities within the limits of sensitivity of our equipment [16, 20–24]. Only in the basic undoped sample, is a very weak emission of oxygen centers detected, provided that they are excited at the maxima of the corresponding bands (6.2, 8.4, and ~10 eV [19, 22, 24, 25]).

An additional emission band at ~4.0 eV was detected in [7] in careful studies of emission of samples with Mn excited at the edge of fundamental absorption of CaF_2 in the region of 10–10.6 eV (see curve *2*a in Fig. 1). The nature of this emission quenched at room temperature is briefly discussed below, in Subsection 2.3.

2.2. Excitation Spectra of Emission of Mn^{2+} Centers

These spectra for several concentrations of phosphors are presented in Fig. 2 for $T = 295$ K and in Fig. 3 for $T = 85$ K. The ordinate of these and all other figures with excitation spectra of steady-state luminescence is

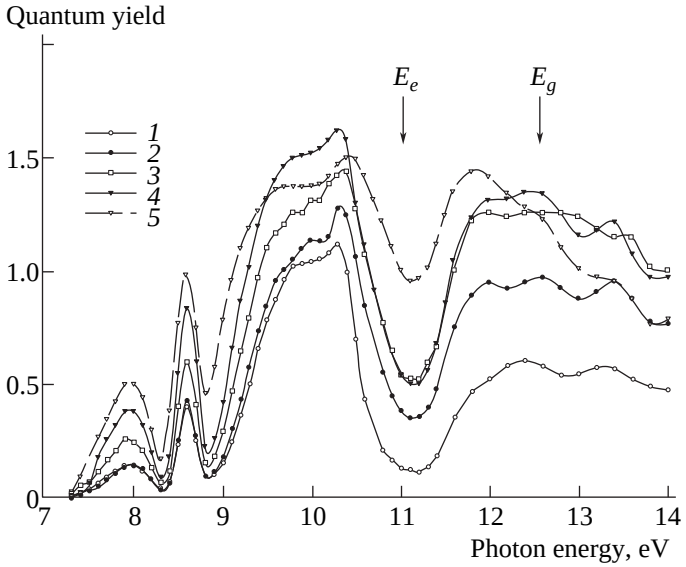

Fig. 2. Excitation spectra of emission of Mn^{2+} centers in CaF_2 : Mn at 293 K for impurity concentrations in the mixture (*1*) 0.01, (*2*) 0.05, (*3*) 0.1, (*4*) 0.82, and (*5*) 2.47 wt. %. In this and in all the following figures, the arrows indicate the locations of the maximum of exciton absorption (E_e) and the forbidden band (E_g) in accordance with [28].

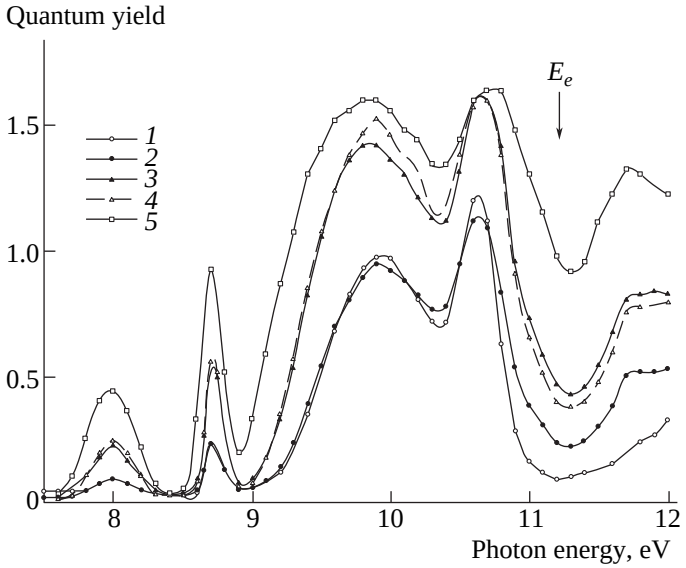

Fig. 3. Excitation spectra of emission of Mn^{2+} centers in CaF_2 : Mn at 85 K. Concentrations are the same as in Fig. 2.

the emission yield measured relative to the emission yield of the reference phosphor—sodium salicylate (all the necessary corrections are made).

From the analysis of all excitation spectra of manganese centers obtained in this work, the following conclusions can be made.

(1) Two narrow excitation bands at 7.9 and 8.6 eV exhibit approximately the same shift by 0.1 eV towards the high-energy side with lowering temperature. Concurrently, their oscillator strengths decrease in approximately the same manner, which is typical of (partially) forbidden transitions. As the Mn concentration increases, the intensity of these bands grows monotonically in approximately the same manner. Apparently, this is representative of an increase in the efficiency of the optical yield from the powder object as the penetration depth of exciting light decreases. Thus, judging from appearances, the bands considered result from transitions inside the electron shell of Mn^{2+} ions. A possible nature of these bands will be discussed in Subsection 2.5.

(2) A wide and clearly nonelementary excitation band is located in the region of 9.1–10.3 eV. The constrained maximum of this band is located at 9.9 eV in the case of liquid nitrogen temperatures. Splitting of this band in

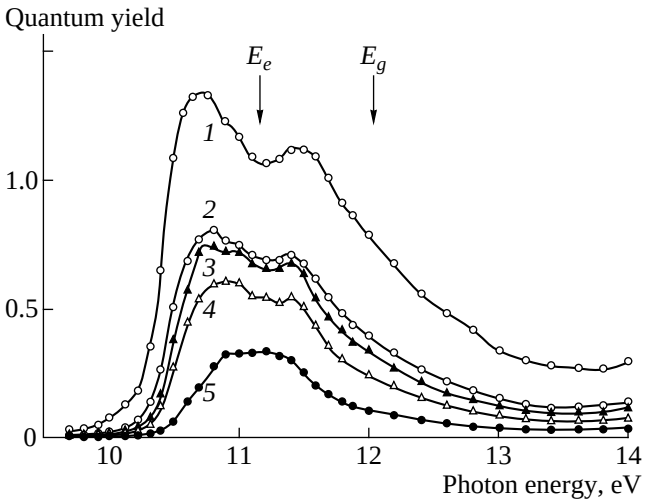

Fig. 4. Excitation spectra of emission of self-trapped excitons in CaF_2 : Mn at 293 K. Concentrations are the same as in Fig. 2.

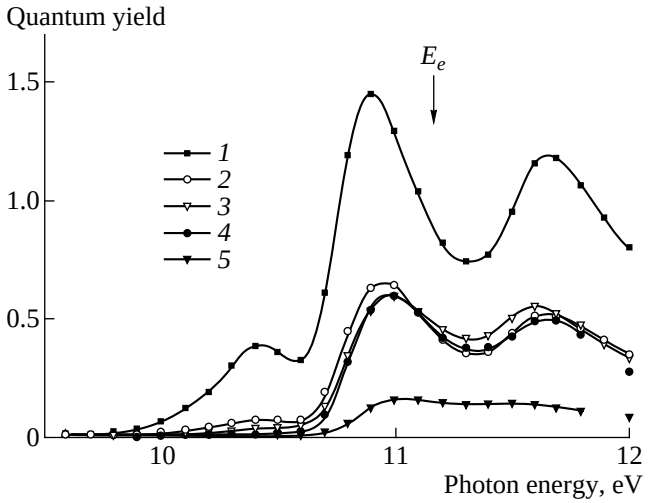

Fig. 5. Excitation spectra of emission of self-trapped excitons in CaF_2 : Mn at 85 K. Concentrations are the same as in Fig. 2.

two will be demonstrated in Subsection 2.4. Absorption in this region possesses a much greater oscillator strength than the bands considered above and is practically independent of temperature, which is typical of allowed transitions. As the Mn concentration C increases, their intensity slowly grows and becomes saturated for high C. The location of these two bands (determined clearly by the manganese impurity) in the vicinity of the fundamental absorption edge attests in favor of their interpretation as excitons localized at impurities (D-excitations, in terms of physics of alkali-halide crystals, see, for instance, [26, 27]). Their possible nature will be considered at greater length in Subsection 2.5.

(3) Apparently, excitation of Mn^{2+} centers by mobile excitons occurs in the region of 10.5–11.9 eV. According to [28], the maximum of the exciton band is located at 11.2 eV at 80 K. Migration energy losses decrease with increasing C (Mn): the dip in the excitation spectrum at 11.2 eV, partially determined by near-surface losses, gradually becomes less pronounced. A temperature decrease from 293 to 85 K does not affect exciton energy transport practically. As the self-trapping (stopping) temperature of an exciton with the $V_k e^-$ structure is unknown for fluorite, on the basis of our data, we can suppose that it is lower than 85 K. Indeed, from the physics of alkali halides [29] we know that the self-trapping temperature of an exciton is 30–40 K lower than the self-trapping (stopping) temperature of a hole with the structure of a V_k center. According to various data [17, 30], the self-trapping temperature of a V_k-center in CaF_2 is in the range of 90–130 K.

(4) The band gap in CaF_2 is 12.1 eV at 80 K [28]. Consequently, recombination luminescence of Mn^{2+} centers is excited with a high enough yield in the region of 12–14 eV. With increasing C (Mn), the emission yield sharply grows (migration energy losses decrease).

2.3. Excitation Spectra of Exciton Emission

These spectra, measured for the same phosphors, are presented in Fig. 4 (T = 293 K) and Fig. 5 (T = 85 K). As in the case of other ionic crystals, emission of relaxed excitons $V_k e^-$ is most efficiently excited within the limits of the exciton absorption band. An ordinary dip resulting from near-the-surface losses and the strong reflection of exciting light from a crystal is observed at the maximum of the band. In the case of interband excitation ($h\nu$ > 12 eV), exciton emission results from recombination of band electrons with not-mobile relaxed holes (V_k-centers). A growth of the concentration of impurity ions leads to the switch of energy transport to Mn^{2+} centers. The exciton emission intensity drops, the drop being strongest in the case of interband excitation (Fig. 4).

Spectra presented in Figs. 4 and 5 were recorded with the use of a UFS-1 optical filter transmitting, apart from exciton emission (4.4 eV), an additional emission band of CaF_2 : Mn at ~4 eV (Fig. 1). This emission is absent in manganese-free samples; it is excited most efficiently in the band with a maximum at 10.4 eV (see curves *1–3* in Fig. 5). As C (Mn) in the mixture increases above 0.05%, the excitation band gradually disappears. In [7], where this emission was described for the first time, the authors assigned it to radiative decay of an exciton localized in the fluorite lattice near a Mn^{2+} ion. Further investigations are required to interpret this band.

2.4. Phosphorescence Excitation Spectra

We failed to detect afterglow in undoped CaF_2 samples in the operating range of temperatures. However, phosphorescence in Mn-containing systems could be easily excited, and its intensity at 85 K was two orders

of magnitude higher than at 293 K. Therefore, at liquid nitrogen temperatures, we even succeeded in measuring the excitation spectrum of weak afterglow in the UV band (4.4 eV), i.e., for radiative decay of relaxed $V_k e^-$ excitons (see curves *3* in Fig. 6). The excitation spectra of the afterglow of Mn^{2+} centers were measured on the same samples with different concentrations of the impurity (a, 0.05% and b, 2.47%) at room (curves *1*) and liquid nitrogen (curves *2*) temperatures.

The analysis of the data in Fig. 6, with the preceding material taken into account, allows the following conclusions to be made.

(1) Indeed, the broad excitation band of Mn^{2+} center emission in the region of 9.1–10.3 eV (see Subsection 2.2) consists of two overlapping bands, whose maxima are located approximately at 9.4 and 10.1 eV. Assuming that they correspond to photogeneration of near-impurity excitons, we denote them as D_1 (9.4 eV) and D_2 (10.1 eV) below.

(2) It is commonly supposed (see, for example, [28, 31]) that the first band of fundamental absorption of CaF_2 at 11.2 eV corresponds to photogeneration of excitons. Dips in all the excitation spectra of recombination luminescence (phosphorescence) that we recorded are in strict agreement with this interpretation. As far as we know, there is no information on excitation spectra of the internal photoelectric effect, formation of peaks of thermostimulated luminescence, etc. in the literature concerning fluorite. Consequently, the excitation spectra of phosphorescence presented in Fig. 6 may be considered as the first experimental evidence of the fact that currentless electronic elementary excitations (excitons) are indeed created in CaF_2 crystals on irradiation in the band at 11.2 eV. With a further growth of the energy of exciting photons (up to 12 eV), the intensity of recombination luminescence excited in both radiation bands regularly grows, reflecting the fact of gradual transition to interband excitation of fluorite.

(3) Only Mn^{2+} centers (the band at 2.5 eV) reveal themselves in D_1 and D_2 absorption bands in the afterglow of CaF_2 : Mn. Consequently, *D* states in CaF_2 : Mn have time to be partially thermoionized during their lifetime, holes remain at their centers (near or at Mn^{2+} ions), and recombination emission appears with subsequent return of electrons from some shallow electron traps. As this process efficiently goes on at liquid nitrogen temperatures, energy levels of both *D*-states and electron capture centers can have a depth of order of 0.1 eV relative to the bottom of the conduction band. Note here that impurity Mn^{2+} ions cannot be these electron traps by themselves, because Mn^{2+} centers are stable up to at least 400 K according to [2, 16, 32].

(4) On excitation in the exciton absorption band, weak phosphorescence appearing in CaF_2 : Mn can be conditioned, as in other ionic crystals, by a number of physical reasons: dissociation of excitons in their collisions with various defects, autoionization in defective surface layer where regions with high electric fields are encountered, generation of *D* states with their subsequent thermoionization in collisions with Mn^{2+} centers, etc. In samples with small impurity concentrations, a part of generated V_k centers has a chance to survive until the arrival of electrons, and UV phosphorescence appears. In samples with much higher manganese concentrations, practically all holes are captured by impurity ions, and UV phosphorescence is no longer observed (compare curves *3*a and *3*b in Fig. 6).

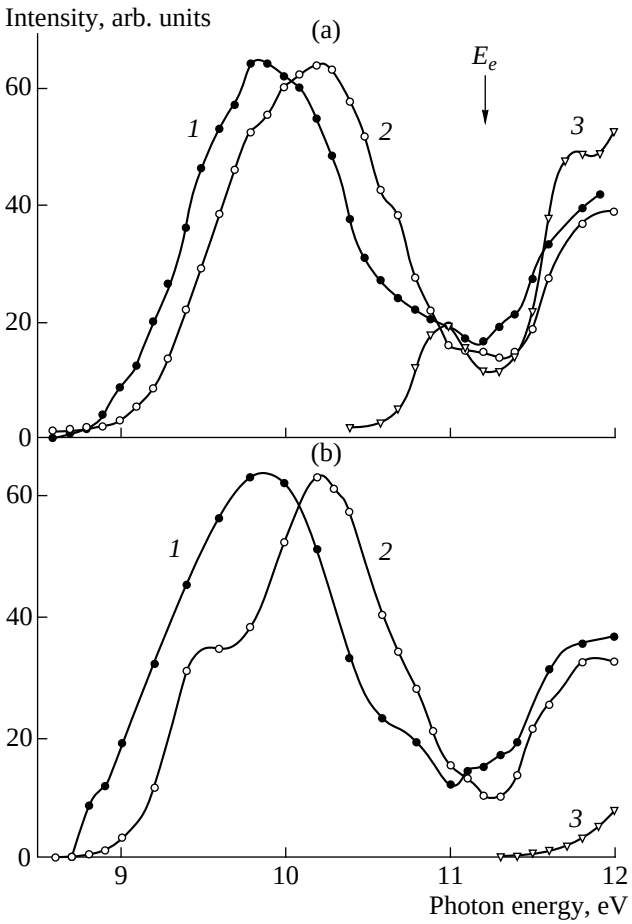

Fig. 6. Excitation spectra of phosphorescence in CaF_2 : Mn. Impurity concentrations in the mixture are (a) 0.05 and (b) 2.47 wt. %; measurement temperatures are (*1*) 293 K and (*2* and *3*) 85 K. Curves (*1*) are multiplied by 100.

2.5. Possible Nature of Absorption Bands of Mn^{2+}-centers in the UV Region

We described two groups of bands of manganese absorption in the CaF_2 lattice. The first of them consists of two narrow bands at 7.9 and 8.6 eV. The second consists of broader and overlapping bands with maxima approximately at 9.4 and 10.1 eV. Figure 7 summarizes the following data of current interest (for room temperature): energy terms of free Mn^{2+} ions for the electronic configurations $3d^4 4s$ and $3d^4 4p$ (at the top of the figure)

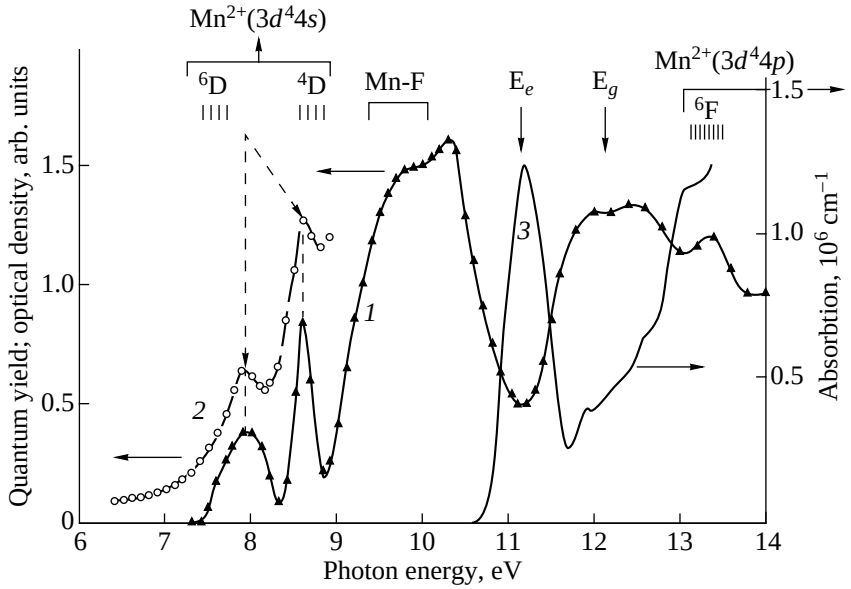

Fig. 7. Excitation spectra of (*1*) emission of Mn^{2+} centers in CaF_2 : Mn (0.82 wt. % in the mixture), (*2* from [11]) absorption of CaF_2 : Mn, and (*3* from [31]) absorption of CaF_2. Terms of levels and configurations of a free Mn^{2+} ion (from [33]) are shown in the upper part. The remaining denotations are given in the text.

[33], the excitation spectrum of emission of Mn^{2+} centers in CaF_2 : Mn (0.82%) (curve *1*, taken from Fig. 2), a fragment of the absorption spectrum of CaF_2 : Mn from [11] (curve *2*), and the spectrum of fundamental absorption of CaF_2 (curve *3* from [31]).

The ground state ^6S of an Mn^{2+} ion ($3d^5$) is split by the crystalline field of the fluorite lattice in the upper doubly degenerate sublevel e_g and the lower triply degenerate sublevel t_{2g} (see, for example, [9, 18]). The distance between them $10Dq$ is 0.71 eV according to the latest data [9]. Transitions from these sublevels to the excited level ^6D ($3d^4 4s$) (Fig. 7) are, judging from appearances, responsible for the first group of bands (at 7.9 and 8.6 eV) of absorption under study. Let us briefly outline the main arguments. Five components of the ^6D multiplet of a free Mn^{2+} ion are located at energies from 7.42 to 7.85 eV [33], which is extremely close to the first band. The distance between the bands detected coincides practically with the splitting of the ground state. The transitions $^6S \longrightarrow {}^6D$ are partially forbidden, which explains the temperature dependence of the band intensities described above. The intensity of the second band at 8.6 eV is approximately twice as large as the intensity of the first band at 7.9 eV, which qualitatively coincides with the relation between the degrees of degeneration of the sublevels e_g and t_{2g}. The next energy level of a free Mn^{2+} ion, which is located in the interval from 8.85 to 8.95 eV [33], corresponds to the ^4D term, hence, a transition to this level will have a much smaller oscillator strength because of the additional forbiddenness associated with nonconservation of multiplicity.

Let us consider now the second group of bands, which was earlier supposed to result from photogeneration of near-impurity electronic excitations (D_1 at ~9.4 and D_2 at ~10.1 eV). The idea of *D* excitation in ionic crystals was first formulated in [26] on the basis of the analysis of spectra of mercury-like impurities in alkali halides. The results of long-lasting studies of these spectra were summarized in [34]: of two basic models, one of which involves excitation (generation of near-impurity excitons), while the other involves the transfer, (electron transition from a level split by an impurity from the top of the valence band to an empty high-energy level of an impurity), the second model was chosen. Let us briefly outline the main arguments in favor of the fact that the bands considered in the case of CaF_2 : Mn are indeed *D* excitations and described most probably by the model of charge phototransport. First, they are located immediately near the edge of fundamental absorption. Second, the magnitude of their intensity and the absence of explicit temperature dependence testify that the transitions are allowed. Third, next energy levels of free Mn^{2+} ions ($3d^4 4p$) are located at energies higher than 13.6 eV (Fig. 7), i.e., too far from D_1 and D_2. Fourth, estimates made in [12, 35] show that *d* impurities in ionic crystals should have two bands of charge phototransport each.

In view of configurational interaction of energy levels of the impurity and energy bands of the host [26, 36], the main contribution to the lower (unexcited) state of *D* excitations is made by the level split from the top of the valence band and additional contribution is made by the ground state level of the impurity. Conversely, the main contribution to the upper (excited) state is made by the

impurity, and an additional contribution is made by the host. Then, qualitatively following the line of [26], we can write down the *D*-transition with charge transfer in CaF_2 : Mn as $F(2p^6)Mn(3d^5) \longrightarrow Mn(3d^54s)F(2p^5)$. The domain of absorption of CaF_2 : Mn that we interpreted as *D* excitations is denoted in Fig. 7 as Mn–F.

In conclusion of this subsection, we comment briefly on the results of two familiar works [11, 12] devoted to the measurement of CaF_2 : Mn absorption in the VUV spectral region. Earlier (see curve *2* in Fig. 7) we already used a fragment of the absorption spectrum measured in [11]. Here, there is complete agreement between our data and the results of their analysis. In [12], the bands at 6.2, 6.7, and 7.2 eV are assigned to absorption of Mn^{2+} centers. We consider this interpretation incorrect for the following reasons. Impurity absorption in CaF_2 : Mn was first measured reliably in [18] using samples 5–7 cm thick with impurity concentrations higher than 10^4 ppm. The sample in [12] was 1–2 mm thick and had *C* (Mn) = 180 ppm. From our data, emission of Mn^{2+} centers is not practically excited in the region of 5.9–7.2 eV. From the data of a number of works (see, for example, [19, 22, 24, 25]), oxygen centers emitting at 2.6 eV [19] absorb efficiently in this region. It is extremely difficult to avoid incorporation of oxygen into fluorite when crystals are synthesized not in HF atmosphere (see, for example, [37–39]). For the last reason, we believe that the absorption spectrum of CaF_2 : Mn measured in [11] was also somewhat distorted in the region of 9.3–10.2 eV. According to [19, 24], it is in this region that one of the intense bands of oxygen absorption is located.

2.6. On the Mechanism of Energy Transport in the CaF_2 : Mn System

The utilization of samples in a wide concentration range and of elementary excitation, i.e., selective production of only excitons or only electron–hole pairs in a crystal by VUV radiation makes it possible to extract the key information on energy transport in a crystal. In particular, this is necessary for decoding the operation of a CaF_2 : Mn dosimeter. We are planning to publish the results of this study elsewhere. Here, we restrict ourselves to the separation (sorting) of mechanisms of energy transfer in two groups, low-efficient and highly efficient.

To the first group belong the following:

(1) The reabsorption mechanism. Its efficiency is low in view of the fact that the oscillator strengths of transitions in Mn^{2+} ions in the spectral region of 2.8–5.3 eV are low (10^{-6}–10^{-7}) [9, 18].

(2) Energy transfer in direct impact of a mobile exciton with a Mn^{2+} center. According to [9], the distance from an Mn^{2+} ion to the surrounding eight F^- ions is decreased by 7% relative to the Ca^{2+}–F^- distance in a regular crystal. The corresponding increase in the distance between ions of the first and the second fluorine coordination shells produces a deformation potential, extensively studied in alkali halides (see [29, 40] and references therein). This distortion of the lattice around a small neutral cation impurity repulses a diffusing exciton with the structure V_ke^- (see references cited above for details).

(3) The electronic recombination process: first, the capture of a hole by a neutral center and then recombination of an electron with the Coulomb center is formed. A relaxed hole in CaF_2, i.e., a V_k center, has the structure of a F_2^- quasi-molecule. Therefore, this channel of energy transport is low-efficient for the same reason as in the case of a V_ke^- exciton.

To the second group belong the following:

(1) The sensitization mechanism, which is efficient owing to a high overlap of the absorption spectra of an Mn^{2+} center and the emission spectra of electrons and owing to a high capacity of manganese centers for resonant interaction with various excited centers (see, for example, [2–6, 20]).

(2) The hole recombination process: first, the capture of an electron by a neutral center and then recombination of a hole with the Coulomb center formed. Judging from appearances, this is the most efficient channel of energy transport in CaF_2 : Mn. Ionization energies of Mn^+ and Ca^+ ions are equal to 15.64 and 11.87 eV, respectively [41]. This is why Mn^+ centers [2, 16, 32], which are stable at least up to 400 K [2], dominate in the family of electronic centers formed in the case of any interband excitation of CaF_2 : Mn at $T < 200$ K. We believe that the *D* state, which we studied above (see subsection 2.5), appears as an intermediate state in the subsequent collision of a diffusing hole with a Coulomb center Mn^+. In the case of nonradiative decay of a *D* excitation, generation of a pair of Frenkel defects takes place, as for instance in the systems KCl : Na [29, 42] and KCl : Tl [29, 43]: an *H* center (fluorine atom in our case) disappears and an F_A center (F_A (Mn) center in our case) is generated. Characteristics of F_A (Mn) centers in CaF_2 : Mn were studied in detail both experimentally [13, 16, 32] and theoretically [14].

CONCLUSIONS

In [7], we started systematic studies of the exciton and the electron–hole processes of energy transport at various temperatures in systems on the basis of CaF_2 (cation impurities Li^+, Na^+, Mg^{2+}, and Mn^{2+}). In this work, the study was extended to the concentration series CaF_2 : Mn (from 0.01 to 2.47 wt. % in the mixture). Spectra of emission, excitation of steady-state luminescence, and phosphorescence of samples excited by monochromatic VUV radiation with quantum energies up to 14 eV at 293 K and up to 12 eV at 85 K were measured.

The nature of the main bands of luminescence of our objects was established earlier. Mn^{2+} centers emit at 2.5 eV (the transition $^4G \longrightarrow {}^6S$ [8, 9]), while relaxed excitons with the structure $V_k e^-$ emit at 4.4 eV [17]. In the case of the host excitation, an increase in the impurity concentration leads to natural redistribution of energy in favor of Mn^{2+} centers. In the case of interband excitation, the rate of this redistribution is much higher than in the case of photoproduction of excitons.

The narrow excitation bands of emission of Mn^{2+} centers at 7.9 and 8.6 eV are assigned to partially forbidden phototransitions of electrons from the ground state ^6S, split by the crystalline field of the host in two sublevels ($10Dq = 0.71$ eV according to [9]), to the high excited state corresponding to the ^6D term of a free Mn^{2+} ion (transitions of the type $3d^5 \longrightarrow 4d^4 4s$).

A broad band of Mn^{2+} center excitation, interpreted as photoproduction of near-impurity *D* excitations, was detected in the region of 9.1–10.3 eV. Both components of the *D* band with maxima at ~9.4 (D_1) and ~10.1 eV (D_2) are assigned to transitions with charge phototransfer. By using the ideas of [26], photoproduction of *D* excitations can be qualitatively represented as the transition $F(2p^6)Mn(3d^5) \longrightarrow Mn(3d^5 4s)F(2p^5)$, i.e., as an allowed electron transition from levels split under the effect of an impurity ion from the top of the valence band to a free orbital of a Mn^{2+} center.

It is concluded from the preliminary comparison of channels of energy transport in CaF_2 : Mn that the following recombination process has the highest efficiency: first, Mn^{2+} ions capture electrons (Mn^+ centers were studied in detail in [2, 16, 32}, and then holes efficiently recombine with Coulomb centers formed (V_k centers in CaF_2 are mobile at least at $T > 130$ K [17]). *D* states appearing in this case experience radiative decay (luminescence of Mn^{2+} centers) or nonradiative decay (generation of F_A (Mn) centers studied in [13, 14, 16] and departure of *H* centers).

ACKNOWLEDGMENTS

The authors are grateful to A.A. Élango for discussion. This study was supported by the European program INCO-COPERNICUS (contract ERBIS 15CT960721).

REFERENCES

1. M. D. Agrawal and K. V. Rao, Phys. Status Solidi A **3** (1), 153 (1970).
2. D. W. McMasters, B. Jassemnejad, and S. W. S. McKeever, J. Phys. D: Appl. Phys. **20** (9), 1182 (1987).
3. B. Jassemnejad, R. J. Abbundi, M. D. Brown, *et al.*, Phys. Status Solidi A **108** (2), 753 (1988).
4. S. C. Sen and H. N. Bose, Z. Phys. **201** (4), 368 (1967); J. L. Patel, B. C. Cavenett, J. J. Davies, *et al.*, Phys. Rev. Lett. **33** (21), 1300 (1974).
5. V. E. Bozhevolnov, L. N. Ivanov, V. K. Kozlov, *et al.*, Phys. Status Solidi B **78** (2), 483 (1976).
6. M. Mizuguchi, H. Hosono, H. Kawazoe, *et al.*, J. Vac. Sci. Technol. A **16** (5), 3052 (1998).
7. V. Denks, A. Maaroos, V. Nagirnyĭ, *et al.*, J. Phys. C: Condens. Matter **11** (15), 3115 (1999).
8. P. J. Alonso and R. Alcalá, J. Lumin. **22** (3), 321 (1981).
9. A. C. Lewandowski and T. M. Wilson, Phys. Rev. B: Condens. Matter **50** (5), 2780 (1994).
10. A. Lira, A. Mendez, L. Dagdug, *et al.*, Phys. Status Solidi B **212** (1), 199 (1999).
11. N. E. Lushchik and Kh. A. Soovik in *Spectroscopy of Crystals*, Ed. by S. V. Grum-Grzhimaĭlo, B. S. Skorobogatov, P. P. Feofilov, and V. I. Cherepanov (Nauka, Moscow, 1970), p. 258.
12. R. K. Bagai and A. V. R. Warrier, Phys. Status Solidi B **73** (2), K123 (1976).
13. J. F. Rhodes, R. J. Abbundi, D. W. Cooke, *et al.*, Phys. Rev. B: Condens. Matter **31** (8), 5393 (1985).
14. A. C. Lewandovski and T. M. Wilson, Phys. Rev. B: Condens. Matter **52** (1), 100 (1995).
15. R. C. Palmer and E. F. Blase, U. S. Patent No. 3,282,855 (1 November 1966).
16. P. J. Alonso and R. Alcalá, J. Lumin. **21** (2), 147 (1980).
17. K. S. Song and R. T. Williams, *Self-Trapped Excitons* (Springer, New York, 1993).
18. S. W. S. McKeever, B. Jassemnejad, and J. F. Landreth, J. Appl. Phys. **60**, 1124 (1986).
19. E. Radzhabov and P. Figura, Phys. Status Solidi B **136** (1), K155 (1986); E. A. Radzhabov, Opt. Spektrosk. **65** (5), 1091 (1988).
20. A. N. Tarashchan, *Luminescence of Minerals* (Naukova Dumka, Kiev, 1978).
21. R. Rauch, R. Reimman, and G. Schwotzer, Phys. Status Solidi A **23** (1), 69 (1974).
22. A. Bohun, L. Roscovcova, M. Svantner, *et al.*, Czech. J. Phys. B **28** (7), 795 (1978).
23. V. A. Arkhangel'skaya, N. E. Lushchik, V. M. Reĭterov, *et al.*, Opt. Spektrosk. **47** (4), 393 (1979).
24. V. A. Arkhangel'skaya, V. M. Reĭterov, and L. M. Trofimova, Zh. Prikl. Spektrosk. **32** (1), 103 (1980).
25. R. Rauch and E. Liebold, Phys. Status Solidi A **64** (2), K165 (1981).
26. R. S. Knox, Phys. Rev. **115** (5), 1095 (1959).
27. E. Vasilchenko, N. Lushchik, and Ch. Lushchik, J. Lumin. **5** (2), 117 (1972).
28. N. C. Amaral, B. Maffeo, and D. Guenzburger, Phys. Status Solidi B **117** (1), 141 (1983).
29. Ch. B. Lushchik and A. Ch. Lushchik, *Decay of Electronic Excitations with the Formation of Defects in Solids* (Nauka, Moscow, 1989).
30. P. J. Call, W. Hayes, J. P. Stoff, *et al.*, J. Phys. C: Condens. Matter **7** (14), 2417 (1974).
31. T. Tomiki and T. Miyata, J. Phys. Soc. Jpn. **27** (3), 658 (1969).
32. R. Alcalá, P. J. Alonso, G. Lalinde, *et al.*, Phys. Status Solidi B **98**, 315 (1980); P. J. Alonso, V. M. Orera, and R. Alcalá, Phys. Status Solidi B **99** (2), 585 (1980).

33. *Atomic Energy Levels*, Ed. by Ch. E. Moore (Nat. Bureau Standards, Washington, 1952), Vol. 2, p. 37.
34. T. Tsuboi and S. Sakoda, Phys. Rev. B: Condens. Matter **22** (10), 4972 (1980).
35. G. S. Zavt and N. N. Kristofel', Ukr. Fiz. Zh. **19** (2), 203 (1974).
36. A. M. Stoneham, *Theory of Defects in Solids: the Electronic Structure of Defects in Insulators and Semiconductors* (Clarendon Press, Oxford, 1975; Mir, Moscow, 1978).
37. C. R. A. Catlow, J. Phys. Chem. Solids **38** (10), 1131 (1977).
38. H. J. Fuchs, W. Karthe, and S. Borner, Phys. Status Solidi B **118** (1), 211 (1983).
39. B. P. Sobolev, Z. I. Zhmurova, V. V. Karelin, *et al.*, in *Growth of Crystals*, Ed. by Kh. S. Bagdasarov period and É. L. Lube (Nauka, Moscow, 1988), Vol. 16, p. 58.
40. V. I. Korepanov, V. M. Lisitsyn, and L. A. Lisitsyna, Izv. Vyssh. Uchebn. Zaved, Fiz., No. 11, 94 (1996).
41. A. A. Radtsig and B. M. Smirnov, *Handbook on Atomic and Molecular Physics* (Atomizdat, Moscow, 1980).
42. Ch. B. Lushchik, R. I. Gindina, N. E. Lushchik, *et al.*, Trudy Inst. Fiz. AN ÉSSR **53**, 146 (1982).
43. Ch. B. Lushchik, E. A. Vasil'chenko, A. Ch. Lushchik, *et al.*, Trudy Inst. Fiz. AN ÉSSR **54**, 5 (1983).

Translated by A. Mozharovskiĭ

Physics of the Solid State, Vol. 42, No. 2, 2000, pp. 270–273. Translated from Fizika Tverdogo Tela, Vol. 42, No. 2, 2000, pp. 263–266.

DEFECTS, DISLOCATIONS, AND PHYSICS OF STRENGTH

Dislocation Interaction with Radiation Defects in Alkali-Halide Crystals

V. A. Zakrevskiĭ and A. V. Shul'diner

Ioffe Physicotechnical Institute, Russian Academy of Sciences, Polytechnicheskaya ul. 26, St. Petersburg, 194021 Russia
E-mail: a.shuldiner@pop.ioffe.rssi.ru

Received July 5, 1999

Abstract—A mechanism of room-temperature irradiation-induced strengthening of alkali-halide crystals (AHCs) is suggested. It is shown that the deformation-stimulated luminescence is a result of the destruction of hole color centers, which strengthen AHCs, by dislocations. © *2000 MAIK "Nauka/Interperiodica".*

INTRODUCTION

The plasticity of crystals is mainly determined by the interaction of dislocations with point defects. Suitable objects for studying the influence of point defects on the plasticity are radiation-colored alkali-halide crystals (AHCs). Irradiation-induced strengthening of AHCs indicates that some of color centers (electron and hole centers, as well as vacancies and interstitial ions) are obstacles for dislocation motion. The electron centers in pure crystals are represented by *F* centers and their aggregates. Among hole centers, self-localized holes (V_k and V_F centers) and relaxed interstitial haloid atoms (*H* centers) have been studied in most detail. All of these represent X_2^- molecules (X is a haloid atom) localized in the lattice in different ways [1, 2].

Vacancies and electron centers are relatively weak obstacles for dislocations, and their contribution to irradiation-induced strengthening is insignificant [3]. Hole centers and interstitials, on the contrary, significantly hinder dislocation slip. It was shown [4] that *H* centers and interstitial haloid ions (*I* centers) are the principal defects that exert strengthening in AHCs at low temperatures. These centers become mobile and vanish in all nominally pure crystals below the liquid-nitrogen temperature. At liquid-nitrogen and higher temperatures, strengthening is ascribed to V_k and V_F centers [5], which become unstable near (below) room temperature. The nature of irradiation-induced strengthening of AHCs at room temperature and higher temperatures remains unclear. It was noted that strengthening may be caused by V_2 and V_3 centers stable at room temperature [3], but their structure remained unknown up to recently. As a result, the micromechanism of overcoming these defects by dislocations also is unknown.

The interaction of dislocations with color centers is accompanied by deformation-stimulated luminescence (DSL) (see [6] and references cited therein). Therefore, detection of DSL may prove to be a suitable technique for studying the influence of point defects on the dislocation motion. Since the behavior of AHCs upon macrodeformation is determined to a significant extent by dislocation interaction with one another [7], it is very difficult to separate the contribution of point obstacles against this background. At the same time, the DSL represents a direct ("unmasked") response of the crystal to the collision of dislocations with radiation point defects. Unfortunately, the application of this method is hampered by the absence of a commonly accepted model of DSL. At present, there exist numerous data which prove that DSL arises as a result of the destruction of color centers by moving dislocations [6], but the nature of the centers destroyed has not been established reliably. In most works, the DSL observed is explained by the ionization of *F* centers by dislocations [6, 8], but in recent years there appeared data which indicate that the dislocations destroy other color centers; namely, in the case of KCl these are V_2 and V_Z centers [9]. The detailed consideration of the interaction of dislocations with irradiation-induced obstacles ("stoppers") on a microscopic level can help clarifying both the nature of DSL and the mechanism of irradiation-induced strengthening. This work is an attempt to solve these problems; its final goal is to determine in great detail the mechanism by which the dislocations surpass point-defect-related obstacles.

EXPERIMENTAL

We used nominally pure single crystals of KCl as the object for the investigation. The crystals were γ-irradiated using ^{60}Co to an absorbed dose of 2 MGy, after which samples with dimensions $5 \times 2 \times 2$ mm were cleaved from the crystals. The concentration of *F* centers in the irradiated crystals reached 5×10^{18} cm^{-3}. The composition and the concentration of the electron-type color centers were controlled by measuring the absorption spectra of the crystals. The information on the hole-type centers was obtained from an analysis of the curves of thermostimulated luminescence (TSL). The temperature was increased linearly (at a rate of

1063-7834/00/4202-0270$20.00

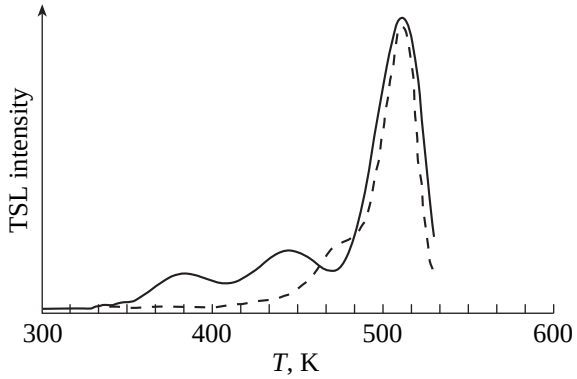

Fig. 1. Thermostimulated luminescence of a γ-irradiated (2 MGy) KCl crystal: solid line, as irradiated; and dashed line, annealed at 445 K for 30 min and cooled to 300 K.

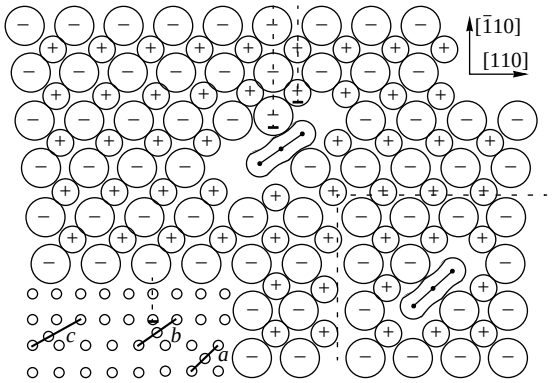

Fig. 2. KCl crystal with X_3^- centers, (001) plane perpendicular to the edge dislocation with a Burgers vector along the [110] direction (schematic).

0.1 K/s). The luminescence intensity was counted using an FÉU-106 photomultiplier. When studying DSL, the load was recorded simultaneously with measuring the luminescence intensity. The rate of deformation was 5×10^{-4} s^{-1}.

RESULTS AND DISCUSSION

In Fig. 1, the solid line shows the TSL curve of a KCl sample irradiated to a high dose (2 MGy). The first two peaks in this curve are due to the destruction of hole V_Z and V_2 centers [2, 10, 11] (peaks at 380 and 450 K, respectively). The mobile H and V_F centers that are formed upon the decay of these centers are recombined with localized electron centers (with F centers among them), generating light emission [1, 2]. The third, most intense peak at 515 K is associated with the thermal ionization of F-type centers [1, 2]. At moderate irradiation doses, this peak is absent because of the absence of hole centers other than V_Z and V_2 in weakly irradiated crystals. The occurrence of an emission maximum at 515 K indicates the formation of hole centers stable at temperatures above 500 K in crystals exposed to large doses of γ radiation. The concentration of these centers may significantly exceed the total concentration of the V_Z and V_2 centers. This circumstance makes it possible to obtain (by annealing the irradiated crystals at temperatures below 500 K) samples completely free of V_Z and V_2 centers but containing sufficiently high concentrations of hole centers of other types and correspondingly high concentrations of electron centers. It is for this reason that we used strongly irradiated crystals in this work, because a comparison of data obtained in experiments with samples both containing V_Z and V_2 centers and free of these defects makes it possible to elucidate the role of these centers and the origin of DSL.

The dashed line in Fig. 1 displays the TSL curve of the sample that was annealed at 445 K for 30 min. The peaks at 380 and 450 K disappeared, but a peak at 470 K, which is related to V_3 centers [1, 11], become visible. The peak at 515 K remained almost unaltered. The measurements of the absorption spectrum show that the number of F centers decreased upon annealing no more than by 10%.

After deformation of unannealed samples, the DSL was similar to that described in literature [12], and the DSL intensity was approximately 8000 cps.

The deformation of annealed samples was also accompanied by DSL, but its intensity was only 500 cps, i.e., it was by an order of magnitude smaller than that recorded prior to the destruction of the V_Z and V_2 centers.

The above data show that the room-temperature DSL of KCl crystals is due to the V_Z and V_2 centers, while the F centers play only a secondary role in this process, contrary to the common opinion. The dislocations appear to destroy V_Z and V_2 centers; in the result, V_F and H centers are formed, which are recombined with the F-type centers. In order to understand how dislocations can destroy hole centers, we should consider the process of their interaction on a microscopic level.

The V_2 centers represent linear molecules of the X_3^- type oriented along ⟨100⟩ directions, located in two anion and one cation lattice sites; these molecules also enter into the V_Z centers [1, 2]. In the case of KCl, these are Cl_3^- molecules. Figure 2 schematically displays the (001) crystal plane of KCl with Cl_3^- molecules oriented along the [010] direction. In the lower right-hand side corner of the figure, an idealized model of the Cl_3^- center is shown in a lattice region that is undisturbed by other defects. The central portion of the figure displays the interaction of a dislocation and a center for one of their possible mutual orientations. The Burgers vector of the dislocation is oriented along the [110] direction and the molecule suffers a tensile stress. In order to more clearly demonstrate the interaction of a dislocation with Cl_3^- centers, in the inset in the lower left-hand side corner of Fig. 2, we show an ultimately simplified

scheme of the same crystal plane with defects (without the adherence to the true relationship between the crystal-chemical radius of the Cl^- ion, the length of the Cl_3^- molecule, and the lattice parameter, and without the cation sublattice). The character *a* in the inset indicates a Cl_3^- center far from a dislocation; the letter *b* denotes a center that is involved in the direct interaction with a dislocation, as in the main part of the figure. It can be seen that an elastic interaction with a dislocation leads to an extension of the molecule (in Fig. 2, the molecule is shown to be extended by 10%). Since the elongation of the bonds in the molecule requires additional stresses, it is obvious that Cl_3^- centers resist the dislocation motion. It can be understood from the figure that the further motion of a dislocation in the same slip plane (i.e., the contact surpassing of an obstacle) is impossible without the breaking of the Cl_3^- molecule. If the intramolecular bonds were retained upon such motion, the molecule would take on the configuration denoted by the letter *c* in the inset. Such a configuration is most likely unstable, because, in particular, it requires a bond elongation by approximately 50% (estimates made below show that at room temperature the bonds become unstable at significantly smaller deformations). We may determine the probability of the destruction of a molecule by a dislocation in the following way.

Atoms in a three-haloid ion Cl_3^- are linked by covalent bonds [13]. For these bonds, the dependence of the interatomic potential U on the interatomic spacing r is well described by the universal function $U(r) = U_0E(A)$, where U_0 is the energy of dissociation of the molecule; E is the Rydberg function; $E(A) = -(I + A)\exp(-A)$; $A = (r - r_0)/l$; r_0 is the equilibrium bond length; $l = (U_0/k_0)^{1/2}$; and k_0 is the force constant [14].

In order to find U_0, we turn to the data obtained in studies of TSL. As was said above, the TSL peak at 450 K is caused by the dissociation of Cl_3^- centers into H and V_F centers. The activation energy for light emission for this peak (1.25 eV [1, 11]) is determined by the energy of dissociation of the Cl_3^- molecule U_0 and the energy required for removing at least one of the centers that are formed upon the dissociation into a neighboring cell (in order to prevent the restoration of the bond). The energy of motion of H centers is a few hundredths of an electron volt [2]; therefore, we can assume $U_0 = 1.25$ eV.

The value of r_0 can be estimated from the following considerations. The position of the maximum of the absorption band of the Cl_3^- centers is known [2] to coincide with that of the Cl_3^- molecules in a solution; therefore, the crystal matrix is only insignificantly deforms the Cl_3^- molecule. According to [13], the r_0 in the X_3^- molecules is approximately 10% longer than the bond length R in the corresponding molecules X_2^0. For Cl_2, we have $R = 2.01 \times 10^{-8}$ cm, and, indeed, $r_0 = 2.21 \times 10^{-8}$ cm. Finally, $k_0 = 0.96$ N/cm [13].

Now, given the $U(r)$ function, we can determine the interatomic interaction force $f(r) = -dU(r)/dr$ and the maximum value of this force f_{max}. We obtained $f_{max} = 1.6 \times 10^{-9}$ N; the bond elongation corresponding to this force is 25%.

It is known that the force of the elastic interaction of a dislocation with an obstacle does not exceed Gb^2 (where G is the shear modulus and b is the Burgers vector) [7]. This force is directed along $\langle 110 \rangle$ and its component in the direction of the molecule extension is only a fraction of the above value Gb^2. For KCl, we have $G = 1.7 \times 10^6$ N/cm^2 and $b = 4.44 \times 10^{-8}$ cm; therefore, $Gb^2 = 3.4 \times 10^{-9}$ N, so that $f_{max} \approx Gb^2/2$. Hence, it appears that the Cl_3^- centers are formidable obstacles for dislocations. At the same time, it should be taken into account that these centers can be destroyed upon the application of a tensile force P which is smaller than f_{max}, since stressed bonds become broken at moderate temperatures by a thermofluctuational mechanism.

The rate of thermoactivated breaking of the bonds is determined by the activation energy $U_P < U_0$ [15]. In this case, U_P is controlled by the experimental conditions via the average time required for the thermoactivated breaking of a stressed bond: $t_P = \tau_0\exp(U_P/kT)$, where τ_0 is the period of atomic vibrations. It is obvious that t_P should not exceed the average time t_S spent by the dislocation on the bypassing of one obstacle; otherwise, the Cl_3^- centers will be bypassed by dislocations by the mechanism of double cross slip or by the Orowan mechanism. In alkali-halide crystals, this time is $t_S \approx d/v$, where d is the average spacing of obstacles and v is the average velocity of dislocation motion. The velocity v can be determined from the equation of plastic deformation $\dot{\varepsilon} = b\rho_m v$, where ρ_m is the density of moving dislocations. For a concentration of the Cl_3^- centers of about 10^{18} cm^{-3}, we have $d \sim 10^{-6}$ cm. Assuming that $\rho_m \sim 10^8$ cm^{-2} [7], we find $t_S \sim 10^{-2}$ s. As a result, we obtain that at 300 K the bond breaks occur at a sufficiently high rate if $U_P \leq 0.6$ eV. Since $U_P = \int_{r_1}^{r_2} [f(r) - P]\,dr$, where r_1 and r_2 are determined by the relationship $f(r_1) = f(r_2) = P$ [15], we can find the force with which the bond should be stretched in order that its activation energy for breaking be reduced from 1.25 to 0.6 eV. It proves to be 0.55×10^{-9} N. The bond elongation in this case is 10%.

Thus, the destruction of Cl_3^- centers and the appearance of DSL are possible at room temperature if the tensile stress acting on the Cl_3^- molecule is about $Gb^2/6$. This value seems to be quite reasonable. If the Cl_3^- molecules form complexes with other defects, which have a lowered dissociation energy, e.g., V_Z centers, the tensile stress can be yet smaller.

The interpretation of DSL as a result of thermoactivated destruction of X_3^- centers by dislocations makes it possible to explain not only the temperature but also the rate dependence of the DSL intensity. It is known that the DSL intensity is proportional to $\dot{\varepsilon}^{-\alpha}$ (where the constant α is less than unity) [6]. From this, it follows that with increasing $\dot{\varepsilon}$ the number of photons emitted during the time corresponding to a unit deformation is decreased, i.e., the probability of the destruction of the X_3^- centers upon their interaction with dislocations is also decreased. The reason may be the decrease in t_S with increasing $\dot{\varepsilon}$.

CONCLUSION

From the above discussion, we may arrive at the following conclusions. Irradiation of alkali-halide crystals causes the formation of hole-type color centers containing X_2^- (H, V_k, and V_1 centers) and X_3^- (V_2 and V_Z centers) molecular ions. The atoms that enter into such centers are displaced noticeably relative to their equilibrium positions in the regular lattice. The spacing of the two haloid atoms decreases by 40% when a V_k center is formed [2] and slightly greater when a V_2 center arises. The changes in the interatomic distances, along with changes in the charge state of the atoms in the defects, lead to lattice distortions around color centers, which undoubtedly hinders dislocation slip. However, when considering the mechanisms of irradiation-induced strengthening of alkali-halide crystals (AHCs), we should take into account (as was shown above) not only lattice distortions, but also the formation in the defects of chemical bonds, which are not characteristic of the regular lattice. The "contact" mechanism of the surpassing of hole centers is impossible without the breaking of intramolecular bonds (in the case of X_3^- centers) or without a reorientation of the centers (in the case of X_2^- centers), which requires additional stresses. At room temperature, X_3^- centers are predominant in AHCs. In KCl crystals (as, seemingly, in other chlorides), the intramolecular bonds in Cl_3^- centers appear to be so strong that the stresses that are required for them to be broken are comparable with maximum possible local stresses. It may be supposed that it is the formation of covalent bonds between the haloid atoms that is the main reason for the development of strengthening in AHCs upon the room-temperature irradiation to moderate doses (until coarse defects are formed).

Upon the destruction of Cl_3^- centers, pairs of mobile H and V_F centers arise. Since these centers move away from the place where the dislocation interacted with an obstacle, the regular lattice is restored there. The recombination of mobile centers with electron-type color centers is accompanied with light emission, which is detected as deformation-stimulated luminescence (DSL).

Note that the reasons for the appearance of DSL cannot be reduced to only the stress-induced dissociation of hole centers. The dislocations not only can destroy the centers, but also displace through small distances. As an example of such a displacement, the above-mentioned reorientation of X_2^- centers can be taken. As another example, F centers located on dislocation slip planes can be sused; they are displaced as a result of deformation shear by one interatomic distance, But for some close pairs of electron and hole centers such a displacement may be sufficient to provide recombination. It is the deformation shear of F centers that may serve the origin of a low-intensity DSL observed after the annealing of X_3^- centers.

Thus, the main conclusions of this work can be formulated as follows. The radiation-induced point defects that exert a strengthening effect on KCl crystals subjected to room-temperature irradiation are Cl_3^- centers. The interaction of these centers with moving dislocations leads to their destruction. The deformation-stimulated luminescence in this temperature range is due to the destruction of hole centers V_2 and V_Z by dislocations.

REFERENCES

1. I. A. Kudryavtseva, E. A. Vasil'chenko, A. Ch. Lushchik, and Ch. B. Lushchik, Fiz. Tverd. Tela (S.-Peterburg) **41** (3), 433 (1999).
2. Ch. B. Lushchik and A. Ch. Lushchik, *Decay of Electron Excitations with the Formation of Defects in Solids* [in Russian] (Nauka, Moscow, 1989).
3. A. V. Gektin, Fiz. Tverd. Tela (Leningrad) **27** (11), 3254 (1985).
4. K. Tanimura, T. Hagihara, M. Fujiwara, and T. Okada, J. Appl. Phys. **49** (11), 5452 (1978).
5. J. S. Nadeau, J. Appl. Phys. **37** (4), 1602 (1966).
6. M. I. Molotskiĭ and S. Z. Shmurak, Phys. Lett. A **166** (3–4), 286 (1992).
7. B. I. Smirnov, *Dislocation Structure and Strengthening of Crystals* [in Russian] (Nauka, Leningrad, 1981).
8. C. T. Butler, Phys. Rev. **141** (2), 750 (1966).
9. A. V. Shuldiner and V. A. Zakrevskiĭ, Radiat. Prot. Dosim. **65** (1–4), 113 (1996).
10. R. I. Gindina, L. A. Ploom, A. A. Maaroos, and Yu. V. Pyllusaar, Zh. Prikl. Spektrosk. **27** (3), 520 (1977).
11. A. A. Nagornyĭ, Izv. Akad. Nauk Latv. SSR, Ser. Fiz. Tekh. Nauk, No. 6, 38 (1979).
12. T. Hagihara, Y. Hayashiuchi, Y. Kojima, *et al.*, Phys. Lett. A **137** (4–5), 213 (1989).
13. G. Pimentel and R. Spratley, *Chemical Bonding Clarified through Quantum Mechanics* (Holden-Day, San Franscisco, 1970; Mir, Moscow, 1973).
14. J. R. V. Smith, H. Schlosser, W. Leaf, *et al.*, Phys. Rev. A **39**, 514 (1989).
15. É. E. Tomashevskiĭ, Fiz. Tverd. Tela (Leningrad) **12** (11), 3202 (1970).

Translated by S.N. Gorin

Physics of the Solid State, Vol. 42, No. 2, 2000, pp. 274–276. Translated from Fizika Tverdogo Tela, Vol. 42, No. 2, 2000, pp. 267–269.

DEFECTS, DISLOCATIONS, AND PHYSICS OF STRENGTH

Deformation of NaCl Crystals under Combined Action of Magnetic and Electric Fields

A. A. Urusovskaya, V. I. Al'shits, N. N. Bekkauer, and A. E. Smirnov

Shubnikov Institute of Crystallography, Russian Academy of Sciences, Leninskiĭ pr. 59, Moscow, 117333 Russia
e-mail: public@mechan.incr.msk.su

Received June 30, 1999; in final form, August 6, 1999.

Abstract—The paper reports observation of a strong macroplastic effect of weak magnetic and electric fields ($B \le 0.4$ T, $E \sim 1$ kV/m) when applied simultaneously to NaCl samples in the course of their active deformation at constant rate ε = const. In the absence of magnetic field, electric effects in the macroplasticity of the same crystals become manifest at fields $E \ge 10^3$ kV/m. Quantitative dependences of the macroplasticity on magnetic and electric fields and on the strain rate have been measured. A physical interpretation of the observed phenomena is proposed. © *2000 MAIK "Nauka/Interperiodica".*

It is well known [1–3] that edge dislocations in alkali halide (AH) crystals undergoing a slip are capable of transporting, without loss, an uncompensated electric charge, whose sign and magnitude are determined by the impurity composition of the crystals and the corresponding supersaturation of the anionic or cationic vacancies. It is this phenomenon that underlies the so-called Stepanov effect [4], which manifests itself in macropolarization of strained AH crystals in the course of their deformation. It is naturally for the same reason that application of an electric field also affects the behavior of a crystal subjected to a mechanical loading. There are the experimental data on the lowering of the plastic-flow stress [5, 6], acceleration of deformation in creep [7], an increase in the strain-induced strengthening rate under active loading [8], and an increase in internal friction [3, 9]. It was established that application of an electric field stimulates activation of additional slip planes [8] and dislocation sources at block boundaries [9], thus giving rise to an increase in the total dislocation density [3]. However, it should be noted that observation of all these effects can be possible only in very high electric fields of the order of 10^5–10^6 V/m.

The observation of the magnetoplastic effect (MPE) [10], which consists in energetically facilitated unpinning of dislocations from point defects in nonmagnetic (including AH) crystals placed in a dc magnetic field $B \sim (0.1–1)$ T, offers new possibilities for increasing the plastic sensitivity to an external action on a crystal. The MPE manifests itself both in an increase of the mobility of single dislocations [11, 12] and, at the macroscopic level, in a considerable lowering of the yield point [13, 14], a decrease in the microhardness [15], and a change in the fundamental characteristics of internal friction [16].

The MPE becomes manifest particularly clearly in an increase of the sensitivity of dislocation pathlength in AH crystals to an external electric field. Application of even a weak magnetic field of a few tenths of a T was shown [11, 17, 18] to increase this sensitivity by two or three orders of magnitude. In other words, single dislocations in an external magnetic field respond strongly already to electric fields $E \sim 10^2$–10^3 V/m.

It is of interest to study the macroplastic response of AH crystals to an electric field in MPE conditions. With this purpose in mind, the present work was aimed at investigating the combined effect of a magnetic and an electric field on macroscopic deformation of NaCl crystals under compression at a constant rate.

1. EXPERIMENTAL TECHNIQUE

The experiments were conducted on the same samples and in the same setup that was employed in [13]. A dc magnetic field was applied perpendicular to the loading axis, and an electric field, along this direction. Brass electrodes were pasted to the sides of corundum dies and were in contact with the sample end faces. The magnetic induction was varied from 0 to 0.4 T, and the electric field, from 0 to 20 kV/m. The samples were deformed at room temperature with rates ranging from 5×10^{-5} to 2×10^{-3} s^{-1}.

2. RESULTS AND DISCUSSION

Figure 1 presents the strain curves obtained under compression of NaCl with different rates in the absence of any field (curve *1*), with only a magnetic field of 0.4 T applied (curve *2*), and under additional application of a 9-kV/m electric field (curve *3*). The magnetic field lowered the curve, including the yield point, reduced the extent of all stages of the deformation, and reduced the strain-induced strengthening coefficient Θ_{II}. Curve *3* is characterized by an additional reduction

1063-7834/00/4202-0274$20.00

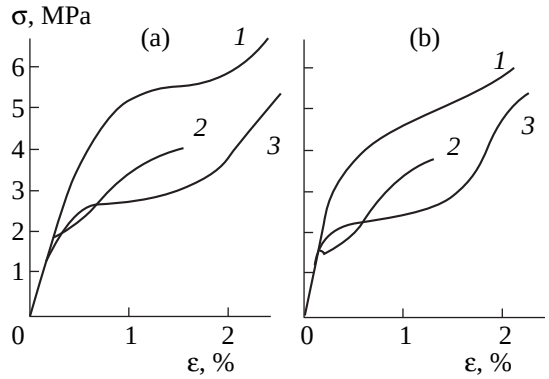

Fig. 1. Strain curves of NaCl crystals compressed (*1*) in the absence of magnetic and electric fields, (*2*) in the presence of the magnetic field $B = 0.4$ T, and (*3*) under combined application of magnetic (0.4 T) and electric (9 kV/m) fields. Strain rate: (a) $\dot{\varepsilon} = 5 \times 10^{-5}$ s^{-1} and (b) $\dot{\varepsilon} = 8 \times 10^{-5}$ s^{-1}.

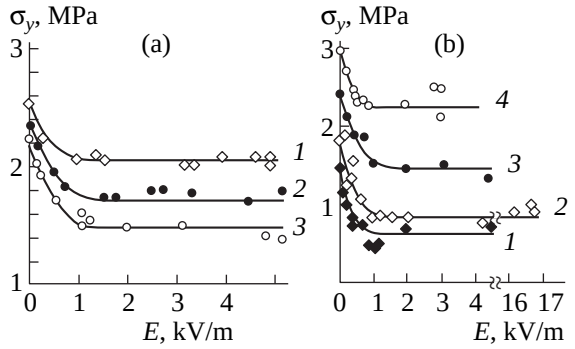

Fig. 2. Dependence of the yield point on electric field for (a) different B = (*1*) 0.2, (*2*) 0.3, and (*3*) 0.4 T and $\dot{\varepsilon} = 5 \times 10^{-4}$ s^{-1} and (b) different $\dot{\varepsilon}$ = (*1*) 5×10^{-5}, (*2*) 8×10^{-5}, (*3*) 2×10^{-4}, and (*4*) 2×10^{-3} s^{-1} and $B = 0.4$ T.

of the yield point, a lengthening of the easy-slip stage, and a decrease in its slope Θ_I, as well as by an increase in the strengthening coefficient immediately after the yield point at the second stage of strengthening Θ_{II} as compared to curve *2*. In the absence of magnetic field, the electric fields applied did not affect in any way the NaCl strain curves. The situation changed only in fields of the order of 10^3 kV/m [8].

The shortening of deformation stages and the lowering of Θ_{II} under the action of magnetic field only is accounted for by a more frequent magnetic-field-stimulated change of active slip systems [13, 14]. Judging from the lengthening of the first deformation stage and the lowering of Θ_I (curve *3*), the electric field, to the contrary, provides conditions favorable for a longer action of the primary slip system in the initial deformation stages. The increase in the strain-induced strengthening coefficients Θ_{II} under combined action of the magnetic and electric fields should be considered as a result of an electric-field-stimulated growth of the dislocation density in accordance with the relation [19]

$$\Theta_{II} \sim Gb\sqrt{\rho},$$

where G is the shear modulus, b is the Burgers vector, and ρ is the dislocation density.

Figure 2a shows the variation of the yield point σ_y with an increase in the electric field E, plotted for different magnetic inductions B.

The experimental curves exhibit two clearly pronounced stages of the observed relations, namely, an initial falloff and subsequent saturation for E above (1–1.5) kV/m. The decrease in σ_y is the larger and the steeper, the higher is B.

Similar dependences were obtained under variation of the strain rate $\dot{\varepsilon}$ at a fixed B (Fig. 2b). The saturated level of E is within the same limits as in Fig. 2a. The rate and depth of the decrease are the stronger, the lower is $\dot{\varepsilon}$. The experiments carried out at $\dot{\varepsilon} = 8 \times 10^{-5}$ s^{-1} showed the saturation level to persist up to $E \geq 20$ kV/m.

Thus, the parameters of NaCl macroplasticity in an external magnetic field also exhibit an increase in the sensitivity to an electric field by several orders of magnitude. Indeed, the effects (the lowering of the flow stress, the increase in the strain-induced strengthening rate, and the increase in the dislocation density) revealed under a combined action of weak magnetic and electric fields ($B \leq 0.4$ T, $E \sim 1$ kV/m) are seen in zero magnetic field only for $E \geq 10^3$ kV/m.

The reason for this appears to be fairly obvious. In both cases, the sensitivity threshold to an electric field is determined from the condition of the electric force, acting on a dislocation, being equal to the resistance meeting its motion. Thus, the well-pronounced lowering of this threshold in a magnetic field reflects, apparently, the corresponding decrease in the dislocation drag after it stops interacting with the main impurity centers as a result of certain spin-dependent transitions in the dislocation-impurity system induced by the external magnetic field.

The saturation of the observed lowering of the yield point σ_y with an increase in the electric field reflects, apparently, the "residual" role of the screw components of dislocation loops in macroplasticity. We can recall that screw dislocations in the main slip systems in AH crystals do not carry any charge. In order for these dislocations to move with a velocity determined by the given strain rate $\dot{\varepsilon}$, one has to apply a certain mechanical stress, and it is this stress that corresponds possibly to the σ_y level for $E \longrightarrow \infty$.

Note that, as $\dot{\varepsilon}$ increases, the maximum depth of the electric-field-induced lowering of the flow stress σ_y decreases (Fig. 2a). This correlates with a decrease in the dynamic charge at edge dislocations observed [20] with an increase in the strain rate $\dot{\varepsilon}$.

REFERENCES

1. A. A. Urusovskaya, Usp. Fiz. Nauk **96** (1), 39 (1968).
2. R. W. Whitworth, Adv. Phys. **24** (2), 203 (1975).
3. N. A. Tyapunina and É. P. Belozerova, Usp. Fiz. Nauk **156** (4), 683 (1988).
4. A. W. Stepanow, Z. Phys. **81** (7/8), 560 (1933).
5. A. N. Kulichenko and B. I. Smirnov, Fiz. Tverd. Tela (Leningrad) **23** (4), 1029 (1981).
6. A. N. Kulichenko and B. I. Smirnov, Fiz. Tverd. Tela (Leningrad) **25** (5), 1523 (1983).
7. N. V. Zagoruĭko and E. D. Shchukin, Kristallografiya **13** (5), 908 (1968).
8. A. A. Urusovskaya, A. E. Smirnov, and N. N. Bekkauer, Izv. Vyssh. Uchebn. Zaved., Chern. Metall. **8**, 15 (1993).
9. É. P. Belozerova, A. A. Svetashov, and N. A. Tyapunina, Kristallografiya **28** (6), 1176 (1983).
10. V. I. Al'shits, E. V. Darinskaya, T. M. Perekalina, *et al.*, Fiz. Tverd. Tela (Leningrad) **29** (2), 567 (1987).
11. V. I. Alshits, E. V. Darinskaya, O. L. Kazakova, *et al.*, Mater. Sci. Eng. A **234–236**, 617 (1997).
12. Yu. I. Golovin and R. B. Morgunov, Zh. Éksp. Teor. Fiz. **115** (2), 605 (1999).
13. A. A. Urusovskaya, V. I. Al'shits, A. E. Smirnov, *et al.*, Pis'ma Zh. Éksp. Teor. Fiz. **65** (6), 470 (1997).
14. V. I. Al'shits, N. N. Bekkauer, A. E. Smirnov, *et al.*, Zh. Éksp. Teor. Fiz. **115** (3), 951 (1999).
15. Yu. I. Golovin, R. B. Morgunov, D. V. Lopatin, *et al.*, Phys. Status Solidi A **160** (1), R3 (1997).
16. É. P. Belozerova, A. A. Svetashov, and V. L. Krasnikov, Izv. Akad. Nauk, Ser. Fiz. **61** (2), 291 (1997).
17. V. I. Al'shits, E. V. Darinskaya, E. Yu. Mikhina, *et al.*, Fiz. Tverd. Tela (Leningrad) **35** (5), 1397 (1993).
18. V. I. Al'shits, E. V. Darinskaya, E. Yu. Mikhina, *et al.*, Fiz. Tverd. Tela (S.-Peterburg) **38** (8), 2426 (1996).
19. N. F. Mott, Philos. Mag. **43** (7), 1151 (1952).
20. V. I. Al'shits, M. V. Galustashvili, and I. M. Paperno, Kristallografiya **20** (6), 1113 (1975).

Translated by G. Skrebtsov

Physics of the Solid State, Vol. 42, No. 2, 2000, pp. 277–279. Translated from Fizika Tverdogo Tela, Vol. 42, No. 2, 2000, pp. 270–272.

DEFECTS, DISLOCATIONS, AND PHYSICS OF STRENGTH

Deformation of LiF Crystals in DC Magnetic Field

V. I. Al'shits, A. A. Urusovskaya, A. E. Smirnov, and N. N. Bekkauer

Shubnikov Institute of Crystallography, Russian Academy of Sciences, Leninskiĭ pr. 59, Moscow, 117333 Russia
e-mail: public@mechan.incr.msk.su

Received July 18, 1999; in final form, August 6, 1999

Abstract—Active deformation of LiF crystals in a dc magnetic field B is shown to produce strong plasticization, which is the more pronounced, the higher is the magnetic induction B and the lower the strain rate $\dot{\varepsilon}$. The measured dependences of the yield point σ_y on B and $\dot{\varepsilon}$ find a reasonable explanation within a simple kinetic model based on the competition between the thermally activated and magnetically stimulated unpinning of dislocations from impurity centers. *© 2000 MAIK "Nauka/Interperiodica".*

The existence of magnetically stimulated unpinning of dislocations from impurity centers in nonmagnetic materials, which was first revealed in NaCl crystals [1], is presently established reliably and has been studied in considerable detail at the level of single dislocations [2–4]. The nature of this phenomenon is usually associated with spin conversion in impurity centers, which results in a rearrangement of their electronic structure and the corresponding weakening of their interaction with dislocations. The time taken for this magnetic unpinning to occur decreases with an increase in the magnetic induction B and is proportional to B^2, and the process itself is observed only in fields B exceeding a certain threshold field B_c^0 and providing a fast enough spin evolution compared to the spin-lattice relaxation time ($\tau_{dp} < \tau_{sl}$).

A manifestation of this effect in microplasticity under active deformation of LiF crystals (loading at a constant rate $\dot{\varepsilon}$ = const) was first reported in our work [5], where in the presence of a magnetic field, we observed a noticeable lowering of the yield point and the strain-induced strengthening rate in stage II of the deformation and an increase of the strengthening rate in stage III. The experiments were carried out in magnetic fields B varied from 0 to 0.48 T and compression rates $\dot{\varepsilon} = (5 \times 10^{-5}–10^{-4})$ s^{-1}. It was also found that the effect follows a threshold behavior both in the field and in the strain rate. It is observed for $B > 0.4$ T and $\dot{\varepsilon} < 10^{-4}$ s^{-1}. Because of the narrow interval of available magnetic fields and the compression rates used, we studied [5] neither the character of the variation in the yield point, with an increase in the magnetic induction, nor the behavior of these thresholds, $B_c(\dot{\varepsilon})$ and $\dot{\varepsilon}_c(B)$. In the present investigation, the strain rate interval was extended considerably toward smaller $\dot{\varepsilon}$. This permitted us to measure for the first time the dependence of the yield point σ_y on B and $\dot{\varepsilon}$, as well as to establish the region $\{B, \dot{\varepsilon}\}$ within which a macroscopic magnetoplastic effect is observed in LiF crystals. The measured relations allow a fairly revealing physical interpretation.

1. EXPERIMENTAL TECHNIQUE

The experiments on deformation in a magnetic field and without it were carried out on a compression stand, in which all of the components within the action of the magnetic field were fabricated of nonmagnetic materials, namely, aluminum, bronze, and brass. The dies were ruby cylinders. The LiF crystals selected for the study were of technical-grade purity. The samples were not subjected to thermal pretreatment. The magnetic field was produced by moving properly a permanent magnet with adjustable poles. The magnetic-field induction B could be varied from 0 to 0.48 T, and the strain rate $\dot{\varepsilon}$, from 2×10^{-6} to 5×10^{-5} s^{-1}. The experiments were run at room temperature. The parallelepiped-shaped samples were cleaved and measured $2.5 \times 2.5 \times 8$ mm. The strain curves were recorded automatically with a KSP-4 recorder.

2. RESULTS

Three-stage strain curves were obtained under compression of LiF crystals with and without application of

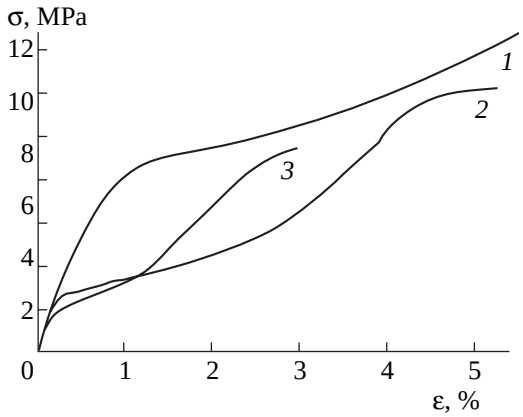

Fig. 1. Strain curves of LiF crystals (*1*) in the absence of magnetic field and in a magnetic field of (*2*) 0.25 and (*3*) 0.48 T. The strain rate is 6×10^{-5}s^{-1}.

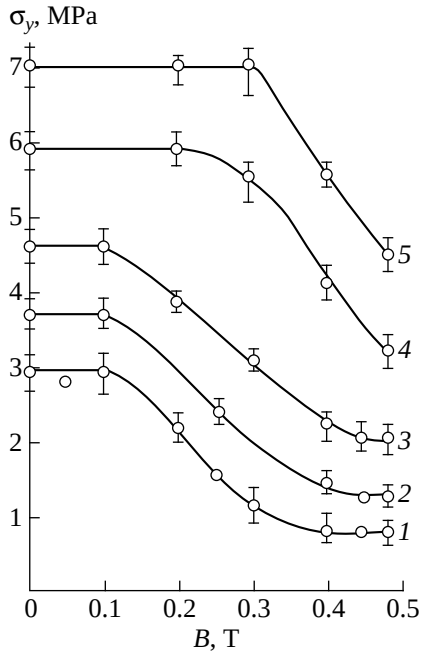

Fig. 2. Yield point σ_y versus magnetic-field induction for different strain rates $\dot{\varepsilon}$ (s^{-1}): (*1*) 2×10^{-6}, (*2*) 3.5×10^{-6}, (*3*) 8×10^{-6}, (*4*) 2×10^{-5}, and (*5*) 5×10^{-5}.

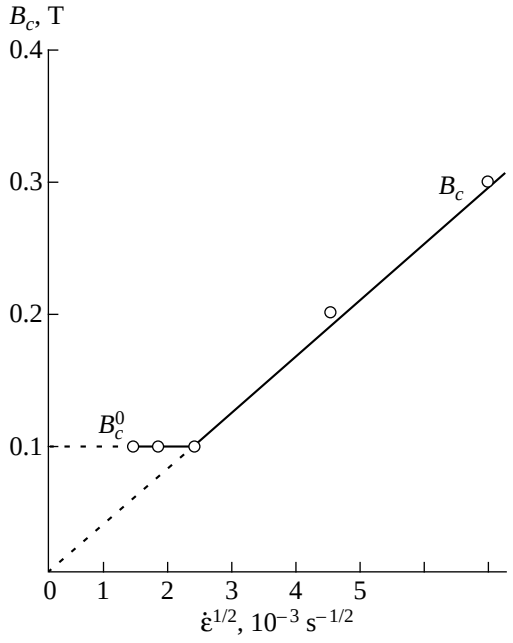

Fig. 3. Dependence of the threshold magnetic induction B_c on $\dot{\varepsilon}$.

magnetic field (Fig. 1). The reproducibility of the strain curves is reliable enough [5]. As is seen from Fig. 1, the magnetic field not only lowers the yield point σ_y, but makes more narrow the strain and stress intervals in each deformation stage. The faster change of the deformation stages shows that the magnetic field activates additional slip systems.

Figure 2 illustrates the magnetic-field dependence of the yield point obtained at different compression rates. It can be seen that the lower the $\dot{\varepsilon}$ value, the faster is the relative decrease in the yield point. At the highest rate, the yield point at the maximum field decreased by a factor 1.5 only, whereas, at the minimum rate, σ_y decreased nearly fourfold. As is seen from Fig. 2, the sensitivity of the yield point to magnetic field becomes noticeable only starting with a certain threshold field B_c, above which σ_y decreases relatively rapidly with an increase in B to approach asymptotically a new, lower $\sigma_y^{(1)}$ level. The magnetic effect observed depends on the strain rate. In particular, the magnetic threshold B_c, while remaining constant ($B_c = B_c^{(0)}$) at low rates $\dot{\varepsilon}$, becomes a function $B_c = B_c^{(0)}\sqrt{\dot{\varepsilon}/\dot{\varepsilon}_c}$ for $\dot{\varepsilon} > \dot{\varepsilon}_c = 6 \times 10^{-6}$ s^{-1} (Fig. 3). On the other hand, this should mean that, at a fixed field $B > B_c^{(0)}$, the $\sigma_y(\dot{\varepsilon})$ dependence can reveal a noticeable magnetic sensitivity only within the range of the $\dot{\varepsilon}$ rates bounded from above: $\dot{\varepsilon} < \dot{\varepsilon}_c B/B_c^{(0)})^2$. It is this factor that becomes manifest in the experimental curves $\sigma_y(\dot{\varepsilon})$ constructed for a series of fixed values of B (Fig. 4).

3. DISCUSSION

Similar data obtained in [6] on NaCl crystals found a reasonable interpretation within the following simple model. In the conditions of active deformation at a constant rate, the yield point corresponds to the stress providing the required velocity of dislocation displacement through the system of local energy barriers. For

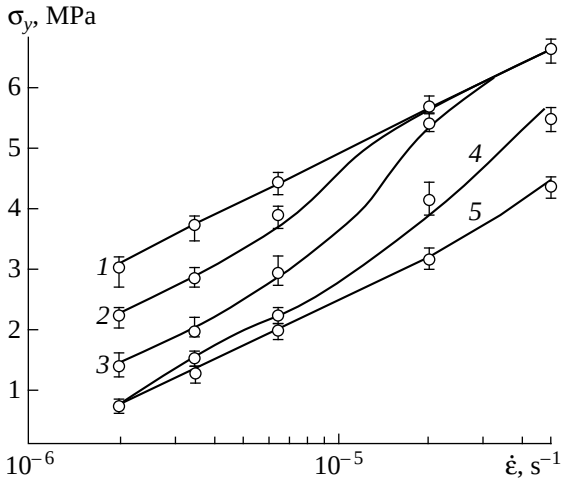

Fig. 4. Strain-rate dependence of the yield point for different magnetic inductions (T): (*1*) 0, (*2*) 0.2, (*3*) 0.3, (*4*) 0.4, and (*5*) 0.48.

$B = 0$, the simplest expression for such a balance can be written in the form

$$\dot{\varepsilon} = \dot{\varepsilon}_0 \exp[-(U - \gamma\sigma_y)/(kT)], \quad (1)$$

where U is the activation energy, γ is the activation volume, σ_y is the flow stress (yield point) for $B = 0$, k is the Boltzmann constant, and T is the absolute temperature.

The linear dependence of σ_y on $\ln\dot{\varepsilon}$ presented in Fig. 4 (curve *1*) for $B = 0$ is a plot of function (1) rewritten in the form

$$\sigma_y = (U/\gamma) + [(kt/\gamma)\ln(\dot{\varepsilon}/\varepsilon_0)]. \quad (2)$$

No noticeable effect of the magnetic field on the yield point should be expected until the time of the magnetically stimulated unpinning of a dislocation from the pinning center $\tau_{dp} = kB^{-2}$ becomes shorter than that required to overcome it by thermal activation

$$\tau_{th} = \tau_0 \exp[(U - \gamma\sigma_y)/(kT)] = \tau_0\dot{\varepsilon}_0/\dot{\varepsilon}. \quad (3)$$

It is this consideration that determines the threshold field $B_c \sim \sqrt{\dot{\varepsilon}}$, which, however, cannot be less than the microscopic threshold $B_c^{(0)}$ of the magnetoplastic effect.

Thus, within the proposed model

$$B_c = \begin{cases} B_c^{(0)}, & \dot{\varepsilon} < \dot{\varepsilon}_c \\ B_c^{(0)}\sqrt{\dot{\varepsilon}/\dot{\varepsilon}_c}, & \dot{\varepsilon} > \dot{\varepsilon}_c, \end{cases} \quad (4)$$

where $\dot{\varepsilon}_c = \dot{\varepsilon}_0\tau_0/\tau_{dp}^{\max}$ and $\tau_{dp}^{\max} = kB_c^{(0)-2}$.

It is readily seen that the $B_c(\dot{\varepsilon})$ relation (4) is in full accord with the experimental curve displayed in Fig. 3.

According to [6], the saturation level $\sigma_y^{(1)}$ at high magnetic fields (see Fig. 2) is determined by the thermally activated process of overcoming the magnetically sensitive local pinning points. It was suggested [6] that magnetically stimulated transitions destroy the main barriers to allow other defects, forming barriers with lower activation energies $U^{(1)}$, to become involved. However, we believe it more reasonable to assume (at least with respect to the LiF crystals studied) that the U barriers, rather than being destroyed, become lowered to the level $U^{(1)}$. This is argued for by curves *1* and *4* in Fig. 4 being nearly parallel, i.e., by the activation volumes, which correspond to the two defect species, considered approximately identical.

REFERENCES

1. V. I. Al'shits, E. V. Darinskaya, T. M. Perekalina, *et al.*, Fiz. Tverd. Tela (Leningrad) **29** (2), 467 (1987).
2. V. I. Al'shits, E. V. Darinskaya, and E. A. Petrzhik, Fiz. Tverd. Tela (Leningrad) **34** (1), 155 (1992).
3. V. I. Al'shits, E. V. Darinskaya, and O. L. Kazakova, Pis'ma Zh. Éksp. Teor. Fiz. **62** (4), 352 (1995).
4. V. I. Al'shits, E. V. Darinskaya, O. L. Kazakova, *et al.*, Pis'ma Zh. Éksp. Teor. Fiz. **63** (8), 628 (1996).
5. A. A. Urusovskaya, V. I. Al'shits, A. E. Smirnov, *et al.*, Pis'ma Zh. Éksp. Teor. Fiz. **66** (6), 470 (1997).
6. V. I. Al'shits, N. N. Bekkauer, A. E. Smirnov, *et al.*, Zh. Éksp. Teor. Fiz. **115** (3), 951 (1999).

Translated by G. Skrebtsov

Physics of the Solid State, Vol. 42, No. 2, 2000, pp. 280–284. Translated from Fizika Tverdogo Tela, Vol. 42, No. 2, 2000, pp. 273–277.

MAGNETISM AND FERROELECTRICITY

On the "Phase Transitions" between Quantum and Classical Behavior in Magnetic Mesoscopic Systems

V. V. Makhro

Bratsk Industrial Institute, Bratsk, 665709 Russia
e-mail: maxpo@mailexcite.com

Received in final form, May 20, 1999

Abstract—The results of theoretical and numerical investigation of thermally stimulated tunneling depinning in mesoscopic systems are presented using $Mn_{12}Ac$ and $CrNi_6$ as examples. It is shown that the boundary between the regions of tunneling and thermally activated depinning interpreted by some authors as a phase transition of the first order is not sharply defined. The effect of absolute spin delocalization in transverse fields weaker than the anisotropy field is studied for the first time. *© 2000 MAIK "Nauka/Interperiodica".*

At present, the role of quantum and classical approaches to the description of mesoscopic systems is widely debated. These systems for their definition should exhibit dualism of quantum and classical properties, because of which the assessment of the adequacy of one or another model to real physical phenomena is essentially difficult. The approach proposed in [1], which implies that the behavior of a mesoscopic system can be separated into two sharply distinguished regions of purely classical and purely quantum behavior, has received certain acceptance. The separation criterion can be any internal parameter of the applied theory or an external parameter, for example, temperature. If the transition between the quantum and classical behavior proceeds sharply, it is classified as a phase transition of the first order, otherwise, the phase transition is of the second order [2–6]. One of the aims of this work was to demonstrate that such a classification is not universally justified as applied to mesoscopic systems, and sufficiently adequate results can be obtained within the framework of only quantum approaches without classical methods.

Most prominent examples of mesoscopic systems in magnetism are provided by systems of two types, namely, boundaries (walls) of magnetic domains and high-spin magnetic clusters, such as $Mn_{12}Ac$, Fe_8, $CrNi_6$, etc. Physically, systems of the two types are very close to each other. In both cases, we deal with bistable systems whose vacuum states are separated with a potential barrier. For domain walls, the barrier is most often due to local defects in the crystal; in high-spin clusters, the major contribution to the potential barrier is made by internal anisotropy.

A transition between vacuum states can be either due to the action of an external field, or a result of thermal activation, or by tunneling. The first mechanism is quite evident, and we will not dwell on it in this paper. The last two mechanisms are of more interest. In the papers referred to above, tunneling and thermal activation are considered as competitive processes. By contrast, it seems to us that, as applied to depinning processes, these mechanisms are cooperative in some sense.

In fact, if a system is in thermal equilibrium with the environment at any nonzero temperature, the probability that it absorbs energy sufficient for overcoming the barrier and changes to the opposite state is nonzero. However, even if the energy absorbed is less than the height of the barrier, the system can penetrate the barrier by tunneling. Note that, along with tunneling, one should also take into account the possibility of overbarrier reflection; therefore, the absorption of external energy higher than that of the barrier does not assure its penetration. Thus, it is necessary to consider the above two mechanisms simultaneously, whereas their separation and contraposition to one another is not universally justified. This approach to tunneling and thermal activation was developed in [7, 8] for domain wall depinning. In this work, we apply the same approach to the analysis of the behavior of other high-spin systems.

1. MAGNETIC MESOSCOPIC MOLECULES: STRUCTURE AND MODELS

In studying physical phenomena stochastic by their nature, it would be desirable to have objects for which the reproducibility of the results is as best as possible. Unfortunately, magnetic domain walls do not belong to these objects for the known reasons. The boundary structure of magnetic domains essentially depends on a particular sample and changes from measurement to measurement. Therefore, the interest that high-spin molecules have attracted recently is quite clear. High-spin molecules possess totally identical magnetic properties and can serve as models of mesoscopic systems. Among these systems, the $Mn_{12}Ac([Mn_{12}O_{12}(CH_3COO)_{16}(H_2O_4)] \times$

1063-7834/00/4202-0280$20.00 © 2000 MAIK "Nauka/Interperiodica"

$2CH_3COOH_4H_2O$) crystal was the best studied. This alloy was synthesized by Lis [9], but the study of its magnetic properties was begun later by Sessoli *et al.* [10]. The works on $Mn_{12}Ac$ were surveyed in detail in [3]. In the $Mn_{12}Ac$ molecule, twelve Mn ions exhibit strong ferromagnetic coupling via superexchange by oxygen bridges. These molecules effectively behave as magnetic clusters with the spin $S = 10$ [10], and very weak interact in crystals, which is supported experimentally by an extremely low Curie point of 0.05 K [11]. At the same time, $Mn_{12}Ac$ is characterized by a very strong uniaxial anisotropy $D \approx 0.75$ K [12, 13]. This anisotropy is responsible for a high potential barrier $U_0 = DS^2 \approx 75$ K between the states $\pm(S)$.

The properties of the $CrNi_6$ molecules with the half-integer spin $S = 15/2$ are quite similar to those of $Mn_{12}Ac$. The Cr(III) ion in the former molecule ($S_{Cr} = 3/2$) is ferromagnetically bound to six Ni(II) ions ($S_{Ni} = 1$) [14]. The height of the potential barrier for this system $U_0 \approx 76$ K is also close to that for the $Mn_{12}Ac$ system. The $Mn_{12}Ac$ and $CrNi_6$ systems are sufficiently adequately described by the Hamiltonian [3]

$$\hat{H} = -DS_z^2 - H_zS_z - H_xS_x. \quad (1)$$

For the sake of simplicity, in equation (1), we use the designation $\mathbf{H} = g\mu_B\mathbf{H}$, where $g = 1.9$. As was mentioned above, in this papers, we do not consider transitions initiated by a longitudinal external field; therefore, without loss of generality, we can replace the Hamiltonian (1) by the Hamiltonian

$$\hat{H} = -DS_z^2 - H_xS_x. \quad (2)$$

Hamiltonian (2) can, in turn, be reduced to the Hamiltonian of a particle in a double-well potential $U(x)$ [15]

$$\hat{H} = -\frac{\nabla^2}{2m} + U(x),$$

where

$$U(x) = \left(S + \frac{1}{2}\right)^2 D(h^2\sinh^2 x - 2h\cosh x) \quad (3)$$

and

$$m = \frac{1}{2D}, \quad h = H_x/((2S+1)D).$$

In what follows, we will consider a one-dimensional problem for a particle of the mass m in a double-well potential (3).

2. TUNNELING AND THERMAL ACTIVATION IN A DOUBLE-WELL POTENTIAL: COMPETITION OR COOPERATION?

The problem of a particle in a double-well potential has long been studied in detail and become a touchstone for the majority of newly developed quantum-mechanical methods [16]. In the conventional formulation of this problem, tunneling between the two lowest "vacuum" states of the system is calculated and the corresponding level splitting is estimated. However, in the case under discussion, we generally deal with tunneling (and equally with over-barrier reflection) of a particle with an arbitrary energy that is not necessarily equal to the energy of the vacuum state. An attempt to solve this problem was made by Chudnovskiĭ in 1992 [1]. He proposed to use a modernized instanton technique for calculating tunneling probability under semiclassical potentials [1]. A characteristic feature of the proposed modernization is the consideration of periodic (with the period $\tau_p = \hbar/k_BT$) instantons (thermones according to the nomenclature [1]); these instantons correspond to particles with an arbitrary energy $E = k_BT$ lower than U_0. To within an exponential precision, the tunneling probability Γ in this case is given by the expression $\Gamma \sim \exp(-S_0/\hbar)$, where S_0 is the action for the classical tunneling solution in the Euclidean time. In view of the law of energy conservation, we can write

$$S_0 = E\oint d\tau = E\sqrt{2m}\int_{b(E)}^{a(E)}\frac{dx}{\sqrt{U-E}},$$

where $a(E)$ and $b(E)$ are classical turning points in the inverted potential $-U(x)$. The preexponential factor can be determined by a conventional method, namely, by calculating fluctuations around the classical instanton solution.

The result obtained in [1] was used to compare the tunneling and thermally activated depinning probabilities. The latter probability is given by the expression $\Gamma_T \sim \exp(-U_0/k_BT)$. Therefore, we can introduce thermodynamic action $S_T = \hbar U_0/k_BT$. By comparing the rates of variation of S_0 and S_T, we can make the conclusion about the predominance of one or another depinning mechanism and about the character of the transition (abrupt or smooth) between the two regions. Up to the present time, the criteria proposed in [1] are still in use in the analysis of thermally stimulated tunneling [2–6]. According to the widely accepted nomenclature, a smooth transition from thermal activation to tunneling is considered as a phase transition of the second order and an abrupt transition, as a phase transition of the first order.

However, it should be noted that this classification and the criteria proposed in [1] are controversial for the following reasons.

First, note that, at any nonzero temperature T, we in fact deal not with a single instanton with the energy $E = k_BT$, but with a ensemble of instantons. The distribution of instantons in the ensemble is determined by the potential range before the barrier. Because of this, comparison of S_0 and S_T at a given T is little informative. The following procedure seems more justified. First, the distribution of instantons is calculated at a

given T; next, the corresponding tunneling probability is calculated for each instanton and multiplied by the probability that this instanton appears in the ensemble. After integration over the whole ensemble, this procedure gives the integral depinning probability at the temperature T. In this procedure, tunneling and thermal activation should not be separated, and it is more convenient to speak about thermally stimulated tunneling.

However, this procedure cannot be implemented within the framework of the instanton approach, because it implies calculations of the probability of the over-barrier reflection for particles in the ensemble with $E > U_0$, which cannot be performed in the instanton technique.

Note also that criteria [1] cannot be applied to mesoscopic systems like $Mn_{12}Ac$ and $CrNi_6$ for another reason: these criteria were derived under the assumption that, in the potential well before the barrier, the spectrum of a particle is quasi-continuous. It will be shown below that this is not the case for high-spin molecules.

Thus, it is necessary to construct an adequate computational procedure for calculating the depinning probability for a mesoscopic system that takes account of both tunneling and thermal activation. Below, we consider a possible variant of this procedure.

3. THERMALLY STIMULATED TUNNELING

Let us turn back to the consideration of a particle of the mass m in a double-well potential (3). We use the following designations $U_{max} = -2S^2Dh$, $U_{min} = -S^2D(1 + h^2)$, and $U_0 = U_{max} - U_{min}$. Depending on the ratio between the well depth U_0 and the particle energy E, the particle can either fall on one of the stationary levels E_n in the well and then can tunnel through the barrier or oscillate within the potential well $U(x)$ at a frequency of

$$\omega_{ext} = \frac{\pi}{\sqrt{m/2}\int\limits_{x_1(E)}^{x_2(E)} dx/\sqrt{E - U(x)}},$$

where x_1 and x_2 are the turning points, if the particle is free and $E > U(x)$. Within the framework of the initial problem, this corresponds to magnetization oscillations between the states $+S$ and $-S$. Strictly specking, the particle with $E > U_{max}$ will have both continuous and discrete spectra. However, as follows from the estimates, the difference between the energy levels in this case is an order of magnitude smaller than the corresponding differences in the spectrum of a localized particle. Therefore, in what follows, we suppose that the spectrum at $E > U_{max}$ is quasi-continuous. It is important that, as the height of the barrier will lower with an increase in the external field, it can appear that the particle will have no stationary states in the corresponding shallow wells. Physically, this means that the particle cannot be localized in such a well. Consequently, depinning become impossible not in the field $h = 1$, but somewhat earlier. With a certain proviso given below, the field in which stationary states for $Mn_{12}Ac$ will disappear is estimated as $h_{cr} \approx 0.89$.

To estimate the depinning probability at a given temperature T, we will used the following computational procedure. Let us consider an ensemble of N identical particles, each of which occurs in the potential well (3). Suppose that the particles of the ensemble are in thermal equilibrium with the environment and obey the Maxwell distribution. The number of particles with the energy $E > U_{max}$ is given by the expression

$$N_{ext} = N\int\limits_{U_0}^{\infty} \frac{2}{\sqrt{\pi}}(k_BT)^{-1.5}\sqrt{E}\exp\left(-\frac{E}{k_BT}\right)dE.$$

Correspondingly, we designate the number of particles in the well as $N_{int} = N - N_{ext}$. In real calculations, we used a certain finite value U_{lim}; these values were chosen so as to obtain a negligible number of particles outside the integration limits and to assure the stability of the computational procedure itself.

Let is divide the energy range from U_0 to U_{lim} into K subintervals of the width δE: $(E_k - \delta E/2, E_k + \delta E/2)$. In each subinterval, we assign all particles the same energy E_k and calculate the probability that a particle penetrates the barrier F_k. Then, $N^*_{ext} = \sum_k N_k F_k$ is the total number of particles among N_{ext} that penetrated the barrier ($N_k = N_{ext}/K$).

If the particles N_{int} are in thermodynamic equilibrium with the environment, their distribution among the levels is described by the Boltzmann law, and the populations of the corresponding levels are given by the expression

$$n_i = N_{int}\frac{\exp(-E_i/k_BT)}{Z},$$

where Z the statistical sum $Z = \sum_i \exp(-E_i/k_BT)$. For each level E_i, we can estimate the corresponding tunneling probability G_i and find the total number of particles penetrated the barrier by tunneling with the use of the equation

$$N^*_{int} = \sum_i n_iG_i.$$

Let us dwell on the calculations is certain detail, in particular, consider the use of approximate methods in the proposed procedure. To assess the probability of passing over the barrier, we used the standard parabolic approximation of the initial potential in the vicinity of

Some characteristics of depinning processes in $Mn_{12}Ac$ at $T = 1$ K for various transverse field parameters h ($N = 100$)

h	0.1	0.3	0.5	0.6	0.7	0.891
Number of levels	7	5	3	2	1	0
Population of the lowest level	100	100	99.993	99.85	99.61	–
Population of the highest level	0	1.615×10^{-11}	1.871×10^{-4}	0.147	99.61	–
Tunneling probability for the lowest level	0	0	1.334×10^{-5}	3.426×10^{-3}	0.334	–
Tunneling probability for the highest level	0.261	0.318	0.325	0.329	0.334	–
Probability of thermal activation	2.23×10^{-20}	3.15×10^{-11}	3.65×10^{-5}	2.80×10^{-3}	0.39	–

its maximum. The WKB solution for a parabola is known to be [17]

$$F_k = \frac{1}{1 + \exp(-2\pi E_k/\sqrt{2D})}.$$

For low-lying levels, we used the quasi-classical solution

$$G = \frac{1}{\pi}\exp\left\{-\frac{1}{2D}\int_{-x_i}^{x_i}\left(\left(S+\frac{1}{2}\right)^2 + D(h^2\sinh^2 x - 2h\cosh x) - E_i\right)dx\right\}.$$

The parameter K was chosen so as to provide the general stability of the computational procedure. Next, the structure of the energy spectrum in the well was determined by approximating the initial potential (3) with the Morse potential $W(X) = A(e^{-2ax} - 2e^{-ax})$. Its spectrum is given by the formula [18]

$$E_i = -A(1 - a\sqrt{D/A}(i + 1/2)). \quad (4)$$

Here, A and a are fitting parameters: $A \approx 1.1U_0$ and a varies from 1.3 for $h = 0.1$ to 2.4 for $h = 0.8$. It is evident that, in the case when the initial potential (3) includes a symmetrical well, the spectrum (4) will be distorted. This will manifests itself as a level broadening in proportion to tunneling probability. However, in the temperature range studied (below 20 K), the population of the levels is low; therefore, the initial estimates obtained in this approximation are quite reasonable. The limiting value of the transverse field, at which the discrete spectrum can occur in the potential well, can be found from the condition $A = D/4$ and is $h_{cr} = 0.89$.

Finally, we will determine the efficient penetrability of a potential barrier as the ratio of the total number of particles penetrated the barrier to the initial number of particles

$$P = \frac{N^*_{int} + N^*_{ext}}{N}.$$

The results of calculations of tunneling probabilities for $Mn_{12}Ac$ and $CrNi_6$ by the proposed procedure are listed in the table and presented in the figure. In both cases, the results of calculations are in good agreement with the experimental data. A comparison of the results of calculations with recent experimental data [19] is of special interest. In [19], depinning in $CrNi_6$ were first studied within a wide temperature range by using the μSR technique, and the tunneling component was estimated separately. Essential evidence for the tunneling character of depinning is it weakly depends on temperature at low T. When interpreting the results, the authors of [19] considered tunneling and thermal activation as independent processes and calculated the resulting depinning probability as the sum of individual tunneling and thermally activated depinning probabilities [19]

$$Q(T) = A_0 + C\exp(-U_0/k_BT),$$

where $A_0 = 0.0085$ s^{-1} is the tunneling depinning probability at $T \longrightarrow 0$ K and $C = 12 \times 10^{-6}$ s^{-1} is the fitting parameter. Note that, in [19], only tunneling from the ground state was taken into account, and tunneling

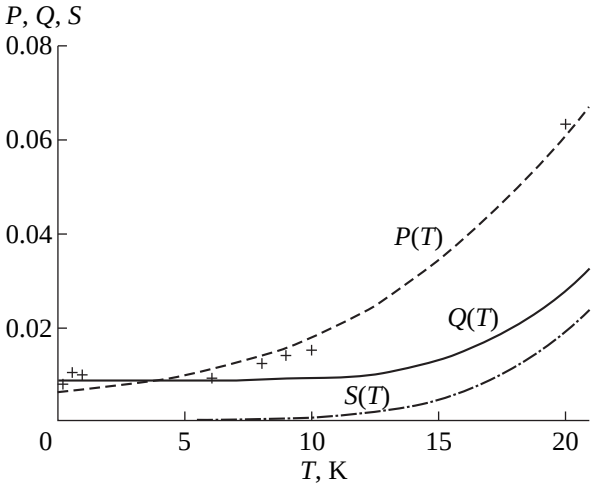

Temperature dependence of the integral depinning probability $P(T)$ calculated by the proposed procedure, the integral depinning probability $Q(T)$ calculated by the procedure [19], and the thermally activated depinning probability $S(T)$. Experimental data [19] are given by crosses.

from excited states was not considered at all. Probably, because of this, the integral depinning probabilities were underestimated in comparison with the experimental data and with the results of calculations by the proposed procedure. For illustration, see curve $P(T)$ in the figure. This curve matches the experimental points satisfactorily. The shape of the experimental curve from [19] strongly suggests that there are no abrupt transitions between the tunneling and thermally activated depinning mechanisms.

Thus, in this work, we presented the procedure for calculating the depinning probability in high-spin clusters. This procedure successively takes account of both physical mechanisms leading to the depinning, namely, tunneling and thermal activation. A characteristic feature of the proposed procedure is that, instead of independent consideration of these mechanisms in different temperature ranges, they are considered simultaneously in the entire temperature range studied (thermally stimulated tunneling). In this case, it is not necessary to separate depinning processes into tunneling and thermally activated ones. Therefore, the concept of phase transitions between these regions does not work. It was also found that, in the fields weaker than the anisotropy field, the effect of spin delocalization is observed. The results obtained are in good agreement with the experimental data reported by other authors.

ACKNOWLEDGMENTS

I am grateful to A.K. Zvezdin for helpful discussions and D.A. Garanin for fruitful discussions, which provided additional insight into the possibility of phase transitions in mesoscopic systems. I am also thankful to A. Keren for providing numerical data on μSR experiments with $CrNi_6$.

REFERENCES

1. E. M. Chudnovsky, Phys. Rev. A **46,** 8011 (1992).
2. E. M. Chudnovsky and D. A. Garanin, Phys. Rev. Lett. **79,** 4469 (1997).
3. D. A. Garanin and E. M. Chudnovsky, Phys. Rev. B: Condens. Matter **56,** 11102 (1997).
4. J.-Q. Liang, H. J. M. Muller-Kirsten, D. K. Park, *et al.*, Phys. Rev. Lett. **81,** 216 (1998).
5. C. S. Park, S.-K. Yoo, D. K. Park, *et al.*, LANL e-print, cond-mat/9807344 (1998).
6. J.-Q. Liang, H. J. M. Muller-Kirsten, D. K. Park, *et al.*, LANL e-print, cond-mat/9805209 (1998).
7. V. V. Makhro, J. Phys. D: Condens. Matter **10,** 6911 (1998).
8. V. V. Makhro, Fiz. Tverd. Tela (S.-Peterburg) **40** (10), 1855 (1998).
9. T. Lis, Acta Crystallogr., Sect. B: Struct. Crystallogr. Cryst. Chem. **36,** 2042 (1980).
10. R. Sessoli, D. Gatteschi, A. Caneschi, *et al.*, Nature (London) **365,** 141 (1993).
11. M. A. Novak and R. Sessoli, in *Quantum Tunneling of Magnetization*, Ed. by L. Gunther and B. Barbara (Kluwer, Dordrecht, 1995).
12. A. Caneschi, D. Gatteschi, R. Sessoli, *et al.*, J. Am. Chem. Soc. **117,** 301 (1991).
13. R. Sessoli, Mol. Cryst. Liq. Cryst. **274,** 801 (1995).
14. T. Mallah, C. Auberger, M. Verdagner, *et al.*, J. Chem. Soc. Chem. Commun. **61** (1995).
15. O. B. Zaslavskiĭ, Phys. Lett. A **145,** 471 (1990).
16. T. Schaefer and E. V. Shuryak, Rev. Mod. Phys. **70,** 323 (1998).
17. E. C. Kemble, Phys. Rev. **48,** 549 (1935).
18. L. D. Landau and E. M. Lifshitz, *Quantum Mechanics: Nonrelativistic Theory* (Nauka, Moscow, 1975).
19. A. Keren, P. Mendels, A. Kratzer, *et al.*, LANL e-print, cond-mat/9806230 (1998).

Translated by E. Rykova

Physics of the Solid State, Vol. 42, No. 2, 2000, pp. 285–291. Translated from Fizika Tverdogo Tela, Vol. 42, No. 2, 2000, pp. 278–283.

MAGNETISM AND FERROELECTRICITY

Anomalies in Thermal Expansion of $DyVO_4$ Induced by Quadrupolar Ordering

Z. A. Kazeĭ*, N. P. Kolmakova, I. B. Krynetskiĭ*, A. A. Sidorenko**, and L. V. Takunov****

** Moscow State University, Vorob'evy gory, Moscow, 119899 Russia*
*** Bryansk State Technical University, Bryansk, 241035 Russia*
e-mail: kazei@plms.phys.msu.su

Received May 26, 1999

Abstract—The thermal expansion of the $DyVO_4$ crystal has been experimentally and theoretically investigated in the range of the Jahn–Teller structural phase transition. The manifestation of totally symmetric magnetoelastic interactions upon this transition has been studied for the first time. It is found that the temperature dependences of the unit-cell and thermal expansion parameters along the nonactive Jahn–Teller direction in the basal plane for the $DyVO_4$ crystal exhibit characteristic magnetoelastic anomalies at $T < T_c$ due to the ordering of quadrupole moments of Dy^{3+} ions. The magnetoelastic contributions of the totally symmetric $\varepsilon^{\alpha 1}$ and $\varepsilon^{\alpha 2}$ and symmetry-lowering ε^{γ} modes to the thermal expansion are calculated within the general crystal-field formalism. The total quadrupolar coefficient G^{γ} and magnetoelastic coefficient B^{γ} are determined from the spectroscopic and spontaneous deformation data. It is demonstrated that the thermal expansion of the $DyVO_4$ crystal in the tetragonal and orthorhombic phases is well described in the framework of the unified model using a common set of interaction parameters for both phases. © *2000 MAIK "Nauka/Interperiodica".*

1. It is well known that rare-earth oxide compounds RXO_4 (X = V, P, or As; R is the rare-earth ion) with a tetragonal zircon structure are characterized by considerable single-ion magnetoelastic and quadrupolar pair interactions. The interaction parameters for totally symmetric and symmetry-lowering modes were determined in detailed investigations of the thermal expansion and magnetostriction in the tetragonal phase with allowance made for all the features of crystal field [1, 2]. These interactions are responsible for appreciable magnetoelastic effects and, in a number of cases ($TbVO_4$, $DyVO_4$, and $TmVO_4$), bring about the spontaneous ordering of quadrupole moments of rare-earth ions [3], which is accompanied by the orthorhombic strain of a crystal lattice. In essence, such a quadrupolar ordering consists in the Jahn–Teller structural phase transitions in rare-earth zircons.

The low-symmetry phases in rare-earth zircons are usually treated on the basis of a model pseudospin Hamiltonian. This approach is applicable for describing only the dominant magnetoelastic effects arising upon ordering of quadrupole moments of rare-earth ions, but fails to carry out consistent comparative analysis of the low-symmetry and tetragonal phases. However, comparison of magnetoelastic interactions of different symmetry for the zircon structure demonstrates that totally symmetric interactions are not negligibly small [4] and also should lead to the magnetoelastic effects observed upon quadrupolar ordering. In particular, according to our investigations of $TbVO_4$ [5], the ordering of quadruple moments of rare-earth ions is accompanied not only by an orthorhombic distortion of the crystal structure, but also by a change in the volume and a change in the degree of lattice tetragonality. It is of special interest to examine similar magnetoelastic effects arising upon quadrupolar ordering in $DyVO_4$ and to compare these effects for two crystals with different types of lattice distortion.

2. The contribution of rare-earth ions to the thermal expansion in the tetragonal and orthorhombic phases in the presence of magnetic field can be calculated with the use of the Hamiltonian $H = H_{CF} + H_{ME} + H_Q + H_Z$, where H_{CF} is the crystal-field Hamiltonian, H_{ME} and H_Q describe the magnetoelastic and quadrupolar pair interactions in terms of the equivalent Stevens operators O_n^m, and H_Z represents the Zeeman coupling to the external magnetic field, that is,

$$H_{CF} = \alpha_J B_2^0 O_2^0 + \beta_J (B_4^0 O_4^0 + B_4^4 O_4^4) + \gamma_J (B_6^0 O_6^0 + B_6^4 O_6^4), \quad (1)$$

$$H_{ME} = -\alpha_J [(B^{\alpha 1}\varepsilon^{\alpha 1} + B^{\alpha 2}\varepsilon^{\alpha 2}) O_2^0 + B^{\gamma}\varepsilon^{\gamma} O_2^2 + B^{\delta}\varepsilon^{\delta} P_{xy}], \quad (2)$$

$$H_Q = -\alpha_J^2 (K^{\alpha}\langle O_2^0\rangle O_2^0 + K^{\gamma}\langle O_2^2\rangle O_2^2 + K^{\delta}\langle P_{xy}\rangle P_{xy}), \quad (3)$$

$$H_Z = g_J \mu_B J H, \quad \left(P_{xy} = \frac{1}{2}(J_x J_y + J_y J_x)\right). \quad (4)$$

In these relationships, α_J, β_J, and γ_J are the Stevens parameters; B_n^m are the crystal-field parameters (their

number for the tetragonal symmetry is equal to five); B^μ are the magnetoelastic coefficients; K^μ are the quadrupolar pair interaction constants; g_J is the Lande factor; J is the angular momentum operator for the rare-earth ion; and μ_B is the Bohr magneton. In the H_{ME} and H_Q Hamiltonians, only the actual invariants for the magnetoelastic effects under consideration are written in an explicit form. The ε-symmetry invariants are omitted, because in the absence of external stresses of the corresponding symmetry for $DyVO_4$, they make no contribution.

The minimization of the free energy with the respect to the strains gives the equilibrium strains expressed in terms of observable quantities of the corresponding quadrupolar operators. The substitution of these equilibrium strains for the ε^μ strains in the magnetoelastic Hamiltonian makes H_{ME} similar to the H_Q Hamiltonian, and both terms can be reduced to the generalized quadrupolar Hamiltonian

$$\begin{aligned} H_{QT} &= H_Q + H_{ME} \\ &= -\alpha_J^2(G^\alpha\langle O_2^0\rangle O_2^2 + G^\gamma\langle O_2^2\rangle O_2^2 + G^\delta\langle P_{xy}\rangle P_{xy}). \end{aligned} \quad (5)$$

The total quadrupolar coefficients G^μ involves the contributions of the single-ion magnetoelastic interaction B^μ and the quadrupolar pair interaction K^μ

$$G^\mu = G^\mu_{ME} + K^\mu = \frac{(B^\mu)^2}{C_0^\mu} + K^\mu \quad (\mu = \gamma, \delta), \quad (6)$$

where C_0^μ is the lattice background elastic constant in the absence of interactions. Note that, for rare-earth zircons, the single-ion magnetoelastic contribution G^μ_{ME}, as a rule, is dominant, and, in the absence of interaction through optic phonons, the relationship $K^\mu/G^\mu_{ME} = -1/3$ is valid for each mode [6].

In the H_{QT} Hamiltonian, the term $\alpha_J^2 G^\gamma\langle O_2^2\rangle O_2^2$ corresponding to the strain of the $\gamma = (B_{1g})$ symmetry is nonzero only either in the presence of external factors, for example, the magnetic field along the [100] axis, or in a low-symmetry phase. In the latter case, there is the spontaneous phase transition followed by the ordering of the quadrupole moments of rare-earth ions $Q_2 = \alpha_J\langle O_2^2\rangle = \alpha_J(1/Z)\sum_i \langle i|O_2^2|i\rangle \exp(-E_i/k_BT)$, where E_i are the energy levels of a rare-earth ion that are calculated using the Hamiltonian $H = H_{CF} + H_{QT}$, and Z is the statistical sum. This implies that, at $T < T_c$, the thermal average of $Q_2(T)$, which is computed in a self-consistent manner, is nonzero in the absence of external magnetic field. The necessary condition of existing this quadrupolar ordering is a sufficiently large value of the total quadrupolar coefficient G^γ and also the appropriate electronic structure of a rare-earth ion with low-lying "quadrupolar" levels. It is these conditions for the Q_2 quadrupole moment that are realized in $DyVO_4$. The ordering of the Q_2 quadrupole moments is attended by the orthorhombic lattice distortion of the B_{1g} type, which is defined as

$$\varepsilon^\gamma = \alpha_J B^\gamma\langle O_2^2\rangle/C_0^\gamma = A^\gamma Q_2 \quad (A^\gamma = B^\gamma/C_0^\gamma).$$

The contribution of rare-earth ions to the thermal expansion can be determined in the conventional way, i.e., by minimizing the free energy, involving magnetoelastic and elastic terms with respect to the strain tensor components. The calculations similar to those conducted in [1] demonstrate that, in the absence of external magnetic field, the contribution to the thermal expansion in the distorted phase along the tetragonal axis is associated only with the totally symmetric modes, namely, the isotropic $\varepsilon^{\alpha 1}$ and tetragonal $\varepsilon^{\alpha 2}$ modes. Moreover, along the [100], [010], and [110] axes, there is the contribution of the spontaneous orthorhombic strain ε^γ, which, for the nonactive Jahn–Teller direction $[110] \equiv a'$, is quadratic in the spontaneous strain, that is,

$$\begin{aligned} \frac{\Delta c_{ME}}{c} &= A_1\Delta Q_0, \quad \frac{\Delta a'_{ME}}{a} = A_2\Delta Q_0 - \frac{3}{4}(A^\gamma Q_2)^2, \\ \frac{\Delta a_{ME}}{a} &= A_2\Delta Q_0 + -\frac{A^\gamma Q_2}{\sqrt{2}}, \\ \frac{\Delta b_{ME}}{b} &= A_2\Delta Q_0 + \frac{A^\gamma Q_2}{\sqrt{2}}, \end{aligned} \quad (7)$$

where $Q_0(T) = \alpha_J\langle O_2^0\rangle = \alpha_J(1/Z)\sum_i \langle i|O_2^2|i\rangle\exp(-E_i/k_BT)$. The expressions for the A_1 and A_2 coefficients that depend on the magnetoelastic and elastic coefficients take the same form as for the tetragonal phase [1].

3. The experiments were performed with single-crystal samples. The crystals were grown from the melt in platinum crucibles by the well-known method of spontaneous crystallization from solution. The magnetoelastic anomalies in the thermal expansion of the $DyVO_4$ crystal upon structural phase transition were investigated using wire strain and capacity-type strain gauges. The relative accuracy of measurements was no worse than 10^{-6}. The measurements were carried out in the presence and absence of magnetic field, which made it possible to control the changes in the domain structure of the sample below the T_c temperature.

4. The lattice distortion and magnetoelastic anomalies of the parameters upon quadrupolar ordering in $DyVO_4$ are considerably less than those in $TbVO_4$, which requires the use of more sensitive techniques. In order to investigate the orthorhombic strain of the B_{1g} symmetry $\varepsilon^\gamma = (b - a)/\sqrt{2a_0}$ (Fig. 1), the thermal expansion $\Delta l/l$ of the $DyVO_4$ crystal along the [100] axis was measured with a capacity-type strain gauge in

the magnetic field H = 20 kOe, which was parallel and perpendicular to the direction of measuring Δl. In this field, the crystal becomes single-domain with the easy magnetization axis aligned along the magnetic field. Therefore, the thermal expansion was measured along the orthorhombic a axis for $\mathbf{H} \parallel [100] \parallel \Delta\mathbf{l}$ and along the b axis for $\mathbf{H} \parallel [010] \perp \Delta\mathbf{l}$ (in the latter case, according to the standard setting for an orthorhombic structure, $a < b$). As can be seen from Fig. 1, the lattice in the absence of magnetic field undergoes a distortion at the temperature $T_c \sim 14$ K (see the inset in Fig. 1), and the orthorhombic strain ε^γ at $T = 0$ K is equal to 36.8×10^{-4}, which is in good agreement with the available data [7].

The anomaly in the thermal expansion of the $DyVO_4$ crystal along the [100] axis at $H = 0$ is equal to 7×10^{-4}, which is substantially less than the spontaneous lattice strain. This means that, in the absence of external magnetic field, the sample at temperatures below T_c is in a polydomain state and exhibits only a slight preferred orientation of the b axes of domains along the direction of measuring Δl. Note also the presence of an appreciable "tail" $\Delta l(T)/l$ at $T > T_c$. This suggests that there exists a distortion of the B_{1g} symmetry above T_c, likely, due to mechanical stresses. Earlier [8], similar effects were observed and discussed for the $TmVO_4$ crystal. The measurements of the thermal expansion in the magnetic field make it possible to stabilize the domain structure and to examine the temperature dependences of the spontaneous strain for a single-domain sample. However, the magnetic field leads to an increases in the transition temperature and a substantial extension of the transition range in the vicinity of T_c. This is consistent with both the results obtained by numerical calculations of the temperature dependence of the lattice distortion for the $DyVO_4$ crystal in magnetic field within the pseudospin formalism [9] and with our computations in the framework of the more general crystal-field formalism (cf. curves *1* and *2* in Fig. 1).

The anomalies observed in the unit-cell parameters $\Delta c/c$ and $\Delta a'/a'$ due to the $\varepsilon^{\alpha 1}$ and $\varepsilon^{\alpha 2}$ totally symmetric magnetoelastic modes upon quadrupolar ordering in the $DyVO_4$ crystal are substantially less than the ε^γ spontaneous orthorhombic strain and, hence, call for special conditions of observation against the background of effects associated with the reorientation of the Jahn–Teller domains. The thermal expansion $\Delta c(T)/c$ along the tetragonal axis of the $DyVO_4$ crystal was measured with strain gauges cemented in the (a–c) and (a'–c) crystal planes. Both dependences show a similar anomalous behavior, which manifests itself in an increase in the $\Delta c/c$ parameter with a decrease in the temperature from 30 K down to T_c = 14 K (Fig. 2, curve *1*) in accord with the theoretical calculations. An increase in $\Delta c/c$ is retarded in the vicinity of T_c, and, below the critical temperature, the parameter $\Delta c/c$ for two measurement conditions exhibits different behavior, which, in turn, disagree with the theoretical predictions. Evidently, such a disagreement is caused by the rearrangement of the domain structure in the crystal below the T_c temperature.

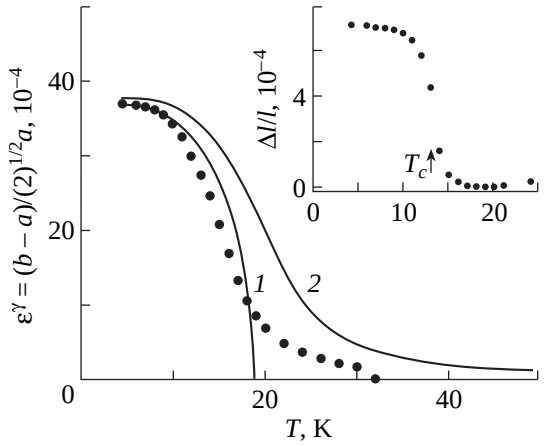

Fig. 1. Experimental (points, H = 20 kOe) and calculated [curves (*1*) H = 0 and (*2*) H = 20 kOe] temperature dependences of the orthorhombic distortion of the γ symmetry for the $DyVO_4$ crystal. The inset shows the temperature dependence of $\Delta l/l$ along the [010] direction in the absence of magnetic field for the polydomain sample.

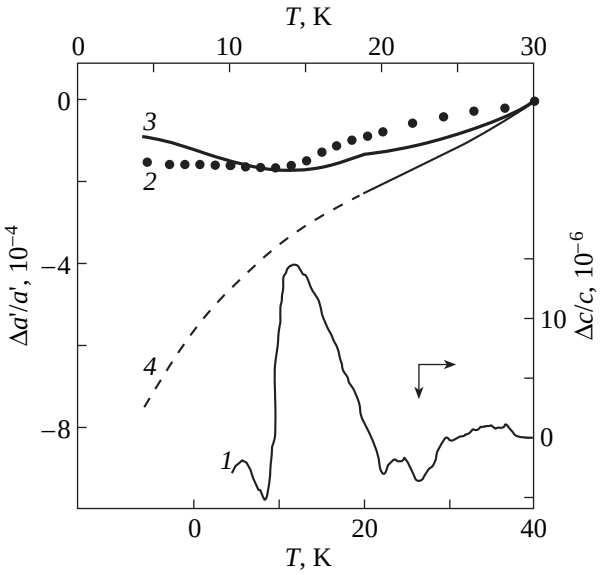

Fig. 2. Experimental temperature dependences of the relative change in the parameters (*1*) $\Delta c/c$ (H = 0) and (*2*) $\Delta a'/a'$ (H = 30 kOe, $\mathbf{H} \parallel [110]$) for the $DyVO_4$ crystal and theoretical curves of the relative change in the parameter $\Delta a'/a'$ at (*3*) H = 30 kOe ($\mathbf{H} \parallel [110]$) and (*4*) H = 0, calculated in the presence and absence of structural transition, respectively.

During the rearrangement of domain structure, the a and b orthorhombic axes in a domain exchange places with each other, which is accompanied by the tensile–compressive local strain of a gauge in the perpendicular direction $\varepsilon \sim (b-a)/a \sim 5 \times 10^{-3}$. Note that, since the length of perpendicular closing links in a wire strain

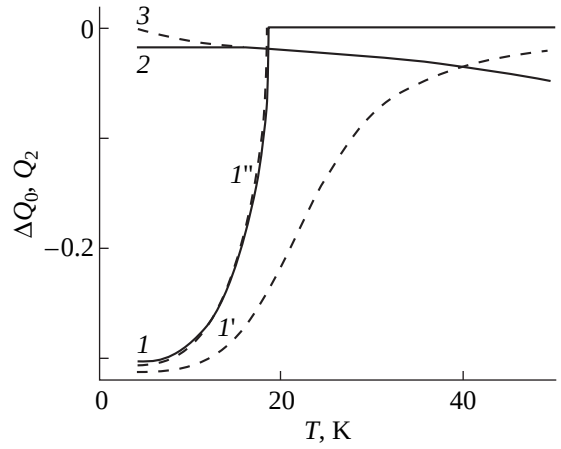

Fig. 3. Calculated temperature dependences of (*1, 1', 1"*) the quadrupole moment Q_2 and the dependences $\Delta Q_0(T) = Q_0(T) - Q_0(0)$ for (*2*) orthorhombic and (*3*) tetragonal phases of the $DyVO_4$ crystal. Magnetic field *H*, kOe: (*1*) 0, (*1'*) 30 (**H** ∥ [100]), and (*1"*) 30 (**H** ∥ [110]).

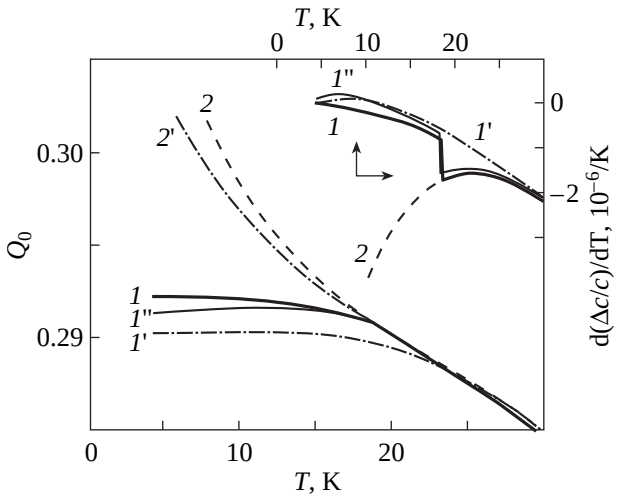

Fig. 4. Calculated temperature dependences of the quadrupole moment $Q_0(T, H)$ in the magnetic field (*1*, *2*) $H = 0$, (*1'*, *2'*) $H = 30$ kOe (**H** ∥ [100]), and (*1"*) $H = 30$ kOe (**H** ∥ [110]) for (*1, 1'*) orthorhombic and (*2, 2'*) tetragonal phases of the $DyVO_4$ crystal. The inset shows the calculated temperature dependences of thermal expansion coefficient $d(\Delta c/c)/dT$ along the tetragonal axis under the same conditions.

gauge is equal to ~ 5% of the length of "operating" links, the strain $\varepsilon \sim 5 \times 10^{-3}$ should result in an anomaly of an order of 25×10^{-5} in the $\Delta c(T)/c$ curve for the single-domain sample along the tetragonal axis. For the polydomain sample in the absence of external magnetic field, the contribution of domain processes is substantially (by about one order of magnitude) less and equal to $\sim 20 \times 10^{-6}$ (Fig. 2). When measuring even in a rather weak magnetic field of 10–20 kOe that stabilizes the domain structure, the jumps in the $\Delta c/c$ dependences disappear. However, the observed behavior of the thermal expansion along the *c* axis is inconsistent with the theoretical calculations. Therefore, the wire strain gauges do not ensure reliable measurements of the anomalies in the $\Delta c/c$ or $\Delta a'/a'$ parameters, which are induced $\varepsilon^{\alpha 1}$ and $\varepsilon^{\alpha 2}$ totally symmetric modes.

The measurements performed with a capacity-type strain gauge are *a priori* more reliable, because they in principle are not affected by the perpendicular strain component (Fig. 2). Actually, the dependence of the $\Delta a'/a'$ parameter along the [110] direction below T_c shows a characteristic anomaly in the form of a plateau (curve *2*), which is in qualitative agreement with the behavior predicted by the crystal-field calculations (curve *3*, see below). In the absence of structural transition at $H = 0$, the thermal expansion of the $DyVO_4$ crystal along the *a'* axis should change with the increasing derivative $d(\Delta a'/a')/dT$ down to 4 K (curve *4*). In order to stabilize the domain structure, the measurements were performed in the constant magnetic field $H = 30$ kOe, which was parallel to the measured strain. In the $DyVO_4$ crystal, the magnetic field **H** ∥ [110] does not give rise to a single-domain structure, but induces extended thin strip domains [10] whose boundaries are perpendicular to the magnetic field and run along planes of the (110) type.

5. The features of the thermal expansion in the $DyVO_4$ crystal upon quadrupolar ordering can be described by the Hamiltonian $H = H_{CF} + H_{QT} + H_Z$ with the use of a common set of interaction parameters for the tetragonal and orthorhombic phases. At present, the problem of the crystal field in $DyVO_4$ is far short of the final solution, since the required spectroscopic data on the Dy^{3+} ion in the tetragonal and orthorhombic phases of $DyVO_4$ are unavailable. The crystal-field parameters available in the literature, for example, in [11], do not describe the known spectroscopic data and, in particular, lead to the splitting of two low-lying Kramers doublets in the tetragonal phase by a magnitude of less than 1.5 cm^{-1} as compared to the experimental value of 9 cm^{-1} [12, 13].

From the available experimental data, we determined the crystal-field parameters ($B_2^0 = -114$ K, $B_4^0 = 50$, $B_4^4 = 973$, $B_6^0 = -59$, and $B_6^4 = 182$ K), which adequately describe the experimental data and agree closely with the sets of parameters for other rare-earth vanadates, for example, $HoVO_4$ [14] whose crystal field is regarded as reliably established. In further calculations, we used these crystal-field parameters, coefficients $A_1 = 0.31 \times 10^{-2}$ and $A_2 = -0.39 \times 10^{-2}$ calculated for the $DyVO_4$ crystal from the anomalies of the thermal expansion in the tetragonal phase [1], and the elastic modulus $C_0^\gamma = 1.24 \times 10^6$ K taken for $DyVO_4$ from [15]. As is customary, we consider the orthorhombic phase of $DyVO_4$ as a small distortion ($\varepsilon^\gamma \sim 10^{-3}$) of the tetragonal phase. Then, it is expedient to use the

same coefficients for the calculation of the magnetoelastic contribution to the thermal expansion in the orthorhombic phase. The orthorhombic parameter of the crystal field $B_2^2 = -\alpha_J G^\gamma \langle O_2^2 \rangle = 57.9$ K was chosen in such a way as to account for the experimental spectral changes in the phase with the quadrupolar ordering [12, 13]. It is known that, at $T > T_c$, two low-lying Kramers doublets of the Dy^{3+} ion in dysprosium vanadate are separated by 9 cm^{-1} (the other excited states are separated by a considerable gap), and, below T_c, the separation between the doublets increases up to 27 cm^{-1}.

With the above parameters, we calculated the temperature dependence of the order parameter of phase transition $Q_2 = \alpha_J \langle O_2^2 \rangle$ (Fig. 3) and determined the critical temperature $T_c = 18.7$ K. This value substantially exceeds the T_c temperature, which was experimentally obtained in the present work and has been known from the literature [16]. It is characteristic that the critical temperature is primarily determined by the gap between the doublets in the orthorhombic phase, and different sets of crystal-field parameters, including the set obtained within the pseudospin formalism, result in virtually the same T_c temperatures. The problem of the overestimated, theoretically calculated transition temperature for $DyVO_4$ is well known in the literature (see, for example, [17]) and concerns the applicability of the mean-field approximation to this crystal. The calculated dependence $Q_2(T)$ reflects the variation in the ε^γ orthorhombic distortion with temperature (Fig. 1, curve *1*). The experimental value of $\varepsilon^\gamma = 36.8 \times 10^{-4}$ at 0 K leads to the magnetoelastic coefficient $B^\gamma = 15 \times 10^3$ K.

The dependence $Q_2(T)$ provides a means of calculating the changes in the spectrum and wave functions of the Dy^{3+} ion below T_c and, then, the temperature dependences of the quadrupole moment $Q_0(T)$ in the orthorhombic (Fig. 3, curve *2*) and tetragonal (Fig. 3, curve *3*) phases. For the Q_0 quadrupole moment, which is nonzero even in the tetragonal phase, the ordering of the quadrupole moments Q_2 is attended by a jump in the dQ_0/dT derivative (Fig. 4), which, in turn, is responsible for the jump in the temperature dependence of the thermal expansion coefficient along the tetragonal axis $d(\Delta c/c)/dT$ or along the nonactive Jahn–Teller direction $d(\Delta a'/a')/dT$. The above-determined values of the B_2^2 parameter and the B^γ magnetoelastic coefficient allow us to calculate the total quadrupolar coefficient $\alpha_J^2 G^\gamma = 7.6$ mK and the magnetoelastic contribution $\alpha_J^2 G_{ME}^\gamma = 7.3$ mK to this coefficient. Therefore, for the $DyVO_4$ crystal, the contribution of the pair quadrupolar interaction K^γ is close to zero (positive, within the limits of experimental error), and the theoretical relationship $K^\gamma / G_{ME}^\gamma = -1/3$ is not valid, which can point to a sizable contribution of optic phonons.

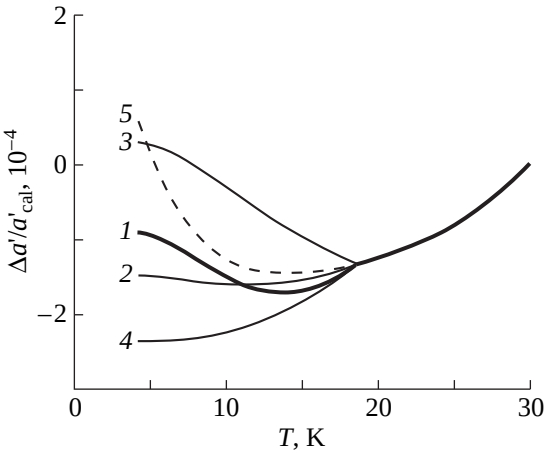

Fig. 5. Calculated contributions to the temperature dependence of (*1*) $\Delta a'/a'$ for the $DyVO_4$ crystal at **H** || [110] in the presence of structural transition: (*2*) totally symmetric $\varepsilon^{\alpha 1}$ and $\varepsilon^{\alpha 2}$, (*3*) orthorhombic ε^δ, and (*4*) orthorhombic ε^γ strain modes. (*5*) The sum of contributions from the totally symmetric $\varepsilon^{\alpha 1}$ and $\varepsilon^{\alpha 2}$ and orthorhombic ε^δ strain modes in the absence of structural transition.

Figures 3 and 4 also demonstrate the calculated dependences $Q_2(T, H)$ and $Q_0(T, H)$ at $H = 30$ kOe (**H** || [100], curves *1'* and *2'*; **H** || [110], curves *1"*), which illustrate how the magnetic field orientation affects the critical temperature, order parameter, and magnetoelastic anomalies of the thermal expansion. It is seen that the *H* field aligned along the direction of the spontaneous orthorhombic strain leads to a smearing of the anomalies in the dependences of the quadrupole moments $Q_2(T, H)$ and $Q_0(T, H)$ and a considerable increase in the transition temperature. The field **H** || [110] with the symmetry different from that of the order parameter produces a different, substantially weaker effect. As can be seen, the transition temperatures slightly decrease (by 0.2 K at a field of 30 kOe), but the anomalies in both dependences $Q_2(T, H)$ and $Q_0(T, H)$ remain pronounced. Specifically, the jump in the temperature dependence of the thermal expansion coefficient along the tetragonal axis $d(\Delta c/c)/dT$ in the field **H** || [110] remains as abrupt as before (see the inset in Fig. 4).

The dependences $Q_2(T, H)$, $Q_{xy}(T, H) = \alpha_J \langle P_{xy} \rangle (T, H)$, and $Q_0(T, H)$ furnish an opportunity to separate different contributions to the thermal expansion of the $DyVO_4$ crystal along the nonactive Jahn–Teller direction $\Delta a'/a'$ (Fig. 5). For the tetragonal phase in the magnetic field **H** || [110], there are only the contributions $(\Delta a'/a')_\alpha = A_2 \Delta Q_0$ and $(\Delta a'/a')_\delta = A^\delta Q_{xy}/\sqrt{2}$, which are brought about by the totally symmetric $\varepsilon^{\alpha 1}$ and $\varepsilon^{\alpha 2}$ and orthorhombic ε^δ modes, respectively. The sum of these contributions above T_c in the presence of structural transition is shown in Fig. 5 by curve *1* and by the dashed line below T_c in the absence of transition. The quadrupolar ordering leads to the change in these con-

tributions (curves *2*, *3*) and gives rise to the additional contribution $(\Delta a'/a')_\gamma = -3(\varepsilon^\gamma)^2/4$ from the ε^γ orthorhombic mode (curve *4*). Resultant curve *5* reasonably well describes the experimental data along the a' axis and, in particular, the characteristic anomaly in the form of a plateau below T_c. Thus, the quadrupolar ordering in $DyVO_4$ is characterized by an inflection point in the $\Delta a'/a'$ curve at the T_c temperature and the change in the sign of $d(\Delta a'/a')/dT$ at lower temperatures. The anomaly at T_c in the experimental dependence of $\Delta a'/a'$ (as in the dependence of $\Delta a/a$ at $H = 0$) is smeared by internal stresses in the crystal, but the change in the sign of the thermal expansion coefficient at a lower temperature is clearly observed (Fig. 2). It is worth noting that the calculated dependence of $\Delta a'/a'$ unexpectedly well quantitatively describes the experimental data, even though the thermal expansion was experimentally measured with respect to the reference sample without corrections for its thermal expansion because of the lack of these data at low temperatures.

It is of interest to compare the magnetoelastic anomalies in the thermal expansion of the $DyVO_4$ and $TbVO_4$ crystals upon quadrupolar ordering [5]. For the $DyVO_4$ crystal, the Q_2 or Q_{xy} spontaneous quadrupole moments responsible for the orthorhombic strain are two times larger and the ε^γ orthorhombic strain, on the contrary, is substantially (approximately five times) less than those for the $TbVO_4$ crystal. This is primarily due to the fact that the elastic constant C_0^γ is larger than the C_0^δ constant for the zircon structure. By contrast, the change in the Q_0 quadrupole moment in the orthorhombic phase with respect to the tetragonal phase (the difference between curves *2* and *3*) for the $DyVO_4$ crystal is two times less than that for the $TbVO_4$ crystal. However, as is seen from Fig. 2, the magnetoelastic anomalies in the thermal expansion upon quadrupolar ordering, which are induced by the totally symmetric interactions and described by the Q_0 quadrupole moment, remain pronounced in the $DyVO_4$ crystal.

6. In the present work, the anomalies observed in the thermal expansion of the $DyVO_4$ crystal due to the ordering of the Q_2 quadrupole moments of the Dy^{3+} ions were studied experimentally and theoretically. The experimental data for the tetragonal and orthorhombic phases are adequately described by the theoretical curves calculated with a common set of interaction parameters for both phases. The magnetoelastic coefficient $B^\gamma = 15.1 \times 10^3$ K for the $DyVO_4$ crystal is close to the values of B^γ for $DyPO_4$ (10.4×10^3 K) and $HoVO_4$ (9.9×10^3 K), which were determined in complex investigations of magnetoelastic effects in the tetragonal phase of these zircons [4, 18]. It was found that, for the $DyVO_4$ crystal, the total quadrupolar coefficient $\alpha_J^2 G^\gamma$ is equal 7.6 mK, and the magnetoelastic contribution $\alpha_J^2 G_{ME}^\gamma$ to this constant is 7.3 mK. Therefore, the contribution of the quadrupolar pair interaction K^γ is close to zero, and the theoretical relationship $K^\gamma/G_{ME}^\gamma = -1/3$ is not valid, which can indicate a significant role of optic phonons. It should be mentioned that, in the zircon family, $DyVO_4$ is the sole crystal characterized by the quadrupolar ordering of the γ symmetry, which explains increased interest in this crystal.

In summary, it should be emphasized that, in the present work, unlike the majority of works dealing with the investigation of distorted phases in rare-earth zircons, the calculations were performed within the framework of the general crystal-field model. In the earlier works, the contribution to the thermal expansion of rare-earth zircons with the cooperative Jahn–Teller effect included only the dominant Jahn–Teller mode, and the contribution of the totally symmetric modes was ignored. Moreover, it was assumed that the ordering of quadrupole moments is accompanied by only the orthorhombic distortion of a crystal in the basal plane and, hence, brings about neither volume nor tetragonal strains. The latter contribution was found to be substantially less than the former contribution due to the hierarchy of magnetoelastic and elastic coefficients in the zircon structure. Nonetheless, we established that the contribution of the totally symmetric modes gives rise to the observable magnetoelastic effects. The calculation of this contribution proportional to the change in the Q_0 quadrupole moment is outside the province of the pseudospin formalism and requires consideration of all the features of mixing in the crystal field. In particular, for the quadrupole moment $Q_0(T)$ that is nonzero even in the tetragonal phase, the ordering of the Q_2 quadrupole moments is attended by the manifestation of the feature in the derivative dQ_0/dT, which, in turn, is responsible for the jump-type anomalies in the temperature dependence of the thermal expansion coefficient along the tetragonal axis or along the nonactive Jahn–Teller direction a' in the basal plane.

ACKNOWLEDGMENTS

This work was supported in part by the Ministry of Education of Russian Federation, project nos. 97-0-7.3-115 and 97-0-7.3-157.

REFERENCES

1. Z. A. Kazeĭ and N. P. Kolmakova, Zh. Éksp. Teor. Fiz. **109** (5), 1687 (1996).
2. P. Morin, J. Rouchy, and Z. Kazei, Phys. Rev. B: Condens. Matter **51** (21), 15103 (1995).
3. G. A. Gehring and K. A. Gehring, Rep. Prog. Phys. **38,** 1 (1975).
4. P. Morin, J. Rouchy, and Z. Kazei, Phys. Rev. B: Condens. Matter **50** (17), 12625 (1994).

5. Z. A. Kazeĭ, N. P. Kolmakova, A. A. Sidorenko, *et al.*, Fiz. Tverd. Tela (S.-Peterburg) **40** (9), 1663 (1998).
6. R. T. Harley, W. Hayes, and S. R. P. Smith, J. Phys. C: Solid State Phys. **5** (12), 1501 (1972).
7. H. Gobel and G. Will, Phys. Status Solidi B **9** (1), 932 (1972).
8. Z. A. Kazeĭ, Fiz. Tverd. Tela (S.-Peterburg) **40** (4), 701 (1998).
9. E. Pytte, Phys. Rev. **9** (3), 932 (1974).
10. A. Kasten and P. J. Becker, Int. J. Magn. **5** (1–3), 157 (1973).
11. M.-D. Guo, A. T. Aldred, and S.-K. Chan, J. Phys. Chem. Solids **48** (3), 229 (1987).
12. R. T. Harley, W. Hayes, and S. R. Smith, Solid State Commun. **9** (9), 515 (1971).
13. C. J. Ellis, K. A. Gehring, M. J. M. Leask, *et al.*, J. Phys. (Paris) **32,** C1-1204 (1971).
14. B. Bleaney, J. F. Gregg, P. Hansen, *et al.*, Proc. R. Soc. London, Ser. A **416** (1850), 63 (1988).
15. R. L. Melcher and B. A. Scott, Phys. Rev. Lett. **28** (10), 607 (1972).
16. A. H. Cooke, C. J. Ellis, K. A. Gehring, *et al.*, Solid State Commun. **8** (9), 689 (1970).
17. G. A. Gehring, A. P. Malozemoff, W. Staude, *et al.*, J. Phys. Chem. Solids **33** (7), 1499 (1972).
18. P. Morin and Z. Kazei, J. Phys.: Condens. Matter **11,** 1289 (1999).

Translated by O. Borovik-Romanova

Physics of the Solid State, Vol. 42, No. 2, 2000, pp. 292–297. Translated from Fizika Tverdogo Tela, Vol. 42, No. 2, 2000, pp. 284–289.

MAGNETISM AND FERROELECTRICITY

Kinetic, Optical, and Elastic Properties of $La_{0.60}Eu_{0.07}Sr_{0.33}MnO_3$

R. I. Zaĭnullina*, N. G. Bebenin*, V. V. Mashkautsan*, A. M. Burkhanov*, Yu. P. Sukhorukov*, V. V. Ustinov*, V. G. Vasil'ev, and B. V. Slobodin****

**Institute of Metal Physics, Ural Division, Russian Academy of Sciences, ul. S. Kovalievskoĭ 18, Yekaterinburg, 620219 Russia*

***Institute of Solid-State Chemistry, Ural Division, Russian Academy of Sciences, Pervomaĭskaya ul. 91, Yekaterinburg, 620219 Russia*

e-mail: elph@ifm.e-burg.su

Received June 8, 1999

Abstract—An experimental study is reported of the temperature dependences of the electrical resistivity and magnetoresistance, thermal and magnetothermal EMF, the Hall effect, optical reflectance, sound velocity, and internal friction of polycrystalline lanthanum manganite $La_{0.60}Eu_{0.07}Sr_{0.33}MnO_3$ carried out within the 77–430-K temperature range. Substitution of a small amount of europium for lanthanum has been found to result in a considerable decrease in the resistivity and a change in the behavior of its temperature dependence. Four characteristic temperatures at which special features are observed in the above properties have been identified. The discussion of the conduction mechanisms involved is based on the concept of mobility edge motion. © *2000 MAIK "Nauka/Interperiodica".*

Intense studies of lanthanum manganites started in 1993, following the discovery of the so-called colossal magnetoresistance (CMR) observed in a temperature range close to room temperature (see reviews [1, 2]). Despite a wealth of papers dealing with the properties of these materials, the nature of the CMR remains unclear. This is due, to a certain extent, to the fact that published experimental results relate, as a rule, to individual properties (primarily to the resistivity and magnetoresistance). Nevertheless, it may be considered established that the colossal magnetoresistance is only one of the specific properties of manganites, which are determined by a strong coupling between the magnetic, electronic, and elastic subsystems of the crystal. It thus follows that the nature of the CMR can be understood only in an integrated investigation of the properties in which these interactions become manifest. With this in mind, we undertook studies of the magnetic, electrical, thermoelectric, galvano- and thermomagnetic, optical, and elastic characteristics of polycrystalline manganite $La_{0.60}Eu_{0.07}Sr_{0.33}MnO_3$. The choice of this composition was motivated by the fact that doping $LaMnO_3$ with 33% Sr produces a material with a high magnetoresistance, while an additional replacement of lanthanum with 7% europium reduces the Curie temperature T_C to values close to room temperature [3]. As will be shown below, such a substitution also brings about a substantial decrease in the resistivity ρ, which is accompanied by a change in the behavior of the temperature dependence $\rho(T)$.

SAMPLES AND EXPERIMENTAL TECHNIQUES

Powders of the nominal composition $La_{0.60}Eu_{0.07}Sr_{0.33}MnO_3$ were prepared by coprecipitation from solutions [4]. Polycrystalline samples were obtained by pressing at room temperature at a pressure of 5 t/cm^2, with a subsequent annealing in an oxygen flow at 1200°C for 12 h. The sample density was 5.2 g/cm^3, which is about 83% of the calculated value. X-ray diffraction measurements showed the samples to be single phase.

The samples prepared for measurement of the kinetic properties (resistivity ρ, the Seebeck coefficient S, and the Hall effect) were parallelepiped-shaped, with dimensions of $10 \times 3 \times 0.9$ mm. The magnetization curves were taken on a vibrating-sample magnetometer on similar, smaller samples in a magnetic field directed as in the Hall-effect measurements. The Curie temperature was determined by the method of thermodynamic coefficients. The resistivity and Hall effect measurements were carried out by the standard dc four-probe technique. The temperature gradient $\Delta T \approx 3$ K in the measurements of the Seebeck coefficient was produced by a heater placed at one end of a sample. The temperatures of the sample ends were monitored with two copper–constantan thermocouples. The thermal emf of a sample was determined potentiometrically between the copper ends of the thermocouples. In all cases, the magnetic field of up to 15 kOe was directed perpendicular to the plate plane. We used indium contacts deposited with an ultrasonic soldering iron.

The optical reflectance was measured in the wavelength range λ of 0.8 to 36 μm within the 293–430-K temperature region.

The sound velocity V and the internal friction Q^{-1} were determined with a composite oscillator at frequencies of 50 to 100 kHz, with quartz transducers used as

piezoresistive sensors. The measurements were made in a helium gas environment within the 80–430-K range.

RESULTS OF MEASUREMENTS

The magnetization curves had the pattern typical of ferromagnets. The Curie temperature determined by the method of thermodynamic coefficients was found to be T_c = 328 K. An analysis of the magnetization curves shows, however, that a weak spontaneous moment persists up to 350 K. For $T < T_c$ and in fields $H \geq 6$ kOe, the magnetization M is described by the relation $M = M_s + \chi H$. Within the temperature range $77 < T < 200$ K, the temperature dependence of M_s is well approximated by the relation $M_s(T) = M_s(0) - \alpha T^{3/2}$, where $\alpha = 1.35 \times 10^{-5}$ G K$^{-3/2}$ and $M_s(0) = 425$ G, which corresponds to 3.3 μ_B/Mn. For $T < 250$ K, one observes, with increasing T, a weak falloff of the susceptibility χ, to be replaced by a sharp growth as one approaches T_C.

Figure 1 presents plots of the temperature dependence of the resistivity and of the Seebeck coefficient. At low temperatures, the resistivity has a metallic character ($d\rho/dT > 0$), reaches a maximum at T_R = 349 K, and then decreases as the temperature continues to increase. At low temperatures, the Seebeck coefficient is positive and reaches a maximum at T = 146 K, only to fall off afterwards monotonically with increasing temperature and to reverse sign at T = 225 K. The absolute values of $d\rho/dT$ and dS/dT pass through a maximum at the same temperature T = 324 K, which is close to T_C.

Figure 2 shows the temperature dependence of the differences $S(H) - S(0)$ and $\rho(0) - \rho(H)$ obtained at H = 10 kOe. Both curves pass through a maximum at $T = T_C$ and practically coincide in shape in the vicinity of T_C. The difference $S(H) - S(0)$ tends to zero as one moves away from the phase-transition point, whereas $\rho(0) - \rho(H)$ is practically temperature independent in the ferromagnetic region.

Figure 3 displays, for a few values of temperatures, the field dependences of the Hall resistance $\rho_H = R_0 B + R_s M$, where R_0 and R_s are the normal and anomalous (spontaneous) Hall coefficients, B is the magnetic induction in the sample, and M is the magnetization [5]. For the geometry of our samples, the demagnetizing factor is close to unity, and therefore one can set $B = H$.

Presented in Fig. 4 are the temperature dependences of R_0 and R_s derived from the $\rho H(H)$ curves as this is done in [6, 7]. Within the temperature range studied, the normal Hall coefficient is positive, which implies a dominant hole contribution to conduction. For $T < 300$ K, the R_0 coefficient is only slightly temperature-dependent and is, on the average, 4.9×10^{-12} Ω cm/G. Above $T > 300$ K, one observes a substantial growth of R_0, which ends at approximately T = 350 K, after which R_0 decreases. The anomalous Hall coefficient is negative and passes through a minimum at T = 355 K (see the inset to Fig. 4). It should be pointed out that for $T > 340$ K, the Hall coefficients are determined within a considerable margin of error (of about 30%). While the $R_0(T)$ and $R_s(T)$ curves

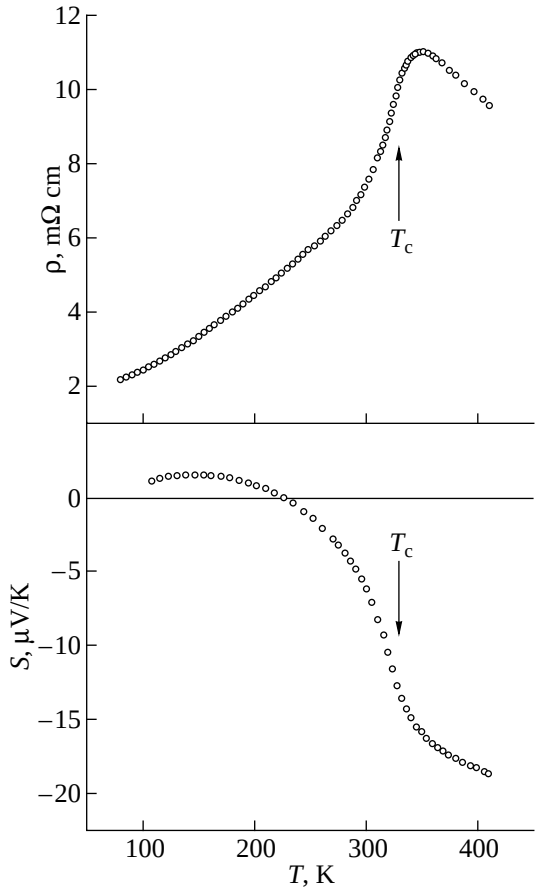

Fig. 1. Temperature dependence of the resistivity ρ and of the Seebeck coefficient S of an $La_{0.60}Eu_{0.07}Sr_{0.33}MnO_3$ sample.

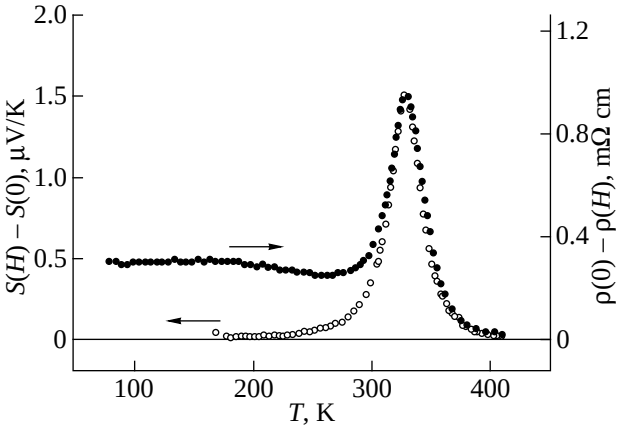

Fig. 2. Temperature dependences of $\rho(0) - \rho(H)$ and $S(H) - S(0)$ obtained at H = 10 kOe.

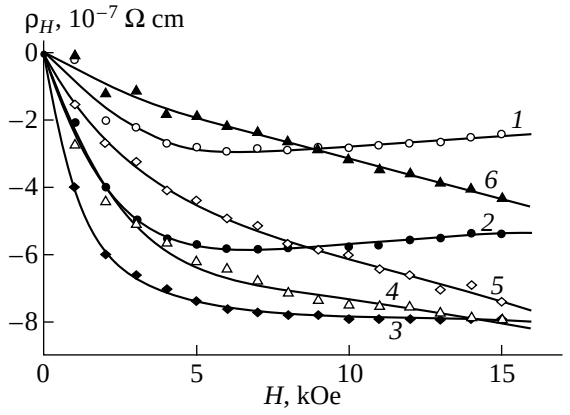

Fig. 3. Isotherms of the Hall resistivity of $La_{0.60}Eu_{0.07}Sr_{0.33}MnO_3$ obtained at different temperatures *T* (K): (*1*) 250, (*2*) 293, (*3*) 324, (*4*) 332, (*5*) 340, and (*6*) 360.

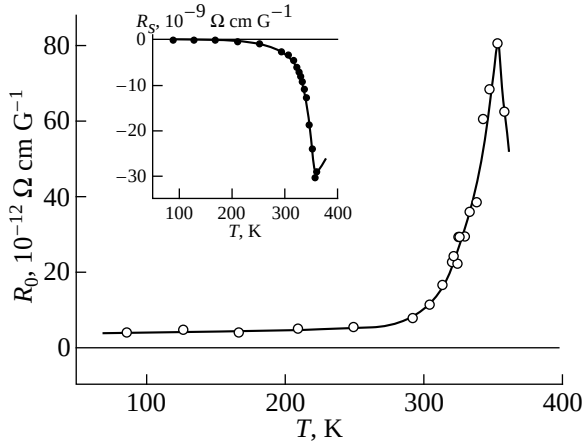

Fig. 4. Temperature dependence of the normal, R_0, and anomalous, R_S (inset), Hall coefficients in $La_{0.60}Eu_{0.07}Sr_{0.33}MnO_3$.

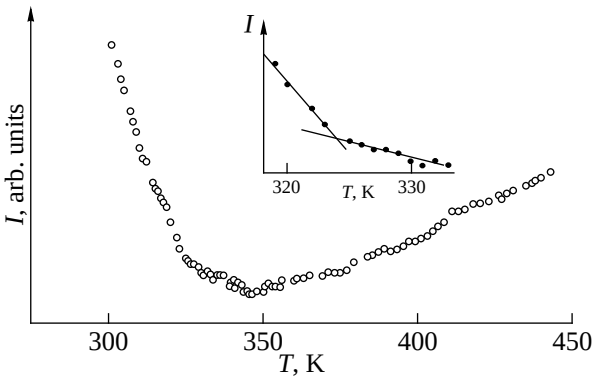

Fig. 5. Temperature dependence of the reflected light intensity at the wavelength λ = 14 μm obtained on an $La_{0.60}Eu_{0.07}Sr_{0.33}MnO_3$ sample.

do not exhibit any features near T_C, the derivatives dR_0/dT and dR_s/dT have extrema at T = 327 K.

Figure 5 shows the temperature dependence of the reflected light intensity I measured at the wavelength λ = 14 μm. This wavelength is convenient for studying the properties of carriers in lanthanum manganites, because it corresponds to the temperature-independent minimum located before the phonon maximum observed in undoped $LaMnO_3$ [8]. The $I(T)$ curve exhibits a break at T = 324 K (see the inset) and a broad minimum at $T \approx 350$ K.

Figure 6 plots the temperature dependences of the sound velocity $V(T)$ and internal friction $Q^{-1}(T)$. The $V(T)$ curve exhibits weak features, to which, in the $dV(T)/dT$ curve (see inset), correspond distinct minima near T_C, at 318 K and at $T_{lat} \approx 395$ K. Internal friction Q^{-1} grows with increasing temperatures to reach a maximum at $T_{lat} \approx 395$ K. No features have been observed in the vicinity of the Curie point in the $Q^{-1}(T)$ relation.

DISCUSSION OF RESULTS

Earlier, we studied the properties of $La_{0.67}Sr_{0.33}MnO_3$ and $La_{0.60}Ce_{0.07}Sr_{0.33}MnO_3$ samples [7] prepared in the same way as the $La_{0.60}Eu_{0.07}Sr_{0.33}MnO_3$ samples in this study. All these samples have a density of about 80% of the theoretical value and practically the same magnetic moment, ≈3.3 μ_B per manganese ion, at T = 77 K. In contrast to doping with cerium, europium doping results in a substantial (by about 40 K) decrease of the Curie temperature. The growth of the paramagnetic contribution to the susceptibility observed to occur in the ferromagnetic region with decreasing temperatures indicates the presence of paramagnetic ions and (or) the existence of a small amount of a ferromagnetic phase with a low (less than 77 K) Curie temperature. It may be conjectured that these paramagnetic ions are europium ions occupying the lanthanum sites, and that the interaction of the magnetic moments of europium with those of manganese is weak. The ferromagnetic phase could be EuO with $T_C < 77$ K.

The persistence of spontaneous magnetization up to 350 K argues for a magnetic nonuniformity of the sample. Note that such a nonuniformity was observed even in single crystals of $La_{0.8}Sr_{0.2}MnO_3$ [9].

The temperature dependence of the resistivity of the manganite samples under study differs substantially from the one we observed on samples of $La_{0.67}Sr_{0.33}MnO_3$ and $La_{0.60}Ce_{0.07}Sr_{0.33}MnO_3$ close in composition, where the temperature dependence had a pattern characteristic of polycrystalline samples with ρ typically near 30–40 mΩ cm. As a result of europium doping, the resistivity decreased substantially (down to 2 mΩ cm at 77 K), and its temperature behavior approached that of $\rho(T)$ for single-crystal samples. Similar changes of the temperature dependences of the resistivity of polycrystalline samples were observed to

occur with increasing crystallite size, which was attained by substantially raising the annealing temperature (see [10] and references therein). It may be conjectured that doping with europium favors an increase in crystallite size during the annealing. Another possible reason for the decrease of the resistivity is the precipitation of a phase with a relatively low resistivity at crystallite boundaries. In this case, such a phase could be EuO doped intrinsically by vacancies of oxygen and (or) trivalent lanthanum, because it is known [11, 12] that this material can have a comparatively low resistivity. It should be stressed, however, that the magnitude of $\rho(T)$ in the ferromagnetic region exceeds, by about one order of magnitude, the resistivity of single-crystal samples with a similar Curie temperature [9, 13].

The experimental data presented in the preceding section permit one to point out three temperatures at which features in properties are observed. This is, first, the temperature of the magnetic phase transition T_C = 328 K, near which features appear in the differential characteristics, namely, extrema in the derivatives $d\rho/dT$, dS/dT, dR_0/dT, dR_s/dT, and dV/dT, maxima in $S(H) - S(0)$ and $\rho(0) - \rho(H)$, and a break in the $I(T)$ curve. The small differences in the position of the anomalies of these quantities can be due to the abovementioned nonuniformity of the sample. Second, it is the temperature $T_R \approx 350$ K, near which one observes features in the quantities associated with charge transport, i.e., ρ, R_0, R_s, and I. Third, it is the temperature $T_{lat} \approx 395$ K, at which one finds features in lattice properties, namely, in the sound velocity and internal friction. Because optical reflectance in the wavelength range considered is only slightly sensitive to grain boundaries, the existence of features at $T = T_C$ and $T = T_R$ is connected primarily with processes inside the crystallites.

We are turning now to a consideration of the conduction mechanisms. The weak temperature dependence of the normal Hall coefficient for $T < 300$ K indicates that, inside the crystallites, the material resides in a metallic state. A straightforward estimation of the carrier concentration n using the $R_0 = (enc)^{-1}$ relation yields $n = 0.75$ carrier per cell. The positive sign of R_0 implies that the dominant carriers are holes. The noticeable difference of this value of n from the one obtained from the chemical formula suggests that carriers of electronic type are also present.

At $T \approx 300$ K, the smooth growth of ρ and of the normal Hall coefficient is replaced by their sharp rise, thus indicating a decrease of the conductivity as a result of a decrease in the carrier concentration. The maxima in $\rho(T)$ (Fig. 1) and $R_0(T)$ (Fig. 4) take place at the same temperature $T_R \approx 350$ K, where it follows that the maximum of resistivity at this temperature originates from the minimum in the concentration of the carriers contributing to the conductivity.

We believe that the temperature dependence of the resistivity and of the Hall effect can be explained as being due to a shift of the hole mobility edge ε_C (without taking into account the electronic contribution). Because the temperature behavior of ε_C near T_C originates from the growth of spin fluctuations [14], all the differential characteristics describing charge transport should have features in the vicinity of this temperature, which is exactly what is observed in experiment. For small values of the relative magnetization $m = M/M_s(0)$ one can write $\varepsilon_C = \Delta_0 - \Delta_1 m^2$, where ε_C is the mobility edge for holes, and Δ_0 and Δ_1 are phenomenological parameters to be found from the experiment. Generally speaking, Δ_0 and Δ_1 are functions of T, but for the sake of simplicity we will consider them to be constants. As this will be seen below, the mobility edge lies near the hole Fermi level ε_F for all temperatures. By Mott [15], in this case, one can write the following expression for the conductivity:

$$\sigma = \sigma_{\min} f(\varepsilon_C), \tag{1}$$

where $\sigma_{\min}$ is the lowest metallic conductivity, and f is the Fermi function. Thus, for the resistivity near the phase-transition temperature we obtain

$$\rho = \rho_m \left(\exp\left(\frac{E_A - \Delta_1 m^2}{T} \right) + 1 \right), \tag{2}$$

where ρ_m = const, and $E_A = \Delta_0 - \varepsilon_F$ is the activation energy in the paramagnetic region at $H = 0$. We used the

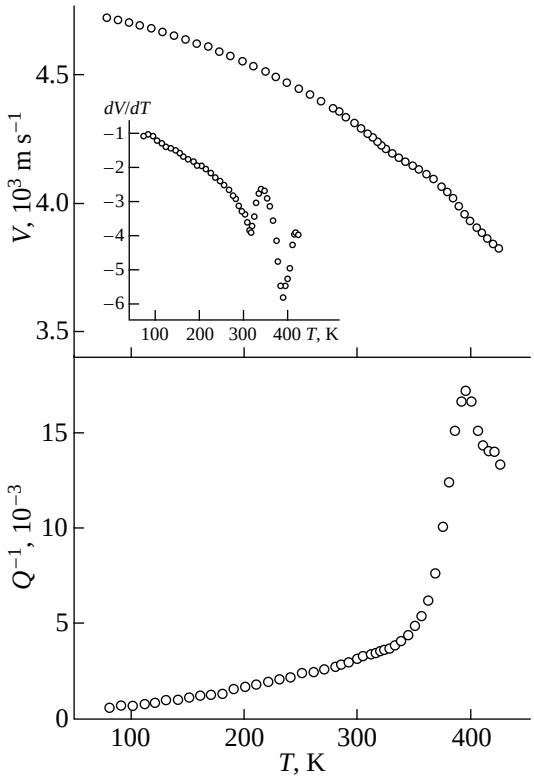

Fig. 6. Temperature dependence of the sound velocity V and internal friction Q^{-1} of an $La_{0.60}Eu_{0.07}Sr_{0.33}MnO_3$ sample.

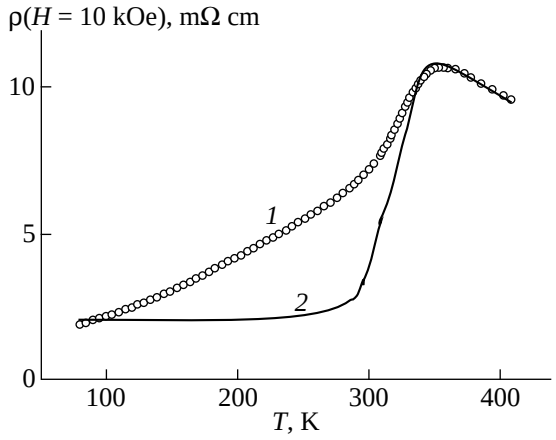

Fig. 7. Experimental (*1*) and calculated (*2*) $\rho(T, H = 10\ \text{kOe})$ curves.

temperature dependence of the resistivity within the 380–410-K range to derive estimates for ρ_m and E_A: $\rho_m = 2.2\ \text{m}\Omega\ \text{cm}$ and $E_A = 530$ K, and, by comparing the temperature dependences of the resistivity at $H = 0$ and $H = 10$ kOe, came to $\Delta_1 \approx 2000$ K. The value of Δ_1 turns out to be substantially smaller than the hole Fermi energy, which is of the order of 2×10^4 K [16, 17], thus validating the application of Eqs. (1) and (2). The estimation of the minimum metallic conductivity by [18] yields $1/\sigma_{\min} \approx 7\ \text{m}\Omega\ \text{cm}$, which coincides in order of magnitude with ρ_m. Calculation of the resistivity from (2) for $H = 0$ and for temperature-independent E_A and Δ_1 yields a sharp peak at the Curie point, rather that a diffuse maximum at $T = T_R > T_C$, as this is observed experimentally. This disagreement may be due, first, to the above-mentioned magnetic nonuniformity of the sample, which should smoothen the resistivity peak and shift it toward higher temperatures, because for $T > T_C$ the dependence of ρ on T is considerably weaker than that in the ferromagnetic region near T_C. Second, our calculations did not take into account the temperature dependence of Δ_0 and Δ_1 in the paramagnetic region near T_C, which also results in a shift of the resistivity maximum toward higher temperatures and its flattening. While estimation of these factors would present difficulties, their role becomes substantially weaker under the application of a strong enough magnetic field, because the temperature dependence of ε_C is dominated in this case by that of the magnetization.

Figure 7 presents the experimental and calculated $\rho(T)$ curves for $H = 10$ kOe. The calculation was done by (2) using the values of E_A and Δ_1 found above, and experimental data on the magnetization for $H = 10$ kOe. One readily sees that Eq. (2) permits one to satisfactorily approximate the shape of the $\rho(T, H = 10\ \text{kOe})$ curve near the maximum, although we could not take the role of the grain boundaries into account. The decrease of the resistivity in the ferromagnetic region found by the calculation is considerably stronger than the experimental one. One can readily see, however, that the calculated temperature dependence of the resistivity very much resembles the $R_0(T)$ relation in Fig. 4. Because the Hall effect in polycrystals reflects the situation inside the crystallites and depends to a much lesser degree on the processes occurring at their boundaries than the resistivity does [19], one can conjecture that the calculated curve correctly approximates, on the whole, the temperature behavior of the resistivity inside the grains, and this refers not only to temperatures $T > T_C$ but also in the ferromagnetic region, at any rate near T_C.

The metal–insulator transition temperature T_{MI}, i.e., the temperature at which the mobility edge crosses the Fermi level, is determined by the condition $m^2 = E_A/\Delta_1$. For $H = 0$ it lies below T_C. Substitution of the above values of E_A and Δ_1 yields $T_{MI} \approx 300$ K, which coincides with the temperature at which a rapid growth of the resistivity and of the normal Hall coefficient sets in. It should be stressed that the resistivity growth in the $T_{MI} < T < T_R$ region, which already belongs to the insulating phase, is caused by a fast increase of the difference $\varepsilon_C - \varepsilon_F$.

We are turning now to a discussion of the results relating to the Seebeck coefficient. The dominance of the hole conduction (which is metallic for $T < 300$ K) should give rise to a positive sign of S and a linear growth of the Seebeck coefficient with temperature for $T < 300$ K, with a subsequent increase near T_{MI} up to about 100 μV/K, followed by the transition to a relation of the const/T type in the paramagnetic region. As seen from Fig. 1, $S > 0$ and it grows with temperature, but only for $T < 146$ K. Having estimated the slope of the $S(T)$ curve in this region, and using the well-known expression for the parabolic band, we find that the hole Fermi energy is about 1–2 eV, which appears quite reasonable. However, as the temperature increases still further, the Seebeck coefficient decreases, to become negative for $T > 225$ K. At first glance, this is at odds with the above suggestion of the dominant hole contribution to conductivity, as well as with the results of band-structure calculations [16], by which the concentration of electrons is less than that of the holes by an order of magnitude. This contradiction is removed, however, if one takes into account that the characteristics of holes and electrons differ substantially [16]. The effective mass of holes is less than the free-electron mass m_0, which accounts for their metallic behavior up to the T_C region. By contrast, the electronic mass is considerably in excess of m_0, which explains the strong trend to localization. This suggests that the negative sign of the Seebeck coefficient is associated not with the electronic contribution to conductivity being dominant, but rather with the large value of the electronic Seebeck coefficient in the insulating state. Because, for $T = T_{MI}$, the hole Seebeck coefficient also reaches high values, the electronic and hole contributions cancel

each other out, to make the Seebeck coefficient comparatively small even in the insulating phase.

As evident from Fig. 2, a magnetic field results in an increase of the hole contribution to the Seebeck coefficient. The reason for the variation of both ρ and S near T_C apparently lies in an increase of the number of holes in delocalized states. The difference $\rho(0) - \rho(H)$ in the ferromagnetic region is practically temperature independent. The magnitude of this difference, about 0.3 mΩ cm, characterizes the contribution of spin-dependent scattering at grain boundaries. It can be assumed that the total contribution of scattering at boundaries to the sample resistivity should be several times larger and, hence, constitute 1–2 mΩ cm, which agrees with low-temperature measurements.

The anomalies observed near $T_{lat} \approx 395$ K are associated mainly with variations of the lattice characteristics, which is evidenced by the presence of a clearly pronounced maximum in the temperature dependence of the internal friction $Q^{-1}(T)$ and of the minimum in $dV(T)/dT$. These anomalies could be assigned to the occurrence of a structural transition or to the onset of charge ordering. The latter, however, hardly appears because the temperature is too high. In order to reveal the lattice changes occurring at 395 K, X-ray diffraction measurements were carried out at 380 and 420 K. Their comparison with each other, as well as with room-temperature diffraction patterns, showed them to be all practically identical. Hence, if any changes in the lattice do take place at 395 K, they are extremely weak. On the whole, the problem of the nature of the strong internal-friction anomaly observed by us remains open.

Thus, our integrated investigation of the properties of the $La_{0.60}Eu_{0.07}Sr_{0.33}MnO_3$ lanthanum manganite allows the following conclusions.

Weak substitution of lanthanum by europium results in a considerable decrease of the resistivity ρ and in the $\rho(T)$ dependence becoming similar to that of single crystals. Such changes were observed earlier only at substantially higher annealing temperatures.

It has been shown that holes are dominant carriers in the ferromagnetic region, although electrons are also present. The small magnitude of the Seebeck coefficient can be accounted for by the competition between the hole and electronic contributions.

Four characteristic temperatures have been pointed out: the metal–insulator transition point $T_{MI} \approx 300$ K, the Curie temperature $T_C = 328$ K, and also $T_R \approx 350$ K and $T_{lat} \approx 395$ K, of which the first three are associated with processes in the electronic and magnetic subsystems, while the latter characterizes the lattice. It has been shown that the features at $T = T_R$ are associated with the minimum of the carrier concentration in delocalized states, rather than with the metal–insulator transition. The temperature dependences of the resistivity and of the Hall effect near T_C can be satisfactorily explained in terms of the concept of a shift of the hole mobility edge.

ACKNOWLEDGMENTS

The authors are indebted to N.I. Taluts for his assistance in X-ray diffraction measurements.

Support of the Russian Basic Research Foundation (grant 97-02-16008) is gratefully acknowledged.

REFERENCES

1. É. L. Nagaev, Usp. Fiz. Nauk **166** (8), 833 (1996).
2. A. P. Ramirez, J. Phys.: Condens. Matter **9** (39), 8171 (1997).
3. A. Nossov, J. Pierre, J. Beille, *et al.*, Eur. Phys. J. B **6**, 467 (1998).
4. V. G. Vasil'ev, A. A. Ivakin, and A. A. Fotiev, Zh. Neorg. Khim. **39** (1), 3 (1994).
5. C. M. Hurd, *Hall Effect in Metals and Alloys* (Plenum Press, N. Y., 1972).
6. N. G. Bebenin, R. I. Zaĭnullina, V. V. Mashkautsan, *et al.*, Zh. Éksp. Teor. Fiz. **113** (3), 981 (1998).
7. R. I. Zaĭnullina, N. G. Bebenin, V. V. Mashkautsan, *et al.*, Fiz. Tverd. Tela (St. Petersburg) **40** (11), 2085 (1998).
8. T. Arima and Y. Tokura, J. Phys. Soc. Jpn. **64**, 2488 (1995).
9. S. E. Lofland, S. M. Bhagat, K. Ghosh, *et al.*, Phys. Rev. B **56** (21), 13705 (1997).
10. A. K. M. Akther Hossain, L. F. Cohen, F. Damay, *et al.*, J. Magn. Magn. Mater. **192**, 263 (1999).
11. A. A. Samokhvalov, in *Rare-Earth Semiconductors* (Nauka, Leningrad, 1977), pp. 5–47.
12. M. Gusgnier, Phys. Status Solidi A **114** (1), 11 (1989).
13. A. Urushibara, Y. Moritomo, T. Arima, *et al.*, Phys. Rev. B **51** (20), 14103 (1995).
14. N. G. Bebenin and V. V. Ustinov, J. Phys.: Condens. Matter **10** (28), 6301 (1998).
15. N. F. Mott, Philos. Mag. **31** (1), 217 (1975).
16. W. E. Pickett and D. J. Singh, J. Magn. Magn. Mater. **172** (3), 237 (1997).
17. D. A. Papaconstantopoulos and W. E. Pickett, Phys. Rev. B **57** (20), 12751 (1998).
18. N. F. Mott and E. A. Davis, *Electronic Processes in Non-Crystalline Materials* (Clarendon Press, Oxford, 1979; Mir, Moscow, 1982).
19. E. V. Kuchis, *Galvanomagnetic Effects and Methods of Their Investigation* (Radio i svyaz', Moscow, 1990).

Translated by G. Skrebtsov

Physics of the Solid State, Vol. 42, No. 2, 2000, pp. 298–304. Translated from Fizika Tverdogo Tela, Vol. 42, No. 2, 2000, pp. 290–296.

MAGNETISM AND FERROELECTRICITY

Linear and Nonlinear Susceptibilities of Samarium Manganites

I. D. Luzyanin, V. A. Ryzhov, S. M. Dunaevskiĭ, V. P. Khavronin, I. I. Larionov, A. V. Lazuta, and Yu. P. Chernenkov

Konstantinov Institute of Nuclear Physics, Russian Academy of Sciences, Gatchina, St. Petersburg, 188350 Russia
e-mail: luzyanin@hep486.pnpi.spb.ru

Received June 11, 1999

Abstract—The temperature and field behaviors of the linear and nonlinear responses to a weak ac magnetic field in the $Sm_{1-x}Sr_xMnO_3$ manganites with x = 0.25, 0.3, and 0.4 have been investigated. It is found that the hysteresis of the second harmonic of magnetization in the dc magnetic field arises in the far-paramagnetic range at $T \leq 180$ K, whereas the hystereses of the linear susceptibility and the dc resistivity are observed at lower temperatures. This phenomenon is associated with the formation of macroscopic ferromagnetic (ferrimagnetic) domains in the paramagnetic matrix. The shape of the temperature dependence of the linear susceptibility at $T > T_c$ is determined by the degree of doping, and the susceptibility itself nonmonotonically depends on *x*. © *2000 MAIK "Nauka/Interperiodica".*

At present, particular emphasis in the field of investigations into the giant magnetoresistance has been placed on research into the partially substituted manganites $RE_{1-x}M_xMnO_3$ (RE = Pr, Nd, Sm, and others; M = Ba, Ca, Sr, and others) synthesized on the basis of rare-earth elements with nonzero local magnetic moment [1–3]. These compounds are characterized by a number of new effects (as compared to the $La_{1-x}M_xMnO_3$ system studied in detail), among which the ferromagnetic (ferrimagnetic) ordering and the absence of the insulator–metal transition (giant magnetoresistance effect) in the $Gd_{0.67}Ca_{0.33}MnO_3$ compound are most intriguing [2]. A rather large number of works are devoted to the magnetic and transport properties of these systems. However, to the best of our knowledge, the nonlinear phenomena that can provide important information about fine details of magnetic interactions have hitherto not been studied.

This work is concerned with the investigation into the temperature and field (in relatively weak external magnetic fields) dependences of the linear and nonlinear susceptibilities and also the dc resistivity of the $Sm_{1-x}Sr_xMnO_3$ manganites. Compared to other compounds, whose phase diagrams were examined in detail [4], samarium manganites are least understood. Their magnetic and transport properties were earlier studied in [1, 3, 5]. The neutron diffraction analysis of the structure of ceramic samples enriched with the Sm^{154} isotope [3, 6] demonstrated that a decrease in the temperature of samples with $x = 0.4$ results in the transition to the unsaturated "ferromagnetic" state [6], which can be interpreted either as a canted ferromagnetic state or a state with the spatial separation of ferromagnetic and antiferromagnetic phases.

Apparently, the nonlinear properties of manganites with the giant magnetoresistance were explored for the first time in the present work. In our opinion, these studies on the nonlinear properties of samarium manganites, together with investigations into the behavior of the linear susceptibility and transport properties, provided new and interesting results. Actually, we revealed the appearance of the hysteresis in the second harmonic of magnetization in the dc magnetic field in the paramagnetic phase, which was accounted for by the formation of macroscopic ferromagnetic (ferrimagnetic) domains. In the earlier work [7], the formation of macroscopic domains with a weak ferromagnetism was observed with this investigation technique upon phase separation of excess oxygen in La_2Cu_{4+x}. Moreover, the results obtained in studies of the linear susceptibility indicate that the paramagnetic susceptibility has a strong and nonmonotonic dependence on the strontium content, whereas the dc resistivity in this range of temperatures only slightly depends on the degree of doping.

1. EXPERIMENTAL

The investigation of the magnetic and transport properties of the $Sm_{1-x}Sr_xMnO_3$ manganites was performed with ceramic samples ($x = 0.25$, 0.3, and 0.4) taken from the same batches as the samples studied in [3, 5, 6]. The X-ray diffraction patterns of the samples were recorded on a DRON-3M diffractometer at room temperature. A pyrolytic graphite crystal was used as a monochromator of the radiation of an X-ray tube with a copper anode. The results obtained in the processing of the X-ray diffraction patterns with the use of the FULLPROF program [8] of the full-profile analysis are

1063-7834/00/4202-0298$20.00

presented in Tables 1 and 2. The unit-cell parameters *a*, *b*, and *c* and the atomic coordinates *X*, *Y*, and *Z* were determined with a rather low accuracy, because the samples had a small volume. The variation in the concentration leads to a monotonic change in all these parameters, except, possibly, the *c* parameter at $x = 0.3$. The symmetry of the unit cell is described by the space group *Pbnm*. An increase in the concentration *x* results in a decrease in the degree of orthorhombicity (i.e., in the difference between the *a* and *b* parameters). This is in agreement with the data obtained in [3], according to which the unit cell for the composition with $x = 0.4$ at $T = 300$ K has the tetragonal symmetry.

For an additional characterization of the samples, their ESR spectra were measured at room temperature on a spectrometer described in [9]. The ESR spectra contain single lines with close values of the *g*-factors and widths (ΔH is about 5 kOe) and differ only in the signal amplitude (normalized to the unit mass). The signal amplitude is minimum for the sample with $x = 0.25$ and increases by about 10% for the sample with $x = 0.3$ and approximately by a factor of two for the sample with $x = 0.4$. It was also found that the dielectric permittivity (conductivity) weakly increases with an increase in the dopant concentration. No signals of magnetic impurities against the background of the signal taken from the main phase are observed in the ESR spectra of the studied samples.

The linear susceptibility was measured at the ac magnetic field amplitude $h_0 \approx 1$ Oe in the frequency range 10^3–10^5 Hz by the phase method [10]. This method is based on the determination of the total impedance of a pickup coil containing the sample at a given frequency and the measurement of the phase shift between the current passing through the pickup coil and the voltage across the coil. The error in the measurement of the ac voltage was no more than 0.05%, and the accuracy of the measurement of the phase shift was no worse than 0.01–0.02 deg. The real (χ') and imaginary (χ'') components of the linear dynamic susceptibility were determined from the parameters of the pickup coil (with and without the sample) in the form $4\pi\chi' = (L_k/L_0 - 1)$ and $4\pi\chi'' = (R_k - R_{k0})/2\pi f L_0$, where L_0 and R_{k0} are the parameters of the pickup coil without sample, L_k and R_k are the parameters of the pickup coil containing the sample, and *f* is the frequency at which the measurements were carried out. At $\chi \approx 0.1$, the errors in determination of the χ' and χ'' values did not exceed 1%. At $\chi < 1$, the errors increased proportionally to a decrease in the susceptibility and reached 100% at $\chi \approx 10^{-4}$.

The second harmonic of magnetization M_2 was measured in parallel dc (H) and ac ($h_0 \approx 45$ Oe) magnetic fields (the fundamental frequency $f = \omega/2\pi = 15.7$ MHz) with a setup described in [11]. The signal of the second harmonic is governed only by the nonlinear properties of the studied material and, unlike the linear susceptibility, does not involve the response of a metering circuit at the fundamental frequency. Therefore, it is necessary to eliminate, as far as possible, the nonlinearity of a transmitter–receiver system, which requires to keep the fundamental frequency from entering the metering circuit. Higher harmonics should also be eliminated, because their entering into a receiver at the output of a generator hinders the recording of a legitimate signal. For these reasons, higher harmonics at the output of a generator and the signal of the fundamental frequency at the input of a receiver were suppressed by more than 120 dB. The dc field was changed from –300 to +300 Oe. The real $\mathrm{Re}\,M_2(H)$ and imaginary $\mathrm{Im}\,M_2(H)$ components of the second harmonic of magnetization were recorded simultaneously. The required phase of the reference voltage at synchronous detectors of the second harmonic was adjusted with a reference signal generated using a nonlinear characteristic of a microwave diode (Schottky-barrier diode A 538A) with a small self-capacitance and a short recovery time. A circuit generating this signal was weakly coupled with a two-frequency resonance system that created the ac field in a sample and carried out the initial separation of a signal with double the fundamental frequency. The phase adjustment was no worse than 0.5 deg. The sensitivity of the M_2 measurements was of an order of 10^{-9} emu.

The method used in the present work for recording the signal of the second harmonic is very sensitive to impurities of ferromagnetic materials (predominantly, iron oxides) in elements of two-frequency resonance system. Special measures, including the application of a galvanic copper coating on conducting parts, made it possible to suppress the "spurious" signal of these fer-

Table 1. Unit cell parameters for the $Sm_{1-x}Sr_xMnO_3$ manganites

x	*a* (Å)	*b* (Å)	*c* (Å)
0.4	5.437(2)	5.437(2)	7.656(1)
0.3	5.432(1)	5.456(1)	7.664(1)
0.25	5.425(1)	5.501(1)	7.650(2)

Table 2. Atomic coordinates

Atom		*X*	*Y*	*Z*
Mn		0.5	0.00	0.00
Sm(Sr)	0.4	–0.008(3)	0.0278(7)	0.25
	0.3	–0.008(1)	0.0300(5)	0.25
	0.25	–0.006(6)	0.0421(8)	0.25
O1	0.4	0.07(2)	0.498(7)	0.25
	0.3	0.06(1)	0.485(5)	0.25
	0.25	0.17(1)	0.390(9)	0.25
O2	0.4	0.72(1)	0.30(1)	0.029(7)
	0.3	0.74(1)	0.31(1)	0.044(4)
	0.25	0.73(1)	0.18(1)	0.047(2)

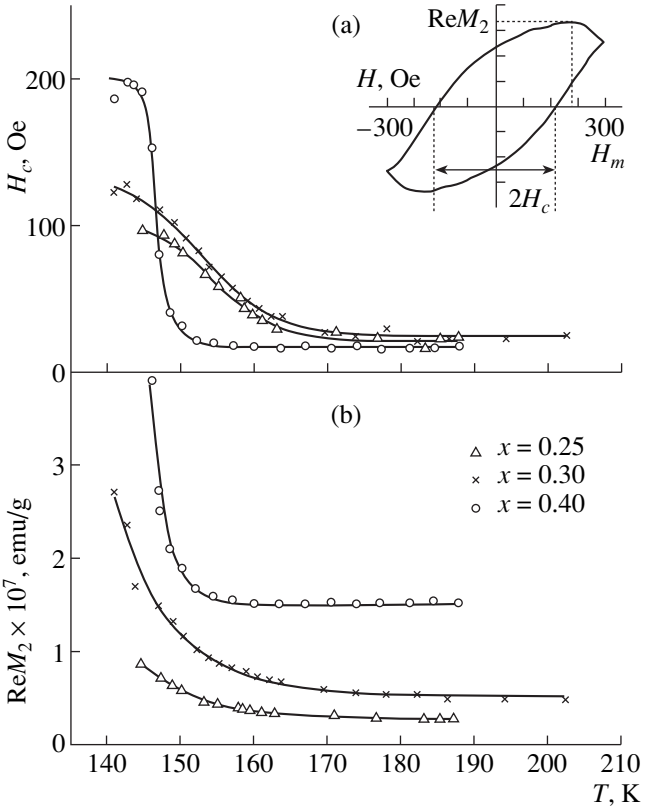

Fig. 1. Temperature dependences of the parameters of the ReM_2 signal without subtraction of the impurity signal for the ceramic $Sm_{1-x}Sr_xMnO_3$ samples with x = 0.25, 0.3, and 0.4: (a) the dependence of the coercive force H_c on T and (b) the dependence of the magnitude of ReM_2 on T. The errors in determination of the parameters are equal to approximately double the size of the symbol designating the experimental point. The inset shows typical ReM_2 signal with a hysteresis loop and illustrates the determination of the characteristic parameters H_c, ReM_2, and H_m.

romagnetic impurities in a material of this resonance system down to the level of internal noise [11]. Control experiments with commercial polycrystalline salts of different metals (both paramagnetic and diamagnetic metals) demonstrated that all these salts contain impurities whose signal exhibits a weak magnetic field hysteresis with the coercive force $H_c \approx 10$–50 Oe. Note that the M_2 and H_c quantities do not depend on temperature in the range 110–350 K. This suggests that impurities form macroscopic, magnetically ordered regions, which can be accomplished in the case of nonuniform distribution of impurities.

The "impurity" signals of M_2 were also observed in the paramagnetic phases of the $Sm_{1-x}Sr_xMnO_3$ samples under consideration. Figure 1 depicts the temperature dependences of the coercive force and the ReM_2 magnitude for the studied samples, which were determined from the unprocessed experimental curves $M_2(H)$ (i.e., in the presence of the impurity signal). The typical experimental dependence of ReM_2 on H with a hysteresis loop is displayed in the inset in Fig. 1. These dependences will be characterized by the following parameters: (i) the signal amplitude at extreme points, (ii) the location of the extreme points H_m in the dc magnetic field (or, to put it differently, on the H-axis), and (iii) the coercive force H_c (see the inset in Fig. 1). The behavior of M_2 was analyzed from the temperature dependences of these parameters. As can be seen from Fig. 1, there is the temperature range in which both parameters H_c and ReM_2 are temperature independent. It seems likely that, in this range, as in the experiments with commercial salts, the signal is induced by magnetic impurities. In order to obtain the signal in the studied compound, this impurity signal was subtracted in the processing of experimental data.

The dc electrical resistivity of the studied samples was measured by the standard four-probe method. The hystereses in the linear susceptibility and the electrical resistivity were investigated in dc magnetic fields up to 500 Oe.

2. RESULTS AND DISCUSSION

2.1. Temperature dependences of the linear susceptibility. The temperature dependences $\chi'(T)$ for the $Sm_{1-x}Sr_xMnO_3$ samples with different degrees of doping were studied in the temperature range 60–230 K. The dependences of $\log\chi'$ on T (Fig. 2) at $H = 0$ are characterized by two temperature range: in one range, the susceptibilities of different samples exhibit a similar behavior, whereas in the other range, the susceptibilities of different samples show strongly different behaviors. The characteristic temperature T_0 that separates these ranges falls in the range 100–130 K for all values of x. At temperatures above T_0, the χ' quantity is a nonmonotonic function of x, and the shape of the $\chi'(T)$ curve is also determined by the doping level. For example, at $T \approx 230$ K, the susceptibility of the sample with $x = 0.3$ is two orders of magnitude less than that of the sample with $x = 0.25$, and the susceptibility of the sample with $x = 0.4$ is intermediate between these values. This behavior of χ' in the paramagnetic phase bears no relation to the above impurities in the studied samples. Indeed, it can be seen from Fig. 1b that ReM_2 monotonically increases with an increase in the strontium concentration; i.e., an increase in the magnetic impurity content does not correlate with the observed dependence $\chi'(x)$. The inset in Fig. 2 demonstrates that, for the $Sm_{0.75}Sr_{0.25}MnO_3$ sample, the dependence $\chi'^{-1}(T)$ in the high-temperature range obeys the Curie–Weiss law $1/\chi = (T + \Theta)/C$ with $\Theta \approx -130$ K, which is characteristic of ferrimagnets and antiferromagnets. At the same time, as the temperature decreases, the susceptibility of the sample with $x = 0.4$ very weakly increases up to $T \approx 120$ K and, then, begins to steeply rise. For the sample with $x = 0.3$, the susceptibility $\chi'(T)$ considerably increases beginning with high tempera-

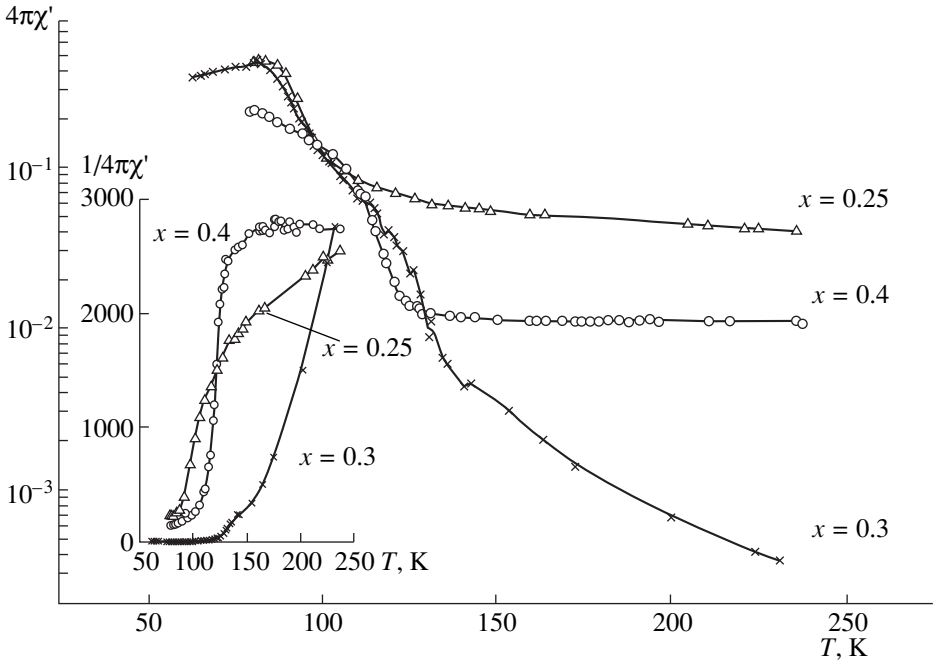

Fig. 2. Temperature dependences of $4\pi\chi'$. The inset shows the dependences of $1/4\pi\chi'$ on T. For convenience of comparison, the values of $1/4\pi\chi'$ are increased by a factor of 100 for the sample with $x = 0.25$ and by a factor of 30 for the sample with $x = 0.4$.

tures, has a nonmonotonic behavior, and, as is seen from Fig. 2, shows inflection points at $T \approx 140$ and 110 K. At temperatures close to T_0, the dependences $\chi'(T)$ for all the samples are virtually coincident and, at $T < T_0$, exhibit a maximum whose location depends on the strontium content.

The experimental determination of the temperature, at which the sample undergoes a transition to the magnetically ordered state, is the most complex problem. In our earlier work [10], the T_c temperatures in simple cubic ferromagnets were determined within the scaling approach, according to which the higher harmonics of magnetization are singular at the Curie point. However, in the studied manganites, the higher harmonics in the low-frequency range were not found, most likely because of their low values (the linear susceptibility itself is rather low). In such complex magnets as manganites, the transition occurs over a rather wide temperature range, and the Curie point is usually taken as either the temperature corresponding to a maximum of the derivative of the susceptibility with respect to temperature (see, for example, [1]) or the temperature of the onset of a sharp increase in the susceptibility (see, for example, [12]). The temperature corresponding to the onset of a sharp increase in the linear susceptibility was taken as the temperature of the magnetic phase transition. Although this definition of the phase transition temperature is evidently conventional in character, it is convenient for comparison of the behavior of the susceptibility in the two aforementioned temperature ranges. The Curie point thus determined is equal to approximately 97 K for the sample with $x = 0.25$ and 130 K for the sample with $x = 0.3$ and virtually coincides with the characteristic temperature T_0 introduced above. The T_c temperature for the sample with $x = 0.4$ is equal to approximately 120 K and agrees with the magnetic ordering temperature obtained in the neutron experiments [6].

In the temperature range 60–230 K, the imaginary component of the susceptibility is rather small in magnitude and can be observed only at high frequencies. The real component of susceptibility virtually does not depend on frequency. Most likely, the imaginary com-

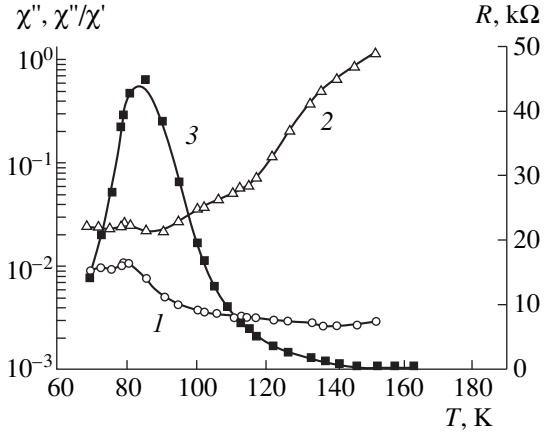

Fig. 3. Temperature dependences of (*1*) χ'', (*2*) $\tan\delta = \chi''/\chi'$, and (*3*) R for the sample with $x = 0.3$.

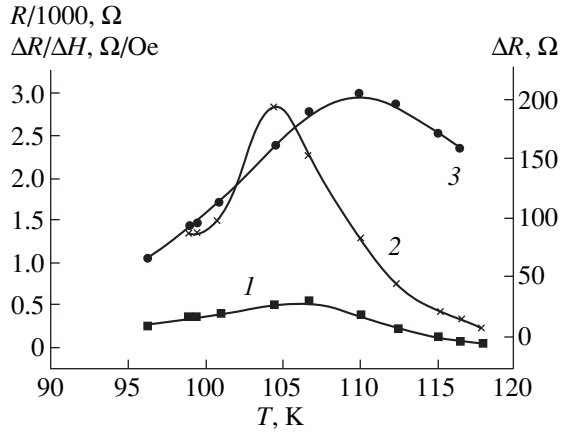

Fig. 4. Fragments of the temperature dependences of (*1*) the difference ΔR between the initial resistivity (at $H = 0$) and the resistivity after returning the dc magnetic field to zero, (*2*) $\Delta R/\Delta H$, and (*3*) R for the sample with $x = 0.4$.

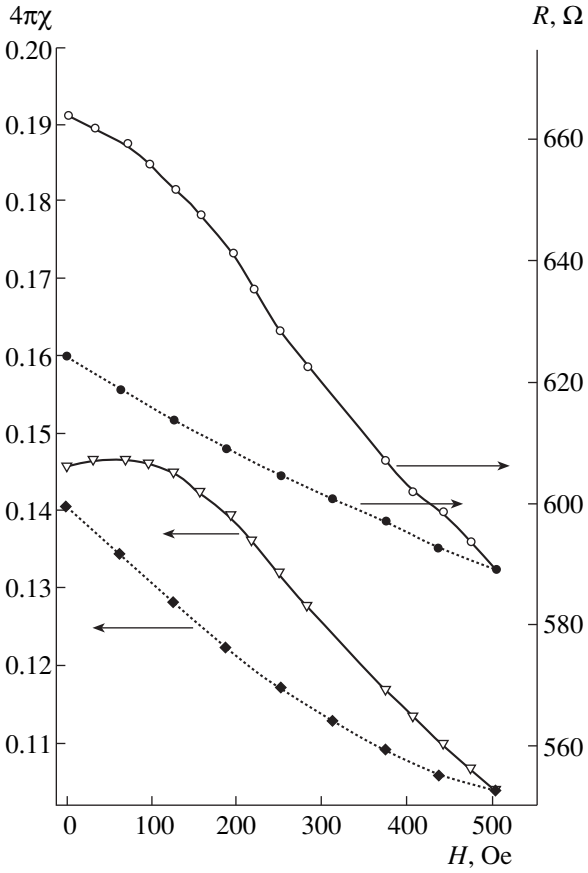

Fig. 5. Hysteresis of the linear susceptibility and the resistivity. Solid lines are the ascending branches, and dashed lines represent the descending branches. Sample with $x = 0.4$.

ponent of susceptibility is predominantly determined by the eddy-current losses in the sample. Indeed, as can be seen from Fig. 3, which depicts the temperature dependences of R, χ'', and $\tan\delta = \chi''/\chi'$ for the sample with $x = 0.3$, a decrease in the loss tangent with a decrease in the temperature correlates with an increase in the resistivity. At the same time, according to the critical retardation phenomenon (an increase in the relaxation time of uniform magnetization at $T \longrightarrow T_c$), the value of $\tan\delta$ should increase as the temperature approaches T_c. Note that the dependence $\chi''(T)$ measured at a frequency of 100 kHz for this sample has a maximum that coincides in temperature ($T \approx 80$ K) with a maximum in the dependence $\chi'(T)$.

2.2. Temperature and field dependences of the resistivity. The resistivity of the samples with $x = 0.3$ and 0.4 was measured in the temperature range 60–300 K. The $R(T)$ curve obtained shows a maximum whose location at T_m also depends on x. The highest resistivity at a maximum is observed for the sample with $x = 0.3$ ($T_m \approx 85$ K, $R(T_m)/R_{300} \approx 10^4$). For the sample with $x = 0.4$, this ratio is one order of magnitude less ($T_m \approx 110$ K). This sample was used to examine in detail the dependence of the resistivity on the dc field. The experimental data demonstrate that, in the magnetic fields from 100 to 500 Oe, the dependence $R(H)$ is virtually linear with $dR/dH \approx 0.4$ Ω/Oe in the vicinity of the maximum in the $R(T)$ curve (an example of this dependence in displayed in Fig. 4). In turn, the dependence of dR/dH on T also exhibits a maximum at $T \approx 107$ K (Fig. 4).

2.3. Hysteresis of the susceptibility and resistivity. The hysteresis phenomena are observed at $T \approx 130$ K for $Sm_{0.7}Sr_{0.3}MnO_3$ and at $T \approx 120$ K for $Sm_{0.6}Sr_{0.4}MnO_3$, i.e., in both cases, virtually at $T \approx T_c$. The magnetic field hystereses of the linear susceptibility and the resistivity were studied in detail for the sample with $x = 0.4$ upon cooling in zero dc field. As an example, Fig. 5 demonstrates the susceptibility and resistivity hysteresis loops. It is of interest that, after returning the field to zero, the susceptibility takes virtually the initial value at $H = 0$, even though the susceptibilities in the ascending and descending branches of the hysteresis loop differ substantially (Fig. 5). At the same time, the resistivity R does not regain its initial values. The temperature dependence of the difference between the initial resistivity R (at $H = 0$) and the resistivity after returning the dc magnetic field to zero also shows a maximum at the temperature that does not coincide with temperatures of the maxima in the dependences $\chi(T)$ and $R(T)$ (Fig. 4).

2.4. Nonlinear phenomena. The appearance of the second harmonic of magnetization M_2 in parallel dc and ac magnetic fields in exchanged magnets with dipole forces is brought about by two factors: the nonlinearity of the magnetization curve and the influence of the ac magnetic field on relaxation processes [13]. As follows from the experimental data, the second factor is insignificant in the studied system. In regard to the nonlinearity of the magnetization curve, in the framework of the perturbation theory, the second harmonic of magnetization M_2 is proportional to $\chi_2(\omega)h_0^2$, where $\chi_2(\omega))$ is the second-order susceptibility with the static limit

$\chi_2(0) = \partial^2 M/\partial H^2$ (M is the static magnetization). Within the simplest relaxation approximation characterized by the relaxation rate Γ, $\chi_2(\omega)$) is described by the Lorentz function. In this case, the real part of the second harmonic of magnetization takes the form $\mathrm{Re}M_2(\omega) = \chi_2(0)/(1 + (2\omega/\Gamma)^2)$, and the imaginary part is given by $\mathrm{Im}M_2 = (2\omega/\Gamma)\mathrm{Re}M_2(\omega)$. From symmetry considerations, it is clear that the M_2 signal in zero external field should be equal to zero when the internal field is absent in a sample. Actually, M_2 is a pseudovector, an even function of h_0, and an odd function of H in the paramagnetic range, and $M_2 = 0$ at $H = 0$. Consequently, M_2 is very sensitive to the appearance of domains with a spontaneous magnetization in a sample, because the dependence of M_2 on H involves the characteristic H hysteresis with $M_2 \neq 0$ at $H = 0$ (see the inset in Fig. 1). Since $M_2 \longrightarrow 0$ at $H \longrightarrow \infty$, at least one extremum should be observed in the dependence $M_2(H)$.

The experiments with the second harmonic of magnetization were carried out in the temperature range 135–230 K. The temperature dependences of the H_c, $\mathrm{Re}M_2$, and H_m parameters (see the inset in Fig. 1a) of the M_2 signal are shown in Fig. 6. The errors in determination of the parameters in this figure are larger than those in Fig. 1 due to the procedure of subtracting the impurity signals. The features of experimental data obtained can be summarized as follows.

(1) The field hysteresis (the coercive force H_c) in the paramagnetic phase is observed in all the compounds. At $T \leq 180$ K, the hysteresis arises in the sample with $x = 0.25$ and 0.3 and at $T \approx 160$ K in the sample with $x = 0.4$, i.e., in all cases, at temperatures appreciably higher than the T_c temperature. It is clear that the appearance of the hysteresis of M_2 in the dc field suggests the formation of macroscopic ferromagnetic (ferrimagnetic) regions (domains) in the paramagnetic phase. Above 155 K, the temperature dependences of the coercive force (Fig. 6a) are approximately identical for all the samples. Apparently, this signifies that both the structure of formed domains and their interaction with the environment are also almost identical in these samples. At lower temperatures, the experimental dependences differ from each other. In particular, the H_c curves have smoothed maxima whose locations depend on the dopant concentration.

(2) Above 150 K, the temperature dependences of $\mathrm{Re}M_2$ are also virtually identical for all the samples (Fig. 6b), whereas their linear susceptibilities differ by several orders of magnitude. In turn, this points to the fact that the formation of new magnetic phase (macroscopic magnetically ordered domains in the paramagnetic matrix) is responsible for the appearance of the M_2 signal.

(3) In the temperature range close to the temperature of the maximum in the dependence $H_c(T)$, the $H_m(T)$ curves show an abrupt change in H_m at various temperatures for different samples (Fig. 6c). This abrupt change correlates with the onset of substantial increase in the M_2 signal (Fig. 6b) and can indicate the completion of forming the domain structure of a new phase, after which its volume begins to increase.

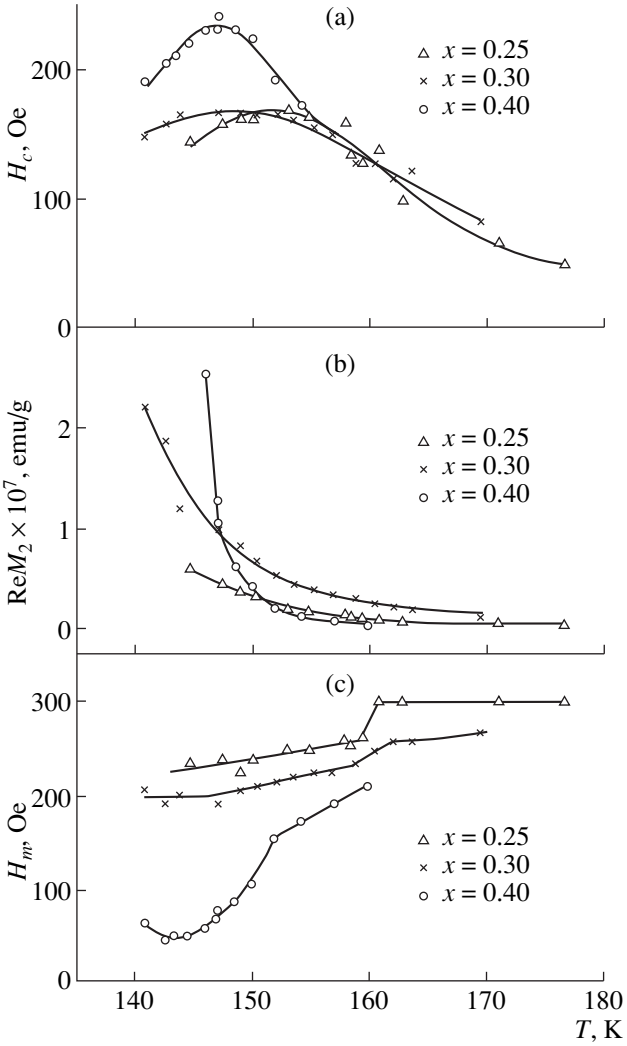

Fig. 6. Temperature dependences of the parameters of the $\mathrm{Re}M_2$ signal after subtraction of the impurity signal: (a) the dependence of the coercive force H_c on T, (b) dependence of the magnitude of $\mathrm{Re}M_2$ on T, and (c) dependence of the location of the signal extremum in the dc magnetic field H_m on T. The errors in determination of the parameters are equal to approximately triple the size of the symbol designating the experimental point.

(4) In our opinion, the monotonic dependence of all the studied parameters of the M_2 signal on x in the temperature range below 150 K as contrasted to the nonmonotonic dependence $\chi(x)$ is of considerable importance. This is a further evidence that the formation of new magnetic phase gives rise to the second harmonic of magnetization. Furthermore, the monotonic dependence on x demonstrates that the change in the concen-

tration of holes (Mn^{+4} centers) appreciably affects the formation of ferromagnetic (ferrimagnetic) domains. Specifically, the rate of change in M_2 with a decrease in the temperature increases as the strontium concentration increases.

It is worth noting that the M_2 signal in the sample with the highest dopant concentration ($x = 0.4$) and the largest content of magnetic impurities (Fig. 1b) is observed up to 170 K, i.e., above the temperature of arising the hysteresis. As follows from the data on $\mathrm{Re}M_2$ with the static limit (Fig. 6), the static properties of ordered domains in all the samples are qualitatively identical, whereas their dynamic behavior is different. Actually, the imaginary component of M_2 is observed only for the sample with $x = 0.3$. Note that the magnitudes of $\mathrm{Im}M_2$ and $\mathrm{Re}M_2$ are virtually equal to each other, and their temperature and field dependences are similar. This implies that, for the sample with $x = 0.3$, the relaxation rate of the magnetic moment of domains contributing to the M_2 signal is comparable to the frequency of the exciting field ($\mathrm{Im}M_2 \sim \omega/\Gamma \mathrm{Re}M_2$). Recall that the largest ratio $R(T_m)/R(300)$ is observed for this sample. Since $\mathrm{Im}M_2$ is not observed for the other samples, it is evident that, in these cases, $\omega/\Gamma \ll 1$.

The experimental results obtained reveal two intriguing features in the behavior of the $Sm_{1-x}Sr_xMnO_3$ manganites. First, the dependence of the linear susceptibility on the strontium concentration is nonmonotonic in the paramagnetic phase. It should be mentioned that a similar nonmonotonic dependence on x is also observed for the temperature $T_c(x)$ and the unit-cell parameter $c(x)$. Second, the field hysteresis in the second harmonic of magnetization arises in the paramagnetic phase. This is likely due to the formation of macroscopic ferromagnetic (ferrimagnetic) domains in the paramagnetic matrix at $T > T_c$. It can be assumed that an increase in the volume of these domains with a further decrease in the temperature gives rise to the magnetic field hysteresis in the susceptibility χ' and the resistivity R at $T \leq T_c$. As follows from the data on $\mathrm{Re}M_2(H, T)$ (Fig. 6), the static properties of ordered domains in all the samples are qualitatively similar, whereas their dynamic behavior is different. Indeed, for the sample with $x = 0.3$ (with the least susceptibility χ' and the largest resistivity R), the relaxation rate of the magnetization turns out comparable to the frequency of the exciting field, and $\Gamma \gg \omega$ for the other two samples. The formation of ferromagnetic (ferrimagnetic) domains can be associated with the electronic phase separation in manganites. This problem is under active study now (see, for example, [14]). The results obtained in this work demonstrate that the concurrent investigations of the linear and nonlinear magnetic phenomena in the paramagnetic phase can provide new and interesting information on physical processes in manganites.

ACKNOWLEDGMENTS

We are grateful to V.A. Trunov, S.V. Maleev, and D.Yu. Chernyshov for their participation in discussions of the results, and I.A. Kiselev for his assistance in performance of experiments.

This work was supported by the Russian Foundation for Basic Research (project no. 97-02-17097) and the State Program "Neutron Investigations of Matter."

REFERENCES

1. F. Damay, N. Nguyen, A. Maignan, *et al.*, Solid State Commun. **98** (11), 997 (1996).
2. G. J. Snyder, C. H. Booth, F. Briges, *et al.*, Phys. Rev. B: Condens. Matter **55** (10), 6453 (1997).
3. S. M. Dunaevskiĭ, A. I. Kurbakov, V. A. Trunov, *et al.*, Fiz. Tverd. Tela (S.-Peterburg) **40** (7), 1271 (1998).
4. R. Maezono, S. Ishihara, and N. Nagaosa, Phys. Rev. B: Condens. Matter **58** (17), 11 583 (1998).
5. S. M. Dunaevskiĭ, A. L. Malyshev, V. V. Popov, *et al.*, Fiz. Tverd. Tela (S.-Peterburg) **39** (10), 1831 (1997).
6. D. Yu. Chernyshov, V. A. Trounov, A. I. Kurbakov, and S. M. Dunaevsky, in *Abstracts of EPDTC-6, Budapest, Hungary, 1998* (Budapest, 1998) p. 223.
7. A. V. Lazuta, V. A. Ryzhov, and T. I. Arbuzova, Physica C (Amsterdam) **295**, 22 (1998).
8. J. Rodriguez-Carvajal, Laboratoire Leon Brillouin, http: //www-llb.cea.fr/fullweb/powder.htm.
9. V. A. Ryzhov, E. I. Zavatskiĭ, V. A. Solov'ev, *et al.*, Zh. Tekh. Fiz. **65** (1), 133 (1995).
10. I. D. Luzyanin and V. P. Khavronin, Zh. Éksp. Teor. Fiz. **85** (3), 1029 (1983).
11. V. A. Ryzhov, I. I. Larionov, and V. N. Fomichev, Zh. Tekh. Fiz. **66** (6), 183 (1996).
12. A. Maignan, C. Martin, F. Damay, *et al.*, Phys. Rev. B: Condens. Matter **58** (5), 2758 (1998).
13. I. I. Larionov, A. V. Lazuta, and V. A. Ryzhov, Zh. Éksp. Teor. Fiz. **100** (6), 1964 (1991).
14. M. R. Ibara and J. V. De Teresa, J. Magn. Magn. Mater. **177–181**, 846 (1998).

Translated by O. Borovik-Romanova

Physics of the Solid State, Vol. 42, No. 2, 2000, pp. 305–307. Translated from Fizika Tverdogo Tela, Vol. 42, No. 2, 2000, pp. 297–299.

MAGNETISM AND FERROELECTRICITY

Effect of Oxygen Non-Stoichiometry on the Antiferromagnet–Ferromagnet Transition in $Nd_{0.5}Ca_{0.5}MnO_{3-\gamma}$ ($\gamma \le 0.12$)

I. O. Troyanchuk*, S. V. Trukhanov*, D. D. Khalyavin*, N. V. Pushkarev*, and G. Szymchak**

**Institute of Solid-State and Semiconductor Physics, Belarussian Academy of Sciences, ul. Brovki 17, Minsk, 220072 Belarus*
***Institute of Physics, Polish Academy of Sciences, Warsaw, 02-668 Poland*
e-mail: troyan@ifft.bas-net.by

Received June 29, 1999

Abstract—A decrease in the oxygen content in $Nd_{0.5}Ca_{0.5}MnO_{3-\gamma}$ down to $\gamma \le 0.12$ is shown to bring about a strong decrease in the magnetic field inducing a transition from the antiferromagnetic charge-ordered to the ferromagnetic charge-disordered state. The ferromagnetic phase in a $Nd_{0.5}Ca_{0.5}MnO_{2.92}$ sample is stable in the absence of an external magnetic field. A further increase in the content of oxygen vacancies stabilizes the antiferromagnetic charge-disordered state. © *2000 MAIK "Nauka/Interperiodica".*

The manganites of lanthanum and rare-earth ions have attracted considerable attention because of an intimate connection between the magnetic, orbital, and charge orderings and the electrical properties [1–4]. These compounds exhibit "colossal" magnetoresistance effects differing in nature. An effect of one type is observed near T_C in ferromagnetic samples, and another type of this effect originates from "melting" of the charge-ordered phase (the phase in which the Mn^{3+} and Mn^{4+} ions are ordered) when subjected to an external magnetic field [2, 4]. In the effect of the latter type, the electrical resistivity can change by ten or even more orders of magnitude. Charge ordering was found in the $La_{1-x}Ca_xMnO_3$ ($x \ge 0.5$), $Pr_{1-x}Ca_xMnO_3$ ($x > 0.3$), and $Nd_{1-x}Ca_xMnO_3$ ($x > 0.3$) phases and the $Nd_{0.5}Sr_{0.5}MnO_3$ compound. The magnetic phase diagrams of $Ln_{1-x}Ca_xMnO_3$ (Ln = Pr, Nd; $0.3 \le x \le 0.5$) were constructed from the measurements in pulsed magnetic fields up to 50 T [5]. According to the data obtained for $Nd_{0.5}Ca_{0.5}MnO_3$, the transition from the antiferromagnetic to the ferromagnetic state is induced by a magnetic field of the order of 30 T. This field varies relatively weakly with temperature down to the charge-ordering point near $T_{CO} = 260$ K. Long-range antiferromagnetic order sets in at $T_N = 180$ K. At the temperature T_{CO}, one observes a sharp maximum in the magnetic susceptibility, which is due apparently to a reversal of the type of short-range magnetic order from antiferromagnetic (low-temperature phase) to ferromagnetic. The magnetic properties of manganites are known to depend strongly on the extent of oxygen stoichiometry. A decrease in the oxygen content in $LaMnO_{3-\gamma}$ brings about destruction of the ferromagnetic ordering [6]. The effect of deviation from oxygen stoichiometry on the charge-ordered state in manganites is not known. In this respect, we have carried out the investigation of the magnetic properties of $Nd_{0.5}Ca_{0.5}MnO_3$ as a function of oxygen content.

1. EXPERIMENTAL

A sample of $Nd_{0.5}Ca_{0.5}MnO_3$ was prepared by the conventional ceramic technology of high-purity grade Nd_2O_3 and MnO_2 oxides and $CaCO_3$ carbonate mixed in the stoichiometric ratio. The precalcination was carried out at 950°C, and the synthesis, at 1500°C in air. The sample was cooled to room temperature at a rate of 80 K/h in order to obtain the compound stoichiometric in oxygen.

The oxygen content was determined by thermogravimetric analysis (high-temperature reduction to the metallic form in a hydrogen flow). X-ray diffraction analysis performed on a DRON-3 diffractometer with CoK_α radiation did not reveal the presence of foreign phase. The magnetic measurements were done on a FONER vibration magnetometer. The samples were reduced in quartz ampules at 800°C using metallic tantalum as oxygen getter. The samples were weighed both before and after the reduction.

2. RESULTS

According to the thermogravimetric analysis, the $Nd_{0.5}Ca_{0.5}MnO_3$ sample cooled at a rate of 80 K/h is stoichiometric in oxygen. The sample has an orthorhombically distorted unit cell. The orthorhombic distortions and the unit-cell volume increased with a decrease in the oxygen content. The increase in the vol-

1063-7834/00/4202-0305$20.00 © 2000 MAIK "Nauka/Interperiodica"

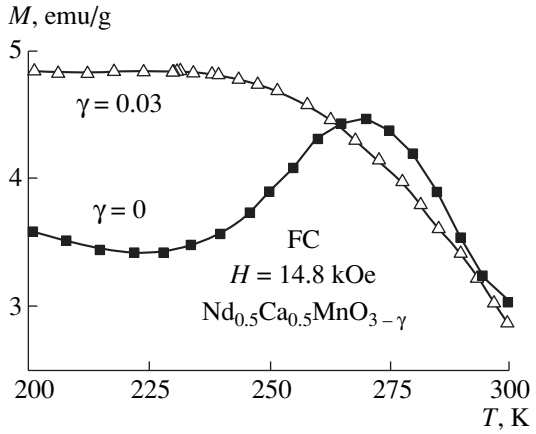

Fig. 1. Temperature dependence of the magnetization of $Nd_{0.5}Ca_{0.5}MnO_{3-\gamma}$ samples for $\gamma = 0$ and 0.03.

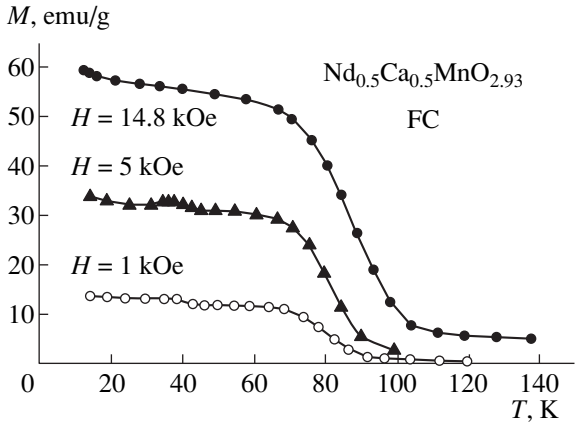

Fig. 2. Temperature dependence of the magnetization of a $Nd_{0.5}Ca_{0.5}MnO_{2.93}$ sample.

ume is due to the transition of manganese ions from the quadrivalent to trivalent state. The ionic radius of the trivalent manganese is considerably larger than that of the quadrivalent species. We have not succeeded in obtaining samples with an oxygen deficiency larger than $\gamma = 0.17$ at 800°C. All the samples with $\gamma \le 0.17$ were single phase and, when oxidized, exhibited properties similar to those of the stoichiometric $Nd_{0.5}Ca_{0.5}MnO_3$.

Figure 1 presents the results of the magnetization measurements performed on the samples with $\gamma = 0$ and 0.03. The sample with $\gamma = 0$ has a magnetization peak in the vicinity of 255 K. A noticeable temperature hysteresis indicates a first-order phase transition. The sample with $\gamma = 0.03$ does not exhibit anomalous behavior of the magnetic properties. Since the magnetization peak at 255 K is due to a charge ordering, it can be assumed that the long-range charge order in the sample with $\gamma = 0.03$ is destroyed.

We did not find anomalous behavior in the magnetic properties associated with charge ordering in any sample with $\gamma \ge 0.03$. However, in samples with $0.05 \le \gamma \le 0.12$, a sharp growth of magnetization is observed below 100 K, which is apparently due to the onset of long-range ferromagnetic ordering. Figure 2 presents the magnetization versus temperature curves measured on the sample with $\gamma = 0.08$ in fields of 1, 5, and 15 kOe. The ferromagnetic transition temperature in 1- and 5-kOe fields lies near 90 K, whereas, at 15 kOe, the transition was observed above 100 K. However, the magnetization measured at 15 kOe (2.6 μ_B per formula unit) is less than the value (3.5 μ_B per formula unit) calculated assuming parallel ordering of the manganese-ion magnetic moments. Figure 3 shows the field dependences of magnetization taken after cooling in zero magnetic field. The field dependences of magnetization exhibit a strong hysteresis originating from a metamagnetic transformation (because the hysteresis increases with the field). The metamagnetic transition is irreversible, because, when repeating the measurements at the same temperature, but with the opposite field direction, the field hysteresis becomes substantially smaller or disappears altogether. At helium temperatures, no metamagnetic behavior was observed. The lowest critical fields inducing the ferromagnetic phase were found near T_C.

As the oxygen-vacancy content increases up to $\gamma = 0.12$, the ferromagnetic behavior becomes less pronounced. In samples with $\gamma > 0.13$, no sharp anomalies in the magnetic properties were observed.

The properties of manganites are usually interpreted in terms of the double-exchange theory, by which the ferromagnetism originates from carrier transitions between ions in different valence states [7]. However, this theory is not capable of accounting for many properties of the manganites [8, 9]. Therefore, we will invoke the mechanism of superexchange interactions between manganese ions in the perovskites [10]. By this mechanism, the exchange interaction between the

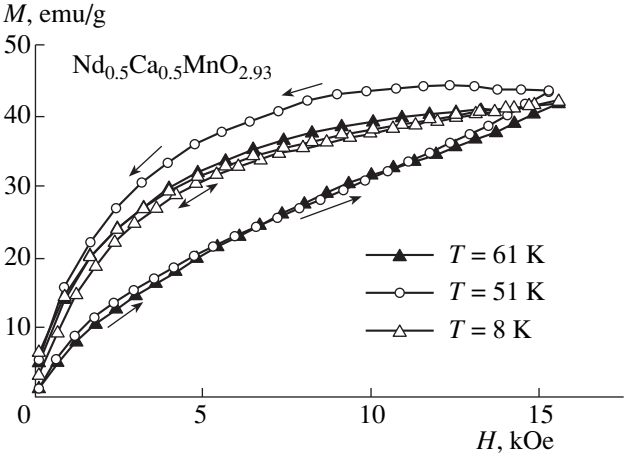

Fig. 3. Field dependence of the magnetization of a $Nd_{0.5}Ca_{0.5}MnO_{2.93}$ sample.

trivalent manganese ions in octahedral positions is anisotropic in the case of orbital ordering (charge ordering in the manganites is always accompanied by an ordering of the Mn^{3+} ion orbitals) and ferromagnetic in the orbitally disordered phase. The exchange interaction between quadrivalent manganese ions is always antiferromagnetic, whereas the exchange interaction between the manganese ions differing in the valence state depends on a number of factors, for example, the Mn–O–Mn angle, the Mn^{3+}/Mn^{4+} ratio, etc. The higher the content of the quadrivalent manganese in a system is, the stronger the antiferromagnetic exchange interactions are. Oxygen vacancies result in a transfer of part of the quadrivalent manganese ions to the trivalent state. This brings about violation of the symmetry in the Mn^{4+} and Mn^{3+} arrangement, thus destroying the charge ordering.

The appearance of excess trivalent manganese results in an enhancement of the ferromagnetic part of the exchange interactions. However, a uniform ferromagnetic state does not form. This can be understood from the following considerations. It is known that $Ca^{2+}Mn^{3+}O_{2.5}$, which has a perovskite-like structure with the trivalent manganese occupying the pentahedra, is an antiferromagnet [11]. Therefore, the exchange interaction between Mn^{3+}–O–Mn^{3+} in the pentahedral coordination is antiferromagnetic. In the $Nd_{0.5}Ca_{0.5}MnO_{3-\gamma}$ composition with a large content of oxygen vacancies, this negative interaction is dominant, which precludes formation of a uniform ferromagnetic state. Within the $0.05 < \gamma \leq 0.12$ concentration interval, the system consists of a ferromagnetic matrix, in which antiferromagnetic clusters with short-range order in the Mn^{3+} and Mn^{4+} ion arrangement are embedded. When placed in an external magnetic field, these clusters transfer gradually to the ferromagnetic state. The metamagnetic transition is diffuse in temperature because of the clusters being distributed nonuniformly in size and composition. It should be pointed out that substitution of iron, titanium, aluminum, cobalt, and nickel ions for part of the manganese ions also reduces the critical fields inducing the ferromagnetic transition [12]. However, in the absence of an external field, doping with these ions does not result in the ferromagnetic state.

ACKNOWLEDGMENTS

This work was supported in part by the Foundation for Basic Research of the Republic of Belarus, grant F98-056.

REFERENCES

1. Z. Jirak, S. Krupicka, Z. Simsa, *et al.*, J. Magn. Magn. Mater. **53**, 153 (1985).
2. P. G. Radaelli, D. E. Cox, M. Marezio, *et al.*, Phys. Rev. B: Condens. Matter **55**, 3015 (1997).
3. C. H. Chen and S.-W. Cheong, Phys. Rev. Lett. **76**, 4042 (1996).
4. Y. Tomioka, A. Asamitsu, H. Kuwahara, *et al.*, Phys. Rev. B: Condens. Matter **53**, 1689 (1996).
5. M. Tokunaga, N. Miura, Y. Tomioka, *et al.*, Phys. Rev. B: Condens. Matter **57**, 5259 (1998).
6. I. O. Troyanchuk, S. N. Pastushonok, A. K. Bogush, *et al.*, Phys. Stat. Sol. B(a) **118**, K111 (1990).
7. C. Zener, Phys. Rev. **82**, 403 (1951).
8. É. L. Nagaev, Usp. Fiz. Nauk **166**, 833 (1966).
9. I. O. Troyanchuk, Zh. Éksp. Teor. Fiz. **102**, 251 (1992).
10. J. B. Goodenough, A. Wold, R. J. Arnott, *et al.*, Phys. Rev. **124**, 373 (1961).
11. K. R. Poppelmeier, M. E. Leonowicz, and J. M. Longo, J. Solid State Chem. **45**, 71 (1982).
12. B. Raveau, A. Maignan, and C. Martin, J. Solid State Chem. **130**, 162 (1997).

Translated by G. Skrebtsov

Physics of the Solid State, Vol. 42, No. 2, 2000, pp. 308–314. Translated from Fizika Tverdogo Tela, Vol. 42, No. 2, 2000, pp. 300–306.

MAGNETISM AND FERROELECTRICITY

Spin-Reorientational Phase Transitions and Magnetoelastic Solitons in an Antiferromagnet with Magnetoelastic Coupling

M. A. Shamsutdinov*, A. T. Kharisov*, and A. P. Tankeev**

**Bashkortostan State University, ul. Frunze 32, Ufa, Bashkortostan, 450074 Russia*
***Institute of Metal Physics, Ural Division, Russian Academy of Sciences, ul. S. Kovalevskoĭ 18, Yekaterinburg, 620219 Russia*

Received May 6, 1999; in final form, July 15, 1999

Abstract—The influence of mechanical stresses and electric and magnetic fields is theoretically investigated on the ground state and the characteristics of linear and nonlinear magnetoelastic waves in a tetragonal antiferromagnet. Magnetic phase diagrams are constructed and the parameters of quasi-acoustic solitons and the region of their stability are determined. © *2000 MAIK "Nauka/Interperiodica".*

INTRODUCTION

In antiferromagnets (AFMs) with magnetoelectric interaction, the electric and magnetic subsystems are coupled, so that the magnetic properties can be changed by applying an electric field and, *vice versa*, the electric properties can be varied by applying a magnetic field [1]. It was found [2] that, in a ferroelectric magnet, the gap in the spin-wave spectrum becomes anisotropic due to magnetoelastic coupling in the case where the antiferromagnetic structure is homogeneous. The magnitude of magnetoelectric effects was shown in [3] to depend crucially on the orientation of the electric and magnetic fields with respect to each other and on the type of magnetic anisotropy. The relative magnitude of acoustic double refraction due to the magnetoelectric effect may be as large as several percentage points. In [4, 5], conditions were found under which additional effective nonlinear elastic moduli appear, which are nonzero only when both a magnetic and an electric field are applied to the material. It was emphasized in the papers mentioned above that the magnetoelectric effects were enhanced near magnetic orientational phase transitions. However, for these effects to be observed, the electric and magnetic fields must be fairly strong. It was also pointed out that a wide variety of nonlinear effects are possible in centroantisymmetric AFMs. A consistent group-theoretic description of tetragonal AFMs was first given by E.A. Turov and his disciples [1, 3–5], which has allowed us to investigate the influence of electric and magnetic fields on the ground state of the magnetoelastic subsystem of these AFMs and on the conditions for the existence of magnetoelastic solitons. In the present paper, this symmetry-based method is also used to investigate nonlinear effects. Nonlinear magnetoelastic waves in magnets without magnetoelectric coupling were treated, e.g., in [6–9]. It is known that directional compression is favorable to an orientational phase transition [10], which may enhance the magnetoelectric effect. In this paper, we investigate the influence of an electric (**E**) and a magnetic (**H**) field on the ground state and stability of magnetoelastic solitons in tetragonal AFMs with easy-plane anisotropy in the vicinity of a magnetic phase transition with varying pressure, in particular.

1. ENERGY DENSITY. SPIN-REORIENTATIONAL PHASE TRANSITIONS

Let us consider an infinite tetragonal two-sublattice AFM with easy-plane anisotropy. We will derive the basic equations starting from the free-energy density F that includes the magnetic, elastic, magnetoelastic, electric-polarization, and magnetoelectric energies [4]:

$$F = F_m + F_e + F_{le} + F_p + F_{mp}, \tag{1}$$

where

$$F_m = 2M_0H_E\mathbf{m}^2 - 2M_0\mathbf{mH} + \frac{1}{2}Kl_z^2 + \frac{1}{2}K_2l_x^2l_y^2 + \frac{1}{2}A\left(\frac{\partial l_i}{\partial x_k}\right)^2,$$

$$F_e = \frac{1}{2}C_{11}(e_{xx}^2 + e_{yy}^2) + C_{12}e_{xx}e_{yy} + C_{13}(e_{xx} + e_{yy})e_{zz} + \frac{1}{2}C_{33}e_{zz}^2 + 2C_{44}(e_{xz}^2 + e_{yz}^2) + 2C_{66}e_{xy}^2 - \sigma_{ik}e_{ik},$$

$$F_{le} = B_{11}(l_x^2e_{xx} + l_y^2e_{yy}) + B_{12}(l_x^2e_{yy} + l_y^2e_{xx}) + B_{13}(e_{xx} + e_{yy})l_z^2 + B_{31}e_{zz}(l_x^2 + l_y^2) + B_{33}e_{zz}l_z^2 + 2B_{44}l_z(e_{xz}l_x + e_{yz}l_y) + 2B_{66}e_{xy}l_xl_y,$$

$$F_p = \frac{1}{2\kappa_\perp}(P_x^2 + P_y^2) + \frac{1}{2\kappa_\parallel}P_z^2 - \mathbf{PE},$$

$$F_{mp} = -2M_0[\gamma_2(l_xP_x + l_yP_y)m_z + \gamma_3(m_xP_x + m_yP_y)l_z + \gamma_4(l_xm_x + l_ym_y)P_z + \gamma_5 l_z m_z P_z].$$

The expression for F_{mp} corresponds to an AFM with a positive-parity magnetic structure $\bar{1}^-4_z^+2_d^- \equiv \bar{1}^-4_z^+2_x^-$. In the expressions presented above, H_E is the exchange field; **m** and **l** are the ferromagnetism and antiferromagnetism vectors, respectively; M_0 is the saturation magnetization of the sublattices; $K > 0$ and K_2 are the magnetic anisotropy constants; A is the exchange stiffness parameter; e_{ik}, C_{ik}, and B_{ik} are the strain tensor components and the elastic and magnetoelastic constants, respectively; σ_{ik} is the external elastic stress tensor; **u** is the elastic displacement vector of an element of the medium; $\kappa_\perp$ and $\kappa_\parallel$ are the electric-polarization constants; γ_i are the magnetoelectric constants; and **P** is the electric-polarization vector.

Let a magnetic field **H** be applied along the z axis, parallel to the C_4 symmetry axis. The electric field **E** lies in the easy plane along the 2_d^- axis, i.e., along the angle bisector between the x and y axes. In this geometry, our results are true for both the positive- and negative-parity magnetic structures of AFMs. The uniaxial stress σ ($\sigma < 0$ corresponds to compression and $\sigma > 0$, to tension) is applied along **E** or perpendicular to it in the easy plane. These directions of the fields **E** and **H** and of the elastic stress σ correspond to a maximum magnitude of the linear magnetoelectric effect. For further consideration, it is convenient to introduce another coordinate frame that is obtained by rotation of the xy plane through an angle $\pi/4$ in the basal plane, i.e., a frame with the x' axis along the 2_d^- axis.

The applied magnetic field is assumed to be much lower than the field at which the sublattices flop over. Therefore, we have $|\mathbf{m}| \ll |\mathbf{l}| \approx 1$. The vector **l** lies in the basal plane in the ground state at $K > 0$; hence, we may write $\mathbf{l} = l(\cos\chi, \sin\chi, 0)$, where χ is the angle between **l** and the x' axis.

Minimizing the free energy density F with respect to the electric polarization **P**, the ferromagnetism vector **m**, and the elastic strain, the following expression is obtained for the free energy in the equilibrium state:

$$F_0 = -M_0H_{ms6} \times \left(eh\cos\chi_0 + \frac{1}{2}\tau\cos 2\chi_0 - \frac{k_2^*}{8}\cos 4\chi_0\right), \quad (2)$$

where

$$H_{ms6} = \frac{B_{66}^2}{2M_0C_{66}}, \quad k_2^* = \frac{K_2^*}{2M_0H_{ms6}},$$

$$K_2^* = K_2 + 2M_0(H_{ms} - H_{ms6}),$$

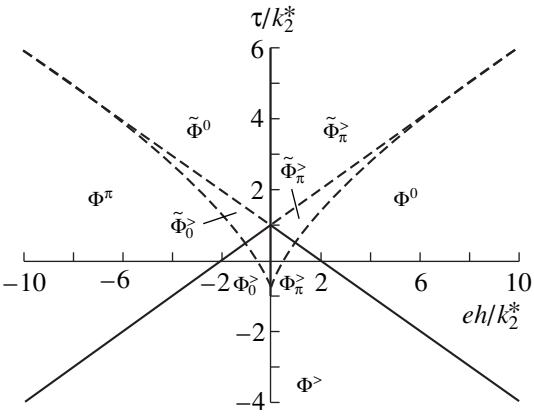

Fig. 1. Magnetic phase diagram for $K_2^* > 0$: bold solid lines are phase transition lines; Φ^0 and Φ^π are symmetric phases; $\Phi^>$, $\Phi_0^>$, and $\Phi_\pi^>$ are doubly degenerate canted phases; dashed lines indicate the boundaries of the metastable phases (marked with tilde).

K_2^* is the magnetostriction-renormalized magnetocrystalline anisotropy constant in the basal plane; $H_{ms} = b^2/[M_0(C_{11} - C_{12})]$ is the magnetostriction field; $b = B_{11} - B_{12}$; and e, h, and τ are the reduced electric and magnetic fields and stress, respectively,

$$e = \gamma_2\kappa_\perp E/H_{ms6}, \quad h = H/H_E, \quad \tau = \sigma\delta/2B_{66}.$$

When the stress σ is applied along **E**, we have $\delta = -1$, but when it is perpendicular to **E**, $\delta = 1$. One of these configurations can be conveniently chosen for experimental measurements.

The angle χ_0 in an equilibrium state is determined by the equation

$$2eh\sin\chi_0 + 2\tau\sin 2\chi_0 - k_2^*\sin 4\chi_0 = 0. \quad (3)$$

The condition for the stability of the ground state with $\chi_0 = 0$ is given by the inequalities

$$2(\tau - k_2^*) + eh \geq 0, \quad eh > 0. \quad (4)$$

Figure 1 shows an eh–τ magnetic-phase diagram for a tetragonal AFM in the case of $K_2^* > 0$. It is seen that, at $\tau/k_2^* > 1$, the symmetric phase Φ^0 with $\chi_0 = 0$ is absolutely stable when $\gamma_2 EH > 0$ and the phase Φ^π with $\chi_0 = \pi$ is absolutely stable when $\gamma_2 EH < 0$. The transition between these phases is of the first order. At $\tau/k_2^* < 1$, the symmetric phase Φ^0 is stable in fairly high electric and magnetic fields. The equality sign of (4) corresponds to the line along which the phase Φ^0 loses its stability. The canted phase is doubly degenerate (when the canted phase χ_0 is stable, the canted phase $2\pi - \chi_0$ is also stable), and the transition between this phase and the symmetric phase is of the second order. In the eh–τ

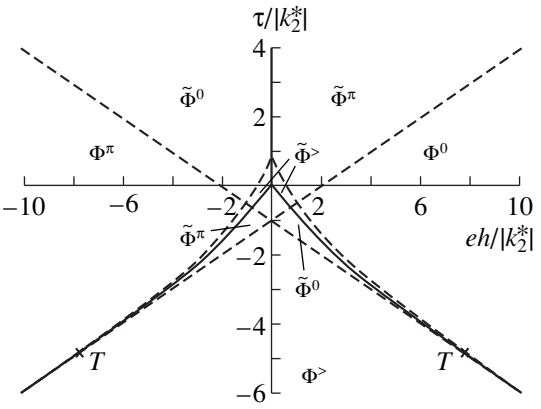

Fig. 2. Magnetic phase diagram for $K_2^* < 0$: the notation as in Fig. 1; *T* are tricritical points.

plane, the point $eh = 0$, $\tau/k_2^* = -1$ corresponds to an ordinary critical point [11]. When $\tau/k_2^* < -1$, the angle χ_0 in the canted phase $\Phi^>$ changes from 0 to π continuously. When $\tau/k_2^* > -1$, the canted phase $\Phi^>$ is represented by two canted phases, $\Phi_0^>$ and $\Phi_\pi^>$, in which the angle χ_0 varies from 0 to $(\pi - \varphi_0)/2$ and from $(\pi + \varphi_0)/2$ to π, respectively. Here, φ_0 changes from 0 to π as τ/k_2^* increases from –1 to 1. The transition between these canted phases is of the first order. The regions of existence of metastable canted phases $\tilde{\Phi}_\pi^>$ and $\tilde{\Phi}_0^>$ expand to the points $eh/k_2^* = \pm 8$ and $\tau/k_2^* = 5$ in the eh–τ plane. The lines separating the regions of the metastable canted phases and those of the stable phases are defined by the equations $eh/k_2^* = \pm(2(\tau/k_2^* + 1)/3)^{3/2}$; the regions of the metastable canted and metastable symmetric phases are separated by lines defined by $eh/k_2^* = \pm 2(\tau/k_2^* - 1)$.

Figure 2 shows an eh–τ diagram for $K_2^* < 0$. The transition between the symmetric phases Φ^0 and Φ^π is of the first order, as in the case of $K_2^* > 0$. However, the transition between the symmetric and canted phases differs from that at $K_2^* > 0$; namely, the former transition is of the second order at $\tau/k_2^* < -5$ and of the first order at $\tau/k_2^* > 5$. Two points (±8, –5) in the eh–τ plane (denoted *T* in Fig. 2) are tricritical points. In the canted phase $\Phi^>$, the angle χ_0 changes from 0 to π continuously at $\tau/k_2^* < -5$, whereas at $\tau/k_2^* > -5$, the angle χ_0 changes from $\varphi_0/2$ to $\pi - \varphi_0/2$. Here, φ_0 varies from 0 to π as τ/k_2^* increases from –5 to 0. The lines separating the regions of the metastable phases, are defined by the equations $eh/k_2^* = \pm(2(1 - \tau/k_2^*)/3)^{3/2}$ and $eh/k_2^* = \pm 2(\tau/k_2^* + 1)$.

2. MAGNETOELASTIC WAVES AND SOLITONS

Let us now consider the effect of external fields and stresses on the spectrum of magnetoelastic waves. The excitation of electric-polarization waves will be ignored; hence, the electric-polarization vector **P** follows magnetoelastic oscillations in a quasi-equilibrium manner. We also neglect damping in the spin and elastic subsystems.

Let us consider waves propagating along the *x*' axis (**k**||*x*'). Starting from the Landau–Lifshitz equation and the equation of motion of an elastic medium, we arrive at the dispersion relation

$$\left[(\omega^2 - c^2k^2 - \omega_{AF}^2)(\omega^2 - S_{44}^2k^2) - \frac{\gamma^2 H_E B_{44}^2 \cos^2\chi_0}{\rho M_0}k^2\right]$$
$$\times\left[(\omega^2 - c^2k^2 - \omega_{QF}^2)(\omega^2 - S_1^2k^2)(\omega^2 - S_2^2k^2)\right.$$
$$-(\omega^2 - S_1^2k^2)\frac{\gamma^2 H_E b^2 \cos^2 2\chi_0}{\rho M_0}k^2$$
$$\left.-(\omega^2 - S_2^2k^2)\frac{\gamma^2 H_E B_{66}^2 \sin^2 2\chi_0}{\rho M_0}k^2\right] = 0,$$

where $c = \gamma\sqrt{AH_E/M_0}$ is the minimum phase velocity of spin waves; ρ is the density of the medium; γ is the gyromagnetic ratio; $S_{ii}^2 = C_{ii}/\rho$ with $i = 4, 6$; $S_1^2 = (C_{11} + C_{12} + 2C_{66})/2\rho$; $S_2^2 = (C_{11} - C_{12})/2\rho$; e_{ik}^0 are spontaneous strains [10]. The solution of this dispersion relation gives five branches of the spectrum: an antiferromagnetic branch with a gap ω_{AF} and a quasi-ferromagnetic branch with a gap ω_{QF}, where

$$\omega_{AF} = \gamma\left\{\frac{H_E}{2M_0}(2K - K_2\cos^2 2\chi_0) + H^2\right.$$
$$+ \kappa_\perp(3\gamma_2 + 2\gamma_3)EH\cos\chi_0 - \frac{H_E}{M_0}[2(B_{31} - B_{33})e_{zz}^0$$
$$+ (B_{11} + B_{12} - 2B_{13})(e_{xx}^0 + e_{yy}^0)$$
$$\left.+ 2B_{66}e_{xy}^0\cos 2\chi_0 - b\sin 2\chi_0(e_{xx}^0 - e_{yy}^0)]\right\}^{1/2},$$

$$\omega_{QF} = \gamma\left\{2H_E H_{ms6}\left[\frac{H_{ms}}{H_{ms6}}\cos^2 2\chi_0 + \sin^2 2\chi_0 + \frac{1}{2}eh\cos\chi_0 + \tau\cos 2\chi_0 - k_2^*\cos 4\chi_0\right]\right\}^{1/2} \quad (5)$$

and three quasi-acoustic branches with velocities $\nu_{x'}$, $\nu_{y'}$, and ν_z, corresponding to waves polarized along the x', y', and z axes, respectively (their expressions are too cumbersome to be presented here). We will analyze the frequencies of only those waves that are significantly affected by the stress and magnetic and electric fields. In the symmetric phase Φ^0, the frequency squared of a quasi-acoustic wave polarized along the y' axis is

$$\omega^2 = S^2k^2 + rk^4, \quad (6)$$

where

$$S^2 = S_2^2\left(1 - \frac{\omega_{ms}^2}{\omega_0^2}\right), \qquad r = \frac{\omega_{ms}^2}{\omega_0^4}(c^2 - S^2)S_2^2. \quad (7)$$

Here, $\omega_0 = \omega_{QF}$ ($\chi_0 = 0$) is the gap in the quasi-ferromagnetic spectrum branch of spin waves in the symmetric phase. The minimum value of the frequency ω_0 at the phase-transition point is the so-called magnetoelastic gap for magnons [10]:

$$\omega_{0\min} = \omega_{ms} = \gamma\sqrt{2H_E H_{ms}}.$$

As the phase transition point is approached by varying the electric field (at fixed magnitudes of the stress and magnetic field), the velocity $\nu_{y'} = S$ of a transverse quasi-acoustic wave can be decreased to zero. In AFMs with a low Neel temperature, the situation may take place where, far from the phase transition point, the velocity of a quasi-acoustic wave S is higher than the minimum phase velocity c of spin waves. Then, as the phase transition point is approached, the situation may become opposite. In this case, the dispersion r of the transverse quasi-acoustic mode changes sign, which allows the magnetoelastic-soliton stability to be controlled by the electric field, as will be shown later.

Let us consider the case of $K_2^* > 0$ and $\tau/k_2^* < 1$, where the transition from the canted phase to the symmetric one is of the second order, as shown above. If $\tau/k_2^* \approx 1$, this transition occurs, when the electric and magnetic fields are varied, at practically attainable fields. Figure 3 shows the quasi-ferromagnetic-branch frequency ω_{QF} (curve *1*), the velocity $\nu_{y'}$ of a quasi-acoustic wave polarized along the y' axis (curve *2*), and the acoustic double-refraction coefficient $\beta = (\nu_z - \nu_{y'})/\nu_z$ (curve *3*) as functions of the electric and magnetic fields for $\tau/k_2^* = 0.8$. It is seen that, in the vicinity of the phase transition when the stress is varied, the double-refraction coefficient may be changed over a wide range with an electric or a magnetic field. Since there are, as far as we know no magnetoelectric crystals, for which all parameters required of our calculations were measured experimentally, we have used typical values of the crystal parameters: $M_0 \approx 150$ G; $H_E \approx 150$ kOe; $\rho \approx 5$ g/cm^3; $c \approx 2\times10^5$ cm/s; $b \approx B_{66} \approx 5\times10^6$ erg/cm^3; $C_{11} \approx 2.2\times10^{12}$ erg/cm^3; $C_{12} \approx 0.8\times10^{12}$ erg/cm^3; $C_{66} \approx 0.5\times10^{12}$ erg/cm^3; $K_2^* \approx 10^3$ erg/cm^3; and $\gamma_2\kappa_\perp \approx 0.3$ (the last value corresponds to the magnetoelastic susceptibility equal to $\alpha \approx 3\times10^{-4}$; the reduced unit of the electric field e is equal, in SI units, to about 10 kV/m in this case).

Now, we will consider nonlinear magnetoelastic excitations from the ground state with $\chi_0 = 0$ propagating along the x' axis. The prime on the coordinates will be dropped in what follows. We restrict our consideration to the frequency range $\omega \ll \sqrt{2H_E H_A}$, where $H_A = K/2M_0$, which allows one to neglect the excitation of the antiferromagnetic spectrum branch of spin waves. In this case, the Lagrangian density has the form

$$L = \frac{M_0}{2\gamma^2 H_E}(\chi_t^2 - c^2\chi_x^2) + M_0 H_{ms6}\left(eh\cos\chi + \frac{1}{2}(1+\tau)\cos 2\chi - \frac{1}{8}k_2\cos 4\chi\right) - \frac{1}{2}bu_{xy}\sin 2\chi$$

$$-\frac{1}{2}B_{66}u_{xx}\cos 2\chi - \frac{1}{2}\rho(S_1^2u_{xx}^2 + S_{44}^2u_{xz}^2 + S_2^2u_{xy}^2 - \mathbf{u}^2).$$

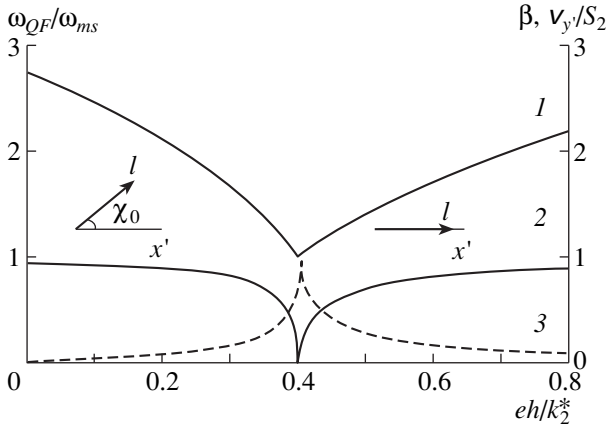

Fig. 3. Quasi-ferromagnetic-branch frequency (curve *1*), quasi-acoustic-branch velocity $\nu_{y'}$ (curve *2*), and double-refraction coefficient β (curve *3*) as functions of the electric e and magnetic h fields for $\tau/k_2^* = 0.8$.

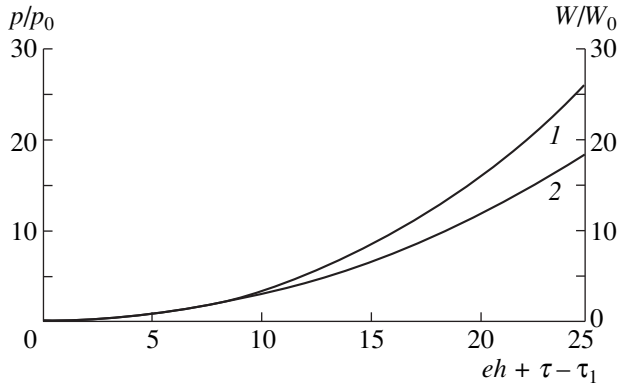

Fig. 4. Momentum (curve *1*) and energy (curve *2*) of a soliton as functions of the quantity $\tau - \tau_1 + eh$.

Here, $u_{xi} = \partial_{ui}/\partial x$, $(i = x, y, z)$ are deviations of the strain tensor components from their values in the ground state, and $k_2 = K_2/2M_0H_{ms6}$.

When considering the coupling of quasi-acoustic waves, we assume that the sublattice magnetization follows elastic-strain variations in a quasi-equilibrium manner. In this case, a reductive perturbation theory can be applied by introducing stretched coordinates [12]. Starting from the Euler–Lagrange equations in which nonlinear terms are kept up to the third order in small deviations χ and u_{xi}, we arrive at the modified Korteweg–de Vries (MKdV) equation for the transverse component of the strain tensor, $U \equiv u_{xy}$,

$$2S\frac{\partial U}{\partial t} - r\frac{\partial^3 U}{\partial \zeta^3} + q\frac{\partial}{\partial \zeta}U^3 = 0,$$

$$q = \frac{5b^4\gamma^8 H_E^4 H_{ms6}}{2\rho M_0^3 \omega_0^8}\left[eh + \frac{8}{5}\left(\tau + 1 - \frac{S_{66}^2}{S_1^2 - S^2}\right)\right]. \quad (8)$$

Here, $\zeta = x - St$. The other nonzero dynamic variables are

$$\chi = \frac{b\gamma^2 H_E}{M_0\omega_0^2}U, \quad u_{xx} = \frac{b^2 B_{66}\gamma^4 H_E^2}{\rho M_0^2(S_1^2 - S^2)\omega_0^4}U^2,$$

$$m_z - m_z^0 = -\frac{\gamma\gamma_2\kappa_\perp E\chi^2 + 2\chi}{4\gamma H_E},$$

$$P_x - P_x^0 = -\frac{M_0\gamma_2\kappa_\perp}{2\gamma H_E}(\gamma H\chi^2 + 2\chi),$$

$$P_y - P_y^0 = -\frac{M_0\gamma_2\kappa_\perp}{\gamma H_E}(\gamma H - \chi)\chi.$$

The NKdV equation (8) has soliton solutions if $rq < 0$ [7]. The single-soliton solution is [12]

$$U = \frac{U_0}{\cosh(\xi/\Delta)},$$

$$U_0 = 2\sqrt{S(\lambda/q)}, \quad \Delta = \sqrt{|r|/(2S\lambda)}, \quad (9)$$

where $\xi = x - x_0 - (S + \lambda)t$. ($\lambda > 0$ and x_0 are real-valued parameters). The parameter λ is the difference of the soliton velocity and the sound velocity S. The perturbation theory is applicable if $\lambda \ll S$. In the case under consideration, $q > 0$; hence, solitons exist if $r < 0$, i.e., $S > c$. With (7), the condition for the existence of a soliton may be written as

$$\frac{\gamma_2\kappa_\perp EH}{H_E} + \left(\frac{H_{ms6}\sigma\delta}{B_{66}} - \frac{K_2^*}{M_0}\right) > \frac{2H_{ms}c^2}{S_2^2 - c^2}, \quad S_2 > c. \quad (10)$$

If $\tau < \tau_1$, where

$$\tau_1 = k_2^* + \frac{H_{ms}c^2}{H_{ms6}(S_2^2 - c^2)}, \quad (11)$$

a soliton can exist only when eh exceeds a critical value $2(\tau_1 - \tau)$. If the opposite inequality takes place, $\tau \geq \tau_1$, a soliton can exist when $eh > 0$. Thus, if the stress magnitude is somewhat smaller than τ_1, the condition for the existence of a soliton can be controlled by applying weak electric and magnetic fields. When $\tau - \tau_1 + eh$ tends to zero, we have $r \longrightarrow 0$ and, therefore, the soliton width Δ also vanishes, while its amplitude does not. At $h = 0.05$ ($H = 7.5$ kOe), $\tau = 50$ ($\sigma = 5 \times 10^8$ dyn/cm^2), $e = 200$ ($E = 67$ esu $= 2$ MV/m), and $\lambda \approx 100$ cm/s, the soliton parameters are as follows: amplitude $\sim 1 \times 10^{-5}$; width $\sim 2 \times 10^{-4}$ cm; velocity $\sim 3 \times 10^5$ cm/s; the amplitude of angular deviations χ of the antiferromagnetism vector ~ 0.03; $m_z - m_z^0 \sim 10^{-5}$; $P_x - P_x^0 \sim 10^{-3}$ esu; and $P_y - P_y^0 \sim 0.1$ esu.

Analysis shows that the energy and the momentum of a soliton consist of two terms, one of which is proportional to the soliton width Δ, while the other is inversely proportional to it. The soliton width can be noticeably changed by varying the applied stress and electric and magnetic fields; hence, the momentum and energy of a soliton can also be profoundly altered. Figure 4 shows the reduced momentum p/p_0 (curve *1*) and energy W/W_0 (curve *2*) of a soliton as functions of the quantity $\tau - \tau_1 + eh$ for moderately small values of Δ (p_0 and W_0 are the soliton momentum and energy, respectively, at $\tau = \tau_1$ and $eh = 5$).

The results presented above are valid with the proviso that $\Delta \gg a_0$ (a_0 is the lattice parameter of the crystal) and $|\mathbf{m}| \ll |\mathbf{l}| \approx 1$. These conditions are not satisfied at $r \longrightarrow 0$. At the same time, in the field geometry considered in this paper, the transverse elastic mode u_y becomes dispersionless and solitons described by (9) do not exist when $r \longrightarrow 0$. As shown above, it is possible to make the quantity r approach zero by varying the applied electric and magnetic fields, thereby causing the solitons indicated above to disappear.

The planar soliton (9) may be unstable with respect to perturbations dependent on the y and z coordinates

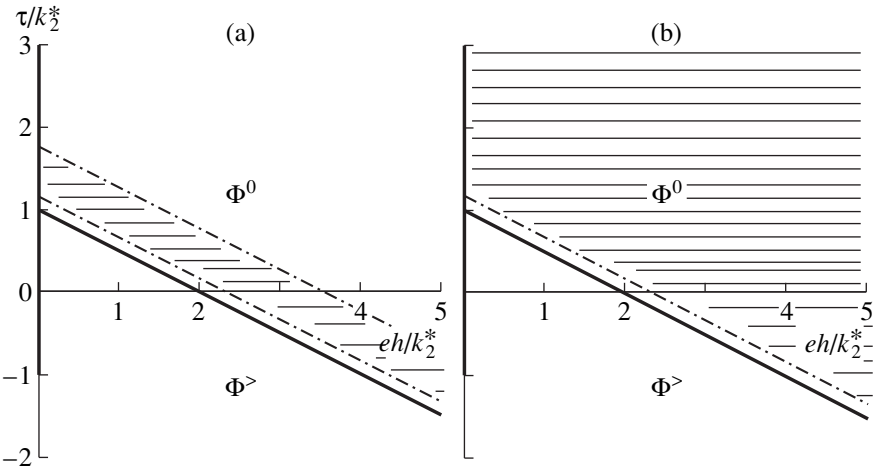

Fig. 5. Diagram showing the influence of stresses and electric and magnetic fields on the stability of an MKdV soliton (the stability region is shown by hatching) for (a) $c < S_5 < S_2$ and (b) $c < S_2 < S_5$.

[7]. Taking into account the weak y and z dependence (in the linear approximation), we arrive at the modified Kadomtsev–Petviashvili equation

$$\frac{\partial}{\partial\zeta}\left(2S\frac{\partial U}{\partial t} - r\frac{\partial^3 U}{\partial\zeta^3} + q\frac{\partial}{\partial\zeta}U^3\right) = -a\frac{\partial^2 U}{\partial y^2} - S_{44}^2\frac{\partial U}{\partial z^2}, \quad (12)$$

where

$$a = S_1^2 - (S_3^2 + S^2)^2/(S_1^2 - S^2),$$

$$S_3 = \sqrt{(C_{11} + C_{12} - 2C_{66})/2\rho}.$$

At $a > 0$, the planar soliton (9) is stable [13]. If the elastic crystalline anisotropy in the basal plane satisfies the condition

$$\frac{C_{11} - C_{12} - 2C_{66}}{C_{11} - C_{12}} > \frac{1}{5 - 2C_{12}/(C_{11} + C_{12})}, \quad (13)$$

the quantity a may change its sign when τ, e, and h are varied. In the case $a < 0$, the planar (one-dimensional) solitons are unstable against goffering [13]. For the values of crystal parameters indicated above, the inequality (13) is satisfied. Therefore, in addition to (10), another condition should be fulfilled for the soliton to be stable; namely, $S < S_5$, or

$$eh + 2(\tau - k_2^*) < \frac{2H_{ms}S_5^2}{H_{ms6}(S_2^2 - S_5^2)}, \quad S_2 < S_5,$$

$$S_5 = \frac{1}{\sqrt{2}}\left[\sqrt{(2S_3^2 + S_1^2)^2 + 4(S_1^4 - S_3^4)} - (2S_3^2 + S_1^2)\right]^{1/2}. \quad (14)$$

With (10) and (14), we arrive at the following results. When $c > S_2$ or $c > S_5$, the soliton is unstable; if $c < S_5 < S_2$, the soliton is stable for τ, e, and h varying within narrow limits (see Fig. 5a); and, finally, when $c < S_2 < S_5$, the soliton is stable in those ranges of τ, e, and h where condition (10) is satisfied (see Fig. 5b).

As shown above, the magnetoelectric coupling may drastically affect magnetic spin-reorientational phase transitions, which occur in easy-plane tetragonal AFMs subjected to external pressure; in eh–τ phase diagrams there appear critical points, tricritical points, etc. When the electric field is varied, a first-order or a second-order phase transition may occur between the symmetric and canted phases, depending on the sign of the anisotropy constant in the basal plane. Near phase transition lines, the velocity of quasi-acoustic waves depends crucially on the electric field strength, which affects the condition for the existence of one-dimensional magnetoelastic solitons.

The magnetoelectric coupling may modify not only the condition of existence, but also the condition for stability of one-dimensional magnetoelastic solitons against their goffering. This takes place for a certain elastic anisotropy strength in the basal plane. Near second-order phase transitions, the conditions for existence and stability of solitons can be controlled by varying one of the three external factors (stress and electric and magnetic fields). Estimates show that substantial changes in the characteristics of magnetoelastic solitons in AFMs with a basal-plane anisotropy constant ~10^2 J/cm^3 can be produced by external fields with a strength easily attainable in experiment ($\sigma \sim 3 \times 10^7$ Pa, $E \sim 1$ MV/m, and $H \sim 1$ MA/m) even at moderate values of the magnetoelectric constant, $\alpha \approx 3 \times 10^{-4}$. The effects considered in this paper may be observed in AFMs such as trirutiles Cr_2TeO_6, V_2WO_6 [14–16], rare-earth phosphates and vanadates ($HoPO_4$ and $GdVO_4$ [17–19]), and compound Sm_2CuO_4 [20].

REFERENCES

1. E. A. Turov, *Kinetic, Optical, and Acoustic Properties of Antiferromagnets* [in Russian], Izd. Ural. Otd. Akad. Nauk, Sverdlovsk (1990).
2. A. I. Popov, G. A. Esina, and A. K. Zvezdin, Fiz. Tverd. Tela (S.-Peterburg) **38** (10), 3091 (1996).
3. E. A. Turov, V. V. Men'shenin, and V. V. Nikolaev, Zh. Éksp. Teor. Fiz. **104** (6), 4157 (1993) [JETP **77**, 1014 (1993)].
4. V. V. Men'shenin and E. A. Turov, Zh. Éksp. Teor. Fiz. **108** (6), 2061 (1995).
5. V. V. Menshenin, I. F. Mirsaev, and E. A. Turov, J. Magn. Magn. Mater. **144**, 1739 (1995).
6. V. I. Ozhogin and A. Yu. Lebedev, J. Magn. Magn. Mater. **15**–**18**, 617 (1980).
7. S. K. Turitsyn and G. E. Fal'kovich, Zh. Éksp. Teor. Fiz. **89** (1), 258 (1985) [Sov. Phys.—JETP **62**, 146 (1985)].
8. V. V. Kiselev and A. P. Tankeev, Fiz. Tverd. Tela (Leningrad) **75** (1), 40 (1993).
9. M. A. Shamsutdinov, A. T. Kharisov, and A. P. Tankeev, Fiz. Met. Metalloved. **85** (1), 43 (1998).
10. I. E. Dikshteĭn, E. A. Turov, and V. G. Shavrov, in *Dynamic and Kinetic Properties of Magnetic Materials* (Nauka, Moscow, 1986), p. 68.
11. L. D. Landau and E. M. Lifshitz, *Statistical Physics*, Part 1 [in Russian], Nauka, Moscow (1995).
12. *Solitons and Nonlinear Wave Equations*, Ed. by R. K. Dodd, J. C. Eilbeck, J. D. Gibbon, and H. C. Morris (Academic, London, 1982; Mir, Moscow, 1988).
13. B. B. Kadomtsev and V. I. Petviashvili, Dokl. Akad. Nauk SSSR **192**, 753 (1970).
14. W. Kunnmann, S. La Placa, L. M. Corliss, *et al.*, J. Phys. Chem. Solids **29**, 1359 (1968).
15. R. M. Hornreich, Int. J. Magn. **4**, 321 (1974).
16. A. H. Cook, S. J. Swithenby, and M. R. Wells, Int. J. Magn. **4**, 309 (1974).
17. G. T. Rado, Phys. Rev. Lett. **23**, 644 (1969).
18. G. T. Rado, J. M. Ferrari, and W. G. Maisch, Phys. Rev. B: Condens. Matter **29**, 4041 (1984).
19. S. Bluck and H. G. Kahle, J. Phys. C **21**, 5193 (1988).
20. H. Wiegelmann, I. M. Vitebsky, A. A. Stepanov, *et al.*, Phys. Rev. B: Condens. Matter **55** (22), 15304 (1997).

Translated by Yu. Epifanov

Physics of the Solid State, Vol. 42, No. 2, 2000, pp. 315–320. Translated from Fizika Tverdogo Tela, Vol. 42, No. 2, 2000, pp. 307–312.

MAGNETISM AND FERROELECTRICITY

Neutron Diffraction Investigation of Structural and Magnetic States of Lithium-Doped Antiferromagnet NiO

A. Z. Men'shikov*, Yu. A. Dorofeev*, A. E. Teplykh*, B. A. Gizhevskiĭ*, and N. A. Mironova**

** Institute of Metal Physics, Ural Division, Russian Academy of Sciences, ul. S. Kovalevskoĭ 18, Yekaterinburg, 620219 Russia*
*** Institute of Physics of Latvia, Salaspils, 229021 Latvia*
e-mail: menshikov@imp.uran.ru

Received July 21, 1999

Abstract—The elastic neutron scattering in polycrystalline samples of the $(Ni_{1-x}Li_x)O$ solid solutions ($x < 0.1$) is investigated by neutron diffraction technique. It is shown for the first time that the doping of nickel monoxide by lithium is accompanied by the formation of vacancies in the anionic sublattice, and the vacancy concentration is equal to the lithium content in the solid solution. The neutral lithium atoms are randomly arranged over sites of the cationic sublattice with possible spatial polarization of a valence electron toward an oxygen vacancy. In the composition range studied, the diamagnetic dilution of nickel monoxide by lithium turns out to be magnetically similar to the dilution with magnesium. In both cases, the Néel temperature and the mean magnetic moment per atom linearly decrease with an increase in concentration of the diamagnetic dopant. *© 2000 MAIK "Nauka/Interperiodica".*

Nickel monoxide with crystal lattice of the NaCl type is the antiferromagnet whose magnetic structure is described by the wavevector $\mathbf{k} = (1/2, 1/2, 1/2)$ [1, 2]. This compound exhibits electrical properties characteristic of a good insulator with an electrical resistivity of about 10^{14} Ω cm [3]. It is revealed [4] that, in the case when magnesium with the same valence as the Ni^{2+} ion serves as a diamagnetic dopant, the electrical resistivity of the $(Ni_{1-x}Mg_x)O$ solid solutions obtained remains unchanged. In these solid solutions, the nickel and magnesium ions are randomly disordered over the cationic sublattice, and the anionic sublattice is completely occupied by oxygen [5–9]. The Néel temperature and the mean magnetic moment per atom linearly decrease with an increase in the concentration x, and, at $x > 0.5$, the antiferromagnetic long-range order breaks down with the formation of a state of the "cluster spin glass" type [8, 9].

Quite a different situation is observed upon diamagnetic dilution with lithium atoms. First and foremost, the doping with lithium leads to a considerable increase in the electrical conductivity of nickel monoxide, since the latter transforms from the insulator to the semiconductor with the hole conductivity [3]. Moreover, the lithium-doped nickel monoxide possesses a low value of the electronic work function, and, hence, this material can be used as a cathode in electromagnetic and electrochemical devices [10, 11]. At the same time, it was found that the cathode functions of lithium-doped nickel monoxide decrease with time due to the contamination with the Ni^{3+} ions and simple cathode dissolution. Berbenni *et al.* [11] made the assumption that such an undesirable side effect is brought about by the defectiveness of the cationic or anionic sublattices in the $(Ni_{1-x}Li_x)O$ solid solutions and attempted to reveal this feature of the sublattices with the use of thermogravimetric and X-ray diffraction analyses. Although the experimental data obtained in [10, 11] indicated the defectiveness of the anionic sublattice, the above assumption was rejected as unreliable because of insufficiently precise measurements.

The problem of the defectiveness of the sublattices in the $(Ni_{1-x}Li_x)O$ solid solutions is of particular importance in determining structural and electronic states of diamagnetic lithium atoms in the NiO lattice. Indeed, in the case of the $(Ni_{1-x}Li_x)O$ solid solutions, the small ionic radius of lithium suggests that lithium atoms can be located either in tetrahedral sites of the oxygen sublattice, when the octahedral sites have already been completely occupied by the Ni^{2+} ions, or in the octahedral sites, when the anionic sublattice is only partially occupied by oxygen atoms.

However, beginning with the work published by Goodenough *et al.* [12], the lithium-doped nickel monoxides have been considered in terms of the formula $(Ni^{2+}_{1-2x}Ni^{3+}_x Li^{+}_x)O$, which suggests that lithium ions occupy only octahedral sites in the anionic sublattice that is completely occupied by oxygen ions. Furthermore, Li *et al.* [13] established that the doping with lith-

ium initially brings about the formation of the $(Ni_{1-x}Li_x)O$ solid solutions with randomly substituted sites in the cationic sublattice of the NaCl-type structure and, then, at $x = 0.5$, leads to the structural transformation from the cubic phase to the $(Ni_{0.5}Li_{0.5})O$ hexagonal phase characterized by an ordered arrangement of Li^+ and Ni^{3+} ions. According to [14, 15], the short-range order is formed even at $x = 0.3$. As a result of the structural rearrangement of atoms in the NaCl-type lattice, the magnetic ordering changes from antiferromagnetic to ferromagnetic through intermediate ferrimagnetic states at $0.3 \le x < 0.5$ [12, 15].

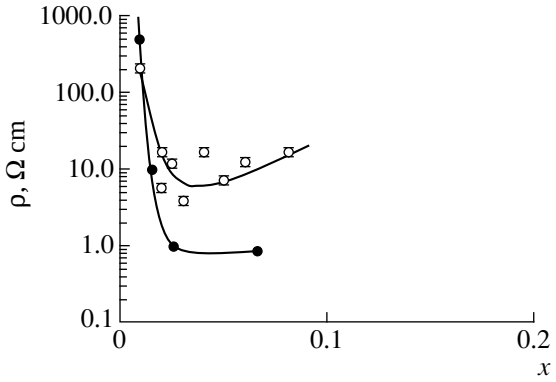

Fig. 1. Dependences of the electrical resistivity on the lithium concentration in NiO at room temperature for single crystals [3] (filled circles) and polycrystalline samples studied in this work (open circles).

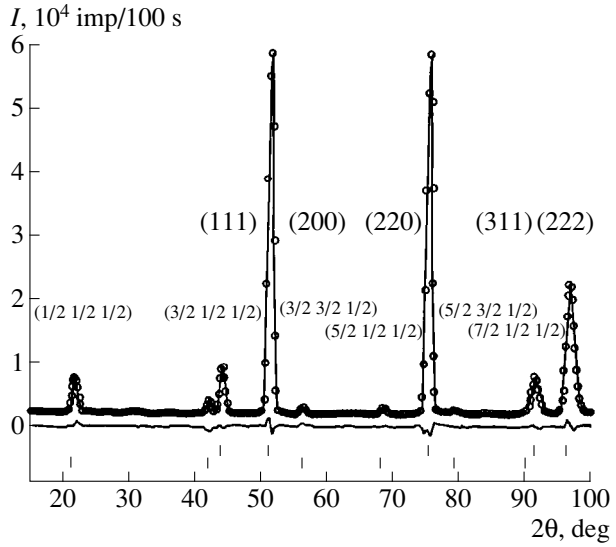

Fig. 2. Neutron diffraction pattern of the $(Ni_{1-x}Li_x)O$ solid solution at $x = 0.03$. The pattern is typical of all the studied compounds. Points are the experimental intensities, solid lines represent the intensities calculated with the assumption of an imperfect oxygen sublattice. The integer and non-integer (*hkl*) indices correspond to the nuclear and magnetic reflections, respectively.

The aim of the present work was to reveal the defectiveness of the structure of lithium-doped nickel monoxide by the neutron diffraction technique. In our case, the neutron diffraction method proved to be more sensitive to structural changes as compared to the X-ray diffraction analysis, because the nuclear-scattering amplitudes for lithium ($b_{Li} = -0.194 \times 10^{-12}$ cm), on the one hand, and nickel ($b_{Ni} = 1.03 \times 10^{-12}$ cm) and oxygen ($b_O = 0.577 \times 10^{-12}$ cm), on the other hand, are different in sign. Moreover, the neutron diffraction technique makes it possible to trace changes in both atomic and magnetic subsystems simultaneously.

1. SAMPLE PREPARATION AND EXPERIMENTAL TECHNIQUE

For experiments, samples of NiO doped with lithium at different concentrations were prepared by the salt decomposition method. Carbonates $NiCO_3$ and Li_2CO_3 (high-purity grade) used as the initial compounds were mixed in molar ratios corresponding to the specified compositions. The mixed aqueous solutions were dried at a temperature of 120–130°C and then were calcinated at 300–800°C to the complete decomposition of salts. The materials thus prepared were carefully ground in an agate mortar, pressed into pellets, and, again, annealed at a temperature of 1200–1300°C for 6–10 h. We synthesized samples of the $(Ni_{1-x}Li_x)O$ solid solutions with the compositions $x =$ 0.01, 0.02, 0.025, 0.03, 0.04, 0.05, 0.06, and 0.08. The values of x corresponded to the specified lithium content and were refined from the unit cell parameters. According to the X-ray diffraction analysis, all the prepared compounds exhibit crystal lattice of the NaCl type without distortions.

In addition, the quality of the prepared samples was checked by measuring the electrical resistivity at room temperature. The data obtained are displayed in Fig. 1. It can be seen that, as the lithium content in NiO increases, the electrical resistivity changes by more than thirteen orders of magnitude. Moreover, the electrical resistivity measured in this work on polycrystalline samples rather well correlates with the data obtained for single crystals in [3].

The elastic neutron-scattering measurements were carried out with the polycrystalline samples in the temperature range 77–550 K, which corresponds to the magnetically ordered state of the studied objects. All the neutron diffraction patterns were obtained in the range $2\theta = 10°$–$110°$ ($\lambda = 1.81$ Å) on a diffractometer installed at a horizontal channel of an IVV-2M reactor (Zarechnyĭ, Russia). The numerical processing of the elastic neutron-scattering data was based on the fitting of calculated and experimental intensities. The calculations were performed with the Rietveld method included in the FULLPROF program [16].

2. RESULTS

Figure 2 demonstrates the neutron diffraction pattern of the $(Ni_{1-x}Li_x)O$ solid solution at the concentration $x = 0.03$. Similar neutron diffraction patterns are observed for the other compositions. Two types of reflections clearly manifest themselves in the elastic neutron-scattering pattern of the studied compounds. These reflections are indexed on the cubic NaCl-type unit cell with the integer and non-integer (*hkl*) values and correspond to nuclear and magnetic reflections, respectively. The latter reflections with the original (1/2 1/2 1/2) reflection indicate the antiferromagnetic ordering of the NiO type. The Néel temperatures of the studied compounds were determined from the temperature dependences of the intensity of the original reflection. A number of these dependences are depicted in Fig. 3. As can be seen, the Néel temperature that corresponds to the zero intensity of this reflection decreases with an increase in the lithium content in NiO. The concentration dependences of the Néel temperatures for the $(Ni_{1-x}Mg_x)O$ and $(Ni_{1-x}Li_x)O$ solid solutions are compared in Fig. 4. It is clear that there is a close correlation between both dependences. These results are in good agreement with the data on the temperature dependence of the magnetic susceptibility [17].

The required data on the other parameters of the atomic and magnetic subsystems of the $(Ni_{1-x}Li_x)O$ solid solutions were obtained by the numerical processing of the neutron diffraction patterns with the use of the FULLPROF program package. In the numerical processing of the neutron diffraction patterns, the variable parameters were three main parameters of the atomic subsystem, namely, the unit cell parameter $a(x)$, the site occupancy of the metal atoms P_{Me}, and the occupancy of the oxygen atoms P_O. The mean magnetic moment $\langle\mu\rangle$ per atom of the antiferromagnetic lattice served as the characteristic parameter of the magnetic subsystem. All the calculations were performed under the assumption that the magnetic structure of the $(Ni_{1-x}Li_x)O$ solid solutions at $x \le 0.1$ is described by the wavevector $\mathbf{k} = (1/2, 1/2, 1/2)$.

The results of numerical calculations unambiguously indicate that, for the $(Ni_{1-x}Li_x)O$ solid solutions, the best discrepancy factor ($R \sim 5\%$) for the experimental and theoretically calculated intensities of nuclear and magnetic reflections is achieved when the nickel and lithium atoms are randomly arranged in the cationic sublattice with an occupancy of 1, and the site occupancy of oxygen sublattice is equal to $1 - x$ (Fig. 5). Similar calculations carried out for the $(Ni_{1-x}Mg_x)O$ solid solutions studied earlier in [8] demonstrate that the oxygen site occupancy of the anionic sublattice is equal to 1. From these facts, it can be concluded that, in this case, there are no errors brought about by the method of processing the neutron diffraction patterns; in other words, we deal with the physical result. This suggests that the anionic sublattice in the

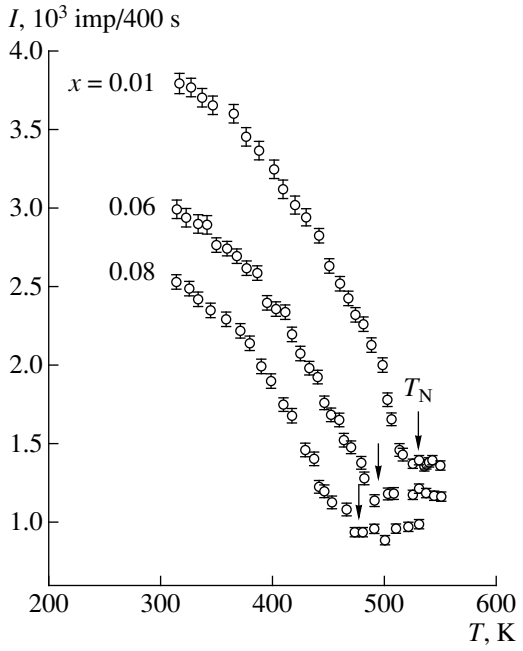

Fig. 3. Temperature dependences of the intensity of the (1/2 1/2 1/2) reflection for the $(Ni_{1-x}Li_x)O$ solid solutions. Arrows indicate the Néel temperatures.

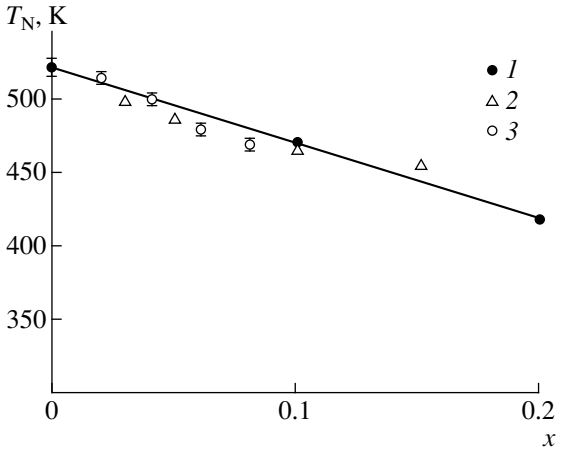

Fig. 4. Concentration dependences of the Néel temperature for the $(Ni_{1-x}Mg_x)O$ and $(Ni_{1-x}Li_x)O$ solid solutions according to the data taken from (*1*) [9], (*2*) [17], and (*3*) this work.

$(Ni_{1-x}Li_x)O$ solid solutions is characterized by the presence of oxygen vacancies whose concentration corresponds to the lithium concentration.

The result obtained was thoroughly analyzed and checked. First of all, we considered two alternative model structures of the $(Ni_{1-x}Li_x)O$ solid solutions. The first model corresponded to the formula $(Ni^{2+}_{1-2x}Ni^{3+}_{x}Li^{+}_{x})O^{2-}$. This implies that the cationic sublattice is completely occupied by the nickel and lithium

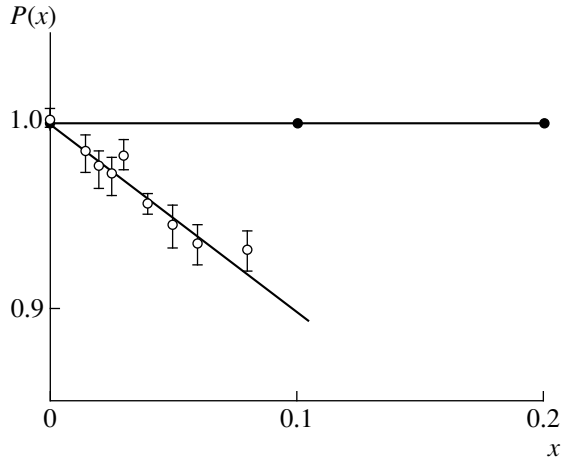

Fig. 5. Oxygen site occupancies of anionic sublattices in the $(Ni_{1-x}Mg_x)O$ (filled circles) and $(Ni_{1-x}Li_x)O$ (open circles) solid solutions. The data are obtained by the fitting of experimental and theoretical intensities with the Rietveld method included in the FULLPROF program.

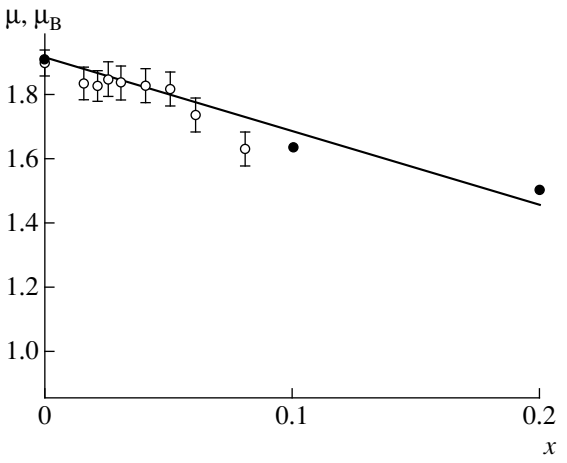

Fig. 6. Concentration dependences of the mean magnetic moment per metal ion in the $(Ni_{1-x}Mg_x)O$ (filled circles) and $(Ni_{1-x}Li_x)O$ (open circles) solid solutions according to the neutron diffraction data obtained in [8] and this work, respectively.

ions, and the anionic sublattice is fully filled by the oxygen ions. The second model was based on the assumption that neutral lithium atoms occupy the tetrahedral sites in the face-centered cubic lattice of oxygen, and the octahedral sites are occupied only by the Ni^{2+} ions. As follows from the calculations performed, in both cases, the discrepancy factors for the experimental and calculated intensities of nuclear reflections are higher than 50%, which indicates the inconsistency of the above models for describing the structural state of lithium atoms in NiO.

In order to obtain further evidence for the defectiveness of the anionic sublattice, the experimental ratios between the integrated intensities of the (111) and (200) nuclear reflections were determined by the independent method (without numerical calculations within the FULLPROF program package). Then, the same ratios were theoretically calculated under the assumption that the oxygen site occupancy P_O of the anionic sublattice is equal to 1 and $1 - x$. The data obtained are summarized in the table. As is seen from the table, the calculated and experimental data are in reasonable agreement when the occupancy of the oxygen sites is equal to $1 - x$. In this case, the intensity ratio $I_{(111)}/I_{(200)}$ is approximately constant over the entire range of compositions, whereas, if the occupancy of the oxygen sublattice is equal to 1, this ratio changes by a factor of about 1.5. Consequently, the inference drawn from the data on the neutron diffraction measurements that the oxygen sublattice in lithium-doped nickel monoxides is imperfect seems to be quite justified.

Experimental and calculated relative intensities of the (111) and (200) reflections for the $(Ni_{1-x}Li_x)O$ solid solutions of different compositions

Concentration	Scattering amplitude	$I_{(111)}/I_{(200)}$		
x	$\langle b \rangle 10^{-12}$ cm	observed	calculated at $P_O = (1-x)$	calculated at $P_O = 1$
0.010	1.020	0.127	0.139	0.132
0.015	1.012	0.135	0.136	0.128
0.020	1.005	0.133	0.137	0.126
0.025	0.999	0.132	0.136	0.123
0.030	0.994	0.139	0.137	0.121
0.040	0.981	0.133	0.135	0.113
0.050	0.968	0.127	0.129	0.110
0.060	0.809	0.133	0.132	0.105
0.080	0.956	0.136	0.135	0.095

Furthermore, the full-profile analysis of neutron diffraction reflections taken from the powder samples enabled us to determine the concentration dependences of the mean magnetic moment per atom $\mu(x)$ and the unit cell parameter $a(x)$, which are displayed in Figs. 6 and 7, respectively. It can be seen from Fig. 6 that the mean magnetic moment $\langle \mu(x) \rangle$ exhibits a linear behavior similar to that observed for the $(Ni_{1-x}Mg_x)O$ solid solutions. At the same time, the unit cell parameters are close to those determined by the X-ray diffraction analysis and somewhat deviate from the dependence $a(x)$ obtained in [12].

3. DISCUSSION

The experimental data obtained permit us to conclude that lithium-doped nickel monoxides are the substitutional solid solutions, in which the lithium atoms are randomly distributed over the completely occupied

cationic sublattice, and the oxygen vacancies with the same concentration are formed in the anionic sublattice. Then, the chemical formula of these solutions should be written as $Ni^{2+}_{1-x}Li_xO^{2-}_{1-x}\square_x$, where $\square$ designates the oxygen vacancy in the anionic sublattice. As follows from this formula, the number of valence electrons of nickel and oxygen ions in lithium-doped NiO remains the same as in undoped NiO. It should be noted that the lithium atoms, which are randomly arranged in the cationic sublattice, are in the neutral state and do not form chemical bonds with oxygen atoms. However, it can be assumed that an outer-shell valence electron of lithium that is described by the wavefunction with the 2*p* symmetry and weakly interacts with the ionic core can be spatially polarized toward an oxygen vacancy. One can also expect the formation of *F*-centers in the anionic sublattice whose concentration corresponds to the concentration of lithium atoms in the solid solution.

We also believe that the low value of electronic work function in these materials can be directly associated with the presence of oxygen vacancies in the anionic sublattice. From the viewpoint of electronic structure, this means that, in defect crystals, the Fermi surface in some points of the reciprocal space is very closely adjacent to the crystal surface. On the other hand, the high hole-type conductivity of lithium-doped nickel monoxides, as compared to the conductivity of the undoped compound, is likely brought about by the formation of an acceptor level induced by doped lithium atoms in the forbidden energy band.

As regards the magnetic properties of lithium-doped nickel monoxides, it should be mentioned that, in the composition range with $x < 0.1$, the compounds remain antiferromagnetic with the same type of magnetic ordering as in undoped nickel monoxide. Note that the substitution of the diamagnetic lithium atom for the magnetic Ni^{2+} ion leads to a linear change in the Néel temperature according to the relationship $T_N = T_N^{NiO}(1 - x)$, where $x < 0.25$. This is consistent with the conclusion of the molecular-field theory considered in [8, 9] for the substitution of the diamagnetic Mg^{2+} ion for the magnetic Ni^{2+} ion. Therefore, in the composition range under consideration, there are no considerable differences in the diamagnetic dilution with magnesium and lithium. This is also evidenced by similar concentration dependences of the mean magnetic moment per atom, which can be also described by the linear law in this composition range: $\langle\mu\rangle = \mu_{Ni}(1 - x) - M_x$, where $\mu_{Ni} = 1.9\mu_B$ is the local magnetic moment at the nickel atoms in the diamagnetically diluted and undiluted NiO, and M_x is the moment induced at the diamagnetic dopant with the direction opposite to the magnetization of the antiferromagnetic sublattice [9].

The similarity in the magnetic properties of the $(Ni_{1-x}Li_x)O$ and $(Ni_{1-x}Mg_x)O$ solid solutions in the composition range $0 \le x < 0.1$ primarily suggests that the exchange interaction between the magnetic nickel ions occurs within the cationic sublattices, which show identical behavior in both systems. In solid solutions of both types, the main parameters of the magnetic subsystem are the exchange integrals $J_1 > 0$, $J_2 < 0$, and $J_3 > 0$ at distances of the first ($r_1 = \frac{\sqrt{2}}{2}a$), second ($r_2 = a$), and third ($r_3 = \sqrt{3}\,a$) nearest neighbors, respectively. This character of the exchange interaction is accomplished solely in solid solutions with the NaCl-type crystal lattice, which, in the $(Ni_{1-x}Li_x)O$ system, is observed only to $x = 0.5$. Then, there occurs the structural transformation from the cubic phase to the $NiLiO_2$ hexagonal phase. The latter phase is characterized by the ordered arrangement of lithium and nickel atoms and also by the ferromagnetic spin ordering. Note that the $NiLiO_2$-type short-range order elements appear already at $x = 0.3$. As a result, in the composition range $0.3 < x < 0.5$, as the diamagnetic atoms occupy one of the antiferromagnetic sublattices, its magnetization becomes less than the magnetization of another sublattice. This gives rise to the ferrimagnetic structure associated with the uncompensated antiferromagnetic sublattices.

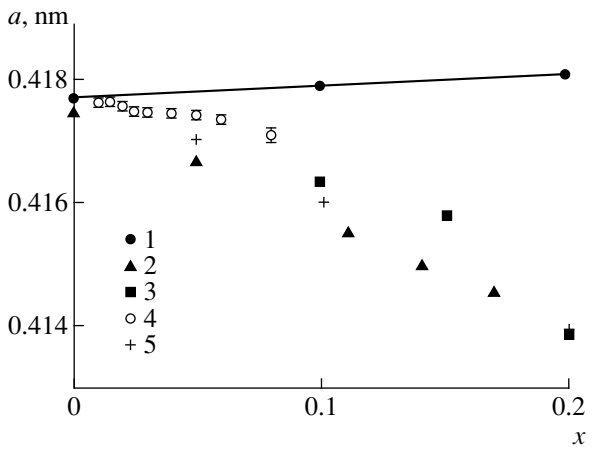

Fig. 7. Concentration dependences of the unit cell parameter for the $(Ni_{1-x}Li_x)O$ and $(Ni_{1-x}Mg_x)O$ solid solutions according to the data taken from (*1*) [8], (*2*) [10], (*3*) [13], (*4*) this work, and (*5*) [12].

The main experimental result of the present neutron diffraction investigation is the revelation of the defectiveness of the oxygen sublattice in lithium-doped NiO. This result could be achieved only with the optimum ratio between the nuclear-scattering amplitudes of lithium, nickel, and oxygen atoms. It is not improbable that the revelation of the defectiveness of the oxygen sublattice in the lithium-doped nickel monoxide will provide an explanation for the specific features of electrical properties of these materials that manifest themselves in the high electrical conductivity and a low value of the electronic work function.

ACKNOWLEDGMENTS

This work was supported by the State Scientific and Technical Program "Topical Directions in Physics of Condensed Matter"—the Direction "Neutron Investigations," project no. 4.

REFERENCES

1. C. G. Shull, W. A. Strausser, and E. O. Wollan, Phys. Rev. **83**, 333 (1951).
2. W. I. Roth, Phys. Rev. **110**, 1333 (1958).
3. S. Koide, J. Phys. Soc. Jpn. **20** (1), 123 (1965).
4. N. I. Mironova and U. A. Ulmanis, *Radiation-Induced Defects and Iron Group Metal Ions in Oxides* (Zinatne, Riga, 1988), p. 202.
5. T. M. Giebultovicz, J. J. Rhyne, M. S. Seehra, *et al.*, J. Phys., Suppl. **49** (12), C8-1105 (1988).
6. Z. Feng, V. Suresh Babu, J. Zhao, *et al.*, J. Appl. Phys. **70**, 6161 (1991).
7. S. Seehra, R. Kannan, and M. Ibrahim, J. Appl. Phys. **73**, 5468 (1993).
8. A. Z. Menshikov, Ya. A. Dorofeev, A. G. Klimenko, *et al.*, Phys. Status Solidi B **164**, 275 (1991).
9. A. Z. Menshikov, Ya. A. Dorofeev, N. A. Mironova, *et al.*, Solid State Commun. **98** (9), 839 (1996).
10. A. Marini, V. Massarotti, V. Berbenni, *et al.*, Solid State Ionics **45**, 143 (1991).
11. V. Berbenni, V. Massarotti, D. Capsoni, *et al.*, Solid State Ionics **48**, 101 (1991).
12. J. B. Goodenough, D. G. Wickhow, and W. J. Croft, J. Phys. Chem. Solids **5**, 107 (1958).
13. W. Li, J. N. Reimers, and J. R. Dahn, Phys. Rev. B: Condens. Matter **46** (6), 3236 (1992).
14. R. Stoyanova, E. Zhecheva, and S. Angelov, Solid State Tech. **59**, 17 (1993).
15. F. Kern and N. Perakis, C. R. Acad. Sci. B **279** (6), 143 (1974).
16. J. Rodríguez-Carvajal, Physica B (Amsterdam) **192**, 55 (1993).
17. A. A. Arkhipov, Izv. AN Latv. SSR, Ser. Fiz. Tekh. Nauk **3**, 13 (1986).
18. J. P. Kemp, P. A. Cox, and J. W. Hodby, J. Phys.: Condens. Matter, No. 2, 6699 (1990).

Translated by O. Borovik-Romanova

Physics of the Solid State, Vol. 42, No. 2, 2000, pp. 321–325. Translated from Fizika Tverdogo Tela, Vol. 42, No. 2, 2000, pp. 313–317.

MAGNETISM AND FERROELECTRICITY

Magnetic Susceptibility and Magnetic-Field Behavior of CuB_2O_4 Copper Metaborate

G. A. Petrakovskiĭ, A. D. Balaev, and A. M. Vorotynov

Kirenskiĭ Institute of Physics, Siberian Division, Russian Academy of Sciences, Akademgorodok, Krasnoyarsk, 660036 Russia

e-mail: gap@cc.krascience.rssi.ru

Received May 18, 1999; in final form, August 17, 1999

Abstract—An experimental study is reported regarding the temperature dependence of the magnetic susceptibility of a CuB_2O_4 tetragonal single crystal within the 4.2–200-K range. It has been established that the magnetic susceptibility exhibits anomalies at 21 and 10 K and depends strongly on crystal orientation in the magnetic field. A study has been carried out of the field dependences of the magnetization of CuB_2O_4 at various temperatures and crystal orientations. It is shown that for $T > 21$ K, the crystal is in a paramagnetic state determined by Cu^{2+} copper ions with an effective magnetic moment of 1.77 μ_B. Within the 10–21 K interval, the field dependence of the magnetization is typical of a weak ferromagnet with magnetic moments of the two antiferromagnetically coupled sublattices lying in the tetragonal plane of the crystal. The spontaneous weakly-ferromagnetic moment is 0.56 emu/g at 10 K. The canting angle of the sublattice magnetic moments, determined by the Dzyaloshinski–Moriya interaction, is 0.49°. It is believed that below 10 K, the CuB_2O_4 crystal retains its easy-plane magnetic structure, but with a zero spontaneous magnetic moment. © *2000 MAIK "Nauka/Interperiodica".*

Copper oxide compounds exhibit a rich variety of electrical and magnetic properties. It is in these compounds that high-temperature superconductivity was discovered and studied extensively. The diversity of the magnetic properties of the cuprates is accounted for by the specific features of the electronic configuration ($3d^0$) of the Cu^{2+} ion, in which it is mainly present in these compounds. The spin of the Cu^{2+} ion is 1/2. From the theoretical viewpoint, this makes the investigation of the properties of such magnets easier. At the same time, the small spin and the possibility of formation of quasi-low-dimensional magnets makes such effects as quantum spin reduction and quantum fluctuations important. One of the interesting quantum effects is the Peierls spin transition in antiferromagnetic chains with an $S = 1/2$ spin. This transition was found to occur in $CuGeO_3$ [1]. The transition is associated with the instability of a uniform antiferromagnetic chain in a three-dimensional phonon system with respect to dimerization and transition to the singlet state of the spin system. The transition of low-dimensional systems to a singlet ground state accompanied by the formation of an energy gap in the spectrum of elementary magnetic excitations is also characteristic of the Holdane systems [2] and systems exhibiting competition among the exchange interactions [3].

In order to understand the nature of the specific properties of the cuprates, one has to comprehensively study their magnetic properties at the level of the electronic structure. This paper presents the results of a measurement of the magnetic characteristics of a single crystal copper metaborate of CuB_2O_4.

EXPERIMENTAL RESULTS

The magnetic properties of a single-crystal of CuB_2O_4 were measured on samples grown from a melt solution by the technology described by us elsewhere [4]. The temperature and field dependences of the magnetic moments were determined with a vibrating-sample magnetometer within the 4.2–200-K temperature range and in magnetic fields of up to 70 kOe.

The temperature dependences of the crystal susceptibility in fields of 350 and 500 Oe obtained for magnetic-field orientations along and perpendicular to the tetragonal axis are shown graphically in Fig. 1. Note the strong anisotropy of the susceptibility. In a magnetic field applied in the basal plane of the crystal, one observes a jump in the susceptibility at 21 K and its fast growth with a further decrease of temperature. At 10 K, the susceptibility decreases in a jump by about an order of magnitude and then increases monotonically as the temperature continues to fall. It should be pointed out that the temperature dependence of the susceptibility measured at 20 kOe does not exhibit any anomalies within the temperature interval specified (Fig. 2). When measured in a magnetic field applied along the tetragonal axis of the crystal, the temperature dependence of the susceptibility is monotonic throughout the temperature and field ranges studied (Fig. 1). The paramagnetic Néel temperature and the effective magnetic

1063-7834/00/4202-0321$20.00 © 2000 MAIK "Nauka/Interperiodica"

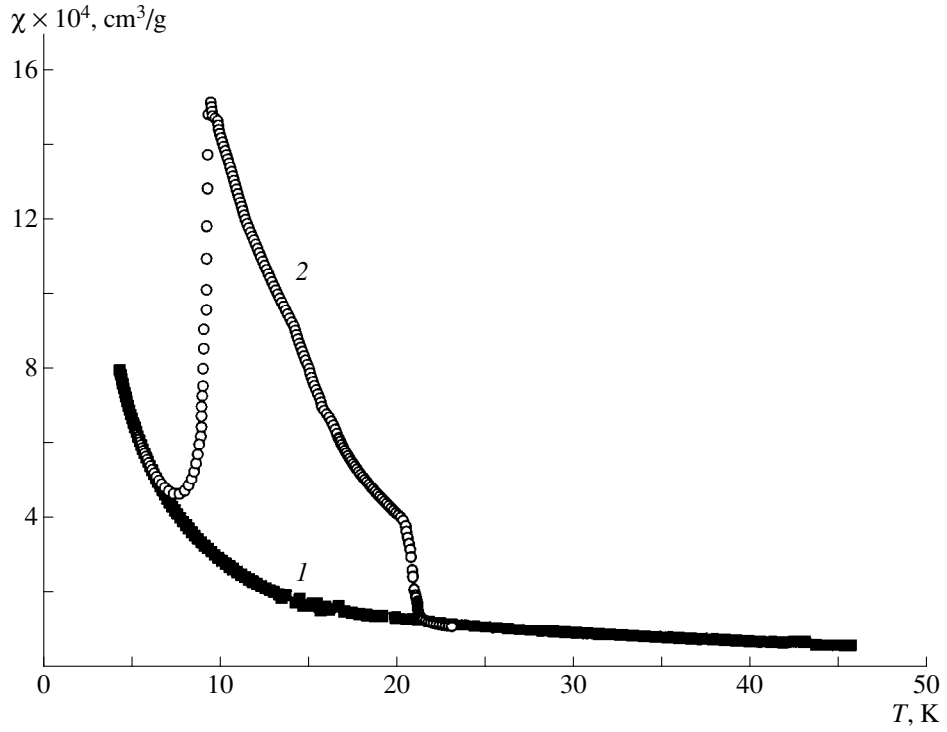

Fig. 1. Temperature dependence of the magnetic susceptibility of single-crystal CuB_2O_4: (*1*) the field is parallel to the tetragonal axis of the crystal (H = 350 Oe), (*2*) the field is parallel to the crystal basal plane (H = 500 Oe).

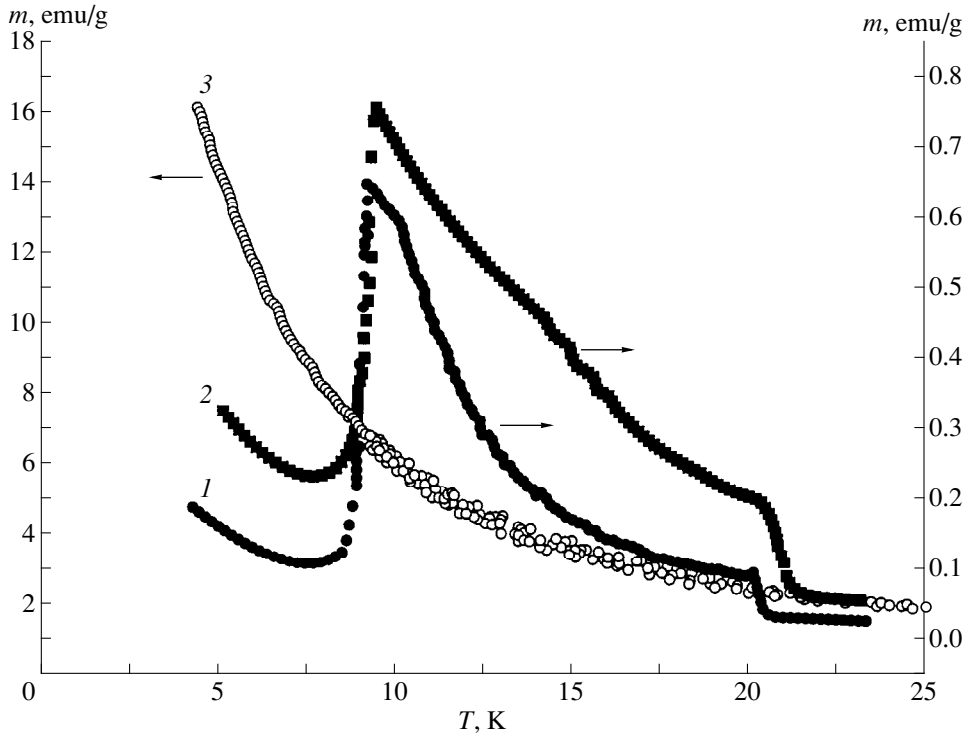

Fig. 2. Temperature dependence of the magnetization of single-crystal CuB_2O_4 plotted for different external magnetic fields H (kOe) applied in the basal plane of the crystal: (*1*) 0.2, (*2*) 0.5, (***3***) 20.

moment of the copper ion derived from the high-temperature part of the magnetic susceptibility are Θ_N = –9.5 K and $\mu_{eff} = 1.77\ \mu_B$, respectively.

To establish the nature of the anomalies in the temperature dependence of the susceptibility, one measured the field dependences of magnetization at various temperatures and for different magnetic-field orientations relative to the crystal axes. The results obtained are shown in Figs. 3 and 4. The field dependences of magnetization obtained with a magnetic field oriented along the tetragonal axis of the crystal are mostly monotonic throughout the temperature interval studied. However, when the magnetic field is oriented in the tetragonal plane, the magnetization exhibits characteristic features. Within the 10–18-K region, the magnetization curves give evidence for the existence of a weak spontaneous magnetic moment in the basal plane of the crystal, which is characteristic of weak ferromagnets. The spontaneous moment is $m_0 = 0.56$ emu/g at $T = 10$ K. As the temperature is brought below 10 K, the spontaneous magnetization vanishes, and a feature typical of a magnetic spin-reorientational transition appears in the magnetization curve. Linear extrapolation of the high-field rectilinear portions (directly above the anomalies characteristic of spin-reorientational transitions) of magnetization curves made within the 10–4.2-K interval again reveals the appearance of a spontaneous magnetic moment above these fields.

The temperature dependences of the spontaneous magnetic moment and of the spin-reorientational transition field obtained in this way are shown graphically in Fig. 5.

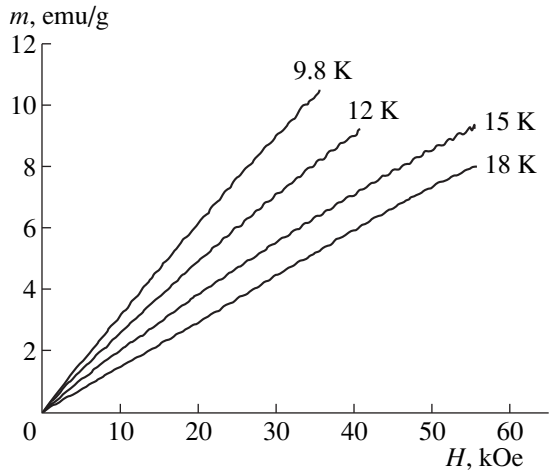

Fig. 3. Field dependence of the magnetization of single-crystal CuB_2O_4. The magnetic field is parallel to the tetragonal axis of the crystal.

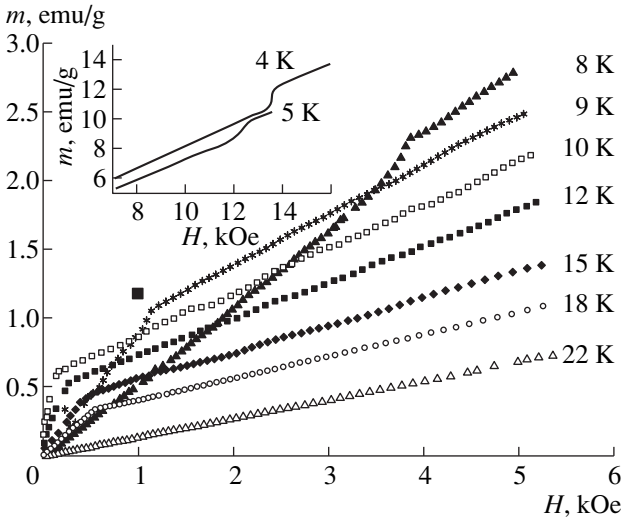

Fig. 4. Field dependence of the magnetization of single-crystal CuB_2O_4. The magnetic field is parallel to the basal plane of the crystal.

DISCUSSION

The CuB_2O_4 metaborate crystallizes in tetragonal symmetry, space group $I42d$ [4]. The unit cell contains 12 formula units, and the cell parameters are a = 11.484 Å and c = 5.620 Å. A symmetry analysis [5] of the crystal structure of CuB_2O_4 showed the possibility of formation of several antiferromagnetic structures, which allow the existence of a small spontaneous magnetic moment in the basal plane of the crystal.

The crystal has two inequivalent copper-ion positions: Cu(1), at the 4*a* site (0, 0, 1/2), and Cu(2), in the 8*d* position (0.08, 1/4, 1/8). As the symmetry-forming elements, one can take, besides the elementary translations, the fourfold inversion axis $(\bar{4})$ and the vertical diagonal plane with a glide along the body diagonal by $1/4(\sigma_d)$. The symmetry-forming elements for the 4*a* position can produce only one parity combination $(\bar{4})^+(\sigma_d)^-$ compatible with the existence of antiferromagnetism. The possible combinations for the 8*d* position are $(\bar{4})^+(\sigma_d)^-$, $(\bar{4})(\sigma_d)^+$, and $(\bar{4})(\sigma_d)^-$. Thus, in this crystal there can exist three antiferromagnetic structures allowing weak ferromagnetism (Fig. 6). The copper-ion magnetic moments lie in the basal plane of the crystal. The second-order invariant in the expression for the free-energy density, which is responsible for the formation of the weak ferromagnetism, in this case, has the form $[\mathbf{ml}]_z$, where **m** and **l** are the ferromagnetism and antiferromagnetism vectors, respectively [5].

The copper ions in the CuB_2O_4 crystal are exchange-coupled through the oxygen and boron ions in the Cu–O–B–O–Cu chain. Note that there is no inversion center on the straight line connecting the nearest copper ions. According to the symmetry rules for determination of the direction of the Dzyaloshinski vector [6], the Cu^{2+} ions can in this case be coupled through the Dzyaloshinski–Moriya interaction, which

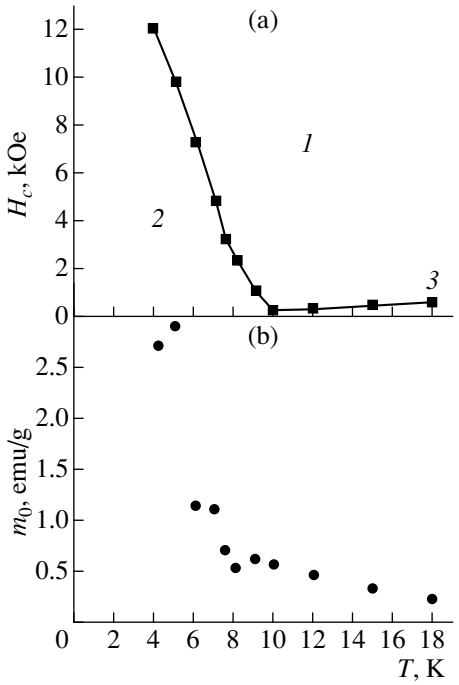

Fig. 5. (a) Temperature dependence of the spin-reorientational transition field H_c: (*1*) region of existence of a weakly ferromagnetic state, (***2***) compensated antiferromagnet; and (b) temperature dependence of the weak magnetic moment m_0 in the basal plane of single-crystal CuB_2O_4. The magnetic field is everywhere parallel to the basal plane of the crystal.

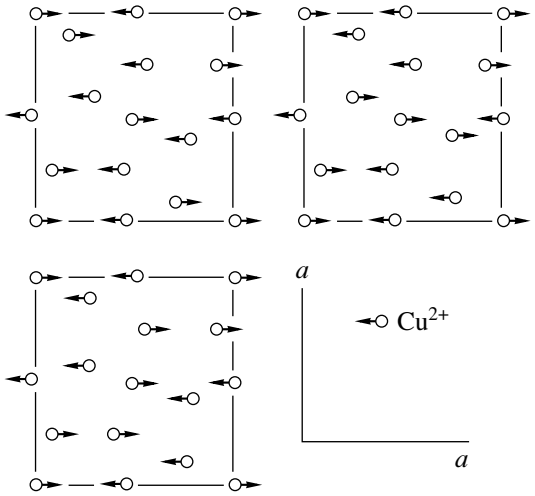

Fig. 6. Three possible antiferromagnetic structures allowing the existence of a weak ferromagnetism in single-crystal CuB_2O_4. The structures are projected onto the tetragonal plane of the crystal.

gives rise to the appearance of a small spontaneous moment due to the weak noncollinearity between the magnetizations of the antiferromagnet sublattices. In view of the fact that a twofold axis passes through the midpoint of the segment that connects the Cu(1) ions, and this axis is perpendicular to the segment and parallel to the tetragonal plane of the crystal, one may conclude that the Dzyaloshinski vector is perpendicular to this axis [6]; it can be directed, for instance, along the *c* axis of the crystal.

With this in mind, and taking into account the available experimental data on magnetization, it appears reasonable to assume that, within the 10–21-K interval, the CuB_2O_4 crystal has an easy-plane magnetic structure with a small spontaneous magnetic moment m_0 = 0.56 emu/g at T = 10 K lying in the basal plane. The canting angle of the sublattice magnetizations is 0.49°. A similar structure is found, for example, in the α-Fe_2O_3 hematite at temperatures above the Morin point [7]. The behavior of such a magnetic structure in magnetic fields can be analyzed using the expression for free energy in the form [7]

$$F = J\mathbf{M}_1\mathbf{M}_2 - D[\mathbf{M}_1 \times \mathbf{M}_2]_2 - \mathbf{H}(\mathbf{M}_1 + \mathbf{M}_2) - K_1(\cos^2\beta_1 + \cos^2\beta_2)/2 - K_2(\cos^4\beta_1 + \cos^4\beta_2)/2, \quad (1)$$

where J is the parameter of the intersublattice exchange interaction, $\mathbf{M}_1$ and $\mathbf{M}_2$ are the magnetizations of the first and second sublattices, $\mathbf{H}$ is the external magnetic field, K_1 and K_2 are the constants of uniaxial magnetocrystalline anisotropy of the second and fourth orders, respectively, and β_1 and β_2 are the angles that the sublattice magnetizations $\mathbf{M}_1$ and $\mathbf{M}_2$, respectively, make with the crystal tetragonal axis. Obviously enough, the easy-plane state occurs in zero external magnetic field for $K_1 < 0$. The presence of the Dzyaloshinski–Moriya interaction gives rise in this case to a weakly ferromagnetic moment m_0 because of the sublattice magnetizations being not collinear. For an external magnetic field $\mathbf{H}$ oriented in the basal plane, the field dependence of the magnetization can be written as

$$m = m_0 + \chi_\perp H, \quad (2)$$

where $\chi_\perp = 1/J$, $m_0 = DM_0/J$, and M_0 is the sublattice magnetization at T = 0 K. The saturation magnetization of single-crystal CuB_2O_4 is $2M_0$ = 160 G. Using (2) and the experimental data of Fig. 4, one can construct the temperature dependence of the Dzyaloshinski field $H_D = DM_0$. The results are shown in Fig. 7. Note the satisfactory agreement of the Dzyaloshinski field thus obtained with its value derived from magnetic resonance data [8]. The effective exchange field $H_E = JM_0$ is estimated as 29 kOe at T = 4.2 K.

An analysis of the field dependences of magnetization in the basal plane obtained at temperatures below 10 K (Fig. 4) indicates the absence of a spontaneous magnetic moment in weak magnetic fields and its formation as the magnetic field increases above a certain critical level. Note that the lower the temperature, the higher the critical field is. The phase boundary constructed in this way, and separating the states with a

weak spontaneous magnetic moment and a weak field-induced magnetic moment, is indicated in Fig. 5a. The vanishing of the spontaneous magnetic moment can be caused, in our opinion, by antiferromagnetic ordering of weak ferromagnetic moments below 10 K. A similar situation was reported by some authors [9, 10]. Besides, the disappearance of the spontaneous magnetic moment can be associated with distortions of the CuB_2O_4 structure, which impose symmetry-induced restrictions on its existence.

As follows from studies of antiferromagnetic resonance in CuB_2O_4 [8], at temperatures below 10 K the magnetic structure of the crystal is also easy plane. This conclusion is also argued for by the observation that the magnetic susceptibility grows monotonically with decreasing temperature, irrespective of the magnetic field orientation relative to the crystallographic axes. In this case, the susceptibility of a sample is determined, for any orientation of the external magnetic field, by the perpendicular susceptibility $\chi_\perp$. Now, if an easy-axis magnetic structure with magnetic moments parallel to the tetragonal axis formed below 10 K, the susceptibility would be strongly anisotropic, and its temperature dependence would be governed by the perpendicular ($\chi_\perp$) and parallel ($\chi_\parallel$) susceptibilities; this is not supported by experimental data.

Note the parts of the magnetization curves for the basal plane of the crystal at temperatures from 18 to 10 K, which lie within the field range of 0 to 600 Oe in Fig. 4. Significantly, these parts of the curves are linear functions of the field, and the field at which the curve slope changes (identified by an arrow) increases with increasing temperature. Fig. 5a also shows the strengths of these fields, which permit one to isolate a certain region (3) in the phase diagram. Assuming this behavior of the magnetization in these temperature and field regions not to be due to the sample becoming a single domain, one could suggest the existence within the 21–10-K interval of one more magnetic phase, the nature of which remains unclear.

Summing up, we can conclude that, for temperatures $T_N > 21$ K, the CuB_2O_4 tetragonal crystal is a paramagnet with an effective magnetic moment $\mu_{eff} = 1.77\mu_B$. The magnetic susceptibility obeys the Curie–Weiss law with a Néel paramagnetic temperature $\Theta = -9.5$ K, which shows antiferromagnetic exchange interactions to be dominant. Below the Néel temperature $T_N = 21$ K, the crystal is in a magnetically ordered state. Within the 10–21-K temperature interval it is a weak ferromagnet with the sublattice magnetic moments lying in the basal plane of the crystal and being slightly noncollinear. At $T = 10$ K, a magnetic phase transition occurs, which results in a disappearance of the weak spontaneous magnetic moment. To reveal the nature of this transition and to better identify the magnetic state of the crystal for $T < 10$ K, antiferromagnetic resonance studies are presently under way, and neutron diffraction measurements on a crystal with the ^{11}B isotope are being planned for the future.

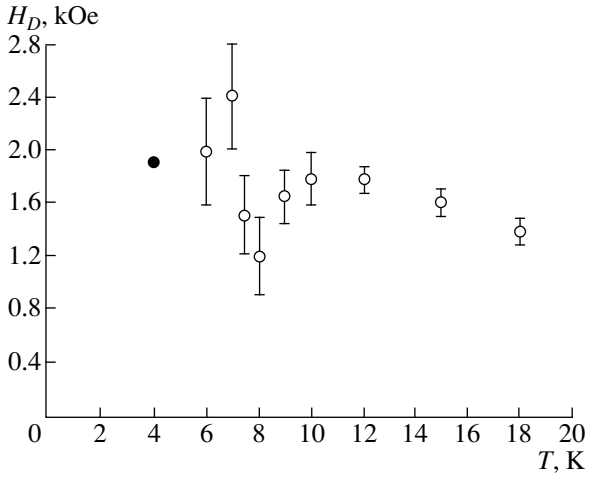

Fig. 7. Temperature dependence of the Dzyaloshinski field H_D in single-crystal CuB_2O_4: the filled circle is antiferromagnetic-resonance data.

ACKNOWLEDGMENTS

The authors express their gratitude to A.I. Pankrats and O.A. Bayukov for fruitful discussions of the experimental results, and to K.A. Sablina for growing single-crystal samples.

Support from the Krasnoyarsk-krai Science Foundation (Grant 8F0156) is gratefully acknowledged.

REFERENCES

1. G. A. Petrakovskiĭ, in *Itinerant Electron Magnetism: Fluctuation Effects*, Ed. by D. Wagner *et al.* (Kluwer Academic, 1998), pp. 437–450.
2. F. D. M. Haldane, Phys. Rev. Lett. **50**, 1153 (1983).
3. Y. Nonomura and M. Suzuki, J. Phys. A **27**, 1127 (1994).
4. G. A. Petrakovskiĭ, K. A. Sablina, D. A. Velikanov, *et al.*, Kristallografiya (in press).
5. E. A. Turov, *Physical Properties of Magnetically-Ordered Crystals* (Izd. Akad. Nauk SSSR, M., 1963).
6. T. Moriya, Phys. Rev. **120**, 91 (1960).
7. I. S. Jacobs, R. A. Beyerlen, S. Foner, *et al.*, Int. J. Magn. **1**, 193 (1971).
8. A. I. Pankrats, G. A. Petrakovskiĭ, and N. V. Volkov, Fiz. Tverd. Tela (in press).
9. A. Rouco, X. Obradors, and F. Pérez, Phys. Rev. B: Condens. Matter **50**, 9924 (1994).
10. A. M. Kadomtseva, A. S. Moskvin, and I. G. Bostrem, Zh. Éksp. Teor. Fiz. **72**, 2286 (1977).

Translated by G. Skrebtsov

Physics of the Solid State, Vol. 42, No. 2, 2000, pp. 326–329. Translated from Fizika Tverdogo Tela, Vol. 42, No. 2, 2000, pp. 318–321.

MAGNETISM AND FERROELECTRICITY

Effect of Magnetic Field on the Chaos Appearance Fields in a Triglycine Sulfate Crystal

S. A. Gridnev*, K. S. Drozhdin, ***, and V. V. Shmykov****

**Voronezh State Technical University, Moskovskiĭ pr. 14, Voronezh, 394026 Russia*
***Voronezh State University, Universitetskaya pl. 1, Voronezh, 394893 Russia*
****Martin Luther University, Halle-Wittenberg, D-06108 Halle, Germany*
e-mail: gridnev@ns1.vstu.zc.ru

Received August 20, 1999

Abstract—Effects of a constant magnetic field, the amplitude of an alternating electric field, and the temperature on the values of fields corresponding to the appearance and disappearance of chaotic oscillations were studied in the ferroelectric phase of a triglycine sulfate crystal. A mechanism of the appearance of a magnetic moment, induced by the repolarization current, during the lateral motion of a 180° domain wall is considered.

INTRODUCTION

Magnetoelectric interactions in nonmagnetic ferroelectric crystals, in which the effects of magnetic field is not related to the crystallographic symmetry laws, draw considerable attention of researchers [1]. Theoretical aspects of the phenomena in ferroelectrics exposed to external magnetic fields were studied within the framework of the vibronic theory [2, 3], a thermodynamic approach [4], and a model of the magnetic moment induced by the crystal repolarization current during the lateral motion of domain walls [5] or interphase boundaries [6]. The related experimental investigations proceed in two main directions: study of the effect of applied magnetic fields upon the fundamental properties of ferroelectrics (such as the Curie temperature, soft mode frequency, etc.) [7–9] and study of the effects related to the interaction of magnetic fields with nonequilibrium domain structure [10–12]. The results of these investigations showed [12] that a noticeable effect of magnetic fields with a strength below 20 kOe is observed only during continuous variation of the temperature in the vicinity of the phase transition temperature, where the domain structure occurs in a nonequilibrium state. However, the published results and their interpretations are rather contradictory, so the problem can hardly be considered as exhaustively studied. In this context, it expedient to continue investigations of the effect of magnetic field on the kinetics of the domain structure variation in ferroelectrics switched by alternating electric field, which is characterized by a change in the spatial arrangement of domain boundaries and is accompanied by dynamic changes in the spontaneous polarization of a crystal.

Since the ferroelectric crystals are essentially nonlinear electric materials, in which the appearance of determinate chaos has been experimentally observed [13, 14], we have used the monitoring of chaotic oscillations as a method sensitive with respect to the domain structure dynamics. Indeed, manifestations of the nonlinearity of a ferroelectric in a dynamic regime under the action of an alternating electric field reflects rearrangements in the domain structure of the crystal.

In this work, we have studied for the first time the effect of a constant magnetic field on the appearance of chaotic oscillations in a serial *LCR* circuit with a nonlinear element represented by a ferroelectric capacitor based on a triglycine sulfate $(CH_2NH_2COOH)_3H_2SO_4$ (TGS) crystal. The crystal was polarized by external sinusoidal voltage at temperatures below the Curie temperature (T_c = 49.5°C).

The choice of a TGS crystal as the object for investigation is explained by the following circumstances. First, the dielectric and polarization properties of TGS, as well as the domain dynamics in this crystal are well studied (TGS is considered as a model system). Second, the domain structure of TGS is characterized by a high mobility and sensitivity with respect to external factors, which allowed us expect significant response to the application of magnetic fields.

EXPERIMENTAL

A TGS crystal was grown by the method of controlled cooling from an oversaturated aqueous TGS solution. The Y-cut samples had a shape of rectangular plates with dimensions $8 \times 4 \times 0.5$ mm and the faces perpendicular to the principal crystallographic axes. Silver electrodes on the large faces were obtained by vacuum deposition.

A sample was placed into a temperature-controlled cell, where the temperature could be varied between 150 and 310 K and maintained constant at a preset level

1063-7834/00/4202-0326$20.00 © 2000 MAIK "Nauka/Interperiodica"

to within 0.2 K. A constant magnetic field was generated by electric magnets and measured with a Hall transducer.

The chaotic oscillations in the circuit were studied using a scheme depicted in Fig. 1. The oscillation modes were monitored by visual observation and their phase portraits were photographed on the oscilloscope screen. The phase portrait represents a $\dot{P}(P)$ function where P is the polarization of the ferroelectric crystal, and $\dot{P}$ is the derivative of this quantity with respect to time.

In this experimental scheme, the oscillation circuit parameters L, C, and R were constant during the measurement cycle, while the amplitude U_0 and frequency ω of the ac voltage applied to the sample and the temperature T of the cell could be varied. In order to obtain a phase portrait on the oscilloscope screen, the voltage U_x from a reference linear capacitor C (proportional to P) was applied to the horizontal plates (X input), and the voltage U_y from the resistor R (proportional to $\dot{P}$) was applied to the vertical plates (Y input).

Behavior of a nonlinear LCR circuit with a ferroelectric crystal can be described by the Duffing equation, well-known in the theory of nonlinear oscillations [13–15]:

$$\ddot{P} + \rho\dot{P} + kP + \gamma P^3 = U_0 \cos\omega t, \qquad (1)$$

where P is the polarization of the ferroelectric crystal, $\rho = R/L$, $k = \alpha d/SL$, $\gamma = \beta d/SL$; d is the sample thickness, S is the electrode area, and α and β are the thermodynamic coefficients in the Landau expansion of the crystal free energy in a series with respect to even powers of the polarization.

An analysis [16] showed that, under certain conditions, equation (1) admits, in addition to periodic solutions, a transition to chaotic oscillations via a sequence of bifurcations of the oscillation period. In experiments, the onset of chaos in the system studied was manifested by the phase trajectory filling some area in the phase space. We have measured an electric field vale E_1, corresponding to the appearance of chaotic oscillations, and the field E_2, at which this regime disappeared on increasing the electric field amplitude at a fixed temperature.

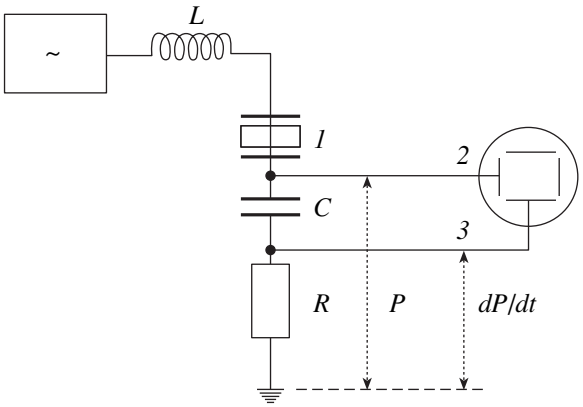

Fig. 1. Schematic diagram of a system used for observation of the phase portrait of a serial resonance circuit with a ferroelectric crystal: (*1*) TGS sample; (*2*) X input of the oscilloscope; (*3*) Y input of the oscilloscope.

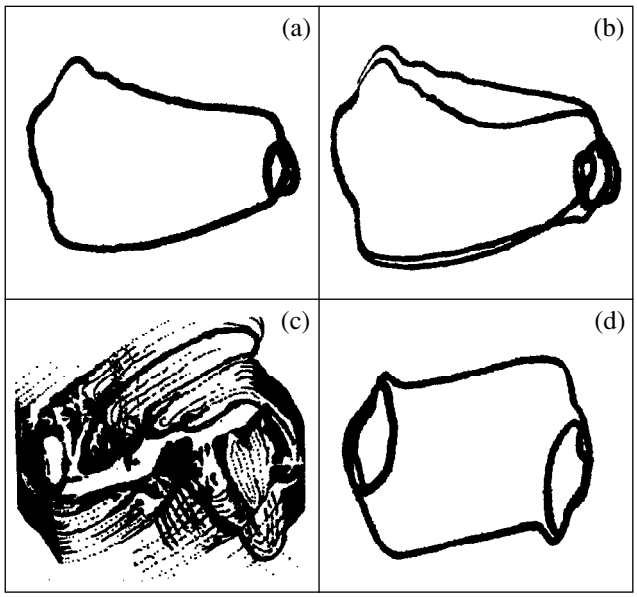

Fig. 2. Typical phase portraits of a circuit with a pure TGS crystal obtained for various amplitudes of the repolarizing electric field E (f = 2 kHz; T = 25°C): (a) $E < E_1$; (b) $E = E_{2T}$, amplitude of the first doubling of the oscillation period; (c) $E_1 < E < E_2$; (d) $E > E_2$.

RESULTS AND DISCUSSION

Since the features of chaotic oscillations in a resonance LCR circuit with a ferroelectric crystal are related to the dynamic properties of a domain structure of this crystal [17, 18], we have studied the behavior of the threshold electric fields E_1 and E_2, corresponding to the appearance and disappearance of chaos in a TGS crystal, depending on the dynamic properties of the domain structure, amplitude of the applied electric field, temperature, and strength of a constant magnetic field.

The results of our investigations showed that the phase portrait of a TGS crystal in a weak alternating electric field represents a close curve (Fig. 2a). As the amplitude of the repolarizing field E increases, a single-period oscillatory process changes to double-period (Fig. 2b). If the field amplitude grows further, the period increases to four-fold, etc., that is, a cascade of period doubling is developed. As a result of sequential

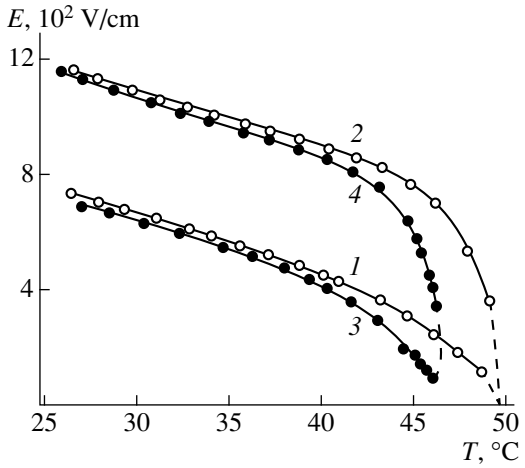

Fig. 3. Temperature dependence of the field strengths (*1*, *3*) E_1 and (*2*, *4*) E_2 at which the chaos appears and disappears, respectively: (*1*, *2*) $H = 0$; (*3*, *4*) $H = 3$ kOe.

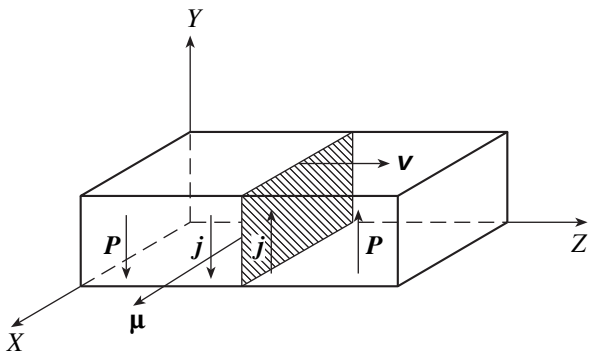

Fig. 4. Schematic diagram illustrating the appearance of a magnetic moment **μ** induced by the repolarization current ***j*** in the region of a domain boundary moving at a velocity ***v*** [12].

development of this cascade process at $E = E_1$, the phase trajectories become open and do not overlap, thus filling some region on the phase plane, which is a manifestation of the chaos onset (Fig. 2c). Further increase in the electric field amplitude to $E = E_2$ results in that the chaotic oscillations disappear (Fig. 2d). Thus, the regime of chaotic oscillations is observed only in the interval between E_1 and E_2.

In agreement with the results of our previous investigations [18, 19], it was found that chaos in the TGS crystals is observed only in the ferroelectric phase, at an alternating field amplitude 2–3 times that of the coercive field strength of a given crystal, and is completely absent in the paraelectric phase of the crystal. Figure 3 shows the temperature dependence of the threshold field amplitudes E_1 and E_2 corresponding to the appearance and disappearance of chaotic oscillations, respectively (curves *1* and *2*). As seen, the width of the interval of the existence of chaotic regimes (E_1–E_2) decreases with increasing temperature, reaching virtually zero on approaching the T_c level. Note also that both the lower (curve *1*) and upper (curve *2*) boundaries of the chaos region decrease with increasing temperature, which confirms the above assumption concerning the domain nature of this phenomenon.

Based on analysis of the numerous experimental data, the following qualitative mechanism of the appearance of chaos in ferroelectric crystals was proposed [19]. Instability of the macroscopic polarization is manifested by a nonregular (with respect to time) behavior of the domain structure of the crystal on the level of individual domain walls and domain nuclei. The nonregularity tends to increase as a result of noncoordinated behavior of a large number of domains characterized by different values of the threshold chaos onset fields. Eventually, this leads to a nonregular macroscopic polarization of the whole crystal, which is manifested by a periodic nonreproducible chaotic variation of the instantaneous P and $\dot{P}$ values. Disappearance of the chaotic oscillations when the electric field amplitude exceeds E_2 results either from synchronization of the behavior of individual oscillating domains or from a decrease in the optimum density of the domain nuclei necessary for the existence of chaos. Synchronization of the domain oscillations is related to the enhanced interaction between the domains, which is caused by the increase in the repolarizing field amplitude up to a level at which the new domains are nucleated very rapidly and almost simultaneously which hinders the development of nonregularity and chaos in the system.

A dominating role of the domain dynamics in the mechanism described above allowed us to expect that the applied magnetic field would modify the conditions of chaos development in a TGS crystal. In our experiments, a constant magnetic field with a strength of $H =$ 3 kOe directed along the X axis of the crystal led to a decrease in the threshold fields E_1 and E_2. The closer the sample temperature to the Curie temperature, the more pronounced was the effect (Fig. 3, curves *3* and *4*). In addition, the application of a magnetic field leads to narrowing of the temperature interval of the existence of chaos in the vicinity of T_c, whereby the chaotic oscillations disappeared at a temperature a few degrees below T_c, rather than exactly at this point. Apparently, the magnetic field modifies the dynamic characteristics of domains in the system studied.

In order to explain the interaction of the magnetic field with the moving domain wall, we may use the concept of a magnetic moment appearing in the domain wall moving in the course of repolarization of a ferroelectric crystal [5, 12]. Figure 4 illustrates the appearance of the magnetic moment in the moving domain wall μ and shows orientation of this moment. Within

the framework of this model, the above effects observed in the magnetic field are explained by the tendency of the magnetic moment of the domain wall to acquire a favorable orientation along the magnetic field. As a result of the combined action of the electric E and magnetic H fields, the velocity of the 180° domain walls oriented along H increases and, hence, the threshold electric field amplitudes E_1 and E_2 decrease. An increase in the temperature decreases the threshold amplitudes and the field strengths necessary for activation of the domain boundary nucleation and motion. This explains a decrease in the electric field amplitudes corresponding to the appearance and disappearance of chaos. The same considerations explain increasing effect of the magnetic field at elevated temperatures, which is manifested by the temperature interval of the existence of chaos being limited on the side of higher temperatures. These results agree with conclusions concerning the dynamics of domain boundaries moving in a magnetic field, made on the basis of direct observations of a nonequilibrium domain structure in a magnetic field [12] and investigation of the dielectric losses related to the relaxation of domain boundaries [20] and chaotic polarization oscillations in a serial resonance circuit with a ferroelectric crystal capacitor [21].

Thus, data on the magnetic domain effect observed and studied in this work allow us to conclude that moving domain boundaries, representing dynamic inhomogeneities in a ferroelectric crystal, possess an effective magnetic moment induced by a repolarization current localized in the vicinity of the domain boundaries.

ACKNOWLEDGMENTS

The authors are grateful to O.A. Kordin for his help in conducting experiments.

REFERENCES

1. H. Schmid, Ferroelectrics **161**, 1 (1994).
2. P. Konsin and N. N. Kristofel', Izv. Akad. Nauk ÉstSSR, Ser. Fiz. Mat. **20** (1), 37 (1975).
3. B. G. Vekhter, V. P. Zenchenko, and I. B. Bersuker, Fiz. Tverd. Tela **18** (8), 2325 (1976).
4. V. N. Novosil'tsev and B. N. Rolov, Uch. Zap. Latv. Gos. Univ. **195**, 163 (1973).
5. S. A. Flerova and I. E. Chupis, Izv. Ross. Akad. Nauk, Ser. Fiz. **57** (3), 20 (1993).
6. S. I. Moiseev and V. N. Nechaev, Izv. Ross. Akad. Nauk, Ser. Fiz. **61** (5), 945 (1997).
7. R. Comes and S. M. Shapiro, Phys. Rev. B: Condens. Matter **24**, 1559 (1981).
8. I. H. Ismailzade and R.H. Ismailov, Ferroelectrics **31**, 165 (1981).
9. S. A. Flerova and O. E. Bochkov, Pis'ma Zh. Éksp. Teor. Fiz. **33** (1), 37 (1981).
10. S. A. Popov, N. A. Tikhomirova, and S. A. Flerova, Kristallografiya **30** (3), 608 (1985).
11. S. A. Flerova and I. L. Tsinman, Kristallografiya **32** (4), 1047 (1987).
12. O. L. Orlov, S. A. Popov, S. A. Flerova, *et al*., Pis'ma Zh. Tekh. Fiz. **14** (2), 118 (1988).
13. J. J. Kim and J. Y. Huang, Phys. Rev. B: Condens. Matter **38**, 11885 (1988).
14. H. Beige M. Diestelhorst, *et al.*, Ferroelectrics **104**, 355 (1990).
15. R. Z. Sagdeev, D. A. Usikov, and G. M. Zaslavsky, *Nonlinear Physics: From the Pendulum to Turbulence and Chaos* (Harwood, Switzerland, 1992).
16. Y. Ueda, J. Stat. Phys. **20**, 181 (1979).
17. S. N. Drozhdin and L. N. Kamysheva, Fiz. Tverd. Tela **34**, 2797 (1992).
18. S. N. Drozhdin, L. N. Kamysheva, and O.M. Golitsina, Ferroelectrics **175**, 119 (1996).
19. S. N. Drozhdin, Candidate's Dissertation in Mathematical Physics (Voronnezh, 1993).
20. S. A. Gridnev, K. S. Drozhdin, and V. V. Shmykov, Kristallografiya **42** (6), 1135 (1997).
21. S. A. Gridnev, K. S. Drozhdin, and V. V. Shmykov, Phys. Status Solidi B **214**, R7 (1999).

Translated by P. Pozdeev

Physics of the Solid State, Vol. 42, No. 2, 2000, pp. 330–333. Translated from Fizika Tverdogo Tela, Vol. 42, No. 2, 2000, pp. 322–325.

LATTICE DYNAMICS AND PHASE TRANSITIONS

Acoustic Emission at Phase Transition in Vanadium Sesquioxide Single Crystals

V. N. Andreev, V. A. Pikulin, and D. I. Frolov

Ioffe Physicotechnical Institute, Russian Academy of Sciences, Politekhnicheskaya ul. 26, St. Petersburg, 194021 Russia

Received in final form, May 20, 1999

Abstract—The metal–semiconductor phase transition in vanadium sesquioxide is investigated by the acoustic emission method. It is shown that the acoustic emission in single crystals of this compound is due to thermoelastic stresses arising in the crystal upon the phase transition. Transformation of the acoustic emission activity and an increase in the phase transition temperature are revealed in the temperature cycling of the sample. Observation of peaks of the acoustic emission activity at a temperature of 5–6 K above the critical temperature indicates that crystal nuclei of the monoclinic phase appear in the high-temperature (trigonal) phase of the crystal.

A stoichiometrically pure vanadium sesquioxide single crystal, when cooled up to ~150 K, undergoes a metal–semiconductor first-order phase transition accompanied by an abrupt increase in the electrical resistance, antiferromagnetic ordering of vanadium spins, and structural transition [1]. Particularly, extensive evidence in the literature devoted to this compound reveals a significant scatter in the experimental data, specifically for the low-temperature phase. Cracking of the single crystal due to a jumpwise change in its volume upon the metal–semiconductor transition is a possible explanation for this situation. The destruction of single crystals at the transition across the critical temperature has not been clearly understood. At the same time, cracking leads to a change in the elastic energy of the crystal. The influence of this energy on the parameters of the phase transition is particularly interesting.

1. EXPERIMENTAL TECHNIQUE

The acoustic emission (AE) method is one of the well-known methods for the investigation of cracking [2]. Elastic waves arising from abrupt local changes of stresses in a material are the source of acoustic emission.

Our experimental setup consisted of a cryostat, a piezoelectric transducer, a preamplifier, a signal processing module, a storage oscilloscope, and a computer. The required temperature of the crystal was held with the cryostat. The temperature was measured by a copper–constantan thermocouple. A specially devised piezoelectric transducer made it possible to substantially reduce spurious noise shielding the studied effect. The preamplifier with an amplification factor of 40 dB amplified the transducer signal. The signal processing module extracted the standard parameters (such as the peak-to-peak amplitude of the signal, signal duration, and the number of intersections with zero) from the AE signal. These parameters were stored on a computer hard disk. The AE signals were simultaneously stored in memory of the storage oscilloscope used to observe the shape of the AE signals.

The experiment was performed as follows. The $5 \times 5 \times 0.5$-mm crystal was directly installed on the surface of a piezoelectric tablet of the transducer. Both transducer and crystal under investigation were mounted in the cryostat. Heating and cooling were performed in the range from room temperature to 145 K at a rate of 1 K/min. As a result of the conducted experiment, the database containing parameters, such as the time of the acoustic signal arrival, the amplitude of AE signal, and the crystal temperature, was stored on the computer hard disk.

2. RESULTS AND DISCUSSION

Figure 1 shows the temperature dependence of the AE activity (the number of events per equal time interval of 10 s) during sample cooling from room temperature to 145 K (Fig. 1a) and during its heating (Fig. 1b). The same temperature dependences of AE activity after four cooling–heating cycles are shown in Figs. 1c and 1d. As is clearly seen from Fig. 1, the peak of AE activity is observed in the vicinity of the phase transition temperature. It can be concluded from the electrical conductivity measurements that these temperatures are equal to 148 K (cooling) and 165 K (heating) for the first switching.

The metal–semiconductor phase transition in V_2O_3 is accompanied by the change in the symmetry from trigonal (space group D_{3d}^6) to monoclinic (space group C_{2h}) with a 1.6% volume increase [1]. Such a symmetry lowering upon the metal–semiconductor transition leads to the formation of twinned domains [3]. Observing the surface of the single crystal [plane (0001)]

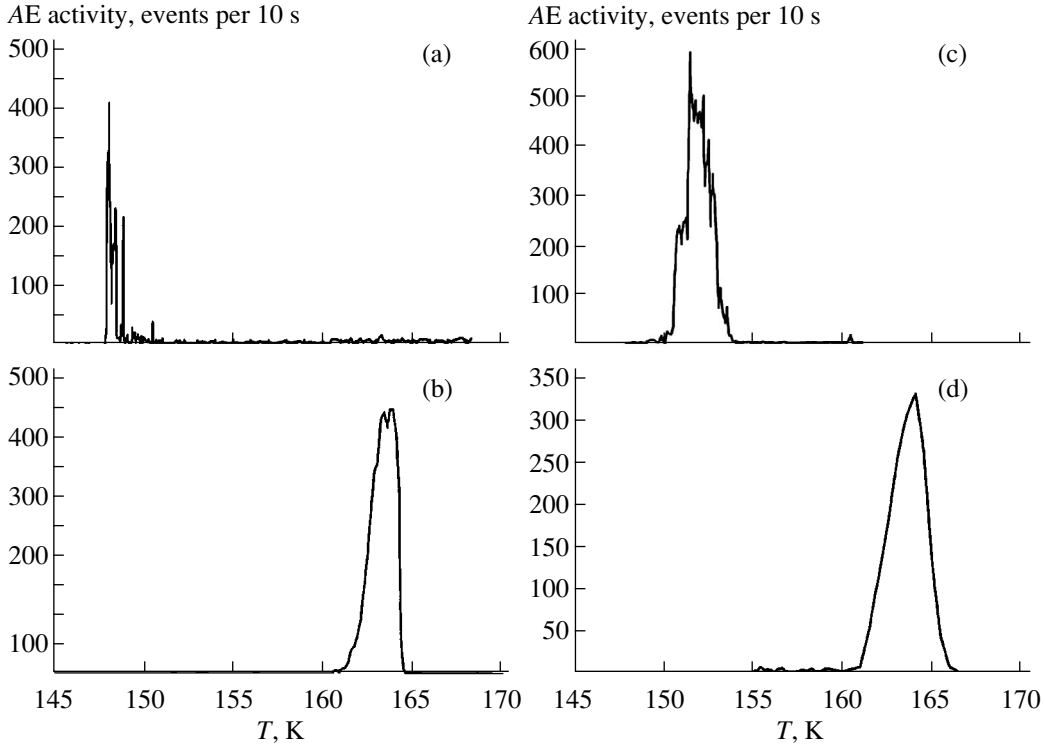

Fig. 1. Temperature dependence of the AE activity in the first cycle of (a) cooling and (b) heating and in the fourth cycle of (c) cooling and (d) heating.

under a microscope, one can see a twin structure (Fig. 2a). It is clear that the monoclinic phase of vanadium sesquioxide consists of twinned domains rotated by 120 degrees. Taking into account the strong anisotropic change in the lattice parameters upon the metal–semiconductor transition, it is clear that strong mechanical stresses should appear on the domain boundaries. These stresses lead to the crystal cracking and give rise to the acoustic emission observed.

The instant release of locked-in stresses on the domain boundaries upon heating results in a further cracking of the single crystal and gives rise to new AE impulses. After the first cooling–heating cycle, a significant amount of cracks appears in the sample (Fig. 2a), so that the sample breaks down into a number of fragments. On further thermocycling, these fragments continue to fall apart into smaller pieces.

As is seen from Figs. 1a and 1b, the dependence of the AE activity exhibits separate peaks after the first cooling and a smoothed peak of the AE activity after the heating. The smoothing of the AE activity peak is observed in the subsequent cooling–heating cycles (Figs. 1c, 1d). We suppose that cracking takes place in each part of the sample simultaneously, and, as the number of cracks increases, the AE activity peak becomes smoother. Comparison of the phase transition temperatures in the first and fourth cooling cycles (Figs. 1a, 1c) shows that the crystal fragmentation leads to an increase in the critical temperature. Since the frag-

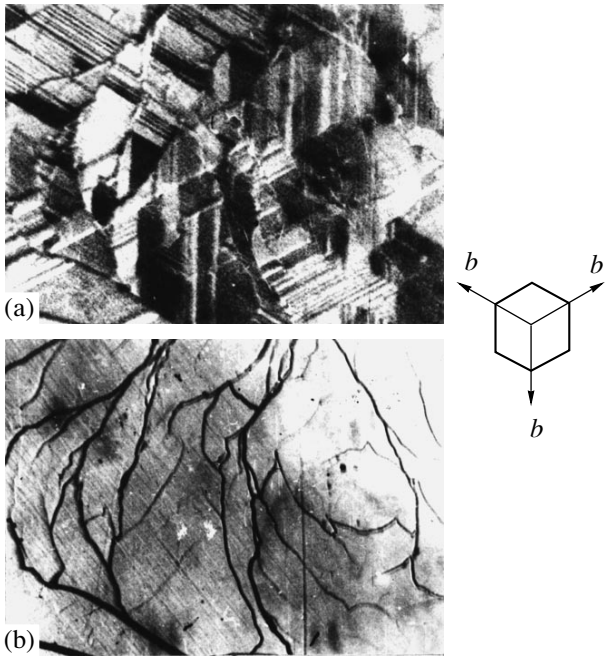

Fig. 2. The surface of vanadium sesquioxide single crystal [plane (0001)] under a polarizing microscope (magnification ×500): (a) domain structure formed upon the transition to the monoclinic phase and (b) trigonal phase (cracks appeared after the first cooling–heating cycle are clearly seen). The inset shows the directions of *b*-axes (hexagonal setting).

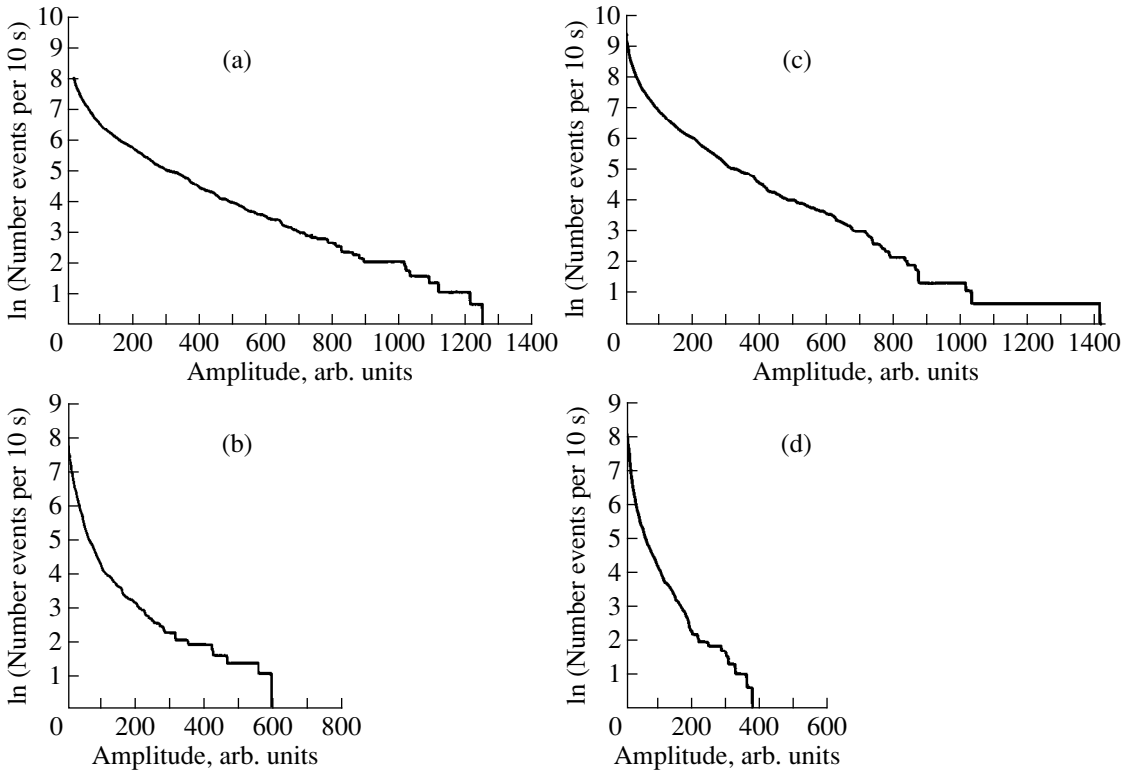

Fig. 3. Amplitude distribution of AE impulses in the first cycle of (a) cooling and (b) heating and in the fourth cycle of (c) cooling and (d) heating.

mentation weakens the locked-in stresses, it is clear that the phase transition temperature depends partly on thermoelastic stresses. The elastic energy of the crystal can be estimated from the ultimate strength of the material and the change in the unit cell volume upon the phase transition. The estimation shows that the elastic energy is equal to ~10 meV per unit cell. This value is almost one-fourth of the latent heat of the transition and, therefore, should influence the phase transition temperature.

Thus, the model of thermoelastic martensitic transformation can be used for the interpretation of some aspects of the phase transition in the vanadium sesquioxide crystal. For example, the mechanism of the hysteresis loop formation can be explained in terms of this model. The V_2O_3 single crystal transforms into the polycrystal during the phase transition. According to the model of martensitic transformation, an increase in the number of small grains during the process of fragmentation increases the dispersion of the critical temperature of the phase transition in a grain [4]. This can result in the broadening of the AE activity peak during thermocycling of the crystal. The assumption that, after the fragmentation of the single crystal, the acoustic emission simultaneously originates from different points inside the crystal is confirmed by the analysis of the amplitude distribution of AE impulses. The amplitude distributions of AE impulses for the first and fourth cooling cycles are shown in Figs. 3a and 3c, respectively. Comparison of these distributions shows that the high-amplitude AE impulses ($A > 800$ arb. units) appear during the first cooling more often than during the fourth cooling. According to [5, 6], there is a correlation between the AE signal amplitude and the size of the arising crack, namely, the AE signal amplitude is directly proportional to the size of a crack.

An increase in the total amount of AE impulses is accompanied with a decrease in the average amplitude of the impulses. For example, 5394 impulses were recorded during the first cooling cycle, and their number increased up to 14041 during the fourth cycle. Therefore, the fragmentation of the existing fragments into smaller pieces continues in the repeated thermocycling. This leads to an increase in the number of AE impulses. By comparing the amplitude distributions during heating and cooling in the first and fourth cooling–heating cycles (Fig. 3), we found that the average amplitudes for the cooling cycle are two times larger than those for the heating cycle. The total number of AE impulses upon cooling is also larger than that upon heating. This is likely due to the fact that the elastic stresses arising upon heating are smaller than those observed upon cooling, and, therefore, the destruction processes are not so catastrophic. This also explains why the phase transition temperature does not change significantly after several cooling–heating cycles.

One of the interesting results of our work is the observation of an increase in the AE activity in the metallic phase of V_2O_3 long before the phase transition. During the first cooling, the AE impulses were recorded approximately 5–6 K above the critical temperature (Fig. 1a). This can be explained by the crystal nucleation of the monoclinic phase at temperatures above the phase transition temperature. Recent EXAFS measurements on V_2O_3 single crystals demonstrated that local monoclinic distortions appear above the phase transition temperature [7]. An increase in the velocity of surface acoustic waves in the metallic phase at a temperature far above the critical temperature was observed in measurements of surface acoustic waves in V_2O_3 single crystals.

This effect was also explained by the appearance of crystal nuclei of the monoclinic phase [8].

Thus, our investigations demonstrated the following.

(1) Acoustic emission is associated with cracking of the V_2O_3 single crystal due to the change in its volume during the phase transition. (2) Acoustic emission was observed at temperatures above the phase transition temperature. The possible cause of such a behavior is the nucleation of the monoclinic (semiconducting) phase within the trigonal (metallic) phase. (3) Cracking raises and extends the range of the phase transition temperature. This indicates that thermoelastic martensitic transitions are very important in vanadium sesquioxide.

REFERENCES

1. B. P. Zakharchenya, A. A. Bugaev, and F. A. Chudnovskiĭ, *A Metal–Semiconductor Phase Transition and Its Application* (Nauka, Leningrad, 1979).
2. V. A. Greshnikov and Yu. B. Drobot, *Acoustical Emission* (Izd. Standartov, Moscow, 1974).
3. V. N. Andreev and F. A. Chudnovskiĭ, Fiz. Tverd. Tela (Leningrad) **17**, 2957 (1975).
4. A. L. Roĭtburd, Usp. Fiz. Nauk **113** (1), 69 (1974).
5. E. Yu. Nefed'ev, V. A. Volkov, A. I. Lyashkov, *et al.*, Defektoskopiya, No. 3, 41 (1986).
6. V. S. Kuksenko, A. I. Lyashkov, V. N. Savel'ev, *et al.*, Mekh. Kompoz. Mater. (Zinatne), No. 4, 710 (1982).
7. A. Frenkel, E. A. Stern, and F. A. Chudnovsky, Solid State Commun. **102**, 637 (1997).
8. E. N. Boborykina, S. E. Nikitin, and F. A. Chudnovskiĭ, Fiz. Tverd. Tela (S.-Peterburg) **37**, 271 (1995).

Translated by A. Poushnov

Physics of the Solid State, Vol. 42, No. 2, 2000, pp. 334–336. Translated from Fizika Tverdogo Tela, Vol. 42, No. 2, 2000, pp. 326–328.

LATTICE DYNAMICS AND PHASE TRANSITIONS

Temperature Effect on Structural Transformations in Nanocrystalline Cobalt Films

G. I. Frolov, V. S. Zhigalov, and V. K. Mal'tsev

Kirenskiĭ Institute of Physics, Siberian Division, Russian Academy of Sciences, Akademgorodok, Krasnoyarsk, 660036 Russia
e-mail: frolov@iph.krasnoyarsk.su

Received April 28, 1999; in final form, July 12, 1999

Abstract—The effect of annealing temperature on the structure and magnetic properties of nanocrystalline cobalt films has been studied by nuclear magnetic resonance (NMR) and magnetometric (vibrational magnetometer) techniques. Interpretation of the experimental data demonstrates that the initial films have an amorphous-like structure due to the high degree of disordering in the intergranular regions and nanoparticles. This structure transforms into the equilibrium polycrystalline state through the formation of a number of intermediate phases. © *2000 MAIK "Nauka/Interperiodica".*

Considerable current interest has been expressed by researchers in nanophase materials—three-dimensional analogs of multilayer structures [1]. These materials possess unusual physical properties owing to the occurrence of new solid states [2]. An example of such materials is provided by nanocrystalline 3*d* metal films prepared by the pulsed plasma deposition [3–6]. The specific features of the pulsed deposition technique are the high pulsed condensation rate (~10^5 A/s) at a pulse length of ~10^{-4} s and at a pulse-duration ratio of ~10^3–10^4, and the high cooling rate of condensate (~10^8 K/s) [5]. The films produced in these technological conditions and under a vacuum of 10^{-6} torr are built up of 3*d* metal nanocrystallites (≤4 nm in size) surrounded by a carbon "coating" [6].

The novelty of the method resides in the fact that the limiting dispersion of crystal structure in the chosen direction is achieved at superhigh condensation rates when the number of arising nuclei is so great that the radius of a critical nucleus coincides with the coalescence radius. On the other hand, the high surface reactivity of nanocrystallites formed under plasma deposition conditions and the large pulse-duration ratio cause the condensate to entrap a large amount of impurity atoms (predominantly, carbon) of residual gases in a vacuum chamber.

Analysis of the available data on the magnetic, electrical, structural, and spectral properties of iron films produced under the given technological conditions [3, 6] suggests that the central region of structural nanoblocks consists predominantly of the phase of supersaturated carbon solution in α-Fe. However, for the cobalt films, this question remains unclear. The point is that the carbon content in the cobalt films is higher than that in the iron films (30 and 20 at. % C, respectively). At the same time, it is known from the data available in the literature that an increase in the carbon content in nanogranular cobalt films leads to a change in the phase composition of the central region of structural blocks; that is, the hexagonal close-packed cobalt phase transforms into the Co_3C phase [7, 8]. Therefore, in order to interpret the unusual properties of nanocrystalline cobalt films, it is necessary to elucidate in detail their initial structure.

In the present work, the effect of annealing temperature on the structure and magnetic properties of cobalt films prepared by the pulsed plasma deposition was studied with the nuclear magnetic resonance (NMR) and magnetometric (vibrational magnetometer) techniques. As is known, the magnitude and distribution of the hyperfine nucleus field in magnetically ordered materials are proportional to the magnetization and carry information on the local electronic and chemical environment of atoms. Therefore, analysis of the NMR spectra makes it possible to elucidate the structure of the studied samples in detail.

The thickness of films deposited onto glass and silicon substrates was equal to 50–100 nm. The samples were subjected to multistage annealing under a vacuum of 10^{-5} torr for 1 h at each fixed temperature T_{an}. The NMR spectra were obtained using the standard spin-echo two-pulse sequence at room temperature.

The NMR spectrum of the initial film is displayed in Fig. 1 (spectrum *a*). It can be seen that the NMR signal is a smeared peak centered at frequency f ~ 190 MHz with a width of ~50 MHz. Upon heating of the sample up to T_{an} = 400–500 K, the spectrum drastically changes. The resonance peak shifts toward the high-frequency range, and its maximum is observed at f = 215 MHz. At T_{an} ~ 400 K, the spectrum involves a long "tail" on the left edge of the line (Fig. 1, spectrum *b*). This tails contains several peaks whose location and

number vary from sample to sample and depend on the carbon content.

A further increase in the annealing temperature brings about the change in the line shape: a symmetric smeared peak (Fig. 1, spectrum *c*) transforms into a narrow peak at $f = 213$ MHz and a "shoulder" in the frequency range 214–221 MHz (Fig. 1, spectrum *d*). At $T_{an} = 700$ K, the peak becomes even narrower without change in the resonance frequency, and the intensity of the shoulder decreases (Fig. 1, spectrum *e*).

Figure 2 depicts the dependence of the magnetization I_s on the annealing temperature for the nanocrystalline cobalt film. The magnetization of the initial film is equal to approximately 850 G, which is considerably less than the magnetization of bulk cobalt samples. The annealing at temperature $T_{an} \le 550$ K leads to a further decrease in the magnetization I_s, whereas, upon annealing at $T_{an} \ge 600$ K, the magnetization increases and virtually reaches the magnitude characteristic of bulk cobalt samples.

Let us consider the experimental data presented in Figs. 1 and 2. The change in the NMR spectra upon annealing of our films qualitatively follows a similar dependence obtained for the cobalt–phosphorus amorphous alloys in [9, 10]. The authors of these works observed the broadening of the NMR line and its shift toward the low-frequency range for amorphous cobalt ribbons and films. A decrease in the NMR frequency and, correspondingly, a decrease in the hyperfine field at cobalt nuclei was accounted for by the electron transfer from phosphorus ions to cobalt ions. According to the X-ray diffraction analysis, our samples consist of nanocrystallites less than 4 nm in size. As follows from the Auger spectroscopic data, these samples contain as much as 30 at. % C. It is assumed that the very broadened NMR spectra of the initial films indicate a high degree of structural disordering, which is determined not only by the intergranular graphite-like regions and a large ratio between the numbers of surface cobalt and bulk cobalt atoms, but also by the disordering of carbon ions dissolved in the cobalt nanoparticles. The latter assumption is confirmed by the presence of satellites in the NMR spectrum of the film after the first annealing. The number of satellites corresponds to the number of carbon ions in the nearest environment of each cobalt ion. This spread in the atomic configurations is responsible for the shape of the spectra of the initial films, which is similar to the shape of the spectra of cobalt–phosphorus amorphous materials.

A similar unusual combination of amorphism and nanocrystallinity was described by Delaunay *et al.* [11]. In this work, the microstructure of granular films prepared by the joint sputtering of cobalt and carbon was investigated at different carbon concentrations and different temperatures of substrate. It was found that the samples containing 27 at. % C are composed of cobalt nanoparticles (~5 nm in diameter) separated by carbon interlayers. However, these authors failed to

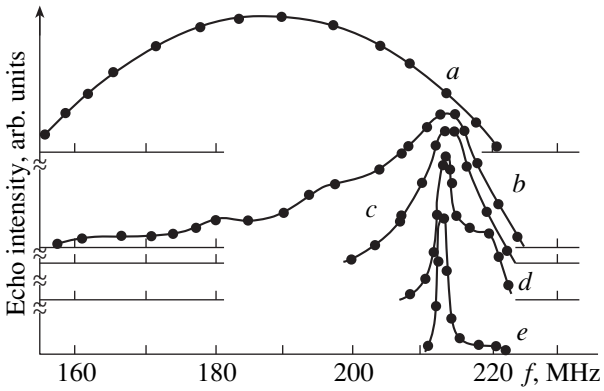

Fig. 1. NMR spectra of cobalt films prepared by pulsed plasma deposition: (*a*) initial film and films annealed at T_{an} = (*b*) 400, (*c*) 500, (*d*) 600, and (*e*) 700 K.

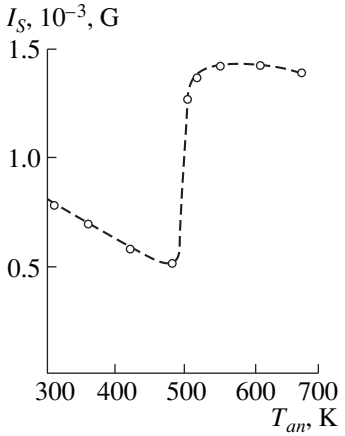

Fig. 2. Dependence of the magnetization I_s on the annealing temperature T_{an} for the nanocrystalline cobalt film.

determine the structure of nanoparticles even with the high-resolution electron microscopy, and, hence, the structure of nanoparticles was interpreted as an amorphous-like structure.

Upon heating of the films up to T_{an} = 400–500 K, carbon is likely to be displaced from the cobalt nanoparticles, and the resonance peak shifts toward the high-frequency range (Fig. 1; spectra *b*, *c*). The NMR signal in the cobalt–phosphorus polycrystalline films is observed at the same frequencies [10]. At room temperature, this signal is a superposition of two resonance lines, which correspond to the face-centered cubic (fcc) and hexagonal close-packed (hcp) phases of cobalt ($f_1 = 213$ MHz and $f_2 = 221$ MHz, respectively). A long tail appeared on the left edge of the NMR line after the first annealing (Fig. 1, spectrum *b*) can be associated with an incomplete displacement of carbon from the cobalt nanoparticles because of low temperature.

The formation of the hcp and fcc magnetic cobalt phases (Fig. 1, spectrum *c*) should seemingly lead to an

increase in the magnetization of samples. However, as is seen from Fig. 2, the value of I_s decreases almost by a factor of 1.5 compared to the magnetization of the initial film. This contradiction can be also explained with the results obtained by Delaunay *et al.* [11], who demonstrated that nanoparticles containing a mixture of the Co_2C and hcp Co phases are formed in the granular cobalt films prepared by the joint sputtering with carbon at the substrate temperature $T = 470$ K. In [11], it was inferred that the carbide compound is formed just at $T = 470$ K. Since the Co_2C phase does not exhibit magnetic properties at room temperature, its formation should cause the overall magnetization to decrease.

At $T_{an} > 600$ K, the NMR line shape changes in the same frequency range: there appears a narrow peak and a broad shoulder, which correspond to a well ordered fcc phase and severely disordered hcp phase of cobalt. According to [11], at $T = 620$ K, the Co_2C phase undergoes decomposition into the hcp cobalt phase and graphite-like carbon. This should be attended by an increase in the magnetization of samples, which is actually observed in Fig. 2.

A further increase in the annealing temperature results in an increase in the amount of the fcc cobalt phase at the expense of a decrease in the content of the hcp cobalt phase (Fig. 1, spectrum *e*); in this case, the magnetization remains virtually constant.

Thus, the investigation into the structure of nanocrystalline cobalt films by the NMR method demonstrated that the initial films consist of the cobalt particles with incorporated carbon atoms. The annealing at $T_{an} > 550$ K results in the formation of a mixture composed of the hcp and fcc cobalt phases. A further increase in the annealing temperature leads to an increase in the content of the fcc phase. The unusual temperature behavior of the magnetization is associated with the formation of the nonmagnetic cobalt carbide phase at $T_{an} = 400$–500 K and its decomposition at $T_{an} > 550$ K.

REFERENCES

1. R. W. Siegel, Phys. Today **10**, 46 (1993).
2. J. P. Perez, V. Dupuis, J. Tuaillon, *et al.*, J. Magn. Magn. Mater. **145** (1–2), 74 (1995).
3. G. I. Frolov, V. S. Zhigalov, S. M. Zharkov, *et al.*, Fiz. Tverd. Tela (S.-Peterburg) **36** (4), 970 (1994).
4. G. I. Frolov, V. S. Zhigalov, A. I. Pol'skiĭ, *et al.*, Fiz. Tverd. Tela (S.-Peterburg) **38** (4), 1208 (1996).
5. V. S. Zhigalov, G. I. Frolov, and L. I. Kveglis, Fiz. Tverd. Tela (S.-Peterburg) **40** (11), 2074 (1998).
6. S. G. Ovchinnikov, B. A. Belyaev, I. S. Edelman, and G. I. Frolov, *Micron–Submicron Technologies for Magnetic Structures*, Preprint No. 776F IF SD RAN (Kirenskiĭ Inst. of Physics, Siberian Division, Russian Academy of Sciences) (1997).
7. Y. Saito, T. Yoshikawa, M. Okuda, *et al.*, J. Appl. Phys. **75** (1), 134 (1994).
8. Y. Yosida, S. Shida, T. Ohsuna, *et al.*, J. Appl. Phys. **76** (8), 4533 (1994).
9. K. Ray, J. Durand, J. I. Budnick, *et al.*, J. Appl. Phys. **49** (3), 1671 (1978).
10. V. K. Mal'tsev, G. I. Fish, and V. I. Tsifrinovich, Fiz. Met. Metalloved. **52** (2), 439 (1981).
11. J. J. Delaunay, T. Hayashi, M. Tomita, *et al.*, J. Appl. Phys. **82** (5), 2200 (1997).

Translated by O. Borovik-Romanova

Physics of the Solid State, Vol. 42, No. 2, 2000, pp. 337–344. Translated from Fizika Tverdogo Tela, Vol. 42, No. 2, 2000, pp. 329–335.

LATTICE DYNAMICS AND PHASE TRANSITIONS

Features of Sound Propagation in the Vicinity of "Symmetry-Dictated" Isostructural Phase Transitions in Ferroelastics

Yu. M. Gufan, E. S. Larin, and A. N. Sadkov

Research Institute of Physics, Rostov State University, pr. Stachki 194, Rostov-on-Don, 344104 Russia

Received April 2, 1999; in final form, July 16, 1999

Abstract—Using a proper ferroelastic phase transition of the tension–compression type as an example, it is shown that, if the order parameter characterizing a structural phase transition allows the existence of a third-power invariant in the Landau potential, then there must be "symmetry-dictated" isostructural phase transition lines in the vicinity of the line of that structural phase transition. These isostructural transitions may manifest themselves both directly and as supercritical anomalies in the behavior of elastic moduli and lattice parameters. These effects are discovered and investigated without invoking the perturbation theory in terms of which the second-order phase transitions are commonly described. A hypothesis is made on the basis of the results obtained that the sound velocity anomalies observed in orthoclase and sanidine crystals are due to the supercritical behavior of the lattice parameters in the vicinity of a symmetry-dictated isostructural phase transition in the prototype phase of these crystals. © *2000 MAIK "Nauka/Interperiodica".*

INTRODUCTION

There are a lot of materials in which the external factors determining the state of the crystal may cause second-order elastic moduli to decrease to such a degree that the crystal lattice becomes unstable against deformation. The phase transitions (PTs) that consist in the occurrence of spontaneous deformation of the crystal lattice are termed ferroelastic [1] by analogy with ferromagnetic and ferroelectric phase transitions. The order parameters (OPs) describing proper ferroelastic phase transitions are proportional to certain linear combinations of the strain-tensor components. In this paper, we will consider only proper ferroelastic PTs. These PTs occur in superconductors which have the β-tungsten structure, such as Nb_3Sn, Nb_3Sb, and V_3Si [2, 3] ($O_h^4 - D_{4h}^9$ phase transitions), in solid solutions of spinels $M_{1-x}Ni_xCr_2O_4$ (M = Cu, Fe) [4, 5] ($O_h^1 - D_{4h}^1 - D_{2h}^{24}$) phase transitions, in Ni–Mn alloys [6], and also in a number of minerals (see, e.g., review [7]). In symmetry terms, all phases on the T–x phase diagram of solid solutions $Nb_3Sn_xSb_{1-x}$ and $M_{1-x}Ni_xCr_2O_4$ are described by the same two-component OP $\boldsymbol{\eta} = (\eta_1, \eta_2)$; in the high-symmetry phase, its components can be considered as a basis for the two-dimensional irreducible representation E_g of the cubic symmetry group of the crystal class O_h [8]. Replacing the proportionality sign by the equality sign, which is of no importance for what follows, we define the OP as

$$\eta_1 = (2u_{zz} - u_{xx} - u_{yy})/\sqrt{6}, \quad \eta_2 = (u_{xx} - u_{yy})/\sqrt{2}, \quad (1)$$

where u_{xx}, u_{yy}, and u_{zz} are the diagonal components of the strain tensor u_{ik}. The concept of the prototype phase [9–11] allows one to describe the PTs between the tetragonal and orthorhombic phases in TeO_2 [12] and solid solutions $YBa_2Cu_3O_{7-y}$ [9, 10] in terms of the same OP. Naturally, the behavior of physical quantities and the features of phase diagrams described by this OP were investigated earlier (see, e.g., [3, 8–10, 13]), and it was emphasized that at least sixth-order terms should be retained in the Landau potential in order to adequately describe the physical characteristics of ferroelastics [8, 13, 14]. However, the methods applied in [8, 13, 14] and approximations used in [7, 10] to investigate the Landau potentials did not allow one to reveal a number of interesting features of the properties of ferroelastics dictated by symmetry.

The objective of this paper is to show that, in addition to PT lines separating phases of different symmetry on phase diagrams of cubic ferroelastics, there must be lines of isostructural PTs separating phases of the same symmetry and structure. An important point is that isostructural PTs in ferroelastics are dictated by symmetry [10]. Furthermore, it will be shown that, even if an experimental phase diagram has no isostructural PT lines, anomalies of physical quantities due to "supercritical" phenomena must take place in the lower-symmetry (tetragonal) phase.

1063-7834/00/4202-0337$20.00

LANDAU THERMODYNAMIC POTENTIAL AND PHASE DIAGRAM

In a cubic crystal, the symmetry change associated with a proper ferroelastic PT of the compression–tension type is described in terms of the two-component OP $\boldsymbol{\eta} = (\eta_1, \eta_2)$ given by (1). In this case, the Landau potential, considered as a function of $\boldsymbol{\eta}$, involves two invariants:

$$I_1 = \eta_1^2 + \eta_2^2, \quad I_2 = \eta_1^3 - 3\eta_1\eta_2^2. \tag{2}$$

A simplest model potential $F = F(I_1, I_2)$ describing a structurally stable state [15, 16] has the form

$$F(I) = a_1 I_1 + a_2 I_1^2 + a_3 I_1^3 + b_1 I_2 + b_2 I_2^2 + \gamma_{12} I_1 I_2, \tag{3}$$

where a_1, a_2, and b_1 are variable parameters dependent on external factors. It is this model that was investigated in [3, 8, 12–14].

The equations of state have the form

$$\begin{aligned} \partial\Phi/\partial\eta_1 &= 2\eta_1\Phi_1 + 3(\eta_1^2 - \eta_2^2)\Phi_2 = 0, \\ \partial\Phi/\partial\eta_2 &= 2\eta_2(\Phi_1 - 3\eta_1\Phi_2) = 0, \end{aligned} \tag{4}$$

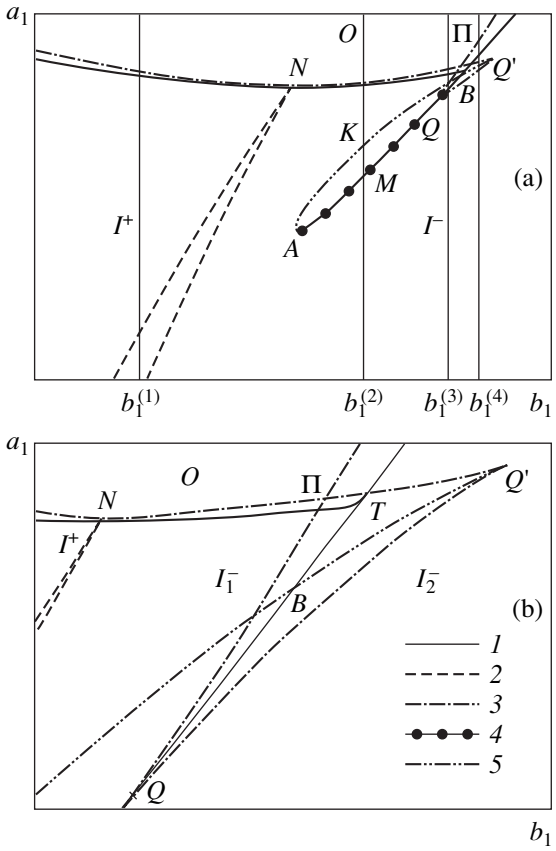

Fig. 1. Phase diagram in the plane of the coefficients a_1 and b_1 involved in the potential F_{el} given by (19). The line designations: *1* is a first-order PT line, *2* is a second-order PT line, *3* is the boundary of a phase stability region, *4* is the line along which the Landau potential (19) is minimum, and *5* is the line along which the potential (19) is maximum.

where Φ is the nonequilibrium potential (3) in the variables η_1 and η_2 and $\Phi_i = \partial F/\partial I_i$ with $i = 1, 2$. It is seen from (4) that the OP describes four phases, the symmetry of which is determined by the conditions

$$0: \ \eta_1 = \eta_2 = 0, \tag{5}$$

$$I^{\pm}: \ \eta_1 \neq 0, \ \eta_2 = 0, \ 2\Phi_1 + 3\eta_1\Phi_2 = 0, \tag{6}$$

$$II: \ \eta_1 \neq 0, \quad \eta_2 \neq 0, \ \Phi_1 = 0, \ \Phi_2 = 0. \tag{7}$$

The phases $I^{\pm}$ (6) have the same (tetragonal) symmetry. However, in the phase I^+ ($\eta_1 > 0$, $\eta_2 = 0$), we have $u_{zz}^T > u_{xx}^T = u_{yy}^T$, that is, the unit cell is lengthened ($c/a > 1$), whereas in the phase $I^{\pm}$ ($\eta_1 < 0$), we have $u_{zz}^T < u_{xx}^T = u_{yy}^T$, that is, the unit cell is shortened ($c/a < 1$). The phases $I^{\pm}$ are anti-isostructural [15].

Let us consider the equation of state for the phases $I^{\pm}$

$$\begin{aligned} &2a_1 + 3b_1\eta_1 + 4a_2\eta_1^2 \\ &+ 5\gamma_{12}\eta_1^3 + 6(a_3 + b_2)\eta_1^4 = 0. \end{aligned} \tag{8}$$

In the general case, equation (8) has four solutions corresponding to critical (extremum) points of the nonequilibrium potential $F(I_1, I_2)$ (3). The regions of existence of the four solutions (8) are determined by the condition

$$\begin{aligned} \partial^2\Phi/\partial\eta_1^2 &= 2a_1 + 6b_1\eta_1 + 12a_2\eta_1^2 \\ &+ 20\gamma_{12}\eta_1^3 + 30(a_3 + b_2)\eta_1^4 = 0. \end{aligned} \tag{9}$$

From (8) and (9), the regions in the space $R^3 = (a_1, b_1, a_2)$ can be found in which the phases I^+ ($\eta_1 > 0$) and I^- ($\eta_1 < 0$) are stable. Let us consider a plane $R^2 = (a_1, b_1)$ in R^3 corresponding to $a_2 = \text{const}$. When $0 < a_2 < 25\gamma_{12}^2/64(a_3 + b_2)$, the boundary of the stability region of the phases $I^{\pm}$ $a_1 = a_1(b_1)$, is fairly complicated (see Fig. 1). This line has cuspidal points Q and Q' and a self-intersection point Π. Figure 1a shows one of the cross sections of the phase diagram. In the region for which Q, Q', and Π are boundary points in Fig. 1, two stable solutions of the equation of state (8) coexist that correspond to minima of $F(I_1, I_2)$. These solutions describe phases of the same symmetry: at $\gamma_{12} > 0$, these phases are I_1^- and I_2^- with $\eta_1(I_1^-) < \eta_1(I_2^-)$, whereas at $\gamma_{12} < 0$, they are I_1^+ and I_2^+ with $\eta_1(I_1^+) < \eta_1(I_2^+)$. It is in this region that an isostructural PT is possible [17]. Therefore, the OP describes both the PT with a symmetry change and the PT in which the symmetry does not change (isostructural PT). We note that the latter PT is of the first order. The line of the isostructural PT terminates, on one side, in the critical point Q (liquid–gas critical point) and, on the other side, in the three-phase point T, at which this line shares its tangent either with

the $0–I_2^-$ or with the $0–I_2^+$ first-order PT line (at $\gamma_{12} > 0$ or $\gamma_{12} < 0$, respectively). The three-phase point T has coordinates

$$a_1^T = \frac{[\gamma_{12}^2 - 4a_2(a_3 + b_2)]^2}{4^3(a_3 + b_2)^3},$$
$$b_1^T = \frac{\gamma_{12}[\gamma_{12}^2 - 4a_2(a_3 + b_2)]}{24(a_3 + b_2)^2}, \quad (10)$$

while the coordinates of the critical point Q are

$$a_1^Q = 2a_2\eta_Q^2 - 5\gamma_{12}\eta_Q^3 + 9(a_3 + b_2)\eta_Q^4,$$
$$b_1^Q = 8a_2\eta_Q/3 - 5\gamma_{12}\eta_Q^2 + 8(a_3 + b_2)\eta_Q^3, \quad (11)$$

where

$$\eta_Q = \{-5\gamma_{12} - [25\gamma_{12}^2 - 64a_2(a_3 + b_2)]^{1/2}\}/24(a_3 + b_2).$$

Along the $0–I^\pm$ first-order PT line we have

$$da_1/db_1\big|_{0-I^\pm} = -\eta_1. \quad (12)$$

The $0–I^-$ and $0–I^+$ first-order PT lines differ in slope at the three-phase point T (Fig. 1). According to (12), the slopes of these lines are

$$da_1/db_1\big|_{0-I_2^-}^{0-I_1^-} = -\eta_1^T(I_1^-, I_2^-), \quad (13)$$

where

$$\eta_1^T(I_1^-, I_2^-) = \{-\gamma_{12} \pm [3\gamma_{12}^2 - 8a_2(a_3 - b_2)]^{1/2}\}/4(a_3 + b_2). \quad (14)$$

A second condition for the stability of the phases $I^\pm$ is given by

$$\partial^2\Phi/\partial\eta_2^2 = 2a_1 - 6b_1\eta_1 + 4a_2\eta_1^2 - 4\gamma_{12}\eta_1^3 + 6a_3\eta_1^4 - 12b_2\eta_1^4 \geq 0. \quad (15)$$

The line given by (8) and (15) (with the equality sign) is the boundary of the region of stability of phase II in the $R^2 = (a_1, b_1)$ plane.

At $4a_2b_2 - \gamma_{12}^2 > 0$, the I^+–II and I^-–II phase transitions occur along the second-order PT lines. In order to investigate the dependence of physical quantities on external factors (temperature, pressure, average concentration, etc.), one should specify the phenomenological parameters of the theory as functions of temperature, pressure, and concentration, thereby choosing a thermodynamic path. For simplicity, we assume that only a_1 depends on the external factors. For the sake of definiteness, let a_1 depend only on temperature, $a_1 = a^0(T - T_c)$, so that the thermodynamic path is a straight line parallel to the Oa_1 axis on the phase diagram (Fig. 1).

THE BEHAVIOR OF PHYSICAL QUANTITIES ALONG A THERMODYNAMIC PATH

The phase diagram in Fig. 1 is obtained without specifying the OP, so that its features are determined only by the OP symmetry properties. To investigate physical properties of crystals at a proper ferroelastic PT, we specify the physical meaning of the OP and write the nonequilibrium elastic energy in the form [7]

$$\Phi_{el} = \sum \alpha_i e_i + 1/2\sum C_{ik}e_ie_k + 1/3!\sum C_{ijk}e_ie_je_k + \ldots + 1/6!\sum C_{ijklmn}e_ie_je_ke_le_me_n, \quad (16)$$

where α_i is the thermal expansion coefficient; C_{ik}, C_{ikl}, …, C_{ijklmn} are the elastic moduli of all orders from the second to the sixth; and e_i ($i = 1,\ldots, 6$) are the strain tensor components in the Voigt notation: $e_1 = u_{xx}$, $e_2 = u_{yy}$, $e_3 = u_{zz}$, $e_4 = 2u_{yz}$, $e_5 = 2u_{xz}$, and $e_6 = 2u_{xy}$. In (16), all possible strains are included. For the description of those properties of phases which are determined by the two-component OP, it is sufficient to put $e_i = 0$ for $i = 4$, 5, 6 in (16). The physical meaning of the phenomenological coefficients in the Landau potential will become clear when we write (16) in terms of the representation basis components (1) and

$$\eta_3 = (u_{xx} + u_{yy} + u_{zz})/\sqrt{3}. \quad (17)$$

From (1) and (17) we obtain

$$u_{xx} = \eta_3/\sqrt{3} - \eta_1/\sqrt{6} + \eta_2/\sqrt{2},$$
$$u_{yy} = \eta_3/\sqrt{3} - \eta_1/\sqrt{6} - \eta_2/\sqrt{2}, \quad (18)$$
$$u_{zz} = \eta_3/\sqrt{3} + \eta_1\sqrt{2}/3.$$

The total Landau potential, expressed in terms of (1) and (17), takes the form

$$F_{el} = AI_3 + BI_3^2 + CI_3^3 + a_1I_1 + a_2I^2 + a_3I^3 + b_1I_2 + b_2I_2^2 + \gamma_{12}I_1I_2 + \gamma_{13}I_1I_3 + \gamma_{23}I_2I_3 + \gamma_{113}I_1^2I_3, \quad (19)$$

where $I_3 = \eta_3$ as given by (17).

Comparing (16) with (19) gives relations between the coefficients involved in the potential F_{el} in (19) and the isothermal elastic moduli C_{ik}, …, C_{ijklmn}

$$A = \alpha\sqrt{3},$$
$$B = (C_{11} + 2C_{12})/2,$$
$$C = (C_{111} + C_{123} + 3C_{112})/3\sqrt{3}, \quad (20)$$
$$a_1 = (C_{11} - C_{12})/2,$$
$$a_2 = (2C_{1111} - 4C_{1112} + C_{1122})/16,$$

$$
\begin{aligned}
a_3 &= C_{111111} - C_{111112} + C_{111122} - C_{111222},\\
b_1 &= (2C_{111} + 2C_{123} - 3C_{112})/6\sqrt{6},\\
b_2 &= C_{111111} - C_{111112} - C_{111122} + 2C_{111222}\\
&\quad + C_{111123} - C_{111223} + C_{112233}/3,\\
\gamma_{12} &= (5C_{11111} - 5C_{11112} + C_{11122}\\
&\quad + 2C_{11123} - C_{11223})/6\sqrt{6},\\
\gamma_{13} &= (2C_{111} - C_{123})/2\sqrt{3},\\
\gamma_{23} &= (2C_{1111} - C_{1112} - C_{1122} + 2C_{1231})/6\sqrt{2},\\
\gamma_{113} &= (10C_{11111} - 4C_{11112} + 2C_{11122}\\
&\quad - 2C_{11123} + C_{11223})/4\sqrt{3}.
\end{aligned}
\tag{21}
$$

In what follows, we assume that, in the cubic phase, $B > 0$, $C > 0$, and $\alpha = 0$ over the entire range of the external parameters.

We investigate the behavior of the physical parameters of the crystal along four thermodynamic paths (see Fig. 1) in the case where $\gamma_{12} > 0$ and $a_1 = a_1^0(T - T_c)$. The following results are obtained.

(1) $b_1^{(1)} < 0$, there occurs the sequence of PTs $0 \xrightarrow{\text{I}} I^+ \xrightarrow{\text{II}}$ II;

(2) $b^A < b_1^{(2)} < b_1^Q$, the PT sequence $0 \xrightarrow{\text{I}} I_1^- \text{ — } I_2^- \xrightarrow{\text{II}}$ II;

(3) $b_1^Q < b_1^{(3)} < b_1^T$, the PT sequence $0 \xrightarrow{\text{I}} I_1^- \xrightarrow{\text{I}} I_2^- \xrightarrow{\text{II}}$ II;

(4) $b_1^{(4)} > b_1^T$, the PT sequence $0 \xrightarrow{\text{I}} I_2^- \xrightarrow{\text{II}}$ II.

The numbers Ⅰ and Ⅱ indicate that the PT is of the first and second order, respectively. The physical quantities show anomalous behavior along dot-and-dash lines in Fig. 1, although there is no phase transition in this "supercritical" region. In each phase, the effective elastic moduli are given by

$$
\begin{aligned}
C_{11}^* &= \partial^2\Phi/\partial u_{xx}^2 = \Phi_{11}/6 + \Phi_{22}/2 + \Phi_{33}/3\\
&\quad - \Phi_{12}/\sqrt{3} - \Phi_{13}\sqrt{2}/3 + \Phi_{23}\sqrt{2}/3,\\
C_{22}^* &= \partial^2\Phi/\partial u_{yy}^2 = \Phi_{11}/6 + \Phi_{22}/2 + \Phi_{33}/3\\
&\quad + \Phi_{12}/\sqrt{3} - \Phi_{13}\sqrt{2}/3 - \Phi_{23}\sqrt{2}/3,\\
C_{33}^* &= \partial^2\Phi/\partial u_{zz}^2 = 2\Phi_{11}/3 + 2\Phi_{13}\sqrt{2}/3 + \Phi_{33}/3,\\
C_{12}^* &= \partial^2\Phi/\partial u_{xx}\partial u_{yy}\\
&= \Phi_{11}/6 - \Phi_{22}/2 + \Phi_{33}/3 - \Phi_{13}\sqrt{2}/3,\\
C_{13}^* &= \partial^2\Phi/\partial u_{xx}\partial u_{zz}\\
&= -\Phi_{11}/3 + \Phi_{33}/3 + \Phi_{12}/\sqrt{3} + \Phi_{13}/3\sqrt{2} + \Phi_{23}/\sqrt{6},\\
C_{23}^* &= \partial^2\Phi/\partial u_{yy}\partial u_{zz}\\
&= -\Phi_{11}/3 + \Phi_{33}/3 - \Phi_{12}/\sqrt{3} + \Phi_{13}/3\sqrt{2} - \Phi_{23}/\sqrt{6},
\end{aligned}
\tag{22}
$$

where $\Phi_{ij} = \partial^2\Phi/\partial\eta_i\partial\eta_j$ and $i, j = 1, 2, 3$.

Expressions (22) give C_{ik}^* as a function of the external parameters for each of the phases. It should be noted that the combinations of the elastic moduli, dictated by symmetry rather than the moduli themselves, commonly show anomalous behavior. Indeed, the crystal becomes unstable against deformation when one of the eigenvalues of the elastic-modulus matrix vanishes.

In the cubic phase, we have

$$
\begin{aligned}
\eta_3^0 &= \eta_1^0 = \eta_2^0 = 0,\\
u_{xx}^0 &= u_{yy}^0 = u_{zz}^0 = 0,
\end{aligned}
\tag{23}
$$

and the "symmetry-dictated" combinations of the elastic moduli are

$$
\begin{aligned}
\lambda_1^0 &= C_{11}^0 + 2C_{12}^0 = 2B,\\
\lambda_2^0 &= C_{11}^0 - C_{12}^0 = 2a_1 = 2a_1^0(T - T_c).
\end{aligned}
\tag{24}
$$

In the tetragonal phases I^+ ($\eta_1^T > 0$) and I^- ($\eta_1^T < 0$), three types of domains are possible,

$$
\begin{aligned}
&1)\ u_{xx}^T = u_{yy}^T = -\eta_1^T/\sqrt{6} + \eta_3^T/\sqrt{3},\\
&\qquad u_{zz}^T = 2\eta_1^T/\sqrt{6} + \eta_3^T/\sqrt{3},\\
&2)\ u_{yy}^T = u_{zz}^T = -\eta_1^T/\sqrt{6} + \eta_3^T/\sqrt{3},\\
&\qquad u_{xx}^T = 2\eta_1^T/\sqrt{6} + \eta_3^T/\sqrt{3},\\
&3)\ u_{xx}^T = u_{zz}^T = -\eta_1^T/\sqrt{6} + \eta_3^T/\sqrt{3},\\
&\qquad u_{yy}^T = 2\eta_1^T/\sqrt{6} + \eta_3^T/\sqrt{3},
\end{aligned}
\tag{25}
$$

where η_3^T is determined from the condition $\partial F/\partial\eta_3 = 0$ at $\eta_2^T = 0$,

$$
\begin{aligned}
\eta_3^T &= [-\gamma_{13}(\eta_1^2 + \eta_2^2) - \gamma_{23}(\eta_1^3 - 3\eta_1\eta_2^2)\\
&\quad - \gamma_{113}(\eta_1^2 + \eta_2^2)^2]/2B.
\end{aligned}
\tag{26}
$$

The relative change in volume for the phases $I^\pm$ is given by the equilibrium value η_3^T,

$$
\begin{aligned}
\Delta V_T/V_0 &\approx \eta_3^T\\
&= -(\eta_1^T)^2[\gamma_{13} - \gamma_{23}\eta_1^T + \gamma_{113}(\eta_1^T)^2]/(C_{11} + 2C_{12}),
\end{aligned}
\tag{27}
$$

where η_1^T is the equilibrium value of the OP in the phases $I^{\pm}$, which is found from the equation of state

$$2a_1 + 3b_1\eta_1^T + 4a_2^*(\eta_1^T)^2 + 5\gamma_{12}^*(\eta_1^T)^3 + 6(a_3^* + b_2^*)(\eta_1^T)^4 = 0, \quad (28)$$

with

$$a_2^* = a_2 - \gamma_{13}^2/4B, \quad \gamma_{12}^* = \gamma_{12} - \gamma_{13}\gamma_{23}/2B,$$

$$b_2^* = b_2 - \gamma_{23}^2/4B, \quad a_3^* = a_3 - \gamma_{13}\gamma_{113}/2B.$$

Equation (28) coincides with the equation of state (8), in which the coefficients are replaced by their renormalized values a_2^*, b_2^*, a_3^*, and γ_{12}^*.

The eigenvalues λ_i^T are given by

$$\lambda_1^T = C_{11}^T - C_{12}^T = \partial^2\Phi/\partial\eta_2^2, \quad (29)$$

$$\lambda_{2,3}^T = \{(C_{11}^T + C_{12}^T + C_{33}^T) \pm [(C_{11}^T + C_{12}^T - C_{33}^T)^2 + 8C_{13}^2]^{1/2}\}/2 = \{(\partial^2\Phi/\partial\eta_3^2 + \partial^2\Phi/\partial\eta_1^2) \pm [(\partial^2\Phi/\partial\eta_3^2 + \partial^2\Phi/\partial\eta_1^2)^2 - 4\Delta]^{1/2}\}/2, \quad (30)$$

where $\Delta = (\partial^2\Phi/\partial\eta_3^2)(\partial^2\Phi/\partial\eta_1^2) - (\partial^2\Phi/\partial\eta_3\partial\eta_1)^2$ and C_{ik}^T are the elastic moduli in the phases $I^{\pm}$. It follows from (29) that the condition $\lambda_1 = 0$ determines the boundary of the stability region of the orthorhombic phase on the phase diagram. The condition $\Delta = 0$ determines the stability limits of the phases $I^{\pm}$ and the region of coexistence of the isostructural phases I_1^- and I_2^-.

When the external parameters are varied along the thermodynamic path $a_1 = a_0(T - T_c)$, $b_1^{(1)} < 0$, $0 < b_1^{(1')} < b_1^{(A)}$ (Fig. 1), the equation of state (28) has only one solution, corresponding to the stable state of the phase I^+ ($b_1 < 0$) or I^- ($b_1 > 0$). This solution may be written as $\eta_1^T = \eta_0^T(T) + \eta^T$, where only the first term

$$\eta_0^T(T) = [-3b_1 \pm (9b_1^2 - 32a_1a_2^*)^{1/2}]/8a_2^* \quad (31)$$

is dependent on the external factors, whereas η^T is determined by higher-order terms in the Landau potential and is independent of the external factors. Therefore, the key features of the anomalous behavior of physical parameters of the crystal are determined by the temperature dependence of η_0^T

$$\eta_0^T(T) = 3\eta_0^T\big|_{T_{pt}}\{1 + [(T_c^* - T)/(T_c^* - T_c)]^{1/2}\}/4, \quad (32)$$

$$T_{pt} = T_c + b_1^2/4a_2^*a_0, \quad T_c^* = T_c + 9b_1^2/32a_2^*a_0,$$
$$\eta_0^T\big|_{T_{pt}} = -b_1/2a_2^*, \quad \eta_0^T\big|_{T_c^*} = -3b_1/8a_2^*, \quad (33)$$

where T_{pt} is the temperature at which the 0–$I^{\pm}$ phase transition occurs, and T_c^* is the temperature at which the phases $I^{\pm}$ become unstable, i.e., $\Delta = 0$ [see the text below (30)],

$$\Delta = 2B(3b_1 + 8a_2^*\eta_0^T)\eta_0^T = 2B(3b_1/8a_2)^2\{[(T_c^* - T)/(T_c^* - T_c)]^{1/2} + (T_c^* - T)/(T_c^* - T_c)\}. \quad (34)$$

The symmetry-dictated combinations of elastic moduli are

$$\lambda_1^T = C_{11}^T - C_{12}^T = -9b_1\eta_0^T = -27b_1\eta_0^T\big|_{T_{pt}}\{1 + [(T_c^* - T)/(T_c^* - T_c)]^{1/2}\}/4,$$
$$(C_{11}^T - C_{12}^T)\big|_{T_{pt}} = -9b_1^2/2a_2, \quad (C_{11}^T - C_{12}^T)\big|_{T_c^*} = 27b_1^2/8a_2. \quad (35)$$

From (35) it follows that, at the temperature T_c^*, where the phases $I^{\pm}$ lose their stability, the combination $C_{11}^T - C_{12}^T$ undergoes a jump

$$(C_{11}^T - C_{12}^T)\big|_{T_c^*} - (C_{11}^0 - C_{12}^0)\big|_{T_c^*} = 45b_1^2/16a_2.$$

The two other eigenvalues, λ_2 and λ_3, have the following form in the vicinity of the PT, $\Delta \longrightarrow 0$:

$$\lambda_2^T = 2C_{11}^0 + C_{12}^0 - \Delta/[2(2C_{11} + C_{12})], \quad \lambda_3^T = \Delta/[2(2C_{11}^0 + C_{12}^0)]. \quad (36)$$

It follows from (36) that one of these eigenvalues has the following temperature dependence:

$$\lambda_3^T = [9(C_{11}^0 + 2C_{12}^0)/64(2C_{11}^0 + C_{12}^0)](\eta_0^T\big|_{T_{pt}})^2 \times \{[(T_c^* - T)/(T_c^* - T_c)]^{1/2} + (T_c^* - T)/(T_c^* - T_c)\}. \quad (37)$$

From (37) we obtain that, at $T \longrightarrow T_c^*$,

$$\lambda_3 \sim (T_c^* - T)^{1/2}, \quad (38)$$

while at the PT point T_{pt}, where $(T_c^* - T_{pt})/(T_c^* - T_c) = 1/9$, we have

$$\lambda_3 = [(C_{11}^0 + 2C_{12}^0)/16(2C_{11}^0 + C_{12}^0)](\eta_0^T\big|_T)^2. \quad (39)$$

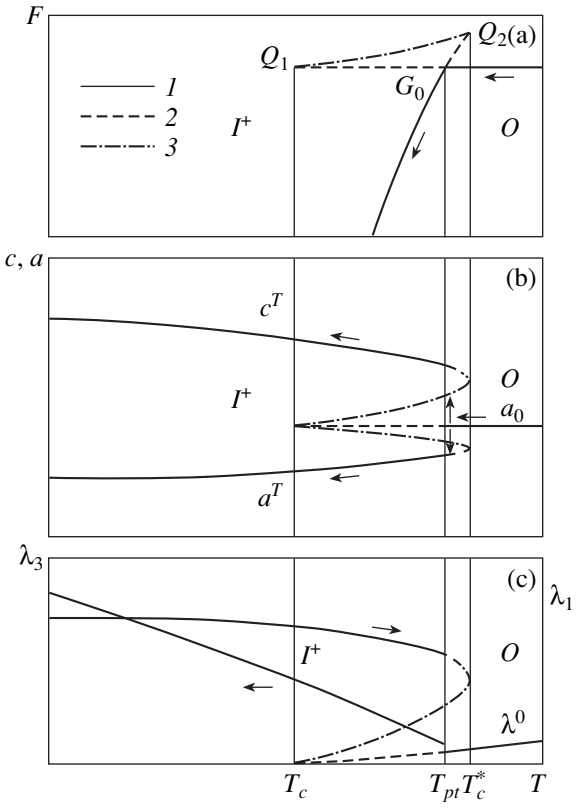

Fig. 2. Temperature dependences of (a) equilibrium values F of the Landau potential (19), (b) the lattice parameters a and c and (c) elastic-modulus combinations λ_1 and λ_3 for a thermodynamic path $b_1^{(1)} < 0$. The line designations: *1* is a line corresponding to equilibrium values of the free energy of stable phases, *2* is a line corresponding to equilibrium values of the free energy of metastable phases, and *3* is a line corresponding to the maximum values $F(T)$ of the nonequilibrium potential (19).

The symmetry-dictated combination

$$\bar{C}_{11}^T - \bar{C}_{12}^T = (C_{11}^T + C_{12}^T + 2C_{33}^T - 4C_{13}^T)/3 = \partial^2\Phi/\partial\eta_1^2, \quad (40)$$

was discussed in detail in [7]. In accordance with [7], the elastic moduli are marked with an overscribed bar in (40). In the tetragonal phase we have

$$\partial^2\Phi/\partial\eta_1^2\big|_{T_c^*} = \eta_0^T(3b_1 + 8a_2\eta_0^T)\big|_{T_c^*} = 4\eta_0^T\big|_T(1 - a_2/a_2^*). \quad (41)$$

Thus, at $\gamma_{13} \neq 0$, the combination $\bar{C}_{11}^T - \bar{C}_{12}^T$ goes soft, but remains nonzero at T_c^*.

Figure 2 shows the temperature dependences of the equilibrium values $F(T)$ of the Landau potential (19), and also $u_{xx} = u_{yy}(T)$, $u_{zz}(T)$, $\lambda_1(T)$, and $\lambda_3(T)$ for a thermodynamic path with $b_1^{(1)} < 0$. At $0 < b_1^{(1')} < b_1^A$, the results for the phases 0 and I are similar to those presented above. In Fig. 2a, point G_0 is the intersection point of two branches of the temperature dependence of the equilibrium free energy; solid lines correspond to the stable phases 0 and I^+, between which a phase transition occurs at point G_0. Lines Q_1G_0 and Q_2G_0 correspond to the equilibrium energy of the phases 0 and I^+ in a metastable state. The end points of these lines Q_1 and Q_2, which are cuspidal points of the $\Phi_{eq}(T)$ line, determine the maximum temperature width of the PT hysteresis between the 0 and I^+ phases. Figure 2b shows the temperature dependences of the lattice parameters a_0, $a^T = a_0(1 + u_{xx}^T)$ (with $u_{xx}^T = u_{yy}^T$), and $c^T = c_0(1 + u_{zz}^T)$. The elastic-modulus combinations $\lambda^0(T)$, $\lambda_1^T(T)$, and $\lambda_3^T(T)$ as functions of temperature are shown in Fig. 2c. It is seen from Figs. 2b and 2c that the temperature dependences of all the physical characteristics exhibit a jump at the first-order PT temperature between the 0 and I^+ phases in accordance with the general consideration.

When the thermodynamic path passes far from point Q (Fig. 1), the temperature dependence of physical characteristics is monotonic in the phase I^+. However, this dependence ceases to be monotonic in the vicinity of the critical point Q. Figure 3 shows the temperature dependence of physical quantities along a thermodynamic path for which $b_1^A < b_1^{(2)} < b_1^Q$. Both the lattice parameters and elastic moduli are seen to exhibit the "supercritical" behavior along this path; namely, their temperature dependence becomes nonmonotonic. In Fig. 1, curve *QABQ'* is constructed, which determines the extremum points in the temperature dependence of $\lambda_3^T(T)$; namely, the extremum points correspond to the intersection points of the thermodynamic path and this line. In Fig. 1, for example, point K corresponds to a maximum of $\lambda_3(T)$ and point M, to its minimum. In Fig. 3c, these points K and M correspond to T_{max} and T_{min}, respectively. In the vicinity of $T = T_{min}$, the lattice parameters also exhibit nonmonotonic change (Fig. 3b): $a(T)$ has a maximum and $c(T)$ has a minimum. In the I^- phase ($c/a < 1$), λ_3 becomes soft at $T = T_{min}$, whereas $\lambda_1(T) = C_{11}^T - C_{12}^T$ reaches its maximum at this point (Fig. 3c). As the thermodynamic path approaches $b_1 = b_1^Q$, the anomalies become more and more pronounced, and at $b_1 = b_1^Q$ and $T = T_Q = a_1^Q/a_0^0 + T_C\lambda_3$, the quantity λ_3 vanishes. In the vicinity of T_Q ($T \longrightarrow T_Q$), we have

$$\lambda_3 \sim |T - T_Q|^{2/3}. \quad (42)$$

For thermodynamic paths for which $b_1^Q < b_1^{(3)} < b_1^T$ (Fig. 1), an isostructural PT occurs at points of the QT

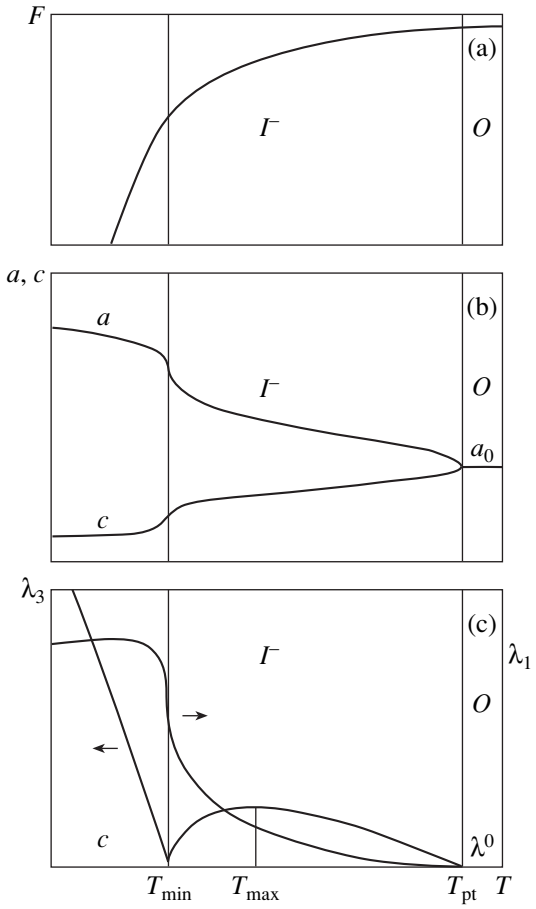

Fig. 3. Temperature dependences of the same physical quantities as in Fig. 2, but along a thermodynamic path $0 < b_1^{(2)} < b_1^A$.

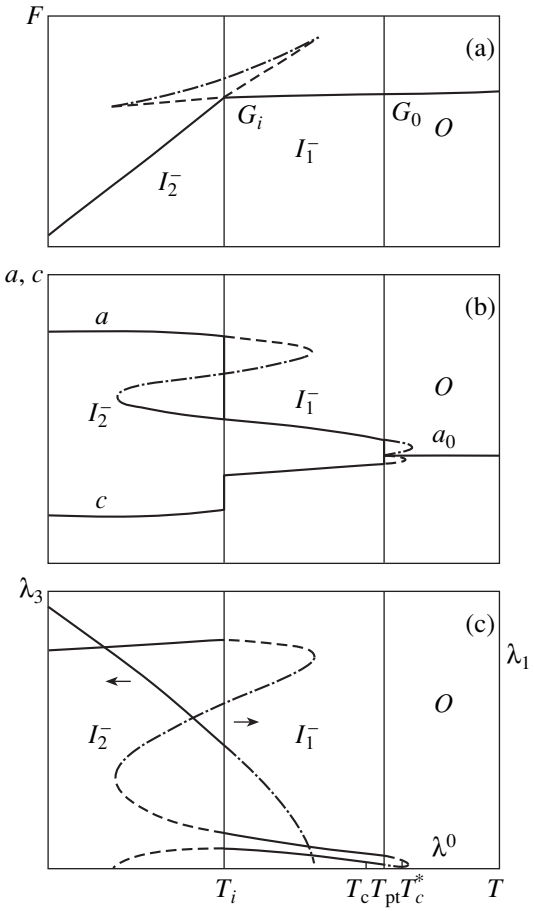

Fig. 4. Temperature dependences of the same physical quantities as in Fig. 2, but along a thermodynamic path $b_1^Q < b_1 < b_1^T$.

line. In Fig. 4a, the temperature T_i of the isostructural PT is given by the abscissa of point G_i. The isostructural PT is of the first order; the jump in the order parameter due to this phase transition increases in value along line QT from zero (at $b = b_1^Q$) to its maximum value at the three-phase point T,

$$\Delta\eta_1^T\big|_T = [3\gamma_{12}^{*2} - 8a_2(a_3^* + b_2^*)]^{1/2}/4(a_3 + b_2). \quad (43)$$

When the thermodynamic path moves away from the critical point Q to $b_1 = b_1^B$, the quantity $\lambda_3(T)$ has a maximum as a function of temperature. This maximum is absent when $b_1^B < b_1 < b_1^T$, and in this case, the isostructural PT is not accompanied by softening of the λ_3; the "softening" takes place for the metastable solution with decreasing temperature and, hence, it may manifest itself in hysteresis phenomena (with rapid enough temperature variations). The $\lambda_1(T)$ dependence shows a positive jump as the temperature is decreased (Fig. 4c).

MANIFESTATIONS OF THE ISOSTRUCTURAL PHASE TRANSITION IN ACOUSTIC PHENOMENA

The dependence of the velocity of sound of different polarization is most commonly used to reveal the effect of external factors on the elastic moduli C_{ik}, although only certain linear combinations can be measured in most cases. In particular, the dependence of λ_3 on the external factors described in this paper must manifest itself in the velocity of longitudinal sound propagating along the inherent direction of the crystal and, therefore, not breaking the symmetry of the tetragonal phase. As far as we know, no direct measurements of this quantity have been made on cubic crystals undergoing a proper ferroelastic phase transition to a tetragonal phase. The velocity of longitudinal sound as a function of temperature was measured, for example, in orthoclase and sanidine [18, 19]. It was found that, as the temperature is increased, the velocity of longitudinal sound along the b axis (twofold axis of symmetry) first decreases, then passes through a minimum, and

increases in both orthoclase and sanidine in a single-phase region. In both the cases, the minimum was reached in the temperature range 400–440°C.

Orthoclase and sanidine crystals have low (monoclinic) symmetry. However, as shown in [10, 11], these crystals, as well as all SiO_2 oxides, have the same cubic prototype phase (the structure from which, for example, all SiO_2 oxides can be obtained as its derivatives). This common prototype phase has the O_h^9 symmetry, and the symmetry of orthoclase and sanidine can be obtained by an antiferroelectric displacement of atoms within a unit cell and its distortion described by two order parameters, e_1 and e_2. Based on these results, one may suppose that the cause of the nonmonotonic temperature dependence of the sound velocity in orthoclase and sanidine is a symmetry-dictated isostructural phase transition in the crystal associated with a ferroelastic phase transition in the prototype phase.

From the theory developed in this paper, it follows that the isostructural PT is dictated by symmetry in this case. Sanidine and orthoclase have a common prototype phase and the same order parameter; this is the reason why the nonmonotonic temperature dependence of the sound velocity takes place in these materials at about the same temperature. If this interpretation of the temperature dependence of the sound velocity is true, then in this temperature range changes must occur in the lattice parameters [see (3) and (4)] and Debye–Waller temperature factors related to each other.

ACKNOWLEDGMENTS

This work was supported by the Russian Foundation for Basic Research.

REFERENCES

1. K. Aizu, J. Phys. Soc. Jpn. **27**, 387 (1969).
2. L. R. Testardi, M. Veger, and I. Goldberg, *Superconducting Compounds with the β-Tungsten Structure* (Mir, Moscow, 1977).
3. J. D. Axe and Y. Yamada, Phys. Rev. B: Condens. Matter **24**, 2567 (1981).
4. A. Wold, R. J. Arnott, E. Wipple, and J. B. Goodenough, J. Appl. Phys. **34**, 1085 (1963).
5. Y. Kino and S. Miyahara, J. Phys. Soc. Jpn. **21**, 2732 (1966).
6. E. Z. Vintaĭkin, D. S. Litvin, and V. D. Udovenko, Fiz. Met. Metalloved. **33**, 77 (1972).
7. M. A. Carpenter, E. K. H. Salje, and A. Graeme-Barber, J. Mineral. **10** (4), 621 (1998).
8. V. P. Sakhnenko and V. M. Talanov, Fiz. Tverd. Tela (Leningrad) **21** (8), 2435 (1979); **22** (3), 785 (1980).
9. Yu. M. Gufan, Pis'ma Zh. Éksp. Teor. Fiz. **61** (8), 646 (1995); Kristallografiya **40** (2), 203 (1995).
10. P. Toledano and V. Dmitriev, *Reconstructive Phase Transitions* (World Scientific, 1996).
11. V. I. Torgashev, Doctoral Dissertation in Mathematical Physics (Rostov-on-Don, 1998).
12. Yu. M. Gufan, V. P. Dmitriev, S. B. Roshal', and V. I. Snezhkov, *Landau Phases in Close-Packed Structures* (Rostov. Gos. Univer., Rostov-on-Don, 1990).
13. E. I. Kut'in, V. L. Lorman, and S. N. Pavlov, Usp. Fiz. Nauk **161** (6), 109 (1991).
14. P. Toledano, T. E. Fejer, and B. A. Auld, Phys. Rev. B: Condens. Matter **27**, 5717 (1983).
15. Yu. M. Gufan, *Structural Phase Transitions* (Nauka, Moscow, 1982).
16. E. S Larin, Candidate's Dissertation in Mathematical Physics (Rostov-on-Don, 1984).
17. Yu. M. Gufan and E. S. Larin, Dokl. Akad. Nauk SSSR **242**, 1311 (1978).
18. I. N. Moshchenko, A. N. Sadkov, V. K. Yatsenko, *et al.*, Izv. Vyssh. Uchebn. Zaved. (Sev.-Kavkaz. region), Estestv. Nauki, No. 4, 56 (1997).
19. E. S. Larin, M. I. Novgorodova, A. N. Sadkov, *et al.*, Izv. Vyssh. Uchebn. Zaved. (Sev.-Kavkaz. region), Estestv. Nauki, No. 3, 57 (1999).

Translated by Yu. Epifanov

Physics of the Solid State, Vol. 42, No. 2, 2000, pp. 345–349. Translated from Fizika Tverdogo Tela, Vol. 42, No. 2, 2000, pp. 336–340.

LATTICE DYNAMICS AND PHASE TRANSITIONS

Polarization-Optical and X-ray Diffraction Investigations on the Symmetry of Distorted Phases of Ammonium Cryolite $(NH_4)_3ScF_6$

S. V. Mel'nikova*, S. V. Misyul', A. F. Bovina*, and M. L. Afanas'ev***

** Kirenskiĭ Institute of Physics, Siberian Division, Russian Academy of Sciences, Akademgorodok, Krasnoyarsk, 660036 Russia*

*** Krasnoyarsk State Agricultural University, pr. Mira 88, Krasnoyarsk, 660049 Russia*

e-mail: flerov@iph.krasnoyarsk.su

Received July 20, 1999

Abstract—Single-crystal plates of different sections of the $(NH_4)_3ScF_6$ crystal have been investigated by polarization-optical microscopy and X-ray diffraction over a wide temperature range, including the temperatures of two known phase transitions and the third transition found recently. It is established that the symmetry of phases changes in the following sequence: $O_h^5 - Fm3m$ ($Z = 4$) $\longleftrightarrow$ $C_{2h}^5 - P12_1/n1$ ($Z = 2$) $\longleftrightarrow$ $C_{2h}^3 - I12/m1$ ($Z = 16$) $\longleftrightarrow$ $C_i^1 - I\bar{1}$ ($Z = 16$). *© 2000 MAIK "Nauka/Interperiodica".*

The crystals $A_3M^{3+}X_6$ with the cryolite structure (space group $Fm3m$, $Z = 4$) belong to one of the related families of perovskite-like compounds. The three-dimensional crystal framework of these compounds is formed by the AX_6 and $M^{3+}X_6$ octahedra shared by their vertices, and the polyhedra arranged between these octahedra are occupied by the A^+ cations. As a rule, fluoride crystals with the atomic cations A^+ undergo structural phase transitions at sufficiently high temperatures, which makes their detailed exploration difficult. In this respect, the ammonium compounds (in which phase transitions have been found rather recently) are more attractive objects of investigations. In many cases, the presence of ammonium in the structure considerably decreases the temperature at which the cubic phase remains stable in these compounds [1–8].

By now, it has been established that, in the majority of ammonium cryolites, the transitions from the cubic phase are associated with the change in the orientational motion of two structural groups: $(NH_4)^+$ and $(MF_6)^{3+}$. The temperature at which the cubic phase loses its stability depends on the size of the M^{3+} ion. This factor also determines the sequence of changes in the symmetry upon phase transitions observed in crystals. The compounds with a small radius of trivalent ion ($R_M^{3+} \leq R_{Fe}^{3+}$) undergo only one phase transformation into the triclinic phase with the hypothetical symmetry $P\bar{1}$ [6, 8]. The compounds with larger-sized cations (Sc or In) are characterized by two phase transitions [8]. More recent research on the heat capacity of the $(NH_4)_3ScF_6$ polycrystalline samples by the adiabatic calorimetry revealed three anomalies at temperatures $T_1 = 330$ K, $T_2 = 293$ K, and $T_3 = 243$ K [9].

In [8], the symmetry of this crystal was found to be cubic ($Fm3m$, $Z = 4$) at temperatures above T_1 and monoclinic ($P2_1/n$, $Z = 2$) at 290 K. The X-ray diffraction analysis of the powders at temperatures corresponding to the G_0, G_1, and G_2 phases showed a substantial splitting of reflections in the diffraction patterns upon transition from the cubic phase, even though no abrupt change were observed in the volume. However, the transition from the G_1 phase at T_2 ($T_{exp} = 290$ K) was not accompanied by changes in the number of reflections and their intensities.

It should be noted that the X-ray diffraction investigations of small-scale structural distortions and changes in the symmetry in perovskite-like crystals are more efficient with single-crystal samples rather than with powders, because the single-crystal experiments provide more detailed information. Actually, a complex sequence of the symmetry changes was revealed in elpasolites upon twinning of their structure when studying the X-ray reflections of oriented single-crystal plates [10, 11]. In this respect, the purpose of the present work was to confirm the existence of three phase transitions found in [9] and to determine the symmetry of distorted phases of the $(NH_4)_3ScF_6$ cryolite.

1. EXPERIMENTAL

The $(NH_4)_3ScF_6$ compound was synthesized from equivalent amounts of NH_4F and Sc_2O_3 in HF (10%).

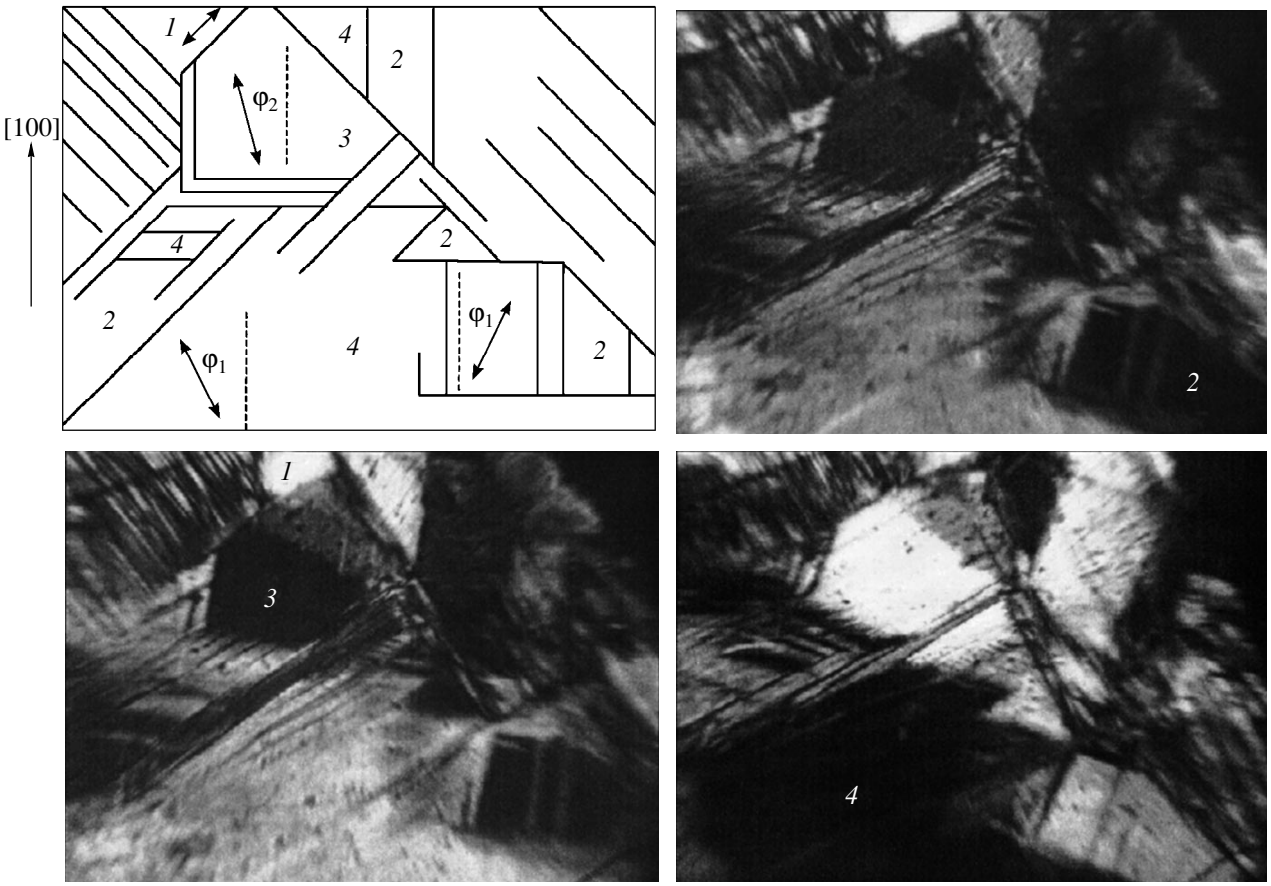

Fig. 1. Photographs of the twinned structure and a scheme of twinning in the $(100)_0$ section of the $(NH_4)_3ScF_6$ crystal at room temperature.

Large-sized faceted single crystals were grown by the slow controlled evaporation of a neutral saturated aqueous solution at a temperature of 305 K for 8 months.

X-ray diffraction analysis of the $(NH_4)_3ScF_6$ crystal was carried out on a DRON-2.0 diffractometer equipped with URNT-180 low-temperature and GPVT-2000 high-temperature attachments (CuK_α radiation, graphite monochromator) over a wide range of temperatures (120–360 K). Single-crystal plates of the $(100)_0$, $(110)_0$, and $(111)_0$ sections and the powders prepared from the $(NH_4)_3ScF_6$ single crystals were used as samples (hereafter, the subscript in the designation of planes and directions indicates the type of the crystal phase).

2. RESULTS

Thin crystal plates of different crystallographic sections were examined under a polarizing microscope. At a sample thickness of 0.1 mm and more, only one phase transition from the cubic phase can be observed at $T_1\downarrow = 326$ K ($T_1\uparrow = 328$ K) upon cooling. This transition is attended by the appearance of crystal twins and cracking. In the polarized light, the studied sample at room temperature has a complex interlacing twinned structure. A further cooling below T_2 and T_3 does not bring about additional changes in the twinning picture; and only when the sample thickness is chosen to be less than 0.5 mm, there appear extended single-domain regions characterized by a clear-cut extinction, in which all three phase transitions take place. Simple observations in polarized light clearly demonstrate only two phase transitions. The twinned structure arises at T_1 and becomes more complex at temperatures below T_3. No changes are observed at temperature $T \approx T_2$.

At room temperature, the thin sample of the $(100)_0$ section is characterized by twin boundaries along the $[100]_0$ and $[110]_0$ directions (Fig. 1). The twins observed can be classified into three types: (1) the extinction direction along $[110]_0$ in the G_1 and G_2 phases (twin 1), (2) the extinction direction differs from $[100]_0$ by the angle $\pm\varphi_1$ and depends on the temperature (twins 2 and 4), and (3) the extinction direction along $[100]_0$ in the G_1 phase and along $[100]_0 \pm \varphi_2$ in the G_2 phase (twin 3). Figure 2 depicts the temperature dependences of the angles of rotation of the optical indicatri-

ces $\varphi_1(T)$ and $\varphi_2(T)$ for different twins in the $(100)_0$ plane. The cooling below $T_1 = 326$ K results in a small disorientation of the optical indicatrices $2\varphi_1$ in twins 2 and 4 ($\varphi_1 \approx 4° \pm 1°$). Somewhat below room temperature ($T_2 = 290$ K), the φ_1 angle sharply increases and becomes equal to $20° \pm 1°$ at temperatures about 230 K. No changes in the twinning picture are observed in this case. A further cooling below T_3 leads to the appearance of additional twins. The clear-cut extinction observed along $[110]_0$ in region 1 is disturbed. The first-order phase transition occurs with a large temperature hysteresis. Note that, upon cooling, the temperature $T_3\downarrow$ of this phase transition is not constant and depends on many factors such as the cooling rate, the choice of the twin under observation, etc. As a result, the temperature hysteresis varies in the range $\Delta T_3 = 30$–13 K. Upon heating, the phase transition is always observed at $T_3\uparrow = 230$ K.

The optical observations in the polarized light indicate that the $(NH_4)_3ScF_6$ crystal undergoes phase transitions in the following order: $Fm3m$ (G_0) ⟷ monoclinic (G_1) ⟷ monoclinic (G_2) ⟷ triclinic (G_3). As follows from the extinctions in twins, the twofold axis in the G_1 and G_2 monoclinic phases lies along the $[110]_0$ direction.

The changes observed in the X-ray diffraction profiles of single-crystal plates and the splittings of reflections in the powder diffraction patterns at different temperatures (see table) suggest at least two phase transitions at $T_1\uparrow = 328$ K and $T_3\uparrow = 230$ K. The initial phase G_0 is the cubic modification with the face-centered unit cell F. The unit cell parameters at 353 K are listed in the table. According to the splittings of the main reflections, the monoclinic symmetry is assigned to the G_1 and G_2 distorted phases, and the triclinic symmetry, to the G_3 phase.

The cooling below T_1 (G_1 phase) gives rise to a set of the (hk0) and (hkl) superstructure reflections, for which the sums ($h + k$), ($h + l$), and ($k + l$) are odd numbers. Among the (h00) and (hh0) reflections, only the reflections with the even indices h are observed (the h, k, and l indices of reflections are chosen with respect to the axes in the unit cell of the G_0 cubic phase). Although the splittings of reflections in the temperature ranges T_1–T_2 and T_2–T_3 virtually coincide and do not indicate phase transitions, apart from the already observed reflections, one can see the superstructure reflections (h + 1/2, h + 1/2, h + 1/2), (h00), and (hh0) (where h is any integer number) at temperatures below T_2. The superstructure reflections found in the G_1 and G_2 phases are also observed in the low-symmetry phase G_3. The splitting of reflections and the appearance of superstructure reflections clearly demonstrate the existence of three phase transitions.

The temperature dependences of the linear and angular unit-cell parameters for the G_0, G_1, G_2, and G_3 phases were determined from the location of components of the (880) reflection (Figs. 3, 4). The scheme of the splitting of this reflection is given in the table. As can be seen from Fig. 3, the linear unit-cell parameters sharply change upon transition from the cubic phase to the G_1 phase. An abrupt change observed in the unit-cell volume at the same temperature is equal to 0.5% V_0. No features in the behavior of the linear unit-cell parameters are observed in the transitions at temperatures T_2 and T_3. The parameters of the monoclinic and triclinic unit cells along the a_i and b_i directions virtually coincide. The temperature dependences of the angular unit-cell parameters (Fig. 4) exhibit three singular

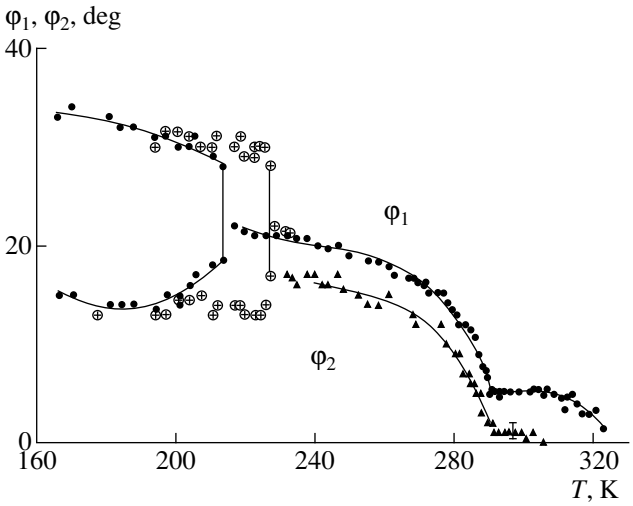

Fig. 2. Temperature dependences of the angle of rotation of the optical indicatrix for $(NH_4)_3ScF_6$.

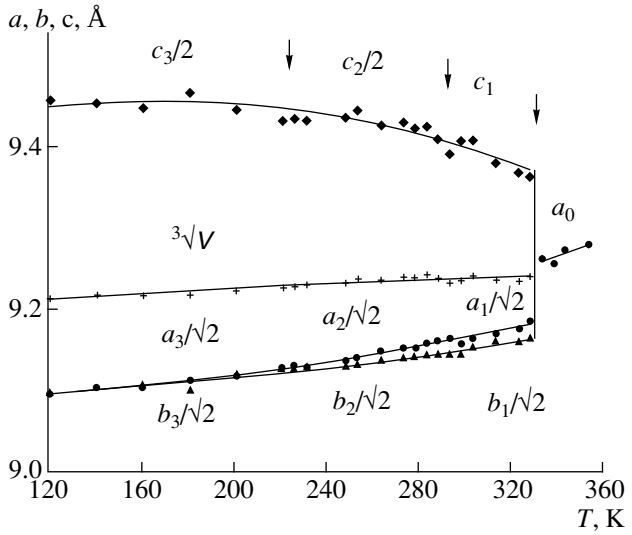

Fig. 3. Temperature dependences of the linear sizes and the volume of the Bravais cell in the $(NH_4)_3ScF_6$ crystal. The unit cell volume is doubled for the G_1 phases and is reduced by a factor of four for the G_2 and G_3 phases.

Crystallographic characteristics of four phases $(NH_4)_3ScF_6$

Phase	G_3	G_2	G_1	G_0
Space group	C_i^1–$I\bar{1}$	C_{2h}^3–$I12/m1$	C_{2h}^5–$P12_1/n1$	O_h^5–$Fm3m$
Z	16	16	2	4
T_{exp}, K	173	273	303	353
Unit-cell parameters				
$\mathbf{a}_i$, Å	$12.874(-\mathbf{b}_0 + \mathbf{c}_0)$	$12.944(-\mathbf{b}_0 + \mathbf{c}_0)$	$6.481(1/2(-\mathbf{b}_0 + \mathbf{c}_0))$	$9.281(\mathbf{a}_0)$
$\mathbf{b}_i$	$12.875(\mathbf{b}_0 + \mathbf{c}_0)$	$12.926(\mathbf{b}_0 + \mathbf{c}_0)$	$6.472(1/2(\mathbf{b}_0 + \mathbf{c}_0))$	$9.281(\mathbf{b}_0)$
$\mathbf{c}_i$	$18.898(2\mathbf{a}_0)$	$18.860(\mathbf{a}_0)$	$9.408(\mathbf{a}_0)$	$9.281(\mathbf{c}_0)$
α, deg	90.19	90	90	90
β, deg	89.60	89.78	89.90	90
γ, deg	90.09	90	90	90
V, Å^3	3132.216	3155.522	394.618	799.308
Scheme of reflection splitting				
(h00)				
(hh0)				
(hhh)				
Presence of superstructure reflections	++	++	+	–

points at temperatures corresponding to the three phase transitions. The temperature behavior of the angle $\beta(T)$ (Fig. 4) is similar in character to that of the rotation angle for the optical indicatrix $\varphi_1(T)$ (Fig. 2).

3. DISCUSSION

In order to determine the space groups of the distorted crystal phases, we take into consideration the following observations: only the centrosymmetric distorted phases are revealed in the family of the $A_3M^{3+}X_6$ crystals [1–11], and, as follows from the polarization-optical experiments, the twofold axis in the G_1 and G_2 monoclinic phases lies along the $[110]_0$ direction, i.e., along the diagonal of the cubic cell face. These factors substantially reduce the number of possible space groups from C_{2h}^1 to C_{2h}^6 for the low-symmetry monoclinic phases and allow an unambiguous choice of the C_i^1 symmetry for the triclinic phase. Analysis of the absences of structure and superstructure reflections and also the splittings of specially chosen reflections in the X-ray diffraction patterns of single-crystal plates makes it possible to choose particular space groups of the distorted phases. The data on the symmetry of the $(NH_4)_3ScF_6$ phases, sizes, and orientation of the unit cells are summarized in the table. It should be mentioned that, in the conventional setting (see [12]), the Bravais cell should be base-centered in the G_2 monoclinic phase and simple in the G_3 triclinic phases. However, for convenience, we chose the body-centered unit cells for the G_2 and G_3 phases. As is seen, the volume of the Bravais cell is two times smaller in the G_1 phase and it is four times larger in the G_2 and G_3 phases as compared to the unit-cell volume in the G_0 phase. At the same time, the primitive cells in the G_0, G_1, G_2, and G_3 phases contain 1, 2, 8, and 8 formula units, respectively.

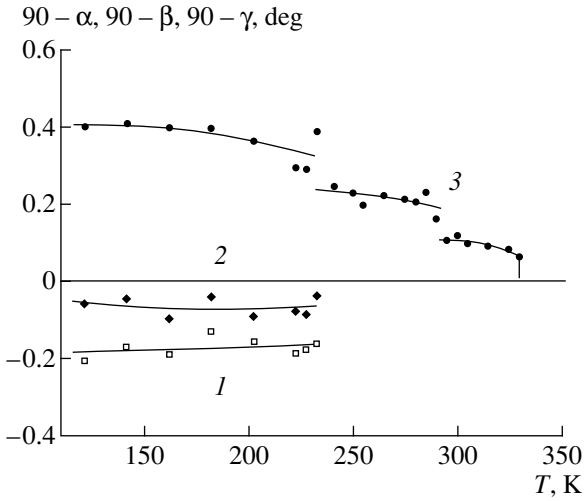

Fig. 4. Temperature dependences of the angular unit-cell parameters of the $(NH_4)_3ScF_6$ crystal: (*1*) 90° – α, (*2*) 90° – γ, and (*3*) 90° – β.

Now, let us consider the probable pattern of structural distortions in the $(NH_4)_3ScF_6$ crystal. For this purpose, we invoke the data of recent calorimetric [9] and NMR investigations of cryolites with M^{3+} = Ga, V, Fe, and In [7]. Reasoning from the results obtained in the works [7, 9], it can be concluded that the phase transitions in the scandium cryolite are accompanied by transformations of the order–disorder type. The phase transition at temperature T_1 is associated with a partial ordering of the ScF_6 rigid octahedral groups and the ordering of the NH_4 tetrahedral groups. The complete ordering of the ScF_6 octahedra is observed at T_2. Most likely, the octahedral and tetrahedral groups in the G_2 and G_3 phases are completely ordered, and these phases differ only in the degree of distortions of the unit cells. The change in the entropy upon complete ordering of octahedral and tetrahedral groups is $\Delta S = R(\ln 2 + \ln 8) = 2.77R$, which is in good agreement with the data obtained in [9] for this crystal. According to [9], the overall change in the entropy during all three phase transitions is $\sum \Delta S_i = (2.50 \pm 0.18)R$.

In closing, we briefly dwell on the work [8], in which the $P\bar{1}$ symmetry was assigned to the G_3 phase. The results of the present work complement, rather than contradict, the data reported in [8]. In [8], the symmetry of the $(NH_4)_3ScF_6$ phases was determined from the splitting of reflections in the X-ray diffraction patterns of powder samples. The translational symmetry is difficult to judge from the data obtained in [8]. In the present work, apart from the point symmetry of all the phases, we revealed the change in the translational symmetry, i.e., the Bravais lattices, which was not found in [8].

ACKNOWLEDGMENTS

This work was supported by the Russian Foundation for Basic Research, project no. 96-15-96700.

REFERENCES

1. S. Morup and N. Thrane, Solid State Commun. **11**, 1319 (1972).
2. K. Moriya, T. Matsuo, H. Suga, *et al.*, Bull. Chem. Soc. Jpn. **50** (8), 1920 (1977).
3. E. G. Steward and H. P. Rocksby, Acta Crystallogr. **6** (1), 49 (1953).
4. H. Bode and E. Voss, Z. Anorg. Allg. Chem. **290** (1–2), 1 (1957).
5. K. Moriya, T. Matsuo, H. Suga, *et al.*, Bull. Chem. Soc. Jpn. **52** (11), 3152 (1979).
6. K. Kobayashi, T. Matsuo, H. Suga, *et al.*, Solid State Commun. **53** (8), 719 (1985).
7. A. Sasaki, Y. Furukawa, and D. Nakamura, Ber. Bunsen-Ges. Phys. Chem. **93**, 1142 (1989).
8. A. Thessaud, S. Khairoun, L. Rabardel, *et al.*, Phys. Status Solidi A **98** (2), 407 (1986).
9. I. N. Flerov, M. V. Gorev, and T. V. Ushakova, Fiz. Tverd. Tela (S.-Peterburg) **41** (3), 523 (1999).
10. K. S. Aleksandrov, S. V. Melnikova, and S. V. Misjul, Phys. Status Solidi A **104**, 545 (1987).
11. I. N. Flerov, M. V. Gorev, S. V. Mel'nikova, *et al.*, Fiz. Tverd. Tela (Leningrad) **34** (7), 2185 (1992).
12. *International Tables for X-ray Crystallography* (Kynoch, Birmingham, 1952), Vol. 1.

Translated by O. Borovik-Romanova

Physics of the Solid State, Vol. 42, No. 2, 2000, pp. 350–355. Translated from Fizika Tverdogo Tela, Vol. 42, No. 2, 2000, pp. 341–346.

LOW-DIMENSIONAL SYSTEMS AND SURFACE PHYSICS

Spin Resonance of Conduction Electrons and EPR of Localized Moments in a Low-Dimensional Organic Conductor $[Pd(dddt)_2]Ag_{1.5}Br_{3.5}$

S. V. Kapel'nitskiĭ* and L. A. Kushch**

**Russian Research Center Kurchatov Institute, pl. Kurchatova 1, Moscow, 123182 Russia*
***Chernogolovka Department, Semenov Institute of Chemical Physics, Russian Academy of Sciences, Chernogolovka, Moscow oblast, 142432 Russia*
e-mail: kapelnitsky@imp.kiae.ru

Received February 17, 1999; in final form, June 21, 1999

Abstract—The EPR spectra of a quasi-two-dimensional organic metal $[Pd(dddt)_2]Ag_{1.5}Br_{3.5}$ contain signals due to the spin resonance of conduction electrons (CESR) and signals due to the localized magnetic moments of Ag^{2+}. The system of Ag^{2+} ions exhibits a strong indirect antiferromagnetic exchange interaction characterized by the Weiss constant $\Theta = -280(25)$ K, which leads to magnetic ordering at a temperature of $T_0 = 70(10)$ K. The same temperature T_0 corresponds to a strong anomaly in the CESR linewidth. The observed anomaly in the CESR linewidth, as well as some features of the temperature dependence of conductivity in the system studied, are explained by the interaction between conduction electrons and Ag^{2+} ions localized in the anion layers (π–*d* interaction) and by antiferromagnetic ordering of the spins of Ag^{2+} magnetic ions. © *2000 MAIK "Nauka/Interperiodica".*

INTRODUCTION

The organic metal $[Pd(dddt)_2]Ag_{1.5}Br_{3.5}$ [1, 2] is a close structural analog of quasi-two-dimensional superconducting salts of the type $(BEDT–TTF)_2X$, where BEDT–TTF is bis(ethylenedithiol)tetrathiafulvalene and X is an anion [3–5]. The crystal structure of $[Pd(dddt)_2]Ag_{1.5}Br_{3.5}$ comprises alternation of conducting cation layers composed of flat organic molecules $Pd(dddt)_2$ and nonconducting anion layers of $Ag_{1.5}Br_{3.5}$. Formally, the molecule of $[Pd(dddt)_2]Ag_{1.5}Br_{3.5}$ differs from BEDT–TTF by the presence of Pd atom instead of two central carbon atoms with double carbon bond.

The transport properties, crystal structure, and electron band structure of $[Pd(dddt)_2]Ag_{1.5}Br_{3.5}$ were studied previously [1, 2]. It was established that this compound exhibits conductivity of the metal type at temperatures up to 1.3 K, with $\sigma_{bc}(300\ \text{K}) = 15\ \Omega^{-1}\ \text{cm}^{-1}$ in the conducting plane *bc*; the resistance anisotropy is $\rho_a/\rho_{bc} \sim 600$ at 300 K and rather weakly varies with the temperature [1, 2]. The quasi-two-dimensional (2D) conductivity of $[Pd(dddt)_2]Ag_{1.5}Br_{3.5}$, like that of the other organic conductors of the BEDT–TTF type, is due to overlap of the $p\pi$ orbitals of sulfur atoms belonging to each couple of neighboring organic molecules.

According to the band structure calculations [2] and taking into account the high conductivity of $[Pd(dddt)_2]Ag_{1.5}Br_{3.5}$, we may suggest that $[Pd(dddt)_2]$ cation has the charge +0.5. Therefore, Ag atoms occur in the divalent state (Ag^{2+}) and we may expect that the nonconducting anion layer contains magnetic ions. In recent years, investigations of the interaction between conduction electrons and magnetic ions localized in the ionic layers of 2D organic conductors and superconductors draw a considerable interest of researchers [6–10]. For example, it was reported that the metal–insulator transition in λ-$(BETS)_2FeCl_4$ (containing Fe^{3+} magnetic ions in the anion layer) is completely suppressed in the magnetic field with a strength of 100 kG [9, 10]. At the same time, interaction between the localized magnetic moments of Fe^{3+} ions and conduction electrons in $((BEDT–TTF)_4[Fe(C_3O_4)_3(H_2O)C_6H_5CN]$ is quite weak and this compound is characterized by a rather high superconducting transition temperature $T_c = 7$ K [7].

We have studied the magnetic properties of $[Pd(dddt)_2]Ag_{1.5}Br_{3.5}$ and the interaction between magnetic moments and conduction electrons in this system by EPR. As is known, a special feature of most of the quasi-2D organic conductors representing cation–radical salts (BEDT–TTF, BEDO, BETS) is a sufficiently large electron relaxation time, which provides conditions for observation of the conduction electron spin resonance (CESR) effect [5]. However, no CESR signals from the cation salts of metal dithiolates [$M(dddt)_2$ and $M(dmit)_2$, where M is a metal] were observed previously, probably, because of a strong spin–orbit coupling of conduction electrons and metal ions, related to mixing of the *d* orbitals of the metal and the ligand orbitals, which leads to considerable broadening of the CESR line.

1063-7834/00/4202-0350$20.00 © 2000 MAIK "Nauka/Interperiodica"

Our measurements showed that the EPR spectra of $[Pd(dddt)_2]Ag_{1.5}Br_{3.5}$ represent a superposition of the CESR signal from the conduction electrons of cation layers and the EPR signal from Ag^{2+} ions localized in the anion layers. An analysis of the temperature variation of parameters of the EPR spectra revealed an antiferromagnetic phase transition in the system of localized ions and showed the presence of the interaction between conduction electrons and magnetic ions. Preliminary results of this work were reported in [11].

SAMPLE PREPARATION AND MEASUREMENTS

The EPR spectra were measured at 9.4 GHz in the temperature range 8–300 K using a Bruker ESP-300 spectrometer equipped with a helium flow cryostat (Oxford Instruments). The sample response was registered as the first derivative of the absorption intensity.

The single-crystal samples of $[Pd(dddt)_2]Ag_{1.5}Br_{3.5}$ were grown at the laboratory of Prof. Yagubskiĭ (Semenov Institute of Chemical Physics, Chernogolovka) [1, 2]. The crystals had the shape of thin plates, with the large face coinciding with the conducting *bc* plane. The EPR spectra were measured using samples composed of several single-crystal plates. The composition samples were prepared by gluing about 10 single crystals with their large face onto a flat teflon substrate. The substrate with single crystals was placed into an ampule filled with helium to provide for a better heat exchange. Most of the measurements were performed with the constant magnetic field oriented in the *bc* plane. For the resistance anisotropy determination, the ampule with a composite sample was rotated about the axis lying in the substrate plane and perpendicular to the constant magnetic field. Control measurements performed on separate single crystals gave approximately the same spectra as those obtained using composite samples.

The magnetic susceptibility χ was determined using the integral intensity of the EPr spectrum. The χ value can be calculated for a spectral component having Lorentzian shape and using the formula $\chi \propto \Delta H_{pp}^2 A_{pp}$, where ΔH_{pp} and A_{pp} are the width and intensity of the EPR line. A standard for the absolute value determination was represented by $CuSO_4 \cdot 5H_2O$. The absolute values of χ at $T > 160$ K correspond to the magnetic susceptibility of a system of noninteracting spins with $S = 1/2$ and a concentration of 1.0 ± 0.5 spins per formula unit. The accuracy of measurements, albeit rather low as a result of considerable uncertainty of the sample mass determination, was nevertheless sufficient to ascertain that the signal observed was not related to some structural defects. The accuracy of determination of the relative χ values was about 3%. The fact that the spectra measured at low temperatures contained a single symmetric line free of the Dyson distortions indicates that a sample crystal thickness was smaller than the skin layer depth, so that the skin effect did not significantly contribute to the error of susceptibility measurements.

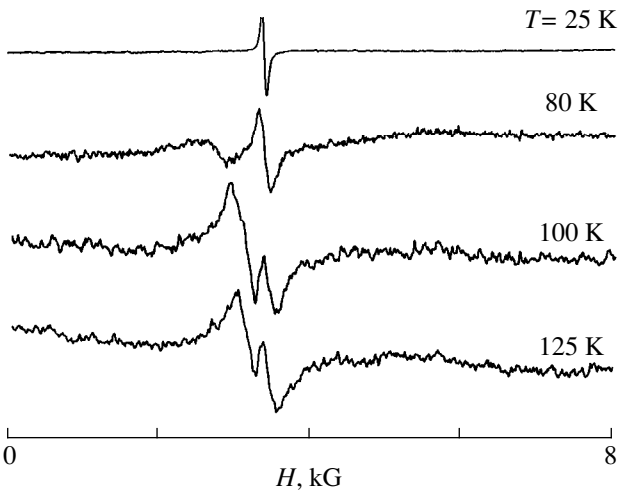

Fig. 1. EPR spectra (absorption derivative) of $[Pd(dddt)_2]Ag_{1.5}Br_{3.5}$ measured at various temperatures ($f = 9.4$ GHz).

RESULTS AND DISCUSSION

The EPR spectra (Fig. 1) contained two components (I and II) differing by the character of the temperature and angular dependences of the EPR line parameters. The spectra measured at $T < 80$ K contained a single component (I), because component II exhibited broadening with decreasing temperature and became unobservable. Lines I and II can be interpreted (see below) as the conduction electron spin resonance (CESR) signal from the cation layers and the EPR signal due to magnetic moments of Ag^{2+} ions localized in the anion layers, respectively.

In poorly resolved spectra, component II can be separated because this line is anisotropic, while component I is almost perfectly isotropic. Figure 2 (curve *a*) shows an EPR spectrum $A(H, \varphi = 0°)$ measured with the magnetic field H oriented in the crystal plane ($\varphi = 0°$). Let the crystal be rotated by a small angle $\delta\varphi$, whereby the shape of the EPR spectrum changes insignificantly and, to the first approximation, only the resonance line position H_{res} slightly varies, which is expressed as $A_{II}(H, \varphi + \Delta\varphi) = A_{II}[H - \Delta\varphi dH_{res}/d\varphi, \varphi]$. Then, $A_{II}(H, \varphi + \Delta\varphi) - A_{II}(H, \varphi) = (-1)(\Delta\varphi dH_{res}/d\varphi)[\partial A_{II}(H, \varphi)/\partial H]$ and we may use the $A(H, \varphi)$ spectra with isotropic (I) and anisotropic (II) components measured at two close orientations of the crystal to separate a signal due the anisotropic component A_{II}:

$$A_{II}(H, \varphi) \propto \int_0^H [A(h, \varphi + \Delta\varphi) - A(h, \varphi)]dh. \qquad (1)$$

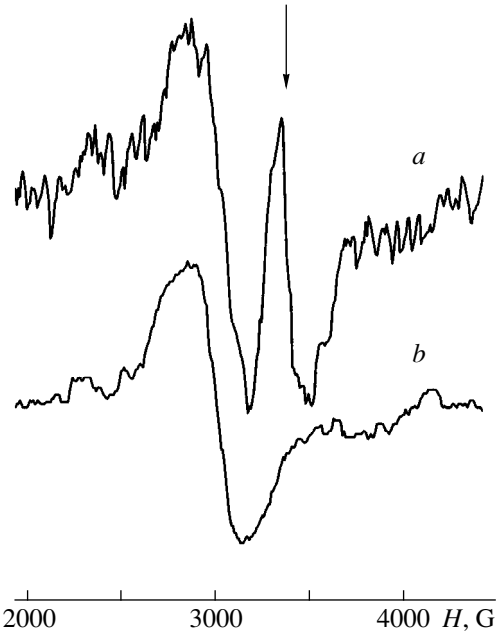

Fig. 2. EPR spectra: (*a*) $A(H, \varphi = 0°)$ measured at $T = 100$ K with the magnetic field H oriented in the crystal plane; (*b*) anisotropic component A_{II} calculated by formula (1). The arrow indicates a resonance field value corresponding to $g = 2.0$.

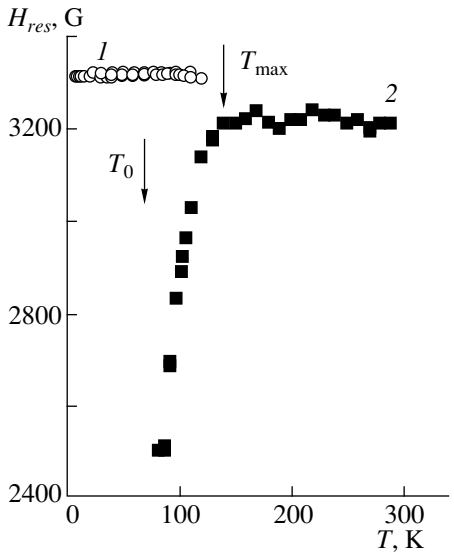

Fig. 3. Plots of the resonance magnetic field versus temperature for (*1*) EPR signal from Ag^{2+} ions (component II) and (*2*) CESR signal (component I). The arrows indicate the temperature of maximum magnetic susceptibility (T_{max}) and the temperature of magnetic ordering (T_0) determined by formula (3).

Figure 2 (curve *b*) shows a spectrum of the anisotropic component $A_{II}(H, \varphi = 0)$ calculated by formula (1) for $\varphi = 0°$, $\Delta\varphi = 10°$. It should be noted that the anisotropy of component II is reliably detected at temperatures up to room temperature.

Figure 3 shows the temperature dependence of the resonance fields of components I and II. Component I is almost isotropic and has a nearly Lorentzian shape. The temperature-independent g value $g_1 = 2.005(5)$ is close to that of the free electron. The spin susceptibility corresponding to this component χ(CESR) (Fig. 4) is also independent of the temperature (magnetic susceptibility of the Pauli type). For these reasons, we have interpreted component I as a CESR signal from conducting cation layers of $Pd(dddt)]_2$.

Figure 4 also shows the total magnetic spin susceptibility χ(total) of $[Pd(dddt)_2]Ag_{1.5}Br_{3.5}$. As seen, the χ(total) value measured in the 90–293-K temperature interval exhibits a maximum at $T_{max} = 140(10)$ K. Since the lines of component II and CESR overlap at $T > 100$ K, we have evaluated χ(II) as the difference χ(II) = χ(total)–χ(CESR), assuming that χ(CESR) = const. As seen from Fig. 4, the temperature variation of χ(total) at $T > 160$ K is well described by a relationship

$$\chi(\text{total}) = \chi(\text{II}) + \text{const}, \qquad (2)$$

where

$$\chi(\text{II}) = C/(T - \Theta)$$

corresponds to the Curie–Weiss law with the Weiss constant $\Theta = -280(25)$ K.

Let us consider in more detail the interpretation of component II. This line may be assigned either to Pd atoms in the $Pd(dddt)_2$ cations or to Ag atoms in the anion layer. The neighboring Pd atoms in $[Pd(dddt)_2]Ag_{1.5}Br_{3.5}$ occur at a distance of 4.16 Å [2], which is greater than the double radius of a Pd ion. If the spins corresponding to component II were uncompensated spins of Pd atoms, we might conclude that the 4*d* moments of Pd interact via the conduction electrons. Since the spins of component II exhibit a strong exchange interaction (characterized by the Weiss constant = –280 K), their coupling with conduction electrons would make the observation of CESR impossible as a result of the line broadening. Thus, the very fact of observation of the CESR signal indicates that Pd atoms occur in a nonmagnetic state. This conclusion agrees with the data of Raman spectroscopy, according to which palladium atoms in $[Pd(dddt)_2]Ag_{1.5}Br_{3.5}$ occur in the divalent state (Pd^{2+}) [12]. Therefore, component II is naturally assigned to Ag ions occurring in the anion layers in a divalent Ag^{2+} state (Ag^{1+} corresponding to a spin singlet). The large value of Θ, obtained by approximation based on formula (2), is evidence of a strong antiferromagnetic exchange interaction between the magnetic moments of Ag^{2+} ions. The interaction is probably mediated by Br atoms also occurring in the anion layer. The corresponding magnetic susceptibility $\chi(Ag^{2+}) = \chi$(II) reaches maximum at $T = T_{max}$ (Fig. 4).

The resonance magnetic field $H_{res}(Ag^{2+})$ is almost constant in the temperature interval from 293 to 150 K. As the temperature decreases, $H_{res}(Ag^{2+})$ drops from

3220(15) G at $T > 150$ K to 2500 G at 90 K (Fig. 3), which corresponds to an increase in the effective g value from $g = 2.06(1)$ to 2.65, respectively. The deviation of $\chi(Ag^{2+})$ from the Curie–Weiss law and the change of the resonance field are explained by the appearance and development of a short-range antiferromagnetic order [13, 14].

The resonance linewidth $\Delta H(Ag^{2+})$ decreases from 700 G at 293 K to a minimum value of 300 G at $T_W = 100$ K and then sharply grows again to 1800 G at 77 K (Fig. 5). On further cooling of the sample, the EPR signal becomes unobservable because of the considerable broadening. The sharp increase in the linewidth with decreasing temperature is indicative of a cooperative character of the magnetic ordering and can be explained by magnetic fluctuations in the vicinity of the transition temperature [14–16]. In order to determine the temperature of the antiferromagnetic ordering, we have described the temperature dependence of $\Delta H(Ag^{2+})$ at $T < 90$ K by an approximate relationship

$$\Delta H(Ag^{2+}) \propto (T - T_0)^{-P}, \qquad (3)$$

where T_0 is the effective Néel temperature. For $P = 1$–2, this approximation yields $T_0 = 70(10)$ K. Although, as seen in Fig. 5, the curve calculated for $P = 1.5$ satisfactorily describes the line broadening, we failed to determine the critical factor P with better precision from the experimental data.

Relationship (3) describes the critical line broadening during the antiferromagnetic ordering in many 3D and nonideal low-dimensional magnetic compounds [14–16], as well as in the spin glasses [17]. As is known, the ideal 2D and 1D Heisenberg ($s = 1/2$) antiferromagnetics cannot feature magnetic ordering at temperatures above zero. However, the presence of even a weak interplanar or interchain exchange interaction ($J_\perp$) allows the antiferromagnetic transition to take place. For $J_\perp \ll J_\parallel$, the transition temperature depends only slightly on $J_\perp$ and is primarily determined by the system dimensionality and the $J_\parallel$ value [18, 19]. An empirical criterion for determination of the magnetic dimensionality is offered by the ratio T_0/T_{max}, where T_0 is the temperature of the 3D antiferromagnetic ordering and T_{max} is the temperature of maximum susceptibility [18, 19]: $T_0/T_{max} < 0.1$ for 1D magnetic systems, $0.25 < T_0/T_{max} < 0.5$ for the 2D systems, and $T_0/T_{max} > 0.9$ for the 3D magnets. In our case, $T_0/T_{max} = 0.5(1)$, which is characteristic of a 2D magnetic system. The interplanar interaction $J_\perp$ can be related to an indirect interaction between Ar^{2+} ions, occurring in the neighboring anion layers, mediated by the conduction electrons of cation layers (π–d exchange). It should be noted that, according to the X-ray diffraction data [1, 2], Ag atoms are randomly arranged in the anion layers. Therefore, the system of interacting Ag^{2+} ions at low temperatures occurs in the state typical of a disordered antiferromagnet. The magnetically ordered state may correspond to a long-range antiferromagnetic order or represent a state of the cluster spin glass type.

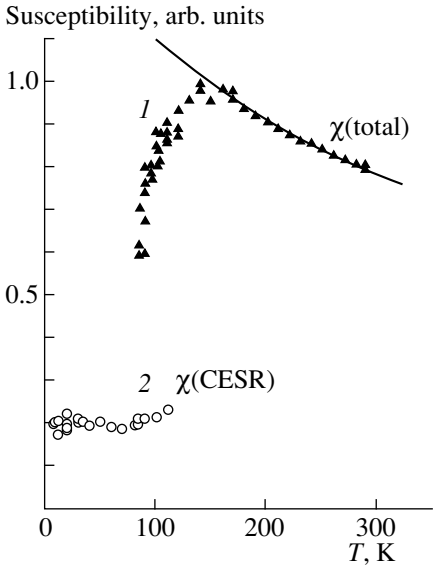

Fig. 4. Temperature variation of the magnetic susceptibilities determined from the integral intensity of lines: (*1*) χ(total) corresponding to the total EPR spectrum; (*2*) χ(CESR) determined for the CESR signal (component I); solid shows the results of calculation by formula (2).

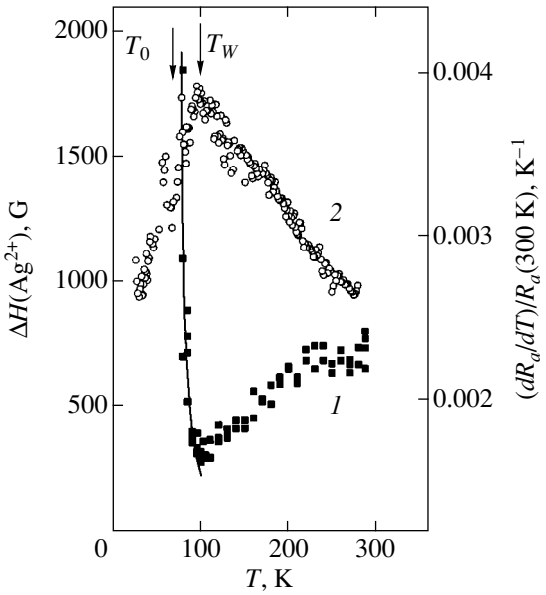

Fig. 5. Temperature variation of (*1*) linewidth $H(Ag^{2+})$ of the EPR signal from Ag^{2+} ions and (*2*) derivative of the electric resistance in the a direction with respect to temperature $(dR_a/dT)/R_a$ (300 K) (for $R_a(T)$ data taken from [2]). Solid line shows the results of calculation by formula (3) for $P = 1.5$ and $T_0 = 70$ K. The arrows indicate T_0 and the temperature T_W of minimum linewidth of the signal from Ag^{2+} ions.

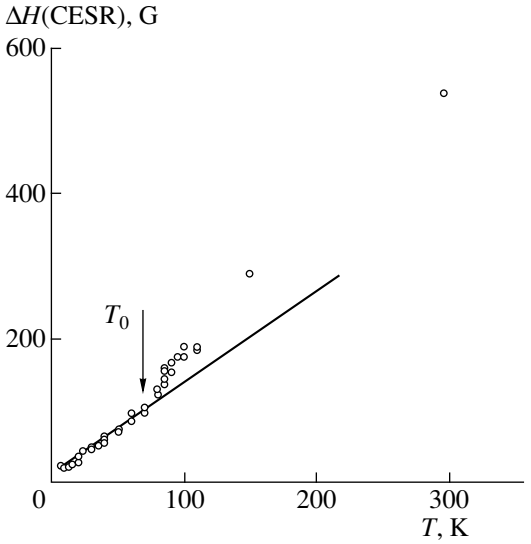

Fig. 6. Temperature variation of the CESR linewidth ΔH(CESR). Solid line corresponds to the slope of the initial portion. The arrow indicates the magnetic ordering temperature T_0 determined by formula (3).

Figure 5 also shows a plot of the derivative dR_a/dT versus temperature, where R_a is the resistance of a sample in the direction perpendicular to the conducting plane *bc* (data taken from [2]). The curve exhibits a well pronounced maximum at $T = 100(7)$ K, which coincides with the temperature T_W of minimum in the linewidth $\Delta H(Ag^{2+})$ of the EPR signal (Fig. 5). No such extremal feature is observed in the temperature dependence of ρ_{bc}, and T_W is only manifested by a bending point observed at the same temperature in the plot of the resistance anisotropy ratio ρ_a/ρ_{bc} versus temperature [2]. As seen in Fig. 5, the temperature T_W, at which the above conductivity features are observed, corresponds to a transition to the state of critical broadening of the Ag^{2+} line described by formula (3).

The maximum observed in the derivative of resistance with respect to the temperature can be related to "freezing" of the Ag^{2+} magnetic moment fluctuations at $T < 100$ K, which leads to suppression of the scattering of conduction electrons with spin reversal. A similar change in the slope of $\rho(T)$ was observed in 3D metals in the vicinity of a temperature corresponding to their magnetic ordering [14, 20].

The organic conductor $[Pd(dddt)_2]Ag_{1.5}Br_{3.5}$ features a rather seldom situation, whereby the conduction electrons, interacting with magnetically ordered localized spins, produce an electron spin resonance signal. Figure 6 shows a plot of the CESR linewidth versus temperature. As seen, the ΔH(CESR) value monotonically increases from 20 G at 8K to 540 G at 293 K. At a temperature of the antiferromagnetic ordering of the spins of Ag^{2+} ions ($T_0 = 70$ K), the slope of the plot of ΔH(CESR) versus temperature increases. Therefore, we may suggest that the change in the slope of the CESR linewidth at this temperature is related to the magnetic ordering of moments of the Ag^{2+} ions and to a change in relaxation of the spins of conduction electrons upon the antiferromagnetic ordering of the moments of localized Ag^{2+} ions.

The anomalies observed in the behavior of the CESR linewidth and the electric resistance near the temperature of the antiferromagnetic ordering of the Ag^{2+} ion moments are apparently caused by interaction between the π electrons of the donor (cation) layers and magnetic ions localized in the anion layers (π–*d* interaction).

CONCLUSIONS

The main results obtained in this work can be summarized as follows.

We have observed the phenomenon of conduction electron spin resonance (CESR) in organic conductors with metal dithiolate cations. It was found that the second EPR component is due to the magnetic Ag^{2+} ions localized in non-conducting anion layers of $[Pd(dddt)_2]Ag_{1.5}Br_{3.5}$. The pattern of temperature variation of the EPR signal from Ag^{2+} ions is indicative of development of a short-range antiferromagnetic ordering of the spins of Ag^{2+} ions at $T < 140$ K, which leads to the establishing of a static antiferromagnetic order at $T_0 = 70(10)$ K. Despite the fact that Ag^{2+} ions are randomly arranged in the anion layer, the antiferromagnetic transition exhibits a cooperative character. Large values of the Weiss constant (–280 K) and the temperature of maximum in the magnetic susceptibility (140 K) are indicative of a strong indirect exchanged interaction between localized Ag^{2+} ions.

It was established that the temperature position of maximum differential resistance in the direction perpendicular to the conducting layers corresponds to the region of transition from a state with dynamic 2D short-range antiferromagnetic order of Ag^{2+} ions in the anion layers to the state of the static antiferromagnetic order. The maximum may reflect a change in the scattering of electrons with spin reversal upon "freezing" of the 2D fluctuations of the magnetic moments of Ag^{2+} ions at $T < 100$ K. The static antiferromagnetic ordering of the localized magnetic moments at $T = T_0$ is accompanied by a change in the slope of the plot of the CESR linewidth ΔH(CESR) versus temperature.

The features observed in the temperature variation of the resistance and the CESR linewidth of $[Pd(dddt)_2]Ag_{1.5}Br_{3.5}$ are apparently caused by the π–*d* interaction between the itinerant π electrons of the donor (cation) layers and magnetic $4d$-Ag^{2+} ions localized in the anion layers.

ACKNOWLEDGMENTS

The authors are grateful to É.B. Yagubskiĭ for his help in formulation of the problem and discussion of the experimental results and to M.A. Chuev for fruitful remarks.

The work was supported by the Russian Foundation for Basic Research, project no. 98-02-17411.

REFERENCES

1. E. B. Yagubskiĭ, L. A. Kushch, V. V. Gritsenko, *et al.*, Synth. Met. **70** (1/3), 1039 (1995).
2. L. A. Kushch, S. V. Konovalikhin, L. I. Buravov, *et al.*, J. Phys. I (France) **6** (12), 1555 (1996).
3. E. B. Yagubskiĭ, I. F. Shchegolev, V. N. Laukhin, *et al.*, Pis'ma Zh. Éksp. Teor. Fiz. **39** (1), 12 (1984).
4. H. Urayama, H. Yamochi, G. Saito, K. Nozawa, *et al.*, Chem. Lett. **1**, 55 (1988).
5. J. M. Williams, J. R. Ferraro, R. J. Thorn, K. D. Carlson, U. Geiser, H. H. Wang, A. M. Kini, and M. H. Whangbo, in *Organic Superconductors* (Including Fullerene) (Prentice Hall, Englewood Cliffs, 1992).
6. T. Mori, Physica C (Amsterdam) **264** (1), 22 (1996).
7. M. Kurmoo, A. W. Graham, P. Day, *et al.*, J. Am. Chem. Soc. **117** (49), 12209 (1995).
8. M. Kurmoo, P. Day, M. Allan, *et al.*, Mol. Cryst. Liq. Cryst. **234** (1), 199 (1993).
9. F. Goze, V. N. Laukhin, K. Brossard, *et al.*, Physica C (Amsterdam) **233** (3/4), 427 (1994).
10. H. Kobayashi, H. Tomita, T. Udagawa, *et al.*, Synth. Met. **70** (1/3), 867 (1995).
11. S. Kapelnitsky, in *Magnetic Resonance and Related Phenomena. Proceedings of the Joint 29th AMPERE–13th ISMAR Int. Conf.* (Technical University, Berlin, 1998), Extended Abstracts, II, p. 1105.
12. H. H. Wang, S. B. Fox, E. B. Yagubskiĭ, *et al.*, J. Am. Chem. Soc. **119** (32), 7601 (1997).
13. K. Nagata and Y. Tazuke, J. Phys. Soc. Jpn. **32** (2), 337 (1972).
14. R. H. Taylor and B. R. Coles, J. Phys. F: Metal Phys. **5** (1), 121 (1974).
15. P. Baillargeon, C. Buorbonnais, S. Tomic, *et al.*, Synth. Met. **27** (3/4), B83 (1988).
16. K. Kawasaki, Prog. Theor. Phys. **39** (2), 285 (1968).
17. S. E. Barnes, Phys. Rev. B: Condens. Matter **30** (7), 3944 (1984).
18. L. J. de Jongh and A. R. Miedema, Adv. Phys. **23** (1), 1 (1974).
19. I. S. Jacobs, J. W. Bray, H. R. Hart, Jr., *et al.*, Phys. Rev. B: Condens. Matter **14** (7), 3036 (1976).
20. R. White and T. Geballe, *Long Range Order in Solids* (Academic Press, New York, 1979).

Translated by P. Pozdeev

Physics of the Solid State, Vol. 42, No. 2, 2000, pp. 356–363. Translated from Fizika Tverdogo Tela, Vol. 42, No. 2, 2000, pp. 347–353.

LOW-DIMENSIONAL SYSTEMS AND SURFACE PHYSICS

Thermodesorption of Silicon from Textured Tantalum Ribbons

V. N. Ageev, E. Yu. Afanas'eva, N. D. Potekhina, and A. Yu. Potekhin

Ioffe Physicotechnical Institute, Russian Academy of Sciences, Politekhnicheskaya ul. 26, St. Petersburg, 194021 Russia

Received May 12, 1999

Abstract—The interaction of silicon with tantalum is studied by the Auger spectroscopy and temperature-controlled desorption technique. It is shown that, at a monolayer coating, the adsorbed silicon atoms penetrate into the bulk of a substrate at temperature $T \geq 1400$ K. The spectral shape and the annealing curves are explained by the influence of the Si–Si lateral repulsion in an adsorbed layer on the desorption and diffusion of the Si atoms into the bulk. Some ratios between the kinetic parameters are determined from analysis of the experimental data. Their application in numerical calculations based on the model proposed earlier makes it possible to determine (from comparison of the calculated and experimental data) the kinetic parameters for all the processes of the interaction between silicon and the tantalum substrate during the temperature-controlled desorption (desorption, transfer into the bulk, diffusion, and migration of silicon onto the surface). An adequate description of the experiment is obtained only under the assumption that the diffusion at the final stages of temperature-controlled desorption after reaching a maximum occurs within a thin layer near the surface, so that the migration of the Si atoms to the surface and desorption proceed more rapidly than their diffusion into the bulk. © *2000 MAIK "Nauka/Interperiodica".*

Although the refractory metal–silicon contacts are promising elements of high-temperature microelectronics, the processes of their formation have thus far been imperfectly understood. For this purpose, it is common practice to examine the system "a semiconductor coated with a metal layer" [1]. In studies performed in our laboratory, we have dealt with the systems "a metal covered with a semiconductor layer." This provides a means for revealing new aspects of the formation of near-the-surface layers in the region of the studied contact. The present work continuities a series of systematic investigations of the interaction between silicon and refractory metals (such as W, Ir, Nb, and Ta [2–8]) by the Auger electron spectroscopy and temperature-controlled desorption technique. The interaction of silicon with tantalum was investigated by the photoelectron spectroscopy in [9]. The diffusion of silicon into tantalum and the silicide formation were examined by the X-ray diffraction in [10].

In this work, we measured the spectra of temperature-controlled desorption, the Auger signals, and the total amount of silicon remaining in a tantalum substrate after the annealing of the tantalum ribbon coated with a monolayer of silicon. The experimental data were compared with the results of calculations of the model system described in [11, 12]. The model system accounts for the processes of penetrating adsorbed atoms into the bulk of metal, their diffusion in the bulk, and transfer onto the surface upon temperature-controlled desorption and annealing. A comparison of the model calculation and the experimental results makes it possible to determine the rate constants for all the processes observed in the system and to refine their physical meaning.

1. EXPERIMENTAL TECHNIQUE

The measurements were performed by the temperature-controlled desorption technique. The desorption products were identified using a time-of-flight mass spectrometer. The pressure of residual gases in the instrument was 10^{-10} Torr. An absorbent was a textured tantalum ribbon with the surface predominantly formed by the (100) face $0.01 \times 1.5 \times 30$ mm in size. The ribbon surface was arranged within view of an ion source of the mass spectrometer. The ribbon was cleaned from carbon according to the standard procedure by the annealing in an oxygen atmosphere followed by temperature-controlled heating.

Silicon was deposited from small bars $1 \times 1 \times 30$ mm in size. The silicon bars were mounted parallel to the tantalum ribbon and then were subjected to dc heating. The ribbon temperature was determined from the temperature dependence of the resistance. This dependence was calibrated with an optical micropyrometer. The tantalum ribbon was heated by a direct current. The ribbon temperature in the course of the "flash" changed linearly with time. The flux of Si atoms was recorded from the flow of Si^+ ions, to which corresponded a 28 line in the mass spectrometer. The flux of Si atoms onto the tantalum ribbon was calibrated by the "quartz balance" method.

The experiments were performed as follows. The tantalum ribbon was heated at a temperature of 2600 K for several seconds. Then, the temperature of ribbon

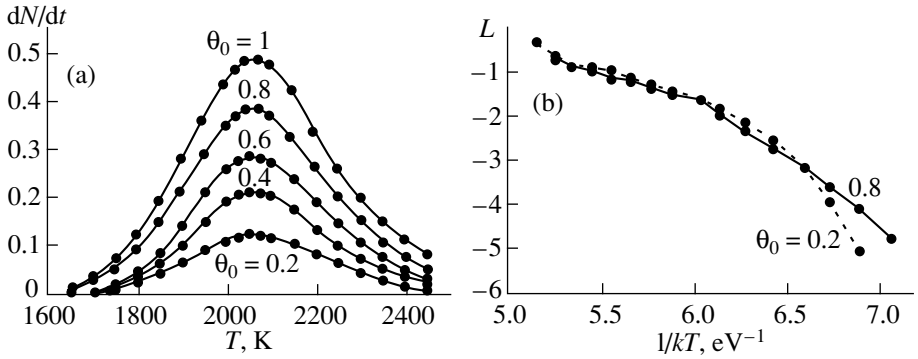

Fig. 1. (a) Experimental spectra of temperature-controlled Si/Ta desorption at the initial silicon coverage $\theta_0 = 0.2$, 0.4, 0.6, 0.8, and 1.0 and (b) dependences of the function $L = \ln(N^{-1}dN/dt)$ on $(kT)^{-1}$ at the coverage $\theta_0 = 0.2$ (dashed line) and 0.8 (solid line).

was decreased to room temperature, silicon was deposited over different time intervals, and the flash was carried out. The annealing of the film with a silicon monolayer applied at $T = 300$ K was carried out at several temperatures T_i in the range 1300–1800 K for 1 min. Prior to measurements, we established that the silicon desorption on the opposite side of the ribbon was absent both in the course of the flash and upon annealing of the ribbon with a silicon layer applied only on one side.

2. RESULTS

Figure 1a demonstrates the spectra of temperature-controlled desorption at the heating rate $\beta = 200$ K s^{-1} and different initial silicon coverages $\theta_0 \leq 1$ for the Ta(100) surface. It is seen that, for all the coverages θ_0, the spectra contain only one maximum. The maximum location and the halfwidth remain unchanged as the θ_0 value increases, which is characteristic of the monoatomic desorption without lateral interactions in an adsorbed layer and without diffusion of adsorbed species into the bulk. In this case, the temperature-controlled desorption is described by the Arrhenius equation with the first-order desorption. However, in our case, the dependence $L(1/kT) = \ln(N^{-1}dN/dt)$, for which the graphs at two θ_0 values are depicted in Fig. 1b, cannot be approximated by the straight line and, hence, cannot be described by the Arrhenius equation. The slope of the initial rectilinear portions of these curves (at $T \lesssim 1800$ K, i.e., $1/kT \gtrsim 6.4$ eV^{-1}) decreases with an increase in the coverage from $E^* \simeq 5.4 \pm 0.2$ eV at $\theta_0 = 0.2$ to $E^* \simeq 3.5 \pm 0.2$ eV at $\theta_0 = 0.8$. At higher temperatures, the $L(1/kT)$ curves become less dependent on θ_0, and their slopes decrease as the temperature increases up to 2200 K.

Since the spectra of temperature-controlled desorption at $\theta_0 \leq 1$ cannot be described by the Arrhenius equation with the first-order desorption, it would be reasonable to consider other processes for their explanation, such as, for example, the diffusion of silicon into the bulk of a tantalum ribbon upon temperature-controlled desorption. In order to verify the possibility of the diffusion process to occur, we studied the dependence of the intensity of the silicon Auger signal on the temperature T_i of annealing a silicon monolayer film on the tantalum substrate. Figure 2 displays the annealing curves (dashed lines) drawn through the experimental points—the temperature dependence of the intensity of the Auger signal (curve *1*) and the dependence of the total amount of silicon remaining in the system after annealing (curve *2*). The solid line corresponds to the theoretical approximation discussed in Section 3.

The decrease in intensity of the Auger signal $I_A(T)$ (curve *1*), which is proportional to the silicon amount in near-the-surface layers, occurs with an increase in the T_i temperature due to the silicon desorption during the annealing and also the diffusion of silicon into the bulk of tantalum. The total amount of silicon remaining in the system $M(T_i)$ decreases only through the desorption in the course of annealing and can be measured by the temperature-controlled desorption technique. Comparison of curves *1* and *2* in Fig. 2 shows that a decrease in the silicon amount in the near-the-surface region (at T_i

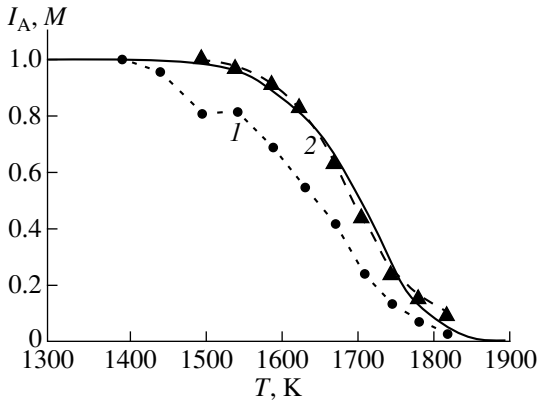

Fig. 2. Dependences of (*1*) the intensity of the Auger signal I_A and (*2*) total amount of silicon $M(T)$ in a tantalum plate after annealing for 60 s on the annealing temperature.

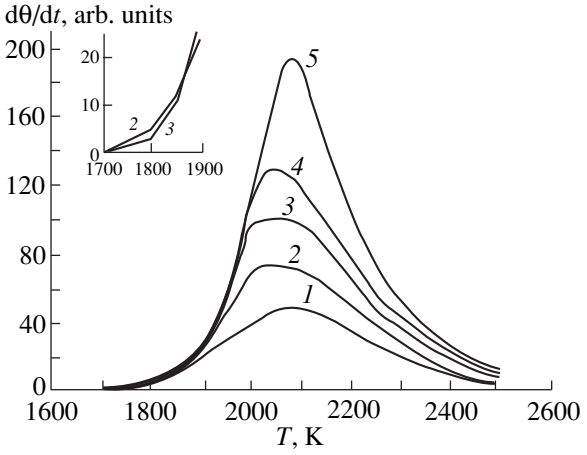

Fig. 3. Experimental spectra of temperature-controlled Si/Ta desorption at large silicon coverage θ_0 = (*1*) 1.2, (*2*) 1.6, (*3*) 2.0, (*4*) 2.4, and (*5*) 3.2.

≥ 1400 K) occurs prior to the desorption and a decrease in M(T_i) (at $T_i \geq 1500$ K). This implies that, in the range $1400 \leq T_i \leq 1500$ K, only the diffusion of silicon into the bulk of tantalum substrate takes place, and, at $T_i \geq 1500$ K, the diffusion of silicon in the bulk is accompanied by its desorption from the surface of tantalum. Below $T_i \leq 1400$ K, the silicon monolayer on the tantalum surface remains stable in both processes.

Figure 3 shows the spectra of temperature-controlled desorption at large silicon coverages $\theta_0 > 1$. The initial portions of the spectra at $\theta_0 = 1.2$ and 1.6 (curves *1*, *2*) differ from those at $\theta_0 > 2$ (curves *3*–*5*). Upon further increase in the coverage, the edges of thermodesorption curves *3*–*5* coincide, and the maxima shift with an increase in θ_0 toward the high-temperature range. This indicates the zero order of desorption, which is characteristic of the desorption from a thick layer of an adsorbate. Indeed, in this case, the dependence of $\ln(N^{-1}dN/dt)$ on $(kT)^{-1}$ is adequately reproduced by the straight line with the slope $E^* = 5.4 \pm 0.2$ eV. As is known [8], upon deposition of silicon on tantalum in the temperature range $1300 < T \leq 1600$ K at the initial coverages $\theta_0 < 2$, silicon is accumulated in near-the-surface region followed by formation of the Ta_5Si_3 silicide. In the case when the deposited silicon coverage becomes somewhat larger, i.e., $\theta_0 \simeq 2$, the structural phase transition from Ta_5Si_3 to Ta_4Si is observed in near-the-surface region. Hence, the differences in the initial portions of the temperature-controlled desorption curves at $\theta_0 < 2$ and $\theta_0 > 2$ are likely accounted for by the desorption of silicon from different silicides, namely, Ta_5Si_3 and Ta_4Si. This process is accompanied by a drastic increase in the rate of dissolution of silicon through the silicide layer [8].

At $\theta_0 \geq 2$, the edges of the desorption curves coincide, and the maxima are shifted to the high-temperature range. The fact that the desorption rate does not depend on the coverage is likely due to the desorption of silicon from the Ta_4Si silicide. The activation energy of desorption, which is found from the dependence $L(1/kT)$, coincides with the desorption energy at small coverages θ_0, i.e., $E_d = 5.4 \pm 0.2$ eV, which indicates a small surface concentration of silicon atoms during the sublimation of silicide.

It should be noted that, if the temperature T_{ads}, at which silicon was deposited on tantalum, is less than 1300 K, the shape of the temperature-controlled desorption curves, unlike the silicon layer on the tungsten surface at $\theta_0 > 1$ [4], does not depend on T_{ads} both at $\theta_0 \leq 1$ and $\theta_0 > 1$, even though the penetration of silicon into tantalum at $\theta_0 > 1$ occurs already at $T > 700$ K [8]. This means that the ultimate concentration profile of silicon in the bulk of tantalum is achieved during the flash.

3. COMPARISON OF EXPERIMENTAL RESULTS AND MODEL CALCULATIONS OF TEMPERATURE-CONTROLLED DESORPTION

As follows from the data shown in Figs. 1–3, the temperature-controlled desorption of Si atoms from the Ta(100) surface is accompanied by the penetration of silicon into the bulk of substrate, which occurs prior to the desorption from the adsorbed layer. A decrease in the slope of the initial portions of the $L(1/kT)$ curves in Fig. 1b with an increase in θ_0 suggests a repulsive interaction between the adsorbed Si atoms on the Ta(100) surface, which is similar to the lateral Si–Si interaction on the W(100) surface [4].

Therefore, in order to describe the spectra of temperature-controlled desorption from submonolayer silicon films on the Ta(100) surface, it is necessary to take into account the diffusion of silicon into the bulk of substrate and its transfer onto the surface in the course of the flash, and also the lateral interaction in the adsorbed layer. The calculation of the model system for describing the spectra of temperature-controlled desorption under these conditions was performed in the earlier works [11, 12]. In these works, we dealt with a symmetric plate of thickness 2*l*. Two surfaces of the plate were coated with a layer of an adsorbate at the initial coverage θ_0. It was assumed that the diffusion and desorption proceed only at $T(t) \geq T_0$. At the initial instant, the volume is free from particles. In the model (Fig. 4), the first subsurface layer serves as a boundary of the remaining volume, which is treated as a continuum. The motion of particles in the continuum is characterized by the diffusion coefficient $D = D_0\exp(-E_m/kT)$. In [11], we described the set of equations for numerical solution to the problem of the concentration changes for particles in an adsorbed layer,

near-the-surface layer, and in the bulk upon temperature-controlled desorption at the condition

$$T(t) = T_0 + \beta t. \quad (1)$$

The temperature-controlled desorption was analyzed at different ratios between the rate constant of desorption k_d, the rate constant of transition from an adsorbed layer to near-the-surface layer k_1, the rate constant of transition from near-the-surface layer to the adsorbed layer k_2, and the diffusion coefficient $D(T)$.

An analogous problem was formulated more recently by Mavrikakis *et al.* [13], who considered the diffusion into the bulk in the course of deposition of an adsorbate. It was demonstrated that the more slowly proceeded the deposition, the higher the diffusion maximum was located in the spectrum in the high-temperature range. In our works, we assumed that the initial coverage has already been specified, and the influence of diffusion was studied only during the temperature-controlled desorption. However, unlike [13], we made allowance for the concentration changes in the subsurface layer at the boundary between the continuum and adsorbed layer [11] instead of the assumption on the quasi-stationary flow of particles at the boundary. One of the purposes of our earlier work [11] was to determine the conditions of forming the quasi-stationary flow at the boundary of continuum. It was shown that the quasi-stationary flow is formed only at the final stages of temperature-controlled desorption after reaching a maximum in the spectrum. Moreover, in [12], unlike [13], we also considered the influence of lateral interactions in an adsorbed layer on the spectra of temperature-controlled desorption.

In the absence of lateral interactions, the rate constants of all the processes follow the Arrhenius equation

$$k_i(T) = k_i^0 \exp(-E_i/kT), \quad (2)$$

where k_i^0 is the preexponential factor of the ith process, and E_i is the activation energy of the ith process. The lateral interactions in the adsorbed layer result in the dependences of k_d and k_1 on the coverage $\theta(t)$. We took this dependence from the lattice-gas theory [14, 15]. The spectrum of temperature-controlled desorption is determined by the flux of desorbable particles

$$J(t) = -dN/dt = N_s k_d(T(t))\theta(t), \quad (3)$$

(where $N(t) = N_s\theta(t)$ is the total number of particles in half the plate, and N_s is the number of adsorption sites per 1 cm^2), and can contain one, two, and three maxima [11, 12]. In the presence of the lateral repulsion in an adsorbed layer, one maximum in the spectrum can be observed only when the repulsion affects both the desorption rate and the diffusion of particles into the bulk; in this case, the diffusion comes before the desorption.

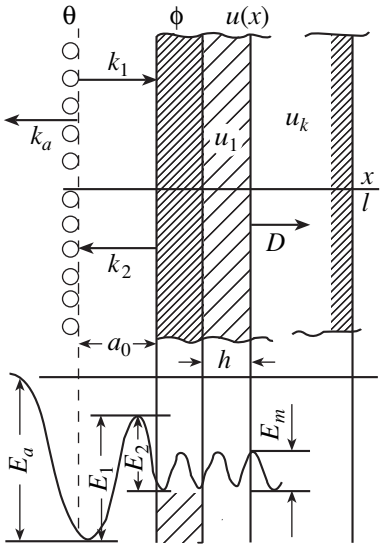

Fig. 4. A schematic model of the studied system.

In order to estimate the ranges of variations in the parameters involved in the calculation, we used the following findings.

(1) The slope of the dependence $L(1/kT) = \ln(N^{-1}dN/dt)$ (Fig. 1b) at small coverages $\theta_0 \longrightarrow 0$ determines the activation energy of desorption, that is,

$$E_d \simeq 5.4 \pm 0.2 \text{ eV}. \quad (4)$$

(2) The change in the slope of the $L(1/kT)$ curve with an increase in the coverage θ_0 gives an estimate of the energy of lateral interaction w from the relationship

$$E_i(\theta) \simeq E_i(0) - z\theta w, \quad (5)$$

where z is the number of the nearest neighbors in an adsorbed layer, and $E_i = E_d$ or E_1.

The energy of the lateral interaction w can be determined using the $E_d(0)$ value found from expression (4) and $E_d(1) \simeq 4.5$ eV. The latter value is taken to be close to the heat of sublimation of silicon, because the $E_d(1)$ energy obtained from the slope of the $L(1/kT)$ curve is not correct. This is explained by the fact that the temperature-controlled desorption occurs, as shown above, after the partial depletion of the adsorbed layer due to the diffusion of silicon into the bulk. In the case of desorption at the coverage $\theta_0 \simeq 1$, the lateral repulsion in the adsorbed layer should give rise to two maxima in the spectrum of temperature-controlled desorption [14, 15]. However, the spectrum of temperature-controlled Si/Ta desorption exhibits only one high-energy peak, which corresponds to small coverages. Hence, from formula (5) at $z = 4$, we obtain the estimate

$$w \simeq 0.25 \pm 0.05 \text{ eV}. \quad (6)$$

(3) The preexponential factors of the desorption process are evaluated from the location of the maximum in the spectrum of temperature-controlled desorp-

Table 1. Variants of the sets of parameters used in calculations

	I		II		III	
	E_i	k_i^0	E_i	k_i^0	E_i	k_i^0
k_d	5.4	5	5.5	8	5.3	7
k_1	4.6	1	4.7	1	4.4	5
k_2	3.4	5	3.5	5	3.0	7
D	2.1×10^{-3}		1.8×10^{-4}		1.6	2×10^{-4}
l_1	$0.15l$		$0.12l$		$0.25l$	

Table 2. Fraction of silicon in substrate after annealing for 60 s at different temperatures T_i (experimental and calculated data correspond to sets of parameters I and III specified in Table 1)

T_i, K	Experiment	I		III
		$l_1 = l$	$l_1 = 0.15l$	$l_1 = 0.25l$
1400	1.0	0.994	0.99	1.0
1500	1.0	0.988	0.98	0.98
1600	0.80–0.89	0.92	0.90	0.88
1700	0.38–0.46	0.72	0.60	0.52
1800	0.10	0.36	0.13	0.06

tion at $T_m \simeq 2060$ K according to the Redhead equation [16], which was derived without regard for diffusion into the bulk, that is,

$$E_d/(kT_m) \simeq \ln(k_d^0 T_m/\beta) - 3.64. \quad (7)$$

Here, the dependences $k_d(T)$ and $T(t)$ are found from equations (1) and (2).

(4) The temperature difference between the onset of the silicon diffusion into the tantalum substrate (T_1 = 1400 K) and the onset of desorption (T_2 = 1500 K) specifies the lower boundary for the difference of E_d and E_1 according to the relationship $k_1(1400\ \text{K}) \simeq k_d(1500\ \text{K})$. By substituting formula (5) for the dependences of the activation energies E_d and E_1 on the coverage into the Arrhenius equation (2) and taking into account the fact that, at T_2 = 1500 K, a certain part of the silicon coverage (about $0.1\theta_0$) passes into the bulk (Fig. 3), we obtain the expression

$$E_1 \simeq (E_d - 0.9\theta_0 zw)\frac{T_1}{T_2} + \theta_0 zw - kT_1 \ln(k_d^0/k_1^0). \quad (8)$$

From this formula at $k_d^0/k_1^0 \simeq$ (1–10), $w = 0.3$, $z = 4$, and $\theta_0 = 1$, it follows that

$$\delta E = E_d - E_1 \geq (0.4\text{–}0.8)\ \text{eV}. \quad (9)$$

(5) According to the theory of annealing a submonolayer in the presence of the diffusion into the bulk [17], the change in intensity of the Auger signal for impurity particles in the surface layer at the initial instants of annealing, i.e., at $t < k_d^{-1}(T)$, is determined by the relationships

$$I_A(t, T) \simeq I_0 \lambda \theta_0 [1 - b(T)\sqrt{t}],$$
$$b(T) = k_1(T)\sqrt{D}/[a_0 k_2(T)]. \quad (10)$$

Here, a_0 is the lattice constant for tantalum, and λ is the penetration depth of the Auger signal for the impurity, which decays with an increase in its distance x from the surface according to the law $I_A(x) = I_0 \exp(-x/\lambda)$, where I_0 is the intensity of the Auger signal from the monolayer. Comparison between the experimental data for the Si/Ta desorption [7] and expression (10) in [17] gives the following relationships

$$E_1 - E_2 \simeq (1.9 - E_m/2)\ \text{eV}; \quad k_2^0/k_1^0 \simeq 5, \quad (11)$$

where E_2 is the activation energy of the reverse transfer of particles from the bulk onto the surface, and E_m is the activation energy of bulk migration.

Expressions (10) and (11) were derived without regard for the fact that the coefficients $k_d(\theta, T)$ and $k_1(\theta, T)$ depend on θ. Hence, the estimates obtained from formulas (11) are tentative and can change with allowance made for these dependences.

(6) In the course of our experiment, no particle transfer to the opposite side of the ribbon 0.01 mm thick was observed. The distributions of particles throughout the bulk, which were calculated at different diffusion coefficients with the parameters meeting conditions (1)–(5), indicate that the silicon atoms do not reach the opposite side of the ribbon upon both annealing and temperature-controlled desorption, provided that the diffusion coefficient is limited by the inequality

$$D(T) \geq 10^{-4} \exp(-1.5\ \text{eV}/kT). \quad (12)$$

From the above considerations, we obtain a set of the initial parameters, which, after additional small variations, provide a more adequate description for the spectra of temperature-controlled desorption (Fig. 1) and the annealing curves (Fig. 2). The initial sets of kinetic parameters at different diffusion coefficients $D(T)$ are listed in Table 1 (variants I and II). The activation energies are given in eV, and the preexponential factors are expressed in units of 10^{13} s^{-1} for k_i^0 and cm^2 s^{-1} for D_0.

The calculations with these parameters for $l = 10^{-3}$ cm rather closely reproduce the main features of the spectrum, in particular, one maximum whose location and halfwidth virtually do not change with changes in the initial coverage θ_0 (Fig. 5). However, unlike the experiment, the calculated spectrum appears to be asymmetric in shape, and the annealing rate at high temperatures is considerably less than the experimental value

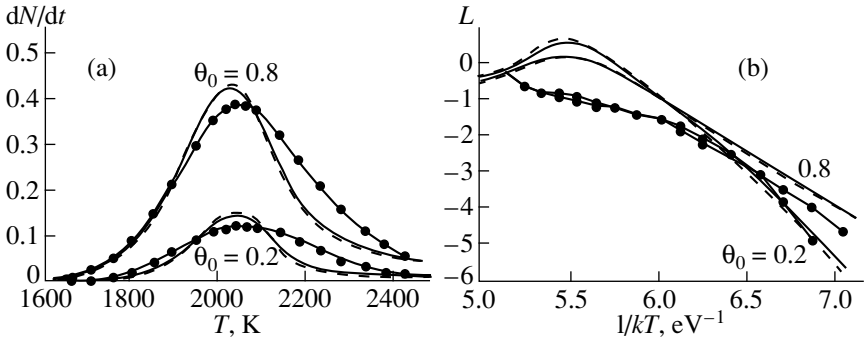

Fig. 5. Calculated (a) spectra of temperature-controlled desorption and (b) function $L(1/kT)$ at sets of parameters I (solid lines) and II (dashed lines) specified in Table 1 and $l_1 = l = 0.001$ cm. Points connected by solid lines represent the experimental data at the coverages (a) $\theta_0 = 0.2$, 0.6, and 1.0 and (b) $\theta_0 = 0.2$ and 0.8.

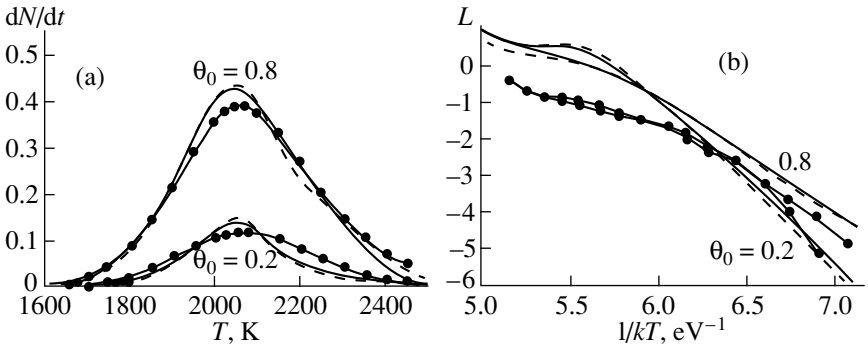

Fig. 6. The same data as in Fig. 5, but at $l_1 < l$ specified in Table 1.

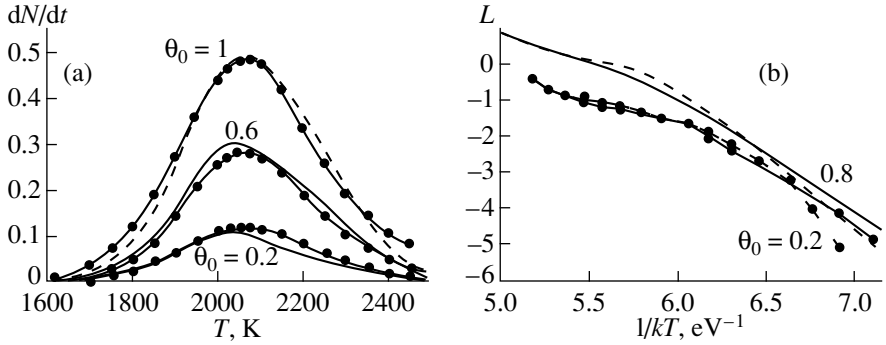

Fig. 7. Calculated (a) spectra of temperature-controlled desorption and (b) function $L(1/kT)$ at set of parameters III specified in Table 1. Points connected by solid lines represent the experimental data at the coverages (a) $\theta_0 = 0.2$, 0.6, and 1.0 and (b) $\theta_0 = 0.2$ and 0.8.

(Table 2, $l_1 = l$). This implies that the amount of silicon remaining in the bulk after the annealing at $T \geq 1700$ K is overestimated in the calculation more than three times irrespective of the diffusion coefficients satisfying condition (12). The additional variations mentioned above, which we produced in the found parameters, did not eliminate this discrepancy with the experimental data. The $L(1/kT)$ function (Fig. 5b) in the calculation ceases to increase and decreases at $T \geq T_m$, which, as was shown in [11, 12], also indicates an increased role of the silicon diffusion into the bulk in our model as compared to the experiment.

The symmetric shape of the calculated spectra can be obtained only by assuming that the diffusion rate drastically decreases in the bulk outside a certain layer with thickness $l_1 \ll l$ in the vicinity of the surface. With this assumption, all the variants specified in Table 1 give the symmetric shape of the spectra similar to those shown in Fig. 6, in which the calculated data were

obtained with the parameters of variants I and II at $l_1 < l$. The behavior of the $L(1/kT)$ function (Fig. 6b) also more closely resembles the behavior of the experimental curves. At high temperatures, the annealing proceeds more rapidly, and the discrepancy between the calculation and the experiment is almost absent, as it is seen from Table 2. Note that, in this variant of the theoretical model, restriction (12) becomes redundant.

A better fitting to the experimental data was achieved with a certain variation in the constants (variant III in Table 1) (Fig. 7). Deviations from conditions (11) in this set of parameters can result from the approximations made in [17] and also from the constraint between the parameters E_i and k_i^0, which makes impossible their unambiguous determination separately from each other. The interrelation between the parameters provides a means for describing the experimental data by different sets of parameters. However, all the found sets only slightly differ from one another, and, in the case of the interaction between the silicon submonolayer and the tantalum substrate, the parameters are limited by the following ranges (the activation energies are given in eV, and the k_i^0 preexponential factors are expressed as 10^{13} s^{-1}):

$$E_d \simeq 5.3\text{–}5.5; \quad k_d^0 \simeq 5\text{–}10;$$
$$E_1 \simeq 4.4\text{–}4.7; \quad k_1^0 \simeq 1\text{–}8;$$
$$E_2 \simeq 3.0\text{–}3.5; \quad k_2^0 \simeq 3\text{–}7;$$
$$E_m \simeq 1.6\text{–}2.1; \quad D_0 \simeq 10^{-4}\text{–}10^{-3}\ \text{cm}^2\ \text{s}^{-1}. \qquad (13)$$

In our model, we assumed that the diffusion rate in the bulk of the plate decreases to zero outside the thin layer near the surface. For the actual system, this means that the diffusion rate of impurity particles in the bulk depends on their concentration or their distance from the surface. We simulated this dependence by the stepwise decrease in $D(T)$ down to zero at $x \geq l_1 = (0.12\text{–}0.25)l$, where l is the thickness of the tantalum plate. The roughness of this model is partly responsible for the inexact description of the calculated dependences dN/dt and $L(1/kT)$ at different coverages θ_0. In particular, the stepwise decrease in the diffusion coefficient leads to a more drastic decay of the high-temperature branch of the spectrum as compared to the experiment. The shape of the experimental curve $L(1/kT)$ is more adequately described by the model with the stepwise dependence of the diffusion coefficient $D(x)$ as compared to the model without this assumption (Figs. 5, 6). The slopes of different portions of the $L(1/kT)$ curve (Fig. 7), which determine the effective activation energies E_i, are in reasonable agreement with the experiment. The remaining quantitative discrepancies can be accounted for by the inaccuracy of both the model and the measurements. The data on annealing, which were calculated with the proposed model (the last column in Table 2 and the solid line in Fig. 2), also agree well with the experiment.

The above calculations showed that a set of conditions (4)–(12) determines rather narrow ranges for variations in the parameters of rate constants specified by relationships (13).

Thus, it was demonstrated that, in the course of the temperature flash, silicon from the submonolayer penetrates into the bulk of substrate (at $T \geq 1400$ K) prior to its desorption (at $T \geq 1500$ K). This explains the presence of only one maximum in the spectrum of temperature-controlled desorption of silicon from the surface of tantalum, even with the lateral repulsion in the adsorbed layer.

From comparison of the calculated and experimental data, it follows that the experimental bell-shaped (almost without diffusion "tail") spectrum can be realized only when the diffusion rate is increased within a certain layer near the surface as compared to the rest of the system. This can be associated with the formation of a silicide layer at $T \geq 1600$ K, which provides the accelerated diffusion of silicon into the bulk and also a more rapid transfer of silicon to the surface through the layer of decomposing silicide in comparison with its penetration farther in the bulk of pure tantalum. Thus, the model with "reflection" of diffusing particles from the boundary of a certain layer near the surface better reproduces the spectrum of temperature-controlled desorption and the annealing rate than the model with a constant diffusion coefficient throughout the bulk of the ribbon.

The approximate values were determined for the activation energies and preexponential factors of the rate constants for all the processes of the interaction between adsorbed silicon atoms and the tantalum substrate.

ACKNOWLEDGMENTS

This work was supported by the "Surface Atomic Structures" Program of the Ministry of Science and Technology of the Russian Federation, project no. 4.5.99.

REFERENCES

1. G. Rossi, Surf. Sci. Rep. **7**, 1 (1987).
2. V. N. Ageev, E. Yu. Afanas'eva, N. R. Gall', *et al.*, Poverkhnost, No. 5, 7 (1987).
3. V. N. Ageev, E. Yu. Afanas'eva, N. R. Gall', *et al.*, Pis'ma Zh. Éksp. Teor. Fiz. **12** (9), 565 (1986).
4. V. N. Ageev and E. Yu. Afanas'eva, Poverkhnost, No. 7, 30 (1987).
5. E. Yu. Afanas'eva, N. D. Potekhina, and S. M. Solov'ev, Fiz. Tverd. Tela (S.-Peterburg) **37** (2), 463 (1995).
6. V. N. Ageev, E. Yu. Afanas'eva, S. M. Solov'ev, *et al.*, Fiz. Tverd. Tela (Leningrad) **35** (2), 481 (1993).

7. N. R. Gall, E. V. Rut'kov, A. Ya. Tontegode, *et al.*, Phys. Low-Dim. Struct. **4/5**, 75 (1996).
8. V. N. Ageev and E. Yu. Afanas'eva, Fiz. Tverd. Tela (S.-Peterburg) **39** (8), 1484 (1997).
9. T. A. Nguyen Tau, V. Azizan, and J. Derrien, Surf. Sci. **189/109**, 339 (1987).
10. G. J. Campisi, A. J. Bevolo, N. R. Shanks, *et al.*, J. Appl. Phys. **53**, 1714 (1982).
11. V. N. Ageev, A. Yu. Potekhin, and N. D. Potekhina, Poverkhnost, No. 1, 31 (1987).
12. V. N. Ageev, A. Yu. Potekhin, and N. D. Potekhina, Poverkhnost, No. 1, 5 (1991).
13. M. Mavrikakis, J. M. Schwank, and Y. L. Gland, Surf. Sci. **355**, 385 (1996).
14. D. L. Adams, Surf. Sci. **42**, 12 (1974).
15. V. P. Zhdanov, *Elementary Physical Chemical Processes on Solid Surfaces* (Plenum, New York, 1991).
16. P. A. Redhead, Vacuum **12** (2), 203 (1962).
17. N. D. Potekhina, Fiz. Tverd. Tela (S.-Peterburg) (1999) (in press).

Translated by O. Borovik-Romanova

Physics of the Solid State, Vol. 42, No. 2, 2000, pp. 364–365. Translated from Fizika Tverdogo Tela, Vol. 42, No. 2, 2000, pp. 354–355.

LOW-DIMENSIONAL SYSTEMS AND SURFACE PHYSICS

Width of Steps on a Rough Surface

A. A. Berzin and A. I. Morozov

Moscow State Institute of Radio Engineering, Electronics, and Automation (Technical University), pr. Vernadskogo 78, Moscow, 117454 Russia
e-mail: morosov@eot-qw.eot.mirea.ac.ru

Received May 18, 1999

Abstract—Computer simulation of a rough surface indicates that a relation exists between the experimentally determined degree of roughness of interlayer boundaries and the correlation length, on the one hand, and the characteristic width of atomic steps on the layer interfaces in multilayered structures, on the other hand. © *2000 MAIK "Nauka/Interperiodica".*

1. Great attention is now paid to studying magnetic and semiconducting multilayered structures. The quality of the interface between the layers may significantly affect the characteristics of such "sandwiches." In particular, in the case of magnetic multilayered structures consisting of alternating ferromagnetic and nonmagnetic metal layers, the roughness, i.e., the existence of atomic steps at the interfaces, may lead under certain conditions to the division of magnetic layers into domains [1]. The main parameter in this case is the characteristic width of the steps, i.e., the characteristic distance between two steps that locally change the thickness of the layer by a monatomic layer.

Usually, correlated and uncorrelated roughnesses are distinguished. In the case of the correlated roughness, the steps arise at the opposite sides of the layer in such a way that its thickness proves to be unaltered on average (Fig. 1a). In the case of the uncorrelated roughness, the steps arise independently (Fig. 1b).

As was shown in [2, 3], X-ray diffraction methods permit one to separate these contributions to the roughness and independently determine the roughness σ (that characterizes the mean-square deviation of the interface from the ideal plane) and the correlation lengths ξ_c and ξ_u for the correlated and uncorrelated roughnesses, respectively. Naturally, the correlation length for the layer thickness coincides with ξ_u.

However, the correlation length does not coincide with the average width of steps. The aim of this work is to find a relation between these two quantities at an arbitrary value of σ.

2. To this end, we performed a computer simulation of the surface roughness. We restricted ourselves to the case where the edges of the steps were parallel (one-dimensional case).

A random set of steps was realized; the probability of the creation of steps of length L was described by the formula [4]

$$P(L) = A\exp\left(-\frac{2L}{\langle L\rangle}\right)L, \quad (1)$$

where $\langle L\rangle$ is the average length of steps, and the constant A is found from the normalization condition. The height of steps was equal to one atomic layer, and the probability of the occurrence of each of the two directions for a jump (upward or downward) $w_\pm$ was described as

$$w_\pm = A'\exp[-(h\pm 1)^2/s^2], \quad (2)$$

where h is the height of the previous step, and the constant s characterizes the degree of roughness of the surface. The value of σ is unambiguously determined by the value of s; the corresponding dependence is shown

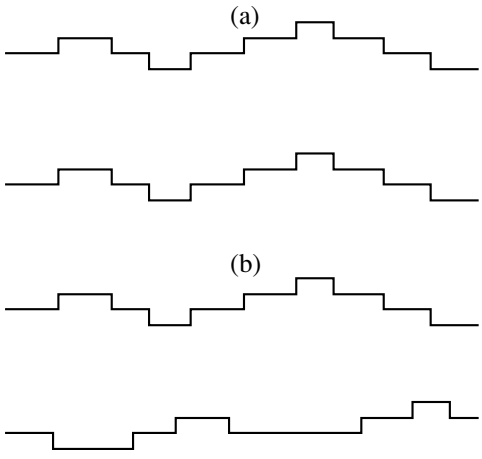

Fig. 1. (a) Correlated and (b) uncorrelated roughnesses on layer interfaces.

1063-7834/00/4202-0364$20.00

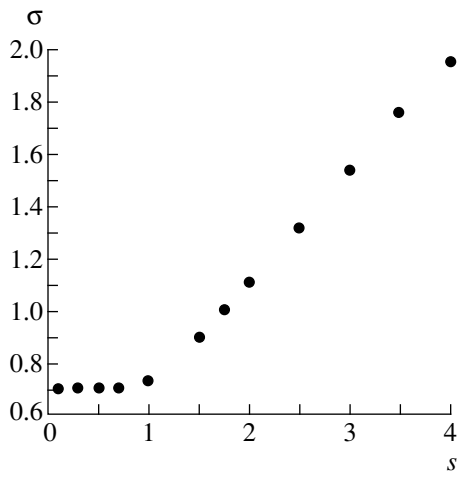

Fig. 2. Variation of the mean-square deviation of the surface from the ideal plane as a function of the parameter *s*.

in Fig. 2. At small σ, the deviations from the level $h = 0$ occur by one layer upward ($h = +1$) or downward ($h = -1$); the steps corresponding to $h = 0$ occur twice as frequently as those with $h = \pm 1$. Therefore, the value of σ is $(2)^{-1/2}$. At $s > 1$, we have

$$\sigma = 0.254 + 0.427s, \quad (3)$$

i.e., σ grows linearly with increasing *s*.

Then, we found the correlation function $K(x) = \langle h(0)h(x)\rangle$. To a good accuracy, this function is approximated by an exponential dependence with a correlation length ξ. For the case at hand ($\sigma \sim 1$, $\langle L\rangle \gg 1$), the ratio $\xi/\langle L\rangle$ is a universal function of σ of the form

$$\xi/\langle L\rangle = (1.71 \pm 0.03)\sigma^{(2.38 \pm 0.03)}. \quad (4)$$

The dependence obtained only weakly depends on the character of the distribution $P(L)$. For example, for steps of a fixed length, we have

$$\xi/\langle L\rangle = (1.52 \pm 0.06)\sigma^{(2.47 \pm 0.03)}. \quad (5)$$

Thus, the results of our simulation make it possible to determine the characteristic width of steps from experimentally determined values of ξ and σ.

REFERENCES

1. A. I. Morozov and A. S. Sigov, Fiz. Tverd. Tela (S.-Peterburg) **39** (7), 1244 (1997).
2. D. E. Savage, J. Kleiner, B. N. Schimke, *et al.*, J. Appl. Phys. **69** (3), 1411 (1991).
3. A. Schreyer, J. F. Ankner, Th. Zeidler, *et al.*, Phys. Rev. B **52** (22), 16066 (1995).
4. P. R. Pukite, C. S. Lent, and P. I. Cohen, Surf. Sci. **161** (1), 39 (1985).

Translated by S. Gorin

Physics of the Solid State, Vol. 42, No. 2, 2000, pp. 366–370. Translated from Fizika Tverdogo Tela, Vol. 42, No. 2, 2000, pp. 356–360.

LOW-DIMENSIONAL SYSTEMS AND SURFACE PHYSICS

Electronic Properties of Cesium Ultrathin Coatings on the Ga-Rich GaAs(100) Surface

G. V. Benemanskaya*, V. P. Evtikhiev*, and G. É. Frank-Kamenetskaya**

** Ioffe Physicotechnical Institute, Russian Academy of Sciences, Politekhnicheskaya ul. 26, St. Petersburg, 194021 Russia*

*** St. Petersburg Technological Institute (Technical University), Moskovskiĭ pr. 26, St. Petersburg, 198013 Russia*

Received May 31, 1999

Abstract—The cesium submonolayer coatings on the Ga-rich GaAs(100) surface at different coverages have been investigated by threshold photoemission spectroscopy. The electronic spectra of surface states and the ionization energies are analyzed. At a cesium coverage of about one-half the monolayer, the spectrum exhibits two narrow adsorption-induced bands below the Fermi level. This indicates that cesium atoms interacting with gallium dimers occupy two nonequivalent positions. It is found that the gallium broken bonds are saturated at the cesium coverage of ~0.7 monolayer, and the adsorption bonding is predominantly covalent in character. At the coverages close to the monolayer, broad bands with energies of 1.9, 2.05, and 2.4 eV have been observed for the first time. These bands can be associated with the excitation of cesium islands, cesium clusters, and surface cesium plasmon, respectively. The results obtained suggest two adsorption stages characterized by the formation of strong and weak bonds. © *2000 MAIK "Nauka/Interperiodica".*

1. INTRODUCTION

For many years, the interaction of metal atoms with a GaAs surface has attracted considerable interest, which stems from the fundamental problems concerning the formation of the metal–semiconductor interface and extensive technical applications of these systems [1, 2]. The high-quality GaAs(100) surface obtained by different methods of growth and surface treatment is of particular importance in producing the Schottky barriers and photoemitters with a high quantum yield.

Recent investigations demonstrate that about ten different reconstructions are observed on an atomically clean GaAs(100) surface. In the general case, one can recognize two classes of reconstructions, in which either arsenic dimers or gallium dimers are formed. In actually observed reconstructions, a part of atoms in the first layer is absent. For example, the GaAs(100) surface that is formed upon annealing at a maximum possible temperature of ~600°C has the $(4 \times 2)/c(8 \times 2)$ structure with gallium dimers, in which each fourth gallium dimer is absent [3]. This leads to the (4×2) periodicity. The (8×2) periodicity is brought about by the spatial displacement of one row of dimers with respect to another row. Since a quarter of gallium atoms is absent in the upper layer, their surface concentration is equal to 3/4 of the monolayer. Note that a monolayer (1 ML) is defined as the density of atoms on the ideal unreconstructed surface GaAs(100) 1×1, and its value is determined as 1 ML = 6.2×10^{14} atoms/cm^2 [1, 4]. The dimerization brings about a twofold decrease in the number of the gallium reactive broken bonds, so that their concentration is equal to the concentration of the surface gallium atoms, i.e., 4.6×10^{14} cm^{-2} (0.75 ML). By now, it is revealed that the GaAs(100) surface has a semiconductor-type electronic surface structure with unoccupied states of Ga broken bonds and occupied states of As broken bonds [5].

As a rule, the dimeric surface structure is retained upon adsorption of cesium atoms, and the adatoms can occupy different nonequivalent positions (the so-called "adsorption sites") above dimers, between atoms in a dimer, between dimer rows, etc. It is clear that the occupation of these sites affects the energy characteristics of interfaces. In the earlier works [6, 7], we established that, upon adsorption on the dimerically reconstructed surface Si(100) 2×1, the cesium atoms sequentially occupy the adsorption sites above dimers (one type of local interactions) and between dimer rows (another type of local interactions). The electronic surface structure of interfaces on silicon substrates and the GaAs(110) surface has been extensively studied by photoemission spectroscopy. However, similar investigations of the Ga-rich GaAs(100) surface were not carried out. Furthermore, neither modification of the existing surface states nor new surface states arising upon adsorption of cesium were examined. The question on the Cs saturating coverage (estimated at 0.5 ML in [4] and 1.0 ML in [8]) also remains open to discussion.

In the present work, the surface photoemission spectra and the ionization energy as functions of coverage for the Cs/Ga-rich GaAs(100) system were studied for the first time. The intensity of Cs source and the cesium coverage were evaluated with an original technique. At a coverage of ~0.5 ML, the spectrum contains

two narrow adsorption-induced bands, which indicates local interactions between the 6*s* valence states of cesium atoms and the s–p^3 orbitals of gallium broken bonds and also the presence of two different adsorption sites. It was found that the development of the cesium-induced bands is completed at a saturating coverage of 0.7 ML. This coating is stable and corresponds to the minimum ionization energy. With a further increase in the deposited amount of cesium, the coating becomes unstable and readily undergoes a partial desorption upon heating of the sample up to 100°C. At the coverages close to a monolayer, the surface photoemission spectra exhibit several broad bands with excitation energies of 2.4, 2.05, and 1.9 eV. The nature of these bands is likely associated with the excitation of cesium surface plasmon, cesium clusters, and cesium islands, respectively. It was revealed that an increase in the cesium coverage leads to a substantial increase in the density of surface states in the forbidden band; however, the spectrum involves the energy gap, and the Cs/Ga-rich GaAs(100) interface remains semiconductor in character over the entire coverage range under consideration.

2. EXPERIMENTAL

In situ measurements were carried out under ultrahigh vacuum at $P < 2 \times 10^{-10}$ Torr and room temperature. The clean GaAs(100) surface (*n*-type, 10^{17} cm^{-3}) was obtained by the thermal elimination (~580°C) of thin protective oxide layer formed preliminarily in a grower. As mentioned above, this temperature treatment brings about the formation of the dimerically reconstructed $(4 \times 8)/c(8 \times 2)$ surface rich with Ga. A high quality of the surface of this sample and the presence of dimer rows were shown by the atomic force microscopy (AFM) (Fig. 1). The electronic properties were investigated by threshold photoemission spectroscopy upon excitation with *s*- and *p*-polarized light [9, 10]. The method is based on the separation of bulk and surface photoemission and also on the effect of the near-threshold enhancement of photoemission from surface states. The *s*-polarized light causes the excitation of only the bulk states of a substrate with the threshold energy $h\nu_s$, which corresponds to the top of the valence band in the bulk, i.e., to the ionization energy ϕ. The *p*-polarized light brings about the excitation of surface bands with the threshold energy $h\nu_p$ due to the interaction with the normal component of the electric vector of light. In the case when the surface band is located at the Fermi level E_F (as in the case of metallization) or has the low-energy edge between the top of the valence band and the Fermi level E_F, the threshold energies can differ appreciably, i.e., $h\nu_s > h\nu_p$. Note that the threshold energy $h\nu_p$ is determined by the location of either the Fermi level E_F or the edge of the surface band. Analysis of the surface photoemission spectra I_p/I_s allows one to determine the energy location of surface bands with optical resolution (~0.02 eV) and also to reveal the presence or absence of the energy gap in the spectrum of surface states.

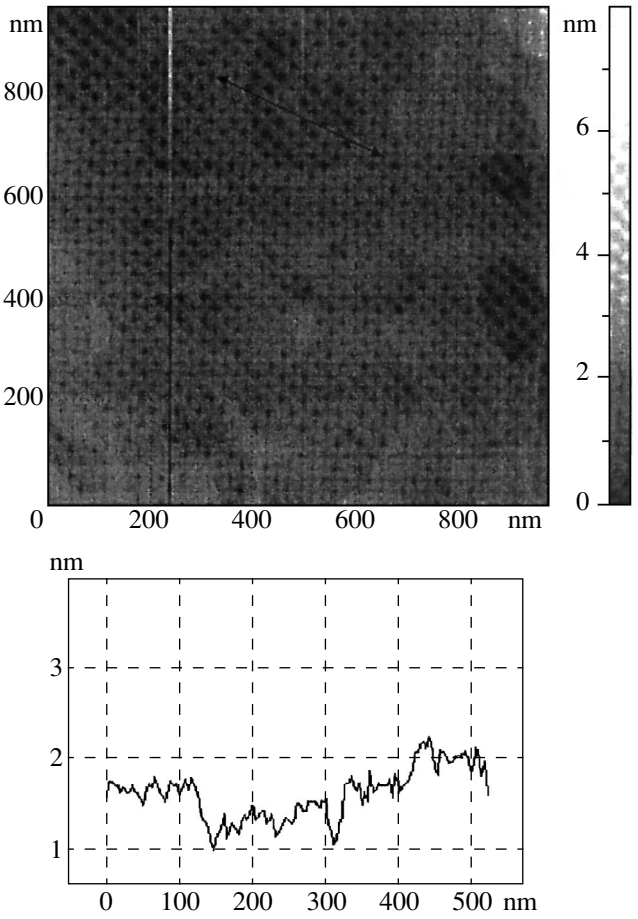

Fig. 1. An AFM image of the clean Ga-rich GaAs(100) surface.

3. RESULTS AND DISCUSSION

For the first time, we observed that the adsorption of cesium on the Ga-rich GaAs(100) surface causes the photoemission threshold energy to sharply increase. Figure 2 demonstrates the threshold energies $h\nu_s = \phi$ and $h\nu_p$ as functions of the cesium submonolayer coverage. It can be seen that both curves have a weakly pronounced minimum at the same coverage θ_{min}. We repeatedly determined the cesium amount at which the saturating coverage θ_{min} corresponds to the minimum ionization energy $\phi_{min} = 1.45$ eV. In order to quantitatively evaluate the deposited amount of cesium, we measured the flux rate of the Cs source. The source intensity was *in situ* determined from the ratio between the times of the cesium deposition onto the studied GaAs(100) surface and onto the pure W(110) surface used as a reference surface. Both samples were simultaneously positioned in a vacuum chamber and were

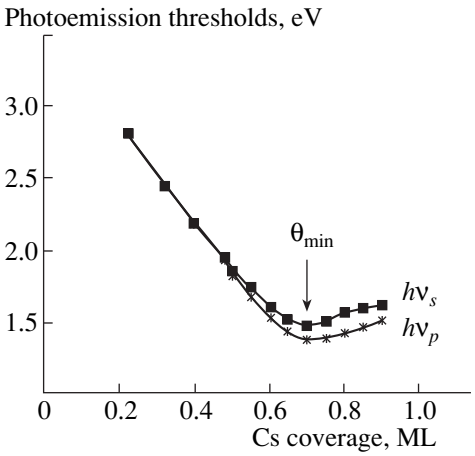

Fig. 2. Dependences of the photoemission threshold energies $h\nu_s$ and $h\nu_p$ on the Cs coverage of the Ga-rich GaAs(100) surface for *s*- and *p*-polarized light.

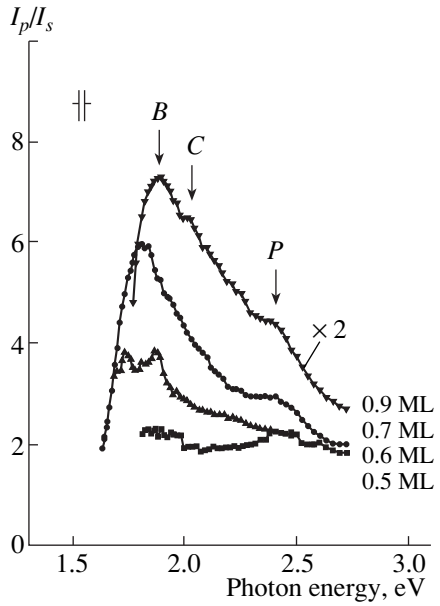

Fig. 3. Surface photoemission spectra I_p/I_s of the Cs/Ga-rich GaAs(100) system at different Cs submonolayer coverages.

placed under a beam of Cs atoms with the use of a manipulator. The accuracy of setting the sample in the same position with respect to the Cs source was controlled with crossed laser beams. The calibration procedure was described in detail in [6].

It was found that the cesium amount required to produce the coverage θ_{min} is equal to $(6.0 \pm 0.2) \times 10^{14}$ atoms/cm^2. The amount of cesium atoms deposited onto the sample surface can be converted to the surface concentration of adsorbed cesium atoms only with the known adhesion coefficient. At present, the accurate data for the entire range of submonolayer coverages are not available. Hence, we can use only the results obtained in [11–13], according to which the adhesion coefficient is equal to unity for the cesium deposition in the coverage range from 0 to 0.5 ML (3.1×10^{14} atoms/cm^2) and, then, beyond this range, drastically decreases by a factor of two or three. Therefore, the error in determination of the cesium coverage varies from ±0.02 to ±0.05 ML in the ranges 0.2–0.5 and 0.5–1.00 ML, respectively. From the cesium amount determined, the coverage $\theta = \theta_{min}$ was estimated at 0.70 ± 0.05 ML. Consequently, it can be concluded that the θ_{min} saturating coverage virtually coincides with the concentration of gallium atoms in the upper surface layer.

As can be seen from Fig. 2, at coverages less than $\theta = 0.5$ ML, the thresholds $h\nu_s$ and $h\nu_p$ are equal to each other; i.e., the surface states in the forbidden band are absent. With a further increase in the coverage, the threshold energies become different, which clearly indicates the appearance of surface states in the forbidden band above the top of the valence band. The difference between the thresholds monotonically increases and becomes as much as 0.18 eV at ~0.9 ML. This suggests the shift of the surface band edge toward the Fermi level. For the cesium coverage in the range from 0.5 to 1.0 ML, the analysis of photoemission in the immediate region of the $h\nu_p$ threshold shows that the density of surface states at the Fermi level E_F is equal to zero; i.e., the edge of the surface band lies between the top of the valence band and the Fermi level E_F. A detailed description of the technique employed was given in [6, 7]. Therefore, we can make the inference that the spectrum of surface states of the Cs/Ga-rich GaAs(100) interface is characterized by the energy gap, and the metallization is absent up to the cesium monolayer coverage.

The surface photoemission spectra I_p/I_s at different cesium coverages are displayed in Fig. 3. These spectra reflect the local density of surface states below the top of the valence band. We succeeded in identifying the surfaces bands. Their modification during the formation of the interface was thoroughly examined. The figure demonstrates a pronounced effect of the increase in the density of states and also the formation of bands induced by the cesium adsorption. It is significant that, at the coverages less than the saturating coverage ($\theta \leq 0.7$ ML), the spectra are stable for many hours. At larger coverages, the intensity of the spectrum decreases with an increase in the time after the deposition. This is caused by the desorption of cesium atoms at room temperature. It was found that, even upon insignificant heating of the interface up to a temperature of 100°C for 60 s, the spectra transform to the spectrum corresponding to $\theta_{min} = 0.7$ ML, no matter what the initial cesium coverage in the range 0.7–1.0 ML has already been deposited. Therefore, the above data suggest a change in the mechanism of the interaction between the surface and adatoms and a change in the

character of the adsorption bond during the formation of the interface. The adsorption observed can be separated into two stages, namely, the cesium chemisorption characterized by the formation of strong bonds and the adsorption of weakly bound cesium.

We revealed that the first stage of adsorption is characterized by the appearance of narrow surface bands induced by the adsorption. Actually, at a coverage of ~0.6 ML, the spectrum contains two narrow (Δ = 0.15 eV) A_1 and A_2 bands with energies of 1.75 and 1.85 eV, respectively. With a slight increase in the coverage up to θ = 0.7 ML, these bands are not resolved and correspond to a maximum at 1.8 eV (Fig. 4a). Analysis of the spectra with a small coverage step demonstrates that the behavior of the A_1 and A_2 bands is similar to that of the bands corresponding to the local interaction of cesium atoms with silicon dimers on the Si(100)-(2 × 1) surface [6, 7]. Taking into account that the formation of the A_1 and A_2 bands is completed at the coverage θ_{min} = 0.7 ML, their origin can be explained by the local interaction of cesium atoms with gallium dimers, which is accompanied by the saturation of all the broken bonds on the Ga-rich GaAs(100) surface.

At the second stage of adsorption, a further increase in the cesium coverage leads to a substantial increase in the intensity of surface photoemission and gives rise to several broad (Δ = 0.2–0.4 eV) bands in the spectrum. The experimental surface photoemission spectrum I_p/I_s for the cesium monolayer coverage and its decomposition is shown in Fig. 4b. It can be clearly seen that the spectrum involves three new peaks *B*, *C*, and *P* at energies of 1.9, 2.05, and 2.4 eV, respectively. It is worth noting that the *B* peak is not associated with the A_1 and A_2 bands, which, according to detailed analysis of the spectra, disappear at a coverage of ~0.85 ML. It should be mentioned once again that the states corresponding to the *B*, *C*, and *P* peaks are unstable and very rapidly disappear upon slight heating of the sample. The intensity of the only peak *P*, which is observed after the heating, decreases more than five times (Fig. 4). As follows from the above results, the origin of the *B*, *C*, and *P* bands can be associated with the formation of Cs–Cs unstable complexes on the GaAs(100) surface such, for example, as quasi-2*D* cesium islands or quasi-3*D* cesium clusters and surface cesium plasmon. In the study of the differential reflectivity spectra, Liebsch *et al.* [14] showed that the surface cesium plasmon is observed upon excitation of monolayer cesium film with the *p*-polarized light at an energy of 2.4 eV. There is recent indirect evidence that cesium clusters or islands can be formed on the GaAs(100) surface [15].

Therefore, the evolution of the spectra of surface states for the Cs/Ga-rich GaAs(100) interface indicates two adsorption stages. This agrees with the data on the thermal desorption of cesium from the Ga-rich GaAs(100) surface [16, 17]. According to our findings, at the cesium coverage less than the saturating coverage, the cesium adsorption is predominantly covalent in character and gives rise to two induced bands below the top of the valence band. All the gallium broken bonds are involved in the adsorption, and the saturating coverage is estimated at ~0.7 ML. The interface has a semiconductor-type electronic structure, and the metallization can be expected only at low temperatures when the second cesium layer can be formed. The development of the cesium-induced bands is completed at the saturating coverage. This implies the completion of the first adsorption stage and the onset of the second stage characterized by the unstable cesium coating with the formation of weak bonds. The second stage of adsorption is accompanied by the appearance of broad photoemis-

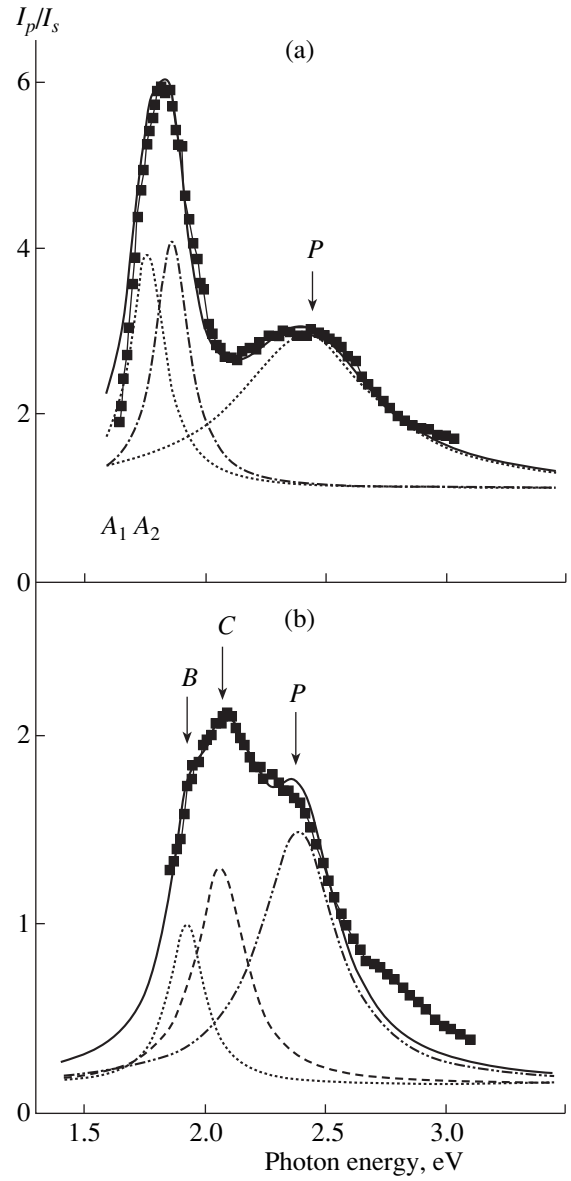

Fig. 4. Surface photoemission spectra I_p/I_s of the Cs/Ga-rich GaAs(100) system and their decomposition for (a) the saturating coverage θ ~ 0.7 ML and (b) the monolayer coverage θ = 1 ML.

sion bands in the spectra, which can be associated with the excitation of surface cesium plasmon and the formation of isolated cesium islands or cesium clusters. The results obtained indicate that the Cs–Ga interaction is stronger than the Cs–Cs interaction.

ACKNOWLEDGMENTS

We are grateful to D.V. Daĭneka, B.A. Bondarev, and A.K. Kryzhanovskiĭ for their assistance in performance of the experiments.

This work was supported by the Russian Foundation for Basic Research (project no. 98-02-18265) and the "Surface Atomic Structures" Program of the Ministry of Science and Technology of the Russian Federation (project no. 99-2.14).

REFERENCES

1. W. Mönch, *Semiconductor Surfaces and Interfaces* (Springer-Verlag, 1992).
2. F. Bechstedt and M. Scheffler, Surf. Sci. Rep. **18**, 145 (1993).
3. M. Vitomirov, A. D. Raisanen, and A. C. Finnerfrock, J. Vac. Sci. Technol., B **10** (4), 1898 (1992).
4. M. Kamaratos and E. Bauer, J. Appl. Phys. **70** (12), 7564 (1991).
5. Yia-Chung Chang, Shang-Fen Ren and D. E. Aspnes, J. Vac. Sci. Technol., A **10** (4), 1856 (1992).
6. G. V. Benemanskaya, D. V. Daineka, and G. É. Frank-Kamenetskaya, Pis'ma Zh. Éksp. Teor. Fiz. **65** (9), 699 (1997).
7. G. V. Benemanskaya, D. V. Daineka, and G. E. Frank-Kamenetskaya, Surf. Rev. Lett. **5** (1), 91 (1998).
8. J. Kim, M. C. Gallagher, and R. F. Willis, Appl. Surf. Sci. **67**, 286 (1993).
9. A. Liebch, G. V. Benemanskaya, and M. N. Lapushkin, Surf. Sci. **302**, 303 (1994).
10. G. V. Benemanskaya, M. N. Lapushkin, and M. I. Urbakh, Zh. Éksp. Teor. Fiz. **102** (5), 1664 (1992).
11. D. Rodway, Surf. Sci. **147**, 103 (1984).
12. G. Vergara, L. J. Gómez, J. Campany, *et al.*, Surf. Sci. **278**, 131 (1992).
13. B. Kierren and D. Paget, J. Vac. Sci. Technol., A **15** (4), 2074 (1997).
14. A. Liebsch, G. Hincelin, and T. Lipez-Rios, Phys. Rev. B: Condens. Matter **41** (15), 10 463 (1990).
15. A. O. Gusev, D. Paget, Y. Ya. Aristov, *et al.*, J. Vac. Sci. Technol., A **15** (1), 192 (1997).
16. H. Gao, J. Vac. Sci. Technol., A **5** (4), 1295 (1987).
17. J. Sakai, G. Mizutani, and S. Ushioda, Appl. Surf. Sci. **64**, 275 (1993).

Translated by O. Borovik-Romanova

Physics of the Solid State, Vol. 42, No. 2, 2000, pp. 371–376. Translated from Fizika Tverdogo Tela, Vol. 42, No. 2, 2000, pp. 361–366.

LOW-DIMENSIONAL SYSTEMS AND SURFACE PHYSICS

Theory of Scanning Capacitance Microscopy

D. B. Balagurov, A. V. Klyuchnik, and Yu. E. Lozovik

Institute of Spectroscopy, Russian Academy of Sciences, Troitsk, Moscow oblast, 142092 Russia
e-mail: lozovik@isan.troitsk.ru

Received June 3, 1999

Abstract—The theory of scanning capacitance microscopy (SCM), used in the examination of a two-dimensional distribution of irregularities in films arranged over metallic substrates, as well as of reliefs of conductive surfaces, is discussed. A realistic model of SCM, which is solvable analytically, is proposed. An explicit solution of the inverse problem of irregularities relief reconstruction (IRR) in SCM is obtained. The possible effects resulting from exciting of free oscillations in the "film–stylus" system of a sonde microscope are analyzed in detail. © *2000 MAIK "Nauka/Interperiodica".*

INTRODUCTION

The scanning capacitance microscopy (SCM) [1–15] is a version of the scanning sonde microscopy, where the value to be directly measured is the mutual capacitance of a conductive stylus and a substrate overlain by a specimen under examination. Because of modern methods being applicable for a measuring capacity up to ~10^{-20} F, the space resolution of the SCM may be more than ~100 nm in a sufficiently wide range of frequencies.

With the SCM, in semiconductor nanostructures, measurements of carrier concentrations were performed (*C–V* method) [3–5] and, in metal–nitride–oxide–semiconductor structures, the experiments on writing and reading of high-density information were carried out [6]. Furthermore, the series of experiments, where the SCM was used for sounding of low-dimensional systems, was performed [7–9]. Local capacitance detecting is used also in combination with the microscopy of atomic forces [11, 12] and with the electrostatic force microscopy [13].

Up to now, in the systems containing a stylus and an inhomogeneous dielectric–substrate layer, investigations of an electric field and a capacitance were performed usually with numeric methods, such as the finite-element method [14], the surface charge method [13], and the image method [15].

In this paper, we discuss a model of the scanning capacitance microscopy, which the following effects take strictly into account. It is assumed that the principal component of the capacity to be measured is determined by the geometry of the system as a whole (by the proportions and the shapes of the stylus, the substrate, etc.) and the slowly varying function of the stylus position. Besides, there is a contribution, which is of the order of the stylus tip size and, in a certain sense, is universal. This component is a function of deviation from the mean values of the quantities under examination (such as permittivity, film width, etc.).

In this work, by analytically solving the electrostatic boundary problem, the addition to the capacity is found to the first order in the fluctuating part of the permittivity and in the function of the relief of the film surface. This approach allows us to obtain an integral equation of a simple form, and its solution is the solution of the inverse problem of reconstruction of the image given by the SCM.

THE MODEL

A. Formulation of the Problem and Basic Equations

Our consideration is based on the scheme presented in Fig. 1. In the oblong spheroidal coordinates, which are coupled with the Cartesian coordinates by the following relations

$$x = a\sqrt{(\xi^2 - 1)(1 - \eta^2)}\cos\varphi,$$

$$y = a\sqrt{(\xi^2 - 1)(1 - \eta^2)}\sin\varphi,$$

$$z = a\xi\eta,$$

(where $\xi > 1$; $-1 < \eta < 1$; φ is the azimuthal angle, and a is a scale factor), the stylus and substrate surfaces are hyperboloids $\eta = \tilde{\eta}$ and $\eta = -\delta\eta$, respectively. The film surface is given by the equation $\eta = \zeta(\mathbf{r})$, where $\zeta(\mathbf{r}) = \zeta(\xi, \varphi)$ is the surface relief function (SRF) (measured in units of a) with $\langle\zeta(\mathbf{r})\rangle = 0$, $|\zeta(\mathbf{r})| \ll |\delta\eta|$; $\mathbf{r} = (x, y)$. Furthermore, we suppose that $1 - \tilde{\eta} \gg 1$ and $\delta\eta \ll 1$, i.e., that the stylus and the film are thin enough. Besides, we assume that the film permittivity is of the form $\varepsilon(\mathbf{r}, \omega) = \varepsilon_0(\omega) + \delta\varepsilon(\mathbf{r}; \omega)$, where the variable part $\delta\varepsilon(\mathbf{r}; \omega) = \delta\varepsilon(\xi, \varphi; \omega)$ satisfies the conditions $\langle\delta\varepsilon(\mathbf{r}; \omega)\rangle = 0$ and $|\delta\varepsilon(\mathbf{r}; \omega)| \ll \{|\varepsilon_0(\omega)|, 1\}$.

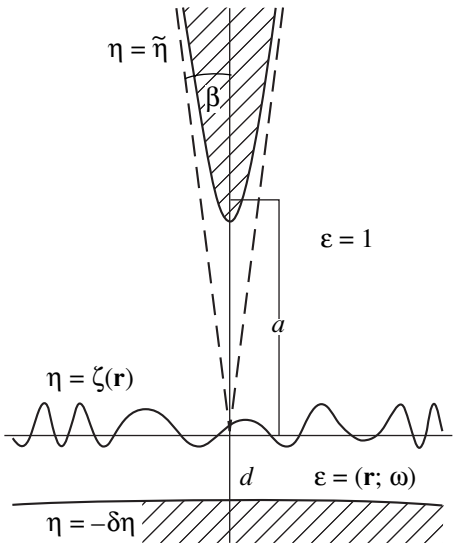

Fig. 1. Model of the SCM usual configuration. The regions $\tilde{\eta} < \eta < 1$ and $-1 < \eta < -\delta\eta$ are corresponded to a perfectly conductive stylus and a substrate respectively. The stylus expansion angle and the average film thickness are defined by the expressions $2\beta = 2\sqrt{2(1-\tilde{\eta})}$ and $d = a\delta\eta$, where a is the focus distance of hyperboloids.

For not-too-high frequency, the capacitance may be determined by solving the boundary problem with respect to the scalar potential u (normalized to the known voltage between the tip and the substrate):

$$\mathrm{div}[(\varepsilon_0 + \delta\varepsilon)\nabla u] = 0, \tag{1}$$

$$u|_{\eta=\tilde{\eta}} = 1, \quad u|_{\eta=-\delta\eta} = 0, \quad u|_{\eta=\zeta-0}^{\eta=\zeta+0} = 0,$$

$$[(\varepsilon_0 + \delta\varepsilon)\mathbf{n}\nabla u]|_{\eta=\zeta-0}^{\eta=\zeta+0} = 0, \tag{2}$$

where n is a normal vector to the irregular surface.

The solution of (1), (2) can be presented in the form of a power series in the $\zeta(\mathbf{r})$ and $\delta\varepsilon(\mathbf{r}; \omega)$ functions. In this case, the zeroth and first power terms are harmonic functions in the intervals $-\delta\eta < \eta < 0$ and $0 < \eta < \tilde{\eta}$, and they satisfy the boundary conditions

$$\begin{aligned} u^{(0)}|_{\eta=\tilde{\eta}} &= 1, \quad u^{(0)}|_{\eta=-\delta\eta} = 0, \\ u^{(0)}|_{\eta=-0}^{\eta=+0} &= [\varepsilon_0 n\nabla u]|_{\eta=-0}^{\eta=+0} = 0, \end{aligned} \tag{3}$$

and

$$\begin{aligned} u^{(1)}|_{\eta=\tilde{\eta}} &= u^{(1)}|_{\eta=-\delta\eta} = 0, \\ u^{(1)}|_{\eta=-0}^{\eta=+0} &= -\frac{\partial u^{(0)}}{\partial\eta}\bigg|_{\eta=-0}^{\eta=+0}\zeta, \\ \left[\varepsilon_0\frac{\partial u^{(1)}}{\partial\eta}\right]\bigg|_{\eta=-0}^{\eta=+0} &= -\left[\delta\varepsilon\frac{\partial u^{(0)}}{\partial\eta}\right]\bigg|_{\eta=-0}^{\eta=+0}. \end{aligned} \tag{4}$$

In the field expansion in powers of the variable parts of the permittivity and of the SRF, the dominant term, which represents the solution of boundary problem (3), takes the form

$$u^{(0)} = \frac{1}{\varepsilon(\eta)\ln(1-\tilde{\eta})}\ln\frac{1-\eta}{1+\eta}. \tag{5}$$

In this relation, $\varepsilon(\eta) = \varepsilon_0(\omega)$ at $-\delta\eta < \eta < 0$ and $\varepsilon(\eta) = 1$ at $0 < \eta < \tilde{\eta}$. Besides, we ignored the terms of higher powers with respect to $\delta\eta$ and $1 - \tilde{\eta}$ here. Including them would result in a shift of the resonance singularity in solution (5) from the point $\varepsilon_0(\omega) = 0$ to $\varepsilon_0(\omega) = \frac{2\delta\eta}{\ln(1-\tilde{\eta})} \ll 1$, which is of no significance in this model. Let us note that, in the plane $z = 0$ (inside the specimen), the electric field intensity dependence on the coordinates is similar to $E^{(0)} \sim (r^2 + a^2)^{-1/2}$, i.e., it involves a characteristic scale parameter a, which is the focus distance of the hyperboloid approximating the stylus.

The solution of (4) can be found in the form of expansion in the complete set of harmonics $e^{im\varphi}P^m_{-1/2+i\tau}(\pm\eta)P^m_{-1/2+i\tau}(\xi)$ for a hyperboloid, where P is the associated Legendre function of the first kind, $m = 0, \pm1, \ldots$; $\tau > 0$. The expression for the field $u^{(1)}$ is given in the Appendix.

B. Analysis of Free Oscillations

As will be shown below, at certain relations between the parameters, the effects associated with excitation of free oscillations become significant. The dispersion law for the free oscillations is specified by the resonance denominator (20) in expression (18) and has the form

$$\varepsilon_0(\omega) = \frac{P^m_{-1/2+i\tau}(\delta\eta) - P^m_{-1/2+i\tau}(-\delta\eta)}{P^m_{-1/2+i\tau}(\delta\eta) + P^m_{-1/2+i\tau}(-\delta\eta)}. \tag{6}$$

Therefore, it was taken into account that in the region where the resonance properties are significant, it is possible to pass to the limit $\tilde{\eta} \longrightarrow 1$ in (20). In Fig. 2, dispersion curves (6) are presented for several values of the integer number m specifying the field dependence on the angle φ.

In the region $|\tau^2\delta\tau| \ll 1$, the dispersion equation has an asymptotic form

$$\begin{aligned} \varepsilon_0(\omega) &= 2\delta\eta\tan\frac{\pi}{2}\left(-\frac{1}{2} + i\tau + m\right) \\ &\times\frac{\Gamma(3/4 + i\tau/2 - m/2)\Gamma(3/4 + i\tau/2 + m/2)}{\Gamma(1/4 + i\tau/2 - m/2)\Gamma(1/4 + i\tau/2 + m/2)}. \end{aligned} \tag{7}$$

For each m, there is a critical value of the permittivity

$$\varepsilon^{\mathscr{C}}_m = 2(-1)^m\delta\eta\frac{\Gamma(3/4 - m/2)\Gamma(3/4 + m/2)}{\Gamma(1/4 - m/2)\Gamma(1/4 + m/2)},$$

above which it is impossible to excite the corresponding free mode. In the region $|\tau^2\delta\eta| \gtrsim 1$, equation (6) takes the form of the dispersion law for a plasmon in a film [16] with a thickness $a\delta\eta$, one of whose surfaces borders on a perfect conductor

$$\varepsilon_0(\omega) = -\tanh\tau\delta\eta. \quad (8)$$

Here, τ/a is the wave number. In this case, the field is mainly concentrated at the dielectric–vacuum boundary, and there is no field–stylus overlapping, which explains the degeneracy in m.

In Fig. 3, in the complex plane τ, the position of the resonance pole with $m = 0$ is shown schematically as a function of the real part of permittivity. The range of permittivity variation from $-1 + 0$ to $\varepsilon_0^{\mathscr{C}} \approx -0.228\delta\eta$ corresponds to the region of the axially-symmetric free-mode existence. Therefore, in (6), taking the ohmic damping into account results in the pole displacing from the real axis into the lower half-plane. Let us note that in parallel with the ohmic damping due to the non-zeroth imaginary part of permittivity, there is radiation damping and damping due to irregularities in the system [16]. The last one may by taken into account only in the second order terms in the functions $\zeta(\mathbf{r})$ and $\delta\varepsilon(\mathbf{r}; \omega)$. The radiation damping is small with respect to the parameter $1 - \tilde{\eta}$.

At $\varepsilon_0'(\omega) = 0$ (more precisely, $\varepsilon_0'(\omega) = \dfrac{2\delta\eta}{\ln(1-\tilde{\eta})}$), this pole is near the point $\tau = -i/2$. In the limit of a perfect metal ($\varepsilon_0'(\omega) = \infty$), the pole goes through the point $\tau = -3i/2$ and reaches $-3i/2 - i\left[\delta\eta - \dfrac{2}{\ln(1-\tilde{\eta})}\right]$ at $\varepsilon_0'(\omega) = -1 - 0$. Let us note that there is also a pole situated symmetrically about $\tau = 0$ to that investigated above.

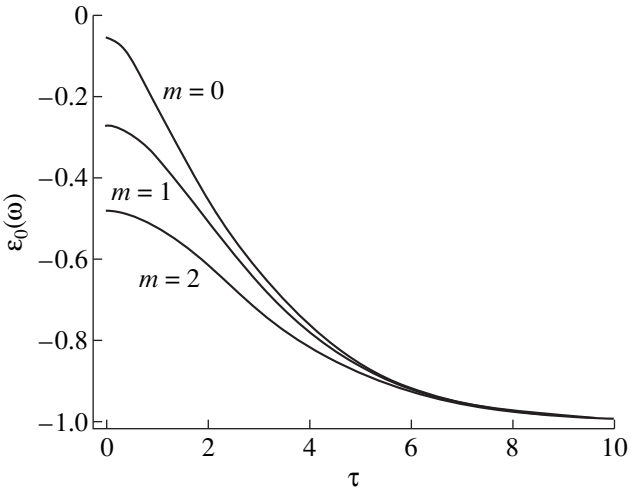

Fig. 2. Resonance permittivity versus the parameter τ for several values of m in the absence of absorption (τ is the parameter of eigenfunctions in problem (1), (2)). The value of the film thickness parameter is $\delta\eta = 0.25$ (see Fig. 1).

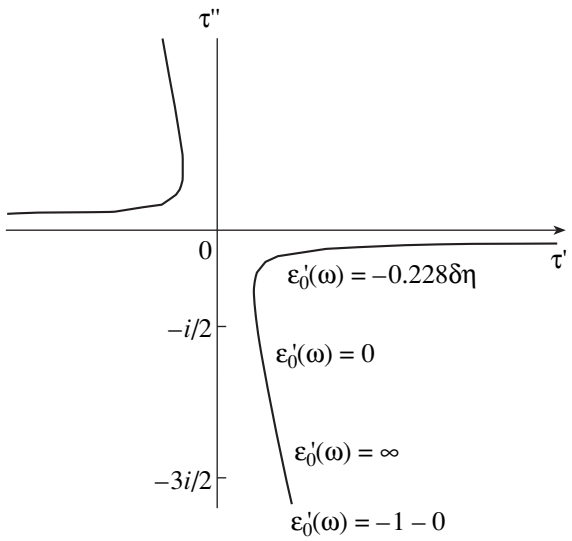

Fig. 3. Trajectory of the resonance pole τ_0 in the complex plane of the eigenfunction parameter as the real part of the permittivity $\varepsilon_0'(\omega)$ is varied.

C. Inverse Problem

Turning to the capacity calculation, let us note that when the system is not finite, the whole capacity is a divergent quantity. To prevent the divergence, it is convenient to cut off the space domain by the spheroid $\xi = \xi_{\mathcal{M}}$, so that the capacity would be calculated by the formula

$$C = -\frac{a(1-\tilde{\eta})}{2\pi}\int_1^{\xi_{\mathcal{M}}}\int_0^{2\pi}\left.\frac{\partial u}{\partial\eta}\right|_{\eta=\tilde{\eta}} d\xi d\varphi. \quad (9)$$

In so doing, it is assumed that, in the region $\xi < \xi_{\mathcal{M}}$, the stylus and substrate surfaces deviate from the hyperbolic surfaces $\eta = \tilde{\eta}$ and $\eta = -\delta\eta$ insignificantly, and $\xi_{\mathcal{M}} \gg 1$.

Just as it would be expected, for the zeroth approximation (5), the capacity $C^{(0)} \sim \xi_{\mathcal{M}}$, calculated by (9), is equivalent to $\xi_{\mathcal{M}}$ and it diverges with the parameter $\xi_{\mathcal{M}}$ being increased. The actual value of the capacity is determined not only by the tip of the stylus, but also by the sizes of the whole stylus, substrate, etc.

It is the addition to the capacity due to the varying components of the permittivity and of the surface relief function (SRF) that is of prime interest. A displacement of the stylus relative to the substrate reduces to change $\zeta(\mathbf{r}')$ by $\eta(\mathbf{r} - \mathbf{r}')$ and $\delta\varepsilon(\mathbf{r}'; \omega)$ by $\delta\varepsilon(\mathbf{r} - \mathbf{r}'; \omega)$, so that the contribution in $C^{(1)}$, linear in these functions, transforms to $C^{(1)}(\mathbf{r})$. Let us note that, in this case, $C^{(0)}$, as well as the cutting parameter, become slowly varying

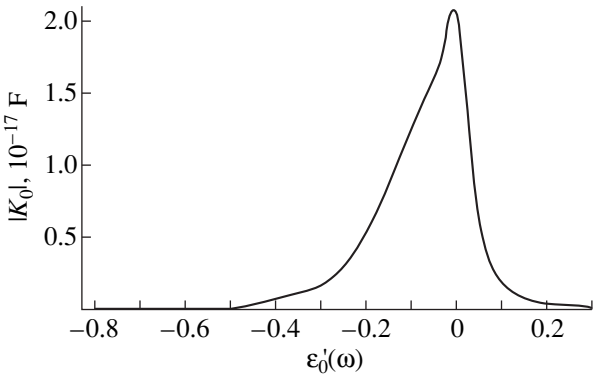

Fig. 4. Kernel amplitude versus the real part of the permittivity in the inverse problem (a = 500 nm, $1 - \tilde{\eta} = 10^{-4}$, $\delta\eta = 0.25$, $\xi_{\mathcal{M}} = 10^3$, and $\varepsilon_0''(\omega) = 0.04$).

functions of coordinates in the film plane with the inherent space scale $\gtrsim \xi_{\mathcal{M}}$.

In the potential $u^{(1)}$ expansion (17), in terms of functions harmonic inside and outside the hyperboloid, only the axially-symmetric term (with $m = 0$) makes a contribution into the function $C^{(1)}(\mathbf{r})$. To separate the fast dependence, it is sufficient to calculate the dominant term of the asymptotic expansion $C^{(1)}(\mathbf{r})$ in powers of the parameter $\xi_{\mathcal{M}} \gg 1$. This is equivalent to the single-pole approximation in integration with respect to τ in (9) and (17), when only the principal pole of the integrand is taken into consideration, for which the distance to the line $\mathrm{Im}\tau = 0$ is minimal. Therefore, the contributions from other poles would have additional factors of the type $\xi_{\mathcal{M}}^{\alpha}$, where $\alpha < 0$.

In calculating the correction to the capacity, two following cases may be differentiated.

(i) When the real part of the permittivity $\varepsilon_0'(\omega) < -1$ or $\varepsilon_0'(\omega) > 0$, then the poles $\tau = \pm i/2$ make the main contribution into the expression under consideration, so that

$$C^{(1)}(\mathbf{r}) = \int d\mathbf{r}' \mathcal{H}_1(\mathbf{r} - \mathbf{r}', \mathbf{r}) \times [\varepsilon_0(\omega)(\varepsilon_0(\omega) - 1)\zeta(\mathbf{r}') + \delta\eta\,\delta\varepsilon(\mathbf{r}'; \omega)], \tag{10}$$

where

$$\mathcal{H}_1 = \frac{1}{\pi\varepsilon_0^2(\omega)\ln^2(1-\tilde{\eta})}\frac{a^2}{\sqrt{(\mathbf{r}-\mathbf{r}')^2 + a^2}}. \tag{11}$$

(ii) If $-1 < \varepsilon_0'(\omega) < 0$, then, as it was noted above (see also Fig. 3), the poles $\tau = \pm i/2$ are located farther from the real axis than the pair of resonance poles $\pm\tau_0$ at $m = 0$. The location of the last ones may be determined from (6), and in regions corresponding to asymptotics (7) and (8), the following equations arise, which couple the capacity with the varying components of the permittivity and of the SRF:

$$C^{(1)}(\mathbf{r}) = \int d\mathbf{r}' \mathcal{H}_2(\mathbf{r} - \mathbf{r}', \mathbf{r}) \times [(\varepsilon_0(\omega) - 1)\,\mathrm{arctanh}\,\varepsilon_0(\omega)\zeta(\mathbf{r}') + \delta\eta\,\delta\varepsilon(\mathbf{r}'; \omega)], \tag{12}$$

where

$$\mathcal{H}_2 = F_2(\tau_0)\frac{a^2(2\xi_{\mathcal{M}}(\mathbf{r}))^{1/2 - i\tau_0}}{\sqrt{(\mathbf{r}-\mathbf{r}')^2 + a^2}} \times P_{-1/2 + i\tau_0}\left(\frac{a}{\sqrt{(\mathbf{r}-\mathbf{r}')^2 + a^2}}\right). \tag{13}$$

Here, at $|\tau_0^2\,\delta\eta| \ll 1$ (in the intervals $-0.228\delta\eta < \varepsilon_0'(\omega) < 0$ or $0 < -\varepsilon_0'(\omega) - 0.228\delta\eta \ll 1$), the value τ_0 is determined from equation (7) with $m = 0$, and at $|\tau_0^2\,\delta\eta| \gtrsim 1$ (in the interval $-1 < \varepsilon_0'(\omega) \lesssim -\sqrt{\delta\eta}$), it is determined from (8). In these intervals, the function F_2 has the following form:

At $|\tau^2\delta\eta| \ll 1$

$$F_2(\tau) = \frac{\sqrt{2}}{\pi\varepsilon_0(\omega)\delta\eta\ln^2(1-\tilde{\eta})} \times \frac{\Gamma(1/4 - i\tau/2)\Gamma(1/4 + i\tau/2)\Gamma(-1/2 + i\tau)}{\Gamma(i\tau)} \times [\psi(3/4 - i\tau/2) - \psi(3/4 + i\tau/2) + \psi(1/4 + i\tau/2) - \psi(1/4 - i\tau/2)]^{-1}, \tag{14}$$

where ψ is the digamma function.

At $|\tau^2\delta\eta| \gtrsim 1$

$$F_2(\tau) = \frac{(1+i)\cosh^2\tau\delta\eta}{\tau\delta\eta^2\ln^2(1-\tilde{\eta})}e^{-\pi\tau/2}. \tag{15}$$

D. Discussion

The solution of the integral Fredholm equations of the first kind, (10) or (12), represents the solution of the inverse problem of the reconstruction of the relief irregularities in the SCM, where, from the measured local capacitance distribution, a combination of the surface relief function and the variable part of the permittivity are determined. Usually, this experiment is of such a nature that on the characteristic scale of the surface under investigation, the variation of $\xi_{\mathcal{M}}(\mathbf{r})$ may be neglected. Therewith, in the case (ii), similar to (i), at the large values of the cutoff parameter $\xi_{\mathcal{M}}$, the dominant term of the asymptotic expressions of the kernel $\mathcal{H}$, written in (11) and (13), is dependent only on the difference $\mathbf{r} - \mathbf{r}'$, which allows us to solve the inverse problem by the Fourier transform. Namely, in (10) and (12),

the combination of the unknown functions is defined by the relation

$$f(\varepsilon_0(\omega))(\varepsilon_0(\omega)-1)\zeta(\mathbf{r})+\delta\eta\,\delta\varepsilon(\mathbf{r};\omega) = \int\frac{d\mathbf{k}}{(2\pi)^2}e^{i\mathbf{kr}}\frac{C^{(1)}(\mathbf{k})}{\mathcal{H}(\mathbf{k})}, \tag{16}$$

where, in the intervals (i) and (ii), the function $f(\varepsilon_0(\omega)) = \varepsilon_0(\omega)$ is equal to $f(\varepsilon_0(\omega)) = \operatorname{arctanh}\varepsilon_0(\omega)$ and $\operatorname{arctanh}\ \varepsilon_0'(\omega)$, respectively. The special form of the kernel, as well as the fact of the mean values $\langle\zeta(\mathbf{r})\rangle$ and $\langle\delta\varepsilon(\mathbf{r};\omega)\rangle$ being equal to zero, permits the existence and the uniqueness of the solution.

The dependence of the kernel maximal value $|\mathcal{H}(0)|$ (at $\mathbf{r} = \mathbf{r}'$) on the real part of the permittivity $\varepsilon_0'(\omega)$ is shown in Fig. 4. It is necessary to note that in the vicinity of the point $\varepsilon_0'(\omega) = 0$, the quantity in question is defined by the ohmic losses. Unlike (i), in the case of normal oscillations exciting (ii), which is difficult to realize in the SCM configuration, the kernel of the inverse problem (12) depends on the cutoff parameter $\xi_{\mathcal{M}}$. This means that, in this interval, the amplitude $|\mathcal{H}(0)|$ is not universal, i.e., it is defined not only by the system geometry near the stylus tip. Moreover, in the case of (ii), the real and imaginary parts of the addition to the capacity are the values of the same order. Let us note that even at the value $\varepsilon_0'(\omega) = -1 + \xi_{\mathcal{M}}^{-2\delta\eta}$, because of fast decreasing of $F_2(\tau)$ at $\tau \longrightarrow +\infty$ (see (15)), the contribution from the resonance pole becomes small, and it would be necessary to take the term (11) into account.

The investigated model allows us to consider the inverse problem, which arises in studying the conductive surface relief by the SCM, as its special case. Namely, from (10) and (13), in the limit $\varepsilon_0'(\omega) = \infty$, we have

$$C^{(1)}(\mathbf{r}) = \int\frac{a^2\zeta(\mathbf{r}')d\mathbf{r}'}{\pi\ln^2(1-\tilde{\tau})\sqrt{(\mathbf{r}-\mathbf{r}')^2+a^2}}.$$

The value of the addition to the capacity to be measured is proportional to the scale parameter a, which, at the same time, is the inherent space scale of the kernel in (10) and (12). This is in accordance with the fact that the capacity measurement errors make up the principal limitations on the space resolution in the SCM. In [2, 10], it was reported that the achievement of the space resolution was approximately equal to 10 nm. The behavior of the inverse problem kernel as a function of the coordinates is in good agreement with the experimental results and the numerical calculations [6, 10, 13–15].

APPENDIX

In the interval $0 < \eta < \tilde{\eta}$, the solution of the boundary problem (4) has a form

$$u^{(1)} = \sum_{m=-\infty}^{\infty}e^{im\varphi}\int_0^{+\infty}[A_m(\tau)P^m_{-1/2+i\tau}(\eta) + B_m(\tau)P^m_{-1/2+i\tau}(-\eta)]P^m_{-1/2+i\tau}(\xi)d\tau. \tag{17}$$

In this relation

$$A_m(\tau) = P^m_{-1/2+i\tau}(-\tilde{\eta})\frac{\mathcal{U}_m(\tau)}{\mathcal{W}_m(\tau)},\qquad B_m(\tau) = -P^m_{-1/2+i\tau}(\tilde{\eta})\frac{\mathcal{U}_m(\tau)}{\mathcal{W}_m(\tau)}, \tag{18}$$

$$\mathcal{U}_m(\tau) = \frac{\alpha_m(\tau)}{P^m_{-1/2+i\tau}(0)}[P^m_{-1/2+i\tau}(\delta\eta)+P^m_{-1/2+i\tau}(-\delta\eta)] + \frac{\beta_m(\tau)}{P^{m'}_{-1/2+i\tau}(0)}[P^m_{-1/2+i\tau}(\delta\eta)-P^m_{-1/2+i\tau}(-\delta\eta)], \tag{19}$$

$$\mathcal{W}_m(\tau) = P^m_{-1/2+i\tau}(-\tilde{\eta})[(\varepsilon_0(\omega)+1)P^m_{-1/2+i\tau}(-\delta\eta) + (\varepsilon_0(\omega)-1)P^m_{-1/2+i\tau}(\delta\eta)] - P^m_{-1/2+i\tau}(\tilde{\eta})[(\varepsilon_0(\omega)-1)P^m_{-1/2+i\tau}(-\delta\eta) + (\varepsilon_0(\omega)+1)P^m_{-1/2+i\tau}(\delta\eta)], \tag{20}$$

with

$$\alpha_m(\tau) = \frac{2(\varepsilon_0(\omega)-1)}{\ln(1-\tilde{\eta})}\tilde{\zeta}_m(\tau),\qquad \beta_m(\tau) = \frac{2}{\varepsilon_0(\omega)\ln(1-\tilde{\eta})}\tilde{\delta\varepsilon}_m(\tau). \tag{21}$$

The functions $\tilde{\zeta}_m(\tau)$ and $\tilde{\delta\varepsilon}_m(\tau)$, which appeared here, are the Fourier and Mehler–Fock-transforms [17] of the varying components of the permittivity and the SRF, respectively, with respect to the variables φ and ξ:

$$\begin{pmatrix}\tilde{\zeta}_m(\tau)\\ \tilde{\delta\varepsilon}(\tau)\end{pmatrix} = \frac{\tau}{\pi}\sinh\pi\tau\,\Gamma\left(\frac{1}{2}-m-i\tau\right)\Gamma\left(\frac{1}{2}-m+i\tau\right) \times\int_0^{2\pi}\frac{d\varphi}{2\pi}e^{-im\varphi}\int_1^{+\infty}d\xi P_{-1/2+i\tau}(\xi)\begin{pmatrix}\zeta(\xi,\varphi)\\ \delta\varepsilon(\xi,\varphi)\end{pmatrix}. \tag{22}$$

ACKNOWLEDGMENTS

The work was supported by the Russian Foundation for Basic Research and by the Programs “Surface Atomic Structures” and “Physics of Solid Nanostructures.”

REFERENCES

1. Y. Martin, D. W. Abraham, and H. K. Wickramasinghe, Appl. Phys. Lett. **52**, 1103 (1988).
2. C. C. Williams, W. P. Hough, and S. A. Rishton, Appl. Phys. Lett. **55**, 203 (1989).
3. A. C. Diebold, M. R. Kump, J. J. Kopanski, *et al.*, J. Vac. Sci. Technol. B **14**, 196 (1996).
4. G. Neubauer, A. Erickson, C. C. Williams, *et al.*, J. Vac. Sci. Technol. B **14**, 426 (1996).
5. A. Erickson, L. Sadwick, G. Neubauer, *et al.*, J. Electr. Mat. **25**, 301 (1996).
6. R. C. Barrett and C. F. Quate, J. Appl. Phys. **70**, 2725 (1991).
7. S. H. Tessmer, P. I. Glicofridis, R. C. Ashoori, *et al.*, Nature **392**, 51 (1998).
8. H. Drexler, D. Leonard, W. Hansen, *et al.*, Phys. Rev. Lett. **73**, 2252 (1994).
9. G. Medeiros-Ribeiro, D. Leonard, and P. M. Petroff, Appl. Phys. Lett. **66**, 1767 (1995).
10. Š. Lányi, J. Török, and P. Řehuřek, Rev. Sci. Instrum. **65**, 2258 (1994).
11. K. Goto and K. Hane, Rev. Sci. Instrum. **68**, 120 (1997).
12. V. A. Bykov, V. V. Losev, and S. A. Saunin, in *Proceedings of the All-Russia Meeting "Sonde Microscopy–99"* (Nizhni Novgorod, 1999).
13. S. Watanabe, K. Hane, T. Ohye, *et al.*, J. Vac. Sci. Technol. B **11**, 1774 (1993).
14. Š. Lányi, J. Török, and P. Řehuřek, J. Vac. Sci. Technol. B **14**, 892 (1996).
15. K. Goto and K. Hane, J. Appl. Phys. **84**, 4043 (1998).
16. Yu. E. Lozovik and A. V. Klyuchnik, in *The Dielectric Function of Condensed Systems*, Ed. by L. V. Keldysh, *et al.* (Elsevier, Netherlands, 1987).
17. V. A. Ditkin and A. P. Prudnikov, *Integral Transforms and Operational Calculus* (Fizmatgiz, Moscow, 1961).

Translated by N. Ostrovskaya

Physics of the Solid State, Vol. 42, No. 2, 2000, pp. 377–380. Translated from Fizika Tverdogo Tela, Vol. 42, No. 2, 2000, pp. 367–370.

LOW-DIMENSIONAL SYSTEMS AND SURFACE PHYSICS

Coadsorption of Silicon and Chalcogen (S, O) Atoms on Heated Re(10$\bar{1}$0) Substrate

N. R. Gall', E. V. Rut'kov, and A. Ya. Tontegode

Ioffe Physicotechnical Institute, Russian Academy of Sciences, Politekhnicheskaya ul. 26, St. Petersburg, 194021 Russia

Received 18 June, 1999

Abstract—The coadsorption of silicon and Group VI elements on the Re(10$\bar{1}$0) surface is investigated by the high-resolution Auger spectroscopy. It is demonstrated that, upon deposition of silicon on the surface oxide or surface sulfide, a part of silicon atoms deposited interacts with chalcogen atoms to be desorbed in the form of SiO or SiS molecules. The rest of silicon atoms occupy the becoming free adsorption sites, thus forming surface silicide. The silicon atoms incorporated into the surface silicide loose their reactivity and coexist on the surface together with adsorbed chalcogen atoms. © *2000 MAIK "Nauka/Interperiodica".*

The coadsorption of different-type atoms on heated transition-metal surfaces is of considerable scientific and practical interest. This is associated with a wide variety of physicochemical processes occurring on the surface and also with practical importance of similar systems. Investigations into multicomponent adsorption systems on the surface of rhenium—an effective commercial catalyst—are essential to the understanding of the processes proceeding in the course of actual catalytic reactions [1].

In the earlier works, we have shown that the high-temperature coadsorption of Si and C atoms causes the displacement of carbon atoms from the surface into the bulk of a rhenium substrate to form the solid solution [2, 3], as is the case on the surface of W or Mo [4, 5]. However, the coadsorption of silicon and chalcogen (S, O) atoms on tungsten initiates quite a different process: at high temperatures, the volatile SiO or SiS molecules are formed on the surface and undergo desorption, while the free adsorption sites are occupied by silicon atoms [5, 6]. In this respect, the question arises as to whether the above processes proceed on the surface of rhenium, which is a Group VII metal, or a distinctly different physical pattern should be observed.

1. EXPERIMENTAL TECHNIQUE

The measurements were carried out in an ultrahigh-vacuum Auger spectrometer ($P \sim 10^{-1}$ Torr) [7]. The substrate was a polycrystalline rhenium ribbon ($1 \times 0.02 \times 40$ mm in size) heated by an alternating current. The ribbon was cleaned by ac heating under ultrahigh vacuum at 2500 K and in an oxygen atmosphere ($P_{O_2} \sim 10^{-6}$ Torr). After cleaning, only the Auger peaks of rhenium were observed in the spectra taken from the ribbon surface. The ribbon was textured during the cleaning. The ribbon surface was formed predominantly by the (10$\bar{1}$0) face with the work function $e\varphi = 5.15$ eV, which is typical of this facet [8]. According to the X-ray diffraction data, the degree of face orientation relative to the surface was 99.9%. The ribbon temperature was measured by a micropyrometer; and, beyond the pyrometric range, it was determined by the linear extrapolation of the dependence of the temperature on filament current.

Oxygen was supplied to the apparatus from a source, in which cesium bichromate was thermally decomposed. Hydrogen sulfide H_2S was introduced in order to apply sulfur on the surface. Silicon was deposited uniformly over the entire ribbon surface from a small bar $1 \times 1 \times 40$ mm in size, which was placed in parallel with the ribbon. The Auger peaks of sulfur at the energy $E = 156$ eV, oxygen at $E = 504$ eV, silicon at $E = 92$ eV, and a triplet of rhenium Auger peaks at $E = 162$–177 eV were used in measurements. For purposes of calibration, the rhenium ribbon was placed alongside the tungsten ribbon, which was cleaned and textured according to the procedure described in [4].

2. OXYGEN ADSORPTION ON THE Re(10$\bar{1}$0) SUBSTRATE

Oxygen adsorption on the Re surface was investigated by different techniques (see references in [9–11]). It is found that exposure of the Re(10$\bar{1}$0) face to an O_2 atmosphere at room temperature up to saturation causes the dissociative oxygen adsorption. However, it should be mentioned that the data available in the literature are derived either from the measurements performed with a sample cooled after heating or from the thermodesorption spectroscopy; i.e., the data thus obtained have a somewhat circumstantial character.

1063-7834/00/4202-0377$20.00 © 2000 MAIK "Nauka/Interperiodica"

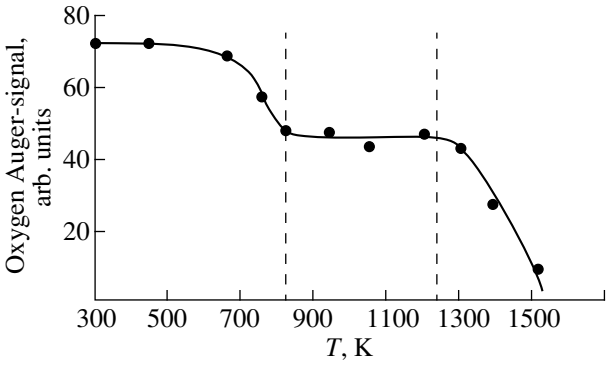

Fig. 1. Variation in the Auger signal of oxygen during the stepwise (at 100 K intervals) annealing of surface rhenium oxide. Conditions: exposure of rhenium to O_2 at $P = 10^{-6}$ Torr and $T = 300$ K for 100 s; annealing at each temperature for 20 s.

It was necessary to obtain and, then, to attest the coverage of the rhenium $(10\bar{1}0)$ surface by oxygen at medium temperatures $T \sim 1000$–1300 K. For this purpose, oxygen was fed into a chamber at room temperature ($P_{O_2} \sim 10^{-6}$ Torr), and two samples, namely, the W(100) and Re$(10\bar{1}0)$ substrates, were exposed simultaneously for time $t = 100$ s.

The KVV Auger lines of oxygen adsorbed on both substrates turned out to be virtually identical in shape. The oxygen concentration on the rhenium surface was determined by comparing the intensities of the signals for both substrates. Indeed, the oxygen concentration in the surface tungsten oxide is $N_O^W = (0.95 \pm 0.05) \times 10^{15}$ atoms/cm^2 [12, 13]. The intensity of the Auger signal from surface oxygen on rhenium is (2 ± 0.4) times less than that on tungsten, i.e., $N_O^{Re} \sim (5 \pm 1) \times 10^{14}$ atoms/cm^2. These estimates are likely to be valid, because the ratio of Auger-signal intensities for clean (W and Re) substrates corresponds to the reference [14]. Moreover, since tungsten and rhenium are neighbors in the periodic table, we can neglect the effects associated with fast backward scattered electrons on both substrates and can compare the amplitudes of Auger peaks for the adsorbate as such.

Figure 1 presents the variation in intensity of the oxygen Auger signal upon heating the rhenium substrate, on which oxygen was adsorbed at room temperature up to saturation. It is seen that, above $T = 650$ K, the Auger signal of oxygen decreases and, at $T = 800$–1250 K, remains constant. As in the preceding case, the concentration of adsorbed oxygen for a plateau at $T = 800$–1250 K (see Fig. 1) was estimated as $N_O^{Re} \sim (3 \pm 0.05) \times 10^{15}$ atoms/cm^2. Taking into account the fact that the surface concentration of rhenium atoms on the $(10\bar{1}0)$ face is $N_{Re}^{pure} \sim 1.3 \times 10^{14}$ atoms/cm^2, we can estimate the stoichiometry of the surface oxide as Re_4O. As is seen from Fig. 1, the complete removal of adsorbed oxygen from the rhenium surface occurs at $T > 1500$ K.

3. SULFUR ADSORPTION ON THE Re$(10\bar{1}0)$ SUBSTRATE

Surface sulfide Re_2S with the sulfur concentration $N_S^{Re} \sim (6.0 \pm 1) \times 10^{14}$ atoms/cm^2 is formed on the Re$(10\bar{1}0)$ surface [15]. The Re_2S surface sulfide is thermally stable up to $T = 1300$ K. At higher temperatures, it undergoes decomposition due to the sulfur thermal desorption. Sulfur does not penetrate into the bulk of metal, and the accumulation of sulfur in the metal neither in the form of a solid solution nor in the form of a bulk sulfide is observed.

4. SILICON ADSORPTION ON THE Re$(10\bar{1}0)$ SUBSTRATE

The silicon adsorption on the Re$(10\bar{1}0)$ substrate was studied in detail in our earlier work [16]. It was found that, at $T = 1350$–1450 K, surface silicide of the ReSi stoichiometry is formed on the surface, and the adsorbate concentration is $N_{Si} \sim 1.3 \times 10^{15}$ atoms/cm^2. Silicon is desorbed from the surface in the temperature range 1500–2000 K. Bulk silicides grow at lower temperatures (900–1300 K). The silicide growth is always preceded by the formation of surface silicide.

5. COADSORPTION OF SILICON AND CHALCOGENS

The variations in intensity of the Auger signals for silicon and sulfur upon deposition of silicon atoms on the surface sulfide at $T = 1200$ K are displayed in Fig. 2. The curve of the silicon deposition on pure rhenium is shown for comparison. As was demonstrated earlier [15], under these conditions, almost all silicon atoms that had already attained the surface remained in the adsorbed layer until the concentration corresponding to the surface silicide was reached.

As can be seen from Fig. 2, the presence of surface sulfide on the rhenium substrate virtually does not affect the character of the curve; however, the silicon accumulation on the surface is considerably retarded. The time required in this case for silicon to attain the saturation, which corresponds to the formation of surface silicide ReSi, is appreciably longer (~190 s instead of ~120 s for the pure metal). The Auger signal of sulfur decreases almost linearly with an increase in the amount of deposited silicon, and, at $t > 190$ s, no sulfur occurs on the surface, since it is completely replaced by adsorbed silicon. The Auger signal of rhenium remains

virtually unchanged during the silicon deposition on the surface silicide. This is explained by the fact that the substrate is shielded by both adsorbates (S and Si) very weakly, and the elimination of sulfur is compensated for by the presence of silicon.

Figure 3 shows the variations in intensity of the Auger signals for both adsorbates upon deposition of Si atoms on the surface oxide Re_4O. It is seen that, in this case, too, the accumulation of silicon is retarded by approximately 25%. This is caused by the presence of adsorbed oxygen in the form of surface oxide on the substrate, whereas unbound oxygen is eliminated from the adsorbed layer.

After the removal of adsorbed chalcogens from the surface and completion of the formation of surface silicide, further deposition of silicon brings about the growth of bulk silicides [15]. However, the discussion of this problem is beyond the scope of the present work.

Now, we consider in more detail the physical meaning of the points depicted in Figs. 2 and 3. The question arises as to whether these points reflect any actual stationary states of the Re–Si–O and Re–Si–S adsorption systems, or they are merely random quantities associated with the kinetics of surface processes. In order to clarify this question, we carried out the following experiment. The Si atoms were deposited onto the surface oxide or surface sulfide in the same fashion as in the aforementioned cases. However, after the deposition of each amount of silicon, the sample was isothermally annealed, and the Auger signals from the adsorbates were recorded. It turned out that such an annealing brought about no significant variations in the surface, and the concentrations of adsorbates remained constant. In other words, all the interactions proceed only immediately during the deposition of silicon atoms, and, thereafter, once the atoms occupied certain "legitimate" adsorption sites, no interaction was observed.

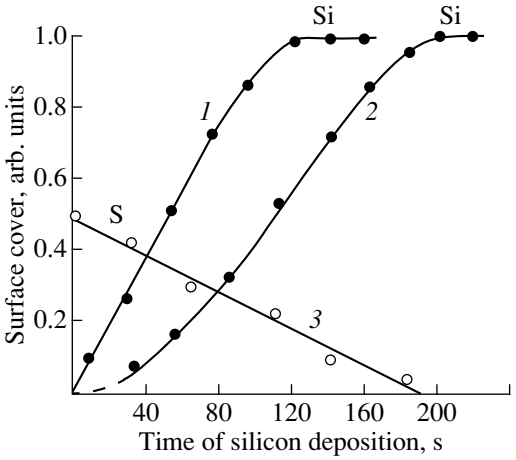

Fig. 2. Variations in the surface concentrations for (*1*) silicon during deposition of Si atoms on the Re(10$\bar{1}$0) substrate at 1200 K, (*2*) silicon, and (*3*) sulfur during deposition of Si atoms by the same flow on the surface sulfide Re_2S at 1200 K. The flux density of silicon atoms is 1.1×10^{13} atoms/(cm^2 s).

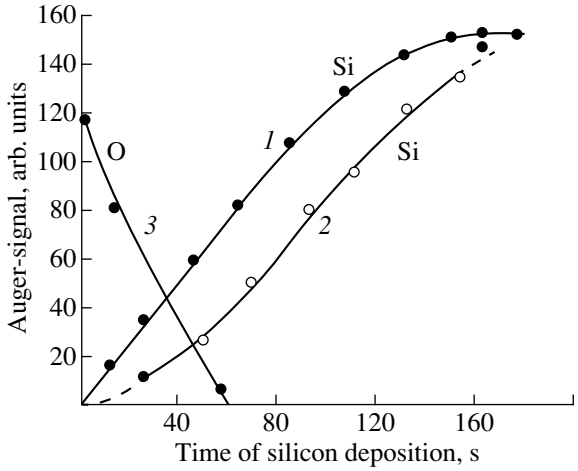

Fig. 3. Variations in the surface concentrations for (*1*) silicon during deposition of Si atoms on the Re(10$\bar{1}$0) substrate at 1200 K, (*2*) sulfur, and (*3*) silicon during deposition of Si atoms by the same flow on the surface oxide Re_4O at 1200 K. The flux density of silicon atoms is 1.2×10^{13} atoms/(cm^2 s).

6. DISCUSSION

Earlier [4, 5], we established that the deposition of silicon on the heated W and Mo surfaces containing adsorbed O and S atoms leads to the formation of volatile diatomic SiS or SiO molecules. These molecules are desorbed from the surface at $T \sim 1100$–1400 K and carry simultaneously both silicon and chalcogen atoms away from the surface. As this takes place, the flux of silicon atoms impinging on the surface is divided into two parts: the atoms, which are embedded into the surface to form the surface silicide, and the atoms, which leave the surface to carry chalcogen atoms away.

An analysis of the curves shown in Figs. 2 and 3 indicates that analogous processes should proceed on the rhenium surface. Actually, sulfur and oxygen themselves can reside on the rhenium surface at 1200 K for an indefinitely long time. The deposition of silicon brings about an irreversible removal of sulfur and oxygen from the surface, so that no subsequent annealing can restore these atoms in the adsorbed layer, even at the temperature of silicon desorption from the surface. On the other hand, in both cases, the time required to accumulate silicon on the surface in the amount corresponding to the surface silicide is in good agreement with that calculated from the particle balance on condition that volatile diatomic molecules SiS or SiO

undergo desorption. Indeed, the sulfur concentration in the surface sulfide is approximately two times less than the silicon concentration in the surface silicide. Hence, in order to remove the sulfur atoms from the surface and to form the surface silicide, the required doze of deposited silicon atoms should be approximately 1.5 times larger than that for the pure metal. For oxygen, contrastingly, this difference amounts to ~25%. This value agrees well with the low concentration of adsorbed O atoms in the surface rhenium oxide Re_4O ($N_O^{Re} \sim 3.0 \times 10^{14}$ atoms/cm^2).

As follows from a more detailed analysis of the data presented in Fig. 2, the silicon amount, which is required for the complete removal of sulfur from the rhenium surface and the subsequent formation of surface silicide, is approximately 10–15% larger than the amount expected from the exact balance of atoms on the surface. Apparently, the part of silicon atoms reaching the surface of the metal, which contains the absorbed sulfur, penetrate from the surface into the bulk of rhenium to form the solid solution [15]. The balance becomes more and more exact as sulfur is removed from the surface. The exact balance between the Si atoms impinging on the surface, the Si and S atoms adsorbed on the surface, and the desorbed SiS molecules is observed when the concentration of surface sulfur is $\sim 2 \times 10^{14}$ atoms/cm^2.

ACKNOWLEDGMENTS

This work was supported by the "Surface Atomic Structures" Program of the Ministry of Science and Technology of the Russian Federation, project no. 4.6.99.

REFERENCES

1. G. K. Boreskov, *Heterogeneous Catalysis* (Nauka, Moscow, 1988).
2. N. R. Gall', E. V. Rut'kov, and A. Ya. Tontegode, Thin Solid Films **266**, 229 (1995).
3. N. R. Gall', E. V. Rut'kov, and A. Ya. Tontegode, Pis'ma Zh. Teor. Fiz. **15** (7), 52 (1989).
4. V. N. Ageev, E. Yu. Afanas'eva, N. R. Gall', *et al.*, Pis'ma Zh. Teor. Fiz. **12** (9), 565 (1986).
5. N. R. Gall', E. V. Rut'kov, A. Ya. Tontegode, *et al.*, Fiz. Tverd. Tela (S.-Peterburg) **38** (8), 2541 (1996).
6. N. R. Gall', E. V. Rut'kov, and A. Ya. Tontegode, Poverkhnost **5**, 55 (1999).
7. N. R. Gall, S. N. Mikhaĭlov, E. V. Rut'kov, *et al.*, Surf. Sci. **191**, 185 (1987).
8. V. S. Fomenko, *A Handbook on Emission Properties of Materials* (Naukova Dumka, Kiev, 1981).
9. F. Zaera and G. A. Somorjai, Surf. Sci. **154**, 303 (1985).
10. V. N. Ageev, Zh. Tekh. Fiz. **40** (8), 1743 (1970).
11. R. Ducros, M. Alnot, J. J. Ehrhardt, *et al.*, Surf. Sci. **94**, 154 (1980).
12. V. N. Ageev and N. I. Ionov, Zh. Tekh. Fiz. **38**, 1149 (1968).
13. N. P. Vas'ko, Yu. G. Ptushinskiĭ, and B. A. Chuĭkov, Surf. Sci. **14**, 448 (1969).
14. L. E. Davice, N. C. McDonald, P. W. Palmberg, G. E. Rich, and R.E. Weber, *Handbook of Auger Electron Spectroscopy* (Physical Electronics, Eden Prerie, 1976), p. 266.
15. N. R. Gall', E. V. Rut'kov, and A. Ya. Tontegode, Pis'ma Zh. Teor. Fiz. **25** (14), 57 (1999).
16. N. R. Gall', E. V. Rut'kov, and A. Ya. Tontegode, Zh. Tekh. Fiz. **60** (4), 125 (1990).

Translated by N. Korovin

Physics of the Solid State, Vol. 42, No. 2, 2000, pp. 381–387. Translated from Fizika Tverdogo Tela, Vol. 42, No. 2, 2000, pp. 371–377.

FULLERENES AND ATOMIC CLUSTERS

Effect of Electron Irradiation on the Spectra of Elementary Excitations in C_{60} Fullerite

Yu. S. Gordeev, V. M. Mikushkin, and V. V. Shnitov

Ioffe Physicotechnical Institute, Russian Academy of Sciences, Politekhnicheskaya ul. 26, St. Petersburg 194021 Russia

Received May 21, 1999

Abstract—Electron irradiation produces changes in the spectra of elementary excitations of C_{60} fullerite, which are manifested by decrease in the π-plasmon energy, bandgap width, and energies of the HOMO–LUMO and other molecular transitions, smoothening of the corresponding spectral features, and significant growth in the quasicontinuous low-energy background intensity, the latter being indicative of an increase in the conductivity. The observed "red shifts" are related to collectivization of a part of the π electrons, the formation of chemical bonds between adjacent molecules (polymerization), and the corresponding increase in the proportion of sp^3-hybridized electrons. Characteristic electron energy loss (EEL) spectra of an intact fullerite sample nonperturbed by the polymerization process were measured. The EEL spectra of fullerite exhibit a multipole structure due to the (σ + π)-plasmon and reveal an exciton feature which is highly sensitive with respect to electron irradiation and can be used to characterize the initial fullerite structure and to indicate the polymerization onset.

INTRODUCTION

The spectra of collective vibrations (plasmons) and one-electron excitations in fullerenes have been extensively studied in recent years. The great majority of these works were performed on solid-state samples–fullerites, representing condensed fullerenes with molecules bound by the van der Waals bonds. The main results were obtained by the method of electron energy loss spectroscopy (EELS). The characteristic EEL spectra were measured using electron beams scattered from thin fullerite films (in the transmission mode) [1–7] and massive samples (in the reflection mode) [8–12] or using the inelastic scattering of X-ray photoelectrons [13, 14]. All these works showed evidence of the excitation of π- and (σ + π)-plasmons with the energies close to those of the graphite plasmons.

At the same time, some details of the spectra of collective vibrations reported by various researchers were significantly different. In particular, the energies of the (σ + π)-plasmon in the spectra of C_{60} fullerites measured in the reflection mode in different works vary in a rather wide interval (25 to 29 eV). Also different were the energies of inelastic electron transitions between occupied and unoccupied molecular states and the numbers of the corresponding peaks in the EEL spectra. One possible reason for these discrepancies can be the destructive action of the probing electron beam. For example, it was reported [15, 16] that exposure to even low-intensity (<50 nA) electron beams for several minutes results in the formation of polymer chains involving a considerable part of fullerite molecules. Subsequent electron irradiation led to profound changes in the fullerite structure, which were manifested by increasing energy of the C KVV Auger electrons from $E = 268.3 \pm 0.2$ eV to the value typical of the ion-bombardment-amorphized graphite ($E = 272.3 \pm 0.2$ eV) and by a decrease in the density of molecular states.

The purpose of this work was to study the effect of electron irradiation on the spectra of elementary electron excitations of C_{60} fullerite and to measure the EEL spectra of a non-destructed fullerite.

EXPERIMENTAL

We have performed three independent experiments using two spectrometers. The need in repeated measurements is explained by rapid electron-stimulated changes in the energy positions of low- intensity spectral features. All fullerite films were prepared *in situ* in the analytical chambers of spectrometers, whereby C_{60} molecules were evaporated from sublimation sources and deposited onto an atomically-clean Si(111) substrate surface at room temperature. The substrate surface was preliminarily cleaned by argon ion bombardment until complete vanishing of the Auger electron lines of carbon and oxygen in the spectra. In the first experiment (*A*), the initial material for the fullerite film preparation was a carbon black containing ~20% fullerenes; samples for the second (*B*) and third (*C*) experiments were prepared from an almost pure (99.9%) C_{60} fullerene powder [17]. Prior to the sample preparation, the sublimation source was preliminarily trained by prolonged heating at 200–250°C for outgassing and removal of the organic solvent molecules from the initial carbon black. The working temperature of the source (320–350°C) ensured the production of required fluxes of the C_{60} fullerene molecules, but was insufficient for effective evaporation of the graphite-

1063-7834/00/4202-0381$20.00 © 2000 MAIK "Nauka/Interperiodica"

like carbon black fragments in the first experiment (*A*). The residual pressure in the analytical chambers of spectrometers during the fullerite film deposition increased to (3–8) × 10^{-9} Torr and rapidly decreased upon termination of the sample preparation process. The sample thicknesses varied from 30 to 100 Å. Film thicknesses in the nanometer range and the corresponding deposition rates were determined by measuring relative intensities of the Auger electron lines from the adsorbate and the substrate [15]. The control EEL spectra were measured on the samples of pyrographite and a graphite amorphized by 2-keV Ar^+ ion bombardment to a dose of $Q = 5 \times 10^{-4}$ C/cm^2. At this ion fluence, the surface layers are etched off and the concentration of defects in the target reaches maximum for the given beam parameters. The structure of pyrographite upon ion cleaning was restored by high-temperature annealing.

Experiments *A* and *B* were performed using an original angular-multichannel energy analyzer of the cone mirror type [18, 19]. This device allows the energy distributions of electrons emitted from a sample to be simultaneously measured in a 0°–80° range of polar angles at a 10° step in the regimes of constant relative or absolute energy resolution. Our measurements were performed in the electron count mode at a constant absolute resolution of $\Delta E = 0.7$ (*A*) and 0.4 eV (*B*) for the transmission energy of $E = 100$ and 30 eV, respectively. The comparatively high resolution achieved in experiment B was in fact limited only by the electron energy scatter in the primary beam generated by a gun with a special oxide cathode. In order to reduce the systematic error and reveal general regularities, the EEL spectra measured at various angles were summed.

Experiment C was performed using a high-purity initial fullerene sample measured in a commercial Leybold-Heraus LHS-11 spectrometer with an absolute energy resolution of $E = 0.9$ eV. The energy scales of the spectrometers were calibrated with respect to the peak of elastically scattered electrons and checked by reference to the standard values of the Auger electron energies of silicon and copper. For the more accurate determination of the positions of spectral features, the EEL spectra were doubly differentiated by numerical techniques: $N(E) \longrightarrow d^2N/dE^2$.

The primary electron beam energies $E_0 = 1200$ (*A*), 1000 (*B*), and 500 eV (*C*) were selected so as to be markedly greater than the characteristic electron energy losses. The EEL measurements under these conditions provided information about the bulk properties of fullerites, rendered the collision regime with respect to the momentum transferred close to that realized in the transmission mode, and allowed justified comparison of the results obtained under analogous conditions. The mean free paths of electrons without inelastic collisions, corresponding to the primary electron energies indicated above, were $\lambda = 30$ (*A*), 27 (*B*), and 20 Å (*C*) as estimated according to [20]. These values indicate that the EEL spectra refer to several layers of molecules and may e considered as characterizing the bulk properties of fullerite.

RESULTS AND DISCUSSION

1. Review Spectra of Electron Energy Losses

Figures 1a and 1c (curves *1*) show the EEL spectra of C_{60} fullerite measured in experiments *A* and *B* in a wide range of energy losses of the inelastically scattered electrons. These spectra display, besides the narrow lines of elastically scattered electrons (centered at the origin of the scale of characteristic energy losses), wide lines corresponding to excitation of the plasma vibrations of π electrons (6.2 eV) and all valence $\sigma + \pi$ electrons (~27 eV). A comparison of the spectra obtained in two independent experiments shows good reproducibility of the plasmon peaks with respect to position, shape, and intensity. A higher energy resolution achieved in experiment *B* even without differentiation reveals additional features on the plasmon peaks. These features are related to the excitation of one-electron molecular transitions. For the comparison, Fig. 1a also presents the spectrum of pyrographite (curve *5*). All spectra are normalized with respect to the peak of elastically scattered electrons, which allows us to compare both energies and the relative probabilities of inelastic excitations in fullerite and graphite samples.

As seen from Fig. 1, the positions and intensities of plasmon peaks in the EEL spectra of fullerite and graphite are close, which reflects common features in the electron structure of these objects. However, there are some significant distinctions as well. First, the spectrum of fullerite exhibits a much less intense continuum in the region of low-energy losses ($\Delta E < 2$ eV). This difference is explained, on the one hand, by the fact that fullerite possesses a wide bandgap ($\Delta = 2.3$ eV [21]) imparting insulator properties to this compound and suppressing transitions with the energies smaller than the bandgap width and, on the other hand, by a relatively high density of unoccupied states at the Fermi level in graphite, which accounts for the high conductivity of graphite and a high probability of the low-energy transitions to these states. Second, the π-plasmon peak of fullerite is about 25% lower than the peak of graphite. This difference is apparently related to an intermediate character of hybridization of the atomic orbitals in fullerite, which falls between the pure sp^2-hybridization of graphite and the pure sp^3-hybridization of diamond (the latter having no weakly bound interplanar π electrons and, hence, no corresponding π-plasmon peak). A reason for the appearance of an admixture of the sp^3-hybridization in fullerite is probably a large curvature of the carbon shell of the C_{60} molecule, which leads to increased overlap of the π orbitals inside the molecule.

2. Electron Energy Loss Functions

Figure 1b shows the electron energy loss functions $\mathrm{Im}(-1/\varepsilon)$ determined in experiment *A* by subtracting from the EEL spectra the contributions due to elastically scattered and multiply scattered electrons (Fig. 1a, curve *6*). The latter contribution was determined using a well-known method [10] based on the solution of an integral equation establishing a relationship between the experimental spectrum of inelastic losses to the $\mathrm{Im}(-1/\varepsilon)$ function averaged over the scattering angle. Figure 1b shows, besides the electron energy loss function of the initial fullerite (curve *1*), the loss functions of a fullerite sample upon electron bombardment (curve *2*) and the fullerite and graphite samples amorphized by Ar^+ ion bombardment (curves *3*, and *4*, respectively). The first important conclusion, which can be drawn from an analysis of Fig. 1b, is that the ion bombardment of fullerite and graphite leads to very similar forms of amorphous carbon characterized by almost identical energy loss functions. The ion-irradiated forms of carbon exhibit, in contrast to the initial pyrographite and fullerite, a markedly lower energy (6.2 ⟶ 4.0 eV) and intensity of the π-plasmon peak. The latter circumstance is evidence of the formation of a large number of diamond bonds characterized by the sp^3 hybridization. The corresponding drop in concentration (n_π) of the out-of-plane π electrons leads to a decrease in the π-plasmon energy ($\hbar^2\omega_\pi^2 \cong 4\pi\hbar^2 n_\pi e^2/m$).

Another important conclusion, also following from analysis of the loss functions, is that determination of the (σ + π)-plasmon energy using the corresponding peak in the initial EEL spectrum leads to considerable systematic errors (~2 eV). Indeed, the (σ + π)-plasmon peak in the EEL spectra is shifted to higher energies (25.1 ⟶ 27 eV) as a result of the increasing contribution due to multiple scattering (Fig. 1a, curve *6*). Since the magnitude of this contribution depends on the primary electron energy and the experimental geometry, the data obtained under different conditions may (and in fact do) vary. At the same time, Fig. 1a shows that this contribution (curve *6*) represents a very slowly increasing monotonic function, which can be approximated by linear functions in particular wide energy intervals. For this reason, the energy position of the (σ + π)-plasmon was determined by the position of minimum in the second derivative of the experimental spectrum. It should be noted that determination of the position of such a broad peak by double differentiation requires measuring the curves with small statistical errors and using an optimum algorithm for smoothening the initial spectra.

3. Multipole Structure of (σ + π)-Plasmon

Figure 2 presents the results of analysis of the doubly differentiated EEL spectra measured in experiments *A*, *B*, and *C*, which may seem rather unexpected. As seen, the differential spectra reveal, instead of a single (σ + π)-plasmon peak, at least three features with the energies $\hbar\omega_1 = 18.0 \pm 0.2$ eV, $\hbar\omega_2 = 23.1 \pm 0.3$ eV, and $\hbar\omega_3 = 26.9 \pm 0.3$ eV. Reproducibility of the results is confirmed by virtually complete coincidence of the independently measured spectra and by the data of Table 1, showing data obtained upon the processing of twenty spectra measured in all the three experiments. The peaks correspond to dipole, quadrupole, and octupole modes of the plasmon spectrum of a cluster described by the following formula [22]:

$$\hbar\omega_l = \sqrt{\frac{3l(l+1)}{2(2l+1)}}\hbar\omega_1. \qquad (1)$$

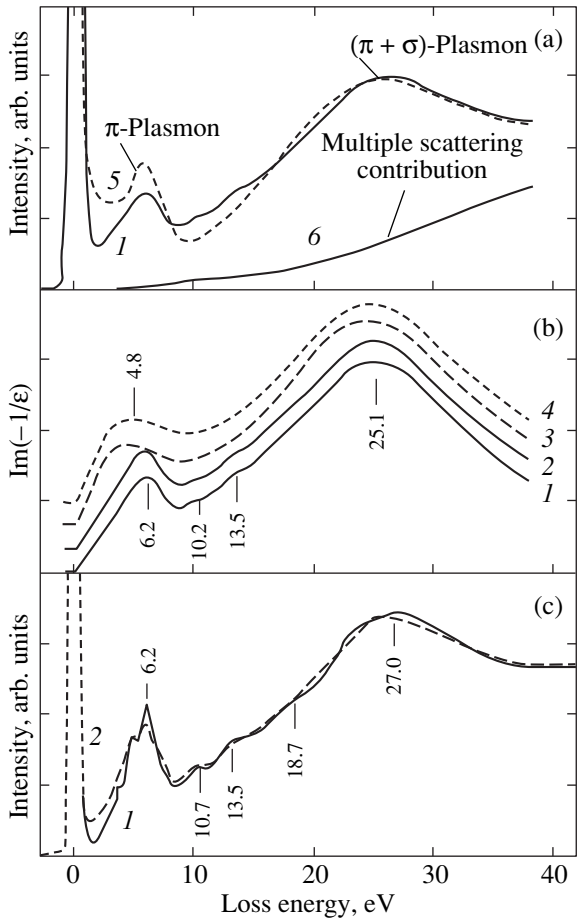

Fig. 1. (a) The results of EEL measurements in experiment *A* showing the spectrum of (*1*) initial fullerite in comparison with that of (*5*) pyrographite and with (*6*) the contribution due to multiple inelastic electron scattering. Part (b) presents the electron energy loss functions determined in experiment *A* for (*1*) initial fullerite, (*2*) fullerite exposed to electron irradiation to a dose of $Q \sim 1$ C/cm^2, (*3*, *4*) fullerite and graphite bombarded with a beam of Ar^+ ions, respectively; (c) EEL spectra measured in experiment *B* for (*1*) the initial fullerite and (*2*) fullerite upon the electron irradiation to a dose of $Q \sim 0.5$ C/cm^2.

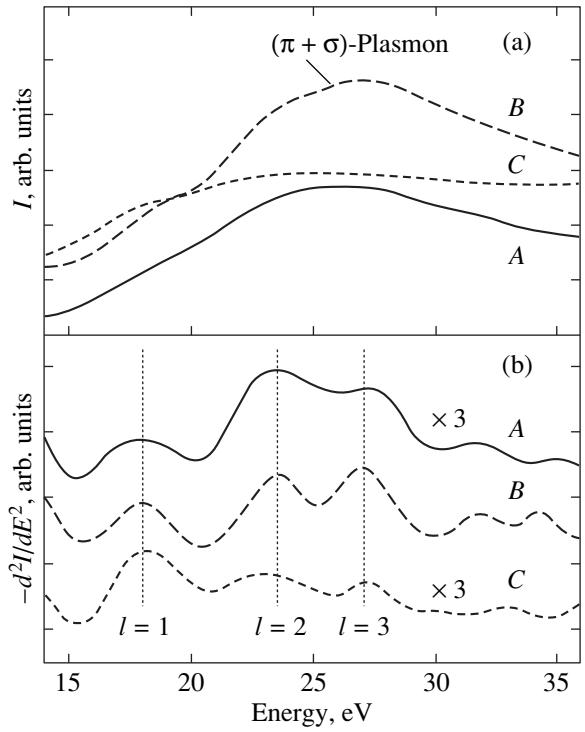

Fig. 2. EEL spectra of C_{60} fullerite measured in experiments *A*, *B*, and *C*: (*1*) initial ("true") spectra and (*2*) their second derivatives.

where l is the angular moment of the plasmon ($l = 1$ for the dipole mode). The energies of various modes of the $(\sigma + \pi)$ electron plasma vibrations in fullerite, determined from direct experimental measurements, have proved to be close to the corresponding values for isolated C_{60} molecules determined in a model experiment with fullerene molecules in the gas phase [23]. Thus, we may conclude that the plasmon spectrum of fullerite possesses a multipole structure very close to that of an isolated fullerene molecule.

4. Molecular Transitions

The pattern of variations of the shape of the energy loss curves show that changes induced by the electron irradiation of fullerite are not as large as those caused by the ion bombardment. Nevertheless, some changes are still observed, showing the same general trends and being rather significant. This statement is illustrated by the high-resolution EEL spectra of fullerite measured in experiment *B* (Fig. 1c). These spectra distinctly reveal narrow peaks superimposed on the wide plasmon lines, which are related to the molecular transitions between occupied and unoccupied states of fullerene molecules: 3.8, 4.9, and 10.7 eV. Electron irradiation to a dose of $Q = 0.5$ C/cm^2 leads to a decrease in intensity of the π-plasmon and molecular peaks. Fragments of the EEL spectra of the initial (curve *1*) and irradiated (curve *2*) fullerite (Fig. 3) show that the electron irradiation induces changes in the electron structure of fullerite toward that of the amorphized graphite (curve *3*). Analysis of these fragments showed, in addition to the above conclusion concerning smoothening of the π-plasmon and molecular peaks, that the electron irradiation (as well as the ion bombardment) decreases the π-plasmon energy and markedly

Table 1. Electron energy losses (eV) in C_{60} fullerite

Sample	This work, $Q = 0.02$ C/cm^2	[3]	[4]	[9]	[10]	[11]	[12]	Assignment
1	1.75	–	–	1.55	–	–	–	Exciton
2	2.40	2.15	2.1	2.2	–	–	–	Forbidden band
3	3.05	2.7	2.8	–	–	–	–	1–0.5'; 0.5–1'
4	3.80	3.5	3.7	3.7	–	–	–	1–1' (HOMO–LUMO)
5	4.90	4.5	5.1	4.8	–	–	–	1–2'; 2–1'
6	5.60	–	–	–	5.6	5.6	–	1–3'
7	6.45	6.5	6.4	6.3	5.8	6.5	6.3	2–2', π-plasmon
8	7.05	–	–	–	–	–	–	2–3'
9	7.65	–	7.5	7.6	–	–	–	3–1'
10	9.4	–	9.5	9.4	–	–	–	3–2'; 3'; 4–1'
11	–	–	–	10.2	–	–	–	4–2'; 3'
12	10.5	–	10.7	–	–	–	–	5–1'; 2'
13	14.2	–	15	12.8	–	–	–	–
14	18.0 ± 0.2	–	–	–	–	–	–	(π + σ)-plasmon, 1 = 1
15	23.1 ± 0.3	–	–	–	–	–	–	(π + σ)-plasmon, 1 = 2
16	26.9 ± 0.3	–	–	–	–	–	–	(π + σ)-plasmon, 1 = 3
17	25	27	25.5	28	25	28	29.2	(π + σ)-plasmon, average value

increases the intensity of continuum in the region of energies $E < 1.5$ eV (below the bandgap width), which is indicative of an increase in conductivity of the electron-irradiated samples.

Let us proceed to spectroscopic analysis of the molecular transitions in fullerite. The energy positions of the molecular peaks were determined by the minima in the second-derivative curves of the EEL spectra. Figure 3 shows correspondence between features in the initial ("true") spectra (Figs. 3a and 3c) and the second derivative (Fig. 3b), which confirms reliable determination of the energies of molecular transitions even in the case of low- intensity peaks measured in experiments *A* and *C* with comparatively low resolution. Table 1 gives a summary of the energies of molecular transitions in a non-destructed C_{60} fullerite obtained in this work and compiled from other works. As seen, some of our values are markedly greater compared to the previously reported ones.

Let us consider in more detail the problem of interpretation of the observed transitions (see Table 1). In most of the previous works, peaks 2 and 3 (with the energy losses 2.1–2.2 and 3.5– 3.7 eV, respectively) were assigned to the bandgap of fullerite and the transitions between highest occupied and lowest unoccupied molecular orbitals (HOMO–LUMO) or $h_u - t_{1u}$. The other loss peaks can be identified based on the values of maximum densities of the occupied (1, 2, 3, …) and unoccupied (1', 2', 3', …) states (Table 2). These values were obtained from the spectra of density of the occupied and unoccupied states measured [21] by the methods of usual and backscattering X-ray photoelectron spectroscopy. In Table 2, positions of the experimental peaks of the density of states are compared to the energies of molecular orbitals (h_u, t_{1u}, t_{1g}, …) forming these states, the correspondence being established using the calculated data from [24].

Assignment of the molecular transitions is presented in the last column of Table 1. The intense peak with the loss energy 3.05–2.9 eV lying between the bandgap width and the HOMO–LUMO (1–1') transition corresponds to the energies of transitions between HOMO and the conduction band bottom (1–0.5') and between the valence band top and LUMO (0.5–1'). The peaks 4, 5, and 6 represent a series of transitions from HOMO to the first, second, and third unoccupied states, peaks 5, 7, and 8 correspond to transitions from the second occupied state to the first, second, and third unoccupied states, and so on. Of special interest is the loss peak with an energy of 1.75 eV. This value is smaller than the bandgap width and almost coincides with the value calculated for the singlet exciton (1.79 eV) [25]. For this reason, we have concluded that a peak of singlet exciton is observed in the EEL spectrum of fullerite. Previously, Lucas *et al.* [9] reported on the observation of a triplet exciton (1.55 eV). Intensity of the exciton peak, as well as the exciton energy, rapidly decrease under the electron irradiation. As shown below, the decrease in energy is related to a decrease in the bandgap of irradiated fullerite. A high sensitivity of the exciton feature with respect to destructive factors (radiation damage) can be used for characterization of the perfect

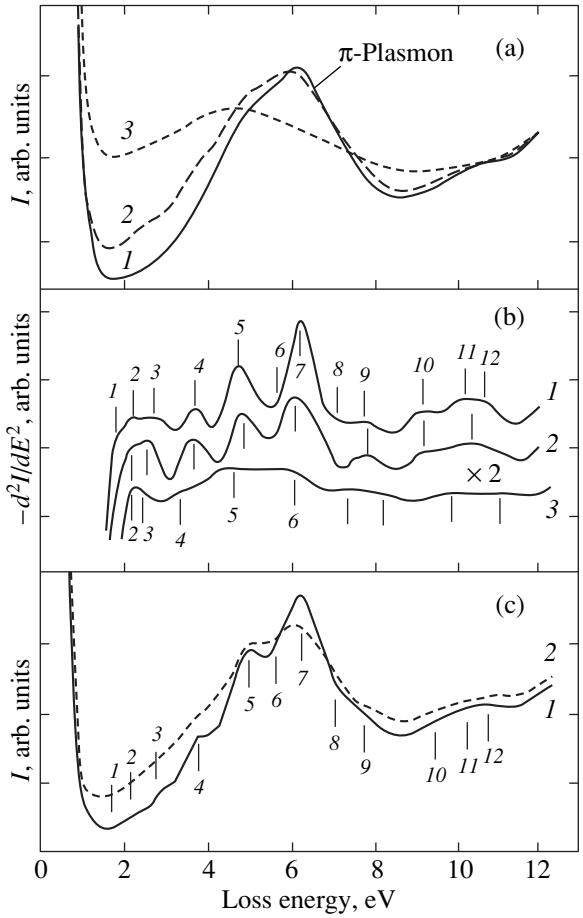

Fig. 3. "True" EEL spectra measured in experiments *A* [(a), true spectra; (b) second derivatives] and *B* (c) of C_{60} fullerite: (*1*) initial; (*2*) after electron irradiation; (*3*) after Ar^+ ion bombardment. Energies of the enumerated features in the initial spectrum (curve *1*) are presented in Table 1.

Table 2. Maxima (eV) of the densities of occupied (1, 2, 3, …) and unoccupied (1', 2', 3') states determined in experiment [21]

Unoccupied states	Occupied states				
	1 (h_u)	2 ($g_g + h_g$)	3 ($g_u + t_{2u} + h_g + t_{1u}$)	4	5
1' ($t_{1u} + t_{1g}$)	3.5	5.0	7.2	8.5	9.7
2' ($h_g + t_{2u} + h_u$)	4.7	6.1	8.3	9.6	10.8
3' (g_g)	5.7	7.1	9.3	10.6	11.8

Note: The correspondence between peaks and orbitals (h_u, t_{1u}, t_{1g}, …) was established using the calculated data from [24]; no data for the states 4 and 5 were presented in [23].

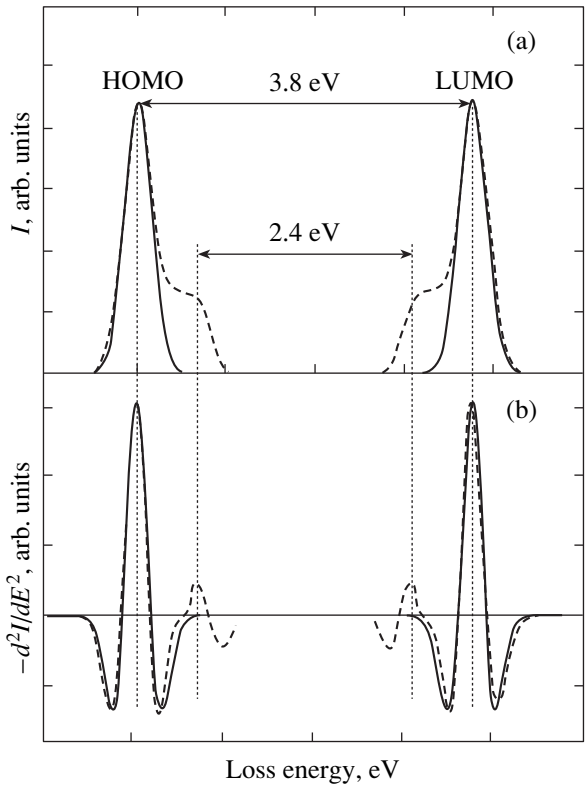

Fig. 4. Schematic diagram of (a) the density of occupied (HOMO) and unoccupied (LUMO) states and (b) the second derivative of this density of states in the vicinity of the forbidden band of an isolated molecule of fullerene (solid curves) and fullerite (dashed curves).

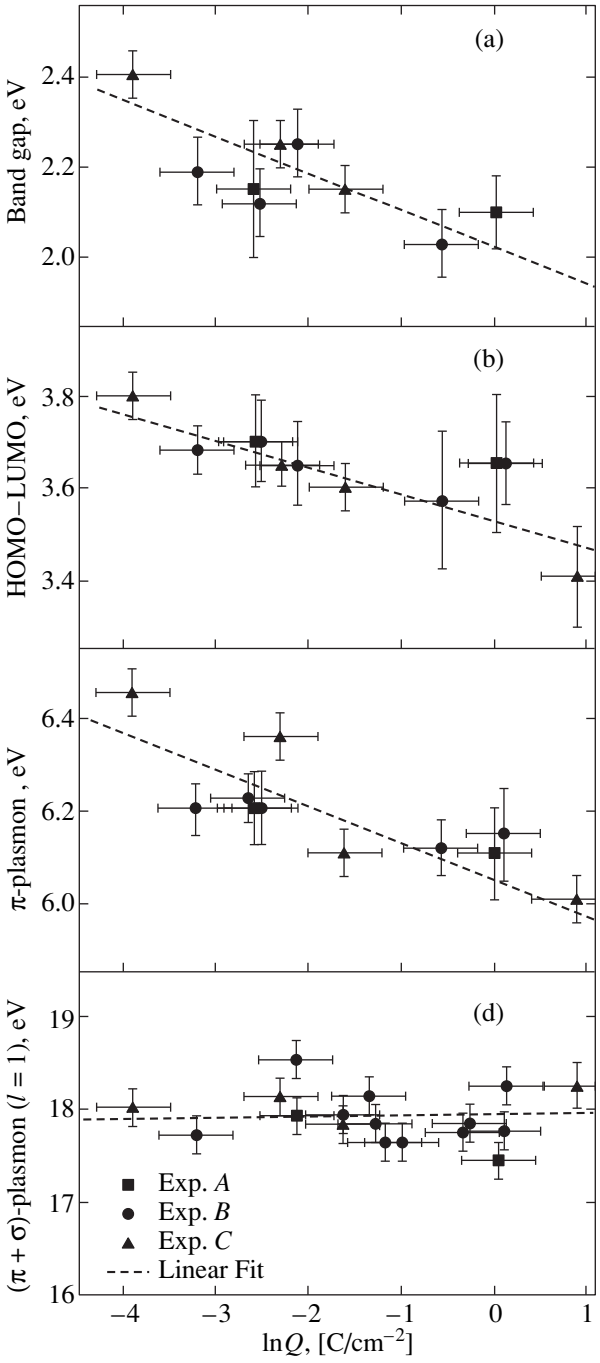

Fig. 5. Plots of (a) bandgap width, (b) energy of the molecular HOMO–LUMO transition, (c) π-plasmon energy, and (d) (σ + π)-plasmon energy in C_{60} fullerite versus the electron irradiation dose Q in the interval Q = 0.02–3.0 C/cm^2. Dashed lies show linear approximations of the experimental plots.

fullerite structure and indication of the onset of polymerization.

Other important conclusions can be made concerning the energy loss corresponding to the bandgap width. First, note that our value (2.4 eV) is markedly greater compared to the data reported previously (2.1–2.2 eV, Table 1) and can be also considered as a characteristic of nonpolymerized fullerite. The very fact that the loss peak can be detected using the second-derivative curve of the EEL spectrum is informative. We may judge on the shape of the density of states near the top of the valence band and the bottom of the conduction band: these regions must appear either as peaks or as shoulders with steps toward the forbidden band (Fig. 4). Otherwise (should these regions be monotonically decaying branches of the HOMO and LUMO peaks as in isolated molecules), the second derivative of the EEL spectrum would not exhibit a minimum. We may suggest that an increase in the density of states and the appearance of steps in the vicinity of the forbidden band are related to the formation of a fullerite crystal from individual molecules. The electron-stimulated polymerization and degradation of fullerite is accompanied by the appearance of additional states in the forbidden band, which increase the conductivity. However, because the density of these states does not exceed the band edge height, the corresponding loss peak is still observed in the EEL spectrum. Therefore, observation of the "bandgap peak" in the spectrum of polymerized fullerite does not contradict the above conclusion concerning a considerable increase in the conductivity.

5. Electron-Stimulated Transformation of Electron and Plasmon Structures

Using the whole body of data gained in experiments *A*, *B*, and *C*, we may construct a plot of the energies of molecular transitions and plasmons versus the electron irradiation dose. Figure 5 shows some examples illustrating the electron-induced decrease in (a) bandgap width, (b) HOMO–LUMO transition energy, and (c) plasmon energy. The errors of these values, determined in experiments *A* and *B*, were estimated using the data obtained in each angular channel of the multichannel spectrometer. The error was typically about ±(0.1–0.2) eV. In experiment *C*, the amount of detected electrons was several times as great as that in experiments *A* and *B* and, hence, the error did not exceed ±(0.05–0.10) eV. Figure 5 demonstrates significant (up to 0.4 eV) electron-induced "red shifts" in the energies of π-plasmon and molecular transitions. The large red shift of the π-plasmon is indicative of a considerable decrease in concentration of the "out-of-plane" π electrons an increase in the proportion of sp^3-hybridized electrons. The observed decrease in the energies of molecular transitions, bandgap width, and the exciton energy are related to the effect of "pulling" of the occupied and free molecular levels toward the Fermi level, that is, to an increase of the occupied and a decrease of the unoccupied levels. An obvious primary reason for this transformation of the molecular levels is the polymerization of fullerite as a result of collectivization of the "out-of-plane" π electrons and the formation of chemical bonds between C_{60} molecules. However, a particular mechanism determining the effect of polymerization on the structure of molecular levels is still unclear. Evidently, this electron structure transformation cannot strongly affect the concentrations of all valence σ + π electrons. Therefore, we may expect that the (σ + π)-plasmon energy would only slightly depend on the dose of electron irradiation. This is confirmed by Fig. 5d showing no significant changes in the energy of the dipole mode of the (σ + π)-plasmon with the electron irradiation dose.

The pattern of changes observed in the EEL spectra indicates that the electron structure of fullerite irradiated with electrons transforms toward that of the amorphous carbon. In the initial stages if irradiation, excitation of the valence electrons by the incident electrons leads to the formation of intermolecular chemical bonds and polymer chains increasing the conductivity of fullerite. The further increase in the electron irradiation dose may result in a considerable degradation of C_{60} molecules, whereby the electron properties of fullerite approach those of amorphous carbon.

ACKNOWLEDGMENTS

This work was supported by the State Scientific Technological Program "Fullerenes and Atomic Clusters", project no. 98090.

REFERENCES

1. J. F. Armbruster, H. A. Romberg, P. Schweiss, *et al.*, Z. Phys. B: Condens. Matter **95**, 469 (1994).
2. D. Li, S. Velásquez, and S. E. Schnatterly, Phys. Rev. B: Condens. Matter **49**, 2969 (1994).
3. E. Sohmen, J. Fink, and W. Kratschmer, Z. Phys. B: Condens. Matter **86**, 87 (1992).
4. R. Kuzuo, M. Terauchi, M. Tanaka, Y. Saito, *et al.*, Jpn. J. Appl. Phys. **30**, L1817 (1991).
5. Y. Saito, H. Shinohara, and A. Ohshita, Jpn. J. Appl. Phys. **30**, L1145 (1991).
6. P. L. Hansen, P. J. Fallon, and W. Kratschmer, Chem. Phys. Lett. **81**, 367 (1991).
7. D. Li, S. Velásquez, and S. E. Schnatterly, Phys. Rev. B: Condens. Matter **49**, 2969 (1994).
8. G. Gensterblum, J. J. Pireaux, P. A. Thiry, *et al.*, Phys. Rev. Lett. **67**, 2171 (1991).
9. A. A. Lucas, G. Gensterblum, J. J. Pireaux, *et al.*, Phys. Rev. B: Condens. Matter **45**, 13694 (1992).
10. Yu. M. Shul'ga, V. I. Rubtsov, and A. S. Lobach, Z. Phys. B: Condens. Matter **93**, 327 (1994).
11. A. M. Shikin, S. A. Gorovikov, G. V. Prudnikova, *et al.*, Mol. Mat. **4**, 113 (1994).
12. W. M. Tong, D. A. A. Olberg, H. K. You, *et al.*, J. Chem. Phys. **95**, 4709 (1991).
13. J. H. Weaver, J. L. Martins, T. Komeda, *et al.*, Phys. Rev. Lett. **66**, 1741 (1991).
14. P. Y. Benning, D. M. Poirier, T. R. Ohno, *et al.*, Phys. Rev. B: Condens. Matter **45**, 6899 (1992).
15. V. M. Mikushkin and V. V. Shnitov, Fiz. Tverd. Tela **39**, 187 (1997).
16. Yu. S. Gordeev, V. M. Mikoushkin, and V. V. Shnitov, Mol. Mat. **11**, 91 (1998).
17. D. Afanas'ev, I. Blinov, A. Bogdanov, *et al.*, Zh. Tekh. Fiz. **64**, 76 (1994).
18. V. M. Mikushkin and V. V. Shnitov, RF Patent No. 1814427; Byull. Izobret. No. 11 (1995).
19. V. V. Shnitov, V. M. Mikoushkin, A. V. Zacharevich, Abstracts of Papers. *The 14th European Conf. on Surface Science* (ECOSS-14) (Leipzig, 1994), p. 76.
20. J. E. Rowe, P. Rudolf, L. H. Tjeng, *et al.*, Int. J. Mod. Phys. B **6**, 3909 (1992).
21. R. W. Lof, M. A. van Veenendaal, B. Koopmans, *et al.*, Phys. Rev. Lett. **68**, 3924 (1992).
22. G. Barton and C. Eberlein, J. Chem. Phys. **95**, 1512 (1991).
23. L. G. Gerchikov, P. V. Efimov, V. M. Mikoushkin, *et al.*, Phys. Rev. Lett. **81**, 2707 (1998).
24. S. Saito and A. Oshiyama, Phys. Rev. Lett. **66**, 2637 (1991).
25. C. Reber, L. Yee, J. McKierman, *et al.*, J. Phys. Chem. **95**, 2127 (1991).

Translated by P. Pozdeev

Physics of the Solid State, Vol. 42, No. 2, 2000, pp. 388–392. Translated from Fizika Tverdogo Tela, Vol. 42, No. 2, 2000, pp. 378–382.

FULLERENES AND ATOMIC CLUSTERS

Ab Initio Calculations of Endo- and Exohedral C_{60} Fullerene Complexes with Li^+ Ion and the Endohedral C_{60} Fullerene Complex with Li_2 Dimer

S. A. Varganov[1, 2], P. V. Avramov[1], and S. G. Ovchinnikov[1, 2]

[1] *Kirenskiĭ Institute of Physics, Siberian Division, Russian Academy of Sciences, Akademgorodok, Krasnoyarsk, 660036 Russia*

[2] *Siberian Aerospace Academy, Krasnoyarsk, 660014 Russia*

Received March 31, 1999; in final form, June 22, 1999

Abstract—The results of *ab initio* Hartree–Fock calculations of endo- and exohedral C_{60} fullerene complexes with the Li^+ ion and Li_2 dimer are presented. The coordination of the Li^+ ion and the Li_2 dimer in the endohedral complexes and the coordination of Li^+ ion in the exohedral complex of C_{60} fullerene are determined by the geometry optimization using the 3-21G basis set. In the endohedral Li^+C_{60} complex, the Li^+ ion is displaced from the center of the C_{60} cage to the centers of carbon hexa- and pentagons by 0.12 nm. In the Li_2 dimer encapsulated inside the C_{60} cage, the distance between the lithium atoms is 0.02 nm longer than that in the free molecule. The calculated total and partial one-electron densities of states of C_{60} fullerene are in good agreement with the experimental photoelectron and X-ray emission spectra. Analysis of one-electron density of states of the endohedral $Li^+@C_{60}$ complex indicates an ionic bonding between the Li atoms and the C_{60} fullerene. In the Li^+C_{60} and $Li^+@C_{60}$ complexes, there is a strong electrostatic interaction between the Li^+ ion and the fullerene.

Metallofullerenes—complexes of metal atoms with a fullerene molecule—are among the derivatives of C_{60} fullerene. These compounds can be subdivided into two types depending on the position of metal atoms relative to the C_{60} cage. In complexes of the first type, metal atoms are arranged outside the fullerene cage; these complexes were named exohedral. The endohedral complexes belong to the second class; in these complexes, metal atoms are encapsulated into the carbon sphere. Complexes of the first class are denoted as MC_{60} and complexes of the second class, as $M@C_{60}$, where M is the metal atom.

Metallofullerenes are of interest because of their widespread application in various branches of science and technology. Actually, solids consisting of exohedral complexes of C_{60} fullerene with some metals exhibit the highest superconducting transition temperatures, except copper-containing HTSC ceramics [1]. Endohedral complexes with the noncentral arrangement of encapsulated atoms can be used for the creation of a new type of ferroelastic materials [2].

In studying complexes of the two classes, one should first determine their geometry, in particular, the mode of the coordination of a metal atom at the carbon wall. At present, experimental studies of these complexes are hampered by the complexity of their synthesis in sufficient amounts and by difficulties of isomer separation.

The theoretical approaches to the determination of the coordination of metal atoms in exo- and endohedral fullerene complexes involve both empirical methods based on the use of the Lennard-Jones interatomic potential [3, 4] and semiempirical and *ab initio* quantum-chemical calculations, which provide approximate solutions of the Schrödinger equation [5–10]. It was shown that many atoms in the endohedral complexes of C_{60} can shift from the center of the fullerene cage. Nonetheless, the mode of atom coordination to the fullerene surface in both endohedral and exohedral complexes have not been understood yet. The problem of possible migration of the encapsulated atom along the inside or the outside surfaces of C_{60} has also not been studied.

The geometry of complexes is responsible for their electronic structure. One of the most efficient techniques for studying the electronic structure of molecules and solids is spectroscopy (photoelectron, inverse photoelectron, and X-ray spectroscopy). The spectroscopic data are often interpreted based on the results of calculations of the electronic structure of the systems under consideration. Although the nature of photoelectron and X-ray spectra is rather complicated, in many cases, they are satisfactorily reproduced in the calculations of the ground states of complexes in the single-electron approximation. For the C_{60} fullerene, this is evident if we compare the total densities of states calculated *ab initio* by the Hartree–Fock method [11] and using the density functional theory [12] with the experimental data of photoelectron and inverse photoelectron spectroscopy. The results of calculations for C_{60}

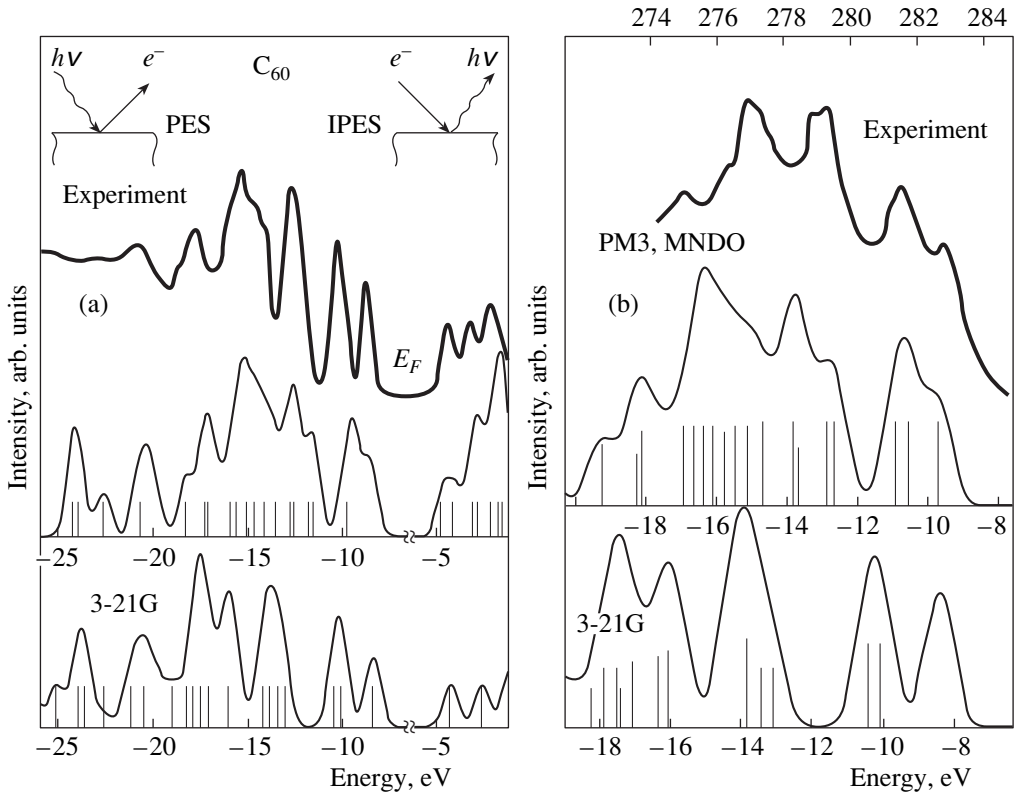

Fig. 1. (a) Photoelectron and inverse photoelectron spectra and (b) X-ray K_α emission spectrum of carbon in C_{60} fullerene. Experimental spectra are taken from (a) [12] and (b) [13].

fullerene, fluorinated $C_{60}F_{24}$ fullerene [13], polymeric fullerene [14], and graphite nanotubes [15] by the semiempirical PM3 method in the Hartree–Fock approximation demonstrate a good agreement between the calculated partial densities of states and the experimental X-ray emission spectra of the above compounds.

In this work, we report the results of *ab initio* Hartree–Fock calculations of endo- and exohedral complexes of C_{60} fullerene with the Li^+ ion and the endohedral complex of C_{60} with the Li_2 dimer. The analysis of the electronic structure of complexes was performed using the calculated total and partial densities of states.

1. METHODS

The calculations were performed by the *ab initio* Hartree–Fock method within the 3-21G basis set using the Direct procedure. The Gamess program [16] and a Dual Pentium-II 266 MHz PC RAM 128 MB were used.

The total densities of states were obtained by the following method. First, the energy spectrum of a complex was constructed. In this complex, each molecular orbital was represented by a line, and the line intensities were assumed equal to unity. Next, each line was replaced by a Gaussian distribution with a halfwidth of 0.4 eV, and the distributions were convoluted at each energy to sum up their intensities.

In constructing the partial density of states of atomic orbitals *x*, the intensity of each line corresponding to the molecular orbital *y* was assumed equal to the sum of squared coefficients of the atomic orbitals *x* in the MO LCAO expansion of the orbital *y*. Next, the partial density of states spectra were constructed by the algorithm similar to that for constructing the total density of states spectra.

2. RESULTS AND DISCUSSION

To assess the correspondence between the calculated electronic structure of C_{60} fullerene and the experimental data, we constructed total and partial densities of states. The experimental photoelectron and inverse photoelectron spectra of the surface of a C_{60} film [12] and the total density of states spectra obtained in *ab initio* calculations with the 3-21G basis set are shown in Fig. 1a. Figure 1b displays the partial densities of states for the *p* AO of carbon atoms in the C_{60} fullerene, which were constructed from the results of *ab initio* calculations, and also the experimental K_α emission spectrum of carbon in C_{60} [13]. For comparison, the figures also present total and partial densities of states calculated by semiempirical MNDO and PM3 methods. It can be

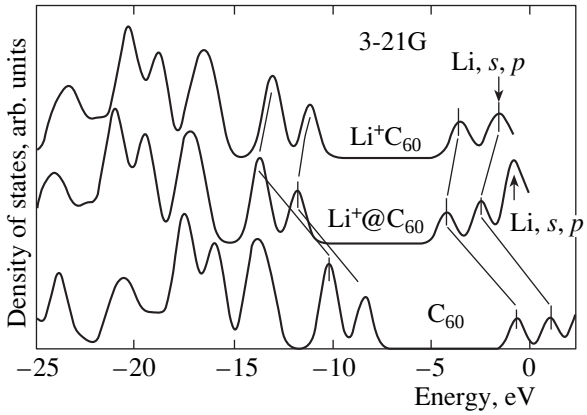

Fig. 2. Total densities of states of the $Li^+@C_{60}$ and Li^+C_{60} complexes.

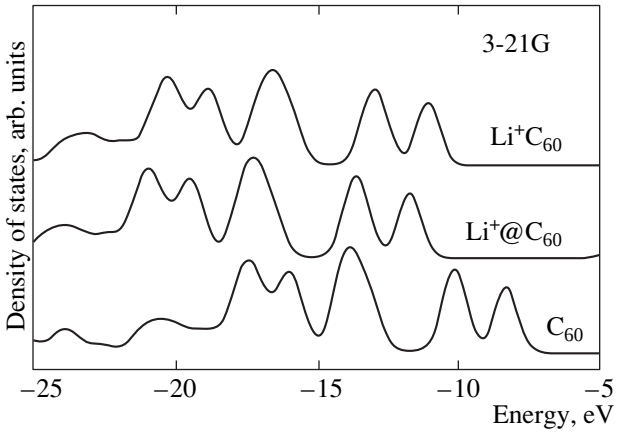

Fig. 3. Partial densities of the *p* states of carbon in the $Li^+@C_{60}$ and Li^+C_{60} complexes.

seen that the results of calculations satisfactorily agree with the experimental data.

The positions of critical points in the potential energy surface of the endo- and exohedral complexes of C_{60} with the Li^+ ion were localized by the geometry optimization procedure using the quasi-Newton–Raphson method. In different calculations, different initial coordination modes of the lithium ion at the surface of the C_{60} fullerene were used. From the reasons of symmetry, the lithium ion was placed near the center of a hexagon of carbon atoms (on the C_3 axis), near the center of a pentagon of carbon atoms (on the C_5 axis), near an edge between two hexagons (on the C_2 axis), near an edge between a hexagon and a pentagon (on the σ_v symmetry plane), near a carbon atom (on another σ_v plane), and at the center of C_{60}. The geometry optimization was performed within the C_{3v}, C_{5v}, C_{2v}, C_s, C_s, and T_h symmetry groups, respectively. The results of calculations of the $Li^+@C_{60}$ and Li^+C_{60} metallocomplexes are listed in Table 1. The following designations are used: $E_{C_{60}}$ is the total energy of C_{60}, E_{Li} is the total energy of the Li atom, $E_{LiC_{60}}$ is the total energy of the LiC_{60} metallocomplex, and $E_{form} = E_{LiC_{60}} - (E_{C_{60}} + E_{Li})$ is the energy of complex formation.

The position of the Li ion in the center of C_{60} does not correspond to a stationary point on the potential energy surface of the complex. The results of calculations for this coordination are presented in order to estimate the energy effect upon the displacement of the lithium ion from the center of C_{60}. The results of calculations indicate that the complexes are thermodynamically stable (the energies of complex formation are negative). It can be seen that the most stable endo- and exohedral complexes are obtained when the lithium atom is arranged at the center of a carbon hexagon. The total energy of the complex is significantly decreased upon the displacement of the lithium ion from the center of the C_{60} cage. The displacement of the lithium atom is about 0.12 nm regardless of the direction.

The total densities of states of the $Li^+@C_{60}$ and Li^+C_{60} complexes are presented in Fig. 2. It can be seen for the endohedral complex that the interaction between the Li^+ ion and the C_{60} sphere results in a pronounced shift of the energy levels without splitting of the levels of Li and of the *p* AO of carbon atoms (Fig. 3). This is indicative of the absence of chemical

Table 1. Calculated properties of the $Li^+@C_{60}$ and Li^+C_{60} complexes

Geometry, symmetry	Complex type	*E*, a.u.	$r_{Li-Co_{60}}$, nm	E_{form}, a.u.	E_{form}, kcal/mol
Center of pentagon, C_{5v}	Endo	–2266.2867802	0.1179	–0.0518927	–32.5632
Center of hexagon, C_{3v}	Endo	–2266.2887585	0.1204	–0.0538710	–33.8046
Hexagon–hexagon edge, C_{2v}	Endo	–2266.2867882	0.1217	–0.0519007	–32.5682
Center of C_{60}, T_h	Endo	–2266.2790085	0.0000	–0.0441210	–27.6864
Center of hexagon, C_{3v}	Endo	–2266.2885003	0.5301	–0.0536128	–33.6426

Note: $E_{Li^+} = -7.1870945$ a.u., $E_{C_{60}} = -2259.047793$ a.u.

Table 2. Calculated properties of the $Li^+@C_{60}$ complex

Geometry, symmetry	E, a.u.	$r_{Li–Li}$, nm	E_{form}, a.u.	E_{form}, kcal/mol
Center of pentagon, C_{5v}	–2273.8284520	0.3008	–0.0114048	–7.15663
Hexagon–hexagon edge, C_{2v}	–2273.8404428	0.3111	–0.0233956	–14.681

Note: E_{Li_2} = –14.7692542 a.u., $E_{C_{60}}$ = –2259.047793 a.u., and $r_{Li–Li}$ = 0.2815 nm.

bonding between the lithium ion and the fullerene cage. In this case, the interaction between the lithium ion and the charged C_{60} sphere is primarily electrostatic. The same is true for the exohedral complex with the only difference that the interaction in this complex is somewhat weaker. This can be explained by the fact that the stability of the 1*s* shell of lithium is very high, and the electron transfer from the lithium ion to the carbon sphere with the formation of an ionic bond is hampered. Therefore, for the lithium atom bearing one electron in the 2*s* shell, the interaction pattern should change dramatically. Thus, we can conclude that the electronic structures calculated for the fullerene metallocomplexes with alkali metal ions are inadequate approximations to the electronic structures of metallocomplexes with alkali metal atoms.

We performed *ab initio* calculations for two modes of coordination of the Li_2 dimer in the endohedral C_{60} fullerene complex. In the first mode, the dimer was arranged on the C_5 symmetry axis (lithium atoms were placed near the centers of carbon pentagons) and, in the second case, on the C_2 axis (lithium atoms were placed near edges between two carbon hexagons). The results of calculations are listed in Table 2. The designations are the same as in Table 1; $r_{Li–Li}$ is the distance between the lithium atoms in the dimer. In two coordination modes, the energy of complex formation is essentially negative, which is indicative of the thermodynamic stability of the complexes. For both modes of coordination, the distance between the lithium atoms in longer than that in the free Li_2 dimer. This enables us to suggest chemical bonding in the fullerene complex.

Figure 4 presents the total densities of states for the endohedral $Li^+@C_{60}$ complex. The orbitals of C_{60} are split for both total and partial densities of *p* states of carbon atoms (Fig. 5). This spitting is due to the lowering of the symmetry of the C_{60} cage upon incorporation of the lithium atoms and partial removal of the degeneracy of the single-electron states of fullerene. For both coordination modes of the dimer, the energy levels of the complex are shifted relative to their positions in the C_{60} fullerene. This indicates the ionic bonding between Li_2 and C_{60}.

An interesting feature is the appearance of a peak in the density of state of the complex almost in the middle of the energy gap of C_{60}. The contributions of *s* and *p* AO of Li to this peak are small; nonetheless, it can be seen from Fig. 4 that this peak consists primarily of the split AOs of carbon. The chief distinguishing feature between complexes with various coordination modes of Li_2 inside the C_{60} cage is that the *p* states of carbon atoms that correspond to HOMO in the density of state of the complex in which Li_2 lies along the C_5 axis of symmetry are split.

Thus, the results of *ab initio* Hartree–Fock calculations are as follows.

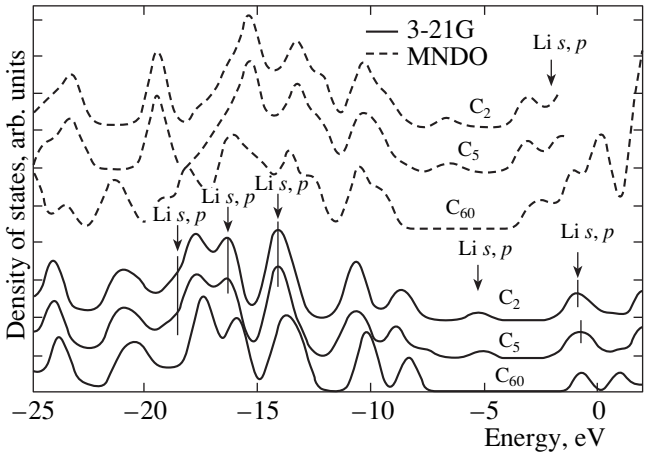

Fig. 4. Total densities of states of the $Li_2@C_{60}$ complex.

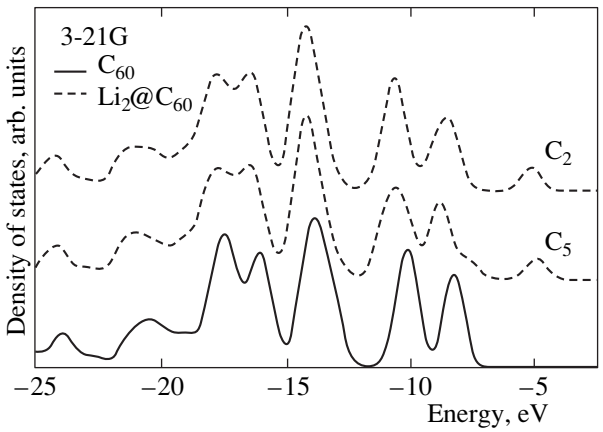

Fig. 5. Partial densities of the *p* states of carbon in the $Li_2@C_{60}$ complex.

In the endohedral complex of C_{60} with the lithium ion, the Li^+ cation is shifted from the center of fullerene cage by 0.12 nm. The most favorable ion coordination in both endohedral and exohedral complexes is the coordination toward a hexagon center.

The interaction between the carbon sphere and lithium atoms in the endohedral $C_{60}@Li_2$ complex is of the ionic character. The distance between the lithium atoms increases from 0.30 to 0.32 nm when they are placed inside the C_{60} cage.

It was also shown that the presentation of the results of quantum-chemical calculations as total and partial densities of states is convenient for the analysis of the electronic structure of large systems such as fullerenes and their derivatives.

ACKNOWLEDGMENTS

This work was performed at the Shared-Access Center for "Quantum-Chemical Calculations of Nanoclusters," which was supported by the Federal Program for Basic Research in Higher Education (project no. 69). We acknowledge financial support by the Russian Foundation for Basic Research (project no. 97-03-33684a), the State Program on Fullerenes and Atomic Clusters (project no. 97018), the Interinstitutional Program for Basic Research in Russian Universities (project no. 2049), and the State Program for High-Temperature Superconductivity (project no. 99019).

REFERENCES

1. A. P. Ramírez, Supercond. Rev. **1** (1–2), 1 (1994).
2. Y. Wang and D. Tomanek, Chem. Phys. Lett. **208** (1–2), 79 (1993).
3. J. Breton, J. González-Platas, and C. Girardet, J. Chem. Phys. **99** (5), 4036 (1993).
4. L. Pang and F. Brisse, J. Phys. Chem. **97** (33), 8562 (1993).
5. J. Cioslowski and E. D. Fleischmann, J. Chem. Phys. **94** (5), 3730 (1991).
6. A. H. H. Chang, W. C. Ermler, and R. M. Pitzer, J. Chem. Phys. **94** (7), 5004 (1991).
7. F. de Proft, C. van Alsenoy, and P. Geerlings, J. Phys. Chem. **100** (18) 7440 (1996).
8. Y. Maruyama, K. Ohno, and K. Esfarjani, Sci. Rep. RITU A **41** (2), 183 (1996).
9. T. Aree and S. Hannongbua, J. Phys. Chem. A **101**, 5551 (1997).
10. S. Patchkovskiĭ and W. Thiel, J. Chem. Phys. **106** (5), 1796 (1997).
11. A. H. H. Chang, W. C. Ermler, and R. M. Pitzer, J. Chem. Phys. **95** (23) 9288 (1991).
12. J. H. Weaver, Acc. Chem. Res. **25** (3), 143 (1992).
13. L. G. Bulusheva, A. V. Okotrub, and N. E. Yudanov, J. Phys. Chem. A **101**, 10018 (1997).
14. A. V. Okotrub, L. G. Bulusheva, and Yu. V. Shvetsov, Phys. Low-Dim. Struct. **5**, **6**, 103 (1997).
15. L. G. Bulusheva, Candidate's Dissertation in Chemistry (Novosibirsk, 1998).
16. M. W. Schmidt, K. K. Baldridge, and J. A. Boatz, J. Comp. Chem. **14**, 1347 (1993).

Translated by E. Rykova